

**Characterization of PFAS and Metal Nanomaterials as
Emerging Contaminants Present in Commercial Products**

**Caractérisation des PFAS et des Nanomatériaux Métalliques
en tant que Contaminants Émergents Présents dans les
Produits Commerciaux**

A thesis submitted to the Division of Graduate Studies of
the Royal Military College of Canada

by

David James Patch, BSc. Chemistry

In Fulfillment of the Requirements for the Doctor of Philosophy in Chemistry and Chemical
Engineering

June 2024

© This thesis may be used within the Department of National Defence but copyright for open
publication and intellectual ownership remains the property of the author.

Abstract

Commercial and industrial products may contain contaminants of emerging concern (CEC), like per- and polyfluoroalkyl substances (PFAS) and metal nanomaterials. Whether present intentionally or incidentally, these CECs pose direct and indirect risks to humans throughout the product's life cycle. Evaluating these risks requires complete characterization of the CECs, and their release potential, which is challenging due to limited analytical reference materials, transformation of the CECs over time, and the need for complementary analytical techniques. The work detailed herein describes the development and validation of complementary analytical methodologies for the complete characterization of PFAS and metal nanomaterials present in, and released from, commercial products.

This work begins with a focus on PFAS, first investigating the transformation of PFAS upon interaction with gamma radiolysis-generated aqueous electrons and hydroxyl radicals. It was found that PFAS are most susceptible to destruction by aqueous electrons, with long-chain PFCAs showing the highest destruction at pH 11, while short-chain PFASAs had the lowest destruction regardless of pH. High-resolution mass spectrometry identified several fluorinated transformation products, providing insight into the mechanisms of PFAS transformation and destruction.

These mechanisms were utilized for analytical applications by developing a three-stage tandem assay for improved PFAS characterization. This assay uses ultraviolet (UV) light to activate oxidizing photosensitizers (potassium/sodium persulfate, hydrogen peroxide) and reducing photosensitizers (sodium sulfite, potassium iodide) under alkaline conditions (sodium hydroxide). In the first stage, the UV-H₂O₂ assay generates hydroxyl radicals to oxidatively break down interfering dissolved organic matter. In the second stage, UV-activated persulfate converts PFAS precursors to terminal PFAS products, which are quantified using liquid chromatography-mass spectrometry (UV-TOP). In the final stage, UV-activated sulfite and iodide generate aqueous electrons to reductively defluorinate PFAS, with the resulting fluoride quantified using a fluoride ion-selective electrode to calculate the concentration of reducible organic fluorine (UV-ROF). This complete tandem UV- H₂O₂-TOP-ROF assay allows for comprehensive PFAS characterization using multiple complementary lines of evidence. The novel tandem assay was first validated with fifteen aqueous film-forming foam (AFFF) formulations and then applied to various commercial products, including cosmetics, textiles, and a waterproofing surface spray.

This work then shifts in focus to metal nanomaterials, using an enhanced analytical approach for their complementary characterization in commercial textiles. Initially, silver and copper-functionalized textiles were synthesized and characterized in the lab using various methods. This was followed by characterizing silver on, and released from, a silver-functionalized commercial textile. Novel physical and chemical weathering techniques simulated active human use, allowing for the determination of the transformation and release of silver nanomaterials throughout the textile's life cycle. The metal nanomaterials were characterized using a novel suite of analytical methodologies, including Fourier-transform infrared spectroscopy, inductively coupled plasma mass spectrometry, x-ray fluorescence spectroscopy, scanning electron microscopy, and x-ray absorption near-edge structure spectroscopy.

The conclusion of this work has resulted in specialized methods allowing for the complete characterization of PFAS and metal nanomaterials present in, and released from, commercial products. This will allow for effective evaluation of the risk of these CECs present in products or the environment and inform decision making processes for involved stakeholders.

Résumé

Les produits commerciaux et industriels peuvent contenir des contaminants émergents (CEC), tels que les substances per- et polyfluoroalkylées (PFAS) et les nanomatériaux métalliques. Qu'ils soient présents intentionnellement ou accidentellement, ces CEC posent des risques directs et indirects pour les humains tout au long du cycle de vie du produit. L'évaluation de ces risques nécessite une caractérisation complète des CEC et de leur potentiel de libération, ce qui est difficile en raison du manque de matériaux de référence analytiques disponibles, de la transformation des CEC au fil du temps et de la nécessité de techniques analytiques complémentaires. Le travail détaillé ici décrit le développement et la validation de méthodologies analytiques complémentaires pour la caractérisation complète des PFAS et des nanomatériaux métalliques présents dans les produits commerciaux et libérés par eux.

Ce travail commence par se concentrer sur les PFAS, en investiguant d'abord la transformation de ces produits lors de leur interaction avec des électrons aqueux et des radicaux hydroxyles générés par radiolyse gamma. Il a été constaté que les PFAS sont les plus susceptibles d'être détruits par les électrons aqueux, les PFCAs à longue chaîne montrant la plus grande destruction à un pH de 11, tandis que les PFAS à chaîne courte avaient la destruction la plus faible, quel que soit le pH. La spectrométrie de masse à haute résolution a identifié plusieurs produits de transformation fluorés, fournissant un aperçu des mécanismes de transformation et de destruction des PFAS. Ces mécanismes ont été utilisés pour des applications analytiques en développant un test en tandem en trois étapes pour une meilleure caractérisation des PFAS. Ce test utilise la lumière ultraviolette (UV) pour activer des photosensibilisateurs oxydants (persulfate de potassium/sodium, peroxyde d'hydrogène) et des photosensibilisateurs réducteurs (sulfite de sodium, iodure de potassium) dans des conditions alcalines (hydroxyde de sodium). Dans la première étape, le test UV- H₂O₂ génère des radicaux hydroxyles pour décomposer de manière oxydative la matière organique dissoute interférente. Dans la deuxième étape, le persulfate activé par UV convertit les précurseurs PFAS en produits PFAS terminaux, qui sont quantifiés en utilisant la chromatographie liquide-spectrométrie de masse (UV-TOP). Dans la dernière étape, le sulfite et l'iodure activés par UV génèrent des électrons aqueux pour défluorer de manière réductrice les PFAS, le fluorure résultant étant quantifié à l'aide d'une électrode sélective de fluorure pour calculer la concentration de fluor organique réductible (UV-ROF). Ce test complet en tandem UV- H₂O₂-TOP-ROF permet une caractérisation complète des PFAS en utilisant plusieurs lignes de preuves complémentaires. Le nouveau test en tandem a d'abord été validé avec quinze formulations de mousse anti-incendie (AFFF) et ensuite appliqué à divers produits commerciaux, y compris les cosmétiques, les textiles et un spray imperméabilisant.

Ce travail se concentre ensuite sur les nanomatériaux métalliques, en utilisant une approche analytique améliorée pour leur caractérisation complémentaire dans les textiles commerciaux. Initialement, des textiles fonctionnalisés avec de l'argent et du cuivre ont été synthétisés et caractérisés en laboratoire en utilisant diverses méthodes. Ensuite, la caractérisation de l'argent présent sur un textile commercial fonctionnalisé à l'argent, et libéré par celui-ci, a été réalisée. Des techniques novatrices de vieillissement physique et chimique ont simulé une utilisation humaine active, permettant de déterminer la transformation et la libération des nanomatériaux d'argent tout au long du cycle de vie du textile. Les nanomatériaux métalliques ont été caractérisés en utilisant une nouvelle suite de méthodologies analytiques, comprenant la spectroscopie infrarouge à transformée de Fourier, la spectrométrie de masse à plasma à couplage inductif, la spectroscopie de fluorescence X, la microscopie électronique à balayage et la spectroscopie d'absorption des rayons X proche de la structure des bords.

La conclusion de ce travail a permis de développer des méthodes spécialisées permettant la caractérisation complète des PFAS et des nanomatériaux métalliques présents dans les produits commerciaux et libérés par eux. Cela permettra une évaluation efficace du risque de ces CEC présents dans les produits ou dans l'environnement, et informera les processus de prise de décision pour les parties prenantes concernées.

Acknowledgements

The work presented herein is the culmination of over seven years of my life's efforts would not be possible without the innumerable contributions, big or small, of many people in my life.

First and foremost, I would like to thank Dr. Kela Weber, for taking a chance on me all those years ago. I know I wasn't the best candidate on paper, but I wouldn't be where I am today if not for you taking the risk that you did. I would also like to thank Dr. Iris Koch, for jumping in without hesitation to supervise me, and being patient with all my revisions and edits. You both have continued to be incredible in your support of me, and I thank you both immensely.

I would also like to thank Dr. Kevin Mumford, Dr. Jennifer Scott, Dr. Dave Major, Dr. Michael Bentel, Dr. Erika Houtz, Dr. Ian Ross, and Daniel Griffiths, for the many hours of mentorship, guidance, and advice. Your contributions, both professional and personal, have been instrumental to my development as a scientist and researcher.

I would like to thank all my close friends for their support, guidance, and laughter during my PhD. To Natalia O'Connor, thank you for all your support, guidance, and incredible ability to keep me on track to finish my current research projects when all I wanted to do was start new ones. You deserve an honorary PhD for putting up with me all these years. To Lauren Turner, thank you for all your support, guidance, and shared commiserations. Your drive for tying up every loose research end rubbed off on me, although I may have overdone it. To Alex Duchense, Zac Yenczek, Tomislav Salamanov, and Damien Figiel thank you for the much-needed video game distractions and always offering an ear to listen.

To all my friends at the Environmental Sciences Group, and the Royal Military College of Canada, thank you for everything you have done, including your contributions, supports, and guidance. Special thanks to Michael DeArruda, Tom Partridge, Taylor Vereecken, Dr. Anbareen Farooq, Clarence McEwen, Kim Sampson, and Dr. Frank Zeman, for constantly going above and beyond to support me.

To my family, including my parents, James and Susan Patch, and my brother Brian, thank you for being the most amazing family a person could ask for. Thank you for always supporting me, giving me a broad range of experiences, and not killing me during my childhood chemistry experiments, like when I covered half the kitchen in sodium acetate, or nearly blew up the garden with homemade fireworks.

Lastly, to everyone who I could not acknowledge directly, I want to thank you, nevertheless. To those who are with us still, I celebrate this accomplishment with you. To those who are with us no longer, I celebrate this accomplishment in your memory. To Joanne, Janet, and Jason, I would not be who I am without your kind words and gentle guidance. You are gone too soon and will be missed eternally.

Co-authorship Statement

This thesis is written in manuscript format, with David Patch being the primary author of the nine chapters. Chapter 3, “Elucidating degradation mechanisms for a range of Per- and Polyfluoroalkyl Substances (PFAS) via controlled irradiation studies”, was co-authored by David Patch, Natalia O’Connor, Iris Koch, Tom Cresswell, Cath Hughes, Justin B. Davies, Jennifer Scott, Denis O’Carroll, and Kela Weber, and was published in *Science of the Total Environment*. Conceptualization was conducted by Patch, Koch, Cresswell, Hughes, Davies, and Weber. Investigation and experimental work were performed by Patch. Formal analysis was performed by Patch and O’Connor. Original draft writing was performed by Patch. Editing and review was performed by all co-authors. [Patch, D., O’Connor, N., Koch, I., Cresswell, T., Hughes, C., Davies, J. B., Scott, J., O’Carroll, D., & Weber, K. (2022). Elucidating degradation mechanisms for a range of per- and polyfluoroalkyl substances (PFAS) via controlled irradiation studies. *Science of the Total Environment*, 832(January), 154941. <https://doi.org/10.1016/j.scitotenv.2022.154941>].

Chapter 4, “Advancing PFAS Characterization: Enhancing the Total Oxidizable Precursor Assay with Improved Sample Processing and UV Activation”, was co-authored by David Patch, Natalia O’Connor, Taylor Vereecken, Daniel Murphy, Gabriel Munoz, Ian Ross, Caitlin Glover, Jennifer Scott, Iris Koch, Sebastien Sauve, Jinxia Liu, and Kela Weber, and was published in *Science of the Total Environment*. Conceptualization was conducted by Patch, Koch, and Weber. Investigation and experimental work were performed by Patch, Murphy, and O’Connor. Formal analysis was performed by Patch. Original draft writing was performed by Patch, with inputs from Ross, O’Connor, Murphy, and Munoz. Editing and review was performed by all co-authors. [Patch, D., O’Connor, N., Vereecken, T., Murphy, D., Munoz, G., Ross, I., Glover, C., Scott, J., Koch, I., Sauvé, S., Liu, J., & Weber, K. (2024). Advancing PFAS characterization: Enhancing the total oxidizable precursor assay with improved sample processing and UV activation. *Science of The Total Environment*, 909 (November 2023), 168145. <https://doi.org/10.1016/j.scitotenv.2023.168145>].

Chapter 5, “Advancing PFAS Characterization: Development and Optimization of a UV- H₂O₂-TOP Assay for Improved PFCA Chain Length Preservation and Organic Matter Tolerance”, was co-authored by David Patch, Natalia O’Connor, Ellie Ahmed, Michael Bentel, Erika Houtz, Ian Ross, Jennifer Scott, Iris Koch, and Kela Weber, and has been published in *Science of the Total Environment*. Conceptualization was conducted by Patch, Koch, and Weber. Investigation and experimental work were performed by Patch, Ahmed, and O’Connor. Resource provision was provided by Houtz and Ross. Formal analysis was performed by Patch, O’Connor, and Bentel. Original draft writing was performed by Patch. Editing and review was performed by all co-authors. [Patch, D., O’Connor, N., Ahmed, E., Houtz, E., Bentel, M., Ross, I., Scott, J., Koch, I., & Weber, K. (2024). Advancing PFAS characterization: Development and optimization of a UV-H₂O₂-TOP assay for improved PFCA chain length preservation and organic matter tolerance. *Science of the Total Environment*, 946. <https://doi.org/10.1016/j.scitotenv.2024.174079>].

Chapter 6, “Shining a Light on Hidden PFAS: Development of a UV-Reducible Organic Fluorine Assay and Tandem UV- H₂O₂-TOP-ROF Assay for Enhanced Analysis of PFAS”, was co-authored

by David Patch, Natalia O'Connor, Ellie Ahmed, Erika Houtz, Michael Bentel, Ian Ross, Jennifer Scott, Iris Koch, and Kela Weber, and is being prepared for submission. Conceptualization was conducted by Patch, Koch, and Weber. Investigation and experimental work were performed by Patch, Ahmed, and O'Connor. Resource provision was provided by Houtz and Ross. Formal analysis was performed by Patch, O'Connor, and Bentel. Original draft writing was performed by Patch. Editing and review was performed by all co-authors.

Chapter 7, "Parsimonious Methodology for Synthesis of Silver and Copper Functionalized Cellulose", was co-authored by David Patch, Natalia O'Connor, Debora Meira, Jennifer Scott, Iris Koch, and Kela Weber, and has been published in *Cellulose*. Conceptualization was conducted by Patch. Investigation and experimental work were performed by Patch. Formal analysis was performed by Patch, O'Connor, and Meira. Original draft writing was performed by Patch, with significant inputs from Scott and Koch. Editing and review was performed by all co-authors. [Patch, D., O'Connor, N., Meira, D., Scott, J., Koch, I., & Weber, K. (2023). Parsimonious methodology for synthesis of silver and copper functionalized cellulose. *Cellulose*, 30(6), 3455–3472. <https://doi.org/10.1007/s10570-023-05099-7>].

Chapter 8, "Development and validation of a method for the weathering and detachment of representative nanomaterials from conventional silver-containing textiles", was co-authored by David Patch, Iris Koch, Derek Peloquin, Denis O'Carroll, and Kela Weber, and was published in *Chemosphere*. Conceptualization was conducted by Patch, O'Carroll, Koch, and Weber. Investigation and experimental work were performed by Patch, with analytical contributions by Peloquin. Original draft writing was performed by Patch, with input from all co-authors. Editing and review was performed by all co-authors. [Patch, D., Koch, I., Peloquin, D., O'Carroll, D., & Weber, K. (2021). Development and validation of a method for the weathering and detachment of representative nanomaterials from conventional silver-containing textiles. *Chemosphere*, 284, 131269. <https://doi.org/https://doi.org/10.1016/j.chemosphere.2021.131269>].

Table of Contents

Abstract	2
Résumé.....	3
Acknowledgements	5
Co-authorship Statement.....	6
List of Figures and Tables	16
1. Introduction	19
1.1. Thesis Organization	23
2. Literature Review	25
2.1. Foreword.....	25
2.1.1. Importance of Water.....	25
2.1.2. Early Civilization’s Utilization of Water.....	25
2.1.3. Lead, the First Emerging Contaminant	25
2.2. History of Organofluorine Chemistry	27
2.1. Synthesis of Per- and Polyfluoroalkyl Substances.....	28
2.2. Classification of PFAS.....	29
2.3. PFAS Applications and Environmental Release	30
2.4. Toxicity, Public Awareness, and Regulation of PFAS	31
2.5. Analysis of PFAS.....	34
2.6. Transformation of PFAS Using Oxidative Systems.....	35
2.6.1. Total Oxidizable Precursor Assay	36
2.7. Transformation of PFAS Using Reductive or Oxidative/Reductive Systems.....	37
2.7.1. Gamma Radiolysis of PFAS.....	38
2.7.2. UV-Activated Reduction of PFAS	40
2.8. Nanomaterials	42
2.9. Nanomaterial Toxicity	42
2.10. Metal Functionalization of Textiles.....	43
2.11. Release of Metals from Textiles	44
2.12. References	47
3. Elucidating Degradation Mechanisms For a Range of Per- and Polyfluoroalkyl Substances (PFAS) via Controlled Irradiation Studies	62
3.1. Abstract.....	63
3.2. Introduction.....	64
3.3. Materials and Methods.....	67
3.3.1. Solution Preparation.....	67

3.3.2.	Gamma Irradiation and Analysis.....	68
3.4.	Results and Discussion	69
3.4.1.	Degradation of Technical Grade PFOS, PFOA and 6:2 FTS	70
3.4.2.	Identification of Fluorinated Transformation Products.....	74
3.4.3.	PFOS Transformation Products	74
3.4.4.	PFOA Transformation Products	76
3.4.5.	6:2 FTS Transformation Products	78
3.4.6.	Initial Fluoride Removal	79
3.4.7.	PFAS Transformation Mechanism	80
3.4.8.	Degradation of PFAS _{13Suite} and Impact of Chain Length.....	84
3.4.9.	Implications for Future Work.....	88
3.5.	Conclusions.....	89
3.6.	Acknowledgements.....	90
3.7.	References.....	91
4.	Advancing PFAS Characterization: Enhancing the Total Oxidizable Precursor Assay with Improved Sample Processing and UV Activation.....	98
4.1.	Abstract.....	99
4.2.	Introduction.....	99
4.3.	Materials and Methods.....	102
4.3.1.	Reagents.....	102
4.3.2.	Review of TOP Assay Methodology.....	103
4.3.3.	Initial TOP Assay Investigations	103
4.3.4.	Chemical Quenching Investigation	103
4.3.5.	Sample Dilution Investigation.....	104
4.3.6.	Sample Volume Justification	104
4.3.7.	Persulfate Determination.....	104
4.3.8.	Initial TOP Assay Investigations	105
4.3.9.	Hydroxyl Radical Investigation using UV/H ₂ O ₂	106
4.3.10.	UV-TOP Assay for AFFF Oxidation	106
4.3.11.	PFAS Analysis.....	106
4.4.	Results and Discussion	107
4.4.1.	Chemical Quenching and Sample Processing.....	107
4.4.2.	Sample Dilution Investigation.....	109
4.4.3.	Thermal and UV-Light Activation	110
4.4.4.	PFCA Yield Comparison to Literature	115

4.4.5.	UV/H ₂ O ₂ System.....	116
4.4.6.	Implementation of the Developed UV-TOP Assay for AFFF Samples.....	117
4.5.	Conclusions.....	123
4.6.	Acknowledgements.....	123
4.7.	References.....	125
5.	Advancing PFAS Characterization: Development and Optimization of a UV-H ₂ O ₂ -TOP Assay for Improved PFCA Chain Length Preservation and Organic Matter Tolerance.....	129
5.1.	Abstract.....	130
5.2.	Introduction.....	131
5.3.	Materials and Methods.....	132
5.3.1.	Reagents	132
5.3.2.	UV-H ₂ O ₂ , UV-TOP, and UV-H ₂ O ₂ -TOP Assays	133
5.3.3.	Method Development and Optimization	134
5.4.	Results and Discussion	135
5.4.1.	UV-H ₂ O ₂ Method Development – Role of pH, Concentration and Activation Time	135
5.4.2.	UV-H ₂ O ₂ -TOP Method Development – Overcoming High Organic Matter Concentrations.....	139
5.4.3.	PFCA Yield of Different Fluorotelomers	141
5.4.4.	Comparison of UV-H ₂ O ₂ -TOP Assay vs. Thermal- and UV-TOP Assay.....	142
5.4.5.	UV-H ₂ O ₂ Assay Mechanism	145
5.5.	Conclusions.....	146
5.6.	Acknowledgements.....	147
5.7.	References.....	148
6.	Shining a Light on Hidden PFAS: Development of a UV-Reducible Organic Fluorine Assay and Tandem UV-H ₂ O ₂ -TOP-ROF Assay for Enhanced Analysis of PFAS.	152
6.1.	Introduction.....	153
6.2.	Materials and Methods.....	155
6.2.1.	Reagents and Materials	155
6.2.2.	UV-H ₂ O ₂ , UV-TOP, and UV-ROF Assays.....	155
6.2.3.	Initial Method Development and Evaluation	156
6.2.4.	PFAS Analysis.....	157
6.2.5.	Fluoride Analysis	158
6.3.	Results and Discussion	158
6.3.1.	Development of UV-ROF, UV-H ₂ O ₂ -ROF, and UV-H ₂ O ₂ -TOP-ROF Assays ..	158
6.3.2.	UV-H ₂ O ₂ -TOP-ROF Assay Evaluation for AFFFs	160

6.3.3.	UV-H ₂ O ₂ -TOP-ROF Assay Application to Other Matrices	163
6.3.4.	UV-H ₂ O ₂ -TOP-ROF Method Analytical Decision Framework	166
6.4.	Conclusions.....	168
6.5.	Acknowledgements.....	169
6.6.	References.....	170
7.	Parsimonious Methodology for Synthesis of Silver and Copper Functionalized Cellulose	173
7.1.	Abstract.....	174
7.2.	Introduction.....	175
7.3.	Materials and Methods.....	177
7.3.1.	Reagents.....	177
7.3.2.	Preparation	177
7.3.3.	Metal Content Determination.....	179
7.3.4.	Metal Speciation	179
7.3.5.	Metal Morphology	180
7.3.6.	Fourier-Transform Infrared Spectroscopy (FTIR) Analysis.....	181
7.3.7.	Ion Selective Electrode (ISE) Analysis	181
7.4.	Results and Discussion	181
7.4.1.	Metal Content and Speciation on Textile	181
7.4.2.	Metal Particle Morphology	185
7.4.3.	Role of Heat in Metal-Textile Synthesis	187
7.4.4.	Silver Copper Competition	188
7.4.5.	Cellulose Analysis.....	190
7.4.6.	Parsimonious Assessment of the Synthesis Methods.....	191
7.4.7.	Metal Cellulose Synthesis Mechanism	192
7.5.	Conclusion	196
7.6.	Acknowledgements.....	197
7.7.	References.....	198
8.	Development and validation of a method for the weathering and detachment of representative nanomaterials from conventional silver-containing textiles	204
8.1.	Abstract.....	205
8.2.	Introduction.....	206
8.3.	Materials and Methods.....	208
8.3.1.	Textile Characterization	208
8.3.2.	Physical Weathering Method	208
8.3.3.	Chemical Weathering Method.....	209

8.3.4.	Combined Physical and Chemical Weathering Method.....	209
8.3.5.	Human Weathering Method	209
8.3.6.	Standard Wash Method	209
8.3.7.	Standard Analytical Suite.....	210
8.3.8.	Single Particle Analysis	210
8.4.	Results and Discussion	211
8.4.1.	No Weathering (Control).....	211
8.4.2.	Physical Weathering.....	214
8.4.3.	Chemical Weathering	215
8.4.4.	Combined Chemical/Physical Weathering.....	216
8.4.5.	Comparison to Human Weathering	217
8.4.6.	Characterization Results and Mechanism	219
8.5.	Conclusion	221
8.6.	Acknowledgements.....	222
8.7.	References.....	223
9.	Conclusions and Recommendations.....	226
9.1.	Investigating the Transformation of PFAS Using Gamma Irradiation	226
9.2.	Development of a Tandem UV-H ₂ O ₂ -TOP-ROF Assay for Enhanced Characterization of PFAS in Commercial Products and Environmental Matrices.....	227
9.3.	Investigating Effective Synthesis Methods for Silver- and Copper-Functionalized Textiles	228
9.4.	Development of a Simulated Weathering Method for Enhanced Characterization of Silver Nanomaterials in Commercial Products and Released Effluent Media.....	229
9.5.	Recommendations for Future Work.....	229
	Appendix A – Supplementary Information for Chapter 3	232
	PFAS and Concentrations Used In Study	232
	Targeted PFAS Analysis.....	234
	Quality Control	236
	Non-Targeted Analysis (PFAS Degradation Products)	236
	Fluoride Analysis	237
	Comparisons of PFOS and PFOA Degradation to Literature	238
	Linear PFOS and 6:2 FTS Degradation Comparison.....	238
	PFOS Transformation Products	239
	PFOA Transformation Products.....	241
	6:2 FTS Transformation Products.....	243

PFAS Transformation Products – High Resolution Analysis.....	244
Statistical Analysis.....	257
Appendix B – Supplemental Information for Chapter 4.....	260
PFAS Analysis	261
Statistical Analysis.....	264
Volume-Normalized Photon Irradiance to the Solution at 254 nm.....	264
Appendix C – Supplemental Information for Chapter 5.....	272
PFAS Analysis	272
Analysis of Butyl Carbitol.....	274
Identification of Organic Matter Inhibition Concentration	274
H ₂ O ₂ Pre-Treatment Initial Method Development.....	274
H ₂ O ₂ Pre-Treatment Method Optimization (Figure 5.1).....	274
Tandem UV- H ₂ O ₂ and UV-TOP Assay (Figure 5.2, 5.3).....	275
Investigation of Persulfate Salt and Concentration (Figure C4).....	275
PFCA Yield of Different Fluorotelomers (Figure 5.4)	275
Thermal-TOP, Tandem UV- H ₂ O ₂ , UV-TOP Validation (Figure 5.5)	275
Extended Results and Discussion	276
Understanding the Role of pH, Concentration, and Activation Rate in the UV-H ₂ O ₂ Assay	276
Selection of Persulfate Salt and Concentration in the UV-H ₂ O ₂ -TOP Assay.....	278
Greyscale Version of Figure 5.5	279
UV-H ₂ O ₂ Transformation Products of 6:2 FTS	280
References.....	281
Appendix D – Supplemental Information for Chapter 6.....	283
PFAS Analysis	283
UV-ROF Validation and Impact of Oxidation Pre-Treatment on UV-ROF Assay (Figure 1).	285
Application of UV-H ₂ O ₂ -TOP-ROF Assay to AFFFs (Figure 2).....	285
Application of the UV-H ₂ O ₂ -TOP-ROF Assay to AFFF Still Bottoms (Figure 3).	285
Application of the UV-H ₂ O ₂ -TOP-ROF Assay to Assorted Samples (Figure 3).	285
Extended Results and Discussion	287
High Resolution Analysis of AFFF Still Bottoms Sample	287
PFAS Composition of Additional Samples Post-UV-H ₂ O ₂ -TOP and Post-dTOP.....	288
UV-H ₂ O ₂ -TOP-ROF Method Analytical Decision Framework Expanded	289
References.....	293
Appendix E – Supplemental Information for Chapter 7.....	296

Metal Content Calibration	296
SEM Sample Preparation Development	297
XANES Relativized Data	300
NaHCO ₃ Role of pH	301
Silver/Copper Competition	302
XANES and FTIR Spectra.....	303
Appendix F – Supplemental Information for Chapter 8.....	306
Analytical Suite.....	306
Total Silver Analysis.....	306
Silver Morphology and Surface Speciation Analysis	306
Bulk Silver Speciation Analysis	306
Standard Wash Method.....	307
Materials	308
Textile Characterization	309
XANES Analysis	311
Statistics on Total/Ionic Releases of Silver.....	325
Appendix G – Supplemental Information for Thesis	331

List of Abbreviations

Acronym	Full name	Acronym	Full name
3M	Minnesota Mining and Manufacturing Company	LC-MS/MS	Liquid chromatography tandem mass spectrometry
6:2 FTS	6:2 Fluorotelomer Sulfonate	MAC	Maximum acceptable concentration
AFFF	Aqueous film forming foam	MCL	Maximum contaminant limit
CEC	Contaminant of Emerging Concern	OECD	Organisation for Economic Co-operation
CIC	Combustion Ion Chromatography	PAPs	Polyfluoroalkyl phosphates
e-aq	Aqueous Electron	PCTFE	Polychlorotrifluoroethylene
ECF	Electrochemical fluorination	PFAIs	Perfluoroalkyl iodides
ECHA	European chemicals agency	PFAS	Per and polyfluoroalkyl substance(s)
FASAAs	N-Alkyl perfluoroalkane sulphonamido acetic acids	PFBS	Perfluorobutane Sulfonic Acid
FASAs	Perfluoroalkane sulphonamides	PFBSs	Perfluoroalkyl sulphonic acids
FASEs	N-Alkyl perfluoroalkane sulphonamido ethanols	PFCAAs	Perfluoroalkyl carboxylic acids
FFTA	Fire fighting training area	PFECAs	Perfluoroether carboxylic acids
F-ICP-MS	Fluorine-Inductively Coupled Plasma Mass Spectrometry	PFESAs	Perfluoroether sulphonic acids
F-NMR	Fluoride-Nuclear Magnetic Resonance	PFOA	Perfluorooctanoic acid
FtACs	Fluorotelomer acrylates	PFOS	Perfluorooctane sulfonate
FtB	Fluorotelomer Betaines	PFPAAs	Perfluoroalkyl phosphonic acids
FtCAs	Fluorotelomer carboxylic acids	PFPIAs	Perfluoroalkyl phosphinic acids
FtIs	Fluorotelomer iodides	PFSA	Perfluorosulfonic Acid
FtMACs	Fluorotelomer methacrylates	PFSAm	Perfluorosulfonamide
FtOHs	Fluorotelomer alcohols	PIGE	Photon Induced Gamma Ray Emission
FtOs	Fluorotelomer olefins	POSF	Perfluorooctane Sulfonyl Fluoride
FTS	Fluorotelomer Sulfonates	PPCPs	Pharmaceuticals and Personal Care Products
FtSA	Fluorotelomer Sulfonic Acid	PTFE	Polytetrafluoroethylene
FtSAAM	Fluorotelomer Sulfonamido Amines	RIS	Reactive iodine species
FtSaB	Fluorotelomer Sulfonamido Betaines	ROF Assay	Reducible Organic Fluorine Assay
FtSOAOS	Fluorotelomer Sulfonyl Amido Sulfonate	SAMPAPs	Perfluorooctane sulphonamido ethanol-based phosphate esters
FtTAOS	Fluorotelomer Thioamido Sulfonates	SERS	Surface Enhanced Raman Spectroscopy
FtTHN	Fluorotelomer Thiohydroxy Ammonium	SPE	Solid phase extraction
FtTP	Fluorotelomer thioether propionate	TFE	Tetrafluoroethylene
FtUCAs	Fluorotelomer unsaturated carboxylic acids	TOC	Total Organic Carbon
GC-MS	Gas chromatography mass spectrometry	TOP Assay	Total Oxidizable Precursor Assay
HPLC	High pressure liquid chromatography	Ultraviolet Light	UV
HPLC-DAD	HPLC-Diode Array Detection	USEPA	United States Environmental Protection Agency
LC-HRMS	Liquid chromatography high resolution mass spectrometry		

List of Figures and Tables

Main Body Figures and Tables		Page
Figure 2.1 – Starting, intermediate, end materials, and applications in the electrochemical fluorination and telomerization synthesis processes. The name of each structure is indicated by the bolded abbreviation. Modified from (Buck et al., 2011; Wang et al., 2014). Example structures can be found in Appendix G1.		29
Figure 2.2 – Structure of N:2 fluorotelomer sulfonamido betaine, a complex zwitterionic fluoroteomer PFAS commonly found in aqueous film forming foam formulations.		30
Figure 2.3 – <i>Modified from (Gaber et al., 2023)</i> . Timeline of notable public health research known by the public (blue) and known from internal industry research reports (orange) detailing awareness of the toxicity of PFAS.		32
Table 2.1 – Guideline (Canada) and regulation (US) values of different PFAS in Canada and the US. HI = Hazard Index, which is the sum of the ratios of the PFAS concentration to their regulatory limit.		34
Table 2.2 - Primary reactive species and chemical yield (G-value) of species generated following radiolysis of water. G-value is the number of charged species (in moles) per 1 joule of absorbed energy, obtained from the literature (Getoff, 1996; Trojanowicz et al., 2018; Wojnárovits and Takács, 2008). In N ₂ saturated solutions, only italicized reactive species are likely.		38
Table 3.1 - Primary reactive species and chemical reaction yield (G-value). G-value is the number of charged species (in moles) per 1 joule of absorbed energy, obtained from the literature (Getoff, 1996; Trojanowicz et al., 2018; Wojnárovits and Takács, 2008). In N ₂ saturated solutions, only italicized reactive species are likely.		65
Figure 3.1 - PFAS degradation of PFOS, PFOA and 6:2 FTS at two different concentrations at pH 7 and 11, and PFAS _{13Suite} at pH 7 and 11. Error bars represent the standard deviation of the replicates (n=3). PFAS _{13Suite} values <5% average standard deviation. Some error bars are too small to be shown.		71
Figure 3.2 - Degradation of branched and linear PFOS as a function of irradiation (1.9 mg PFOS/L). Error bars represent the standard deviation of the replicates (n=3). Some error bars are too small to be shown.		72
Figure 3.3 - Degradation of PFOS with subsequent generation of quantified PFCAs and semi-quantified PFOS transformation products at pH 7 and 11. Left Y-axis for PFOS, right Y-axis for PFCA and transformed PFOS. Error bars are standard deviation of replicates. Some error bars are too small to be shown. N=1 for transformation product analysis.		75
Figure 3.4 - Degradation of PFOA with subsequent generation of quantified PFCAs and semi-quantified PFOA transformation products at pH 7 and 11. Left Y-axis for PFOA, right Y-axis for PFCA and transformed PFOA. Error bars are standard deviation of replicates. Some error bars are too small to be shown. N=1 for transformation product analysis.		77
Figure 3.5 - Degradation of 6:2 FTS with subsequent generation of semi-quantified 6:2 FTS transformation products at pH 7 and 11. Left Y-axis for 6:2 FTS, right Y-axis for transformed 6:2 FTS. Error bars are standard deviation of replicates. Some error bars are too small to be shown. N=1 for transformation product analysis.		78
Figure 3.6 - Chromatograms of -F/+H PFOS at pH 7 (A); -F/+H PFOS at pH 11 (B); -F/+OH PFOS at pH 7 (C), -F/+OH PFOS at pH 11 (D); 6:2 FTS (E); and -4F/+4H PFOS at pH 7 (F)		79
Scheme 3.1 - Proposed mechanisms for α -position C-F bond breakage of PFAS leading to fluorine substitution or and chain shortening. The table shown communicates some of the substituted PFAS found relevant to pathways A and B.		82
Figure 3.7 - First order transformation rate constant (from 0-5 kGy) for PFCAs plotted as a function of carbon length during PFAS suite irradiation to identify comparative trends.		87
Table 3.2 -Unquantified degradation products of PFOS, PFOA, 6:2 FTS, and PFAS _{13Suite}		88
Figure 4.1 – Influence of quenching and dilution protocol on the thermal-activated TOP assay on PFOS recovery. PFOS reported as uncorrected (blue), and mass-label corrected (red). Mass-labelled PFOS was added after oxidation but before quenching and dilution. The dashed line indicates 70% recovery. Error bars shown are the standard deviation from triplicates trials.		108
Figure 4.2 – Recovery of PFOS (~1 mg/L) following a six-hour TOP assay oxidation, chemical quenching with 4% methanolic acetic acid, and diluted to different final compositions of water and methanol.		110
Figure 4.3 – Iodometric spectrophotometric determination of persulfate as a function of time following thermal (85°C) or UV (254 nm, 36W) activation.		111
Figure 4.4 – Investigation of PFOS, PFOA, and 6:2 FTS following thermal and UV-activated TOP assay. One mL samples were quenched immediately with 0.25 mL of acidified methanol (4% acetic acid) and sub-sampled.		112
Figure 4.5 – PFCA yield with respect to time following the thermal-activated (top) and UV-activated (bottom) TOP assays. Samples were run for six hours and quenched with methanolic acetic acid (4%) before sample dilution. TFA was analyzed for but not identified in any of the samples.		114

Figure 4.6 – PFCA composition following oxidative transformation of 6:2 FTS in this work and others (Al Amin et al., 2021; Dai et al., 2019; Eriksson et al., 2022; Fan et al., 2021; Houtz and Sedlak, 2012; Larsson et al., 2018; Martin et al., 2019; Tsou et al., 2023; Zhang et al., 2021; Zweigle et al., 2022). PFCA yields greater than 100% were relativized to 100% (Table B1 for reaction conditions). Studies that measured PFPrA are indicated with *, whereas studies that measured both PFPrA and TFA are indicated with **. Unless otherwise stated, studies used heat as an activation source.	115
Figure 4.7 – PFOS, PFOA, and 6:2 FTS following UV/H ₂ O ₂ oxidation for six hours. Error bars are too small to be shown.	116
Figure 4.8 – PFAS concentration pre- and post- UV-activated TOP assay for four hours. Samples were amended with M ₈ FOSA and MPFAC-MXA before oxidation to track PFAS recovery and oxidative completion. PFAS were quantified with a standard analytical suite (solid border PFAS), expanded analytical suite (dashed border, solid colour), and semi-quantified using appropriate homologues (dashed border, pattern fill) (top).	118
Table 4.1 – Concentration of PFAS pre- and post- oxidation, grouped by PFAS type and analytical suite, with the total PFAS yield post-oxidation calculated by analytical suite.	119
Figure 4.9 – Relativized PFAS across the seven different AFFF samples showing PFCA yield trends. Fluorotelomers grouped by their fluorinated chain length. Concentrations at pre- or post- TOP assay have been relativized to the sum of the quantified and semi-quantified PFAS at the pre- or post- TOP assay stage.	121
Table 4.2 – Recovery of mass-labelled PFAS added pre-oxidation and evaluated post-oxidation.	122
Table 5.1 – Summary of method development and optimization employed in this study. (LC-MS/MS = liquid chromatography mass tandem mass spectrometry. GC-MS= gas chromatography mass spectrometry. TOC = Total organic carbon determination. Iodo determ = iodometric colorimetric determination of H ₂ O ₂).	134
Figure 5.1 – UV-H ₂ O ₂ system. Investigating transformation (or oxidation) of 6:2 FTS as a function of pH (A) and H ₂ O ₂ concentration (B), transformation (or oxidation) of butyl carbitol and total organic carbon as a function of H ₂ O ₂ concentration (C), and H ₂ O ₂ concentration as a function of UV-activation time (D) (A=500 mM H ₂ O ₂ , D=100 mM H ₂ O ₂). Reactions performed at pH 5.7 is unless otherwise stated. Error bars represent the standard deviation of triplicate samples.	136
Figure 5.2 – Concentration of PFCAs and 6:2 FTS following application of the UV-TOP (60 mM KPS, 150 mM NaOH), UV-H ₂ O ₂ assay (500 mM H ₂ O ₂ , 22 hours) and the UV-H ₂ O ₂ -TOP assay, with different concentrations of butyl carbitol (BC). Error bars represent the standard deviation of triplicate samples.	139
Figure 5.3 – PFCA yield of PFAA precursors with different concentrations of total organic carbon (mg TOC/L, substrate in parentheses) following application of 12 hour thermal TOP assay (Tsou et al., 2023), 1 hour UV TOP assay (Glover et al., 2024), 2 hour UV-TOP assay (developed in (Patch et al., 2024), evaluated w/ TOC in this study), and 22 hour/4 hour UV-H ₂ O ₂ -TOP assay (developed and evaluated in this study). SRNOM = Suwannee River natural organic matter.	140
Figure 5.4 – PFCA composition of different fluorotelomers following application of the UV- H ₂ O ₂ -TOP assay (500 mM H ₂ O ₂ , activated with UV for 22 hours, followed by 60 mM NaPS, 150 mM NaOH, activated with UV for 4 hours).	142
Figure 5.5 – (Top) Absolute concentration of PFAS following application of the thermal- or UV-H ₂ O ₂ -TOP assay to five AFFFs , and (Bottom) relativized composition of PFCAs following the oxidation of 6:2 FTS in three different studies (Fan et al., 2021; Glover et al., 2024, Tsou et al., 2023), and this study, as well as PFCA composition following the oxidation of the four PFAA-precursor containing AFFFs studied using the stand-alone 12-hour thermal TOP assay, stand-alone UV-TOP assay, and the UV-H ₂ O ₂ -TOP assay ().	143
Figure 5.6 – Transformation mechanism of 6:2 FTS oxidatively converted into PFCAs in the UV- H ₂ O ₂ system at neutral pH, with inlaid identified structures and their experimentally measured masses.	145
Table 6.1 – Summarized method development, validation, and implementation employed across this study. (LC-MS/MS = liquid chromatography mass tandem mass spectrometry. GC-MS= gas chromatography mass spectrometry. TOC = Total organic carbon determination. Iodo determ = iodometric colorimetric determination of H ₂ O ₂ . F-ISE = fluoride-ion selective electrode). For assays including multiple steps, time is indicated for each step with / (e.g. UV-H ₂ O ₂ -TOP would be the UV-H ₂ O ₂ assay for 22 hours, followed by the UV-TOP assay for four hours).	157
Figure 6.1 – UV-ROF assay applied to different dilutions of N. Foam-PFCA AFFF directly (A), after UV-H ₂ O ₂ pre-treatment (B) or to 10 μM 6:2 FTS after UV-H ₂ O ₂ -TOP (C). UV-ROF conditions: 50 mM Na ₂ SO ₃ , 10 mM KI, 10 mM NaHCO ₃ , 150 mM NaOH for 4 h; UV-H ₂ O ₂ conditions: 500 mM H ₂ O ₂ for 22 hours; UV-H ₂ O ₂ -TOP conditions: 500 mM H ₂ O ₂ for 22 hours, then 60 mM NaPS, 150 mM NaOH for 4 hours.	159

Figure 6.2 – Concentration of PFAS in AFFF formulations evaluated pre-TOP assay and post UV-H ₂ O ₂ -TOP assay (100 mM H ₂ O ₂ /2h, 60 mM NaPS, 150 mM NaOH 12h), with semi-quantified PFAS in dashed borders with pattern fill (A). Organic fluorine concentrations (mM) calculated from the pre- and post-TOP assay target analysis, and the free fluoride measured after application of the UV-ROF assay. Semi-quantified concentrations excluded the organic fluorine concentrations (B). AFFF with asterisks (*) have also been characterized in previous works (Patch et al. 2024). (ΣFOSA = FOSA, Me-FOSAA, Et-FOSAA; ΣX:2 FTS = 4:2, 6:2, 8:2 FTS; ΣX:2 FtSaB = 8:2 FtSaB, 10:2 FtSaB, semi-quantified using 6:2 FtSaB; ΣX:2 FtTaoS = 6:2, 8:2, semi-quantified using 6:2 FTS; Σ7,9,11:X FTB = 7:3, 7:1:2, 9:3, 9:1:2, 11:3, 11:1:2 FtB, semi-quantified using 5:3 or 5:1:2 FtB).	161
Figure 6.3 – Concentration (A) and relative composition (B) of organic fluorine evaluated after UV-H ₂ O ₂ -TOP-ROF assay, compared to concentration (C) and relative composition (D) of organic fluorine evaluated after the dTOP-ROF assay. <i>UV-H₂O₂-TOP conditions</i> : 500 mM H ₂ O ₂ for 22 hours, then 60 mM NaPS, 150 mM NaOH for 4 hours; <i>UV-ROF conditions</i> : 50 mM Na ₂ SO ₃ , 10 mM KI, 10 mM NaHCO ₃ , 150 mM NaOH for 4 h; <i>dTOP conditions</i> : 200 mM NaPS, 500 mM NaOH for 24 hours.	164
Table 6.2 – Developed methodologies for implementation of the UV-H ₂ O ₂ -TOP-ROF assay on simple/complex aqueous samples, soils, PFAS-impacted surface swabs, personal care products, and textiles.	167
Table 7.1 - Overall synthesis steps performed, including reagents added at each step and analytical methods employed.	178
Figure 7.1 - Silver nanoparticles found in the cross-section of the cotton fiber following NaHCO ₃ silver treatment method.	180
Figure 7.2 - Photographic images taken of textiles post-treatment using eight synthesis methods.	182
Figure 7.3 - Concentration of metal present in the textile following treatment with (A) 1mM silver, (B) 1mM copper, and (C) combined 0.5 mM/0.5 mM silver/copper. CuX are samples that do not have speciation data available. D are samples that were not detected by XRF but have speciation data available.	183
Figure 7.4 - Concentration of silver over time with two different temperature profiles using NaHCO ₃ synthesis method.	184
Figure 7.5 - SEM analysis, EDX spectra, and ImageJ particle number/diameter determination of silver nanomaterials (A-C) and copper oxide nanomaterials (C-E) using NaHCO ₃ (A/C), NaOH (B/D), and NaBH ₄ (C/E) synthesis methods.	186
Figure 7.6: SEM analysis (top) and EDX elemental analysis (bottom) on silver (red) and copper (green) nanomaterials following NaHCO ₃ (A), NaOH (B), and NaBH ₄ (C) synthesis methods.	187
Figure 7.7 - Photographic images of the synthesis of silver, copper, and silver/copper treated cotton textiles with three different water bath heat treatments using the NaOH/NH ₃ Version 1 synthesis method and 10 mM of starting metal concentration. Starred values have one replicate under XRF detection limits.	188
Figure 7.8 - Investigation into the effect of reagent concentration on resulting concentration in the textile using the NaOH/NH ₃ Version 1 synthesis method by using a fixed ratio of silver/copper (left) and a variable ratio of silver:copper, with silver held constant at 1 mM (except for 0:1, which had no silver and 1 mM copper) (right).	190
Figure 7.9 - ATR-FTIR absorbance spectra for cotton samples using Methods 2 (NaHCO ₃), 5 (NaOH) and 8 (NaBH ₄) with silver, copper, and silver/copper.	191
Figure 8.1 – SEM imaging of the X-Static® silver coated fiber in the athletic textile following: (A) no chemical/physical weathering after washing; (B) PhW-W after washing; (C) CW/PhW-W; and (D) human weathering before washing.	212
Figure 8.2 – Total concentration, size distribution (A) and speciation (B) of released silver after various weathering methods, with Ag being elemental silver. Human trial data in the left figure was obtained from literature (Gagnon et al., 2019) and only distinguished particulate and ionic silver. (Control = no weathering; PhW-S = physical weathering with stretching; PhW-W = physical weathering with simulated walking; CW = chemical weathering; Human Trials = human release from literature).	213
Figure 8.3 – Single particle analysis of released wash water from a ‘control’ textile (A) (no sweat, no weathering) compared to released wash water following sweat exposure (B) and combined chemical/physical weathering (C, D) treatments.	214
Figure 8.4 – SEM imaging of released silver particles from: (A) a control textile; (B) a CW/PhW-W textile; and (C) a human-weathered textile (C). SEM imaging (left-most panels) shows large micron-sized silver plates surrounded by smaller spherical nanomaterials. EDX overlay shows silver (red, middle panels) and chloride (blue, right-most panels) co-location.	216
Table 8.1 – Summary of results from various complementary analytical techniques. A, B, C superscripts used to denote statistically different groups, Tukey P<0.05. (Control = no weathering; PhW = average physical weathering; CW = chemical weathering; Human weathering = human release rates from literature (Gagnon et al., 2019))	220

1. Introduction

Contaminants of emerging concern (CECs), also known as micropollutants or emerging contaminants, represent a growing class of pollutants whose classification is based on fitting one or more of the following criteria: they have emerged recently due to human manufacturing or synthesis; they have been newly identified due to advancements in analytical chemistry; they possess the potential to harm organisms at environmentally significant concentrations; and they are potential subjects for future regulatory action or updates to existing regulations (EPA, 2008; K'oreje et al., 2020; Yadav et al., 2021). Examples of CECs include polybrominated diphenyl ethers, pharmaceuticals and personal care products (PPCPs), endocrine-disrupting chemicals, per- and polyfluorinated alkyl substances (PFAS), and nanomaterials. Humans are routinely exposed to CECs due to their incorporation into everyday commercial products, further driving the importance in the evaluation of these materials. Studying CECs presents various challenges, such as the need for robust analytical instrumentation to detect these compounds and the complexity of assessing their transformations during usage and release. For PFAS, this thesis is focused on the development of advanced chemical assays to improve PFAS characterization. For nanomaterials, this thesis is focused on developing simulated weathering protocols to characterize the transformation and release potential of nanomaterials during active human use of textiles. Consequently, this thesis aims to develop robust analytical methodologies for PFAS, and nanomaterials present in commercial products.

Per- and polyfluoroalkyl substances (PFAS) are a large class of synthetic organofluorine compounds with unique physicochemical properties, including high thermal/chemical stability, high tensioactivity, hydrophobicity, and oleophobicity. These properties of PFAS have led to them being extensively employed in manufacturing since the early 1950's (Buck et al., 2011). As occurred with lead, many manufacturers saw the advantages of PFAS when used in industrial applications and sought to leverage those advantages in commercial products, including cosmetic makeups, clothing, food packaging, and textile finishing products (Gebbinck et al., 2015; Lu et al., 2017; Schultes et al., 2018; Zafeiraki et al., 2014). PFAS applications continue to expand despite numerous warnings related to their toxicity (Gaber et al., 2023; Grandjean, 2018), and now, due in part to its widespread incorporation into commercial and industrial products, PFAS are found everywhere (Hogue, 2019; Jian et al., 2017; Paul et al., 2009; Wang et al., 2014, 2014). PFAS have been found in every feasible environmental matrix, including air, water, soil, sediment, glacier ice, and various biological organisms, including humans (Chen et al., 2016; Ericson Jogsten et al.,

2012; Garnett et al., 2021; Huber et al., 2011; Möller et al., 2010; Quiñones and Snyder, 2009; Zacs and Bartkevics, 2016). PFAS have been the focus of a growing body of research identifying their toxicological impacts on humans, with links to cancer, kidney/liver disease, neurological and development issues in children, and reduced vaccination immune response (Bell et al., 2021; Caverly Rae et al., 2015; Kwok et al., 2013; Olsen et al., 2017; Pelch et al., 2019; Shih et al., 2021; Zhang et al., 2022).

In response to this growing body of literature, government organizations around the world have been instituting legislation regulating the manufacturing, import, and use of PFAS, as well as identifying limits for the concentration of PFAS in drinking water, groundwater, and soil. To address increasingly stringent PFAS regulations, two fields of research have been a significant focus for academic, industry, and government groups: analysis and remediation. Significant efforts have been invested to identify the most effective ways of analyzing this expanding class of over 15,000 compounds and once detected at above-regulation concentrations, identifying ways to effectively remove and/or destroy PFAS from systems of concern, such as drinking water. From a remediation standpoint, several technologies have been identified as capable of destructively removing PFAS from water, including sonolysis, thermal, ultraviolet light (UV) activated photosensitizers, electron beam, and gamma irradiation. Gamma irradiation is particularly of interest for its application to remediating PFAS because it can be used to generate a broad range of reactive radical species capable of degrading PFAS, including reducing radicals like the aqueous electron (e^-_{aq}) and oxidizing radicals like hydroxyl radicals (OH \cdot). One of the limitations of gamma irradiation is the requirement for existing irradiation infrastructure, which can be quite prohibitive. However, the same reactive radicals that are generated using the gamma radiolysis of water can be replicated by using UV-activated photosensitizers, like sodium sulfite or potassium iodide (which generate e^-_{aq} , alongside other radical species) and sodium or potassium persulfate (which generate sulfate radicals, alongside other radical species). The portable and low-cost nature of UV-activation technologies makes them conducive to both remediation and analytical applications. To this end, the focus of this thesis builds upon previous works to advance the remediation and analysis of PFAS, with a focus on the development of UV-activated oxidative and reductive assays for characterization of PFAS present in aqueous matrices.

Defined as “having at least one dimension between approximately 1 and 100 nanometers” (Health, 2010), nanomaterials and their unique distinction from bulk material have led to their use in many

commercial applications. Aside from being able to use small concentrations of nanoparticles to imbue a material with a desired property, the advantages of nanoparticles come from the wide variety of size, shape, and chemical properties available to manufacturers. For example, carbon nanoparticles in the shapes of nano-rods, wires, and tubes are often used in bicycles, aerospace engineering, printed transistors, and high-tensile strength fibres, where the shape of the nanoparticles can drastically alter a material's thermal/electrical conductivity, weight-to-strength ratio, and elasticity (De Volder et al., 2013). Metal nanoparticles such as copper, silicon dioxide and titanium dioxide are often used in products including shampoo, toothpaste, dietary supplements, skin creams and sun lotions (Kessler, 2011). Despite the different metal nanoparticles used in commercial products, two of the most common metals incorporated into commercial products are silver and copper, which are either added directly to the commercial product in nanoparticulate form or is added in a form which may generate incidental or weathered nanoparticles. This distinction is critical, and identifying the initial functionalization of metal present in a commercial product is important in determining the potential for its release into the environment and human receptors. Furthermore, it is important to simulate commercial product use as accurately as possible, as different factors (e.g. chemical environment, physical stress) can alter the concentration, type, or speciation of released metal nanomaterials. To this end, the thesis concludes by first investigating effective synthesis methods to add silver and copper materials onto textiles, and then investigates the characterization and release of silver nanomaterials from commercially available silver-functionalized textiles.

The overall goal of this research is to characterize PFAS, and metal nanomaterials present in commercial products and, for metal nanomaterials, evaluate their release into the environment. The objective of this research is therefore divided into two focus areas: PFAS and metal nanomaterials.

For PFAS, the sub-goal of this research is to investigate the use of reductive and oxidative techniques for their remediative and analytical applications to PFAS. Specifically, using a cobalt-60 gamma source, gamma irradiation will be used to generate reductive (e.g. aqueous electrons, e^-_{aq}) and oxidative (e.g. hydroxyl radicals, OH^\cdot) species for their remediative application to PFAS. The objective of this gamma-irradiation driven research is to evaluate the transformation of PFAS as it undergoes degradation, for the purposes of elucidating insights into the roles that different reactive radical species play in destroying these highly recalcitrant organofluorine molecules. Following this work, a UV lamp emitting light at 254 nm will be used alongside different

photosensitizers to develop analytical applications suitable for enhancing the characterization of PFAS in aqueous matrices. Specifically, this analytical work will first focus on using UV-light to activate potassium persulfate, then later hydrogen peroxide and sodium persulfate, to generate hydroxyl radicals capable of oxidatively converting perfluoroalkyl acid (PFAA) precursors into terminal PFAS products (referred to as the TOP assay). The gamma irradiation and UV-oxidation research will form the basis of further work to develop a tandem UV-light activated oxidation/reduction assay. This tandem assay will first oxidizing PFAA precursors into terminal perfluorocarboxylic acids (PFCAs), which are analyzed using LC-MS/MS, and then mineralizing the terminal PFAS products into free fluoride using aqueous electrons and other reactive radicals generated by UV-light activated sulfite and iodide under alkaline conditions.

For metal nanomaterials, the sub-goal of this research is to apply already developed analytical methodologies in a complementary nature to characterize both the material present in the commercial product, and after it is released from the product. This was accomplished first by functionalizing cellulose with metal nanomaterials in the lab to provide insights into how different synthesis routes can influence metal nanomaterial characteristics, and to evaluate the effectiveness of different analytical techniques for characterizing the metal-functionalized textiles. Secondly, a silver-functionalized commercial textile was studied to evaluate the characteristics of the metal both on and released from the textile as a function of different simulated use methods. These simulated use methods, also referred to as artificial weathering experiments, were performed to simulate active human use of the textiles to enable accurate characterization without the need for human volunteers.

The conclusion of this work will result in methods capable of comprehensively characterizing PFAS and metal nanomaterials present in different industry and commercial products. For PFAS, these methods include oxidation- and reduction- driven chemical assays used to convert PFAS into quantifiable end-products. The development and optimization of these assays allows for them to be easily incorporated into existing commercial and research analytical laboratories. For metal nanomaterials, this work details the use of existing analytical methods in a complementary nature, providing a multiple-lines-of-evidence approach in characterizing the morphology, speciation, and concentration of silver and/or copper nanomaterials present on or released from textiles.

1.1. Thesis Organization

This thesis is presented in a manuscript style, consisting of nine chapters plus seven appendices, listed below. Chapters 3, 4, 7, and 8 have been published in academic journals and have been modified from their published versions. Chapter 5 has been accepted for publication and is currently undergoing revisions. Chapter 6 will be submitted for publication following the publication of Chapter 5.

Chapter 1 offers a background on the research topic, objectives, and structure of the thesis.

Chapter 2 provides a literature review of the background information of the thesis, including information on PFAS, gamma irradiation of PFAS, UV-activated oxidation of PFAS, UV-activated reduction of PFAS, as well as metal nanomaterials and their presence in textiles.

Chapter 3 provides a detailed investigation into the use of gamma irradiation to degrade PFAS, with the goal of elucidating destruction reactions mechanisms based on the reactive radical species in the system and the transformation products identified using high resolution mass spectrometry.

Chapter 4 provides a detailed investigation into the use of UV-light to activate potassium persulfate under alkaline conditions for the TOP assay and its application to PFAS present in different legacy and modern AFFF formulations.

Chapter 5 provides a detailed investigation into the use of UV-light to activate hydrogen peroxide under neutral conditions as an oxidative pre-treatment to remove dissolved organic matter, before completely converting PFAA precursors to terminal PFAS products using the previously developed UV-TOP assay. The tandem UV-H₂O₂-TOP assay is compared to the standard thermal TOP assay, before being applied to different AFFF formulations.

Chapter 6 provides a detailed investigation into the use of UV-light to activate sodium sulfite and potassium iodide under alkaline conditions to completely mineralize PFAS in aqueous matrices for the analytical determination of the organic fluorine concentration present within a matrix. This reducible organic fluorine assay (UV-ROF) is further modified to be incorporated into the UV-H₂O₂-TOP assay, after which this tandem UV-H₂O₂-TOP-ROF assay is applied to fifteen AFFF samples and an assortment of commercial products to determine the post-oxidation PFAS concentration and post-mineralization free fluoride concentration. Chapter 6 concludes with a

methodological framework describing different method modifications to apply the developed methods to different samples and matrices.

Chapter 7 provides a detailed investigation into the synthesis of silver- and copper- functionalized cellulose textiles and their characterization using x-ray fluorescence spectroscopy (XRF), x-ray absorption near edge structure (XANES), attenuated total reflection-fourier transform infrared spectroscopy (ATR-FTIR), scanning electron microscopy (SEM), energy dispersive x-ray spectroscopy (EDX), and silver ion selective electrode (Ag-ISE).

Chapter 8 provides a detailed investigation into the characterization of a silver-functionalized commercial textile. Different chemical and physical weathering methods were employed to simulate human use of the textile, with the methods being evaluated against data collected from real human trials.

Chapter 9 summarizes the overall outcomes of the thesis and provides recommendations for future work.

Appendix A-G contains supplemental information for Chapters 3-9 respectively.

2. Literature Review

2.1. Foreword

2.1.1.Importance of Water

Water is the single most important resource on Earth, valued for its ability to sustain life. Of the 1.3 billion cubic kilometers of water present on the Earth, only ~0.8% (~11 million cubic kilometers) is available as fresh water not locked up in glaciers (Water Science School, 2019, 2018). That same fresh water is used by trillions of organisms every day to maintain regular function. Therefore, any issues that would affect water availability or quality poses a direct threat to life and the environment. One such issue that humanity continues to face is the presence of chemical or biological contaminants in drinking water systems. As society's grasp of science increases, so too does the complexity of contaminants entering the environment.

2.1.2.Early Civilization's Utilization of Water

Early human civilizations settled along waterways to take advantage of the readily available fresh water for drinking and irrigation. As civilizations expanded so did architecture to handle increasing water demands. As early as 4000 BC human societies begin to employ water treatment, with the goal of aesthetic improvements to appearance, taste, and odour (EPA, 2000). Ancient Sanskrit and Greek writings identify the first water treatment methods utilized filtering through charcoal, exposure to sunlight, boiling, or straining (Hosseiny et al., 2021; Lofrano and Brown, 2010; Vuorinen et al., 2007). Later developments by ancient Egyptians in 1500 BC saw the use of alum (aluminium sulfate) to clarify water through the aggregation of suspended particles. Accounts written by Herodotus (484-425 BC) identified that many kings during travel would only drink water that was boiled and stored in silver vessels to preserve and further improve the aesthetics of the water (Gale and Stos-Gale, 1981; Herodotus, 2008; Simpson, 2005). Up to this point the main contamination of drinking water is attributable to suspended debris and biological organisms which were addressed through the practices of the time.

2.1.3.Lead, the First Emerging Contaminant

Following the expansion of the Roman Empire there was a need to transport water very far distances. To accomplish this, city architects and engineers employed lead (plumbum) pipes, which were advantageous due to their low melting point, ease of working, and resistance to corrosion (Delile et al., 2014). While lead minerals were used in Ancient Egyptian cosmetic make-ups, lead's rise to popularity in the Roman Empire led to an expansion of its applications, including being

added to food and drinks (Eisinger, 1982). Writers including Cato the Elder (234–149 BC), Columella (4-70 AD), and Pliny the Elder (23-79 AD) all recommended the use of lead-coated vessels for preparation of sweeteners which would later be added to wine and food (Waldron, 1973). This was done to take advantage of the natural sweetness of lead (II) acetate and to avoid the bitterness of verdigris (copper chloride, carbonate, or acetate) that would form from brass or copper vessels (Waldron, 1973). Despite warnings by Vitruvius (80-15 BC) regarding the negative health effects of lead, this practice went on for an extended time (Hodge, 1981). While it is currently contested, one popular theory attributes the fall of the Roman Empire to widespread lead poisoning caused by lead pipes and ingestion of lead (II) acetate (Delile et al., 2014; Gilfillan, 1965; Hernberg, 2000; Phillips, 1984). Those afflicted by lead poisoning were referred to as ‘saturnine’, being dark and cynical in disposition.

Lead rose to prominence again during the renaissance, where it was used heavily in alchemical rituals, to once again adulterate wine, and in printing presses. The last two examples were noted for resulting in significant lead poisoning to those exposed, either through imbibing of the wine or inhalation of lead dust during the printing process (Ehrenberg, 1947; Habashi, 1998; Kauffman, 1985; Periodicals, 1849; Read, 1951).

Lead continued to be used quite heavily during the Industrial Revolution, this time through the creation of lead paints. Lead was added to paints to impart water-resistance and improve the appearance of the final painted product. Due to the widespread use of lead paint as well as increased rates of mining and production, cases of lead poisoning continued to rise with links to gout and mental disorders being identified in the 19th century. By the end of the 19th century the first laws were introduced in the UK aimed at decreasing lead poisoning in factories. The rest of the 20th century saw increased legislation and efforts around the world to curb the global impact of lead, with some countries (like the USA) being slow to adopt legislative limits due to pressures from lead reliant industries (Markowitz and Rosner, 2000). The last push in efforts to globally phase-out lead have been complicated considerations as to the usefulness of its addition in products, balanced against the toxicity risk posed by its presence. The first example of this is the use of tetraethyl lead in gasoline (anti-knocking agent), a practice which lasted until 2000. A second example of this is the use of lead in pipes, fittings, fixtures, solder, and flux for drinking water pipes, which was only regulated by the US EPA in 2020 through modification of the Reduction of Lead in Drinking Water Act. This regulation requires the materials to be ‘lead free’, which is defined as containing no more

than 0.2% lead in solder and flux, and no more than 0.25% lead in pipes, fittings, and fixtures. However, these regulations do not apply to materials in contact with non-potable water, or certain household appliances like toilets, bidets, clothes washing machines, or fire suppression sprinklers. Globally, certain countries are still increasing their mining and production of lead, such as China, where it is readily used in paints. This usage has resulted in various recalls over the past decade due to concerns with imported, lead-painted children's toys.

While lead today is understood to be a legacy contaminant, its emergence during the Roman Empire marks the first incidence of a chemical contaminant being introduced into the environment (and humans) through anthropogenic activities. In the case of lead, it took close to 1800 years before science was advanced enough to confidently identify lead's hazards to human health, and an additional 200 years after that before legislation was widespread enough to reduce its exposure to people and the environment. The 2000-year transition of lead from an emerging contaminant with unknown health effects to its status as a legacy contaminant is a useful parallel to many of the emerging contaminants currently being investigated today.

2.2. History of Organofluorine Chemistry

In its pure form, fluorine exists as a gaseous diatomic molecule with each fluorine atom consisting of nine protons, nine electrons, and ten neutrons. It is the lightest halide and is notorious for its extreme reactivity, undergoing chemical reactions with all other elements except for noble gases. With a Pauling electronegativity of 3.98, fluorine is highly electron withdrawing, forming very strong chemical bonds with several different elements, including carbon (strongest organic bond) and silicon (strongest inorganic bond).

Fluorine was first identified in 1810 by Andre-Marie Ampere, who postulated that hydrogen and the yet discovered fluorine constituted hydrofluoric acid (at the time referred to as fluorspar acid, due to its derivation from fluorspar and sulfuric acid) (Greenwood and Earnshaw, 1984). Ampere would attempt to isolate pure fluorine through the electrolysis of hydrofluoric acid, but struggled in the face of the destructive nature of hydrofluoric acid, noting; *'The liquid fluoric acid immediately destroys glass and all animal and vegetable substances, it acts on all bodies containing metallic oxides, and I know of no substances which are not rapidly dissolved or decomposed by it, except metals, charcoal, phosphorus, sulfur, and certain combinations of chlorine'* (Goldwhite, 1989). It would not be until 1886 that fluorine would be isolated by Henri Moissan, who achieved the feat through the electrolysis of molten potassium hydrogen difluoride

and hydrogen fluoride, an accomplishment that would earn him the Nobel Prize in chemistry in 1906 (Banks, 1986).

Due to the reactive and corrosive nature of elemental fluorine, meaningful development of organofluorine compounds would not begin until 1928, where General Motors, in collaboration with Dupont, would synthesize dichlorodifluoromethane (Freon®-113) as part of efforts to identify inert refrigerants (Mackay, 1991). Further development of organofluorine compounds, in particular fluoropolymers, would take place during the Manhattan Project to produce the atomic bomb, led by the efforts of Joseph Simons. Simons identified a large-scale method to produce industrial fluorocarbons through the electrolysis of organic substrates like octane sulfonyl fluoride ($C_8H_{17}SO_2F$) in the presence of anhydrous hydrofluoric acid, resulting in complete substitution of hydrogens with fluorine atoms. This process, referred to as electrochemical fluorination (ECF), or the Simon's Process, would be patented by Simons and two others from the Minnesota Mining and Manufacturing company (3M) (Mackay, 1991). Further work by Robert Haszeldine would develop the telomerization process, which used perfluoroalkyl iodides to synthesize fluorotelomer olefins, sulfonic acids, and alcohols (Haszeldine, 1953, 1953; Haszeldine et al., 1976). These two processes formed the foundation for the synthesis of per- and polyfluoroalkyl substances (PFAS).

2.1. Synthesis of Per- and Polyfluoroalkyl Substances

Per- and polyfluoroalkyl substances (PFAS) are a class of synthetic organofluorine compounds that have been employed since the early 1940's for use in a variety of applications seeking to take advantage of their unique physicochemical properties. These properties, including thermal resistance, chemical resistance, oleophobicity, hydrophobicity, and interfacial activity arise from the specific design of these organofluorine compounds. PFAS are synthesized through two main processes, the ECF process, and the telomerization process (Buck et al., 2011) (Figure 2.1).


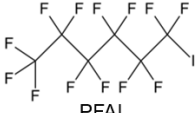


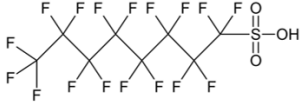

Synthesis Process	Electrochemical Fluorination	Telomerization
Starting Material	 POSF, POCF	 PFAI
Intermediate Material	 FOSA, FOSE	 FTI
End Material	 PFOS, MeFOSA, EtFOSA, SFP	 FTS, FTOH, diPAP, FTAC, FTMAC, SFP
Applications	Surfactants, Aqueous Film Forming Foams, Surface Treatments, Fluoropolymer Production	

Figure 2.1 – Starting, intermediate, end materials, and applications in the electrochemical fluorination and telomerization synthesis processes. The name of each structure is indicated by the bolded abbreviation. Modified from (Buck et al., 2011; Wang et al., 2014). Example structures can be found in Appendix G1.

The electrochemical fluorination process uses starting materials including perfluorooctane sulfonyl fluoride (POSF), and perfluorooctane carbonyl fluoride, to synthesize perfluorosuldonamides (PFSAMs), perfluorosulfonamidoethanols (PFOSEs), perfluorooctane sulfonic acid (PFOS) and perfluorooctanoic acid (PFOA) respectively.

In the telomerization process, perfluoroalkyl iodides are first reacted with ethylene to form fluorotelomer iodides, which are subsequently converted into a broad assortment of chemistries including fluorotelomer sulfonic acids (FTSAs), fluorotelomer alcohols (FTOHs), fluorotelomer (meth)acrylates, (FTACs, FTMACs), and fluorotelomer mono/diphosphate esters (monoPAPs, diPAPs). The fluorotelomer (meth)acrylates and alcohols can subsequently be modified into side-chain fluorinated polymers (SFPs), which are typically used for textile or surface treatments.

2.2. Classification of PFAS

The exact definition of what constitutes a PFAS molecule is constantly being updated, but at a minimum, PFAS consist of a perfluoroalkyl backbone chain typically classified by having at least one fully fluorinated methyl or methylene carbon atom (Wang et al., 2021). Beyond this definition, PFAS are typically defined as non-polymeric (discrete molecules of defined molecular weight, e.g.

PFOS) or polymeric (repeating chains of defined molecular units, e.g. polytetrafluoroethylene). While many academic and government efforts are focused on non-polymeric PFAS, there is an increasing interest in polymeric PFAS, due to the presence of non-polymeric PFAS used as polymer processing aids, or the ability for polymeric PFAS to break down into non-polymeric PFAS, as is the case with side-chain fluoropolymers (Glüge et al., 2020; Lohmann et al., 2020).

Non-polymeric PFAS, herein simply referred to as PFAS, typically contain one (or more) non-fluorinated functional groups that are used to tailor the molecular chemistry to a specific application. These functional groups can be as simple as a non-fluorinated alkyl chain in the middle or end of the molecule (e.g. C_2H_4), or contain different functional groups such as carboxylates, sulfonates, phosphates, amines, and betaines (Buck et al., 2011; Wang et al., 2014, 2014). These chemistries can also be easily combined to further drive molecular complexity, an example of this being the combination of a perfluoroalkyl tail with a C_2H_4 intermediate chain (fluorotelomer), a sulfonamide functional group, and a betaine functional group, to form the PFAS molecule N:2 fluorotelomer sulfonamido betaine (Figure 2.2).

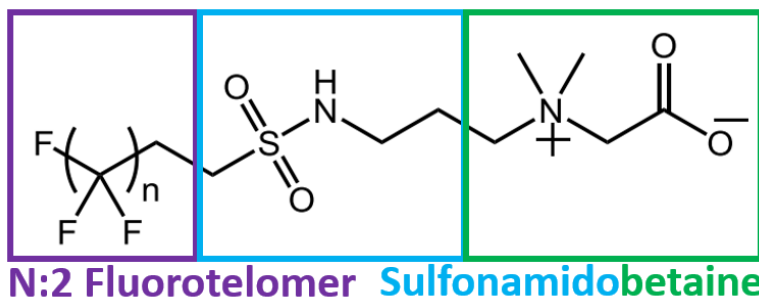


Figure 2.2 – Structure of N:2 fluorotelomer sulfonamido betaine, a complex zwitterionic fluorotelomer PFAS commonly found in aqueous film forming foam formulations.

Depending on the specific definition used for PFAS, it is estimated that over 38,000 PFAS molecules have been identified, with the list continuing to grow daily (Buck et al., 2021; Lea et al., 2022; Williams et al., 2022). While PFAS are typically classified based on their functional chemistry, they can also be classified based on their industrial and commercial applications.

2.3. PFAS Applications and Environmental Release

PFAS in various forms are produced globally by major manufacturers including, but not limited to, 3M, DuPont, Chemours Clariant, Daikan, and AGC Chemicals (Boucher et al., 2019; Jian et al., 2017; Paul et al., 2009; Wang et al., 2017, 2014, 2014). Both polymeric and non-polymeric PFAS

are produced and used extensively in industrial and commercial applications including aqueous film forming foams (AFFF), surface-treatment sprays, food packaging materials, textiles, electronics manufacturing, metal plating processes, and cosmetics (Herzke et al., 2012; Liu et al., 2014; Pan et al., 2021; Robel et al., 2017; Schultes et al., 2018; Wang et al., 2014; Zafeiraki et al., 2014). The widespread application of PFAS in various products or processes are highly concerning due to their propensity for release into the environment or as a direct exposure route to humans (Barzen-Hanson et al., 2017; Gebbink et al., 2015; Houtz et al., 2013; Lu et al., 2017; Nickerson et al., 2020; Robel et al., 2017; Schellenberger et al., 2022; Schultes et al., 2018; Zhu and Kannan, 2020; Zweigle et al., 2023).

Since their development in the early 1950's, it is estimated that upwards of 21,000 tonnes of perfluorocarboxylic acids (PFCAs) and 12,000 tonnes of PFOS and related precursors have been released globally into the environment from various sources (Boucher et al., 2019; Paul et al., 2009; Wang et al., 2017, 2014, 2014). The release of PFAS into the environment can occur through accidental spills, but also includes several documented instances of illegal release events from manufacturing facilities in North America and Europe (Baker, 2022; Hogue, 2019; Nakayama et al., 2007; Quiñones and Snyder, 2009; Willach et al., 2016), as well as being released through the exploitation of loopholes in mandated reporting requirements (Brennan et al., 2021; Hayes, 2022; Holmes, 2021). Whether released accidentally, intentionally, or across the life cycle of a PFAS-containing commercial/industrial product, PFAS will eventually enter the environment, after which they will be taken up by different biological receptors, including humans.

2.4. Toxicity, Public Awareness, and Regulation of PFAS

PFAS have been linked to several negative health effects, including increases to cholesterol, changes in liver function, reduced vaccination response, neurological/development issues in children, and cancer (Ahrens and Bundschuh, 2014; Caverly Rae et al., 2015; Granum et al., 2013; Nabb et al., 2007; Shih et al., 2021; Zhang et al., 2022). Many of these negative toxicological associations were identified more than 30 years later than when they were identified by the PFAS manufacturers themselves (Benesh, 2022; Environmental Working Group (EWG), 2019).

Despite internal reports by 3M identifying the toxicity of PFAS as early as the 1970s and the US FDA being made aware of these reports at the time (Benesh, 2022), decades passed before PFAS's potential for harm to the environment and humans was identified formally to the public. Mirroring

efforts employed by the lead industry in the early 1900's, this delay in public awareness was due in part to active efforts by manufacturers like DuPont and 3M to hide the toxicity concerns surrounding PFAS (Environmental Working Group (EWG), 2019; Gaber et al., 2023; Grandjean, 2018; Paul, 2001).

In the face of increasing pressure and lawsuits in preparation, 3M instituted a 'voluntary' phase-out of PFOS and PFOA in 2002, with many postulating this phase-out was an attempt to save face and get ahead of the backlash before it came out to the public first (Gaber et al., 2023; Grandjean, 2018). Even after information surrounding the toxicity of PFAS became available to the public, DuPont continued to exert pressure on government bodies like the EPA to certify products like Teflon and PFOA as safe, with internal e-mails in 2006 identifying "We need [the] EPA to quickly (like first thing tomorrow) say the following: 1. Consumer products sold under the Teflon® brand are safe. [and] 2. Further, to date, there are no human health effects known to be caused by PFOA". This would be despite Dupont and 3M being aware of the toxicity of PFOA and PFOS as early as 1970 (Figure 2.3).

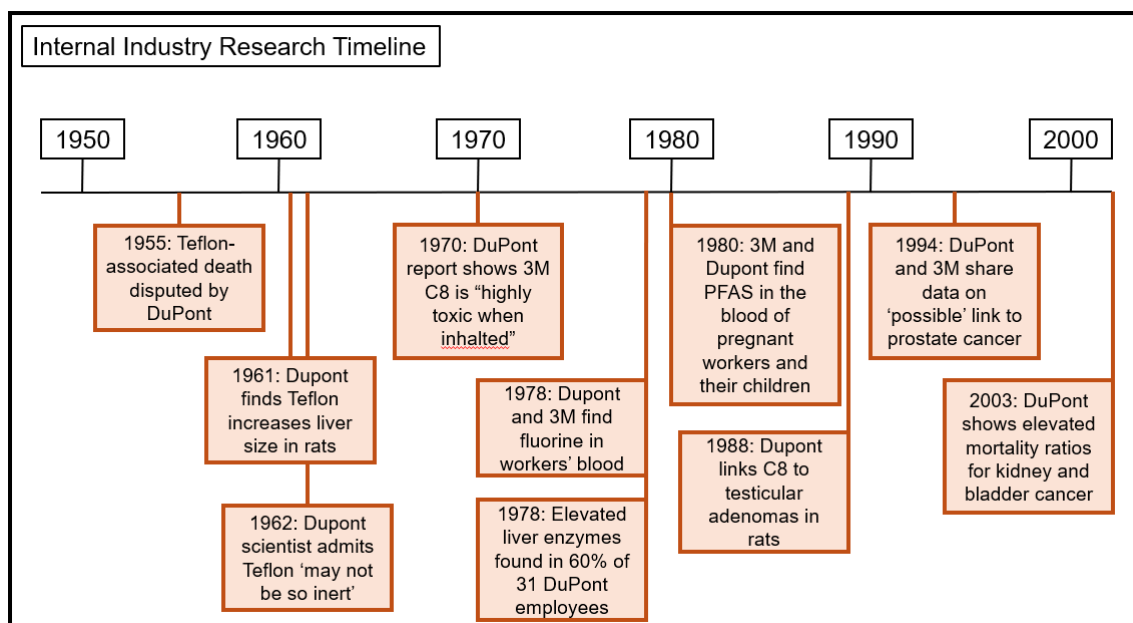


Figure 2.3 – Modified from (Gaber et al., 2023). Timeline of notable public health research known by the public (blue) and known from internal industry research reports (orange) detailing awareness of the toxicity of PFAS.

Following the 3M-instituted phase-out of PFOS and PFOA in 2002, there was a noted decrease in the concentration of these PFAS compounds in the blood of North American populations (Olsen et

al., 2017; Yeung et al., 2008). However, global production of these PFAS shifted to other countries including Russia, China, and India. Additionally, 3M and other PFAS manufacturers would simply shift to newer PFAS formulations that had not yet been regulated. These ‘modern’ PFAS formulations would include fluorotelomers (e.g. 6:2 FTS, 6:2 FTOH, 6:2 FtSaB), perfluoroethers (e.g. GenX), and perfluorosulfonamides (Barzen-Hanson and Field, 2015; Gomis et al., 2015; Heydebreck et al., 2015; Rayne and Forest, 2009; Strynar et al., 2015; Wang et al., 2013). These newer PFAS compounds have been found to either have toxicities similar to PFOS/PFOA or have the ability to transform into regulated PFAS (Caverly Rae et al., 2015; Gannon et al., 2016; Gomis et al., 2015; Hoke et al., 2016; Wang et al., 2015). For example, 6:2 FTOH (unregulated) has been found to degrade into 6:2 fluorotelomer unsaturated aldehyde (6:2 FTUAL) (unregulated) in different environmental and biological receptors. Once formed, 6:2 FTUAL exhibits a significantly higher (>100x) toxicity than PFCAs like PFHxA, which it will eventually degrade into (regulated) (Folkerson et al., 2023; Rand et al., 2014).

Numerous governmental institutions across the world have begun to regulate PFAS in response to their association with negative health effects. In Canada, PFOS, PFOA, long-chain PFCAs, and their salts and precursors are prohibited from manufacture, use, sale, or import under the Canadian Environmental Protection Act, with an allowable incidental total concentration of the PFAS at 1 mg/L each (Government of Canada, 2022). Canada also has, in draft, established drinking water guidelines for PFAS set at 30 ng/L for a total sum of PFAS, based on the list of PFAS specified in EPA 537.1 or EPA 533 (Southerland and Birnbaum, 2023). In Europe, PFAS are listed under the Registration, Evaluation, Authorisation, and Restriction of Chemicals (REACH) list of substances of very high concern, with the European Environmental Agency limiting total PFAS in drinking water at 500 ppt, with individual PFAS limited at 100 ppt (Sadia et al., 2023). In the US, PFOS and PFOA have been designated as hazardous substances under the Comprehensive Environmental Response, Compensation, and Liability Act (CERCLA). Additionally, the Environmental Protection Agency has set Maximum Contaminant Levels for PFOS/PFOA at 4 ng/L, PFHxS, PFNA, and HFPO-DA at 10 ng/L, and a hazard index of 1 (unitless) for mixtures of PFHxS, PFNA, HFPO-DA, and PFBS (PFAS National Primary Drinking Water Regulation 2024) under the Clean Water Act.

Table 2.1 – Criterion values of different PFAS in drinking water in Canada, Europe and the US. HI = Hazard Index, which is the sum of the ratios of the PFAS concentration to their regulatory limit (Cordner et al., 2019; PFAS National Primary Drinking Water Regulation, 2021).

Limit (ng/L)	PFOS	PFOA	PFHxS	PFNA	HFPO-DA	PFBS	Σ PFAS
Canada (MAC)	600	200			-		-
Canada (HI)	1				-		
Canada (Draft)	-						30 (EPA 537.1/533)
USA	4	4	10	10	10	-	-
USA (HI)	-	-	1				-
Europe	-						100

In the face of stringent PFAS regulations, analytical laboratories are developing increasingly sensitive analytical methodologies to detect PFAS in a variety of matrices, including waters, soils, biosolids, sediments, and air (US EPA, 2023).

2.5. Analysis of PFAS

Current analytical methodologies utilized for the characterization of PFAS in environmental matrices rely on the use of liquid chromatography tandem mass spectrometry. In order of increasing mass resolution (and complexity), different mass spectrometers have been employed for PFAS analysis, including triple quadrupole mass spectrometry (LC-MS/MS), time of flight mass spectrometry (LC-ToF-MS), ion trap high resolution mass spectrometry (LC-HRMS), or fourier-transform ion cyclotron resonance mass spectrometry (FTICR-MS) (D’Agostino and Mabury, 2014; Liu et al., 2015; Patch et al., 2022; Strynar et al., 2015; Zacs and Bartkevics, 2016). Several newer methodologies have been developed for the characterization of PFAS, including fluorine inductively coupled plasma mass spectrometry (F-ICP-MS), fluorine nuclear magnetic resonance imaging (¹⁹F-NMR), combustion ion chromatography (CIC), gas chromatography mass spectrometry (GC-MS), surface enhanced raman scattering spectroscopy (SERS), and photon induced gamma emission (PIGE) (Heuckeroth et al., 2021; Lewis et al., 2023; Rehman et al., 2023; Tabassum et al., 2024). The most sensitive and established technique, LC-MS/MS, is used in commercial analytical laboratories to characterize PFAS in accordance with validated EPA methods. The EPA published their first PFAS analytical method (Method 537) in 2009, which allowed for the determination of 14 PFAS compounds in drinking water by using solid-phase extraction (SPE) and LC-MS/MS. This method would see significant iterations over the next nine years, resulting in EPA Method 537.1, which expanded the targeted analytical suite to 18 PFAS compounds. In the following years, the EPA would publish several different methods for the analysis of PFAS in various matrices, including drinking water (Method 533), non-drinking waters

(Method 8327), and wastewater, surface water, groundwater, soil, biosolids, sediment, landfill leachate, and fish tissue (Method 1633). The EPA is now developing PFAS analysis methods for air emissions, including the Other Test Method (OTM)-45 and OTM-50. (Darlington et al., 2018; Kuzniewski, 2022) (Agency, 2021; US EPA, 2023). One of the major drawbacks with many of these methods is their reliance on commercially available reference standards, which limits PFAS analysis to 40-50 compounds out of the over 9,000 compounds currently identified. These ‘unknown’ PFAS, also referred to as hidden PFAS, PFAS/PFAA precursors, or PFAS dark matter, are organofluorine compounds not directly quantifiable using standard LC-MS/MS methods. Many of the compounds have been shown to degrade into quantifiable (target, known) PFAS in different environmental matrices, which can complicate efforts in evaluating the total risk posed by PFAS present in different matrices. Some of the aforementioned analytical methods, such as CIC, F-NMR or PIGE, circumvent this issue by analyzing the fluoride element itself, but these methods can often struggle with sensitive detection of PFAS and require expensive existing infrastructure. To better support existing LC-MS/MS methodologies, many groups have employed chemical assays to transform ‘unknown’ PFAS into quantifiable, terminal products, such as PFCAs, or free fluoride. By understanding the underlying principles of these assays, it is possible to either optimize them further to improve their robustness and ease-of-use, or develop novel chemical assays to further complement PFAS analysis in complex environmental matrices.

2.6. Transformation of PFAS Using Oxidative Systems

In aqueous systems, oxidation-based processes are ones that increase the oxidation number of a given atom or substrate. This can be achieved through the direct transfer of an electron from the substrate to the oxidizing species (single-electron transfer), through the removal of a hydrogen radical (hydrogen atom abstraction), through the addition of oxygen to the substrate, or through addition of the oxidant to double bonds. Oxidizing species can be generated directly from water using high energy radiolysis/photolysis (e.g. gamma irradiation, electron beam, UV_{185nm}), or through the activation of specific oxidizing reagents like hydrogen peroxide, sodium persulfate, ozone, or halogens (Chen et al., 2022a; Kim et al., 2019; Morgan et al., 1988; Wang et al., 2000, 2016; Wenk et al., 2013). Oxidizing species have different properties in terms of their optimal pH range, half-lives, oxidizing potential, selectivity, and main oxidation mechanism. For example, hydrogen peroxide can be activated using UV light to generate hydroxyl radicals, which have a half life of 20 nanoseconds, are strongest under acidic conditions ($E^0=2.8$ V), and non-selectively

oxidize substrates through radical adduct formation and hydrogen atom abstraction mechanisms (Duan et al., 2022). Comparatively, the persulfate anion can be activated using UV light, heat, or aqueous electron transfer to generate sulfate radicals, which have a longer half-life (30-40 μ s), similar oxidation potential ($E^0=2.6$ V) and exhibit a higher reactivity with certain electron-rich organic species like aromatic, sulfur, or nitrogen-containing compounds (Das et al., 1999; Duan et al., 2022).

When applying oxidizing species to the transformation of PFAS, either for remediative or analytical applications, it is important to identify the susceptibility of different PFAS molecules to oxidation. It is well understood that of the three most common classes of PFAS (PFASs, PFCAs, and fluorotelomers), fluorotelomers are susceptible to oxidative conversion to PFCAs by hydroxyl radicals (Houtz and Sedlak, 2012), PFCAs are susceptible to oxidative degradation by sulfate radicals (Frank, Matthew G. annis, Watkins, 2019; Hori et al., 2005; Liu et al., 2012; Yang et al., 2020), and PFASs are generally resistant to oxidation, although some studies have identified the oxidative degradation of PFOS using UV/Fe³⁺-activated persulfate under acidic conditions (Lai et al., 2024; Yang et al., 2020). The oxidative conversion of fluorotelomers to PFCAs is particularly beneficial for analytical applications as it can convert a wide range of PFAA precursors into quantifiable PFCAs, a process referred to as the total oxidizable precursor (TOP) assay.

2.6.1. Total Oxidizable Precursor Assay

One of the challenges in evaluating the risk posed by PFAS in the environment is considering the potential for ‘unknown’, uncharacterized PFAS to either transform into regulated PFAS, or themselves become regulated through ever-evolving guidelines and analytical procedures. With this in mind, analytical methods capable of improving the characterization of unknown PFAS are critical to holistically evaluate the risk present on a site.

Developed by Houtz and Sedlak, the TOP assay uses hydroxyl radicals to oxidatively convert PFAA precursors, such as 6:2 fluorotelomer sulfonate (6:2 FTS) to terminal PFCA products (Houtz and Sedlak, 2012). This is typically achieved through the thermal or UV-activation of the persulfate anion which generates sulfate radicals (eq 1) that, under alkaline conditions, are converted to hydroxyl radicals (eq 2).



As discussed previously, hydroxyl radicals can break down organic molecules through H-atom abstraction mechanisms. When applied to PFAA precursors, the hydroxyl radicals only break down the non-fluorinated components which react with dissolved oxygen and other reactive oxygen species (ROS) to generate shorter-chain PFCAs (Zhang et al., 2021). The exact mechanism can differ by activation type and oxidant but work by Zhang (2021) used density functional theory calculations supported by experimental data to identify that 6:2 FTS transforms to PFHpA and C₆F₁₃, the latter of which further reacts to produce C₂-C₆ PFCAs.

Since its development, the TOP assay has been developed by numerous academic and commercial labs with a variety of modifications, including different reagent concentrations (Göckener et al., 2020; Nolan et al., 2019), different oxidants (Kaiser et al., 2021), UV-activation (Fan et al., 2021; Patch et al., 2024), direct quantification of ultra-short chain PFCAs (Janda et al., 2019; Neuwald et al., 2022), H₂O₂ pre-oxidation (Hutchinson et al., 2020), identification of total organic carbon limitations (Glover et al., 2024; Tsou et al., 2023) and scale-down of sample volumes (Tsou et al., 2023). However, many of these modifications are often explored individually, with little consideration of how the integration of these modifications may improve the accuracy or robustness of the TOP assay.

This lack of robustness in the TOP assay has been noted in multiple inter-laboratory studies, identifying that in its current state, the TOP assay is more useful as a semi-quantitative tool and cannot be considered a true quantitative analytical method (Iavetz et al., 2019; Nolan et al., 2019). Many authors have identified scenarios where the TOP assay results in incomplete oxidation of PFAA precursors, due to oxidant exhaustion caused by dissolved organic matter competition.

In one interlaboratory study between three labs, PFCA variation in post-oxidation samples was found to be as high as 67% (Nolan et al., 2019). In the same study in a high organic carbon containing sample (120 mg/L TOC as diluted worm farm liquid), the sum of PFAA precursors found between labs was found to differ by more than 85% (relative percent difference).

2.7. Transformation of PFAS Using Reductive or Oxidative/Reductive Systems

In aqueous systems, reduction-based processes are ones that decrease the oxidation number of a given atom or substrate. This is often achieved through direct transfer of an electron to the substrate from the reducing species but can also be achieved through direct acceptance (nucleophilic attack) by an aqueous electron. When speaking of reduction reactions in a classic chemical synthesis

context, reduction reactions often occur through direct electron transfer. However, in the context of this thesis, reduction reactions occur through reaction with aqueous electrons. An aqueous electron is a discrete electron trapped in a cavity stabilized by four to six water molecules through hydrogen bonding interactions (Hart, 1964; Hart et al., 1965; Schwarz, 1992). Aqueous electrons can be generated directly from water using high energy radiolysis/photolysis (e.g. gamma irradiation, electron beam, UV_{185nm}), or through the UV-activation of specific reducing reagents (referred to as photosensitizers) like sodium sulfite, potassium iodide, or phenol (Bhattacharyya et al., 2020; Deister and Warneck, 1990; Gu et al., 2017; Jortner et al., 1963; Li and Hoffman, 1999; Li et al., 2014; Neta and Huie, 1985; Park et al., 2011; Yu et al., 2018). Both radiolysis and photosensitizer systems have unique advantages and disadvantages for their general application, and application to PFAS.

2.7.1. Gamma Radiolysis of PFAS

One of the advantages of the gamma radiolysis of aqueous solutions is the ability to generate reactive species without the input of chemical reagents, which can increase costs and result in environmentally harmful chemical species, such as halogenated disinfection byproducts (Dong et al., 2019; Ike et al., 2019; Wenk et al., 2013). Furthermore, the breadth of generated reactive radical species can be significantly reduced by purging the aqueous system with an inert gas like nitrogen or argon. In nitrogen-purged systems, most of the generated reactive species are the aqueous electron and hydroxyl radical, with minor relative amounts of hydrogen radicals (Table 2.2).

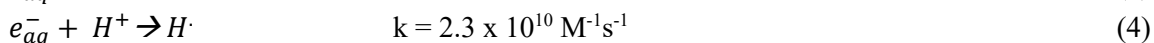
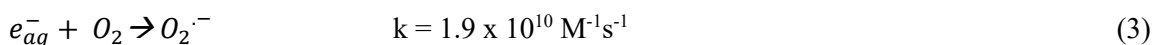
Table 2.2 - Primary reactive species and chemical yield (G-value) of species generated following radiolysis of water. G-value is the number of charged species (in moles) per 1 joule of absorbed energy, obtained from the literature (Getoff, 1996; Trojanowicz et al., 2018; Wojnárovits and Takács, 2008). In N₂ saturated solutions, only italicized reactive species are likely.

Reactive Species	<i>e⁻ (aqueous)</i>	<i>·H</i>	<i>·OH</i>	<i>H₂</i>	HO ₂ ⁻	H ⁺	OH ⁻
G-Value	0.27	0.06	0.28	0.045	0.07	0.32	0.05

As seen in Table 2.1, the two most abundantly generated species are the aqueous electron (*e⁻_{aq}*) and the hydroxyl radical, commonly considered to be the simplest reductant and oxidant respectively. It is for this reason that the gamma irradiation is often considered a mixed redox system, as it can generate both types of reactive species. However, this is not always beneficial, as these two reactive

species can terminate one another if generated too quickly or abundantly, a process referred to as geminate recombination (Kim et al., 2018; Maza et al., 2024; Wang et al., 2016).

Several studies have investigated the use of gamma irradiation to degrade PFAS. Work by Zhang et al. (2014) examined gamma irradiation of PFOA as a function of pH, oxygen saturation, and identified reactive species with scavenger experiments observing 99% mineralization of PFOA at pH 13 under N₂ purging following 126 kGy. Formation and subsequent degradation of shorter chain perfluorocarboxylic acids (PFCAs) was observed. Through scavenging experiments Zhang identified aqueous electrons as being responsible for initial PFOA degradation, with hydroxyl radicals being responsible for complete defluorination (Zhang et al., 2014). Several additional studies, either using gamma irradiation or electron beam radiolysis would identify higher rates of PFAS degradation at higher pH and under anoxic conditions, concluding that protons and dissolved oxygen were two species capable of rapidly scavenging aqueous electrons from the system (Kowald et al., 2021; Lassalle et al., 2021; Trojanowicz et al., 2020, 2019, 2018) (eq 3, 4).



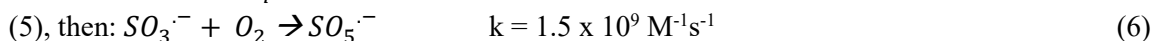
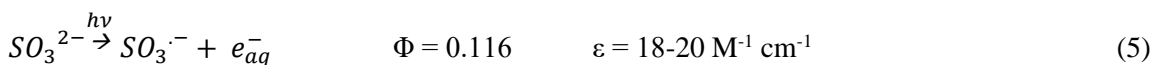
Work by Trojanowicz et al (2019) investigated the degradation of PFOA and PFOS using both electron beam and gamma irradiation, reinforcing other studies that identified the aqueous electron as responsible for initiating PFAS degradation, with the hydroxyl and hydrogen radicals participating in subsequent reactions (Trojanowicz et al., 2020, 2019). Using gamma irradiation, PFOS reached 90% degradation after 10 kGy of irradiation at pH 7. Trojanowicz also identified preferential destruction of branched isomers compared to their linear counterparts and identified alkyl-substituted PFAS transformation products resulting from the dimerization of alkyl radicals (using tert-butanol as an alkyl source). Several gamma irradiation studies have identified the importance of oxidative radicals (e.g. hydroxyl radical) in driving PFAS defluorination after aqueous electron-initiated degradation, however the exact mechanism of PFAS breakdown is still being investigated.

One of the intermediate steps in PFAS destruction is the formation of different PFAS transformation products. These PFAS transformation products, also referred to as products of incomplete degradation (PIDs), complicate efforts to close the mass balance of a remediation process, as they are not easily quantified using standard mass spectrometric methods. Furthermore,

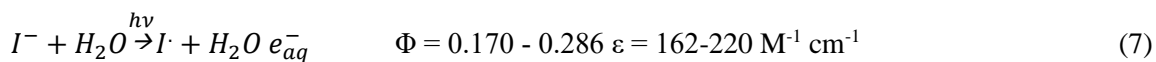
there are concerns that these PIDs can have similar, or greater toxicities to their parent PFAS compounds. One of the most common PFAS transformation products are PFCAs, and -F/+H exchanged PFAS. Using PFOS as an example, expected PFAS transformation products would be PFOA (and shorter PFCAs), and various -nF/+nH PFOS exchanged molecules. The -4F/+4H exchanged PFOS is effectively 6:2 FTS, albeit likely isomerically different. Given that both PFCAs and 6:2 FTS have measured toxicological effects, this further reinforces the issues posed by the formation of PFAS transformation products.

2.7.2. UV-Activated Reduction of PFAS

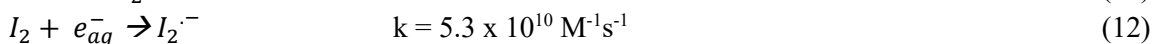
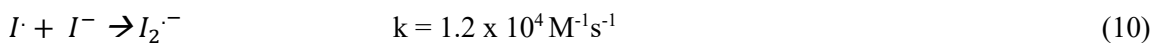
The advantages of UV-activated reduction systems are the reduced infrastructure requirements, ease of use, and ability to tailor the system chemistry to achieve specific desirable reactions. The UV reduction system relies on different photosensitizers to generate aqueous electrons which occur following UV-activation. The efficiency in which reducing reagents can generate aqueous electrons is dictated by their molar absorptivity and quantum yield, with molar absorptivity being a measure of the efficiency of photon capture by a given chemical species at a given photon wavelength, and quantum yield being the ratio of photochemical reactions that occur per absorbed photon (Sauer et al., 2004). Of the various photosensitizers investigated, sulfite and iodide have been identified as particularly promising due to their effectiveness in degrading PFAS independently (UV/S and UV/I respectively) and together (UV/S+I). Independently, UV/S and UV/I systems have been investigated for their degradation of a variety of PFAS, including PFOS, PFOA, 6:2 FTS, GenX, F-53B, and dilute AFFF mixtures (Abusallout et al., 2021; Bao et al., 2019; Bentel et al., 2020, 2019; Liu et al., 2021; Park et al., 2011; Tenorio et al., 2020). In both systems, aqueous electrons have been identified as the dominant reactive species, with iodide radicals potentially serving as a secondary oxidizing species, or a potential nucleophile (as identified by conversion of PFOS to perfluorooctane iodide) (Park et al., 2011, 2009). The strengths and drawbacks of both systems have also been discussed across several studies. In the UV/S system, the generation of aqueous electrons also results in the generate of sulfite radicals (eq 5), which can remove dissolved oxygen through a chain initiated autooxidation reaction (Das, 2001) (eq 6), thus promoting more effective aqueous electron generation.



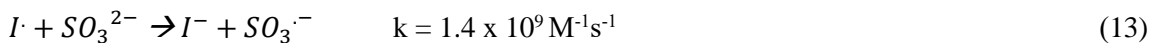
However, the low molar absorptivity and quantum yield of the sulfite anion can result in slow reactions, requiring longer overall energy inputs. In contrast, the UV/I system has a high molar absorptivity and quantum yield, allowing for the rapid generation of aqueous electrons (eq 7).



However, the UV/I system has no inherent dissolved oxygen removal method, requiring manual purging of dissolved oxygen, and as the system proceeds the overall effectiveness decreases due to the accumulation of reactive iodine species, which scavenge free iodide anions and aqueous electrons (eq 8-10) (Park et al., 2011, 2009).



In the combined UV/S+I system, a synergistic relationship emerges in which the iodide anion acts as the primary photosensitizer (due to the higher molar absorptivity and quantum yield), and sulfite reduces the iodide radical back to the iodide anion, thereby effectively regenerating the reaction and allowing iodide to act as a quasi-photocatalyst (eq 13) (Yu et al., 2018).



Furthermore, the resultant sulfite radicals can remove dissolved oxygen as previously discussed, generating the peroxymonosulfate radical (eq 6). Following this, the peroxymonosulfate radical can react with sulfite (eq 14) or itself (eq 15) to generate sulfate radicals, which themselves will be converted into hydroxyl radicals under high pH conditions (eq 16).



The generation of the hydroxyl radicals is critical because, as identified in the gamma irradiation studies, hydroxyl radicals and other oxidizing radicals are critical for facilitating defluorination of PFAS transformation products following their aqueous electron-initiated degradation (O'Connor et al., 2023, 2024). To this end, the combined UV/S+I system is an effective technology for

remediating PFAS in aqueous systems, achieving complete defluorination of PFOS, PFOA, 6:2 FTS, PFBS, and dilute AFFF formulations in less than 8-12 hours (O'Connor et al., 2023, 2024). The ability to achieve complete defluorination of PFAS in aqueous matrices presents itself as an attractive option for modification into a robust analytical assay for the determination of organic fluorine present in a sample. This type of reducible organic fluorine assay would be further enhanced by taking place after an oxidation pre-treatment step to remove dissolved organic matter and other interferents, something that has been employed with success in the remediation research area (Liu et al., 2021).

2.8. *Nanomaterials*

Inspired by Richard Feynman in his famous 1959 talk *There's Plenty of Room at The Bottom*, nanotechnology is a field that examines the direct manipulation of matter at the nanometer scale, mainly atoms, molecules, and supermolecules (Drexler, 1986). Nanotechnology focuses on the difference between the bulk material and the nanoscale material and exploits those differences to synthesize materials with unique properties. As a material approaches the nanoscale, its surface area – volume ratio increases rapidly, and many physiochemical properties of the material become different than the properties of the bulk material including reactivity, strength, diffusivity, elasticity, electrical conductivity, and thermal conductivity. When a dimension of a material becomes smaller than the wavelength of visible light and is at the same scale as biological supermolecules (DNA/proteins) the material can be used in a wide range of applications, including but not limited to; medical probing, DNA-labelling, quantum computing, nanometer-resolution microscopy techniques, catalysis, drug delivery, material coatings, energy generation, energy storing, 3D tissue engineering, and more. The applications of nanotechnology continue to increase when examining the growing incorporation of nanoparticles into commercial products, particularly in textiles (Guo et al., 2021; Salama et al., 2021).

2.9. *Nanomaterial Toxicity*

Both silver and copper are recognized as having antimicrobial, antiviral, and/or antifungal properties (Asghar et al., 2018; Chen and Chiang, 2008; Dural Erem et al., 2011; Hebeish et al., 2011; MacKeen et al., 1987; Xu et al., 2018). In the case of silver nanomaterials, the exact mechanism of toxicity is still under investigation, but is thought to be either due to the metal

nanomaterial itself interacting with the microbial cell walls and deactivating key enzymes, or direct penetration of the microbial cell followed by rapid dissolution of the nanomaterial into highly toxic silver ions (Fabrega et al., 2009; Morones et al., 2005; Reidy et al., 2013; Sun et al., 2005). In the case of copper nanomaterials, it is hypothesized that copper oxide nanomaterials can disrupt host cell recognition by denaturing the protein structures on viral surfaces, leading to inactivation of viruses regardless of the presence of a viral envelope (Minoshima et al., 2016). In biological receptors, such as humans, the toxicity of silver and copper is highly dependent on its chemical form (e.g. ionic, nanoparticulate, pure, oxide, etc), and the mode of exposure (dermal contact, inhalation, ingestion). In general, the effects of silver on human receptors are limited to the development of argyria, loss of night vision, and the potential for skin damage upon direct contact (Chang et al., 2006; Lu et al., 2010). In the case of copper, there is more research identifying negative health effects, in particular their toxicity to lung cells upon inhalation (Ahamed et al., 2015). These findings were further reinforced during the COVID-19 pandemic, during which several copper-functionalized textiles were brought to market for use in personal face masks without consideration as to the risk of inhalation (Jung et al., 2021; Wang and Wang, 2023). There are currently no guidance values for nanomaterials in Canada, although Health Canada is taking a three phased approach to addressing nanomaterials on the Domestic Substance list, including establishing a list of existing nanomaterials, prioritizing nanomaterials for risk assessment, and investigating substances identified for further work (Health Canada 2022).

2.10. Metal Functionalization of Textiles

Metal and metal oxide nanoparticles are often utilized in functionalized textiles as these materials have enhanced stability and antibacterial efficacy over other forms. Silver is often selected for antibacterial applications, and copper is selected for antiviral and antifungal applications (Fauss, 2008; Idumah, 2021; Vance et al., 2015). While these applications are typically marketed for athletic wear, there has been renewed interest in the application of these materials in medical textiles after the COVID-19 pandemic (Idumah, 2021). Other than antimicrobial activity, nanomaterials are used in textiles to add unique properties such as increased conductivity (Gasana et al., 2006; Root et al., 2018), self-cleaning (Allahyarzadeh et al., 2013), electromagnetic interference shielding (Lu et al., 2010) and ultraviolet shielding (Shateri-Khalilabad et al., 2017). Furthermore, recent developments in ‘smart’ textiles have seen many of these properties combined into one material, with traditional and green synthesis techniques used to achieve these multi-

functional materials (Assylbekova et al., 2022; Baldwin et al., 2021; Darabi et al., 2020; Dhanawansha et al., 2020; Galante et al., 2022; Ibrahim et al., 2021; Salama et al., 2021; Wibawa et al., 2021; Zhu et al., 2020, 2020).

Synthesis of metal-functionalized textiles is typically performed either ex-situ (nanomaterials are prepared externally and added to the textile) or in-situ (nanomaterials are prepared with the textile directly). The ex-situ approach typically employs an immersion bath or dry padding to add the nanomaterials onto the textile but can struggle with nanomaterial stability (Anita et al., 2011; El-Rafie et al., 2013; Hasan, 2018; Rajendra et al., 2010). The in-situ approach typically uses an electroless plating or chemical reduction method to convert ionic metals to their metal or metal oxide counterparts, which are then stabilized by the textile polymer matrix (Chen et al., 2017; Liu et al., 2017; Rafique et al., 2017; Root et al., 2018; Srikar et al., 2016). Some of these in-situ methods use an added reducing agent (e.g., glucose) (Vigneshwaran et al., 2006) or use the textile polymer itself (e.g., cellulose in cotton textiles) as the reducing agent (Allahyarzadeh et al., 2013; Maryan et al., 2015; Montazer and Allahyarzadeh, 2013). While the in-situ synthesis method typically results in more stable nanomaterials, there still exists the potential for the release of these metals from the textile into the environment, or humans.

2.11. Release of Metals from Textiles

Within the metal-functionalized textile market, the majority of the textiles are functionalized with silver, which is reflected in the literature (Fauss, 2008; Vance et al., 2015). It is hypothesized that many of the conclusions drawn in the silver-release literature will be at least partially applicable to copper-functionalized textiles if and when they see widespread commercialization.

Across the active life cycle of metal-functionalized textiles, it is possible for metals (e.g. silver) to be released, either during washing, or during wear and use. The silver release characteristics of textiles are heavily influenced by several variables including; initial species, manufacturing method, physical use, sunlight, humidity, chemical interactions with detergent and sweat, friction during the washing cycle, temperature, textile components and textile functionalization (Benn and Westerhoff, 2008; Ding et al., 2016; Glover et al., 2011; Lombi et al., 2014; Quadros et al., 2013; Von Goetz et al., 2013; Wagener et al., 2016). The numerous variables heavily affect the concentration, size, and shape of the silver, which once released can undergo transformations either in the immediate environment, or end-destination environments.

The initial speciation of silver is very important in determining its relative silver release. Information from various antimicrobial textile patents show that the silver in commercially available textiles can be grouped under one of three types: metallic bulk silver, silver nanoparticles, or silver salts. Typically, silver salts result in the largest relative silver release, while bulk silver results in the largest overall silver release for a given wash event (Nowack et al., 2011). The amount of silver released is also heavily influenced by how the silver is incorporated into the textile during the manufacturing process. For silver salt containing textiles, the manufacturing process either involves soaking the textile in the silver salt solution and drying it or embedding the silver salts into the inner fibers of the textile (Wagener et al., 2016). Silver nanoparticle-based textiles often have the silver nanoparticles mounted to a metal or polymer matrix that keeps them adhered to the fibers. For metallic silver-based textiles, the fibres are often coated in a layer of silver through electroless deposition processes and then incorporated into the textile yarn during manufacturing. Each of these manufacturing processes can result in the same type of silver species releasing differently based on how strongly bound it is to the textile or how easily it is exposed to the external environment.

During its regular use silver-containing textiles can undergo physical weathering (stretching, friction), chemical weathering (dissolution into sweat, water) (Benn and Westerhoff, 2008; Kulthong et al., 2010; Von Goetz et al., 2013), and ageing from the sun (Ding et al., 2016). The various stresses that the textile undergo affect not only the silver in the textile, but the textile itself.

Therefore, when examining release of silver from textiles it is important to examine the effects of repeated usage as well, as an older or heavily worn textile may release silver differently. When the silver is mobilized from the textile and released into a transport media, it can undergo various transformations (Mitrano et al., 2015). The media can be sweat adsorbed to the fiber, detergent solution, water, urine, blood, or even the air (Glover et al., 2011).

Once released the initial silver species could be present as silver nanoparticles, micrometer scale silver, or ionic silver. Given the media the silver was released into various transformations can occur. Silver ions can precipitate out as silver chloride, silver sulfide, silver chloro-complexes, or undergo reduction reactions to form silver nanoparticles (Von Goetz et al., 2013). Silver nanoparticles, either present from the release or the result of ionic transformation, can aggregate with other nanoparticles, develop precipitate coatings, or dissolve into silver ions. These transformations can occur quickly or happen across a time scale of days or weeks (Mitrano et al.,

2014. When silver is released into urine, blood, saliva, or the air it can accumulate in biological systems. In the case of detergent solution release, the silver will be transported into the wastewater system where it can ultimately end up in terrestrial or aquatic systems based on the wastewater treatment processes (Benn and Westerhoff, 2008; Colman et al., 2013).

2.12. References

- Abusallout, I., Wang, J., Hanigan, D., 2021. Emerging investigator series: Rapid defluorination of 22 per- and polyfluoroalkyl substances in water using sulfite irradiated by medium-pressure UV. *Environ Sci (Camb)* 7, 1552–1562. <https://doi.org/10.1039/d1ew00221j>
- Agency, U.S.E.P., 2021. EPA Method 8327 Per- and Polyfluoroalkyl Substances (PFAS) By Liquid Chromatography/Tandem Mass Spectrometry (LC/MS/MS).
- Ahamed, M., Akhtar, M.J., Alhadlaq, H.A., Alrokayan, S.A., 2015. Assessment of the lung toxicity of copper oxide nanoparticles: Current status. *Nanomedicine* 10, 2365–2377. <https://doi.org/10.2217/nnm.15.72>
- Ahrens, L., Bundschuh, M., 2014. Fate and effects of poly- and perfluoroalkyl substances in the aquatic environment: A review. *Environ Toxicol Chem* 33, 1921–1929. <https://doi.org/10.1002/etc.2663>
- Allahyarzadeh, V., Montazer, M., Nejad, N.H., Samadi, N., 2013a. In situ synthesis of nano silver on polyester using NaOH/Nano TiO₂. *J Appl Polym Sci* 129, 892–900. <https://doi.org/10.1002/app.38907>
- Anita, S., Ramachandran, T., Rajendran, R., Koushik, cv, Mahalakshmi, M., 2011. A study of the antimicrobial property of encapsulated copper oxide nanoparticles on cotton fabric. *Textile Research Journal* 81, 1081–1088. <https://doi.org/10.1177/0040517510397577>
- Asghar, M.A.A., Zahir, E., Shahid, S.M., Khan, M.N., Asghar, M.A.A., Iqbal, J., Walker, G., 2018. Iron, copper and silver nanoparticles: Green synthesis using green and black tea leaves extracts and evaluation of antibacterial, antifungal and aflatoxin B1 adsorption activity. *LWT - Food Science and Technology* 90, 98–107. <https://doi.org/10.1016/j.lwt.2017.12.009>
- Assylbekova, G., Alotaibi, H.F., Yegemberdiyeva, S., Suigenbayeva, A., Sataev, M., Koshkarbaeva, S., Abdurazova, P., Sakibayeva, S., Prokopovich, P., 2022. Sunlight induced synthesis of silver nanoparticles on cellulose for the preparation of antimicrobial textiles. *J Photochem Photobiol* 11. <https://doi.org/10.1016/j.jpap.2022.100134>
- Baker, S., 2022. 3M's 'Forever Chemicals' Crisis Has Come to Europe. Bloomberg.
- Baldwin, S.J., Slaine, P.D., Keltie, E., Palit, S., McKinnell, S.L., Longpré, B.E., Ko, K.R., Green, J., Markle, G., Kim, J.S., McCormick, C., Frampton, J.P., 2021. Non-Woven Textiles Formed from Contact Drawn Poly(ethylene oxide) Fibers Provide Tunable Filtration and Virucidal Properties via Entrapment of Silver Nanoparticles. *ACS Appl Polym Mater* 3, 4245–4255. <https://doi.org/10.1021/acsapm.1c00697>
- Banks, R.E., 1986. Chapter 1 ISOLATION OF FLUORINE BY MOISSAN: SETTING THE SCENE, *Journal of Fluorine Chemistry*.
- Bao, Y., Huang, J., Cagnetta, G., Yu, G., 2019. Removal of F-53B as PFOS alternative in chrome plating wastewater by UV/Sulfite reduction. *Water Res* 163, 114907. <https://doi.org/10.1016/j.watres.2019.114907>
- Barzen-Hanson, K.A., Field, J.A., 2015. Discovery and implications of C2 and C3 perfluoroalkyl sulfonates in aqueous film-forming foams and groundwater. *Environ. Sci. Technol. Lett.* 2, 95.
- Barzen-Hanson, K.A., Roberts, S.C., Choyke, S., Oetjen, K., McAlees, A., Riddell, N., McCrindle, R., Ferguson, P.L., Higgins, C.P., Field, J.A., 2017. Discovery of 40 Classes of Per- and Polyfluoroalkyl Substances in Historical Aqueous Film-Forming Foams (AFFFs) and AFFF-Impacted Groundwater. *Environ Sci Technol.* <https://doi.org/10.1021/acs.est.6b05843>
- Benesh, M., 2022. For decades, the FDA knew toxic “forever chemicals” were dangerous but continued to allow their use [WWW Document]. EWG. URL <https://www.ewg.org/research/decades-fda-knew-toxic-forever-chemicals-were-dangerous-continued-allow-their-use> (accessed 10.9.22).

- Benn, T.M., Westerhoff, P., 2008. Nanoparticle silver released into water from commercially available sock fabrics. *Environ Sci Technol*. <https://doi.org/10.1021/es7032718>
- Bentel, M.J., Liu, Z., Yu, Y., Gao, J., Men, Y., Liu, J., 2020. Enhanced Degradation of Perfluorocarboxylic Acids (PFCAs) by UV/Sulfite Treatment: Reaction Mechanisms and System Efficiencies at pH 12. *Environ Sci Technol Lett* 7, 351–357. <https://doi.org/10.1021/acs.estlett.0c00236>
- Bentel, M.J., Yu, Y., Xu, L., Li, Z., Wong, B.M., Men, Y., Liu, J., 2019. Defluorination of Per- and Polyfluoroalkyl Substances (PFASs) with Hydrated Electrons: Structural Dependence and Implications to PFAS Remediation and Management. *Environ Sci Technol* 53, 3718–3728. <https://doi.org/10.1021/acs.est.8b06648>
- Bhattacharyya, D., Mizuno, H., Rizzuto, A.M., Zhang, Y., Saykally, R.J., Bradforth, S.E., 2020. New Insights into the Charge-Transfer-to-Solvent Spectrum of Aqueous Iodide: Surface versus Bulk. *J Phys Chem Lett* 11, 1656–1661. <https://doi.org/10.1021/acs.jpcclett.9b03857>
- Boucher, J.M., Cousins, I.T., Scheringer, M., Hungerbühler, K., Wang, Z., 2019. Toward a Comprehensive Global Emission Inventory of C4-C10 Perfluoroalkanesulfonic Acids (PFASs) and Related Precursors: Focus on the Life Cycle of C6- and C10-Based Products. *Environ Sci Technol Lett* 6, 1–7. <https://doi.org/10.1021/acs.estlett.8b00531>
- Brennan, N.M., Evans, A.T., Fritz, M.K., Peak, S.A., von Holst, H.E., 2021. Trends in the regulation of per- and polyfluoroalkyl substances (PFAS): A scoping review. *Int J Environ Res Public Health* 18. <https://doi.org/10.3390/ijerph182010900>
- Buck, R.C., Franklin, J., Berger, U., Conder, J.M., Cousins, I.T., Voigt, P. De, Jensen, A.A., Kannan, K., Mabury, S.A., van Leeuwen, S.P.J., 2011. Perfluoroalkyl and polyfluoroalkyl substances in the environment: Terminology, classification, and origins. *Integr Environ Assess Manag* 7, 513–541. <https://doi.org/10.1002/ieam.258>
- Buck, R.C., Korzeniowski, S.H., Laganis, E., Adamsky, F., 2021. Identification and classification of commercially relevant per- and poly-fluoroalkyl substances (PFAS). *Integr Environ Assess Manag* 17, 1045–1055. <https://doi.org/10.1002/ieam.4450>
- Caverly Rae, J.M., Craig, L., Slone, T.W., Frame, S.R., Buxton, L.W., Kennedy, G.L., 2015. Evaluation of chronic toxicity and carcinogenicity of ammonium 2,3,3,3-tetrafluoro-2-(heptafluoropropoxy)-propanoate in Sprague–Dawley rats. *Toxicol. Rep.* 2, 939.
- Chang, A.L.S., Khosravi, V., Egbert, B., 2006. A case of argyria after colloidal silver ingestion. *J Cutan Pathol* 33, 809–811. <https://doi.org/10.1111/j.1600-0560.2006.00557.x>
- Chen, C.Y., Chiang, C.L., 2008. Preparation of cotton fibers with antibacterial silver nanoparticles. *Mater Lett* 62, 3607–3609. <https://doi.org/10.1016/j.matlet.2008.04.008>
- Chen, G., Liu, S., Shi, Q., Gan, J., Jin, B., Men, Y., Liu, H., 2022. Hydrogen-polarized vacuum ultraviolet photolysis system for enhanced destruction of perfluoroalkyl substances. *Journal of Hazardous Materials Letters* 3, 100072. <https://doi.org/10.1016/j.hazl.2022.100072>
- Chen, H., Liao, F., Yuan, Z., Han, X., Xu, C., 2017. Simple and fast fabrication of conductive silver coatings on carbon fabrics via an electroless plating technique. *Mater Lett* 196, 205–208. <https://doi.org/10.1016/j.matlet.2017.03.070>
- Colman, B.P., Arnaout, C.L., Anciaux, S., Gunsch, C.K., Hochella, M.F., Kim, B., Lowry, G. V., McGill, B.M., Reinsch, B.C., Richardson, C.J., Unrine, J.M., Wright, J.P., Yin, L., Bernhardt, E.S., 2013. Low Concentrations of Silver Nanoparticles in Biosolids Cause Adverse Ecosystem Responses under Realistic Field Scenario. *PLoS One*. <https://doi.org/10.1371/journal.pone.0057189>

- D'Agostino, L.A., Mabury, S.A., 2014. Identification of Novel Fluorinated Surfactants in Aqueous Film Forming Foams and Commercial Surfactant Concentrates. *Environ Sci Technol* 48, 121–129. <https://doi.org/10.1021/es403729e>
- Darabi, S., Hummel, M., Rantasalo, S., Rissanen, M., Öberg Månsson, I., Hilke, H., Hwang, B., Skrifvars, M., Hamed, M.M., Sixta, H., Lund, A., Müller, C., 2020. Green Conducting Cellulose Yarns for Machine-Sewn Electronic Textiles. *ACS Appl Mater Interfaces* 12, 56403–56412. <https://doi.org/10.1021/acsami.0c15399>
- Darlington, R., Barth, E., McKernan, J., 2018. The Challenges of PFAS Remediation EPA Public Access. *Ecosyst Serv* 23, 58–60.
- Das, T.N., 2001. Reactivity and role of SO₅^{•-} radical in aqueous medium chain oxidation of sulfite to sulfate and atmospheric sulfuric acid generation. *Journal of Physical Chemistry A* 105, 9142–9155. <https://doi.org/10.1021/jp011255h>
- Das, T.N., Huie, R.E., Neta, P., 1999. Reduction potentials of SO₃ center dot-, SO₅ center dot-, and S₄O₆ center dot 3- radicals in aqueous solution. *Journal of Physical Chemistry A* 103, 3581–3588.
- Deister, Ursula., Warneck, P., 1990. Photooxidation of sulfite (SO₃²⁻) in aqueous solution. *American Chemical Society* 94, 2191–2198.
- Delile, H., Blichert-Toft, J., Goiran, J.P., Keay, S., Albarède, F., 2014. Lead in ancient Rome's city waters. *Proc Natl Acad Sci U S A* 111, 6594–6599. <https://doi.org/10.1073/pnas.1400097111>
- Dhanawansha, K.B., Senadeera, R., Gunathilake, S.S., Dassanayake, B.S., 2020. Silver nanowire-containing wearable thermogenic smart textiles with washing stability. *Adv Nano Res* 9, 123–131. <https://doi.org/10.12989/anr.2020.9.2.123>
- Ding, D., Chen, L., Dong, S., Cai, H., Chen, J., Jiang, C., Cai, T., 2016. Natural ageing process accelerates the release of Ag from functional textile in various exposure scenarios. *Sci Rep* 6, 37314. <https://doi.org/10.1038/srep37314>
- Dong, H., Qiang, Z., Richardson, S.D., 2019. Formation of Iodinated Disinfection Byproducts (I-DBPs) in Drinking Water: Emerging Concerns and Current Issues. *Acc Chem Res* 52, 896–905. <https://doi.org/10.1021/acs.accounts.8b00641>
- Drexler, E., 1986. The coming era of nanotechnology.
- Duan, X., Niu, X., Gao, J., Waclawek, S., Tang, L., Dionysiou, D.D., 2022. Comparison of sulfate radical with other reactive species. *Curr Opin Chem Eng*. <https://doi.org/10.1016/j.coche.2022.100867>
- Dural Erem, A., Ozcan, G., Skrifvars, M., 2011. Antibacterial activity of PA6/ZnO nanocomposite fibers. *Textile Research Journal* 81, 1638–1646. <https://doi.org/10.1177/0040517511407380>
- Ehrenberg, W., 1947. History of Alchemy and Early Chemistry. *Nature* 160, 330–331. <https://doi.org/10.1038/159333a0>
- Eisinger, J., 1982. Lead and Wine Eberhard Gockel and the Colica Pictonum. *Med Hist* 26, 279–302. <https://doi.org/10.1017/S0025727300041508>
- El-Rafie, H.M., El-Rafie, M.H., Zahran, M.K., 2013. Green synthesis of silver nanoparticles using polysaccharides extracted from marine macro algae. *Carbohydr Polym* 96, 403–410. <https://doi.org/10.1016/j.carbpol.2013.03.071>
- Environmental Working Group (EWG), 2019. For 50 years, polluters knew pfas chemicals were dangerous but hid risks from public 1–26.

- EPA, 2000. The History of Drinking Water Treatment. EPA.
- Fabrega, J., Renshaw, J.C., Lead, J.R., 2009. Interactions of silver nanoparticles with *Pseudomonas putida* biofilms. *Environ Sci Technol* 43, 9004–9009. <https://doi.org/10.1021/es901706j>
- Fan, X., Bao, Y., Mumtaz, M., Huang, J., Yu, G., 2021. Determination of total oxidizable precursors in foam surfactants and foam contaminated water based on UV-activated persulfate oxidation. *Science of the Total Environment* 763, 142943. <https://doi.org/10.1016/j.scitotenv.2020.142943>
- Fauss, E., 2008. The Silver Nanotechnology Commercial Inventory.
- Frank, Matthew G. annis, Watkins, M., 2019. Treatment of Perfluoroalkyl Acids by Heat-Activated Persulfate Under Conditions Representative of In Situ Chemical Oxidation. *Chemosphere* 1, 678–687. <https://doi.org/10.1016/j.chemosphere.2018.04.128>. Treatment
- Gaber, N., Bero, L., Woodruff, T.J., 2023. The Devil they Knew: Chemical Documents Analysis of Industry Influence on PFAS Science. *Ann Glob Health* 89, 37. <https://doi.org/10.5334/aogh.4013>
- Galante, A.J., Pilsbury, B.C., Yates, K.A., LeMieux, M., Bain, D.J., Shanks, R.M.Q., Romanowski, E.G., Leu, P.W., 2022. Reactive silver inks for antiviral, repellent medical textiles with ultrasonic bleach washing durability compared to silver nanoparticles. *PLoS One* 17, e0270718. <https://doi.org/10.1371/journal.pone.0270718>
- Gale, N.H., Stos-Gale, Z., 1981. Lead and Silver in the Ancient Aegean.
- Gannon, S.A., Fasano, W.J., Mawn, M.P., Nabb, D.L., Buck, R.C., Buxton, L.W., Jepson, G.W., Frame, S.R., 2016. Absorption, distribution, metabolism, excretion, and kinetics of 2,3,3,3-tetrafluoro-2-(heptafluoropropoxy)propanoic acid ammonium salt following a single dose in rat, mouse, and cynomolgus monkey. *Toxicology* 340, 1.
- Gasana, E., Westbroek, P., Hakuzimana, J., de Clerck, K., Prinotakis, G., Kiekens, P., Tseles, D., 2006. Electroconductive textile structures through electroless deposition of polypyrrole and copper at polyaramide surfaces. *Surf Coat Technol* 201, 3547–3551. <https://doi.org/10.1016/j.surfcoat.2006.08.128>
- Gebbink, W.A., Glynn, A., Darnerud, P.O., Berger, U., 2015. Perfluoroalkyl acids and their precursors in Swedish food: The relative importance of direct and indirect dietary exposure. *Environmental Pollution* 198, 108–115. <https://doi.org/10.1016/j.envpol.2014.12.022>
- Getoff, N., 1996. Radiation-induced degradation of water pollutants - State of the art. *Radiation Physics and Chemistry* 47, 581–593. [https://doi.org/10.1016/0969-806X\(95\)00059-7](https://doi.org/10.1016/0969-806X(95)00059-7)
- Gilfillan, S.C., 1965. Lead Poisoning and the Fall of Rome. *J Occup Environ Med* 7.
- Glover, C.M., Pazoki, F., Munoz, G., Sauv e, S., Liu, J., 2024. Applying the modified UV-activated TOP assay to complex matrices impacted by aqueous film-forming foams. *Science of the Total Environment* 924. <https://doi.org/10.1016/j.scitotenv.2024.171292>
- Glover, R.D., Miller, J.M., Hutchison, J.E., 2011. Generation of metal nanoparticles from silver and copper objects: Nanoparticle dynamics on surfaces and potential sources of nanoparticles in the environment. *ACS Nano* 5, 8950–8957. <https://doi.org/10.1021/nn2031319>
- Gl uge, J., Scheringer, M., Cousins, I.T., Dewitt, J.C., Goldenman, G., Herzke, D., Lohmann, R., Ng, C.A., Trier, X., Wang, Z., 2020. An overview of the uses of per- And polyfluoroalkyl substances (PFAS). *Environ Sci Process Impacts* 22, 2345–2373. <https://doi.org/10.1039/d0em00291g>
- G ockener, B., Eichhorn, M., L ammer, R., Kotthoff, M., Kowalczyk, J., Numata, J., Schafft, H., Lahrssen-Wiederholt, M., B ucking, M., 2020. Transfer of Per- And Polyfluoroalkyl Substances (PFAS) from Feed into

the Eggs of Laying Hens. Part 1: Analytical Results including a Modified Total Oxidizable Precursor Assay. *J Agric Food Chem*. <https://doi.org/10.1021/acs.jafc.0c04456>

Goldwhite, H., 1989. *Chemical Notes, Hints, Suggestions and Objects of Pursuit" of 1822*, Peregrinus, London, 1991. 11. W. T, Brande, *A Manual of Chemistry, Elements of Chemical Philosophy*, Part. Dawson & Son Ltd.

Gomis, M.I., Wang, Z., Scheringer, M., Cousins, I.T., 2015. A modeling assessment of the physicochemical properties and environmental fate of emerging and novel per- and polyfluoroalkyl substances. *Sci. Total Environ*. 505, 981.

Government of Canada, 2022. *Prohibition of Certain Toxic Substances Regulations, 2022* [WWW Document]. *Canada Gazette*.

Grandjean, P., 2018. Delayed discovery, dissemination, and decisions on intervention in environmental health: A case study on immunotoxicity of perfluorinated alkylate substances. *Environ Health* 17, 1–6. <https://doi.org/10.1186/s12940-018-0405-y>

Granum, B., Haug, L.S., Namork, E., Stølevik, S.B., Thomsen, C., Aaberge, I.S., Van Loveren, H., Løvik, M., Nygaard, U.C., 2013. Pre-natal exposure to perfluoroalkyl substances may be associated with altered vaccine antibody levels and immune-related health outcomes in early childhood. *J Immunotoxicol* 10, 373–379. <https://doi.org/10.3109/1547691X.2012.755580>

Greenwood, N.N., Earnshaw, A., 1984. *Chemistry of the Elements*. Elsevier Science & Technology.

Gu, J., Ma, J., Jiang, J., Yang, L., Yang, J., Zhang, J., Chi, H., Song, Y., Sun, S., Tian, W.Q., 2017. Hydrated electron (eaq⁻) generation from phenol/UV: Efficiency, influencing factors, and mechanism. *Appl Catal B* 200, 585–593. <https://doi.org/10.1016/j.apcatb.2016.07.034>

Guo, Z., Wang, Y., Huang, J., Zhang, S., Zhang, R., Ye, D., Cai, G., Yang, H., Gu, S., Xu, W., 2021. Multi-functional and water-resistant conductive silver nanoparticle-decorated cotton textiles with excellent joule heating performances and human motion monitoring. *Cellulose* 28, 7483–7495. <https://doi.org/10.1007/s10570-021-03955-y>

Habashi, F., 1998. The age of alchemy History of chemistry, metallurgy, and civilisation. *Interdisciplinary Science Reviews* 23, 348–361. <https://doi.org/10.1179/030801898789764336>

Hart, E., 1964. The Hydrated Electron 146.

Hart, E., Gordon, S., Fielden, E., 1965. Reaction of the Hydrated Electron with Water.

Hasan, R., 2018. Production of Antimicrobial Textiles by Using Copper Oxide Nanoparticles. *International Journal of Contemporary Research and Review* 9, 20195–20202. <https://doi.org/10.15520/ijcrr/2018/9/08/564>

Haszeldine, R.N., 1953a. 676. Fluoro-olefins. Part II. Synthesis and reactions of some 3 : 3 : 3-trihalogenopropenes. *Journal of the Chemical Society (Resumed)* 3371–3378. <https://doi.org/10.1039/JR9530003371>

Haszeldine, R.N., 1953b. 715. The addition of free radicals to unsaturated systems. Part IV. The direction of radical addition to hexafluoropropene. *Journal of the Chemical Society (Resumed)* 3559–3564. <https://doi.org/10.1039/JR9530003559>

Haszeldine, R.N., Hobson, D.L., Taylor, D.R., 1976. Organophosphorus chemistry. Part 19. Free-radical addition of dialkyl phosphites to polyfluoro-olefins. *J Fluor Chem* 8, 115–124. [https://doi.org/https://doi.org/10.1016/S0022-1139\(00\)82689-5](https://doi.org/https://doi.org/10.1016/S0022-1139(00)82689-5)

Hayes, J., 2022. Dow, 3M and others likely exploit loophole to avoid reporting 'forever chemicals' releases [WWW Document]. Environmental Working Group. URL <https://www.ewg.org/news-insights/news/2022/09/dow-3m-and-others-likely-exploit-loophole-avoid-reporting-forever> (accessed 12.9.22).

Health Canada. Environment and Climate Change Canada, 2022. Guidance document for the New Substances Notification Regulations (Chemicals and Polymers).

Hebeish, A., El-Naggar, M.E., Fouda, M.M.G., Ramadan, M.A., Al-Deyab, S.S., El-Rafie, M.H., 2011. Highly effective antibacterial textiles containing green synthesized silver nanoparticles. *Carbohydr Polym* 86, 936–940. <https://doi.org/10.1016/j.carbpol.2011.05.048>

Herodotus, B., 2008. *The History Of Herodotus Volume 1 (of 2) THE HISTORY OF HERODOTUS*.

Herzke, D., Olsson, E., Posner, S., 2012. Perfluoroalkyl and polyfluoroalkyl substances (PFASs) in consumer products in Norway - A pilot study. *Chemosphere* 88, 980–987. <https://doi.org/10.1016/j.chemosphere.2012.03.035>

Heuckeroth, S., Nxumalo, T.N., Raab, A., Feldmann, J., 2021. Fluorine-Specific Detection Using ICP-MS Helps to Identify PFAS Degradation Products in Nontargeted Analysis. *Anal Chem* 93, 6335–6341. <https://doi.org/10.1021/acs.analchem.1c00031>

Heydebreck, F., Tang, J., Xie, Z., Ebinghaus, R., 2015. Alternative and legacy perfluoroalkyl substances: Differences between european and chinese river/estuary systems. *Environ. Sci. Technol.* 49, 8386.

Hodge, A.T., 1981. Vitruvius, Lead Pipes and Lead Poisoning. *American Journal of Archaeology* 85, 486–491. <https://doi.org/10.2307/504874>

Hogue, C., 2019. 3M admits to unlawful release of PFAS. *C&EN Global Enterprise* 97, 16. <https://doi.org/10.1021/cen-09726-polcon1>

Hoke, R.A., Ferrell, B.D., Sloman, T.L., Buck, R.C., Buxton, L.W., 2016. Aquatic hazard, bioaccumulation and screening risk assessment for ammonium 2,3,3,3-tetrafluoro-2-(heptafluoropropoxy)-propanoate. *Chemosphere* 149, 336.

Holmes, T., 2021. Potential Biden Administration Changes. *Journal AWWA* 113, 5–5. <https://doi.org/10.1002/awwa.1645>

Hori, H., Yamamoto, A., Hayakawa, E., Taniyasu, S., Yamashita, N., Kutsuna, S., Kiatagawa, H., Arakawa, R., 2005. Efficient decomposition of environmentally persistent perfluorocarboxylic acids by use of persulfate as a photochemical oxidant. *Environ Sci Technol* 39, 2383–2388. <https://doi.org/10.1021/es0484754>

Hosseiny, S.H., Bozorg-Haddad, O., Bocchiola, D., 2021. 9 - Water, culture, civilization, and history, in: Bozorg-Haddad, O. (Ed.), *Economical, Political, and Social Issues in Water Resources*. Elsevier, pp. 189–216. <https://doi.org/https://doi.org/10.1016/B978-0-323-90567-1.00010-3>

Houtz, E.F., Higgins, C.P., Field, J.A., Sedlak, D.L., 2013. Persistence of perfluoroalkyl acid precursors in AFFF-impacted groundwater and soil. *Environ Sci Technol* 47, 8187–8195. <https://doi.org/10.1021/es4018877>

Houtz, E.F., Sedlak, D.L., 2012. Oxidative conversion as a means of detecting precursors to perfluoroalkyl acids in urban runoff. *Environ Sci Technol* 46, 9342–9349. <https://doi.org/10.1021/es302274g>

Hutchinson, S., Rieck, T., Wu, X.L., 2020. Advanced PFAS precursor digestion methods for biosolids. *Environmental Chemistry* 17, 558–567. <https://doi.org/10.1071/EN20008>

- Iavetz, R., Lewin, M., Morschel, G., Slee, D., Lim, C., Nolan, A., Grimison, C., Centner, M., Mcgrath, S., Symons, B., 2019. PFAS TOP Assay Interlaboratory Study Supporting Analytical Laboratories 557–558.
- Ibrahim, H.M., Zaghloul, S., Hashem, M., El-Shafei, A., 2021. A green approach to improve the antibacterial properties of cellulose based fabrics using *Moringa oleifera* extract in presence of silver nanoparticles. *Cellulose* 28, 549–564. <https://doi.org/10.1007/s10570-020-03518-7>
- Idumah, C.I., 2021. Influence of nanotechnology in polymeric textiles, applications, and fight against COVID-19. *Journal of the Textile Institute* 112, 2056–2076. <https://doi.org/10.1080/00405000.2020.1858600>
- Ike, I.A., Karanfil, T., Cho, J., Hur, J., 2019. Oxidation byproducts from the degradation of dissolved organic matter by advanced oxidation processes – A critical review. *Water Res* 164. <https://doi.org/10.1016/j.watres.2019.114929>
- Janda, J., Nödler, K., Scheurer, M., Happel, O., Nürenberg, G., Zwiener, C., Lange, F.T., 2019. Closing the gap-inclusion of ultrashort-chain perfluoroalkyl carboxylic acids in the total oxidizable precursor (TOP) assay protocol. *Environ Sci Process Impacts* 21, 1926–1935. <https://doi.org/10.1039/c9em00169g>
- Jian, J.M., Guo, Y., Zeng, L., Liang-Ying, L., Lu, X., Wang, F., Zeng, E.Y., 2017. Global distribution of perfluorochemicals (PFCs) in potential human exposure source—A review. *Environ Int* 108, 51–62. <https://doi.org/10.1016/j.envint.2017.07.024>
- Jortner, J., Ottolenghi, M., Stein, G., 1963. The Formation of Solvated Electrons in the Photochemistry of the Phenolate Ion in Aqueous Solutions. *J Am Chem Soc* 85, 2712–2715. <https://doi.org/10.1021/ja00901a007>
- Jung, S., Byeon, E.Y., Kim, D.G., Lee, D.G., Ryoo, S., Lee, Sanggu, Shin, C.W., Jang, H.W., Yang, J.Y., Kim, H.J., Lee, Seunghun, 2021. Copper-coated polypropylene filter face mask with SARS-COV-2 antiviral ability. *Polymers (Basel)* 13. <https://doi.org/10.3390/polym13091367>
- Kaiser, A.M., Saracevic, E., Schaar, H.P., Weiss, S., Hornek-Gausterer, R., 2021. Ozone as oxidizing agent for the total oxidizable precursor (TOP) assay and as a preceding step for activated carbon treatments concerning per- and polyfluoroalkyl substance removal. *J Environ Manage* 300, 113692. <https://doi.org/10.1016/j.jenvman.2021.113692>
- Kauffman, G.B., 1985. The role of gold in alchemy. Part II. *Gold Bull* 18, 69–78. <https://doi.org/10.1007/BF03214689>
- Kim, T.H., Lee, S.H., Kim, H.Y., Doudrick, K., Yu, S., Kim, S.D., 2019. Decomposition of perfluorooctane sulfonate (PFOS) using a hybrid process with electron beam and chemical oxidants. *Chemical Engineering Journal* 361, 1363–1370. <https://doi.org/10.1016/j.cej.2018.10.195>
- Kim, T.H., Yu, S., Choi, Y., Jeong, T.Y., Kim, S.D., 2018. Profiling the decomposition products of perfluorooctane sulfonate (PFOS) irradiated using an electron beam. *Science of the Total Environment* 631–632, 1295–1303. <https://doi.org/10.1016/j.scitotenv.2018.03.055>
- Kowald, C., Brorman, E., Shankar, S., Klemashevich, C., Staack, D., Pillai, S.D., 2021. PFOA and PFOS breakdown in experimental sand, laboratory-grade water, investigation-derived groundwater and wastewater effluent samples at 50 kGy electron beam dose. *Radiation Physics and Chemistry* 180. <https://doi.org/10.1016/j.radphyschem.2020.109323>
- Kulthong, K., Srisung, S., Boonpavanitchakul, K., Kangwansupamonkon, W., Maniratanachote, R., 2010. Determination of silver nanoparticle release from antibacterial fabrics into artificial sweat. Part *Fibre Toxicol* 7. <https://doi.org/10.1186/1743-8977-7-8>

- Kuzniewski, S., 2022. EPA's detection methods, the drinking water treatability database, and innovative technologies for PFAS remediation. *Remediation* 32, 309–323. <https://doi.org/10.1002/rem.21730>
- Lai, Y., Wang, Y., Zhang, S., Duan, A., 2024. Kinetics and mechanism analysis of advanced oxidation degradation of PFOA/PFOS by UV/Fe³⁺ and persulfate: A DFT study. *Chemosphere* 357. <https://doi.org/10.1016/j.chemosphere.2024.141951>
- Lassalle, J., Gao, R., Rodi, R., Kowald, C., Feng, M., Sharma, V.K., Hoelen, T., Bireta, P., Houtz, E.F., Staack, D., Pillai, S.D., 2021. Degradation of PFOS and PFOA in soil and groundwater samples by high dose Electron Beam Technology. *Radiation Physics and Chemistry* 189, 109705. <https://doi.org/10.1016/j.radphyschem.2021.109705>
- Lea, I.A., Pham, L.L., Antonijevic, T., Thompson, C., Borghoff, S.J., 2022. Assessment of the applicability of the threshold of toxicological concern for per- and polyfluoroalkyl substances. *Regulatory Toxicology and Pharmacology* 133. <https://doi.org/10.1016/j.yrtph.2022.105190>
- Lewis, R.E., Huang, C.H., White, J.C., Haynes, C.L., 2023. Using 19F NMR to Investigate Cationic Carbon Dot Association with Per- and Polyfluoroalkyl Substances (PFAS). *ACS Nanoscience Au* 3, 408–417. <https://doi.org/10.1021/acsnanoscienceau.3c00022>
- Li, C., Hoffman, M.Z., 1999. One-Electron Redox Potentials of Phenols in Aqueous Solution. *Journal of Physical Chemistry B* 103, 6653–6656. <https://doi.org/10.1021/jp983819w>
- Li, X., Fang, J., Liu, G., Zhang, S., Pan, B., Ma, J., 2014. Kinetics and efficiency of the hydrated electron-induced dehalogenation by the sulfite/UV process. *Water Res* 62, 220–228. <https://doi.org/10.1016/j.watres.2014.05.051>
- Liu, C.S., Higgins, C.P., Wang, F., Shih, K., 2012. Effect of temperature on oxidative transformation of perfluorooctanoic acid (PFOA) by persulfate activation in water. *Sep Purif Technol* 91, 46–51. <https://doi.org/10.1016/j.seppur.2011.09.047>
- Liu, K.G., Abbasi, A.R., Azadbakht, A., Hu, M.L., Morsali, A., 2017. Deposition of silver nanoparticles on polyester fiber under ultrasound irradiations. *Ultrason Sonochem* 34, 13–18. <https://doi.org/10.1016/j.ultsonch.2016.04.006>
- Liu, X., Guo, Z., Krebs, K.A., Pope, R.H., Roache, N.F., 2014. Concentrations and trends of perfluorinated chemicals in potential indoor sources from 2007 through 2011 in the US. *Chemosphere* 98, 51–57. <https://doi.org/10.1016/j.chemosphere.2013.10.001>
- Liu, Y., Pereira, A.D.S., Martin, J.W., 2015. Discovery of C5-C17 Poly- and perfluoroalkyl substances in water by in-line Spe-HPLC-Orbitrap with in-source fragmentation flagging. *Anal Chem* 87, 4260–4268. <https://doi.org/10.1021/acs.analchem.5b00039>
- Liu, Z., Bentel, M.J., Yu, Y., Ren, C., Gao, J., Pulikkal, V.F., Sun, M., Men, Y., Liu, J., 2021. Near-Quantitative Defluorination of Perfluorinated and Fluorotelomer Carboxylates and Sulfonates with Integrated Oxidation and Reduction. *Environ Sci Technol* 55, 7052–7062. <https://doi.org/10.1021/acs.est.1c00353>
- Lofrano, G., Brown, J., 2010. Wastewater management through the ages: A history of mankind. *Science of the Total Environment*. <https://doi.org/10.1016/j.scitotenv.2010.07.062>
- Lohmann, R., Cousins, I.T., Dewitt, J.C., Glüge, J., Goldenman, G., Herzke, D., Lindstrom, A.B., Miller, M.F., Ng, C.A., Patton, S., Scheringer, M., Trier, X., Wang, Z., 2020. Are Fluoropolymers Really of Low Concern for Human and Environmental Health and Separate from Other PFAS? *Environ Sci Technol* 54, 12820–12828. <https://doi.org/10.1021/acs.est.0c03244>

- Lombi, E., Donner, E., Scheckel, K.G., Sekine, R., Lorenz, C., Goetz, N. Von, Nowack, B., 2014. Silver speciation and release in commercial antimicrobial textiles as influenced by washing. *Chemosphere*. <https://doi.org/10.1016/j.chemosphere.2014.03.116>
- Lu, G.H., Gai, N., Zhang, P., Piao, H.T., Chen, S., Wang, X.C., Jiao, X.C., Yin, X.C., Tan, K.Y., Yang, Y.L., 2017. Perfluoroalkyl acids in surface waters and tapwater in the Qiantang River watershed—Influences from paper, textile, and leather industries. *Chemosphere* 185, 610–617. <https://doi.org/10.1016/j.chemosphere.2017.06.139>
- Lu, W., Senapati, D., Wang, S., Tovmachenko, O., Singh, A.K., Yu, H., Ray, P.C., 2010. Effect of surface coating on the toxicity of silver nanomaterials on human skin keratinocytes. *Chem Phys Lett* 487, 92–96. <https://doi.org/10.1016/j.cplett.2010.01.027>
- Lu, Y., Jiang, S., Huang, Y., 2010. Ultrasonic-assisted electroless deposition of Ag on PET fabric with low silver content for EMI shielding. *Surf Coat Technol* 204, 2829–2833. <https://doi.org/10.1016/j.surfcoat.2010.02.061>
- Mackay, N., 1991. A Chemical History of 3M.
- MacKeen, P.C., Person, S., Warner, S.C., Snipes, W., Stevens, S.E., 1987. Silver-coated nylon fiber as an antibacterial agent. *Antimicrob Agents Chemother* 31, 93–99. <https://doi.org/10.1128/AAC.31.1.93>
- Markowitz, Rosner, 2000. The Role of The Lead Industry in a Public Health Tragedy, 1900-1955. *Am J Public Health*.
- Maryan, A.S., Montazer, M., Harifi, T., 2015. Synthesis of nano silver on cellulosic denim fabric producing yellow colored garment with antibacterial properties. *Carbohydr Polym* 115, 568–574. <https://doi.org/10.1016/j.carbpol.2014.08.100>
- Maza, W.A., Breslin, V.M., Owrutsky, J.C., 2024. Early steps in the advanced reduction process of the hydrated electron: lessons learned from transient spectroscopy. *Curr Opin Chem Eng*. <https://doi.org/10.1016/j.coche.2024.101015>
- Minoshima, M., Lu, Y., Kimura, T., Nakano, R., Ishiguro, H., Kubota, Y., Hashimoto, K., Sunada, K., 2016. Comparison of the antiviral effect of solid-state copper and silver compounds. *J Hazard Mater* 312, 1–7. <https://doi.org/10.1016/j.jhazmat.2016.03.023>
- Mitrano, D.M., Motellier, S., Clavaguera, S., Nowack, B., 2015. Review of nanomaterial aging and transformations through the life cycle of nano-enhanced products. *Environ Int* 77, 132–147. <https://doi.org/10.1016/j.envint.2015.01.013>
- Mitrano, D.M., Ranville, J.F., Bednar, A., Kazor, K., Hering, A.S., Higgins, C.P., n.d. Tracking dissolution of silver nanoparticles at environmentally relevant concentrations in laboratory, natural, and processed waters using single particle ICP-MS (spICP-MS). <https://doi.org/10.1039/c3en00108c>
- Montazer, M., Allahyarzadeh, V., 2013. Electroless plating of silver nanoparticles/nanolayer on polyester fabric using AgNO₃/NaOH and ammonia. *Ind Eng Chem Res* 52, 8436–8444. <https://doi.org/10.1021/ie400804n>
- Morgan, M.S., Van Trieste, P.F., Garlick, S.M., Mahon, M.J., Smith, A.L., 1988. Ultraviolet molar absorptivities of aqueous hydrogen peroxide and hydroperoxyl ion. *Anal Chim Acta* 215, 325–329. [https://doi.org/10.1016/S0003-2670\(00\)85294-0](https://doi.org/10.1016/S0003-2670(00)85294-0)
- Morones, J.R., Elechiguerra, J.L., Camacho, A., Holt, K., Kouri, J.B., Ram, J.T., Yacaman, M.J., 2005. The bactericidal effect of silver nanoparticles. *Nanotech* 2346–2353. <https://doi.org/10.1088/0957-4484/16/10/059>

- Nabb, D.L., Szostek, B., Himmelstein, M.W., Mawn, M.P., Gargas, M.I., Sweeney, L.M., Stadler, J.C., Buck, R.C., Fasano, W.J., 2007. In vitro metabolism of 8-2 fluorotelomer alcohol: Interspecies comparisons and metabolic pathway refinement. *Toxicological Sciences* 100, 333–344. <https://doi.org/10.1093/toxsci/kfm230>
- Nakayama, S., Strynar, M.J., Helfant, L., Egeghy, P., Ye, X., Lindstrom, A.B., 2007. Perfluorinated compounds in the Cape Fear drainage basin in North Carolina. *Environ. Sci. Technol.* 41, 5271.
- Neta, P., Huie, R.E., 1985. Free-Radical Chemistry of Sulfite, *Environmental Health Perspectives*.
- Neuwald, I.J., Hu, D., Wiegand, H.L., Valkov, V., Borchers, U., Karsten, N., Scheurer, M., Hale, S.E., Arp, H.P.H., Zahn, D., 2022. Ultra-Short-Chain PFASs in the Sources of German Drinking Water: Prevalent, Overlooked, Difficult to Remove, and Unregulated. <https://doi.org/10.1021/acs.est.1c07949>
- Nickerson, A., Maizel, A.C., Kulkarni, P.R., Adamson, D.T., Kornuc, J.J., Higgins, C.P., 2020. Enhanced Extraction of AFFF-Associated PFASs from Source Zone Soils. *Environ Sci Technol* 54, 4952–4962. <https://doi.org/10.1021/acs.est.0c00792>
- Nolan, A., Grimison, C., Javetz, R., Slee, D., Lim, C., 2019. Improving Measurement Reliability of the PFAS TOP Assay 559–560.
- Nowack, B., Krug, H.F., Height, M., 2011. 120 years of nanosilver history: Implications for policy makers. *Environ Sci Technol.* <https://doi.org/10.1021/es103316q>
- O'Connor, N., Patch, D., Noble, D., Scott, J., Koch, I., Mumford, K.G., Weber, K., 2023. Forever no more : Complete mineralization of per- and polyfluoroalkyl substances (PFAS) using an optimized UV / sulfite / iodide system. *Science of the Total Environment* 888, 164137. <https://doi.org/10.1016/j.scitotenv.2023.164137>
- Olsen, G.W., Mair, D.C., Lange, C.C., Harrington, L.M., Church, T.R., Goldberg, C.L., Herron, R.M., Hanna, H., Nobiletti, J.B., Rios, J.A., Reagen, W.K., Ley, C.A., 2017. Per- and polyfluoroalkyl substances (PFAS) in American Red Cross adult blood donors, 2000–2015. *Environ Res* 157, 87–95. <https://doi.org/10.1016/j.envres.2017.05.013>
- Pan, C.-G., Xiao, S.-K., Yu, K.-F., Wu, Q., Wang, Y.-H., 2021. Legacy and alternative per- and polyfluoroalkyl substances in a subtropical marine food web from the Beibu Gulf, South China: Fate, trophic transfer and health risk assessment. *J Hazard Mater* 403, 123618. <https://doi.org/10.1016/j.jhazmat.2020.123618>
- Park, H., Vecitis, C.D., Cheng, J., Choi, W., Mader, B.T., Hoffmann, M.R., 2009. Reductive defluorination of aqueous perfluorinated alkyl surfactants: Effects of ionic headgroup and chain length. *Journal of Physical Chemistry A* 113, 690–696. <https://doi.org/10.1021/jp807116q>
- Park, H., Vecitis, C.D., Cheng, J., Dalleska, N.F., Mader, B.T., Hoffmann, M.R., 2011. Reductive degradation of perfluoroalkyl compounds with aquated electrons generated from iodide photolysis at 254 nm. *Photochemical and Photobiological Sciences* 10, 1945–1953. <https://doi.org/10.1039/c1pp05270e>
- Patch, D., O'Connor, N., Koch, I., Cresswell, T., Hughes, C., Davies, J.B., Scott, J., O'Carroll, D., Weber, K., 2022. Elucidating degradation mechanisms for a range of per- and polyfluoroalkyl substances (PFAS) via controlled irradiation studies. *Science of the Total Environment* 832, 154941. <https://doi.org/10.1016/j.scitotenv.2022.154941>
- Patch, D., O'Connor, N., Vereecken, T., Murphy, D., Munoz, G., Ross, I., Glover, C., Scott, J., Koch, I., Sauv e, S., Liu, J., Weber, K., 2024. Advancing PFAS characterization: Enhancing the total oxidizable precursor assay with improved sample processing and UV activation. *Science of The Total Environment* 909, 168145. <https://doi.org/10.1016/j.scitotenv.2023.168145>

- Paul, A.G., Jones, K.C., Sweetman, A.J., 2009. A first global production, emission, and environmental inventory for perfluorooctane sulfonate. *Environ Sci Technol* 43, 386–392. <https://doi.org/10.1021/es802216n>
- Paul, S., 2001. Epidemiology , 220-3W-05 Medical Department 3M Company Protocol Number (not applicable) IRB Approval I . 3M Medical Department , 220-3W-05 , St . Paul , MN 55144-1000 "(Corrections made from previous version) 2482163–2482225.
- Periodicals, A., 1849. Alchemy, ancient and modern. *The Eclectic Magazine of Foreign Literature*.
- PFAS National Primary Drinking Water Regulation, n.d.
- Phillips, C.R., 1984. Old Wine in Old Lead Bottles: Nriagu on the Fall of Rome. *The Classical World* 78, 29–33. <https://doi.org/10.2307/4349661>
- Quadros, M.E., Pierson, R., Tulve, N.S., Willis, R., Rogers, K., Thomas, T.A., Marr, L.C., 2013. Release of silver from nanotechnology-based consumer products for children. *Environ Sci Technol*. <https://doi.org/10.1021/es4015844>
- Quiñones, O., Snyder, S.A., 2009. Occurrence of perfluoroalkyl carboxylates and sulfonates in drinking water utilities and related waters from the United States. *Environ. Sci. Technol.* 43, 9089.
- Rafique, M., Sadaf, I., Rafique, M.S., Tahir, M.B., 2017. A review on green synthesis of silver nanoparticles and their applications. *Artif Cells Nanomed Biotechnol* 45, 1272–1291. <https://doi.org/10.1080/21691401.2016.1241792>
- Rajendra, R., Balakumar, C., Ahammed, H., Jayakumar, S., Vaideki, K., Rajesh, E., 2010. Use of zinc oxide nano particles for production of antimicrobial textiles. *International Journal of Engineering, Science and Technology* 2, 202–208. <https://doi.org/10.4314/ijest.v2i1.59113>
- Rayne, S., Forest, K., 2009. Perfluoroalkyl sulfonic and carboxylic acids: A critical review of physicochemical properties, levels and patterns in waters and wastewaters, and treatment methods. *J. Environ. Sci. Health, Part A: Toxic/Hazard. Subst. Environ. Eng.* 44, 1145.
- Read, J., 1951. Alchemy and Alchemists. *Nature* 167, 773/774.
- Rehman, A.U., Crimi, M., Andreescu, S., 2023. Current and emerging analytical techniques for the determination of PFAS in environmental samples. *Trends in Environmental Analytical Chemistry*. <https://doi.org/10.1016/j.teac.2023.e00198>
- Reidy, B., Haase, A., Luch, A., Dawson, K.A., Lynch, I., 2013. Mechanisms of silver nanoparticle release, transformation and toxicity: A critical review of current knowledge and recommendations for future studies and applications. *Materials* 6, 2295–2350. <https://doi.org/10.3390/ma6062295>
- Robel, A.E., Marshall, K., Dickinson, M., Lunderberg, D., Butt, C., Peaslee, G., Stapleton, H.M., Field, J.A., 2017. Closing the Mass Balance on Fluorine on Papers and Textiles. *Environ Sci Technol* 51, 9022–9032. <https://doi.org/10.1021/acs.est.7b02080>
- Root, W., Aguiló-Aguayo, N., Pham, T., Bechtold, T., 2018a. Conductive layers through electroless deposition of copper on woven cellulose lyocell fabrics. *Surf Coat Technol* 348, 13–21. <https://doi.org/10.1016/j.surfcoat.2018.05.033>
- Sadia, M., Nollen, I., Helmus, R., Ter Laak, T.L., Béen, F., Praetorius, A., Van Wezel, A.P., 2023. Occurrence, Fate, and Related Health Risks of PFAS in Raw and Produced Drinking Water. *Environ Sci Technol* 57, 3062–3074. <https://doi.org/10.1021/acs.est.2c06015>

- Salama, A., Abouzeid, R.E., Owda, M.E., Cruz-Maya, I., Guarino, V., 2021. Cellulose–silver composites materials: Preparation and applications. *Biomolecules*. <https://doi.org/10.3390/biom11111684>
- Sauer, M.C., Crowell, R.A., Shkrob, I.A., 2004. Electron photodetachment from aqueous anions. 1. Quantum yields for generation of hydrated electron by 193 and 248 nm laser photoexcitation of miscellaneous inorganic anions. *Journal of Physical Chemistry A* 108, 5490–5502. <https://doi.org/10.1021/jp049722t>
- Schellenberger, S., Liagkouridis, I., Awad, R., Khan, S., Plassmann, M., Peters, G., Benskin, J.P., Cousins, I.T., 2022. An Outdoor Aging Study to Investigate the Release of Per- and Polyfluoroalkyl Substances (PFAS) from Functional Textiles. *Environ Sci Technol* 56, 3471–3479. <https://doi.org/10.1021/acs.est.1c06812>
- Schultes, L., Vestergren, R., Volkova, K., Westberg, E., Jacobson, T., Benskin, J.P., 2018. Per- and polyfluoroalkyl substances and fluorine mass balance in cosmetic products from the Swedish market: Implications for environmental emissions and human exposure. *Environ Sci Process Impacts* 20, 1680–1690. <https://doi.org/10.1039/c8em00368h>
- Schwarz, H., 1992. Reaction of the Hydrated Electron with Water. *Molecular Crystals and Liquid* 96, 4087.
- Shateri-Khalilabad, M., Yazdanshenas, M.E., Etemadifar, A., 2017. Fabricating multifunctional silver nanoparticles-coated cotton fabric. *Arabian Journal of Chemistry* 10, S2355–S2362. <https://doi.org/10.1016/j.arabjc.2013.08.013>
- Shih, Y.H., Blomberg, A.J., Bind, M.A., Holm, D., Nielsen, F., Heilmann, C., Weihe, P., Grandjean, P., 2021. Serum vaccine antibody concentrations in adults exposed to per- and polyfluoroalkyl substances: A birth cohort in the Faroe Islands. *J Immunotoxicol* 18, 85–92. <https://doi.org/10.1080/1547691X.2021.1922957>
- Simpson, J., 2005. The Royal Table.
- Southerland, E., Birnbaum, L.S., 2023. What Limits Will the World Health Organization Recommend for PFOA and PFOS in Drinking Water? *Environ Sci Technol* 57, 7103–7105. <https://doi.org/10.1021/acs.est.3c02260>
- Srikanth, S.K., Giri, D.D., Pal, D.B., Mishra, P.K., Upadhyay, S.N., 2016. Green Synthesis of Silver Nanoparticles: A Review. *Green and Sustainable Chemistry*. *Green and Sustainable Chemistry* 6, 34–56. <https://doi.org/10.4236/gsc.2016.61004>
- Strynar, M., Dagnino, S., McMahan, R., Liang, S., Lindstrom, A., Andersen, E., McMillan, L., Thurman, M., Ferrer, I., Ball, C., 2015. Identification of novel perfluoroalkyl ether carboxylic acids (PFECAs) and sulfonic acids (PFESAs) in natural waters using accurate mass time-of-flight mass spectrometry (TOFMS). *Environ. Sci. Technol.* 49, 11622.
- Sun, R.W., Chen, R., Chung, N, Ho, C, Lin, C., Che, C.-M.C.-M., El-Sayed, M.A., Ho, Silver nanoparticles fabricated in Hepes buffer exhibit cytoprotective activities toward HIV-1 infected cells. *Chemical Communications* 37, 5059. <https://doi.org/10.1039/b510984a>
- Tabassum, S., Ahmed, A., Rahman, S., Tithi, M.R., Mehjabin, M., Dristy, J.T., 2024. Recent Advancements in Per-and Polyfluoroalkyl Substances (PFAS) Detection by Sensors and Surface-Enhanced Raman Scattering (SERS) Method: A Review. <https://doi.org/10.20944/preprints202401.1557.v1>
- Tenorio, R., Liu, J., Xiao, X., Maizel, A., Higgins, C.P., Schaefer, C.E., Strathmann, T.J., 2020. Destruction of Per-and Polyfluoroalkyl Substances (PFASs) in Aqueous Film-Forming Foam (AFFF) with UV-Sulfite Photoreductive Treatment. *Environ Sci Technol* 54, 6957–6967. <https://doi.org/10.1021/acs.est.0c00961>
- Trojanowicz, M., Bartosiewicz, I., Bojanowska-Czajka, A., Kulisa, K., Szreder, T., Bobrowski, K., Nichipor, H., Garcia-Reyes, J.F., Natęcz-Jawecki, G., Męczyńska-Wielgosz, S., Kisała, J., 2019. Application of

ionizing radiation in decomposition of perfluorooctanoate (PFOA) in waters. *Chemical Engineering Journal* 357, 698–714. <https://doi.org/10.1016/j.cej.2018.09.065>

Trojanowicz, M., Bartosiewicz, I., Bojanowska-Czajka, A., Szreder, T., Bobrowski, K., Nałęcz-Jawecki, G., Męczyńska-Wielgosz, S., Nichipor, H., 2020. Application of ionizing radiation in decomposition of perfluorooctane sulfonate (PFOS) in aqueous solutions. *Chemical Engineering Journal* 379, 122303. <https://doi.org/10.1016/j.cej.2019.122303>

Trojanowicz, M., Bobrowski, K., Szostek, B., Bojanowska-Czajka, A., Szreder, T., Bartoszewicz, I., Kulisa, K., 2018a. A survey of analytical methods employed for monitoring of Advanced Oxidation/Reduction Processes for decomposition of selected perfluorinated environmental pollutants. *Talanta* 177, 122–141. <https://doi.org/10.1016/j.talanta.2017.09.002>

Trojanowicz, M., Bojanowska-Czajka, A., Bartosiewicz, I., Kulisa, K., 2018b. Advanced Oxidation/Reduction Processes treatment for aqueous perfluorooctanoate (PFOA) and perfluorooctanesulfonate (PFOS) – A review of recent advances. *Chemical Engineering Journal* 336, 170–199. <https://doi.org/10.1016/j.cej.2017.10.153>

Tsou, K., Antell, E., Duan, Y., Olivares, C.I., Yi, S., Alvarez-Cohen, L., Sedlak, D.L., 2023. Improved Total Oxidizable Precursor Assay for Quantifying Polyfluorinated Compounds Amenable to Oxidative Conversion to Perfluoroalkyl Carboxylic Acids. *ACS ES and T Water*. <https://doi.org/10.1021/acsestwater.3c00224>

US EPA, 2023. 4 th Draft Method 1633 * Analysis of Per- and Polyfluoroalkyl Substances (PFAS) in Aqueous , Solid , Biosolids , and Tissue Samples by LC-MS / MS.

Vance, M.E., Kuiken, T., Vejerano, E.P., McGinnis, S.P., Hochella, M.F., Hull, D.R., 2015. Nanotechnology in the real world: Redeveloping the nanomaterial consumer products inventory. *Beilstein Journal of Nanotechnology* 6, 1769–1780. <https://doi.org/10.3762/bjnano.6.181>

Vigneshwaran, N., Nachane, R.P., Balasubramanya, R.H., Varadarajan, P. v., 2006. A novel one-pot “green” synthesis of stable silver nanoparticles using soluble starch. *Carbohydr Res* 341, 2012–2018. <https://doi.org/10.1016/j.carres.2006.04.042>

Von Goetz, N., Lorenz, C., Windler, L., Nowack, B., Heuberger, M., Hungerbühler, K., 2013. Migration of Ag- and TiO₂-(nano)particles from textiles into artificial sweat under physical stress: Experiments and exposure modeling. *Environ Sci Technol*. <https://doi.org/10.1021/es304329w>

Vuorinen, H.S., Juuti, P.S., Katko, T.S., 2007. History of water and health from ancient civilizations to modern times. *Water Supply* 7, 49–57. <https://doi.org/10.2166/ws.2007.006>

Wagener, S., Dommershausen, N., Jungnickel, H., Laux, P., Mitrano, D., Nowack, B., Schneider, G., Luch, A., 2016. Textile Functionalization and Its Effects on the Release of Silver Nanoparticles into Artificial Sweat. *Environ Sci Technol*. <https://doi.org/10.1021/acs.est.5b06137>

Waldron, H.A., 1973. Lead poisoning in the ancient world. *Med Hist* 17, 391–399. <https://doi.org/10.1017/S0025727300019013>

Wang, G.S., Hsieh, S.T., Hong, C.S., 2000. Destruction of humic acid in water by UV light - Catalyzed oxidation with hydrogen peroxide. *Water Res* 34, 3882–3887. [https://doi.org/10.1016/S0043-1354\(00\)00120-2](https://doi.org/10.1016/S0043-1354(00)00120-2)

Wang, L., Batchelor, B., Pillai, S.D., Botlaguduru, V.S.V., 2016. Electron beam treatment for potable water reuse: Removal of bromate and perfluorooctanoic acid. *Chemical Engineering Journal* 302, 58–68. <https://doi.org/10.1016/j.cej.2016.05.034>

- Wang, X., Wang, W.-X., 2023. Copper Leachability from Cu Nanoparticle-Containing Face Masks and Associated Subcellular Impacts. *Environ Sci Technol Lett* 10, 186–191. <https://doi.org/10.1021/acs.estlett.2c00954>
- Wang, Z., Boucher, J.M., Scheringer, M., Cousins, I.T., Hungerbühler, K., 2017. Toward a Comprehensive Global Emission Inventory of C4-C10 Perfluoroalkanesulfonic Acids (PFSA) and Related Precursors: Focus on the Life Cycle of C8-Based Products and Ongoing Industrial Transition. *Environ Sci Technol* 51, 4482–4493. <https://doi.org/10.1021/acs.est.6b06191>
- Wang, Z., Buser, A.M., Cousins, I.T., Demattio, S., Drost, W., Johansson, O., Ohno, K., Patlewicz, G., Richard, A.M., Walker, G.W., White, G.S., Leinala, E., 2021. A New OECD Definition for Per- And Polyfluoroalkyl Substances. *Environ Sci Technol* 55, 15575–15578. <https://doi.org/10.1021/acs.est.1c06896>
- Wang, Z., Cousins, I.T., Scheringer, M., Buck, R.C., Hungerbühler, K., 2014a. Global emission inventories for C4-C14 perfluoroalkyl carboxylic acid (PFCA) homologues from 1951 to 2030, Part I: Production and emissions from quantifiable sources. *Environ Int.* <https://doi.org/10.1016/j.envint.2014.04.013>
- Wang, Z., Cousins, I.T., Scheringer, M., Buck, R.C., Hungerbühler, K., 2014b. Global emission inventories for C4–C14 perfluoroalkyl carboxylic acid (PFCA) homologues from 1951 to 2030, part II: The remaining pieces of the puzzle. *Environ Int* 69, 166–176. <https://doi.org/10.1016/j.envint.2014.04.006>
- Wang, Z., Cousins, I.T., Scheringer, M., Buck, R.C., Hungerbühler, K., 2014c. Global emission inventories for C4-C14perfluoroalkyl carboxylic acid (PFCA) homologues from 1951 to 2030, Part I: Production and emissions from quantifiable sources. *Environ Int* 70, 62–75. <https://doi.org/10.1016/j.envint.2014.04.013>
- Wang, Z., Cousins, I.T., Scheringer, M., Hungerbuehler, K., 2015. Hazard assessment of fluorinated alternatives to long-chain perfluoroalkyl acids (PFAAs) and their precursors: Status quo, ongoing challenges and possible solutions. *Environ. Int.* 75, 172.
- Wang, Z., Cousins, I.T., Scheringer, M., Hungerbühler, K., 2013. Fluorinated alternatives to long-chain perfluoroalkyl carboxylic acids (PFCAs), perfluoroalkane sulfonic acids (PFSA) and their potential precursors. *Environ. Int.* 60, 242.
- Water Science School, 2019. How Much Water is There on Earth? [WWW Document]. USGS.
- Water Science School, 2018. Where is Earth's Water? [WWW Document]. USGS.
- Wenk, J., Aeschbacher, M., Salhi, E., Canonica, S., Von Gunten, U., Sander, M., 2013. Chemical oxidation of dissolved organic matter by chlorine dioxide, chlorine, and ozone: Effects on its optical and antioxidant properties. *Environ Sci Technol* 47, 11147–11156. <https://doi.org/10.1021/es402516b>
- Wibawa, P.J., Nur, M., Asy'ari, M., Wijanarka, W., Susanto, H., Sutanto, H., Nur, H., 2021. Green synthesized silver nanoparticles immobilized on activated carbon nanoparticles: Antibacterial activity enhancement study and its application on textiles fabrics. *Molecules* 26. <https://doi.org/10.3390/molecules26133790>
- Willach, S., Brauch, H.-J., Lange, F.T., 2016. Contribution of selected perfluoroalkyl and polyfluoroalkyl substances to the adsorbable organically bound fluorine in German rivers and in a highly contaminated groundwater. *Chemosphere* 145, 342.
- Williams, A.J., Gaines, L.G.T., Grulke, C.M., Lowe, C.N., Sinclair, G.F.B., Samano, V., Thillainadarajah, I., Meyer, B., Patlewicz, G., Richard, A.M., 2022. Assembly and Curation of Lists of Per- and Polyfluoroalkyl Substances (PFAS) to Support Environmental Science Research. *Front Environ Sci* 10. <https://doi.org/10.3389/fenvs.2022.850019>
- Wojnárovits, L., Takács, E., 2008. Irradiation treatment of azo dye containing wastewater: An overview. *Radiation Physics and Chemistry* 77, 225–244. <https://doi.org/10.1016/j.radphyschem.2007.05.003>

- Xu, Q., Ke, X., Ge, N., Shen, L., Zhang, Y., Fu, F., Liu, X., 2018. Preparation of Copper Nanoparticles Coated Cotton Fabrics with Durable Antibacterial Properties. *Fibers and Polymers* 19, 1004–1013. <https://doi.org/10.1007/s12221-018-8067-5>
- Yang, L., He, L., Xue, J., Ma, Y., Xie, Z., Wu, L., Huang, M., Zhang, Z., 2020. Persulfate-based degradation of perfluorooctanoic acid (PFOA) and perfluorooctane sulfonate (PFOS) in aqueous solution: Review on influences, mechanisms and prospective. *J Hazard Mater*. <https://doi.org/10.1016/j.jhazmat.2020.122405>
- Yeung, L.W., Wang, Y., Giesy, J.P., Lam, P.K.S., Miyake, Y., Taniyasu, S., Yamashita, N., Yu, H., Jiang, G., Wu, Y., Li, J., Wang, Y., 2008. Perfluorinated compounds and total and extractable organic fluorine in human blood samples from China. *Environ Sci Technol* 42, 8140–8145. <https://doi.org/10.1021/es800631n>
- Yu, K., Li, X., Chen, L., Fang, J., Chen, H., Li, Q., Chi, N., Ma, J., 2018. Mechanism and efficiency of contaminant reduction by hydrated electron in the sulfite/iodide/UV process. *Water Res* 129, 357–364. <https://doi.org/10.1016/j.watres.2017.11.030>
- Zacs, D., Bartkevics, V., 2016. Trace determination of perfluorooctane sulfonate and perfluorooctanoic acid in environmental samples (surface water, wastewater, biota, sediments, and sewage sludge) using liquid chromatography – Orbitrap mass spectrometry. *J Chromatogr A* 1473, 109–121. <https://doi.org/10.1016/j.chroma.2016.10.060>
- Zafeiraki, E., Costopoulou, D., Vassiliadou, I., Bakeas, E., Leondiadis, L., 2014. Determination of perfluorinated compounds (PFCs) in various foodstuff packaging materials used in the Greek market. *Chemosphere* 94, 169–176. <https://doi.org/10.1016/j.chemosphere.2013.09.092>
- Zhang, X., Xue, L., Deji, Z., Wang, X., Liu, P., Lu, J., Zhou, R., Huang, Z., 2022. Effects of exposure to per- and polyfluoroalkyl substances on vaccine antibodies: A systematic review and meta-analysis based on epidemiological studies. *Environmental Pollution*. <https://doi.org/10.1016/j.envpol.2022.119442>
- Zhang, Y., Liu, J., Ghoshal, S., Moores, A., 2021. Density Functional Theory Calculations Decipher Complex Reaction Pathways of 6:2 Fluorotelomer Sulfonate to Perfluoroalkyl Carboxylates Initiated by Hydroxyl Radical. *Environ Sci Technol* 55, 16655–16664. <https://doi.org/10.1021/acs.est.1c05549>
- Zhang, Z., Chen, J.J., Lyu, X.J., Yin, H., Sheng, G.P., 2014. Complete mineralization of perfluorooctanoic acid (PFOA) by γ -irradiation in aqueous solution. *Sci Rep* 4, 1–6. <https://doi.org/10.1038/srep07418>
- Zhu, H., Kannan, K., 2020. Total oxidizable precursor assay in the determination of perfluoroalkyl acids in textiles collected from the United States. *Environmental Pollution* 265, 114940. <https://doi.org/10.1016/j.envpol.2020.114940>
- Zhu, H.W., Gao, H.L., Zhao, H.Y., Ge, J., Hu, B.C., Huang, J., Yu, S.H., 2020a. Printable elastic silver nanowire-based conductor for washable electronic textiles. *Nano Res* 13, 2879–2884. <https://doi.org/10.1007/s12274-020-2947-x>
- Zhu, H.W., Gao, H.L., Zhao, H.Y., Ge, J., Hu, B.C., Huang, J., Yu, S.H., 2020b. Printable elastic silver nanowire-based conductor for washable electronic textiles. *Nano Res* 13, 2879–2884. <https://doi.org/10.1007/s12274-020-2947-x>
- Zweigle, J., Capitain, C., Simon, F., Roesch, P., Bugsel, B., Zwiener, C., 2023. Non-extractable PFAS in functional textiles - characterization by complementary methods: oxidation, hydrolysis, and fluorine sum parameters. *Environ Sci Process Impacts* 25, 1298–1310. <https://doi.org/10.1039/d3em00131h>

3. Elucidating Degradation Mechanisms For a Range of Per- and Polyfluoroalkyl Substances (PFAS) via Controlled Irradiation Studies

David Patch†, Natalia O'Connor†, Iris Koch†, Tom Cresswell‡‡, Cath Hughes‡‡, Justin B. Davies‡‡, Jennifer Scott†, Denis O'Carroll†‡, Kela Weber†‡*

† Department of Chemistry and Chemical Engineering, Royal Military College of Canada, Kingston, ON, Canada K7K 7B4.

‡ School of Civil and Environmental Engineering, University of New South Wales, Sydney NSW 2052, Australia

‡‡ Australian Nuclear Science and Technology Organisation, Australia

* Corresponding Author:

Email: Kela.Weber@rmc.ca

Phone: 613-541-6000 ext. 6610

3.1. Abstract

Per- and polyfluoroalkyl substances (PFAS) are a challenging class of environmental pollutants due to a lack of available destructive remediation technologies. Understanding the fundamental mechanisms for degradation of PFAS is key for the development of field scalable and in-situ destructive based remediation technologies. This study aimed to elucidate and refine the current understanding of PFAS degradation mechanisms in water through a series of controlled gamma irradiation studies. Gamma irradiation of PFAS was performed using a cobalt-60 source in a batch irradiation up to 80 kGy at the Australian Nuclear Science and Technology Organization. Perfluorooctanoic acid (PFOA), perfluorooctanesulfonic acid (PFOS), 6:2 fluorotelomer sulfonate (6:2 FTS), and a suite of thirteen different PFAS (including C4-C12 PFCAs, C4, C6, C8 PFSAs, and FOSA) were irradiated to investigate degradation, influence of pH, chain length, and transformation. High resolution mass spectrometry was used to identify more than 80 fluorinated transformation products throughout the degradation experiments. These included the -F/+H, -F/+OH, -F/CH₂OH exchanged PFAS and n-1 PFCA, amongst others. Given the reactive species present (hydroxyl radicals ($\cdot\text{OH}$), hydrogen radicals ($\cdot\text{H}$) and aqueous electrons (e^-_{aq})), and the degradation products formed it was shown that aqueous electrons were the key reactive species responsible for initial PFAS degradation. Most importantly, based on degradation product formation, we found that the initial -F/+H does not have to occur at the α -fluoride (nearest the functional head group), rather occurring throughout the chain length leading to more complex degradation pathways than previously postulated. While our results support some of the reaction steps postulated in the literature, we have developed a unified 16 step and 3 pathway schematic of degradation supported by experimental observations.

3.2. Introduction

Per- and polyfluoroalkyl substances (PFAS) are a family of compounds containing one or more fully fluorinated carbon atoms that are used in a variety of applications to take advantage of their unique properties including chemical/thermal stability, surfactant properties, and hydrophobic/lipophobic nature (Buck et al., 2011). PFAS are used in numerous applications including aqueous film forming foam (AFFF) for firefighting, stain-repellant sprays, food packaging materials, textiles, electronics manufacturing, and cosmetics (Herzke et al., 2012; Liu et al., 2014; Pan et al., 2021; Robel et al., 2017; Schultes et al., 2018; Wang et al., 2014; Zafeiraki et al., 2014). The unique chemical nature and widespread use of AFFF have resulted in the extensive spread of PFAS, with the class of chemicals being detected in environmental systems, wildlife, and humans across the world (Axmon et al., 2014; Gebbink et al., 2015; Hansen et al., 2016; Knobeloch et al., 2012; Okada et al., 2013; Olsen et al., 2017; Tian et al., 2016; Winkens et al., 2017). The global contamination of PFAS has raised concerns as to the toxicological impact on humans with links to issues with kidney, liver, and reproductive function in adults and suppressed immune response to vaccines and neurological/behavioural issues in children, although some studies draw conflicting conclusions (Bentel et al., 2020; Granum et al., 2013; Petersen et al., 2018; Schrenk et al., 2020; Stanifer et al., 2018; Sunderland et al., 2019; Tsai et al., 2015; Ye et al., 2018).

The high bond dissociation energy (BDE) of the C-F bond, variable functional group chemistry, variable fluorocarbon chain lengths, and other chemical properties of PFAS make remediation efforts difficult (Bentel et al., 2020, 2019; Dombrowski et al., 2018; Kucharzyk et al., 2017; Liu et al., 2021; Mahinroosta and Senevirathna, 2020; Merino et al., 2016; Rayne and Forest, 2009; Trojanowicz et al., 2020, 2019, 2018; Vecitis et al., 2009; Wang et al., 2017). Research for remediation of PFAS-impacted water has investigated the use of bioremediation, fungal degradation, sonochemical destruction, chemical oxidation, and chemical reduction (Hori et al., 2008, 2005; Houtz and Sedlak, 2012; Merino et al., 2016; Tseng, 2012). Chemical oxidation and reduction have shown promise for their ability to degrade PFAS through the generation of several reactive species. The generation of these reactive species is greatly influenced by the reagents added, activator, presence of a catalyst, pH, oxygen content, and concentration of reagent (Arvaniti et al., 2015; Bentel et al., 2019; Dombrowski et al., 2018; Kucharzyk et al., 2017; Ochoa-Herrera et al., 2008; Ochoa-Herrera and Sierra-Alvarez, 2008; Ross et al., 2018; Trojanowicz et al., 2020, 2019, 2018). The roles of pH and oxygen have been found to be particularly important because of

either scavenging of reactive species, or promotion of electrostatic coordination to catalysts at lower pH. While numerous reactive species are generated because of chemical oxidation reactions, only some of them can cleave the strong C-F bonds (116 kcal/mol) present in PFAS. It has been suggested that because of the variable chemistry found in PFAS mixtures (sulfonates, carboxylates, telomers, etc.), technologies that can facilitate both oxidative and reductive species will be most effective for treating the broad range of PFAS found in the environment (Al Amin et al., 2021; Dombrowski et al., 2018; Mejia-Avenidaño et al., 2017a; Munoz and Liu, 2017).

One of the drawbacks of chemical oxidation/reduction technologies is the addition of reagents, which can increase costs and result in introduction or creation of environmentally harmful pollutants, including halogenated disinfection by-products (Dong et al., 2019; Ike et al., 2019; Wenk et al., 2013). One of the advantages of irradiation-based chemical oxidation/reduction technologies (i.e., the use of ionizing radiation) is that reactive species can be generated from water itself, without requiring the addition of reagents. The production of active species (Table 1) has led to the study of gamma irradiation to degrade persistent organic pollutants (Getoff, 1996; Trojanowicz et al., 2020, 2019; Wojnárovits and Takács, 2008; Zhang and Yu, 2004; Zhang et al., 2014).

Table 3.1 - Primary reactive species and chemical reaction yield (G-value). G-value is the number of charged species (in moles) per 1 joule of absorbed energy, obtained from the literature (Getoff, 1996; Trojanowicz et al., 2018; Wojnárovits and Takács, 2008). In N₂ saturated solutions, only italicized reactive species are likely.

Reactive Species	<i>e⁻ (aqueous)</i>	<i>·H</i>	<i>·OH</i>	<i>H₂</i>	HO ₂ ⁻	H ⁺	OH ⁻
G-Value	0.27	0.06	0.28	0.045	0.07	0.32	0.05

There have been several studies investigating the use of gamma irradiation, electron beam, or plasma to degrade PFAS. Work by Zhang et al. (2014) examined gamma irradiation of PFOA as a function of pH, oxygen saturation, and identified reactive species with scavenger experiments observing 99% mineralization of PFOA at pH 13 under N₂ purging following 126 kGy. Formation and subsequent degradation of shorter chain perfluorocarboxylic acids (PFCAs) was observed. Through scavenging experiments Zhang identified aqueous electrons as being responsible for initial PFOA degradation, with ·OH radicals being responsible for complete defluorination (Zhang

et al., 2014). Wang et al. (2016) investigated the use of electron beam for removal of bromate and PFOA for potable water reuse. It was determined that PFOA was effectively mineralized with the addition of nitrate and with an increase to the solution alkalinity. It was also found that humic acid and oxygen in the solution reduced the total defluorination of PFOA by scavenging reactive species such as OH radicals (Wang et al., 2016). Work by Kim et al. (2018, 2019) investigated the decomposition of PFOS using electron beam independently and with chemical oxidants (Kim et al., 2019, 2018). PFOS was degraded 68% following 2000 kGy of electron beam irradiation from a starting concentration of 100 mg/L. At lower concentrations of PFOS the decomposition efficiency was higher, reaching a maximum of 92% decomposition of PFOS at 0.1 mg/L following 2000 kGy of electron beam irradiation. Similar decomposition of PFOS was observed at 100 kGy of irradiation when irradiated in the presence of 5 mM sodium persulfate. Works by Trojanowicz et al. (2019, 2020) contrasted the use of gamma or electron beam radiation for the radiolytic degradation of PFOA and PFOS. It was found that gamma irradiation outperformed electron beam for degradation of PFOA at equivalent absorbed doses. As electron beam results in a high amount of absorbed dose in a short amount of time, radical recombination can occur resulting in a lower concentration of reactive species relative to the energy input. As was found in similar work, oxygen was identified as a scavenger of reactive species responsible for PFAS degradation, and decomposition efficiencies improved in argon saturated samples. Under optimal conditions close to 100% of PFOA and 90% of PFOS was degraded following 50 kGy and 10 kGy of gamma irradiation respectively. In these studies, the formation of shorter-chained PFAS carboxylates as well as -F/+H exchanged and unsaturated polyfluorinated alkyl substances has been observed. Work by Kowald et al examined the degradation of PFOS and PFOA in sand, groundwater, and wastewater effluent using up to 50 kGy of electron beam dose, identifying that while PFOA underwent complete degradation at 50 kGy further optimization and higher doses would be required to fully degrade PFOS (Kowald et al., 2021). Work by Singh et al. (2019) examined the use of plasma technology to degrade PFAS in water, identifying aqueous electrons and argon ions as the main species responsible for degradation. Formation of PFCAs, trace amounts of 78 PFAS related transformation products, and gas-phase products were identified, including cyclic perfluoroalkanes (Singh et al., 2019).

There are several hypothesized mechanisms that attempt to identify the degradation pathway of PFAS (Arvaniti et al., 2015; Bentel et al., 2019; Dombrowski et al., 2018; Hori et al., 2008, 2005;

Kucharzyk et al., 2017; Ross et al., 2018; Trojanowicz et al., 2020, 2019; Zhang et al., 2014). Many of the mechanisms identify aqueous electrons, hydroxyl radicals, hydrogen radicals, and hydroxide ions as hypothesized active species that participate in one (or more) of the degradation steps. The initial step is commonly hypothesized to be aqueous electron attack of the PFAS, generating a double negatively charged radical PFAS molecule (Bentel et al., 2019; Trojanowicz et al., 2020, 2019; Zhang et al., 2014). This radical PFAS species then either results in ejection of the functional group or the ejection of an α -fluoride. Subsequent steps involve attacking the resulting partially transformed PFAS radical with a variety of radical species, which in turn degrade into shorter-chained PFCAs (per- and polyfluorinated carboxylic acids).

The present study seeks to investigate the transformation products and mechanism of degradation for PFAS following gamma irradiation for a broad suite of PFAS including PFCAs, PFSAs (perfluorosulfonic acids), FOSA (perfluorooctanesulfonamide), and 6:2 FTS. This study also examines the influence of pH, initial concentration, and chain length on total degradation, degradation rate constants, and byproduct formation. By identifying the degradation mechanism and identified products following irradiation this study will lend itself to improving existing remediation technologies and development of new remediation technologies, including those that combine multiple effective reactive species.

3.3. Materials and Methods

3.3.1. Solution Preparation

All PFAS except for 6:2 FTS were purchased as powders from Synquest Labs (>97% purity) and used to prepare high concentration stock solutions (Table A1). PFOS was purchased as technical grade, consisting of 25% branched isomers and 75% linear isomers. 6:2 FTS was purchased from Wellington Laboratories (50 ug/mL in methanol). Stock solutions of PFOS and PFOA were individually prepared in deionized water, whereas stock solutions of 6:2 FTS and the suite of PFAS (PFAS_{13Suite}) were prepared in methanol. Methanol was used to allow for complete dissolution of all the PFAS, and it has been found in literature that small amounts of methanol do not interfere with aqueous electrons for degrading PFAS (Abusallout et al., 2021; Bentel et al., 2019). The addition of alcohol has also been found to enhance degradation and defluorination of PFOS and PFOA using gamma irradiation through the scavenging of hydroxyl radicals (Trojanowicz et al., 2020, 2019). Low concentrations of methanol have been shown to scavenge hydroxyl radicals, but recent research has identified the potential for the formation of hydrogen peroxide, a hydroxyl

radical precursor, when scavenged by methanol in the presence of dissolved oxygen. Given the anaerobic conditions of this investigation, it is unlikely that hydrogen peroxide was formed (Wang et al., 2022). Before preparing samples, an anaerobic glove box was purged with N₂ gas for one week and then tested with a resazurin-based anaerobic indicator strip (Thermo Scientific Oxoid Resazurin Anaerobic Indicator). After three days the strip remained colorless, indicating <0.5% O₂ concentration in the atmosphere of the glove box. The glove box was flushed with a constant stream of N₂ gas and fresh resazurin strips were opened each day of sample preparation to ensure anaerobic conditions (Hall and Denning, 1994; Sakaguchi et al., 1993). Deionized water (18 MΩ, Milli-Q Direct 8) was degassed with heat (70° C), stirring, and sparging with N₂ for one hour before sealing and transporting into the glove box. Sodium hydroxide solution (5 M) as well as working solutions of PFOS, PFOA, 6:2 FTS, and PFAS_{13Suite} were prepared externally in the previously de-gassed deionized water, transported into the box, and sparged with N₂ for 20 minutes to ensure oxygen removal. Sodium hydroxide pellets were purchased from VWR (>97% purity, ACS). Samples were prepared by the addition of appropriate PFAS standard solutions (to reach target PFAS concentration, Table A2) into a 100 mL beaker of deionized water (<1% methanol after dilution for 6:2 FTS and PFAS_{13Suite}), adjusting the pH when necessary, with sodium hydroxide, and sub-sampling into 2 mL crimp-cap HPLC vials (Agilent Technologies). The sealed HPLC vials were then placed into a plastic rack with a lid and vacuum-sealed into plastic bags inside the glove box (White Dolphin Food Vacuum Sealer). An oxygen strip was then opened and placed outside the first vacuum seal bag, which was then vacuum sealed into two more bags sequentially. The triple sealed sample racks were removed from the glove box, autoclaved at 121 °C for 30 minutes, vacuum sealed one more time, and shipped to the Australian Nuclear Science and Technology Organisation (ANSTO) (New South Wales, Australia) for gamma irradiation. Each prepared rack corresponded to a different total dose amount and contained triplicate samples for each of the different trials under investigation.

3.3.2. Gamma Irradiation and Analysis

Samples remained within the vacuum-sealed bags and were irradiated by exposure to a plaque cobalt-60 source in a batch irradiator at ANSTO (1.37 kGy/hour). The radiation dose distribution within the sample rack was measured by placing ceric-cerous dosimeters in an empty rack to obtain the minimum and maximum dose rates. This information was used to calculate the exposure time for each target dose, and the minimum and maximum doses to each rack. Dosimeters were sited

on the outside of each sealed sample rack to verify the doses received. Eight racks were irradiated to doses of 0 (i.e., non-irradiation control), 1, 2.5, 5, 10, 20, 40 & 80 kGy. Control samples were also prepared that were not shipped or irradiated and analyzed alongside the shipped and irradiated samples. Samples were then analyzed using an Agilent 6460 LC-MS for targeted PFAS analysis, and on a ThermoFisher Orbitrap Exploris 120 for non-targeted, high-resolution analysis of PFAS degradation products. More information can be found in the SI (Table A3).

3.4. Results and Discussion

Several previous studies have demonstrated the radical decomposition of PFOS, PFOA, and to a lesser extent 6:2 FTS as well as a suite of PFCAs and PFSA's varying by chain length. Depending on the irradiation source, chemical additives, and scavengers present, several reactive species can be generated. It has been shown that the decomposition of PFOA and 6:2 FTS can be carried out by using oxidative and reductive species, whereas PFOS requires reductive species for at least its initial degradation, with further reduction or oxidation allowing for complete mineralization (Abusallout et al., 2021; Bentel et al., 2020, 2019; Houtz and Sedlak, 2012; Kim et al., 2019; Kowald et al., 2021; Liu et al., 2021; Trojanowicz et al., 2020, 2019, 2018; Wang et al., 2016; Zhang et al., 2014).

In nitrogen-purged waters the reactive species that can be generated through gamma irradiation are the hydroxide radical, aqueous electron, and hydrogen radical (1).



The number in the parentheses indicate the G-values (radiation chemical yield) expressed in number of charged species (in moles) generated per 1 joule of absorbed energy (Getoff, 1996; Trojanowicz et al., 2018). These reactive species are heavily influenced by pH, as at higher pH the hydrogen radical can undergo reaction with hydroxide ions (2) ($\text{pK}_a = 9.1$), resulting in the generation of additional aqueous electrons (Trojanowicz et al., 2019), whereas at low pH the aqueous electron can undergo reaction with protons to form hydrogen radicals (3) which are less effective reducing reagents.



Additionally, OH radicals react with methanol and other alcohols, as is the case in this study with 6:2 FTS and the PFAS_{13Suite} (4) (Arlos et al., 2017; Armstrong, 1969; Múčka et al., 2013; Trojanowicz et al., 2019).



The total degradation, rate of reaction and resultant transformation products of PFOS, PFOA, 6:2 FTS and PFAS_{13Suite} will vary as a function of the main reactive species being generated. In the irradiation experiments performed in this study it is expected that PFOS and PFOA will be exposed to aqueous electrons, hydroxyl radicals, and hydrogen radicals. With the presence of methanol, it is expected that 6:2 FTS and the PFAS_{13Suite} will be exposed to aqueous electrons and hydrogen radicals only.

3.4.1. Degradation of Technical Grade PFOS, PFOA and 6:2 FTS

In nitrogen-purged neutral (pH 7) and alkaline (pH 11) solutions, the extent of radiolytic degradation was investigated for PFOS, PFOA and 6:2 FTS (Figure 3.1) at two different concentrations. Zero and first order kinetic fits were investigated for various dosage ranges (Table A4, A5, A6).

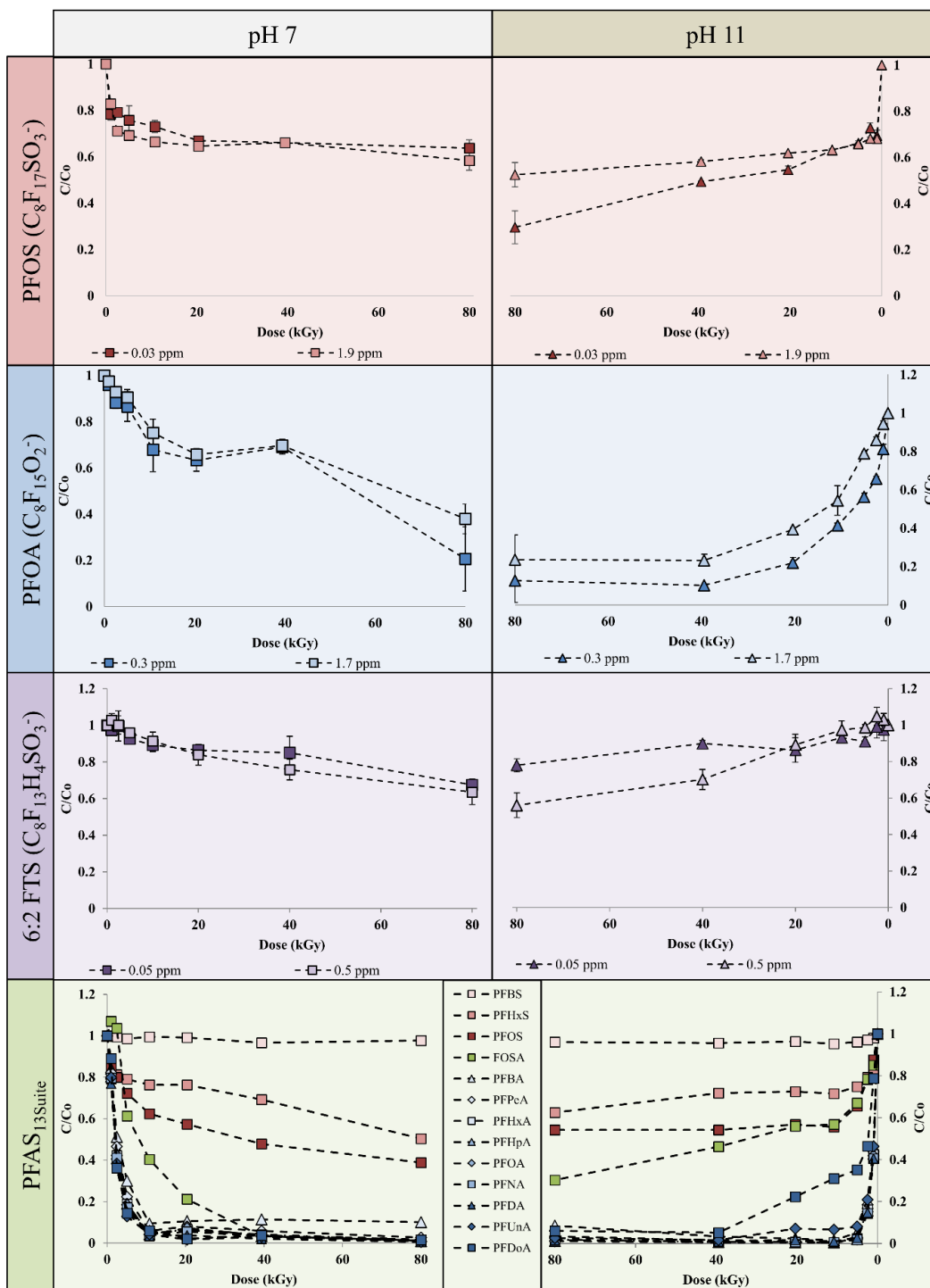


Figure 3.1 - PFAS degradation of PFOS, PFOA and 6:2 FTS at two different concentrations at pH 7 and 11, and PFAS_{13Suite} at pH 7 and 11. Error bars represent the standard deviation of the replicates (n=3). PFAS_{13Suite} values <5% average standard deviation. Some error bars are too small to be shown.

The largest degradation of PFOS was found to occur with the smaller concentration at pH 11 ($70 \pm 7\%$) (Figure 3.1). It was determined that the various branched isomers of PFOS were more susceptible to degradation than their linear isomer counterpart. The branched PFOS isomers at both pH 7 and 11 experienced close to 100% degradation, whereas the linear isomers only experienced 22% (pH 7) and 30% (pH 11) (Figure 3.2). The rate constant for PFOS is more accurately calculated when the branched and linear isomers are considered separately. At pH 11, the first order rate constant for the sum of PFOS was found to be 0.005 kGy^{-1} ($R^2 0.48$). However, the linear PFOS was found to degrade following a first order rate constant of 0.004 kGy^{-1} ($R^2 0.84$) and branched PFOS degraded too rapidly for an accurate rate law calculation. The same trend is observed at pH 7 when comparing total PFOS (0.004 kGy^{-1} , $R^2 0.46$) and linear PFOS (0.003 kGy^{-1} , $R^2 0.8$).

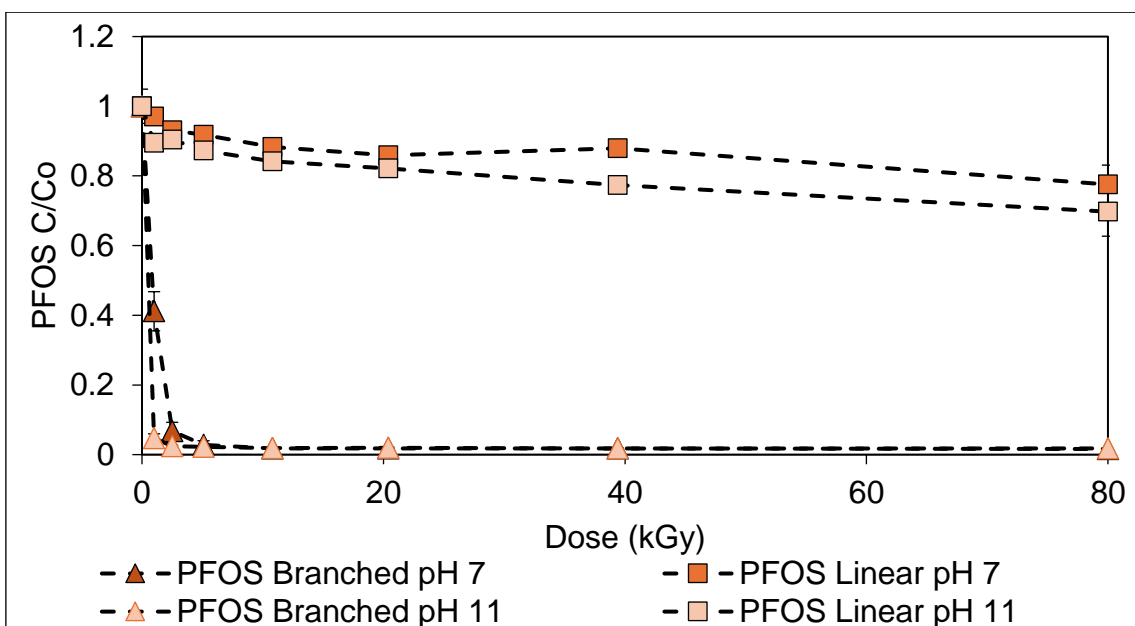


Figure 3.2 - Degradation of branched and linear PFOS as a function of irradiation (1.9 mg PFOS/L). Error bars represent the standard deviation of the replicates ($n=3$). Some error bars are too small to be shown.

Numerous studies have identified the susceptibility of branched PFOS isomers to degradation (Ochoa-Herrera et al., 2008; Trojanowicz et al., 2020; Yamamoto et al., 2007). This enhanced susceptibility is likely due to the tertiary C-F bonds found in the $-\text{CF}_3$ branched isomer, which have a higher electron affinity than their straight chain counterparts (Paul et al., 2004), allowing for easier attack of the branched PFOS by generated aqueous electrons (Ochoa-Herrera et al., 2008).

Given the resistance of PFOS to degradation by hydroxyl radicals, the initial degradation of PFOS occurs following attack by generated aqueous electrons. The increased yield of aqueous electrons under alkaline conditions (eq 2) and the higher ratio of reactive species relative to the amount of PFOS present are responsible for the high degradation observed.

The degradation of PFOA was found to be statistically similar amongst the range of concentrations and pHs used, although the degradation occurred most rapidly at pH 11 with the lower concentration of PFOA (87 ± 11 %), with a first order rate constant of 0.11 kGy^{-1} (Figure 3.1, Table A5). This enhanced rate of degradation is likely caused by the higher ratio of reactive species, specifically aqueous electrons, generated under alkaline conditions. It is generally understood that hydroxyl radicals alone are not capable of initiating the degradation of PFOA (Javed et al., 2020), but they have been shown to enhance defluorination (Zhang et al., 2014) and be potentially capable of degrading PFOA at elevated temperatures (Liu et al., 2012; Yang et al., 2020).

The largest degradation of 6:2 FTS was found to occur with the larger concentration at pH 11 (44 ± 7 %) with a zero-order rate constant of $0.003 \text{ mg 6:2 FTS/L} \cdot \text{kGy}$. Due to the presence of methanol, the initial degradation of 6:2 FTS is caused by aqueous electron attack only. The kinetic degradation trend for 6:2 FTS is comparable to the kinetic degradation trend of PFOS, which provides insight into their degradation mechanism, as the two compounds are structurally identical except fluorine saturation (Figure A1). This, as well as results showing that PFOA was more readily degraded than PFOS, further reinforces observations that the sulfonate functional group for 6:2 FTS and PFOS plays a larger role in its resistance to degradation than the extent of its fluorination. The difficulty in degrading PFOS compared to PFOA is generally understood in literature (Dombrowski et al., 2018; Kowald et al., 2021; Li et al., 2020; Ochoa-Herrera and Sierra-Alvarez, 2008; Trojanowicz et al., 2020, 2019). For example, work by Kowald et al. (2021) identified that PFOA underwent rapid degradation compared to PFOS and 6:2 FTS following 50 kGy of electron beam irradiation, and identified the sulfonate group as being integral to the stability of PFOS in water (Kowald et al., 2021). This resistance to degradation is hypothesized to be a result of the C-S bond energy, as well as the higher electron density of three oxygens in the sulfonate headgroup compared to the two oxygens in the carboxylate headgroup. Lastly, the electron withdrawing nature of the oxygens in the carboxylate functional group result in a partial positive charge for the carbanion, making it susceptible to attack by aqueous electrons.

The PFAS degradation trends observed for PFOS, PFOA, and PFAS_{13Suite} show rapid degradation with low irradiation doses, with higher irradiation doses resulting in slower or stagnant degradation. While first and zero order rate constants were applied to the PFAS, the lack of perfect fits reinforces the complex reaction pathways occurring. The complexity is likely a result of competition between different fluorinated transformation products (and initial PFAS species) for the generated reactive species, especially if the products are less stable and outcompete the initial PFAS species present.

3.4.2. Identification of Fluorinated Transformation Products

The propensity for PFAS to undergo transformation following remediation makes assessing overall mass balance difficult, especially in situations where the measurement of free fluoride ions is either not possible or is found to be significantly lower than expected. While initial PFAS degradation may result in the formation of quantifiable shorter-chained PFCAs, there is the potential for several unquantifiable fluorinated products to be created. Identifying these fluorinated transformation products provides the evidence required to determine overall reaction mechanism (s) and allows for better estimations for mass balance closure.

3.4.3. PFOS Transformation Products

Following the degradation of PFOS (1.9 mg/L) a total of 0.01 mg/L of C₄-C₉ PFCAs were identified at pH 7, and 0.06 mg/L of C₄-C₈ PFCAs were identified at pH 11 (Figure 3.3, S2), corresponding to less than 5% (mol%) of the original PFOS concentration at pH 11. Unexpectedly, PFNA (0.005 mg/L) made up half the amount of transformed PFCA identified following dosage of 20 kGy and higher at pH 7, but not at pH 11 (Figure A2). The formation of a larger-chain PFCA from PFOS degradation was unexpected and indicates a CF₃ radical addition mechanism, which is potentially generated from the degradation of the branched PFOS isomers.

Several substituted PFOS molecules were also identified, with the substitutions including -F/+H, -F/+OH, -F/+CH₃, -F/+OCH₃, and -F/+C₂H₅O₂ (Figure 3.3, A3, Table A7, A10). Additionally, some of the resulting PFCAs underwent subsequent reaction to form similar substituted PFCA molecules. Previous authors have identified a number of these products, including the -F/+H and -F/+OH substituted PFAS (Bentel et al., 2019; Singh et al., 2019). Identification of these transformation products is an important first step in understanding potential transformation mechanisms that occur during reductive degradation of PFAS. It is important to note that while LC-HRMS provides insights into product mass, it does not allow for detailed identification of

structure. For example, the -F/+OCH₃ substitution (C-O bond formation) could also be -F/+CH₂OH (C-C bond formation). The hypothesized substitutions are based on the most probably structure, but future work would benefit from the inclusion of analytical techniques that would allow for additional structural identification (e.g., nuclear magnetic resonance) as well as techniques to measure volatile degradation products (gas chromatography-MS).

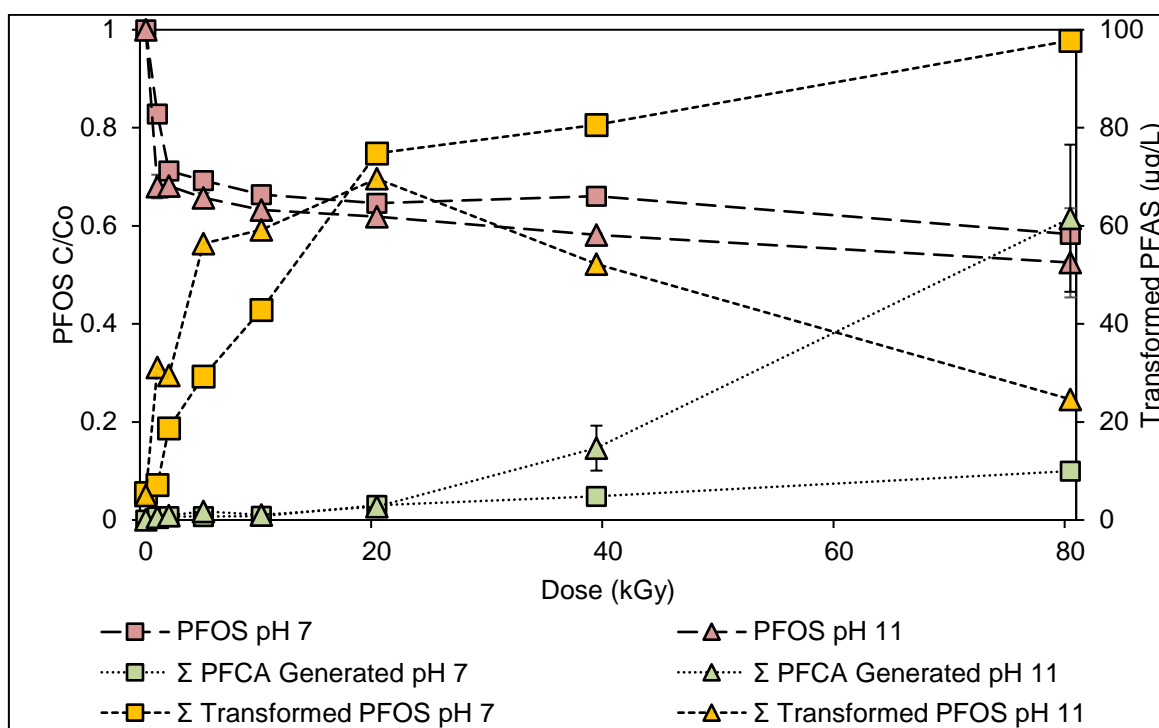


Figure 3.3 - Degradation of PFOS with subsequent generation of quantified PFCAs and semi-quantified PFOS transformation products at pH 7 and 11. Left Y-axis for PFOS, right Y-axis for PFCAs and transformed PFOS. Error bars are standard deviation of replicates. Some error bars are too small to be shown. N=1 for transformation product analysis.

The concentration or intensity of the PFAS transformation products at each dosage is likely the summation of competing synthesis and degradation. This can be seen clearly when examining PFBA at both pH 7 and 11 (Figure A2) as well as the unsaturated PFOS alkene and other transformation products (Figure A3). Interestingly, the degradation of PFOS results in initial increases to PFBA before any of the other quantified PFCAs. This is likely a partial analytical artifact due to the lower detection limit of PFBA compared to PFOA/PFHpA. However, the initial increase of PFBA seems to be more rapid than the loss of PFOA, suggesting a potential fluoride loss and oxidation of the center of the PFOS chain, or degradation of shorter-chained fluorinated impurities.

Among the unquantified PFOS transformation products, the identification of up to five -F/+H exchange is most interesting as it indicates the ease at which five heterolytic C-F bond cleavages can occur compared to a homolytic C-C bond cleavage. Under both neutral and alkaline conditions, the intensity of the -F/+H exchanged PFOS peaks at 20 kGy, with the intensity staying the same at pH 7 but decreasing at pH 11 with increasing irradiation. The higher intensity of the -F/+H exchanged product at pH 7 is supported by the higher amount of hydrogen radicals under neutral conditions. Despite the high bond energy of the C-F bond, the withdrawing nature of the fluorine atoms allows subsequent radical-induced C-F bond breakage to occur.

The identification of various alkyl, alkoxy, and carboxyl substituted PFAS was unexpected as there are no major carbon sources present in the PFOS solution that underwent degradation. It is hypothesized that impurities in the PFOS stock solution or the PFOS itself are the source of the carbon radicals as they degrade down. It is important to note that while these alkyl transformations are detected, their intensity is at least three orders of magnitude smaller than the parent PFOS molecule, indicating that these transformation products are very minor components.

Lastly, the identification of the unsaturated PFOS alkene provides some insight into a potential site for further reactivity. The PFOS alkene ($C_8F_{15}SO_3^-$) is identified in the unirradiated PFOS samples, indicating it is present initially as an impurity from the PFOS. Under neutral conditions the intensity of the alkene decreases following initial irradiation at 1 kGy but increases with subsequent irradiation. Under alkaline conditions the intensity increases with irradiation until 5 kGy, at which point it steadily decreases. At its peak the alkene under alkaline conditions is almost an order of magnitude in intensity higher than under neutral conditions, indicating a pH-dependent transformation mechanism. This alkene can be attacked through a variety of processes (hydrolysis, radical combination, etc) resulting in transformation into various fluorinated compounds.

3.4.4. PFOA Transformation Products

Compared to PFOS, which had minor amounts of quantified PFCAs following degradation, large concentrations of shorter-chained PFCAs were found following PFOA degradation at both pH 7 and 11 (Figure A4). A total of 0.03 mg/L of C4-C7 PFCAs were identified at pH 7, and 0.86 mg/L of C4-C7 PFCAs were identified at pH 11, corresponding to a concentration of 2 mol% and 61 mol% of the original PFOA concentration. When considering the undegraded PFOA, $85 \pm 23\%$ of the total PFAS is accounted for following 80 kGy of irradiation at pH 11. Traces of C3 and C2 PFAS were also detected but their concentrations were too low to quantify.

The remaining mass balance of the degraded PFOA consists of the several non-quantifiable fluorinated degradation products identified, including -F/+H exchanged, -F/+OR exchanged, and alkylated PFOA (Figure 3.4, A5, Table A8, A10).

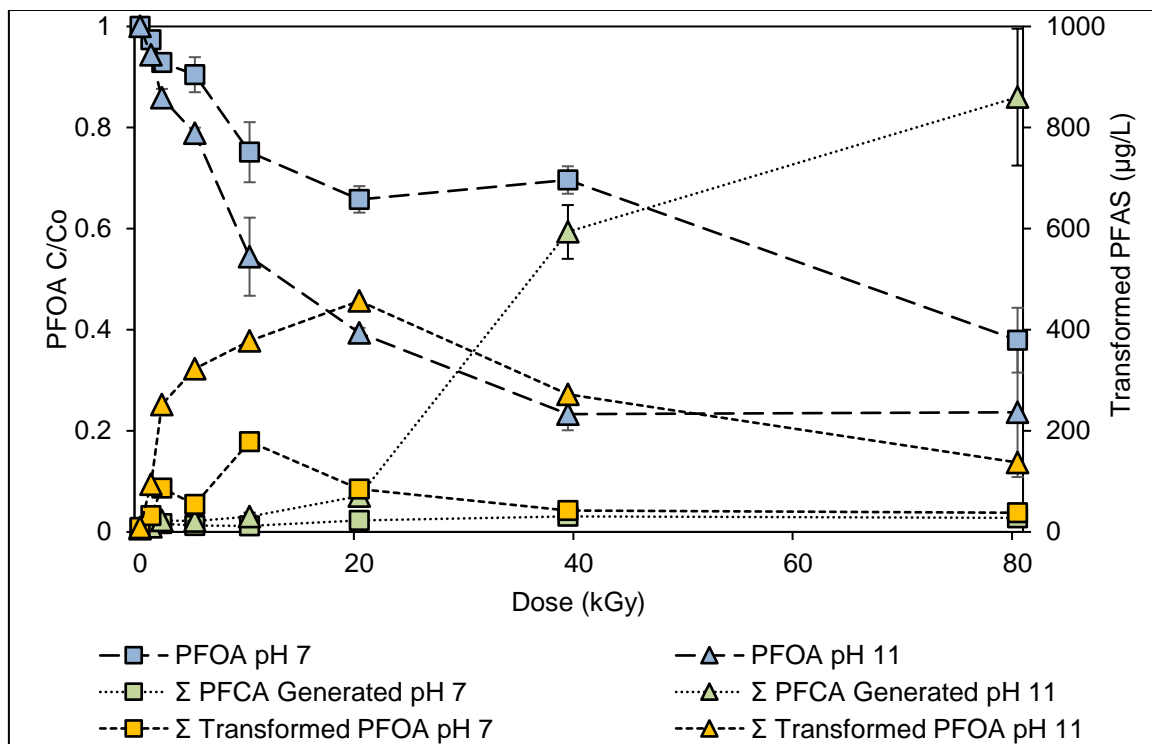


Figure 3.4 - Degradation of PFOA with subsequent generation of quantified PFCAs and semi-quantified PFOA transformation products at pH 7 and 11. Left Y-axis for PFOA, right Y-axis for PFCA and transformed PFOA. Error bars are standard deviation of replicates. Some error bars are too small to be shown. N=1 for transformation product analysis.

The intensity of the first -F/+H exchanged PFOA is within an order of magnitude of the PFOA intensity at the same dosage, accounting for a considerable amount of the mass balance under alkaline conditions (Figure A4). PFOA was only found to undergo a maximum of two -F/+H transformations, with the first -F/+H exchange being almost two orders of magnitude higher in intensity than the second -F/+H exchange. This contrasts with PFOS, which underwent a total of five -F/+H exchanges. This suggests that, whereas PFOS undergoes multiple -F/+H exchanges upon attack by aqueous electrons, the majority of PFOA will transform through a separate pathway. Based on the transformation products identified and the trends in their occurrence, this pathway is likely a chain-shortening transformation pathway. Based on the sum of PFCAs generated following degradation, the chain-shortening pathway is a major transformation mechanism for PFOA but a minor transformation mechanism for PFOS.

3.4.5.6:2 FTS Transformation Products

For 6:2 FTS no shorter-chained PFCAs were found in the high concentration trials at both pH 7 and 11. However, similarly to those found following PFOA and PFOS degradation, several non-quantifiable fluorinated degradation products were identified, including -F/+H exchanged 6:2 FTS, alkylated 6:2 FTS, and alcohol/alkoxy substituted 6:2 FTS (Figure 3.5, Figure A5, Table A9, A10). Like PFOS, 6:2 FTS was found to undergo substantial -F/+H exchange, with an additional six substitutions occurring.

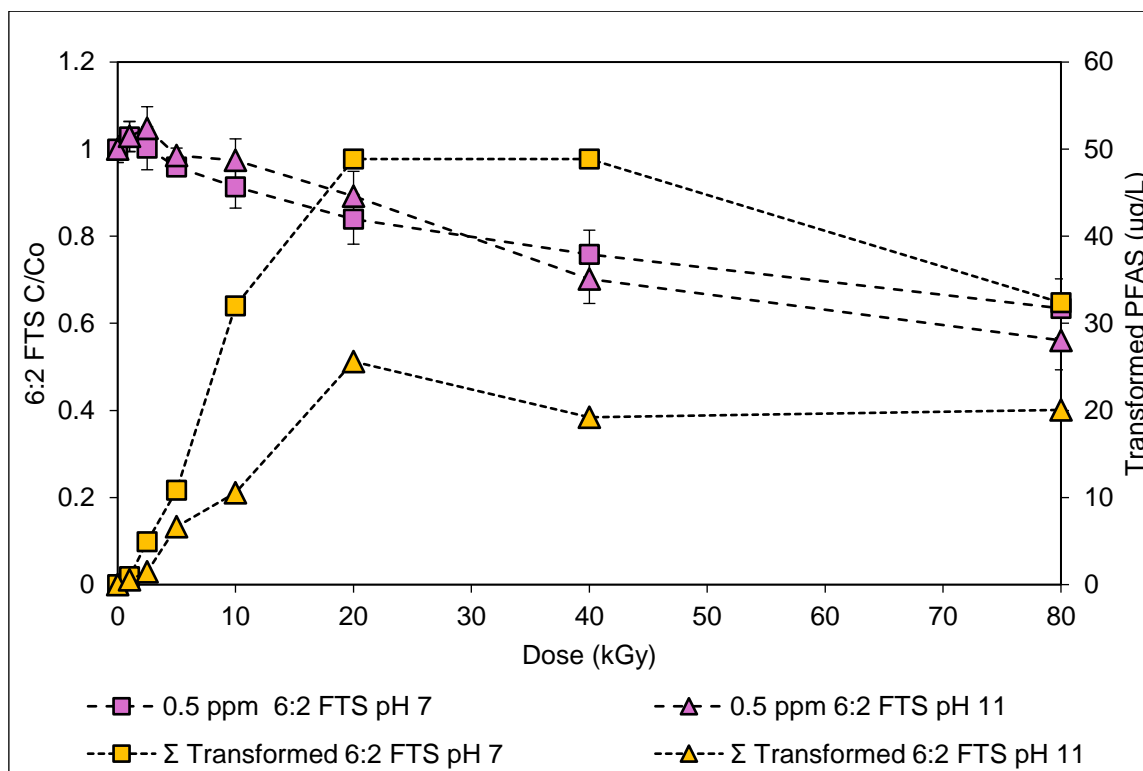


Figure 3.5 - Degradation of 6:2 FTS with subsequent generation of semi-quantified 6:2 FTS transformation products at pH 7 and 11. Left Y-axis for 6:2 FTS, right Y-axis for transformed 6:2 FTS. Error bars are standard deviation of replicates. Some error bars are too small to be shown. N=1 for transformation product analysis.

The lack of shorter-chained PFCAs identified following 6:2 FTS degradation is due to the presence of methanol, which scavenges hydroxyl radicals. For fluorotelomers, hydroxyl radicals allow for a hydrogen abstraction mechanism to occur, resulting in a radical fluorotelomer molecule that can undergo subsequent reaction, including substitution, double-bond formation, or functional group elimination(Liu et al., 2021).

3.4.6. Initial Fluoride Removal

It has been previously hypothesized that PFOS degradation occurs through removal of an α -fluoride (Bentel et al., 2020, 2019). This hypothesis was supported by molecular modelling, identifying the α -position fluoride as being most susceptible to bond breakage following the addition of an electron to the PFAS structure (Bentel et al., 2019).

In the present study, the chromatographic resolution was optimized to separate and identify different isomers of the various -F/+X substituted PFAS. Inspection of the -F/+H, -F/+OH, and -4F/+4H chromatograms identify multiple peaks, which correspond to multiple isomers, providing chromatographic evidence that the initial fluoride removal does not take place solely at the α -position (Figure 3.6).

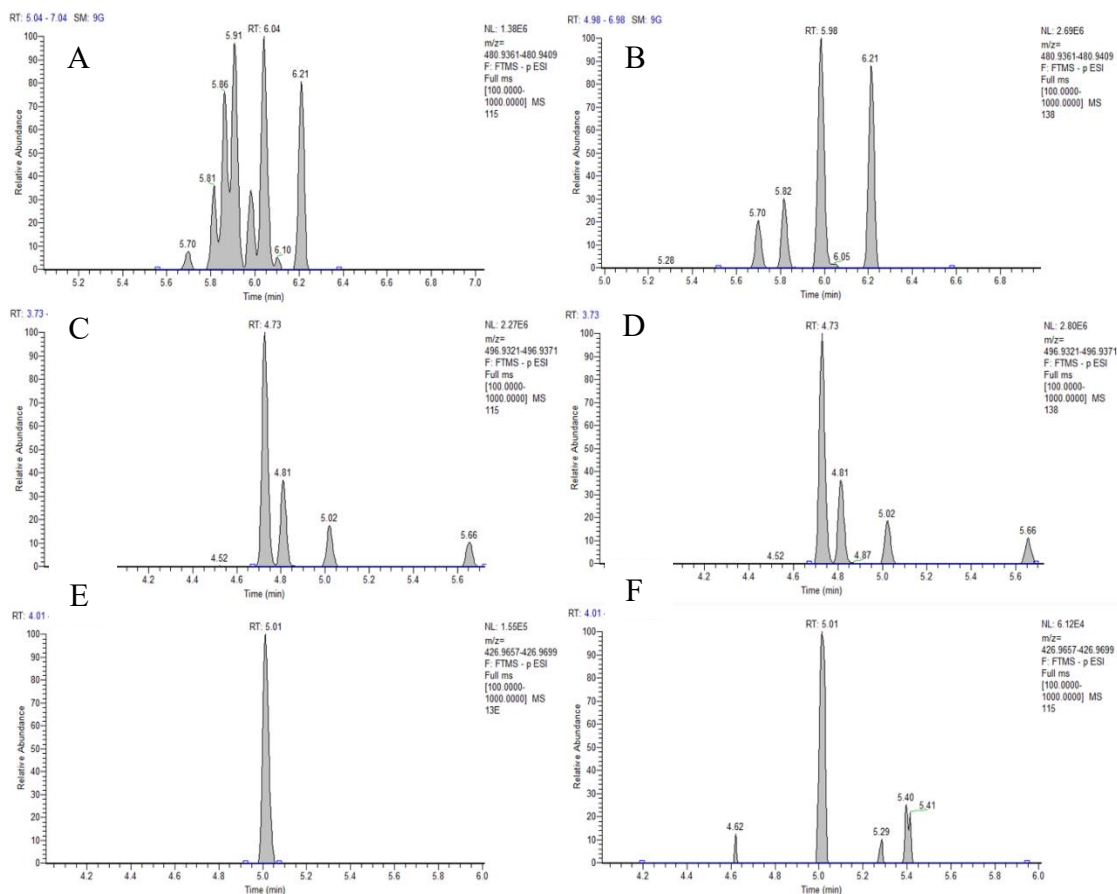


Figure 3.6 - Chromatograms of -F/+H PFOS at pH 7 (A); -F/+H PFOS at pH 11 (B); -F/+OH PFOS at pH 7 (C), -F/+OH PFOS at pH 11 (D); 6:2 FTS (E); and -4F/+4H PFOS at pH 7 (F)

Inspection of the -F/+H exchanged PFOS at pH 7 (Figure 3.6A) shows eight different chromatographic peaks with varying intensities, suggesting that each of the eight carbons in PFOS can undergo the initial fluoride removal and subsequent attack by a hydrogen radical. At pH 11 (Figure 3.6B), only four peaks and a right shoulder can be identified, suggesting less +H substitution can occur. We hypothesize that this is due to the conversion of hydrogen radicals to aqueous electrons under alkaline conditions, resulting in fewer hydrogen radicals for the substitution. Inspection of the -F/+OH exchanged PFOS at pH 7 and 11 (Figure 3.6C, D) shows four baseline separated peaks. The different -F/+OH isomers have different retention times, caused by the location of the hydroxyl group. Different -F/+H and -F/+OH isomers were also found for PFOA, and to a lesser extent 6:2 FTS.

Lastly, inspection of the -4F/+4H exchanged PFOS (Figure 3.6F), which has the same mass (m/z 426.9679) as 6:2 FTS (Figure 3.6E), provides additional evidence for the non- α fluoride removal. If -F/+H exchange occurs at the α -fluoride and moves down the chain, the two chromatograms should be identical because the compounds are the same. Instead, the -4F/+4H PFOS created from the degradation of PFOS (Figure 3.6F) shows four, potentially five different peaks, compared to one 6:2 FTS peak (Figure 3.6E). This confirms that the carbon position at which fluorides are initially removed may vary, resulting in an assortment of polyfluorinated products.

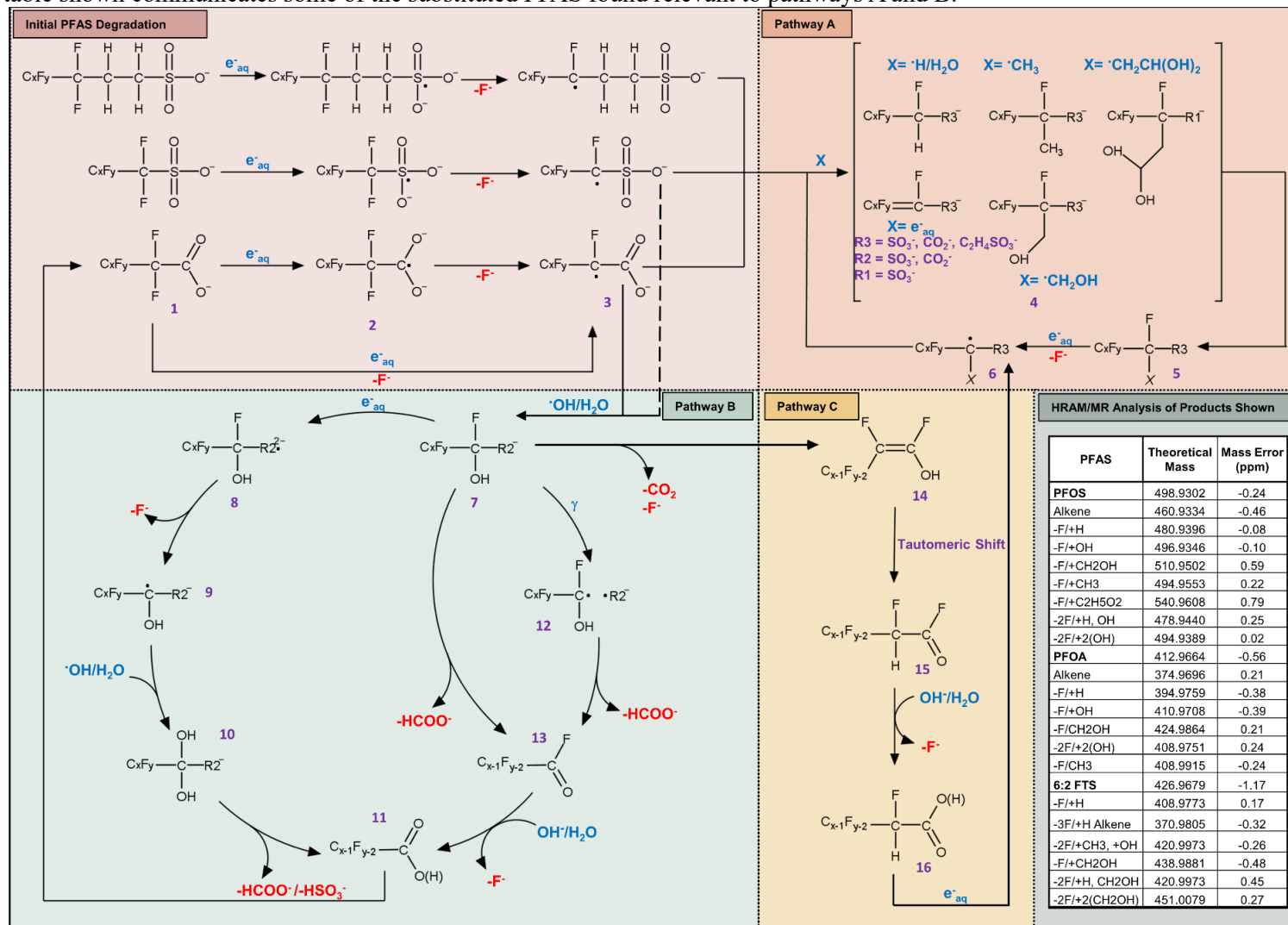
There is the potential for fluoride atom rearrangements within the PFOS molecule following initial radical attack, causing the molecule to stabilize the radical charge closer to the middle of the chain (van Hoomissen and Vyas, 2017). Future work would benefit from NMR to confirm the observations made here. The $n > 1$ -F_n/+H_n exchanged PFOS products are degraded with increasing irradiation, indicating that they are likely degraded more readily than the parent PFOS molecule (Figure A3).

3.4.7. PFAS Transformation Mechanism

It is well known that the initial degradation of PFAS by gamma irradiation is due to attack by aqueous electrons (Kowald et al., 2021; Trojanowicz et al., 2020, 2019, 2018). This is not only supported by literature, but also supported by observations in this study of enhanced degradation under alkaline conditions, which favours aqueous electron generation (Christiane, 2000). The degradation of high concentrations of PFAS and the use of high-resolution spectrometry in this study has allowed for the identification of numerous fluorinated transformation products, each with varying intensities and kinetics. By connecting these transformation products together in the

shortest number of reactions, a simplified overarching transformation mechanism can be proposed (Scheme 1). For simplicity, the degradation mechanism of PFAS will be discussed and illustrated assuming α -fluoride loss, although evidence in this study supports that an initial fluoride removal is possible along the carbon chain.

Scheme 3.1 - Proposed mechanisms for α -position C-F bond breakage of PFAS leading to fluorine substitution or and chain shortening. The table shown communicates some of the substituted PFAS found relevant to pathways A and B.



As described by others, the transition from PFAS (**1**) to compound **3** is most likely the first step of the degradation mechanism. In one route, the addition of an aqueous electron to PFAS (**1**) results in a highly unstable, radical double anion (**2**). Loss of a fluoride and electron rearrangement consequently reestablishes the functional group moiety and relocates the radical to the α -carbon for PFOS/PFOA, and the first fluorinated carbon for 6:2 FTS (**3**). In a second route, direct attack of the C-F bond by an aqueous electron occurs, resulting in direct formation of the radical PFAS without the need for electron rearrangement (**3**). The observations in this study of non α -fluoride loss support both direct C-F bond attack and radical rearrangement, either towards loss of the α -fluoride or another fluoride along the chain via a 1,2-fluorine atom rearrangement (van Hooymissen and Vyas, 2017). Once the PFAS radical has been created (**3**), two different reaction pathways are possible depending on the radical species that attacks the PFAS molecule. In pathway A, electron recombination with a hydrogen radical (generated directly by gamma irradiation or via hydrogen abstraction from water), alkyl radical, carbanion radical, alkoxy radical, or aqueous electron will result in a number of substituted products (**4**), which have all been identified in this study (Table A7-A10). Subsequent attack by an aqueous electron will result in a radical-substituted PFAS (**6**), which will once again react with the radicals to create more varied substitutions. This supports the observations of multiple -F/+H exchanged PFOS and 6:2 FTS molecules. The identification of -CF₃/+H exchanged PFOS also supports earlier discussion as to the degradation pathway for branched PFOS isomers.

In pathway B, electron recombination with a hydroxyl radical, either directly from the reaction media or via hydroxy abstraction from water, results in the formation of the -F/+OH exchanged PFCA (the α -hydroxy PFAS, compound **7**) which is observed experimentally.

From **7**, the most likely reaction involves attack by an aqueous electron, forming the radical double anion (**8**), which loses an α -fluoride upon electron rearrangement to the radical α -hydroxy PFAS (**9**), similar to that described above for **1** to **3**. Attack by a hydroxyl radical (or hydroxyabstraction from water) results in the α -dihydroxy PFAS (**10**, observed experimentally). Decarboxylation by release of formate, which has been identified in the literature (Trojanowicz et al., 2020, 2019), forms the n-1 PFCA (**11**).

Alternatively, from **7**, electron rearrangement and release of the formate anion directly (Pathway **B**) would form the n-1 acyl fluoride (**13**). Hydrolysis of the carbonyl fluoride with either water or a hydroxide ion would result in the n-1 PFCA (**11**). As the driving force for this rearrangement is

not well-understood, pathway **B** may be less likely than **A**. It is also possible that interaction of **7** with a gamma photon could result in homolytic cleavage of the C-C bond (**12**). The newly formed radicals could then undergo an immediate radical disproportionation, where the CO₂-radical abstracts the hydroxy-hydrogen to produce formate, and the hydroxy-carbon radical, having essentially undergone an elimination reaction, rearranges to form the carbonyl (**13**).

The n-1 PFCA (**11**) may continue to react with aqueous electrons and follow the same degradation pathways to reduce the length of the carbon chain, producing formate and fluoride ions. Although we did not probe for the production of formate in this work, others have detected it during degradation reactions.

Many of the proposed degradation mechanisms in the literature instead postulate CO₂ as being released during decarboxylation of the PFCA head group. However, to achieve electron balance, direct release of CO₂ in a reducing environment would result in formation of an unstable carbanion (in fact, the dearth of accessible electrophiles in the basic, reducing medium would more likely encourage the reverse reaction of the carbanion with CO₂ to form the carboxylate). Regardless, the most likely scenario that involves loss of CO₂ and formation of one of the identified products may involve direct decarboxylation of the α -hydroxy PFAS (**7**) (Pathway **C**). The carbanion generated in this case would rearrange via loss of the β -fluoride to the n-1 perfluorinated enol (**14**). Base-catalyzed tautomerization to the -F/+H exchanged acyl fluoride (**15**), followed by hydrolysis, would result in the -F/+H exchanged n-1 PFCA (**16**) with consequent release of fluoride (or HF). As above for pathway **B**, the driving force for the direct loss of CO₂ from an α -hydroxy carboxylate under these conditions is not well understood. As such, the -F/+H-exchanged n-1 PFCA is most likely formed upon degradation of the n-1 PFCA (**9**) following the mechanism described above for (**7**). Of the possible variations of mechanisms presented, the mechanism that follows the numerical order of compounds **1-11** is most likely as it does not rely on direct interaction of the molecule with a gamma photon (a rare event) and relies mainly on the generation of aqueous electrons, which have been identified in previous works.

3.4.8. Degradation of PFAS_{13Suite} and Impact of Chain Length

Following the single PFAS irradiation experiments, the degradation of PFAS_{13Suite} in nitrogen-purged neutral (pH 7) and alkaline (pH 11) solutions was investigated (Figure 3.1). With the presence of methanol (1%) scavenging hydroxyl radicals, the only reactive species expected are aqueous electrons and hydrogen radicals.

At the high concentration of the PFAS_{13Suite} trials, (~0.1 mg/L per individual PFAS) PFCAs underwent, on average, 98±2% degradation at pH 7 and 97±3% at pH 11. PFBA had the lowest total degradation of 90% at pH 7 and 92% at pH 11 (Figure 3.1). This is due to smaller chain PFAS being resistant to degradation. It was found that PFOA in the combined trials had a total degradation of 99% at pH 7 and 11, higher than its total degradation at either pH or concentration (62–87)% when irradiated independently. It was originally hypothesized that total degradation of PFOA would be equal to or less than that observed in the independent irradiation trials, as it was expected that larger chain PFAS (C9-C12 PFCAs) would degrade into PFOA, and that other species would concurrently utilize energy/reactive species. However, the presence of methanol and the scavenging of hydroxyl radicals results in an aqueous-electron dominant degradation mechanism (Pathway A), resulting in more complete degradation of PFOA and the other PFCAs.

The three PFASs experienced different amounts of degradation as a function of their chain length. PFOS underwent total degradations of 61±1% at pH 7 and 46±3% at pH 11; PFHxS underwent total degradations of 50±1% at pH 7 and 38±0% at pH 11; and PFBS underwent total degradations of 2±1% at pH 7 and 4±1% at pH 11 (Figure 3.1). Other researchers have also observed this difficulty in degrading shorter-chained PFASs (Bentel et al., 2019). The resistance of PFBS to degradation and increased rate constant of larger-chained PFCAs indicates that the length of the PFAS chain plays a key role in degradation. While these C-F bond energies have been calculated in other literature and were found to be higher with smaller molecules, it is also possible that the helical nature of the C-F bonds plays a role in protecting the PFAS molecule from degradation. As the chain length of the molecule increases, it is easier for the C-C bonds to rotate and the C-F bond to be exposed to attack the by a reactive species. It is also possible that the higher bond energies are more difficult to break via direct aqueous electron attack, as suggested in Scheme 1.

FOSA, the sulfonamide, experienced different degradation amounts due to pH, with a total degradation of 99±1% at pH 7 and 70±3% at pH 11 (Figure 3.1). This difference in degradation is a result of differences in the overall charge of FOSA as a function of pH (pKa =6.24) (Rayne and Forest, 2009). Under neutral conditions there will likely be a distribution of neutral and anionic FOSA, with neutral FOSA is easier to attack with an aqueous electron than the anionic FOSA. At pH 11 all the FOSA will be in the anionic form, which is more difficult to attack with an aqueous electron due to the negative charge of the molecule and the negative charge of the electron. As many AFFF formulations contain FOSA or PFHxSA precursors with large nonfluorinated

headgroups, this has implications for the ideal pH at which to degrade AFFF components more completely.

The total concentration of fluoride in the PFAS_{13Suite} 80 kGy dosed samples was analyzed at both pH 7 and 11. Based on the total PFAS degradation, 103 ±3% and 90±3% of the expected fluoride concentration was measured at pH 7 and 11 assuming complete mineralization of the degraded PFAS. This suggests that, unlike PFOS and PFOA trials where the initial PFAS degraded into PFCAs and polyfluorinated compounds, the PFAS degraded in the mixture were more easily mineralized. This is due to the presence of methanol resulting in aqueous electron dominant degradation mechanisms.

First order and zero order rates were calculated for all PFAS between various dosages (Table A4-A6). As was also observed with the PFOA-only irradiation trials, PFCAs were found to degrade almost twice as fast at pH 11 compared to 7, with an average first order rate constant of 0.34±0.05 kGy⁻¹ at pH 7 and 0.63±0.18 kGy⁻¹ at pH 11. An exception to this was PFUnA, which had similar rates of degradation at both pH's, and PFDoA, which degraded twice as fast at pH 7. At pH 7 there is an increase in rate constant as a function of increasing carbon length. At pH 11, this trend holds true until PFDA, in which the rate constant decreases dramatically with increasing carbon length (Figure 3.7, A5). This could be due to the longer-chain PFCAs being easier to degrade under neutral conditions, having pKa compared to shorter- and medium-chain PFCAs and therefore a larger fraction of neutral molecules, which could be less repulsive to aqueous electron attack than anionic forms. However, the pKa of even long-chain PFCAs is still quite low, suggesting all of the compound will still be in the anionic form, and differences would be very small.

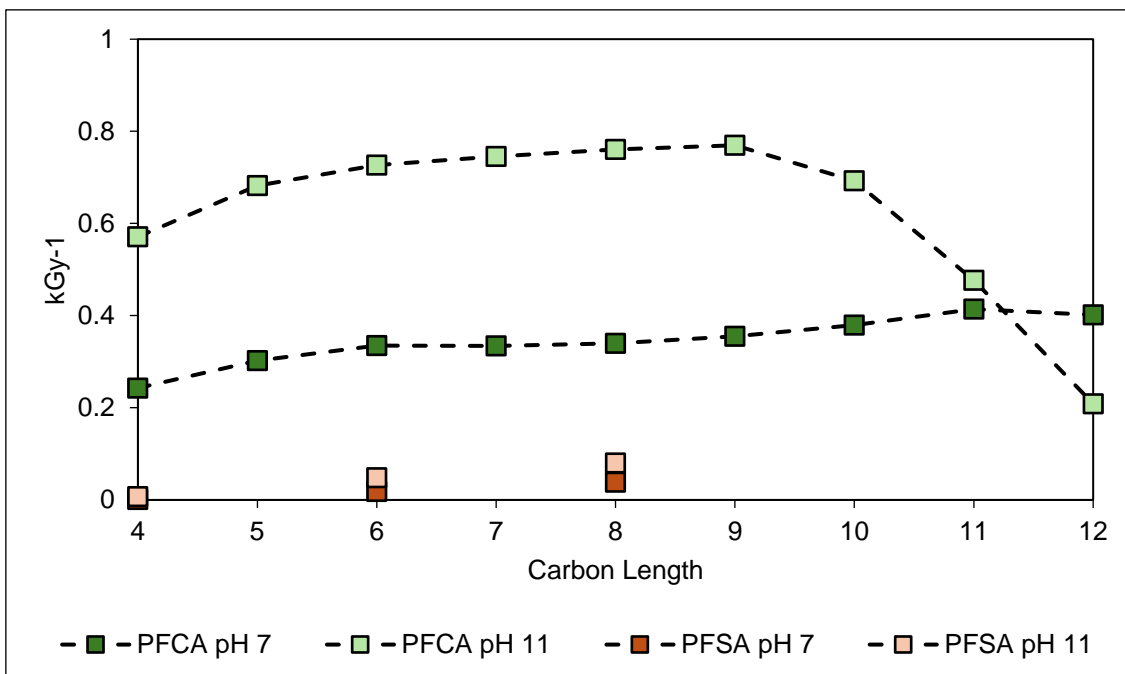


Figure 3.7 - First order transformation rate constant (from 0-5 kGy) for PFCAs plotted as a function of carbon length during PFAS suite irradiation to identify comparative trends.

It was also observed that PFOA in the PFAS_{13Suite} degraded 7-10 times faster than when irradiated independently, providing further evidence of an enhanced degradation mechanism in the presence of methanol. Fluorinated transformation products similar to those found with PFOS/PFOA degradation were identified when analyzing the PFAS_{13Suite} samples, but due to the lower concentration of these PFAS only a handful of products could be found, likely due to their intensity relative to the other identified degradation products. The two main groups of products identified were the -F/+H, -F/+OH, and -F/+CH₂OH exchanged PFAS. These were found for all PFCAs, PFSA (except PFBS, due to lack of degradation), and FOSA (Table 3.2).

Table 3.2 - Unquantified degradation products of PFOS, PFOA, 6:2 FTS, and PFAS_{13Suite}

	PFOS	PFOA	6:2 FTS	PFAS_{13Suite}
PFCA	CF ₃ (CF ₂) _n COOH (n=0-7)	CF ₃ (CF ₂) _n COOH (n=0-5)		
Alkene	PFOS Alkene	PFOA Alkene	6:2 FTS -3F/ +H, Alkene	
-F/+H	PFOS -F _n /+H _n (n=1-5)	PFOA -F/+H (n=1,2)	6:2 FTS -F _n /+H _n (n=1-6)	PFCA/PFSA -F/+H
-F/ +Alkylation	PFOS -F/+C _n H _{2n+1} (n=1,2)	PFOA -F/+C _n H _{2n+1} (n=1)		
-F/+OH	PFOS -F _n /+(OH) _n (n=1,2)	PFOA -F _n /+(OH) _n (n=1,2)	6:2 FTS -2F/+CH ₃ , +OH	PFCA/PFSA/PFOA -F/+OH
	PFOS -2F/ +H, OH			
-F/ +CxHyOz	PFOS -F/+C _n H _{2n} OH (n=1-3)	PFOA -F/+C _n H _{2n} OH (n=1-4)	6:2 FTS -F _n /+(CH ₂ OH) _n (n=1,2)	PFCA/PFSA/PFOA -F/+CH ₂ OH
	PFOS -F/+C _n H _{2n-1} (OH) ₂ (n=2-6)		6:2 FTS -3F/+2H, CH ₂ OH	
Other	C ₇ F ₁₄ HSO ₃			
	C ₈ F ₁₇ SO ₂			
	C ₈ F ₁₇ SO ₄			

3.4.9. Implications for Future Work

The mechanistic and transformation product information obtained from this investigation can help in understanding degradation observed in PFAS remediation studies. Achieving mass balance is critical when evaluating the remediation effectiveness of PFAS destruction technologies. Examining the degradation of PFAS in a controlled system (N₂ purged DI water) allowed for a fundamental investigation into PFAS degradation and transformation. Semi-quantification of fluorinated transformation products can assist in achieving mass balance and allow for better estimations of overall remediation effectiveness. Having established this fundamental understanding, a more comprehensive investigation can be performed with environmentally relevant PFAS-contaminated water.

Many authors have identified possible challenges that arise when scaling up irradiation-based PFAS treatment technologies. There are many scavengers present in natural waters that may interfere with the radicals generated by water-radiolysis remediation technologies (gamma, electron beam, UV to a lesser extent). Aqueous electrons, identified in this study and others as being critical for PFAS degradation, are rapidly scavenged by dissolved oxygen ($1.9 \times 10^{10} \text{ M}^{-1} \text{ s}^{-1}$) (Trojanowicz et al., 2020, 2019, 2018; Zhang et al., 2014) . While dissolved oxygen can be

removed from a system via purging with inert gas (most commonly N₂ or Ar₂), the use of purging can limit scalability and applicability to treating environmentally relevant systems. To address this, future work would benefit from investigating the use of dissolved oxygen scavengers. Reagents such as sulfite, bisulfite, bicarbonate and diethylaminoethanol are used in large quantities to remove dissolved oxygen in boiler feed water and gas hydrate applications (Alef et al., 2018). Other aqueous electron scavengers include nitrate ($9.7 \times 10^9 \text{ M}^{-1} \text{ s}^{-1}$), nitrite ($3.5 \times 10^6 \text{ M}^{-1} \text{ s}^{-1}$), and chloride ($<1.0 \times 10^6 \text{ M}^{-1} \text{ s}^{-1}$) (Trojanowicz, 2020). Removal of the resulting excess nitrate from water could be accomplished using ion-exchange resins or reverse osmosis, although it is possible to remove nitrate via reduction to ammonia with iron or aluminum (Sharma and Chander Sobti, 2012; Shrimali et al., 2001).

Work by Lyu et al. (2015) identified enhanced degradation of PFOS in natural waters compared to DI water, attributed to either oxidative DOM-derived intermediates or through hydroxyl radical quenching (Lyu et al., 2015). Dissolved organic matter (DOM) present in natural waters has been shown to scavenge hydroxyl radicals from radiolysis processes ($2.0 \times 10^8 \text{ M}^{-1} \text{ s}^{-1}$) (Trojanowicz, 2020). As identified in the present study, the presence of hydroxyl radicals causes PFAS to undergo an inefficient chain-shortening degradation mechanism instead of a direct defluorination mechanism. Therefore, the presence of DOM or other hydroxyl scavengers would enhance PFAS degradation, thereby supporting observations made by Lyu et al. (2015) and others. While the addition of alcohols to scavenge hydroxyl radicals is being performed in literature, future work would benefit from LC-HRMS, NMR, and GC-MS analysis to identify additional transformation products and elucidate the exact mechanism (s) that occur in the presence of DOM or added scavengers.

3.5. Conclusions

This study examined the gamma irradiation of PFAS at different concentrations, chain lengths, fluorine saturation, functional group and pH. Insights and experimental evidence gained by this investigation support previous postulations and conclusions that the reactive species responsible for the initial transformation of PFAS is the aqueous electron (Trojanowicz et al., 2020, 2019). The enhanced degradation of PFCAs in methanol-spiked aqueous solutions provides further evidence of the effectiveness of aqueous-electron dominant degradation processes, as it was identified that the chain-shortening mechanism for PFCAs is a mineralization-inefficient process. This identification is important because it further supports that reductive-based aqueous remediation

technologies will have more success compared to oxidation-based aqueous remediation technologies.

Through the identification of >80 fluorinated transformation products using high-resolution mass spectrometry we have expanded the current understanding in the literature to generate experimental evidence for a unified 3 pathway and 16 step reaction schematic for PFAS irradiation in water. We have also identified that the α -fluoride is not always the first step for a H⁺/F⁻ exchange; rather this exchange can occur throughout the chain length. Our results support and are supported by observed success in technologies that facilitate a reductive environment in non-aqueous conditions, such as thermal or ball-milling based technologies (Duchesne et al., 2020; Turner et al., 2021; Zhang et al., 2013).

The effective transformation of PFCAs, especially mixtures of different PFCAs, suggest that this technique could be tailored for applications to sites with predominantly PFCA contamination. The possible protective helical nature of the PFAS chain might also indicate that a minimum activation energy, in the form of temperature, may be required to allow for untwisting of the PFAS structure and subsequent attack. Lastly, linear PFOS and 6:2 FTS were found to have similar trends in their degradation, suggesting the sulfonate functional group has a large impact on the resistance to degradation. This suggests that, where possible, oxidation of sulfonate-containing fluorotelomers followed by reduction of the resulting PFCAs may be a more effective remediation option than attempting direct reduction.

3.6. Acknowledgements

This work was supported by Natural Sciences and Engineering Research Council (Canada) Discovery grants of Weber and Koch. The authors would like to acknowledge Tyler Buote for hands-on assistance with sample preparation, and Mike DeArruda for packing, shipping, and receiving of samples for international transport.

3.7. References

- Abusallout, I., Wang, J., Hanigan, D., 2021. Emerging investigator series: rapid defluorination of 22 per- and polyfluoroalkyl substances in water using sulfite irradiated by medium-pressure UV. *Environmental Science: Water Research & Technology* 7, 1552–1562. <https://doi.org/10.1039/d1ew00221j>
- Al Amin, M., Luo, Y., Nolan, A., Robinson, F., Niu, J., Warner, S., Liu, Y., Dharmarajan, R., Mallavarapu, M., Naidu, R., Fang, C., 2021. Total oxidisable precursor assay towards selective detection of PFAS in AFFF. *Journal of Cleaner Production*. Elsevier Ltd. <https://doi.org/10.1016/j.jclepro.2021.129568>
- Alef, K., Iglauer, S., Barifcani, A., 2018. Effect of Dissolved Oxygen, Sodium Bisulfite, and Oxygen Scavengers on Methane Hydrate Inhibition. *Journal of Chemical and Engineering Data* 63, 1821–1826. <https://doi.org/10.1021/acs.jced.8b00150>
- Arlos, M.J., Liang, R., Li Chun Fong, L.C.M., Zhou, N.Y., Ptacek, C.J., Andrews, S.A., Servos, M.R., 2017. Influence of methanol when used as a water-miscible carrier of pharmaceuticals in TiO₂ photocatalytic degradation experiments. *Journal of Environmental Chemical Engineering* 5, 4497–4504. <https://doi.org/10.1016/j.jece.2017.08.048>
- Armstrong, W.A., 1969. Relative rate constants for reactions of hydroxyl radicals from the reaction of Fe (II) or Ti(III) with H₂O₂. *Canadian Journal of Chemistry* 47, 3737–3744. <https://doi.org/10.1139/v69-623>
- Arvaniti, O.S., Hwang, Y., Andersen, H.R., Stasinakis, A.S., Thomaidis, N.S., Aloupi, M., 2015. Reductive degradation of perfluorinated compounds in water using Mg-aminoclay coated nanoscale zero valent iron. *Chemical Engineering Journal* 262, 133–139. <https://doi.org/10.1016/j.cej.2014.09.079>
- Axmon, A., Axelsson, J., Jakobsson, K., Lindh, C.H., Jönsson, B.A.G., 2014. Time trends between 1987 and 2007 for perfluoroalkyl acids in plasma from Swedish women. *Chemosphere* 102, 61–67. <https://doi.org/10.1016/j.chemosphere.2013.12.021>
- Bentel, M.J., Liu, Z., Yu, Y., Gao, J., Men, Y., Liu, J., 2020. Enhanced Degradation of Perfluorocarboxylic Acids (PFCAs) by UV/Sulfite Treatment: Reaction Mechanisms and System Efficiencies at pH 12. *Environmental Science and Technology Letters* 7, 351–357. <https://doi.org/10.1021/acs.estlett.0c00236>
- Bentel, M.J., Yu, Y., Xu, L., Li, Z., Wong, B.M., Men, Y., Liu, J., 2019. Defluorination of Per- and Polyfluoroalkyl Substances (PFASs) with Hydrated Electrons: Structural Dependence and Implications to PFAS Remediation and Management. *Environmental Science and Technology* 53, 3718–3728. <https://doi.org/10.1021/acs.est.8b06648>
- Buck, R.C., Franklin, J., Berger, U., Conder, J.M., Cousins, I.T., Voogt, P. de, Jensen, A.A., Kannan, K., Mabury, S.A., van Leeuwen, S.P.J., 2011. Perfluoroalkyl and polyfluoroalkyl substances in the environment: Terminology, classification, and origins. *Integrated Environmental Assessment and Management* 7, 513–541. <https://doi.org/10.1002/ieam.258>
- Christiane, F., 2000. The Effect of pH on Water Radiolysis: A Still Open Question. *Research on Chemical Intermediates* 26, 549–565.
- Dombrowski, P.M., Kakarla, P., Caldicott, W., Chin, Y., Sadeghi, V., Bogdan, D., Barajas-Rodriguez, F., Chiang, S.Y.D., 2018. Technology review and evaluation of different chemical oxidation conditions on treatability of PFAS. *Remediation* 28, 135–150. <https://doi.org/10.1002/rem.21555>
- Dong, H., Qiang, Z., Richardson, S.D., 2019. Formation of Iodinated Disinfection Byproducts (I-DBPs) in Drinking Water: Emerging Concerns and Current Issues. *Accounts of Chemical Research* 52, 896–905. <https://doi.org/10.1021/acs.accounts.8b00641>

- Duchesne, A.L., Brown, J.K., Patch, D.J., Major, D., Weber, K.P., Gerhard, J.I., 2020. Remediation of PFAS-Contaminated Soil and Granular Activated Carbon by Smoldering Combustion. *Environmental Science and Technology* 54, 12631–12640. <https://doi.org/10.1021/acs.est.0c03058>
- Gebbink, W.A., Glynn, A., Berger, U., 2015. Temporal changes (1997-2012) of perfluoroalkyl acids and selected precursors (including isomers) in Swedish human serum. *Environmental Pollution* 199, 166–173. <https://doi.org/10.1016/j.envpol.2015.01.024>
- Getoff, N., 1996. Radiation-induced degradation of water pollutants - State of the art. *Radiation Physics and Chemistry* 47, 581–593. [https://doi.org/10.1016/0969-806X\(95\)00059-7](https://doi.org/10.1016/0969-806X(95)00059-7)
- Granum, B., Haug, L.S., Namork, E., Stølevik, S.B., Thomsen, C., Aaberge, I.S., Van Loveren, H., Løvik, M., Nygaard, U.C., 2013. Pre-natal exposure to perfluoroalkyl substances may be associated with altered vaccine antibody levels and immune-related health outcomes in early childhood. *Journal of Immunotoxicology* 10, 373–379. <https://doi.org/10.3109/1547691X.2012.755580>
- Hall, L.A., Denning, D.W., 1994. Oxygen requirements of *Aspergillus* species, *J. Med. Microbiol.*
- Hansen, S., Vestergren, R., Herzke, D., Melhus, M., Evenset, A., Hanssen, L., Brustad, M., Sandanger, T.M., 2016. Exposure to per- and polyfluoroalkyl substances through the consumption of fish from lakes affected by aqueous film-forming foam emissions — A combined epidemiological and exposure modeling approach. The SAMINOR 2 Clinical Study. *Environment International* 94, 272–282. <https://doi.org/10.1016/j.envint.2016.05.030>
- Herzke, D., Olsson, E., Posner, S., 2012. Perfluoroalkyl and polyfluoroalkyl substances (PFASs) in consumer products in Norway - A pilot study. *Chemosphere* 88, 980–987. <https://doi.org/10.1016/j.chemosphere.2012.03.035>
- Hori, H., Nagaoka, Y., Sano, T., Kutsuna, S., 2008. Iron-induced decomposition of perfluorohexanesulfonate in sub- and supercritical water. *Chemosphere* 70, 800–806. <https://doi.org/10.1016/j.chemosphere.2007.07.015>
- Hori, H., Yamamoto, A., Hayakawa, E., Taniyasu, S., Yamashita, N., Kutsuna, S., Kiatagawa, H., Arakawa, R., 2005. Efficient decomposition of environmentally persistent perfluorocarboxylic acids by use of persulfate as a photochemical oxidant. *Environmental Science and Technology* 39, 2383–2388. <https://doi.org/10.1021/es0484754>
- Houtz, E.F., Sedlak, D.L., 2012. Oxidative conversion as a means of detecting precursors to perfluoro-alkyl acids in urban runoff. *Environmental Science and Technology* 46, 9342–9349. <https://doi.org/10.1021/es302274g>
- Ike, I.A., Karanfil, T., Cho, J., Hur, J., 2019. Oxidation byproducts from the degradation of dissolved organic matter by advanced oxidation processes – A critical review. *Water Research* 164. <https://doi.org/10.1016/j.watres.2019.114929>
- Javed, H., Lyu, C., Sun, R., Zhang, D., Alvarez, P.J.J., 2020. Discerning the inefficacy of hydroxyl radicals during perfluorooctanoic acid degradation. *Chemosphere* 247. <https://doi.org/10.1016/j.chemosphere.2020.125883>
- Kim, T.H., Lee, S.H., Kim, H.Y., Doudrick, K., Yu, S., Kim, S.D., 2019. Decomposition of perfluorooctane sulfonate (PFOS) using a hybrid process with electron beam and chemical oxidants. *Chemical Engineering Journal* 361, 1363–1370. <https://doi.org/10.1016/j.cej.2018.10.195>
- Kim, T.H., Yu, S., Choi, Y., Jeong, T.Y., Kim, S.D., 2018. Profiling the decomposition products of perfluorooctane sulfonate (PFOS) irradiated using an electron beam. *Science of the Total Environment* 631–632, 1295–1303. <https://doi.org/10.1016/j.scitotenv.2018.03.055>

- Knobeloch, L., Imm, P., Anderson, H., 2012. Perfluoroalkyl chemicals in vacuum cleaner dust from 39 Wisconsin homes. *Chemosphere* 88, 779–783. <https://doi.org/10.1016/j.chemosphere.2012.03.082>
- Kowald, C., Brorman, E., Shankar, S., Klemashevich, C., Staack, D., Pillai, S.D., 2021. PFOA and PFOS breakdown in experimental sand, laboratory-grade water, investigation-derived groundwater and wastewater effluent samples at 50 kGy electron beam dose. *Radiation Physics and Chemistry* 180. <https://doi.org/10.1016/j.radphyschem.2020.109323>
- Kucharzyk, K.H., Darlington, R., Benotti, M., Deeb, R., Hawley, E., 2017. Novel treatment technologies for PFAS compounds: A critical review. *Journal of Environmental Management* 204, 757–764. <https://doi.org/10.1016/j.jenvman.2017.08.016>
- Li, F., Yang, N., Yang, Z., Cao, W., Zhou, Z., Liao, X., Sun, W., Yuan, B., 2020. Biomimetic degradability of linear perfluorooctanesulfonate (L-PFOS): Degradation products and pathways. *Chemosphere* 259, 127502. <https://doi.org/10.1016/j.chemosphere.2020.127502>
- Liu, C.S., Higgins, C.P., Wang, F., Shih, K., 2012. Effect of temperature on oxidative transformation of perfluorooctanoic acid (PFOA) by persulfate activation in water. *Separation and Purification Technology* 91, 46–51. <https://doi.org/10.1016/j.seppur.2011.09.047>
- Liu, X., Guo, Z., Krebs, K.A., Pope, R.H., Roache, N.F., 2014. Concentrations and trends of perfluorinated chemicals in potential indoor sources from 2007 through 2011 in the US. *Chemosphere* 98, 51–57. <https://doi.org/10.1016/j.chemosphere.2013.10.001>
- Liu, Z., Bentel, M.J., Yu, Y., Ren, C., Gao, J., Pulikkal, V.F., Sun, M., Men, Y., Liu, J., 2021. Near-Quantitative Defluorination of Perfluorinated and Fluorotelomer Carboxylates and Sulfonates with Integrated Oxidation and Reduction. *Environmental Science and Technology* 55, 7052–7062. <https://doi.org/10.1021/acs.est.1c00353>
- Lyu, X.J., Li, W.W., Lam, P.K.S., Yu, H.Q., 2015. Photodegradation of perfluorooctane sulfonate in environmental matrices. *Separation and Purification Technology* 151, 172–176. <https://doi.org/10.1016/j.seppur.2015.07.049>
- Mahinroosta, R., Senevirathna, L., 2020. A review of the emerging treatment technologies for PFAS contaminated soils. *Journal of environmental management* 255, 109896. <https://doi.org/10.1016/j.jenvman.2019.109896>
- Mejia-Avenidaño, S., Munoz, G., Sauvé, S., Liu, J., 2017. Assessment of the Influence of Soil Characteristics and Hydrocarbon Fuel Cocontamination on the Solvent Extraction of Perfluoroalkyl and Polyfluoroalkyl Substances. *Analytical Chemistry* 89, 2539–2546. <https://doi.org/10.1021/acs.analchem.6b04746>
- Merino, N., Qu, Y., Deeb, R.A., Hawley, E.L., Hoffmann, M.R., Mahendra, S., 2016. Degradation and Removal Methods for Perfluoroalkyl and Polyfluoroalkyl Substances in Water. *Environmental Engineering Science* 33, 615–649. <https://doi.org/10.1089/ees.2016.0233>
- Můčka, V., Bláha, P., Čuba, V., Červenák, J., 2013. Influence of various scavengers of •OH radicals on the radiation sensitivity of yeast and bacteria. *International Journal of Radiation Biology* 89, 1045–1052. <https://doi.org/10.3109/09553002.2013.817702>
- Munoz, G., Liu, J., 2017. Assessment of the Influence of Soil Characteristics and Hydrocarbon Fuel Cocontamination on the Solvent Extraction of Perfluoroalkyl and Polyfluoroalkyl Substances. <https://doi.org/10.1021/acs.analchem.6b04746>
- Ochoa-Herrera, V., Sierra-Alvarez, R., 2008. Removal of perfluorinated surfactants by sorption onto granular activated carbon, zeolite and sludge. *Chemosphere*. <https://doi.org/10.1016/j.chemosphere.2008.04.029>

- Ochoa-Herrera, V., Sierra-Alvarez, R., Somogyi, A., Jacobsen, N.E., Wysocki, V.H., Field, J.A., 2008. Reductive defluorination of perfluorooctane sulfonate. *Environmental Science and Technology* 42, 3260–3264. <https://doi.org/10.1021/es702842q>
- Okada, E., Kashino, I., Matsuura, H., Sasaki, S., Miyashita, C., Yamamoto, J., Ikeno, T., Ito, Y.M., Matsumura, T., Tamakoshi, A., Kishi, R., 2013. Temporal trends of perfluoroalkyl acids in plasma samples of pregnant women in Hokkaido, Japan, 2003-2011. *Environment International* 60, 89–96. <https://doi.org/10.1016/j.envint.2013.07.013>
- Olsen, G.W., Mair, D.C., Lange, C.C., Harrington, L.M., Church, T.R., Goldberg, C.L., Herron, R.M., Hanna, H., Nobiletti, J.B., Rios, J.A., Reagen, W.K., Ley, C.A., 2017. Per- and polyfluoroalkyl substances (PFAS) in American Red Cross adult blood donors, 2000–2015. *Environmental Research* 157, 87–95. <https://doi.org/10.1016/j.envres.2017.05.013>
- Pan, C.-G., Xiao, S.-K., Yu, K.-F., Wu, Q., Wang, Y.-H., 2021. Legacy and alternative per- and polyfluoroalkyl substances in a subtropical marine food web from the Beibu Gulf, South China: Fate, trophic transfer and health risk assessment. *Journal of Hazardous Materials* 403, 123618. <https://doi.org/https://doi.org/10.1016/j.jhazmat.2020.123618>
- Paul, A., Wannere, C.S., Schaefer, H.F., 2004. Do linear-chain perfluoroalkanes bind an electron? *Journal of Physical Chemistry A* 108, 9428–9434. <https://doi.org/10.1021/jp0312417>
- Petersen, M.S., Halling, J., Jørgensen, N., Nielsen, F., Grandjean, P., Jensen, T.K., Weihe, P., 2018. Reproductive function in a population of young faroese men with elevated exposure to polychlorinated biphenyls (PCBs) and perfluorinated alkylate substances (PFAS). *International Journal of Environmental Research and Public Health* 15, 1–14. <https://doi.org/10.3390/ijerph15091880>
- Rayne, S., Forest, K., 2009a. Perfluoroalkyl sulfonic and carboxylic acids: A critical review of physico-chemical properties, levels and patterns in waters and wastewaters, and treatment methods. *Journal of Environmental Science and Health - Part A Toxic/Hazardous Substances and Environmental Engineering* 44, 1145–1199. <https://doi.org/10.1080/10934520903139811>
- Rayne, S., Forest, K., 2009b. Comment on “perfluoroalkyl contaminants in an arctic marine food web: Trophic magnification and wildlife exposure.” *Environmental Science and Technology* 43, 6112. <https://doi.org/10.1021/es9013079>
- Robel, A.E., Marshall, K., Dickinson, M., Lunderberg, D., Butt, C., Peaslee, G., Stapleton, H.M., Field, J.A., 2017. Closing the Mass Balance on Fluorine on Papers and Textiles. *Environmental Science and Technology* 51, 9022–9032. <https://doi.org/10.1021/acs.est.7b02080>
- Ross, I., McDonough, J., Miles, J., Storch, P., Thelakkat Kochunarayanan, P., Kalve, E., Hurst, J., S. Dasgupta, S., Burdick, J., 2018. A review of emerging technologies for remediation of PFASs. *Remediation* 28, 101–126. <https://doi.org/10.1002/rem.21553>
- Sakaguchi, H., Hagiwara, H., Fukumori, Y., Tamaura, Y., Funaki, M., Hirose, S., 1993. Oxygen concentration-dependent induction of a 140-kDa protein in magnetic bacterium *Magnetospirillum magnetotacticum* MS-1. *FEMS Microbiology Letters* 107, 169–173. <https://doi.org/10.1111/j.1574-6968.1993.tb06025.x>
- Schrenk, D., Bignami, M., Bodin, L., Chipman, J.K., del Mazo, J., Grasl-Kraupp, B., Hogstrand, C., Hoogenboom, L., Leblanc, J.C., Nebbia, C.S., Nielsen, E., Ntzani, E., Petersen, A., Sand, S., Vleminckx, C., Wallace, H., Barregård, L., Ceccatelli, S., Cravedi, J.P., Halldorsson, T.I., Haug, L.S., Johansson, N., Knutsen, H.K., Rose, M., Roudot, A.C., Van Loveren, H., Vollmer, G., Mac-kay, K., Riolo, F., Schwerdtle, T., 2020. Risk to human health related to the presence of perfluoro-alkyl substances in food. *EFSA Journal* 18, e06223. <https://doi.org/10.2903/j.efsa.2020.6223>

- Schultes, L., Vestergren, R., Volkova, K., Westberg, E., Jacobson, T., Benskin, J.P., 2018. Per- and polyfluoroalkyl substances and fluorine mass balance in cosmetic products from the Swedish market: Implications for environmental emissions and human exposure. *Environmental Science: Processes and Impacts* 20, 1680–1690. <https://doi.org/10.1039/c8em00368h>
- Sharma, S.K., Chander Sobti, R., 2012. Nitrate Removal from Ground Water: A Review.
- Shrimali, M, Singh, K.P., 2001. New methods of nitrate removal from water.
- Singh, R.K., Fernando, S., Baygi, S.F., Multari, N., Thagard, S.M., Holsen, T.M., 2019. Breakdown Products from Perfluorinated Alkyl Substances (PFAS) Degradation in a Plasma-Based Water Treatment Process. *Environmental Science and Technology* 53, 2731–2738. <https://doi.org/10.1021/acs.est.8b07031>
- Stanifer, J.W., Stapleton, H.M., Souma, T., Wittmer, A., Zhao, X., Boulware, L.E., 2018. Perfluorinated chemicals as emerging environmental threats to kidney health: A scoping review. *Clinical Journal of the American Society of Nephrology* 13, 1479–1492. <https://doi.org/10.2215/CJN.04670418>
- Sunderland, E.M., Hu, X.C., Dassuncao, C., Tokranov, A.K., Wagner, C.C., Allen, J.G., 2019. A re-view of the pathways of human exposure to poly- and perfluoroalkyl substances (PFASs) and pre-sent understanding of health effects. *Journal of Exposure Science and Environmental Epidemiology* 29, 131–147. <https://doi.org/10.1038/s41370-018-0094-1>
- Tian, Z., Kim, S.-K.K., Shoeib, M., Oh, J.-E.E., Park, J.-E.E., 2016. Human exposure to per- and polyfluoroalkyl substances (PFASs) via house dust in Korea: Implication to exposure pathway. *Science of the Total Environment* 553, 266–275. <https://doi.org/10.1016/j.scitotenv.2016.02.087>
- Trojanowicz, M., 2020. Removal of persistent organic pollutants (POPs) from waters and wastewaters by the use of ionizing radiation. *Science of the Total Environment*. <https://doi.org/10.1016/j.scitotenv.2019.134425>
- Trojanowicz, M., Bartosiewicz, I., Bojanowska-Czajka, A., Kulisa, K., Szreder, T., Bobrowski, K., Nichipor, H., Garcia-Reyes, J.F., Naęcz-Jawecki, G., Męczyńska-Wielgosz, S., Kisała, J., 2019. Application of ionizing radiation in decomposition of perfluorooctanoate (PFOA) in waters. *Chemical Engineering Journal* 357, 698–714. <https://doi.org/10.1016/j.cej.2018.09.065>
- Trojanowicz, M., Bartosiewicz, I., Bojanowska-Czajka, A., Szreder, T., Bobrowski, K., Naęcz-Jawecki, G., Męczyńska-Wielgosz, S., Nichipor, H., 2020. Application of ionizing radiation in decomposition of perfluorooctane sulfonate (PFOS) in aqueous solutions. *Chemical Engineering Journal* 379, 122303. <https://doi.org/10.1016/j.cej.2019.122303>
- Trojanowicz, M., Bobrowski, K., Szostek, B., Bojanowska-Czajka, A., Szreder, T., Bartoszewicz, I., Kulisa, K., 2018a. A survey of analytical methods employed for monitoring of Advanced Oxidation/Reduction Processes for decomposition of selected perfluorinated environmental pollutants. *Talanta* 177, 122–141. <https://doi.org/10.1016/j.talanta.2017.09.002>
- Trojanowicz, M., Bojanowska-Czajka, A., Bartosiewicz, I., Kulisa, K., 2018b. Advanced Oxidation/Reduction Processes treatment for aqueous perfluorooctanoate (PFOA) and perfluorooctanesulfonate (PFOS) – A review of recent advances. *Chemical Engineering Journal* 336, 170–199. <https://doi.org/10.1016/j.cej.2017.10.153>
- Tsai, M.-S.S., Lin, C.-C.C.-Y.Y.C.C., Lin, C.-C.C.-Y.Y.C.C., Chen, M.-H.H., Hsu, S.H.J.J., Chien, K.-L.L., Sung, F.-C.C., Chen, P.-C.C., Su, T.-C.C., 2015. Association between perfluoroalkyl substances and reproductive hormones in adolescents and young adults. *International Journal of Hygiene and Environmental Health* 218, 437–443. <https://doi.org/10.1016/j.ijheh.2015.03.008>
- Tseng, N.S., 2012. Feasibility of Biodegradation of Polyfluoroalkyl and Perfluoroalkyl Substances. *eScholarship* 23, 401–516.

- Turner, L.P., Kueper, B.H., Jaansalu, K.M., Patch, D.J., Battye, N., El-Sharnouby, O., Mumford, K.G., Weber, K.P., 2021. Mechanochemical remediation of perfluorooctanesulfonic acid (PFOS) and perfluorooctanoic acid (PFOA) amended sand and aqueous film-forming foam (AFFF) impacted soil by planetary ball milling. *Science of the Total Environment* 765, 142722. <https://doi.org/10.1016/j.scitotenv.2020.142722>
- van Hoomissen, D.J., Vyas, S., 2017. 1,2-Fluorine Radical Rearrangements: Isomerization Events in Perfluorinated Radicals. *Journal of Physical Chemistry A* 121, 8675–8687. <https://doi.org/10.1021/acs.jpca.7b08895>
- Vecitis, C.D., Park, H., Cheng, J., Mader, B.T., Hoffmann, M.R., 2009. Treatment technologies for aqueous perfluorooctanesulfonate (PFOS) and perfluorooctanoate (PFOA). *Frontiers of Environmental Science and Engineering in China* 3, 129–151. <https://doi.org/10.1007/s11783-009-0022-7>
- Wang, L., Batchelor, B., Pillai, S.D., Botlaguduru, V.S.V., 2016. Electron beam treatment for potable water reuse: Removal of bromate and perfluorooctanoic acid. *Chemical Engineering Journal* 302, 58–68. <https://doi.org/10.1016/j.cej.2016.05.034>
- Wang, L., Li, B., Dionysiou, D.D., Chen, B., Yang, J., Li, J., 2022. Overlooked Formation of H₂O₂ during the Hydroxyl Radical-Scavenging Process When Using Alcohols as Scavengers. *Environmental Science & Technology*. <https://doi.org/10.1021/acs.est.1c03796>
- Wang, S., Yang, Q., Chen, F., Sun, J., Luo, K., Yao, F., Wang, X., Wang, D., Li, X., Zeng, G., 2017. Photocatalytic degradation of perfluorooctanoic acid and perfluorooctane sulfonate in water: A critical review. *Chemical Engineering Journal* 328, 927–942. <https://doi.org/10.1016/j.cej.2017.07.076>
- Wang, Z., Cousins, I.T., Scheringer, M., Buck, R.C., Hungerbühler, K., 2014. Global emission inventories for C₄–C₁₄ perfluoroalkyl carboxylic acid (PFCA) homologues from 1951 to 2030, part II: The remaining pieces of the puzzle. *Environment International* 69, 166–176. <https://doi.org/10.1016/j.envint.2014.04.006>
- Wenk, J., Aeschbacher, M., Salhi, E., Canonica, S., von Gunten, U., Sander, M., 2013. Chemical oxidation of dissolved organic matter by chlorine dioxide, chlorine, and ozone: Effects on its optical and antioxidant properties. *Environmental Science and Technology* 47, 11147–11156. <https://doi.org/10.1021/es402516b>
- Winkens, K., Vestergren, R., Berger, U., Cousins, I.T., 2017. Early life exposure to per- and polyfluoroalkyl substances (PFASs): A critical review. *Emerging Contaminants* 3, 55–68. <https://doi.org/10.1016/j.emcon.2017.05.001>
- Wojnárovits, L., Takács, E., 2008. Irradiation treatment of azo dye containing wastewater: An over-view. *Radiation Physics and Chemistry* 77, 225–244. <https://doi.org/10.1016/j.radphyschem.2007.05.003>
- Yamamoto, T., Noma, Y., Sakai, S.I., Shibata, Y., 2007. Photodegradation of perfluorooctane sulfonate by UV irradiation in water and alkaline 2-propanol. *Environmental Science and Technology* 41, 5660–5665. <https://doi.org/10.1021/es0706504>
- Yang, L., He, L., Xue, J., Ma, Y., Xie, Z., Wu, L., Huang, M., Zhang, Z., 2020. Persulfate-based degradation of perfluorooctanoic acid (PFOA) and perfluorooctane sulfonate (PFOS) in aqueous solution: Review on influences, mechanisms and prospective. *Journal of Hazardous Materials*. <https://doi.org/10.1016/j.jhazmat.2020.122405>
- Ye, X., Kato, K., Wong, L.Y., Jia, T., Kalathil, A., Latremouille, J., Calafat, A.M., 2018. Per- and polyfluoroalkyl substances in sera from children 3 to 11 years of age participating in the National Health and Nutrition Examination Survey 2013–2014. *International Journal of Hygiene and Environmental Health* 221, 9–16. <https://doi.org/10.1016/j.ijheh.2017.09.011>
- Zafeiraki, E., Costopoulou, D., Vassiliadou, I., Bakeas, E., Leondiadis, L., 2014. Determination of perfluorinated compounds (PFCs) in various foodstuff packaging materials used in the Greek market. *Chemosphere* 94, 169–176. <https://doi.org/10.1016/j.chemosphere.2013.09.092>

Zhang, K., Huang, J., Yu, G., Zhang, Q., Deng, S., Wang, B., 2013. Destruction of Perfluorooctane Sulfonate (PFOS) and Perfluorooctanoic Acid (PFOA) by Ball Milling. *Environmental Science & Technology* 47, 6471–6477. <https://doi.org/10.1021/es400346n>

Zhang, S.J., Yu, H.Q., 2004. Radiation-induced degradation of polyvinyl alcohol in aqueous solutions. *Water Research* 38, 309–316. <https://doi.org/10.1016/j.watres.2003.09.020>

Zhang, Z., Chen, J.-J., Lyu, X.-J., Yin, H., Sheng, G.-P., 2014a. Complete mineralization of perfluorooctanoic acid (PFOA) by γ -irradiation in aqueous solution. *Scientific Reports* 4, 7418. <https://doi.org/10.1038/srep07418>

Zhang, Z., Chen, J.J., Lyu, X.J., Yin, H., Sheng, G.P., 2014b. Complete mineralization of perfluorooctanoic acid (PFOA) by γ -irradiation in aqueous solution. *Scientific Reports* 4, 1–6. <https://doi.org/10.1038/srep07418>

4. Advancing PFAS Characterization: Enhancing the Total Oxidizable Precursor Assay with Improved Sample Processing and UV Activation

David Patch†, Natalia O'Connor†, Taylor Vereecken†, Daniel Murphy†, Gabriel Munoz††, Ian Ross††††, Caitlin Glover ††, Jennifer Scott†, Iris Koch†, Sébastien Sauvé†††, Jinxia Liu ††, Kela Weber†*

† Environmental Sciences Group, Department of Chemistry and Chemical Engineering, Royal Military College of Canada, Kingston, ON, Canada K7K 7B4.

†† Brace Water Center, Department of Civil Engineering, McGill University, Montreal, QB, Canada H3A 0G4

††† Département de chimie, Université de Montréal, Montréal, QC, Canada H2V 0B3.

†††† CDM Smith, 75 State St #701, Boston, MA 02109

* Corresponding Author:

Email: Kela.Weber@rmc.ca

Phone: 613-541-6000 ext. 3633

The authors declare no competing financial interest.

4.1. Abstract

Per- and polyfluoroalkyl substances (PFAS) encompass over 9,000 chemicals utilized in various industrial and commercial applications. However, the quantification of PFAS using standard commercial analytical methods is currently limited to less than 50 selected compounds. To address this issue, the total oxidizable precursor (TOP) assay was developed, allowing for the oxidative conversion of previously undetectable PFAS precursors into measurable PFAS. This study investigated different sample processing methods to address post-oxidation PFAS loss identified in literature. Using PFOS as a probe molecule, up to 50% loss of PFOS was identified during sample work-up. It was determined that the use of mass labelled PFOS and methanolic acetic acid to chemically quench the sample post-oxidation improved PFOS recovery and allowed for correction of any remaining PFOS loss. The use of ultraviolet (UV) light was then investigated as an activator in contrast to the standard thermal activation method. A comparative evaluation was conducted to assess the recovery and conversion of perfluorooctanoic acid (PFOA), PFOS, and 6:2 fluorotelomer sulfonate (6:2 FTS) using both the heat-activated and UV-activated TOP assays. Results demonstrated that the UV-activated TOP assay achieved complete (100%) oxidation of 6:2 FTS within 7.5 minutes, resulting in a total yield of generated perfluorinated carboxylic acids (PFCAs) at $108\pm 8\%$. The study concluded by investigating the UV-activated TOP assay for its application various aqueous film forming foam (AFFF) formulations and two AFFF samples drained from military aircraft rescue firefighting vehicles (ARFFVs). Analysis of these AFFF samples were supported by high resolution mass spectrometry and an expanded analytical suite, identifying several fluorotelomer precursors. The findings of this study provide compelling evidence that modifications in sample processing, work-up procedures, expansion of initial PFAS calibration standards, and UV-activation methods enhance the TOP assay, positioning it as a more reliable and quantitative analytical tool for PFAS characterization.

4.2. Introduction

Per- and polyfluoroalkyl substances (PFAS) are a class of recalcitrant anthropogenic organic compounds, some of which have been manufactured since the 1930s (Hendricks, 1953). These chemicals, characterized by one or more carbon-fluorine moieties ($-\text{CF}_2$ or $-\text{CF}_3$) (Wang et al., 2021), are used in a variety of applications to take advantage of their unique physicochemical properties. PFAS have been found in several commercial and industrial products including Class B firefighting foams such as aqueous film forming foam (AFFF), surface treatment coatings, food

packaging, textiles, electronics manufacturing, and cosmetics. With several negative health effects being attributed to PFAS exposure (liver damage, increased rates of cancer, in-utero developmental issues), many jurisdictions have established drinking water guidelines (Gaber et al., 2023; Gilliland, 1992; Mackay, 1991; Nordby and Luck, 1955; Reinhardt et al., 1973; Renfrew and Pearson, 2021). However, as the number of identified PFAS compounds approach 15,000, there exists a need for expanded analytical methodology to allow for a more comprehensive characterization of the total PFAS load in a sample. One method that has been used by both research and commercial analytical laboratories is the total oxidizable precursor (TOP) assay.

Developed by Houtz and Sedlak (2012), the TOP assay uses hydroxyl radicals to oxidatively transform PFAS precursors, such as fluorotelomers, perfluorosulfonamides, and polyfluoroethers into terminal PFCAs and perfluoroethers (Zhang et al., 2019). This assay relies on the activation of potassium persulfate (KPS) under alkaline conditions to generate hydroxyl radicals from sulfate radicals. This is typically performed through the thermal activation of KPS under alkaline conditions but can be done with UV or sonolysis. Following activation, the persulfate anion is converted into two sulfate radicals (1), which then react with excess hydroxy ions to create sulfate ions and hydroxyl radicals (2).



The generated hydroxyl radicals are capable of oxidizing fluorotelomer PFAS through an H-atom abstraction, with the resulting PFAS radical then reacting with dissolved oxygen to generate shorter-chain PFCAs (Zhang et al., 2021). Work by Zhang (2021) used density functional theory calculations supported by experimental data to identify that 6:2 FTS transforms to PFHpA and C₆F₁₃; the latter of which further reacts to produce C2-C6 PFCAs.

While hydroxyl radicals have been shown capable of oxidizing fluorotelomer PFAS, it is generally accepted that perfluorooctane sulfonic acid (PFOS) and perfluorooctanoic acid (PFOA) are resistant to hydroxyl-radical initiated oxidation (Dombrowski et al., 2018). For example, work by Javed (2020) identified only ~7% defluorination of PFOA using UV/H₂O₂ and ~10% defluorination with UV only, suggesting that PFCAs are resistant to oxidation by hydroxyl radicals, and degradation observed in previous UV/H₂O₂ studies was due to UV irradiation only (Javed et al., 2020). When PFCA degradation is observed using the UV/KPS system, it is attributed to the

oxidation of the PFCAs by sulfate radicals, which occur under acidic environments or can remain in the system if they are generated at a rate faster than the reaction with hydroxide ions to form hydroxyl radicals (Zhang et al., 2021).

Since its development, the TOP assay has been employed by numerous academic and commercial groups with a variety of modifications (Al Amin et al., 2021; Göckener et al., 2020; Houtz et al., 2018; Houtz and Sedlak, 2012; Janda et al., 2019; Liu et al., 2022; Martin et al., 2019; Schellenberger et al., 2022). The most common modifications include increasing the concentration of oxidant or base, usually to compensate for samples that have high organic matter content, which can compete for hydroxyl radicals. Work by Hutchinson et al. (2020) employed a hydrogen peroxide digestion before the TOP assay to break down the background organic matter, which improved PFAS oxidation yields.

Limited modifications have been made to the oxidant itself or the activation source. Work by Kaiser (2021) investigated the use of ozone as an oxidant for the TOP assay (Kaiser et al., 2021). While ozone was successful in partially oxidizing some of the PFAS precursors, it resulted in 6:2 fluorotelomer sulfonate as a post-oxidation product, suggesting that many other PFAS precursors may be incompletely oxidized. Work by Fan (2021) used a 16 x 14-watt UV system (254 nm) to activate the KPS instead of heat. The use of UV was found to result in faster oxidation and improved PFAS recoveries.

While the TOP assay is useful as a semi-quantitative tool, it is not regarded as robust enough to be considered a true quantitative analytical method (Nolan et al., 2019; “Proficiency Test Report AQA 19-19 PFAS TOP Assay in Water,” 2020). When applied in interlaboratory studies it was observed that the oxidant was exhausted before complete PFAS precursor oxidation could be achieved, especially in AFFF products, environmental samples with high concentrations of precursors, or in samples with high levels of total organic carbon (TOC) (Nolan et al., 2019). In one interlaboratory study between three labs, PFCA variation in post-oxidation samples were found to be as high as 67% (Nolan et al., 2019). In the same study in a high organic carbon containing sample (120 mg/L TOC, diluted worm farm liquid), the sum of PFAA precursors found between labs was found to differ by more than 85% (relative percent difference). In a second interlaboratory study between twenty-two labs, the TOP assay was employed with various modifications including: multiple oxidation cycles; increases to reagent concentrations; different sample pretreatments; different extraction parameters; and modified clean-up/quenching protocols (“Proficiency Test Report AQA

19-19 PFAS TOP Assay in Water,” 2020). The study determined that while most of the participants satisfied the PFAS National Environmental Management Plan quality assurance protocols, long-chain perfluorocarboxylic (PFCAs) and perfluorosulfonic acids (PFSAs) were found to be underreported in post-oxidation samples, and analytical uncertainty measurements were expanded to upwards of 500% of the reported value. This underreporting, or incomplete recovery of PFSAs and PFCAs following sample oxidation has also been noted extensively in the literature (Al Amin et al., 2021; Houtz and Sedlak, 2012; Tenorio et al., 2020; Zhang et al., 2021).

One of the main ways to account for incomplete recovery of PFAS is through the incorporation of regular QA/QC measures including mass labelled surrogates, spiked samples, sample duplicates, molar yield determination and methods to evaluate complete oxidation. However, these practices are not consistently applied to TOP assay analysis, which further contributes to poor PFAS recoveries and precludes it from use as a dedicated analytical tool (Ateia et al., 2023; Göckener et al., 2022; Janda et al., 2019; Rodowa et al., 2020; Schaefer et al., 2022).

Significant improvements to sample reproducibility and PFAS recovery are required to transition the TOP assay from a screening tool to a validated analytical protocol. The present study seeks to develop an improved understanding of the standard thermal-activated TOP assay and compare it to an improved UV-activated TOP assay for use with aqueous matrices. To achieve this, the roles of activator, quenching, methanol addition, and sample cleanup are investigated. The modified thermal and UV-TOP assays are then applied to several dilute AFFF samples. The information from this investigation, in particular the UV-TOP assay, will form the foundation for a validated analytical protocol by identifying factors affecting the reproducibility of the TOP assay and avoiding challenges associated with thermal activation.

4.3. Materials and Methods

4.3.1. Reagents

PFOS, PFOA, and 6:2 FTS were purchased as powders from Synquest Labs (>97%) and used to prepare high concentration stock solutions by dissolving the powders in deionized water. PFOS was purchased as a technical grade product, containing 25% branched isomers and 75% linear isomers. Analytical PFAS standards (SI) were purchased from Wellington Labs and diluted with basic methanol (0.1% ammonium hydroxide, VWR) to different concentrations for calibration purposes. Mass labelled PFAS (MPFAC-MXA and M8FOSA) were purchased from Wellington

Labs, with the M8FOSA and MPFAC-MXA being evaporated under nitrogen and then dissolved in water. This was done to avoid adding methanol to the TOP assay before oxidation, which would quench the reaction before it could start. Perfluoropropanoic acid (PFPrA) was purchased from Sigma Aldrich (97%) for calibration purposes. Potassium persulfate (KPS) (ACS grade), sodium hydroxide (ACS grade), ultra-micro UV-transparent cuvettes (BrandTech®), cuvette lids, hydrogen peroxide (30%) and methanol (ACS grade) were purchased from VWR. LC-MS grade water and acetonitrile were purchased from Canadian Life Sciences. Double deionized (DI) water (18 M Ω) was acquired from an in-house Milli-Q® Direct 8 water purification system.

4.3.2. Review of TOP Assay Methodology

A review of TOP assay methods was performed to identify key operational parameters and common modifications (Table B1). Seven key parameters were identified including oxidant type/concentration, base type/concentration, activator, oxidation time, quenching protocol, methanol addition, and sample clean-up/processing. This initial review of TOP assay methodology was performed to better inform the methodology for the rest of the investigation, including experimentation into chemical quenching, sample dilution, and different activation types.

4.3.3. Initial TOP Assay Investigations

Following the review of TOP assay methodologies, several investigations were performed to further investigate chemical quenching, sample dilution, persulfate concentration, and the effect of activator type on PFCA yield. These investigations were performed using the thermal-activated and/or UV-activated TOP assay, with reagent concentrations identical to those originally developed by Houtz and Sedlak. Where applicable, solutions were prepared and sub-sampled (1 mL) into either 2 mL UV-transparent cuvettes (UV TOP development) or 2 mL Eppendorf tubes (Thermal TOP development) (Sigma Aldrich). The UV cuvettes were loaded into a custom 3D printed cuvette holder, and the Eppendorf tubes were loaded into an Eppendorf tube rack. The UV TOP assay solution was activated using a UV lamp (Coospider UVC Ozone Free Germicidal Bulb, 36 W 254 nm) for up to six hours. The cuvettes were positioned 3.5 cm away from the UV lamp and were subjected to 2.6 J s⁻¹ L⁻¹ of photon irradiance (determined using chemical actinometry, details in the SI). The thermal TOP assay solution was activated using a water bath (VWR® Digital General Purpose Water Bath) at 85°C for up to six hours.

4.3.4. Chemical Quenching Investigation

Identification of optimal chemical quenching protocols (used to chemically quench the sulfate and hydroxyl radicals) was investigated by subjecting 1 mL samples of PFOS-spiked DI water amended with TOP reagents (60 mM KPS, 150 mM NaOH) to thermal activation (85°C, 6 hours). PFOS was selected due to its susceptibility for poor recoveries in high ionic strength solutions and its immunity to oxidation (Steffens et al., 2021). Samples were prepared in 1.5 mL polypropylene Eppendorf tubes. After six hours, the samples were spiked with mass labelled PFAS (MPFAC-MXA) and quenched at three different time intervals (immediately, following cooling in an ice bath for five minutes, or after cooling for four hours at room temperature) with either acetic acid (10 μ L glacial acetic acid) or acidified methanol (250 μ L 4% acetic acid in methanol). The samples were then either sub-sampled and diluted with basic methanol (10x dilution v:v) or the whole sample diluted with basic methanol (10x dilution v:v) and analyzed using LC-HRMS.

4.3.5. Sample Dilution Investigation

Observations of salt precipitate forming following direct dilution with methanol in the quenching investigation prompted an experiment aimed at optimal sample dilution protocols. Specifically, PFOS (~1 mg/L) was amended to a final concentration of 60 mM KPS and 150 mM NaOH and subjected to the UV-activated (254 nm, 36 W) TOP assay for six hours. Following oxidation, samples were chemically quenched with 4% acetic acid in methanol (250 μ L of acidified methanol to 1 mL of sample) and diluted 20x with methanol, 10x with methanol, and 10x with various compositions of water and methanol.

4.3.6. Sample Volume Justification

Applications of the TOP assay typically require large sample volumes, upwards of 125 mL or more. In this study the TOP assay was scaled down to allow for increased experimental throughput and enable the use of mass labelled PFAS compounds at a lower cost per sample. This scaling-down of the TOP assay volume size has been reported in literature and yields results comparable to those produced following the oxidation of larger sample volumes (Tsou et al., 2023).

4.3.7. Persulfate Determination

Several TOP assay publications have extended the duration of the TOP assay past six hours, hypothesizing that more time is required to completely activate the persulfate anion (Table B1). Other authors have sought out different activators entirely, seeking more rapid activation of the

persulfate anion. Therefore, the activation rate of persulfate was investigated following both thermal and UV-activation for up to six hours.

The activation rate of persulfate was determined using a method modified from Liang (2008) (Liang et al., 2008). In brief, a standard TOP assay solution without PFAS (60 mM KPS, 150 mM NaOH) was prepared in either UV-transmissible cuvettes or 1.5 mL Eppendorf tubes and subjected to activation for six hours. Samples were taken over time and prepared to a final concentration of 70 mM of NaHCO₃, 60 mM of KI, and a KPS concentration between 0.02 and 0.1 mM. Following the addition of KI and NaHCO₃, samples were left to react in the dark at room temperature for 20 minutes. The remaining KPS in the samples reacted with KI to form I₂ which reacts with excess I⁻ to form I₃⁻ (Burgess and Davidson, 2012). The triiodide complex was then measured at 352 nm with a UV-vis spectrometer. KPS did not decrease in concentration in the UV-free control sample, indicating that UV light is required to initiate the reaction.

4.3.8. Initial TOP Assay Investigations

Volumes of PFOS, PFOA, and 6:2 FTS stock solutions were (first individually, then together) added to a 50 mL volumetric flask alongside NaOH (0.30 grams, 150 mM) and KPS (0.81 grams, 60 mM) before being dissolved with deionized water and mixed for 20 minutes to fully dissolve all reagents. One mL aliquots of the PFAS TOP assay solution were then pipetted into either 2 mL UV-transparent cuvettes (UV TOP development) or 1.5 mL Eppendorf tubes (Thermal TOP development) (Sigma Aldrich). Over the course of the TOP assay oxidation, both systems were destructively sampled by removing cuvettes or tubes at different time points (0, 15, 30, 60, 120, 240, 360 minutes). Cuvettes and tubes were hand-inverted to mix the headspace/pull condensation back into the sample and then immediately quenched with acidified methanol (4% acetic acid in methanol). Samples were stored at 4°C overnight before being subsampled (0.1 mL), diluted with basic (0.1% ammonium hydroxide) methanol (0.9 mL), and centrifuged (14,000x RPM for 10 minutes) to precipitate and remove excess salt (if present). Storing the samples overnight with the addition of methanol was found to allow for desorption of any PFAS from the vessel walls. Samples were then analyzed for PFAS using liquid chromatography-mass spectrometry described in section 2.6.

4.3.9. Hydroxyl Radical Investigation using UV/H₂O₂

Initial findings of PFCAs converting into shorter-chain PFCAs following the TOP assay were initially unexpected. To confirm that hydroxyl radicals alone are incapable of degrading PFCAs, an investigation was performed where PFOS, PFOA, and 6:2 FTS were oxidized using a UV/H₂O₂ system for six hours. PFOS, PFOA, and 6:2 FTS were prepared in UV-transmissible cuvettes and amended with H₂O₂ to a final concentration of 100 mM H₂O₂. Following oxidation, samples were diluted directly with 1:1 water/methanol and analyzed.

4.3.10. UV-TOP Assay for AFFF Oxidation

The UV-activated TOP assay (4 hours) was employed to oxidize five different AFFF formulations and two AFFF samples drained from two aircraft rescue and firefighting vehicles (ARFFVs). The samples include two legacy AFFF products (National Foam 1982, 3M 1980), three modern AFFF products (National Foam 1990, Ansul 2010, Solberg date unknown), and the two ARFFV samples (Firetruck 1 and Firetruck 2).

Samples were diluted 1,000x with deionized water and stored at 4°C before use. Samples were then diluted 10x with DI water, amended with KPS (60 mM) and NaOH (150 mM) and spiked with both MPFAC-MXA and M₈FOSA (~10 ppb) before oxidation. Samples were then subjected to the TOP assay for four hours (UV-light). Samples were then quenched with acidified methanol (4 % acetic acid v/v) after the oxidation reaction and left overnight at 4°C. Samples were diluted 20x with 1:1 H₂O/MeOH and transferred into HPLC vials for analysis. Samples were diluted with 1:1 H₂O/MeOH as it was found to improve the recovery of PFAS and improved chromatographic sharpness of PFPrA.

4.3.11. PFAS Analysis

Detailed information on the analytical methodology employed in this study can be found in the SI and in previous work (Duchesne et al., 2020; O'Connor et al., 2023; Patch et al., 2022; Turner et al., 2021). In brief, samples were analyzed on either an Agilent 6460 LC-MS/MS coupled to an Agilent 6460 HPLC system (standard PFAS analytical suite, Table B2), or on a ThermoFisher Exploris 120 Orbitrap coupled to a Vanquish uHPLC system (standard and screening PFAS analytical suite, Table B4, B5). Analysis of trifluoroacetic acid (TFA) and perfluoropropanoic acid (PFPrA) was exclusive to the Agilent 6460 LC-MS, which was used without any sample diversion to waste to avoid missing the early-eluting analytes. For the analysis of the AFFF samples, the

standard analytical suite was expanded to include three fluorotelomers; 6:2 fluorotelomer sulfonamidobetaine (6:2 FtSaB), 5:3 fluorotelomer betaine (5:3 FTB), and 5:1:2 FTB (Wellington Labs). These standards were prepared into a calibration curve with water/methanol and used for quantification of the parent compounds as well as semi-quantitation of their related homologues (e.g. 8:2 FtSaB, 7:3 FTB, etc).

4.4. Results and Discussion

The standard concentrations of KPS and NaOH as used by Houtz and Sedlak (2012) were employed for initial TOP assay evaluation. Parameter investigation focused first on quenching and sample dilution protocols, as these were most inconsistently employed across studies. Following this, the use of UV-activation as an alternative to thermal-activation was explored using PFOS, PFOA, and 6:2 FTS as model PFAS. The improved TOP assay protocol was then implemented on AFFF samples to confirm its effectiveness.

4.4.1. Chemical Quenching and Sample Processing

Following implementation of the thermal-activated TOP assay, samples often undergo chemical quenching (to stop any further oxidation by hydroxyl and/or sulfate radicals) and processing (e.g. dilution with various solvents, solid-phase extraction). Before a full investigation of the TOP assay, preliminary experiments were performed to identify any PFAS loss that could be occurring during quenching and sample dilution, as this is the part of the TOP assay method most inconsistently applied across literature. It was hypothesized that observations of PFAS loss in literature could be attributed to several possible phenomena, including sorption of PFAS to the reactor walls (investigated with methanol addition), volatilization of PFAS during the thermal activation (investigated with different waiting periods before quenching), stratification of PFAS at the air-water interface (investigated with whole vs sub-sampling dilution), or salting out effects that have been identified in literature as present under high ionic strength conditions (investigated in section 3.2) (Steffens et al., 2021).

Most studies that neutralized the samples post-oxidation employed hydrochloric acid, to ensure complete neutralization of the base (Table B1). However, some studies used weak acids or buffers to neutralize the reaction, which was seen as advantageous due to avoiding possible over-acidification of the sample. For these reasons, samples were neutralized with acetic acid instead of hydrochloric acid.

For the purposes of data evaluation, loss will be identified as being significant (statistically significant when compared to another set) or substantial (PFOS loss being greater than 30%) (Table B3 and B4 for three-way ANOVA and one-way ANOVA statistical comparisons).

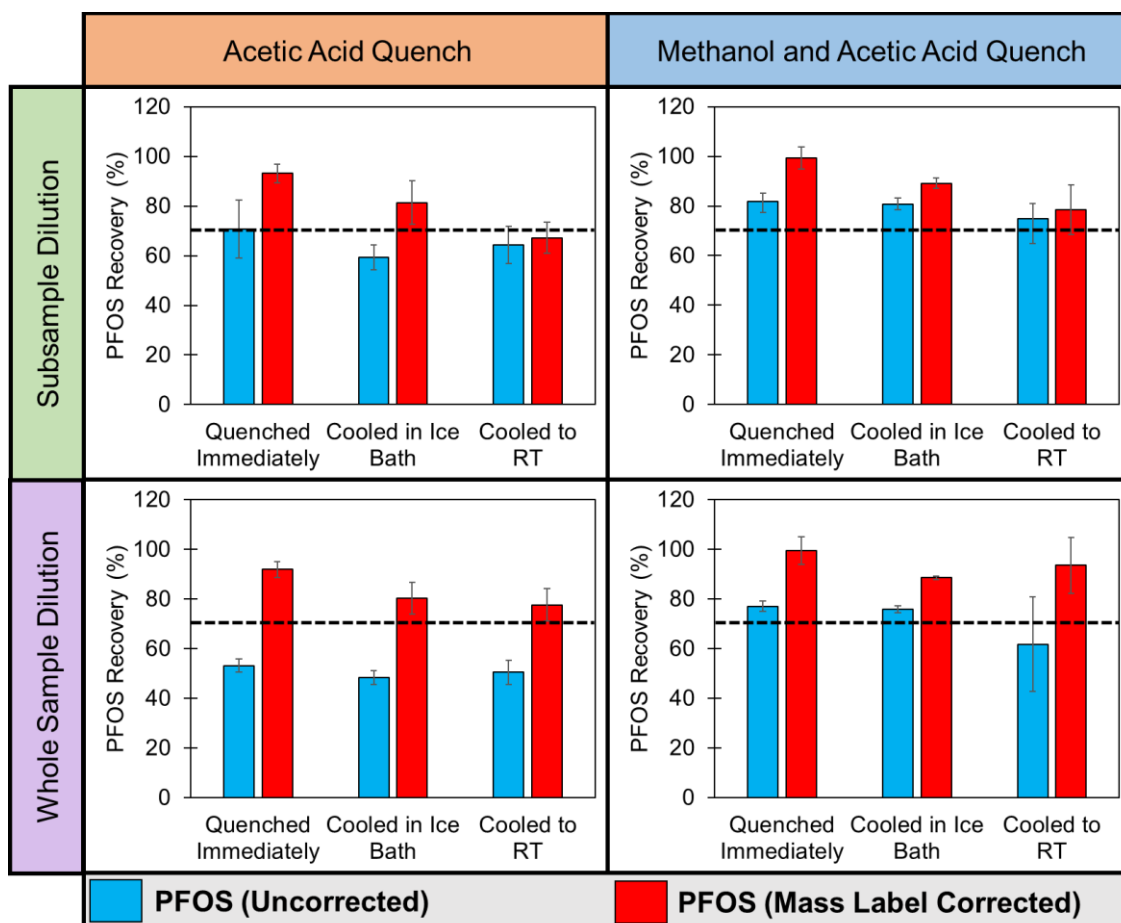


Figure 4.1 – Influence of quenching and dilution protocol on the thermal-activated TOP assay on PFOS recovery. PFOS reported as uncorrected (blue), and mass-label corrected (red). Mass-labelled PFOS was added after oxidation but before quenching and dilution. The dashed line indicates 70% recovery. Error bars shown are the standard deviation from triplicates trials.

Substantial (>30%) and significant PFOS loss was observed following the thermal-activated TOP assay for several quenching/sampling combinations, with the extent of loss varying with overall quenching/dilution protocol (Figure 4.1, Table B2, B3). Quenching immediately with methanolic acetic acid, followed by subsample dilution prior to analysis resulted in the lowest loss of PFOS ($18 \pm 4\%$), whereas quenching with acetic acid followed by dilution of the whole sample prior to analysis resulted in the highest loss of PFOS, regardless of quench time (42 - 60%).

The use of mass labelled PFOS after oxidation but before quenching allowed for acceptable correction of the majority of the lost PFOS. The exception was when quenching was conducted with acetic acid (no methanol) after cooling to room temperature, with dilution of a sub-sample prior to analysis, which resulted in substantial PFOS loss ($33\pm 9\%$, thus $>30\%$) even after correction for the recovery of the mass labelled PFOS.

The improved PFOS recoveries following methanol addition indicates that sorptive loss is a key contributing factor to PFOS loss, as adding methanol allows for desorption of PFAS from the cuvette walls back into the solution. The use of mass labelled PFOS provides evidence that some PFAS is lost in the dilution work-up, indicating that aggregation, enhanced interfacial activity, or a salting out effect is occurring. Work by Steffens et al (2021) identified $>50\%$ PFOS loss in NaCl or KCl solutions at salt concentrations of 500 mM (Steffens et al., 2021). The total concentration of salts in the samples here is approximately 270 mM assuming full conversion of KPS, and thus, it is possible that the same aggregation-based loss is occurring in this study. Salt precipitation could be visually observed during the dilution phase, which could be further driving PFOS loss because of its occlusion into the precipitate crystal structure or interactions with the salt.

The use of methanolic acetic acid, immediate quenching of the samples, and incorporation of mass labelled PFAS before sample quenching/dilution allowed for correction of procedural losses and enabled more accurate quantification.

4.4.2. Sample Dilution Investigation

Implementation of optimal chemical quenching protocols improved PFOS recovery from $\sim 50\%$ to $\sim 80\%$, with the use of mass labelled PFOS allowing for further correction. While the use of mass labelled PFAS surrogates is a critical component of PFAS analysis, over-reliance on their use may result in issues when analyzing PFAS that do not have associated mass labelled surrogates. Therefore, to further improve PFAS recovery, a second sample preparation investigation was performed to examine the optimal dilution protocol to employ after chemical quenching. It was hypothesized that the remaining 20% of PFAS loss was due to the salting out effect, which was supported by the visual observation of salt precipitates forming when the post-oxidation samples were diluted with straight methanol. To confirm this hypothesis, PFOS samples post-oxidation were diluted either 20x with methanol (0.05 mL of sample, 0.95 mL of methanol), 10x with methanol (0.1 mL of sample, 0.9 mL of methanol), or 10x with various compositions of water and

methanol. The effect of increasing water composition on the recovery of PFOS can be seen below (Figure 4.2).

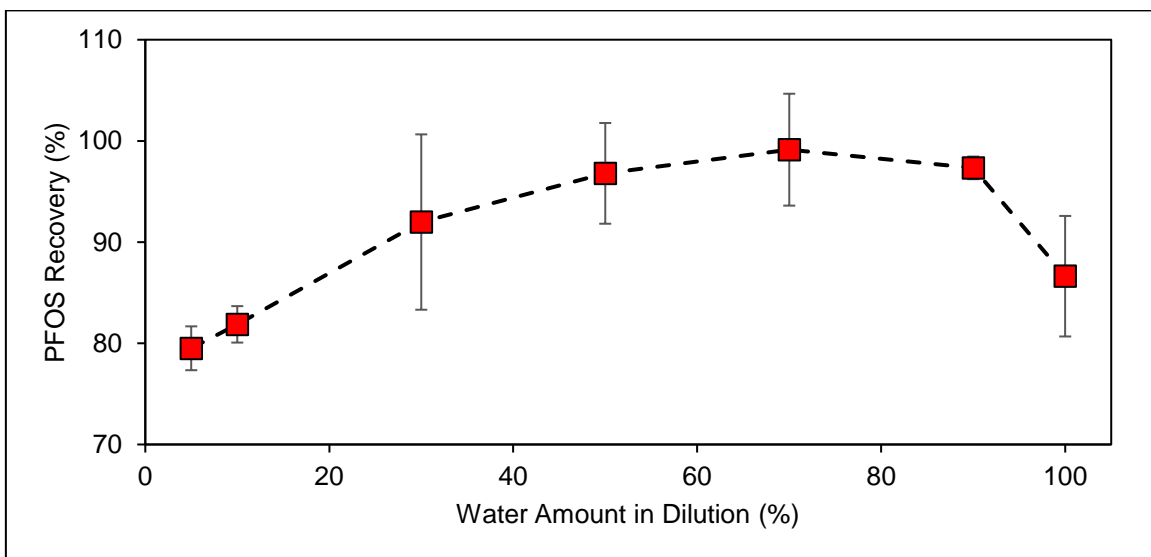


Figure 4.2 – Recovery of PFOS (~1 mg/L) following a six-hour TOP assay oxidation, chemical quenching with 4% methanolic acetic acid, and diluted to different final compositions of water and methanol.

As was identified in the quenching protocol investigation, dilution with pure methanol after oxidation and chemical quenching resulted in ~80% of the PFOS being recovered. Increasing the amount of water present in the final sample dilution resulted in improved PFOS recovery, with 70% water content resulting in $99\pm 6\%$ recovery of PFOS. However, if samples were diluted with pure deionized water, recovery of PFOS dropped to $87\pm 6\%$, potentially due to sorption to the HPLC vials. Following this investigation, it was decided that all samples post-oxidation would be chemically quenched as previously described, and then diluted at least 10x with 1:1 water/methanol solution. This also aligns well with protocols in EPA method 8327, which observed the best recovery of PFAS in aqueous samples when they contained an organic cosolvent at a composition of 50% (Agency, 2021).

4.4.3. Thermal and UV-Light Activation

Several authors have investigated different durations for the thermal-activated TOP assay, suggesting incomplete activation of the oxidant during the standard six-hour duration (Janda et al., 2019; Neuwald et al., 2022; Tsou et al., 2023). It was hypothesized that the use of a sufficiently strong UV lamp at 254 nm would allow for a faster activation of KPS than the standard thermal

method. To confirm this hypothesis, photometric determination of the persulfate anion was employed to monitor the rate of KPS activation in the thermal and UV-activated TOP assay (Figure 4.3).

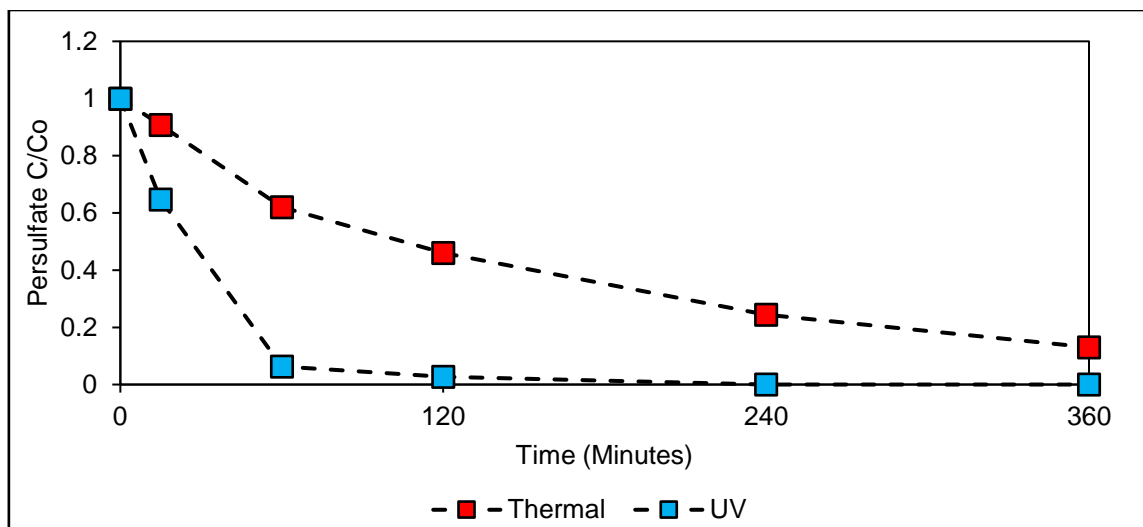


Figure 4.3 – Iodometric spectrophotometric determination of persulfate as a function of time following thermal (85°C) or UV (254 nm, 36W) activation.

The use of UV light resulted in substantially faster activation of KPS, with 93% being activated by one hour, 97% activated by two hours and no detectable amount by four hours. In contrast, thermal activation only resulted in 86% of KPS being activated within six hours. This indicates that the standard six-hour thermal activated TOP assay does not completely consume the applied oxidant, and supports modifications made in literature that employ the TOP assay for up to 20 hours of thermal activation (Janda et al., 2019; Neuwald et al., 2022).

PFOS, PFOA, and 6:2 FTS were subjected to the thermal and UV-TOP assays for six hours to understand the major differences of the two systems (Figure 4.4). Given the resistance of PFOS and PFOA to hydroxyl radical oxidation, it was expected that 6:2 FTS would undergo complete conversion to PFCAs while PFOS and PFOA would remain untouched (Javed et al., 2020).

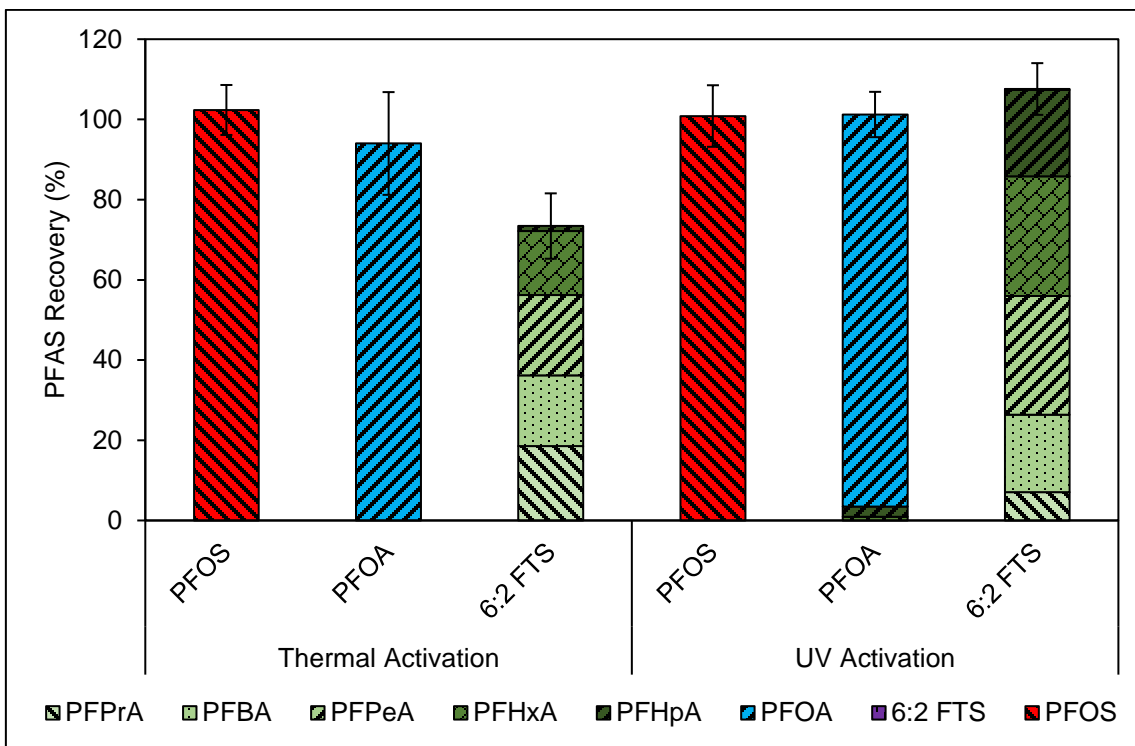


Figure 4.4 – Investigation of PFOS, PFOA, and 6:2 FTS following thermal and UV-activated TOP assay. One mL samples were quenched immediately with 0.25 mL of acidified methanol (4% acetic acid) and sub-sampled.

It was identified both in literature and initial trials performed in this study that substantial (>50%) loss of PFOS can occur following application of the TOP assay (Figure B1). This loss of PFOS is unexpected due to the resistance of PFOS to oxidative transformation by hydroxyl radicals. However, following incorporation of the quenching protocols developed in this study, PFOS showed complete recovery in both the thermal and UV-activated TOP systems, with recoveries of $102\pm 4\%$ and $101\pm 2\%$ respectively.

Initial trials with applying the TOP assay to PFOA found significant conversion to PFCAs, which was originally unexpected due to the resistance of PFCAs to conversion by hydroxyl radicals (Figure B2). It was later identified that the pH of the samples during the oxidation shifted from basic to acidic (potentially due to slightly acidic samples or insufficient concentration of NaOH) (Figure B2, B3). It was found that as long as the post-oxidation sample has a pH greater than 7, then conversion of PFCAs to shorter-chained products should not occur (Figure B3). After ensuring appropriate pH of the samples post-oxidation, the thermal-TOP assay was found to result in near-complete recovery of PFOA. Following the UV-activated TOP assay, some small conversion of

PFOA to PFHpA and PFHxA was identified, despite the final pH being higher than 9. It is hypothesized that this conversion is due to the rate of sulfate radical generation is slightly faster than its conversion to hydroxyl radicals, resulting in some sulfate radicals existing long enough to attack the PFOA molecules and initiate oxidative transformation (Zhang et al., 2021).

As expected, 6:2 FTS underwent rapid transformation in both the thermal and UV-activated systems. In the thermal-activated system, 6:2 FTS was non-detectable by two hours (Figure 4.5). In the UV-activated system, 6:2 FTS was non-detectable within the first fifteen minutes. The UV-activated TOP assay was repeated with increased sampling points, where it was identified that 6:2 FTS reached complete oxidation by 5 minutes (Figure B4). In the UV-activated system, $108 \pm 8\%$ of PFAS recovered from the initial 6:2 FTS consisted of shorter-chain PFCAs, whereas only $73 \pm 8\%$ of PFAS could be recovered following thermal activation (Figure 4.5). The amount of PFHpA generated (22%) following UV activation was substantially higher than that generated following thermal activation (1%).

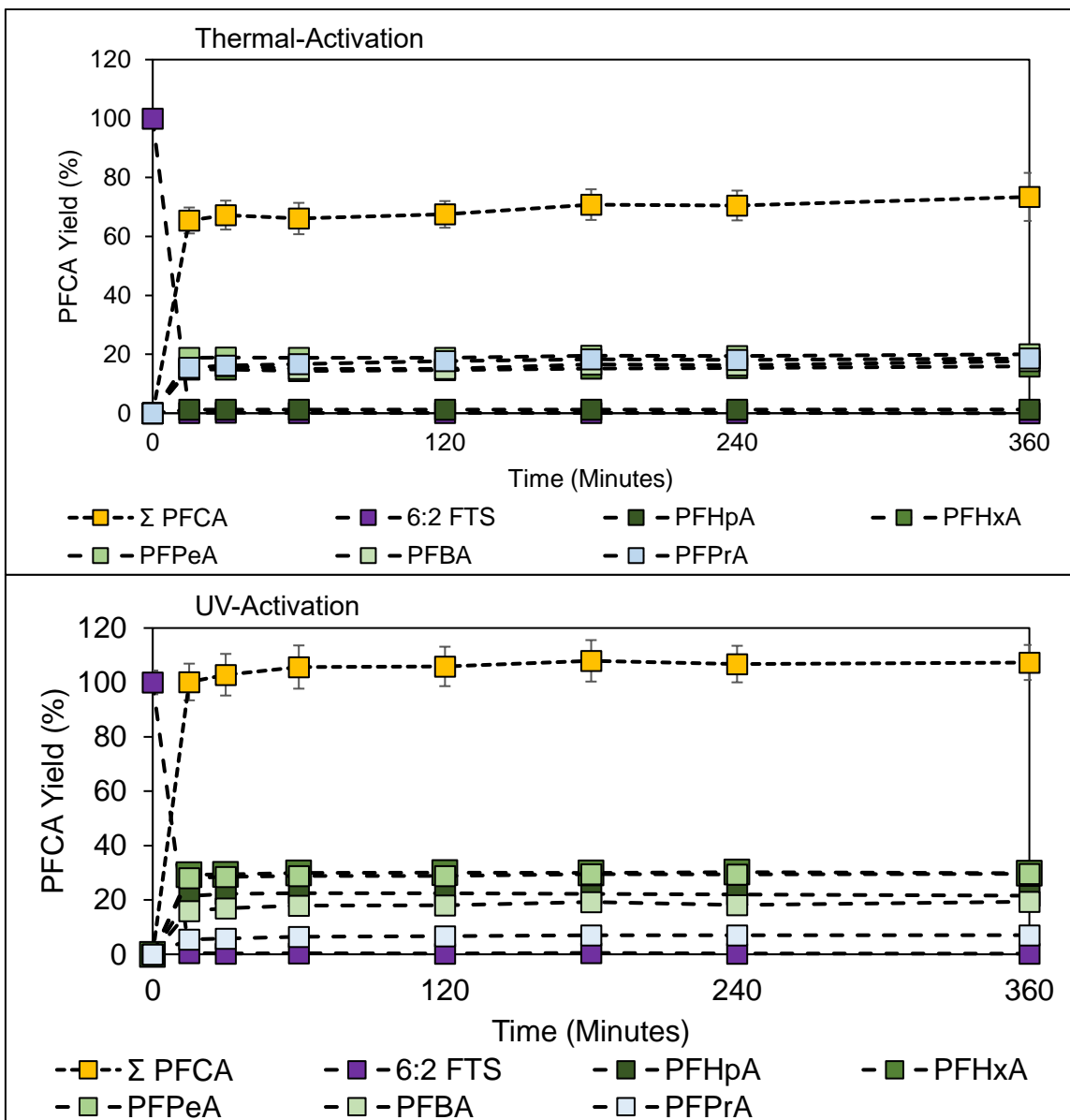


Figure 4.5 – PFCA yield with respect to time following the thermal-activated (top) and UV-activated (bottom) TOP assays. Samples were run for six hours and quenched with methanolic acetic acid (4%) before sample dilution. TFA was analyzed for but not identified in any of the samples.

It is hypothesized that the energy imparted by the thermal-activated TOP assay may result in an ‘unraveling’ of the PFAS structure, allowing 6:2 FTS to transform through reaction pathways that generate shorter-chain PFCAs. Density functional theory calculations performed by Zhang (2021) identify several thermodynamically favored and unfavored reaction pathways for 6:2 FTS, with the calculations being performed at standard temperature. It is therefore possible that the thermal-

activated TOP assay provides higher activation energies, facilitating more varied reaction pathways that lower the overall yield based on measured PFCAs.

4.4.4. PFCA Yield Comparison to Literature

The PFCA signatures following 6:2 FTS oxidation in this study were compared to data taken from the literature (Figure 4.6).

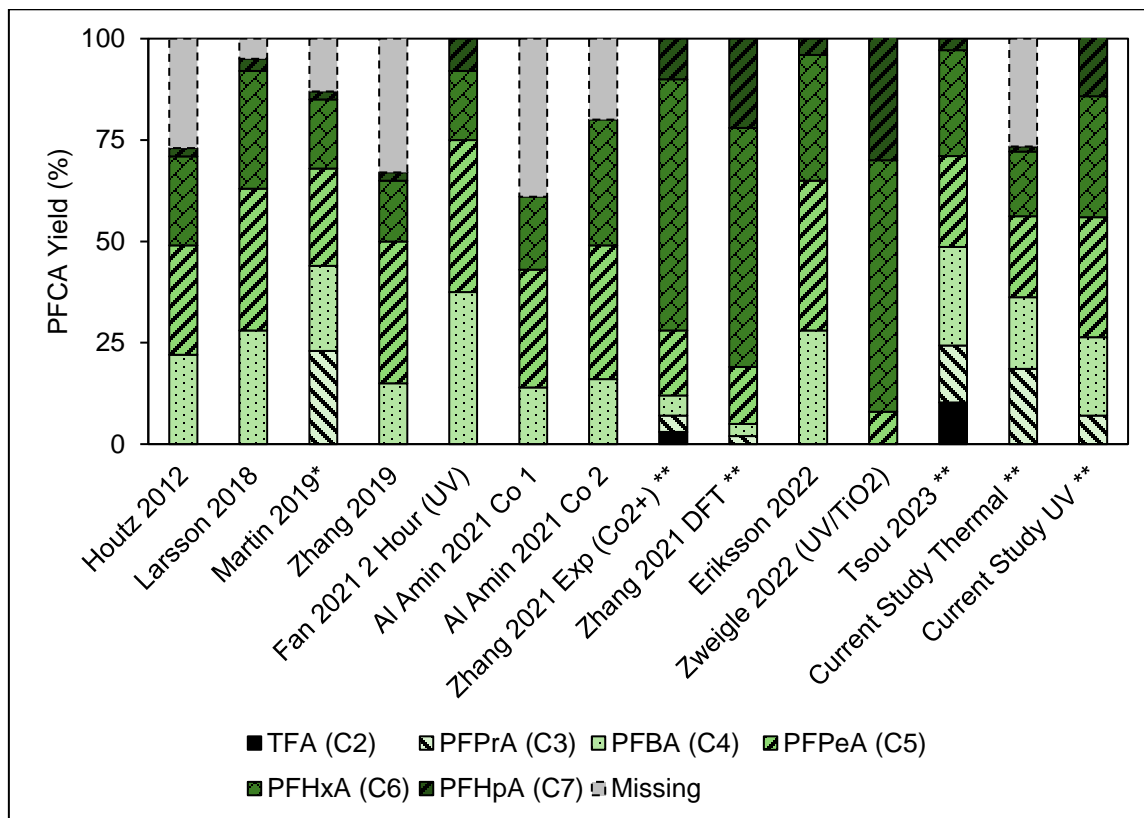


Figure 4.6 – PFCA composition following oxidative transformation of 6:2 FTS in this work and others (Al Amin et al., 2021; Dai et al., 2019; Eriksson et al., 2022; Fan et al., 2021; Houtz and Sedlak, 2012; Larsson et al., 2018; Martin et al., 2019; Tsou et al., 2023; Zhang et al., 2021; Zweigle et al., 2022). PFCA yields greater than 100% were relativized to 100% (Table B1 for reaction conditions). Studies that measured PFPrA are indicated with *, whereas studies that measured both PFPrA and TFA are indicated with **. Unless otherwise stated, studies used heat as an activation source.

The PFCA yield following the thermal-activated oxidative transformation of 6:2 FTS in this study aligns closely with several studies, including works by Houtz (2012), Zhang (2019), Al-Amin (2021), and to a lesser extent Larsson (2018) and Martin (2019). Of the six studies that employed thermal-activation, only two studies (Eriksson and Tsou) achieved complete mass balance closure.

While it is unknown how Eriksson achieved mass balance closure using the standard thermal TOP assay conditions, the expansion of Tsou’s analytical suite to include PFPrA and TFA (accounting for ~25% of their PFCA yield) and their thermal TOP assay being run for 12 hours both contributed to their complete mass balance closure.

While the use of UV-light to activate the TOP assay is not as well studied, results from both literature and this study indicate it is a technique that yields a complete PFCA yield, with higher proportions of PFHpA and PFHxA. The PFCA yield in this study aligns closely with work by Zhang (2021). Work by Zweigle (2022) utilized UV-light and titanium oxide to generate hydroxyl radicals, allowing their method to avoid the use of KPS and NaOH entirely (Zweigle et al., 2022).

4.4.5. UV/H₂O₂ System

A handful of studies have investigated the use of hydrogen peroxide as a pre-treatment to samples before implementing the TOP assay. To identify if hydrogen peroxide could be used as a stand-alone oxidant for the TOP assay, a UV/H₂O₂ experiment was performed using 100 mM H₂O₂ and the same UV system (Figure 4.7).

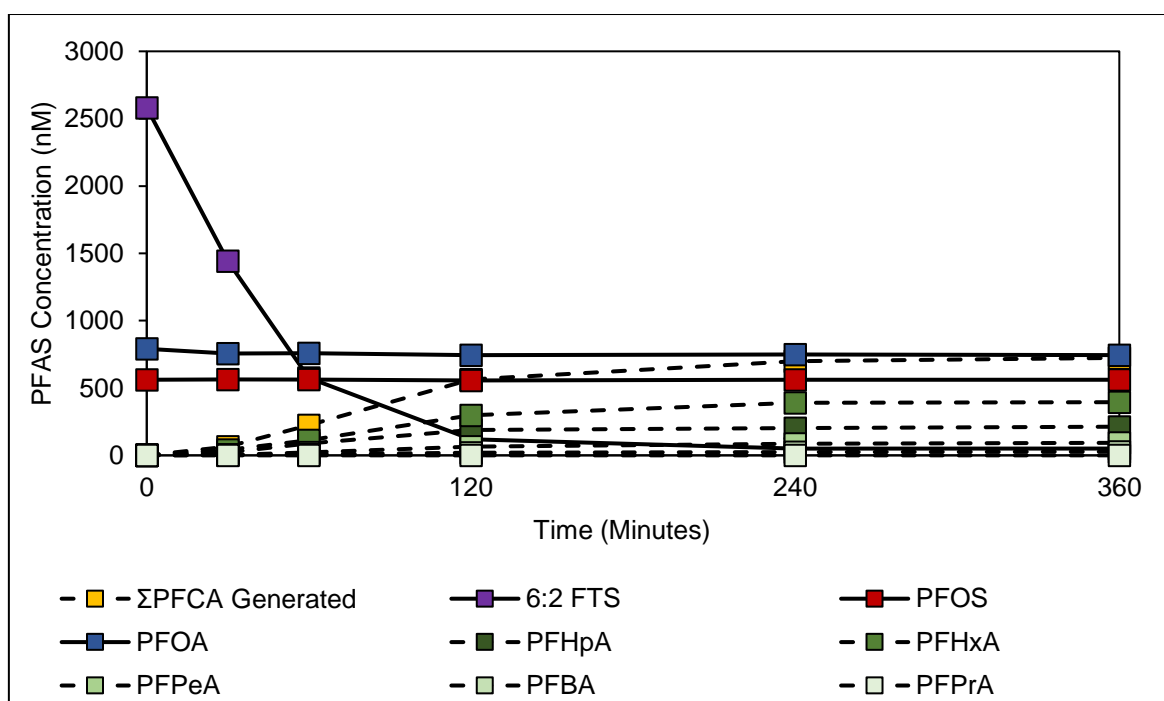


Figure 4.7 – PFOS, PFOA, and 6:2 FTS following UV/H₂O₂ oxidation for six hours. Error bars are too small to be shown.

As expected, 6:2 FTS underwent oxidation in the presence of hydroxyl radicals in the UV/H₂O₂ system, and the resultant PFCAs, however at a much slower rate than the UV/KPS system. Additionally, a significant amount of PFAS following the oxidation of 6:2 FTS could not be accounted for, likely indicating incomplete oxidation. The ability for H₂O₂ to oxidize only 6:2 FTS while leaving PFCAs untouched makes it an attractive candidate for use to oxidize samples containing low PFAS concentrations but high organic matter, as employed by (Hutchinson et al., 2020). However, its inability to achieve complete PFCA yield following oxidation of 6:2 FTS limits its ability to be used as the main oxidant, instead lending itself for use as a pre-oxidative treatment.

4.4.6. Implementation of the Developed UV-TOP Assay for AFFF Samples

The effectiveness of the UV-activated TOP assay was evaluated against seven different AFFF samples: five AFFF formulations, and two AFFVs drained from aircraft rescue firefighting vehicles (ARFFVs). The two samples drained from the ARFFVs were of particular interest as initial visual inspection showed them to be heterogeneous in composition, with a gel-like phase settling to the bottom and a less viscous liquid phase settling at the top. This observation could indicate either a weathering of the AFFF over time, or the formation of self-assembled structures on the surfaces of the ARFFV tank, pipes, and drains. The concentration of PFAS before and after oxidation, quantified using targeted, expanded, and semi-quantified analytical suites can be seen below (Figure 4.8, S6, Table 1).

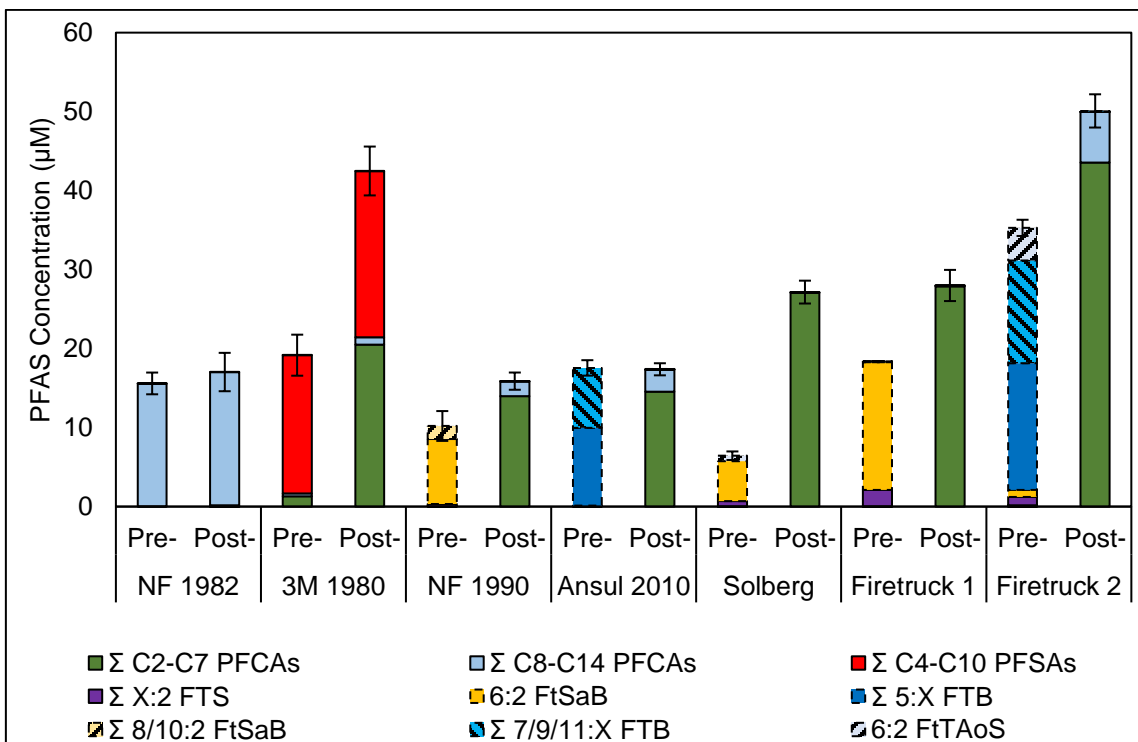


Figure 4.8 – PFAS concentration pre- and post- UV-activated TOP assay for four hours. Samples were amended with M₈FOSA and MPFAC-MXA before oxidation to track PFAS recovery and oxidative completion. PFAS were quantified with a standard analytical suite (solid border PFAS), expanded analytical suite (dashed border, solid colour), and semi-quantified using appropriate homologues (dashed border, pattern fill) (top).

Analysis of the National Foam 1982 sample (NF 1982) revealed an odd-numbered PFCA dominant composition (C7, C9, C11, C13) consisting of linear isomers only. High resolution analysis did not reveal any precursors present, and the total PFAS yield only increased 9% after implementation of the TOP assay, likely a result of analytical deviation.

Analysis of the 3M 1980 sample revealed an expected composition of linear and branched PFSAs, with a smaller amount of linear and branched PFCAs (Figure B5). High resolution analysis revealed several precursors (Table B5), but all in very low amounts of peak area. It is possible that other, more prevalent precursors were not identified in significant intensity due to poor ionization or the precursors themselves not being detectable via LC-HRMS. The total PFAS concentration increased by a factor of 2.2 after implementation of the TOP assay, with PFHxA being highest in concentration. This suggests that a significant amount of the precursors are C6 sulfonamides which would oxidize into PFHxA. The PFCAs generated in the 3M sample post-oxidation were found to

contain branched isomers, indicating that the precursors themselves consist of branched and linear isotopes (Figure B5).

Due to the lack of precursors in the NF 1982 AFFF, and the difficulty in identifying precursors in the 3M 1980, the final post-oxidation TOP yield was the same regardless of analytical suite used to quantify the data. However, analysis of the modern AFFF samples, including those drained from ARFFVs, identified that the TOP yield would be heavily influenced by the characterization of the pre-oxidation PFAS concentration, as more accurate quantitation would decrease the overall TOP yield assessed post-oxidation (Table 1).

Table 4.1 – Concentration of PFAS pre- and post- oxidation, grouped by PFAS type and analytical suite, with the total PFAS yield post-oxidation calculated by analytical suite.

Analysis	PFAS	NF 1982		3M 1980		NF 1990		Ansul 2010		Solberg		Firetruck 1		Firetruck 2	
		Pre-	Post-	Pre-	Post-	Pre-	Post-	Pre-	Post-	Pre-	Post-	Pre-	Post-	Pre-	Post-
Target	Σ C ₂ -C7 PFCAs	0.1	0.2	1.3	20	0	14	0	15	0	27	0	28	0.2	44
	Σ C8-C14 PFCAs	16	17	0.4	0.9	0	1.9	0	2.8	0	0.1	0	0.1	0	6.4
	Σ C4-C10 PFSAs	0	0	18	21	0	0	0	0	0	0	0	0	0	0
	Σ X:2 FTS	0	0	0	0	0.3	0	0.1	0	0.7	0	2	0	1.1	0.01
Expanded	6:2 FtSaB	0	0	0	0	8.2	0	0	0	5.1	0	16	0	0.9	0
	Σ 5:X FTB	0	0	0	0	0	0	10	0	0	0	0.1	0	16	0
Semi-Quant	Σ 8/10:2 FtSaB	0	0	0	0	1.7	0	0	0	0	0	0	0	0	0
	Σ FTB	0	0	0	0	0	0	7.6	0	0	0	0	0	13	0.1
	Σ FtTAoS	0	0	0	0	0	0	0	0	0.7	0	0	0	4.1	0
Σ PFAS (Target) (μM)						0.3		0.14		0.7		2.1		1.2	
Σ PFAS (T + Expanded) (μM)		15.6	17.0	19.2	42.5	8.5	15.9	10.0	17.4	5.8	27.2	18.4	28.0	18.2	50.0
Σ PFAS (T + E + Semi-Q) (μM)						10.2		17.6		6.4				35.3	
TOP Yield (Target)						50		128		40		13		40	
TOP Yield (T + Expanded)		1.09		2.2		1.9		1.7		4.7		1.5		2.8	
TOP Yield (T + E + Semi-Q)						1.6		1.0		4.2				1.4	

Target analysis of the three modern and two drained AFFF samples pre-oxidation identified low concentrations of fluorotelomer sulfonates, making the five samples almost indistinguishable from one another. It is only with the expanded analytical suite that the dominant PFAS precursors are identified (NF 1990 = FtSaB, Ansul = FTB, Solberg = FtSaB/FtTAoS, Firetruck 1 = FtSaB, Firetruck 2 = mix of precursors). Interestingly, the Solberg AFFF only contained 6:2 FtSaB and 6:2 FtTAoS precursors, whereas the other AFFFs contained commonly found homologues of the parent compounds. For example, high resolution analysis of the Ansul AFFF revealed seventeen different fluorotelomer betaine homologues, including 5:X (quantified) 7:X, 9:X, 11:X, 4:N, 6:N, 8:N, and 10:N (semi-quantified) (X=3 or 1:2, N=2, 4, or 1:3) (Table B6).

Analysis of the AFFF drained from the second ARFFV indicated a mix of initial PFAS groups, including 6:2 FTS, 8:2 FTS, 6:2 FtSaB, 5:3 FTB, 5:1:2 FTB, and traces of PFCA/PFSAs. High

resolution analysis also indicated the presence of other FT homologues, 6:2 FTTAoS, 6:2 fluorotelomer thiohydroxyl ammonium (6:2 FTSHA), and several oxidation byproducts of 6:2 FTTAoS, including 6:2 FTSOAoS, and 6:2 FTTHN (Balgooyen and Remucal, 2023; Harding-Marjanovic et al., 2015). The various PFAS groups found in the sample drained from this firetruck indicate that this vehicle has likely been refilled with different manufactured formulations over its active use. More importantly, the identification of these different formulations suggests that previous PFAS can remain present in an ARFFV for an extended duration, potentially due to sorption to the walls of the tank and the formation of self-assembled structures. Additionally, the observation of oxidative transformation products of 6:2 FTTAoS suggests that PFAS can transform over time in the tank.

The results identified in the analysis of the AFFF samples identify that target analysis of PFCAs, PFSAAs, and a few select PFAS precursors alone is not enough to sufficiently describe the PFAS present in AFFF, and by extension AFFF-impacted soil and water. Both the improved thermal-activated TOP assay and UV-activated TOP assay represent a major complementary analytical technique to be used alongside normal target analysis. The incorporation of ultra-short chain PFAS (e.g., PFPrA, TFA), common AFFF fluorotelomers (e.g., 6:2 FtSaB, 5:3 FTB, 5:1:2 FT), additional sample processing, statistical analysis, and LC-HRMS further improves the characterization of the PFAS load present in each matrix. Examining the PFCA composition of a sample post-oxidation can be used to provide information as to initial fluorotelomer chain lengths, with more foundational data allowing for more detailed prediction and modelling.

4.4.7. PFCA Composition Related to Fluorotelomer Chain Length

The AFFF samples investigated in this study can be broadly classified into three groups: legacy AFFF with no precursors (National Foam 1982), legacy AFFF with electrochemical fluorination precursors (3M 1980), and modern AFFFs with fluorotelomer precursors (National Foam 1990, Ansul 2010, Solberg, Firetruck 1, Firetruck 2). While identifying the first two groups is straight forward, there can be difficulties when characterizing different modern AFFFs, as their precursors can oxidatively transform into similar ratios of products. However, by examining the chain length of generated PFCAs post-oxidation we can identify potential post-oxidation PFCA ‘fingerprints’ to provide information as to the fluorotelomer chain length present. This is particularly useful for scenarios in which high resolution mass spectrometry is not available (Figure 4.9).

AFFF		NF 1982		3M 1980		NF 1990		Ansul 2010		Solberg		Firetruck 1		Firetruck 2	
PFAS		Pre-	Post-	Pre-	Post-	Pre-	Post-	Pre-	Post-	Pre-	Post-	Pre-	Post-	Pre-	Post-
PFCA	PFPrA	0	0	1	5	0	10	1	2	0	13	0	14	0	10
	PFBA	0	0	0	9	0	27	0	21	0	35	0	34	0	22
	PFPeA	0	0	1	8	0	23	0	19	0	29	0	29	0	22
	PFHxA	0	0	4	26	0	19	0	20	1	17	1	18	1	22
	PFHpA	0	1	1	1	0	10	0	13	0	5	0	5	0	2
	PFOA	1	3	2	3	0	7	1	10	0	0	0	0	1	7
	PFNA	89	84	0	0	0	3	0	4	0	0	0	0	0	3
	PFDA	0	1	0	0	0	2	0	2	0	0	0	0	0	1
	PFUnDA	8	10	0	0	0	0	0	0	0	0	0	0	0	0
	PFDoDA	1	0	0	0	0	0	0	1	0	0	0	0	0	0
	PFTTrDA	1	1	0	0	0	0	0	0	0	0	0	0	0	0
PFTeDA	0	0	0	0	0	0	0	0	0	0	0	0	0	0	
Fluorotelomers	Σ 4:X FT	0	0	0	0	0	0	0	0	0	0	0	0	0	0
	Σ 5:X FT	0	0	0	0	0	0	56	0	0	0	0	0	46	0
	Σ 6:X FT	0	0	0	0	83	1	1	0	99	1	98	1	17	1
	Σ 7:X FT	0	0	0	0	0	0	34	0	0	0	0	0	28	1
	Σ 8:X FT	0	0	0	0	13	0	1	0	0	0	1	0	1	0
	Σ 9:X FT	0	0	0	0	0	0	9	0	0	0	0	0	8	0
	Σ 10:X FT	0	0	0	0	4	0	0	0	0	0	0	0	0	0
	Σ PFASs	0	0	91	49	0	0	0	0	0	0	0	0	0	1
Σ PFAS (Quant + Semi-Quant μ M)	16	17	19	42	10	16	18	17	6	27	19	28	35	51	

Figure 4.9 – Relativized PFAS across the seven different AFFF samples showing PFCA yield trends. Fluorotelomers grouped by their fluorinated chain length. Concentrations at pre- or post-TOP assay have been relativized to the sum of the quantified and semi-quantified PFAS at the pre- or post- TOP assay stage.

Among the five modern AFFF samples analyzed (NF 1990, Ansul 2010, Firetruck 2), three were found to exhibit long-chain (C8 or greater) PFCAs after oxidation, indicative of 7:X fluorotelomers or longer. This was corroborated by high-resolution mass spectrometry data, which identified the presence of 6:2, 8:2, and 10:2 FtSAB compounds in the NF 1990 sample, as well as various chain-length FTB compounds in the Ansul and Firetruck 2 samples. Notably, the PFCA profile in the FT-dominant AFFF samples showed comparable yields of C4, C5, and C6 PFCAs. In contrast, the two AFFF samples that lacked PFCAs longer than PFHpA did not contain any fluorotelomers longer than 6:X.

The ability to differentiate between different PFAS fluorotelomer chain lengths and structures based on the corresponding PFCA yield provides further evidence in support of the TOP assay's application as a forensic tool (Antell et al., 2023). Improving upon existing forensic TOP assay methodologies through the use of UV-light as an activator will further strengthen this application.

2.1 Quality Control and Inter-Instrument Variability Assessment

The use of mass-labelled PFAS (MPFAC-MXA and M₈FOSA) before oxidation allowed for evaluation of overall PFAS recovery, PFAS oxidation, and evaluation of any PFCA overoxidation (Table 2).

Table 4.2 – Recovery of mass-labelled PFAS added pre-oxidation and evaluated post-oxidation.

Source	PFAS	PFAS Recovery (%)
MPFAC-MXA	M ₄ PFBA	105±5
	M ₂ PFHxA	101±9
	M ₄ PFOA	102±5
	M ₅ PFNA	112±13
	M ₂ PFDA	101±20
	M ₂ PFUnDA	70±36
	M ₂ PFHxS	103±5
M ₈ FOSA	M ₄ PFOS	113±14
	M ₇ PFHpA	3±3
	M ₈ PFOA	114±15
	M ₈ FOSA	0

Overall, PFAS recovery was found to be between 81-127%, excluding M₂PFUnDA which had the lowest recovery (70±30%). In all samples, M₈FOSA was found to undergo complete oxidation, with the total PFCA yield being 117±18%. M₈PFOA made up more than 97% of the generated PFCAs, indicating minimal PFCA conversion.

Several interlaboratory reports identified significant differences determined PFAS concentrations in the same samples, both pre- and post-oxidation. One of the potential reasons for this is inter-instrument variability between multiple labs. To investigate this, the inter-instrument variability was also evaluated in this study, with the analysis of the AFFFs being performed on two different instruments (target analytical suite on LC-MS/MS and the target, expanded, and semi quantified analytical suites on the LC-HRMS). Excluding the pre-TOP assay analysis for the Ansul 2010 sample, which was below the limit of quantitation for the LC-MS/MS, overall variability was found to be 10±6%. This indicates overall good agreement between the two instruments, which operate under different principles (multiple reaction monitoring vs single ion monitoring), different manufacturers (Agilent vs Thermo Fisher) and differ in manufacturing date by more than 10 years. This suggests that differences in PFAS quantitation identified between labs may be attributable to differences in calibration standards, calibration methods, or sample-preparation methods.

4.5. Conclusions

This study aimed to optimize thermal and UV-activated TOP assays for enhanced characterization of PFAS precursors in aqueous samples. Several advantages were observed when using the UV-activated system as compared to the standard thermal-activated system. These advantages included quicker sample oxidation, better preservation of the perfluoroalkyl chain in the precursor structure, and improved PFAS yield. We also explored the significance of quenching and sample dilution, concluding that quenching with methanolic acetic acid and diluting with a 1:1 water/methanol mixture were the best methods to prevent substantial PFAS loss. Additionally, the incorporation of mass labeled PFAS before oxidation was determined to be the optimal quality assurance protocol. This ensures complete oxidation of PFAS precursors, allows for monitoring of the extent of PFCA conversion, and accounts for any PFAS loss during the quenching and sample dilution/processing stages.

Furthermore, the application of the developed UV-activated TOP assay to various AFFF samples revealed distinct PFCA yield compositions dependent on the initial fluorotelomer chain length. These findings, supported by an expanded analytical suite and high-resolution mass spectrometry semi-quantification, provide additional evidence for the TOP assay's value as a forensic tool.

Future research could benefit from optimizing the UV reactor setup to accommodate larger sample volumes while maintaining high sample throughput. This optimization would align the method more closely with existing USEPA and commercial methodologies.

Additionally, while this work has underscored the significance of the TOP assay, it has also highlighted the need for other complementary analytical tools to fully characterize the PFAS load in each sample. Future research should focus on developing a comprehensive PFAS analytical workflow that incorporates target PFAS analysis, UV-TOP assay analysis, and, if possible, a chemical assay version of the total organic fluorine assay based on UV-activated reduction remediation technology (O'Connor et al., 2023) Such an approach would allow for a comprehensive characterization of PFAS in various matrices, providing an additional analytical tool for risk assessors, site owners, and PFAS remediation specialists.

4.6. Acknowledgements

This work was supported by Natural Sciences and Engineering Research Council (Canada) Discovery grants of Weber and Koch, as well as the Strategic Environmental Research and

Development Program (ER19-1157) under Liu and Weber. The authors would like to acknowledge Cassie Tuttle for her assistance with actinometry experiments. The authors would also like to acknowledge Nick Battye, Rick Dunning, Stefanie Goure, and Dana Pantea for their assistance in acquiring AFFF samples taken from aircraft rescue and firefighting vehicles.

4.7. References

- Agency, U.S.E.P., 2021. EPA Method 8327 Per- and Polyfluoroalkyl Substances (PFAS) By Liquid Chromatography/Tandem Mass Spectrometry (LC/MS/MS).
- Al Amin, M., Luo, Y., Nolan, A., Robinson, F., Niu, J., Warner, S., Liu, Y., Dharmarajan, R., Mallavarapu, M., Naidu, R., Fang, C., 2021. Total oxidisable precursor assay towards selective detection of PFAS in AFFF. *J Clean Prod* 328, 129568. <https://doi.org/10.1016/j.jclepro.2021.129568>
- Antell, E.H., Yi, S., Olivares, C.I., Ruyle, B.J., Kim, J.T., Tsou, K., Dixit, F., Alvarez-Cohen, L., Sedlak, D.L., 2023. The Total Oxidizable Precursor (TOP) Assay as a Forensic Tool for Per- and Polyfluoroalkyl Substances (PFAS) Source Apportionment. *ACS ES and T Water*. <https://doi.org/10.1021/acsestwater.3c00106>
- Ateia, M., Chiang, D., Cashman, M., Acheson, C., 2023. Total Oxidizable Precursor (TOP) Assay—Best Practices, Capabilities and Limitations for PFAS Site Investigation and Remediation. *Environ Sci Technol Lett*. <https://doi.org/10.1021/acs.estlett.3c00061>
- Balگوoyen, S., Remucal, C.K., 2023. Impacts of Environmental and Engineered Processes on the PFAS Fingerprint of Fluorotelomer-Based AFFF. *Environ Sci Technol* 57, 244–254. <https://doi.org/10.1021/acs.est.2c06600>
- Burgess, A.E., Davidson, J.C., 2012. A kinetic-equilibrium study of a triiodide concentration maximum formed by the persulfate-iodide reaction. *J Chem Educ* 89, 814–816. <https://doi.org/10.1021/ed200055t>
- Dai, X., Xie, Z., Dorian, B., Gray, S., Zhang, J., 2019. Comparative study of PFAS treatment by UV, UV/ozone, and fractionations with air and ozonated air. *Environ Sci (Camb)* 5, 1897–1907. <https://doi.org/10.1039/c9ew00701f>
- Dombrowski, P.M., Kakarla, P., Caldicott, W., Chin, Y., Sadeghi, V., Bogdan, D., Barajas-Rodriguez, F., Chiang, S.Y.D., 2018. Technology review and evaluation of different chemical oxidation conditions on treatability of PFAS. *Remediation* 28, 135–150. <https://doi.org/10.1002/rem.21555>
- Duchesne, A.L., Brown, J.K., Patch, D.J., Major, D., Weber, K.P., Gerhard, J.I., 2020. Remediation of PFAS-Contaminated Soil and Granular Activated Carbon by Smoldering Combustion. *Environ Sci Technol* 54, 12631–12640. <https://doi.org/10.1021/acs.est.0c03058>
- Eriksson, U., Yeung, L.W.Y., Fredriksson, F., Anna, K., 2022. Analysis and characterization of novel fluorinated compounds used in surface treatments products. *Chemosphere* 302. <https://doi.org/10.1016/j.chemosphere.2022.134720>
- Fan, X., Bao, Y., Mumtaz, M., Huang, J., Yu, G., 2021. Determination of total oxidizable precursors in foam surfactants and foam contaminated water based on UV-activated persulfate oxidation. *Science of the Total Environment* 763, 142943. <https://doi.org/10.1016/j.scitotenv.2020.142943>
- Gaber, N., Bero, L., Woodruff, T.J., 2023. The Devil they Knew: Chemical Documents Analysis of Industry Influence on PFAS Science. *Ann Glob Health* 89, 37. <https://doi.org/10.5334/aogh.4013>
- Gilliand, F.D., 1992. Fluorocarbons and Human Health: Studies in an Occupational Cohort.
- Göckener, B., Eichhorn, M., Lämmer, R., Kotthoff, M., Kowalczyk, J., Numata, J., Schafft, H., Lahrssen-Wiederholt, M., Bücking, M., 2020. Transfer of Per- And Polyfluoroalkyl Substances (PFAS) from Feed into the Eggs of Laying Hens. Part 1: Analytical Results including a Modified Total Oxidizable Precursor Assay. *J Agric Food Chem*. <https://doi.org/10.1021/acs.jafc.0c04456>
- Göckener, B., Lange, F.T., Lesmeister, L., Gökçe, E., Dahme, H.U., Bandow, N., Biegel-Engler, A., 2022. Digging deep—implementation, standardisation and interpretation of a total oxidisable precursor (TOP)

- assay within the regulatory context of per- and polyfluoroalkyl substances (PFASs) in soil. *Environ Sci Eur* 34, 1–9. <https://doi.org/10.1186/s12302-022-00631-1>
- Harding-Marjanovic, K.C., Houtz, E.F., Yi, S., Field, J.A., Sedlak, D.L., Alvarez-Cohen, L., 2015. Aerobic Biotransformation of Fluorotelomer Thioether Amido Sulfonate (Lodyne) in AFFF-Amended Microcosms. *Environ Sci Technol* 49, 7666–7674. <https://doi.org/10.1021/acs.est.5b01219>
- Hendricks, J., 1953. *Industrial Fluorochemicals*.
- Houtz, E., Wang, M., Park, J.S., 2018. Identification and Fate of Aqueous Film Forming Foam Derived Per- and Polyfluoroalkyl Substances in a Wastewater Treatment Plant. *Environ Sci Technol* 52, 13212–13221. <https://doi.org/10.1021/acs.est.8b04028>
- Houtz, E.F., Sedlak, D.L., 2012. Oxidative conversion as a means of detecting precursors to perfluoroalkyl acids in urban runoff. *Environ Sci Technol* 46, 9342–9349. <https://doi.org/10.1021/es302274g>
- Hutchinson, S., Rieck, T., Wu, X.L., 2020. Advanced PFAS precursor digestion methods for biosolids. *Environmental Chemistry* 17, 558–567. <https://doi.org/10.1071/EN20008>
- Janda, J., Nödler, K., Scheurer, M., Happel, O., Nürenberg, G., Zwiener, C., Lange, F.T., 2019. Closing the gap-inclusion of ultrashort-chain perfluoroalkyl carboxylic acids in the total oxidizable precursor (TOP) assay protocol. *Environ Sci Process Impacts* 21, 1926–1935. <https://doi.org/10.1039/c9em00169g>
- Javed, H., Lyu, C., Sun, R., Zhang, D., Alvarez, P.J.J., 2020. Discerning the inefficacy of hydroxyl radicals during perfluorooctanoic acid degradation. *Chemosphere* 247. <https://doi.org/10.1016/j.chemosphere.2020.125883>
- Kaiser, A.M., Saracevic, E., Schaar, H.P., Weiss, S., Hornek-Gausterer, R., 2021. Ozone as oxidizing agent for the total oxidizable precursor (TOP) assay and as a preceding step for activated carbon treatments concerning per- and polyfluoroalkyl substance removal. *J Environ Manage* 300, 113692. <https://doi.org/10.1016/j.jenvman.2021.113692>
- Larsson, P., Yeung, L., Kärrman, A., 2018. A study to understand the information gap between total organofluorine analysis and total oxidizable precursor assay on polyfluoroalkyl/perfluoroalkyl substances (PFASs).
- Liang, C., Huang, C.F., Mohanty, N., Kurakalva, R.M., 2008. A rapid spectrophotometric determination of persulfate anion in ISCO. *Chemosphere* 73, 1540–1543. <https://doi.org/10.1016/j.chemosphere.2008.08.043>
- Liu, M., Munoz, G., Vo Duy, S., Sauv e, S., Liu, J., 2022. Per- and Polyfluoroalkyl Substances in Contaminated Soil and Groundwater at Airports: A Canadian Case Study. *Environ Sci Technol* 56, 885–895. <https://doi.org/10.1021/acs.est.1c04798>
- Mackay, N., 1991. *A Chemical History of 3M*.
- Martin, D., Munoz, G., Mejia-Avenda o, S., Duy, S.V., Yao, Y., Volchek, K., Brown, C.E., Liu, J., Sauv e, S., 2019. Zwitterionic, cationic, and anionic perfluoroalkyl and polyfluoroalkyl substances integrated into total oxidizable precursor assay of contaminated groundwater. *Talanta* 195, 533–542. <https://doi.org/10.1016/j.talanta.2018.11.093>
- Neuwald, I.J., Hu, D., Wiegand, H.L., Valkov, V., Borchers, U., Karsten, N., Scheurer, M., Hale, S.E., Arp, H.P.H., Zahn, D., 2022. Ultra-Short-Chain PFASs in the Sources of German Drinking Water: Prevalent, Overlooked, Difficult to Remove, and Unregulated. <https://doi.org/10.1021/acs.est.1c07949>
- Nolan, A., Grimison, C., Iavetz, R., Slee, D., Lim, C., 2019a. Improving Measurement Reliability of the PFAS TOP Assay 559–560.

- Nolan, A., Grimison, C., Iavetz, R., Slee, D., Lim, C., 2019b. Improving Measurement Reliability of the PFAS TOP Assay 559–560.
- Nordby, G.L., Luck, M.J., 1955. Perfluorooctanoic Acid Interactions with Human Serum Albumin.
- O'Connor, N., Patch, D., Noble, D., Scott, J., Koch, I., Mumford, K.G., Weber, K., 2023. Forever no more : Complete mineralization of per - and poly fluoroalkyl substances (PFAS) using an optimized UV / sulfite / iodide system. *Science of the Total Environment* 888, 164137. <https://doi.org/10.1016/j.scitotenv.2023.164137>
- Patch, D., O'Connor, N., Koch, I., Cresswell, T., Hughes, C., Davies, J.B., Scott, J., O'Carroll, D., Weber, K., 2022. Elucidating degradation mechanisms for a range of per- and polyfluoroalkyl substances (PFAS) via controlled irradiation studies. *Science of the Total Environment* 832, 154941. <https://doi.org/10.1016/j.scitotenv.2022.154941>
- Proficiency Test Report AQA 19-19 PFAS TOP Assay in Water, 2020.
- Reinhardt, Barnes, S., Morgan, Hood, Sherman, Hornberger, Griffith, 1973. Ninety-Day Feeding Study in Rats and Dogs With Zonyl RP. Sherman, Henry Barnes, John Aftosmis, James Reinhardt, Charles.
- Renfrew, D., Pearson, T.W., 2021. The Social Life of the “Forever Chemical” PFAS Pollution Legacies and Toxic Events. *Environment and Society: Advances in Research* 12, 146–163. <https://doi.org/10.3167/ARES.2021.120109>
- Rodowa, A.E., Knappe, D.R.U., Chiang, S.Y.D., Pohlmann, D., Varley, C., Bodour, A., Field, J.A., 2020. Pilot scale removal of per- and polyfluoroalkyl substances and precursors from AFFF-impacted groundwater by granular activated carbon. *Environ Sci (Camb)* 6, 1083–1094. <https://doi.org/10.1039/c9ew00936a>
- Schaefer, C.E., Hooper, J., Modiri-Gharehveran, M., Drennan, D.M., Beecher, N., Lee, L., 2022. Release of Poly- and Perfluoroalkyl Substances from Finished Biosolids in Soil Mesocosms. *Water Res* 217, 118405. <https://doi.org/10.1016/j.watres.2022.118405>
- Schellenberger, S., Liagkouridis, I., Awad, R., Khan, S., Plassmann, M., Peters, G., Benskin, J.P., Cousins, I.T., 2022. An Outdoor Aging Study to Investigate the Release of Per- and Polyfluoroalkyl Substances (PFAS) from Functional Textiles. *Environ Sci Technol* 56, 3471–3479. <https://doi.org/10.1021/acs.est.1c06812>
- Steffens, S.D., Cook, E.K., Sedlak, D.L., Alvarez-Cohen, L., 2021. Under-reporting Potential of Perfluorooctanesulfonic Acid (PFOS) under High-Ionic Strength Conditions. *Environ Sci Technol Lett* 8, 1032–1037. <https://doi.org/10.1021/acs.estlett.1c00762>
- Tenorio, R., Liu, J., Xiao, X., Maizel, A., Higgins, C.P., Schaefer, C.E., Strathmann, T.J., 2020. Destruction of Per-and Polyfluoroalkyl Substances (PFASs) in Aqueous Film-Forming Foam (AFFF) with UV-Sulfite Photoreductive Treatment. *Environ Sci Technol* 54, 6957–6967. <https://doi.org/10.1021/acs.est.0c00961>
- Tsou, K., Antell, E., Duan, Y., Olivares, C.I., Yi, S., Alvarez-Cohen, L., Sedlak, D.L., 2023. Improved Total Oxidizable Precursor Assay for Quantifying Polyfluorinated Compounds Amenable to Oxidative Conversion to Perfluoroalkyl Carboxylic Acids. *ACS ES and T Water*. <https://doi.org/10.1021/acsestwater.3c00224>
- Turner, L.P., Kueper, B.H., Jaansalu, K.M., Patch, D.J., Battye, N., El-Sharnouby, O., Mumford, K.G., Weber, K.P., 2021. Mechanochemical remediation of perfluorooctanesulfonic acid (PFOS) and perfluorooctanoic acid (PFOA) amended sand and aqueous film-forming foam (AFFF) impacted soil by planetary ball milling. *Science of the Total Environment* 765, 142722. <https://doi.org/10.1016/j.scitotenv.2020.142722>
- Wang, Z., Buser, A.M., Cousins, I.T., Demattio, S., Drost, W., Johansson, O., Ohno, K., Patlewicz, G., Richard, A.M., Walker, G.W., White, G.S., Leinala, E., 2021. A New OECD Definition for Per- And Polyfluoroalkyl Substances. *Environ Sci Technol* 55, 15575–15578. <https://doi.org/10.1021/acs.est.1c06896>

Zhang, C., Hopkins, Z.R., McCord, J., Strynar, M.J., Knappe, D.R.U., 2019. Fate of Per- And Polyfluoroalkyl Ether Acids in the Total Oxidizable Precursor Assay and Implications for the Analysis of Impacted Water. *Environ Sci Technol Lett* 6, 662–668. <https://doi.org/10.1021/acs.estlett.9b00525>

Zhang, Y., Liu, J., Ghoshal, S., Moores, A., 2021. Density Functional Theory Calculations Decipher Complex Reaction Pathways of 6:2 Fluorotelomer Sulfonate to Perfluoroalkyl Carboxylates Initiated by Hydroxyl Radical. *Environ Sci Technol* 55, 16655–16664. <https://doi.org/10.1021/acs.est.1c05549>

Zweigle, J., Bugsel, B., Capitain, C., Zwiener, C., 2022. PhotoTOP: PFAS Precursor Characterization by UV/TiO₂ Photocatalysis. *Environ Sci Technol* 56, 15728–15736. <https://doi.org/10.1021/acs.est.2c05652>

5. Advancing PFAS Characterization: Development and Optimization of a UV-H₂O₂-TOP Assay for Improved PFCA Chain Length Preservation and Organic Matter Tolerance

David Patch†, Natalia O'Connor†, Ellie Ahmed†, Michael Bentel††, Erika Houtz†††, Ian Ross††††, Jennifer Scott†, Iris Koch†, Kela Weber†*

† Environmental Sciences Group, Department of Chemistry and Chemical Engineering, Royal Military College of Canada, Kingston, ON, Canada K7K 7B4.

†† Department of Chemical and Environmental Engineering, University of Cincinnati.

††† ECT2, 125 Industrial Way, Portland, ME 04103

†††† CDM Smith, 75 State St #701, Boston, MA 02109

* Corresponding Author:

Email: Kela.Weber@rmc.ca

Phone: 613-541-6000 ext. 3633

The authors declare no competing financial interest.

5.1. Abstract

As per- and polyfluoroalkyl substances (PFAS) infiltrate the environment via industrial, commercial, and domestic sources, the demand for robust, cost-effective, and straightforward analytical assays intensifies to enhance PFAS characterization and quantification. To address this demand, this study introduces a novel UV-H₂O₂-TOP assay, identifying optimal parameters such as pH (5-9), oxidant concentration (500 mM H₂O₂), activation rate (63 mM H₂O₂ h⁻¹), and an acceptable total organic carbon (TOC) limit (~1000 mg/L TOC) to achieve maximum PFAA precursor conversion. Additional work was performed further optimizing the UV-TOP assay, by confirming its superiority to heat activation, identifying the effectiveness of different persulfate salts, and investigating different concentrations of sodium persulfate and sodium hydroxide at a 1:2.5 ratio on PFCA yield. Our investigation concluded by applying the UV-H₂O₂-TOP assay, using sodium persulfate as the TOP assay oxidant, to 6:2 FTS and five different AFFF samples. High-resolution mass spectrometry and an expanded analytical suite support sample analysis, facilitating direct quantification of ultra-short chain perfluoroalkyl carboxylates (PFCAs) and common fluorotelomer compounds including 5:3/5:1:2 fluorotelomer betaine and 6:2 fluorotelomer sulfonamido betaine. Results highlight several advantages of this tandem UV-activated method, including enhanced preservation of perfluoroalkyl chains (post-oxidation of 6:2 fluorotelomer sulfonate resulted in 29% PFHpA, 47% PFHxA, 25% C3-C5 PFCA), capacity to handle high TOC limits (1000 mg/L TOC), and ability to incorporate higher persulfate concentrations in a single oxidation cycle.

5.2. Introduction

Per- and polyfluoroalkyl substances (PFAS) are a class of recalcitrant anthropogenic chemicals manufactured in bulk quantities since the 1930's, characterized by one or more carbon-fluorine ($-CF_2/-CF_3$) moieties (Hendricks, 1953; Wang et al., 2021). Manufacturers use PFAS in a variety of products (e.g. aqueous film-forming foam (AFFF), consumer products, textile treatments) to take advantage of their unique physicochemical properties (Barzen-Hanson et al., 2017; Bečanová et al., 2016; Herzke et al., 2012; Kotthoff et al., 2015; Liagkouridis et al., 2022; Xia et al., 2022). The high degree of stability of fluorocarbon compounds, which has been well known since the 1940's, results in PFAS being extremely environmentally persistent. Due to this environmental persistence, PFAS have been consistently detected in matrices such as surface water, groundwater, and drinking water. Due to the negative health effects associated with some PFAS, many governmental organizations are establishing PFAS guideline limits for soil, water, and consumer products (Brennan et al., 2021). As PFAS regulations continue to develop, so do the analytical methods used to characterize the total PFAS load present in a given matrix.

Work by Houtz and Sedlak (2012) concentrated on adapting a conventional remediation method, chemical oxidation, into an innovative analytical assay. This assay, referred to as the total oxidizable precursor (TOP) assay, employed potassium persulfate in heated ($85^{\circ}C$) and highly alkaline ($pH > 13$) conditions to oxidatively convert polyfluorinated compounds (referred to herein as PFAA precursors) into terminal PFCAs, enabling the detection of otherwise hidden PFAS (Houtz et al., 2018, 2013; Houtz and Sedlak, 2012b). The TOP assay has since been employed by research groups and commercial analytical labs to oxidatively convert PFAA precursors into terminal PFCAs and improve characterization of total PFAS loads. Since its development in 2012, various modifications to the TOP assay have been explored including increased reagent concentrations, multiple oxidation cycles, and the use of different activators (Al Amin et al., 2021b; Casson and Chiang, 2018; Dai et al., 2019; Eriksson et al., 2022; Iavetz et al., 2019; Janda et al., 2019; Kaiser et al., 2021; Martin et al., 2019; Nolan et al., 2019b; Zhu and Kannan, 2020). Current challenges facing the TOP assay include achieving complete PFAS precursor oxidation in high organic matter matrices (Antell et al., 2023; Nolan et al., 2019b; Tsou et al., 2023) and achieving complete recovery of PFAS post-oxidation (Steffens et al., 2021). Work by Tsou et al. (2023) identified that the TOP assay could be scaled down from the standard 125 mL working volume to a 1 mL working volume, increasing sample throughput while reducing resource investment per sample. Work by

Patch et al. (2024) further expanded on this smaller sample volume and identified several TOP assay modifications to improve PFAS recovery, including the use of ultraviolet (UV) light as an activator, the use of mass labelled perfluorooctane sulfonamide (FOSA) to measure oxidation completion, and the use of 1:1 water/methanol when diluting samples post-oxidation to avoid a loss of PFAS due to precipitation of salts from the high ionic strength solution (Patch et al., 2022; Singh et al., 2019b; Steffens et al., 2021). However, one of the biggest challenges for the TOP assay is its difficulty in overcoming high organic matter matrices, which can consume oxidant and lead to incomplete PFAS oxidation and poor PFAS recovery.

The present study sought to develop an integrated, UV-H₂O₂-TOP assay to achieve improved PFAS characterization over the standard thermal-activated TOP assay and UV-TOP assay. To this end, this manuscript focuses on three main objectives: 1) the development of an optimized pre-oxidation assay using UV-activated hydrogen peroxide (H₂O₂) to reduce or eliminate initial organic matter present, 2) the investigation into different persulfate salts and different concentrations of sodium persulfate, and 3) the application of the UV-H₂O₂-TOP assay through its application to 6:2 FTS and five AFFF samples.

5.3. *Materials and Methods*

5.3.1. *Reagents*

6:2 fluorotelomer sulfonate (FTS) was purchased as a powder from Synquest Labs (>97% purity) and used to prepare high concentration stock solutions by dissolving the powder in MilliQ® deionized water. Analytical PFAS standards, including 5:3 FtB, 5:1:2 FtB, 6:2 FtSaB, 6:2 FTS, 8:2 FTS, and 6:2 FTOH were purchased from Wellington Labs (Guelph, Ontario) and were either diluted with 1:1 water/methanol to different concentrations for calibration purposes, or evaporated to dryness and reconstituted in DI water for oxidation experiments. Trifluoroacetic acid (TFA) and perfluoropropanoic acid (PFPrA) was purchased from Sigma Aldrich (97%) for calibration purposes. AFFF formulations were sourced from internal inventories and have been characterized in previous work (Patch et al., 2024). The AFFF formulations include a PFCA-dominant AFFF (N. Foam 1982); a PFSA-dominant AFFF (3M 1980); a 6:2, 8:2, 10:2 FtSaB-dominant AFFF (N. Foam 1990); a 5:1:2, 7:1:2 FtB-dominant AFFF (Ansul 2012); and a 6:2 fluorotelomer-dominant AFFF (Solberg). In the Solberg AFFF, the 6:2 fluorotelomers consist mainly of 6:2 FTS, 6:2 FtSaB, 6:2 FtTAoS, and (identified in this study), 6:2 fluorotelomer sulfonamido propyl methyl hydroxymethyl ammonium (6:2 FTtSaPrMeOHMeAN), which has been previously identified in

similar Solberg AFFF formulations by Luo et al. (Luo et al., 2020). Dilute (1000x) AFFF stock solutions were prepared in DI water gravimetrically, by first weighing out 0.05 grams of AFFF concentrate, and diluting it with DI water to 50 grams total. Dilute AFFF stocks were then mixed on an end-over-end mixer for 24 hours to ensure proper dissolution of the concentrate. Potassium persulfate (KPS; ACS grade), sodium persulfate (NaPS), ammonium persulfate (AmmPS) sodium hydroxide (NaOH; ACS grade), UV-transparent cuvettes (BrandTech®), cuvette lids, hydrogen peroxide (H₂O₂; 30%), butyl carbitol (BC), and methanol (ACS grade) were purchased from VWR. LC-MS grade water and acetonitrile were purchased from Canadian Life Sciences. Double deionized (DI) water (18 MΩ•cm) was acquired from an in-house Milli-Q® Direct 8 water purification system.

5.3.2. UV-H₂O₂, UV-TOP, and UV-H₂O₂-TOP Assays

Throughout this work the UV-activated H₂O₂ and TOP assays are employed to investigate different parameters or methodologies. For the UV-activated H₂O₂ assay, samples are amended with H₂O₂ (100 mM or 500 mM, unless otherwise stated), sub-sampled into 1 mL UV-transmissible cuvettes, and subjected to UV-activation for up to 22 hours (254 nm, 36 watt lamp, ~2.6 J s⁻¹ L⁻¹ of photon irradiance, described in Patch et al., 2022). For the UV-activated TOP assay, samples are amended with 60 mM KPS or NaPS and 150 mM NaOH (unless otherwise stated), sub-sampled into 1 mL UV-transmissible cuvettes, and subjected to UV-activation for at least 4 hours, up to 22 hours (experiment dependent) (Patch et al., 2024).

This work builds upon previous works by Patch et al. (2024) and Tsou et al. (2024), who both identified effective applications of the TOP assay to low volume samples (Patch et al., 2024; Tsou et al., 2023). Working with low volume samples takes advantage of higher sample throughput and reduced resource investment.

Previously, Patch et al. (2024) identified that a 10,000x dilution of AFFFs was required to achieve complete oxidation of PFAA precursors. With the objective of this work being the evaluation of the UV-H₂O₂-TOP assay on high dissolved organic carbon samples, the AFFFs employed in this study were only diluted 1000x before oxidation, and all AFFF samples were prepared in triplicate by diluting them directly from concentrate stocks. Due to this, the use of mass-labelled surrogates could not be used as they would be over-diluted during sample dilution for analysis. To compensate for this, native PFAS (PFOS, PFOA, and 6:2 FTS) were used as internal standards, added at concentrations of 1 mg/L each to three method blank samples, and to one replicate from each

triplicate AFFF sample, before application of the UV- H₂O₂-TOP assay. Samples were prepared in batches of 24, with six diluted AFFFs in triplicate (18), three PFAS-amended method blanks (3), and three undiluted method blanks (3). The overall recovery of PFAS in the PFAS-amended method blanks and diluted AFFF samples amended with PFAS was found to be between 70-110%. No corrections were made based on PFAS or fluoride recovery

5.3.3. Method Development and Optimization

For a summarized list of experiments performed, please see Table 5.1. For a complete description of experiments, please see the Supporting Information (SI). Trials for all experiments were performed in triplicate, with presented data shown as the average of all three trials. Error bars for all trials represent the standard deviation of the triplicates.

Table 5.1 – Summarized method development and optimization employed across this study. (LC-MS/MS = liquid chromatography mass tandem mass spectrometry. GC-MS= gas chromatography mass spectrometry. TOC = Total organic carbon determination. Iodo determ = iodometric colorimetric determination of H₂O₂).

	Experiment Objective	Specific Variable	Probe Molecule (Concentration)	Assay Type (Concentration)	Assay Time (Hours)	Analysis	Figure(s)
Method Development	UV-H ₂ O ₂ Optimal pH	pH 2.6, 5, 5.7, 6.6, 9.2, 11, 13	6:2 FTS (7 µM)	H ₂ O ₂ (500 mM)	22	LC-MS/MS	1, S1
	UV-H ₂ O ₂ Optimal Conc	H ₂ O ₂ (0.1-4000 mM)	6:2 FTS (4 µM)	H ₂ O ₂ (Variable)	22	LC-MS/MS	1, S2
	UV-H ₂ O ₂ Optimal Conc	H ₂ O ₂ (0.1-4000 mM)	Butyl Carbitol (10 mM)	H ₂ O ₂ (Variable)	22	GC-MS, TOC	1
	UV-H ₂ O ₂ Activation Time	Time	H ₂ O ₂ (100 mM)	H ₂ O ₂ (100 mM)	2.5	Iodo. Determ.	1, S3
Method Optimization	Impact of Organic Matter	Butyl Carbitol (0-100 mM)	6:2 FTS (6 µM)	TOP (60 mM KPS, 150 mM NaOH), H ₂ O ₂ (500 mM), H ₂ O ₂ -TOP (as above)	4, 22, 22/4	LC-MS/MS	2, 3
	Oxidant Type	KPS, NaPS, AmmPS	6:2 FTS	UV-TOP (60 mM persulfate, 150 mM NaOH)	12	LC-MS/MS	S4
	Oxidant Concentration	NaPS (1-200 mM) NaOH = 2.5x NaPS Conc	6:2 FTS, PFOS, PFOA	UV-H ₂ O ₂ -TOP (500 mM H ₂ O ₂ , variable TOP reagents)	22/12	LC-MS/MS	S4
	Fluorotelomer Evaluation	Different Single Fluorotelomers	5:3/5:1:2 FtB, 6:2 FtSaB, 6:2 FTS, 8:2 FTS, 6:2 FTOH	UV-H ₂ O ₂ -TOP (500 mM H ₂ O ₂ , then 60 mM NaPS, 150 mM NaOH)	22/4	LC-MS/MS	4
	Impact of TOP Activator	Thermal, UV Activation	6:2 FTS, Five AFFFs	Thermal (60 mM NaPS, 150 mM NaOH), UV-H ₂ O ₂ -TOP (500 mM H ₂ O ₂ , then 60 mM NaPS, 150 mM NaOH)	Thermal (85°C) =12h UV=22/12h	LC-MS/MS	5, S5

PFAS Analysis

Detailed information on the analytical methodology employed in this study can be found in the SI and in several previous works (O'Connor et al., 2023; Patch et al., 2022; Turner et al., 2021). Samples were directly analyzed using an expanded target analytical suite (Table S1) on an Agilent 6460 LC-MS/MS and a ThermoFisher Orbitrap Exploris 120 LC-HRMS. Routine analysis of TFA and PFPrA was exclusive to the Agilent 6460 LC-MS/MS and was achieved using an analytical column longer than that used for other PFAS (150 mm ACME C18 column) and no diverter valve, resulting in the quantitation of the poorly retained TFA and PFPrA. TFA and PFPrA were quantified in SIM mode through the acquisition of 113 m/z and 163 m/z in negative acquisition mode respectively. Where necessary, concentrations of TFA and PFPrA were confirmed using the Orbitrap LC-HRMS, which provided accurate mass confirmation of the compounds. However, this was not applied to every sample due to the introduction of significant salt concentrations into the mass spectrometer as a consequence of not employing a diverter valve. Samples suspected to contain unknown PFAS (e.g. AFFF) were semi-quantified exclusively on the ThermoFisher Orbitrap Exploris 120 using suspect screening databases previously built for AFFFs and PFAS degradation products (O'Connor et al., 2023; Patch et al., 2024). Inter-instrument variability for these instruments was evaluated in previous work and found to be less than 20% including error. Inter-instrument variability was monitored throughout this study and was found to agree with previous work and be less than 20%. In scenarios where the deviation on PFAS concentrations between instruments was found to exceed 20%, both samples and calibration standards were re-prepared and re-analyzed.

5.4. Results and Discussion

5.4.1. UV-H₂O₂ Method Development – Role of pH, Concentration and Activation Time

Numerous studies have identified the ability for dissolved organic matter (DOM) to interfere with the TOP assay, and potentially reduction-based technologies (Fennell et al., 2023, 2022, 2021; Tsou et al., 2023). Several authors identify the need for dilution or multiple applications of the TOP assay when dealing with samples with high organic matter (Nolan et al., 2019b). However, this comes with the drawback of additional salt input into the system, which has been identified in previous studies to result in under-reporting of PFAS due to various salting-out phenomena (Steffens et al., 2021). Instead, work by Hutchinson has proposed the use of H₂O₂ as an effective

pre-treatment method for dealing with samples containing high organic matter without the input of additional salts (Hutchinson et al., 2020).

The use of H_2O_2 to oxidize organic matter has been investigated across numerous studies, with inconsistent conclusions as to the optimal pH, concentration, or activation time required to achieve effective oxidation. Therefore, a series of experiments varying these parameters were performed to develop the UV- H_2O_2 assay method and follow the oxidation of 6:2 FtS to PFCAs, either stand-alone or in the presence of organic matter, (Figure 5.1).

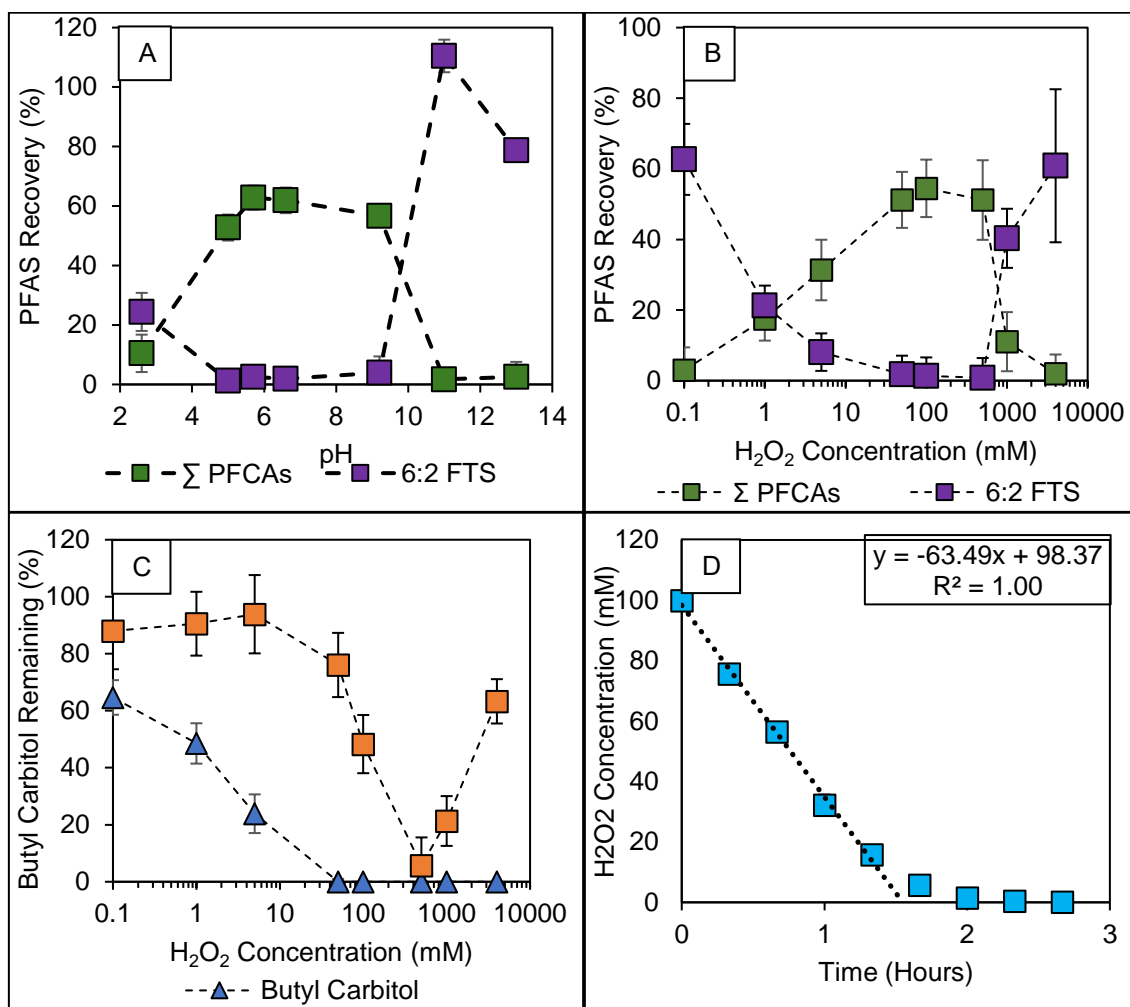


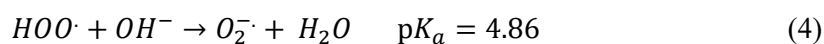
Figure 5.1 – UV- H_2O_2 system. (A) Investigating transformation (or oxidation) of 6:2 FtS as a function of pH and (B) H_2O_2 concentration, (C) transformation (or oxidation) of butyl carbitol and total organic carbon as a function of H_2O_2 concentration, and (D) H_2O_2 concentration as a function of UV-activation time. (A=500 mM H_2O_2 , D=100 mM H_2O_2). Reactions performed at pH 5.7 is unless otherwise stated. Error bars represent the standard deviation of triplicate samples.

Following oxidation of 6:2 FTS in the UV-H₂O₂ system, it was identified that the highest yield of PFCAs (62±1%) is achieved following the application of 500 mM of H₂O₂ for 22 hours with a pH of 5.7 (unadjusted). Following oxidation of butyl carbitol in the UV-H₂O₂ system, it was identified that 50 mM of H₂O₂ was required to degrade the parent butyl carbitol molecule, but maximum total organic carbon removal (mineralization of the butyl carbitol) was achieved at 500 mM of H₂O₂. For details on the specific PFCA product composition under different scenarios, please see the SI.

Understanding the influence of pH on UV-activated H₂O₂ is complex, due to the role of pH on both the parent molecule and resultant photolysis-generated oxidizing radical. H₂O₂ is a common peroxyacid with a pK_a of 11.6, molar absorptivity of ~ 18 M⁻¹ cm⁻¹, and a quantum yield of 1.15 (Goldstein et al., 2007; Morgan et al., 1988; Yin et al., 2023). Following activation with UV-light, H₂O₂ is converted into two hydroxyl radicals (Eq. 1), with a standard reduction potential of 1.8 V (Buxton et al., 1988).

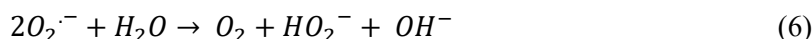
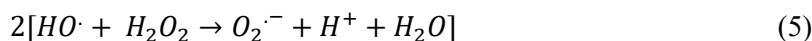


Both H₂O₂ and hydroxyl radicals have optimal pHs at which they operate. Under alkaline conditions (pH > 11), H₂O₂ loses a proton to form the hydroperoxyl anion (HOO⁻), which, following activation by UV, generates the weakly oxidizing hydroperoxyl radical (HOO[·]). This radical, likewise, loses a proton to form the superoxide radical anion (Eq. 2, 3, 4) (Zhao et al., 2013).



As observed in this study, at pH 11 and higher 6:2 FTS shows little-to-no reactivity, likely due to the hydroperoxyl radical and superoxide being weaker oxidants than the hydroxyl radical (Nakabayashi and Nosaka, 2015). Additionally, as conditions shift to a more acidic environment, the yield of PFCAs begins to decrease, suggesting reduced reactivity of H₂O₂ or the hydroxyl radical (X. Liu et al., 2013; Molot et al., 2005).

In the case of concentration, there is a balance between sufficient H₂O₂ to effectively break down the concentration of organic substrate present, and excessive H₂O₂ to avoid scavenging of hydroxyl radicals (Eq. 5, 6) and breakdown of H₂O₂ to oxygen and water (Eq. 7).



The results from Figure 1C reveal that the most effective removal of TOC (94±10%) is achieved at a concentration of 500 mM H₂O₂. Considering an initial TOC concentration of 960 mg/L (approximately 10 mM of BC), this suggests that ~17 g/L H₂O₂ (500 mM) is needed to degrade 0.96 g/L of TOC, resulting in an oxidant-to-TOC ratio of ~17:1. Notably, higher concentrations of H₂O₂ led to diminished TOC removal (Eq. 5-7). Therefore, it is apparent that samples with TOC concentrations exceeding 1 g/L will necessitate dilution prior to the 500 mM UV-H₂O₂ application or may require multiple rounds of UV-H₂O₂ at 500 mM H₂O₂.

Lastly, identifying the rate of H₂O₂ activation for the UV lamp system is important to ensure complete consumption of the initial oxidant concentration. This was achieved using an iodometric determination method, which has the advantage of allowing for sensitive monitoring of H₂O₂ through the oxidative formation of triiodide. One drawback of this method however is the time sensitivity of the solutions used in the determination, which lose stability after ~4 hours. This precluded evaluation of the activation rate of the 500 mM H₂O₂ system, as attempts to make a new solution halfway through the determination resulted in significant data discrepancies. To this end, the H₂O₂-activation rate was evaluated using an initial H₂O₂ concentration of 50 mM to ensure accurate measurement using the iodometric determination. With a photon fluence rate of ~2.6 J s⁻¹ L⁻¹ (previously characterized in Patch et al. 2024), H₂O₂ was consumed at a zero-order rate of ~64 mM per hour for the first 80 mM of H₂O₂, with the rate then shifting to an apparent first-order rate of 3.83 h⁻¹ for the last 20 mM of H₂O₂. This resulted in ~98% activation of H₂O₂ within two hours, and >99.9% activation within 2.7 hours. When applying this rate to 500 mM of H₂O₂, and assuming the shift from zero-order to first-order is concentration-dependent, it can be assumed that the first 480 mM of H₂O₂ will be consumed after 8 hours, and >99% will be consumed by 10 hours. Despite being completed by 10 hours, the UV-H₂O₂ assay was often employed overnight (~22 hours) for ease of use. When applied for 22 hours to a solution containing 6:2 FTS, PFOS and PFOA, PFAS

recovery was found to be >95%, indicating there is no negative effect of the assay being applied for an extended period of time (Figure C4).

5.4.2. UV-H₂O₂-TOP Method Development – Overcoming High Organic Matter Concentrations

The development and optimization of the UV-H₂O₂ assay identified that, under neutral pH to slightly alkaline conditions (pH 5.0-9.2), 500 mM of H₂O₂ was the ideal concentration to degrade BC, with the activation time of this assay being at least 10 hours, with no detriment up to 22 hours. To evaluate the effectiveness of the UV-H₂O₂ assay on overcoming the effect of dissolved organic matter as a co-constituent, the UV-TOP, UV-H₂O₂, and UV-H₂O₂-TOP assays were performed on a solution of 6:2 FTS with a variable concentration of BC (Figure 5.2).

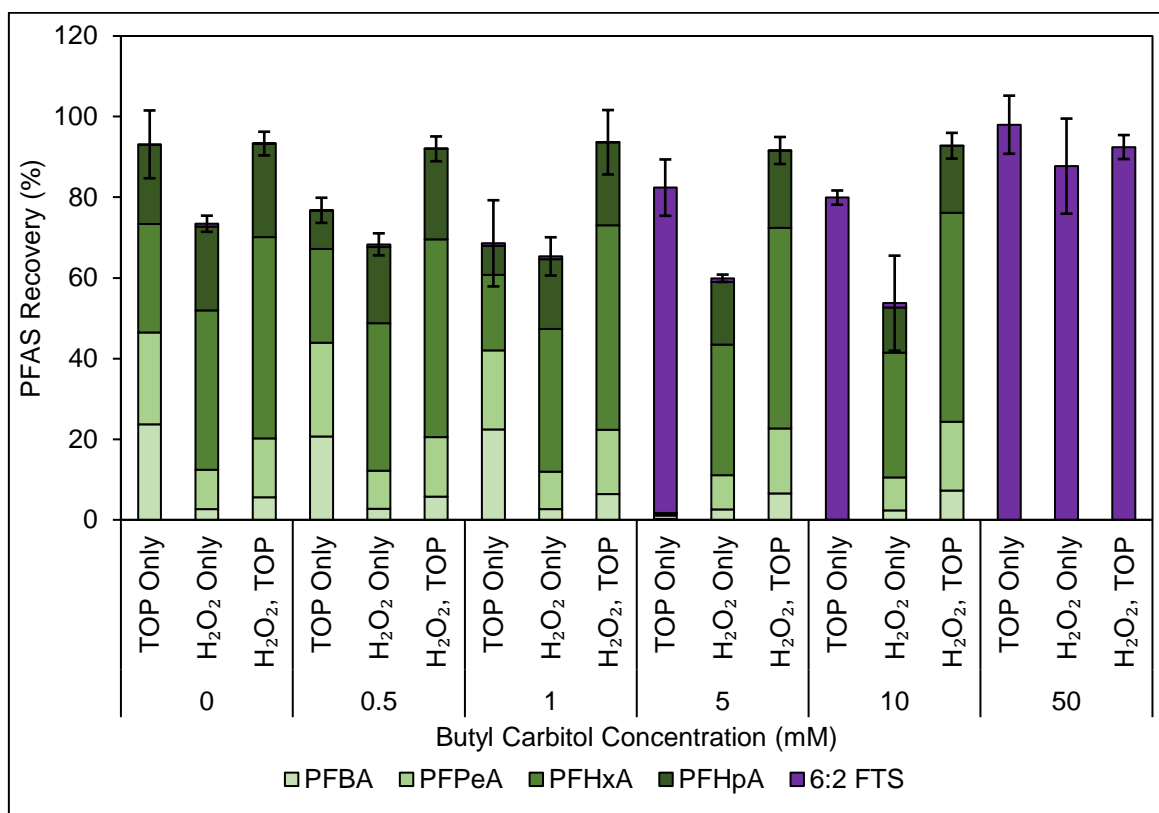


Figure 5.2 – Concentration of PFCAs and 6:2 FTS following application of the UV-TOP (60 mM KPS, 150 mM NaOH), UV-H₂O₂ assay (500 mM H₂O₂, 22 hours) and the UV-H₂O₂-TOP assay, with different concentrations of butyl carbitol (BC). Error bars represent the standard deviation of triplicate samples.

Whereas the UV-TOP assay alone was incapable of oxidizing 6:2 FTS at 5 mM of BC or greater, the UV-H₂O₂ assay achieved oxidation of 6:2 FTS in the presence of up to 10 mM of BC. As identified in previous trials, the UV-H₂O₂ assay does not result in complete recovery of PFCAs, due to partially oxidized transformation products (e.g. C₈F₁₃H₂(OH)₂SO₃⁻) identified herein (Figure C6). Incorporation of the TOP assay following the UV-H₂O₂ assay completes the oxidation of the partially oxidized transformation products, resulting in >90% molar yield of measurable PFCA products from 6:2 FTS up to 10 mM of BC. As observed previously, the UV-H₂O₂-TOP assay results in a shift to the PFCA composition, resulting in >70% of the PFCA composition being PFHpA and PFHxA, compared to ~50% with just UV-TOP assay alone. This shift to longer-chain PFCA products allows for further preservation of the PFAS precursor chain structure, allowing for better identification as to the chain length of precursors in unknown samples.

These results align well with other works investigating the ability for different dissolved organic carbon substrates to interfere with the TOP assay effectiveness (Figure 5.3, Glover et al., 2024; Tsou et al., 2023).

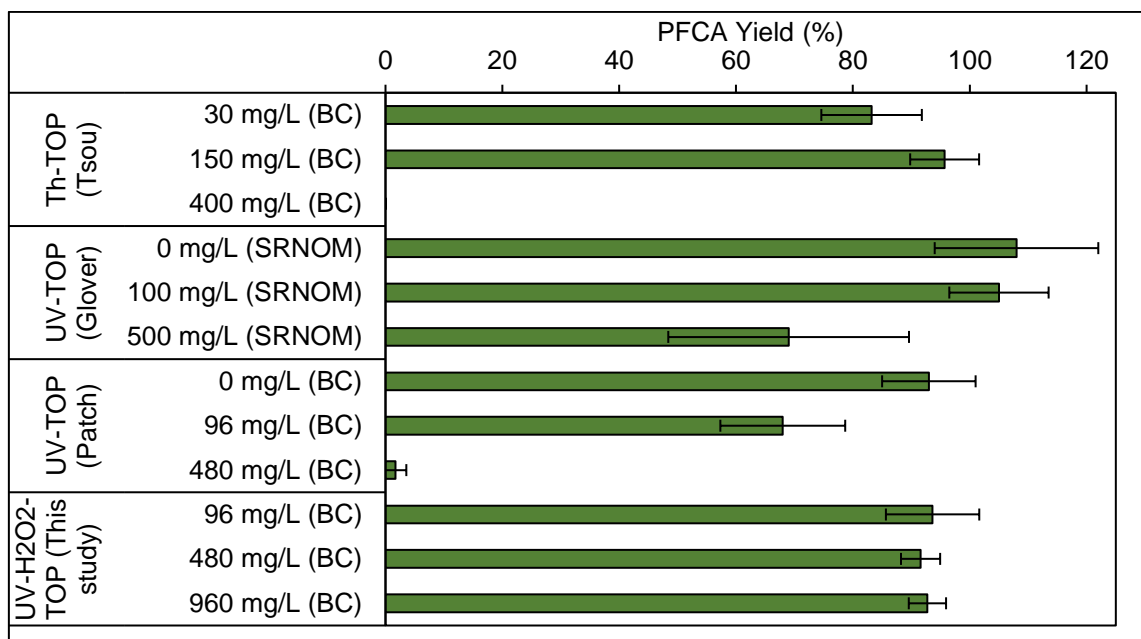


Figure 5.3 – PFCA yield of PFAA precursors with different concentrations of total organic carbon (mg TOC/L, substrate in parentheses) following application of 12 hour thermal TOP assay (Tsou et al., 2023), 1 hour UV TOP assay (Caitlin M. Glover et al., 2024b), 2 hour UV-TOP assay (developed in (Patch et al., 2024), evaluated w/ TOC in this study), and 22 hour/4 hour UV-H₂O₂-TOP assay (developed and evaluated in this study). SRNOM = Suwannee River natural organic matter.

Using Suwannee River natural organic matter (SRNOM) as the model substrate, Glover identified an acceptable TOC limit of 100 mg/L, with significant (<70% PFCA yield) oxidation inhibition at 500 mg/L using 6:2 FTS as a probe molecule (Caitlin M. Glover et al., 2024b). Using BC as the model substrate, Tsou (Tsou et al., 2023) identified an acceptable TOC limit of 150 mg/L, with the next concentration evaluated (400 mg/L) resulting in no oxidation of M₈FOSA. Using the same organic matter substrate as Tsou (BC), Patch identified significant oxidation inhibition of 6:2 FTS at 96 mg/L of TOC (68±11% PFCA yield), and almost no oxidation of 6:2 FTS at 480 mg/L TOC (2±2% PFCA yield). However, the exact concentration of TOC may not be as important as the different compounds that make up the TOC. When comparing TOC limits identified by Glover and Tsou, butyl carbitol inhibits oxidation more than SRNOM, suggesting that both the concentration and type of dissolved organic matter will affect TOP assay effectiveness. This further reinforces the advantage of the UV- H₂O₂-TOP assay, as it allows for the handling of higher concentrations of TOC present in samples, providing users flexibility in deciding if sample dilution is required in samples with high TOC but low PFAS concentration. The upper TOC limit evaluated in this study (960 mg/L TOC) is significantly higher than concentrations found in typical groundwater and is closer to that found in groundwater near landfills (~500 mg/L TOC) (Koda et al., 2017; Lyon et al., 2011). While this TOC limit is lower than what would be found in untreated landfill leachate (>3000 mg/L) (Makhatova et al., 2020), any sample composed of untreated landfill leachate would likely require significant pre-treatment methods (e.g. filtering, dilution, liquid-liquid extraction, alkaline digestion) before any oxidative assays could be employed.

5.4.3. PFCA Yield of Different Fluorotelomers

Initial development of the UV-H₂O₂-TOP assay identified enhanced PFCA preservation compared to standalone UV-TOP when applied to 6:2 FTS. Using sodium persulfate as an alternate oxidant (Figure C4), the UV-H₂O₂-TOP assay was re-applied to 6:2 FTS and several other standalone fluorotelomers, including 5:3 FtB, 5:1:2 FtB, 6:2 FtSaB, 8:2 FTS, and 6:2 FTOH, to identify differences in the PFCA composition post-oxidation (Figure 5.4).

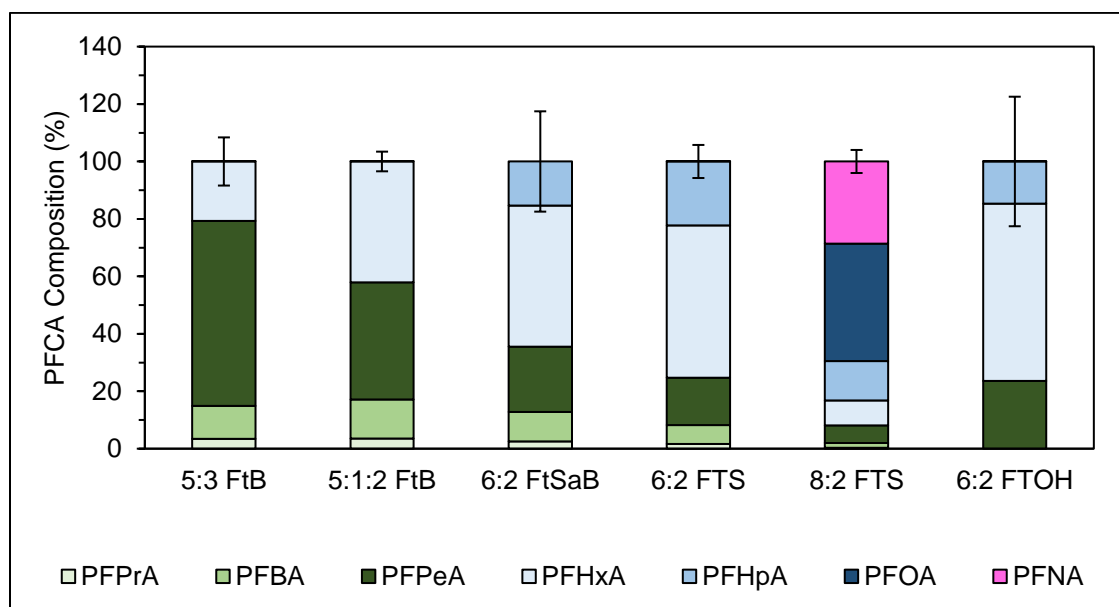


Figure 5.4 – PFCA composition of different fluorotelomers following application of the UV- H_2O_2 -TOP assay (500 mM H_2O_2 , activated with UV for 22 hours, followed by 60 mM NaPS, 150 mM NaOH, activated with UV for 4 hours).

The trend in PFCA composition following oxidation of the fluorotelomers aligned with expectations, with majority of the PFCAs having a chain length of N or N+1, where N is the fluorinated chain length (e.g. 6:2 FTS consists mainly of PFHpA and PFHxA). Interestingly, there was more PFHxA found after the oxidation of 5:1:2 FtB compared to 5:3 FtB, indicating the partially fluorinated carbon results in more formation of the N+1 PFCA. The PFCA profile of 6:2 FTS, 6:2 FtSaB, and 6:2 FTOH were all very similar, except that 6:2 FTOH had no PFPeA or PFBA present. These results suggest that while the PFAS functional group may have a minor role in the post-oxidation PFCA profile, the fluorinated alkyl chain length is what dictates the overall composition trend.

5.4.4. Comparison of UV- H_2O_2 -TOP Assay vs. Thermal- and UV-TOP Assay

Following evaluation of different individual fluorotelomers, the UV- H_2O_2 -TOP assay was applied to different AFFFs, with comparisons to both the thermal-TOP assay and standalone UV-TOP assay (Figure 5.5, grayscale version Figure C5).

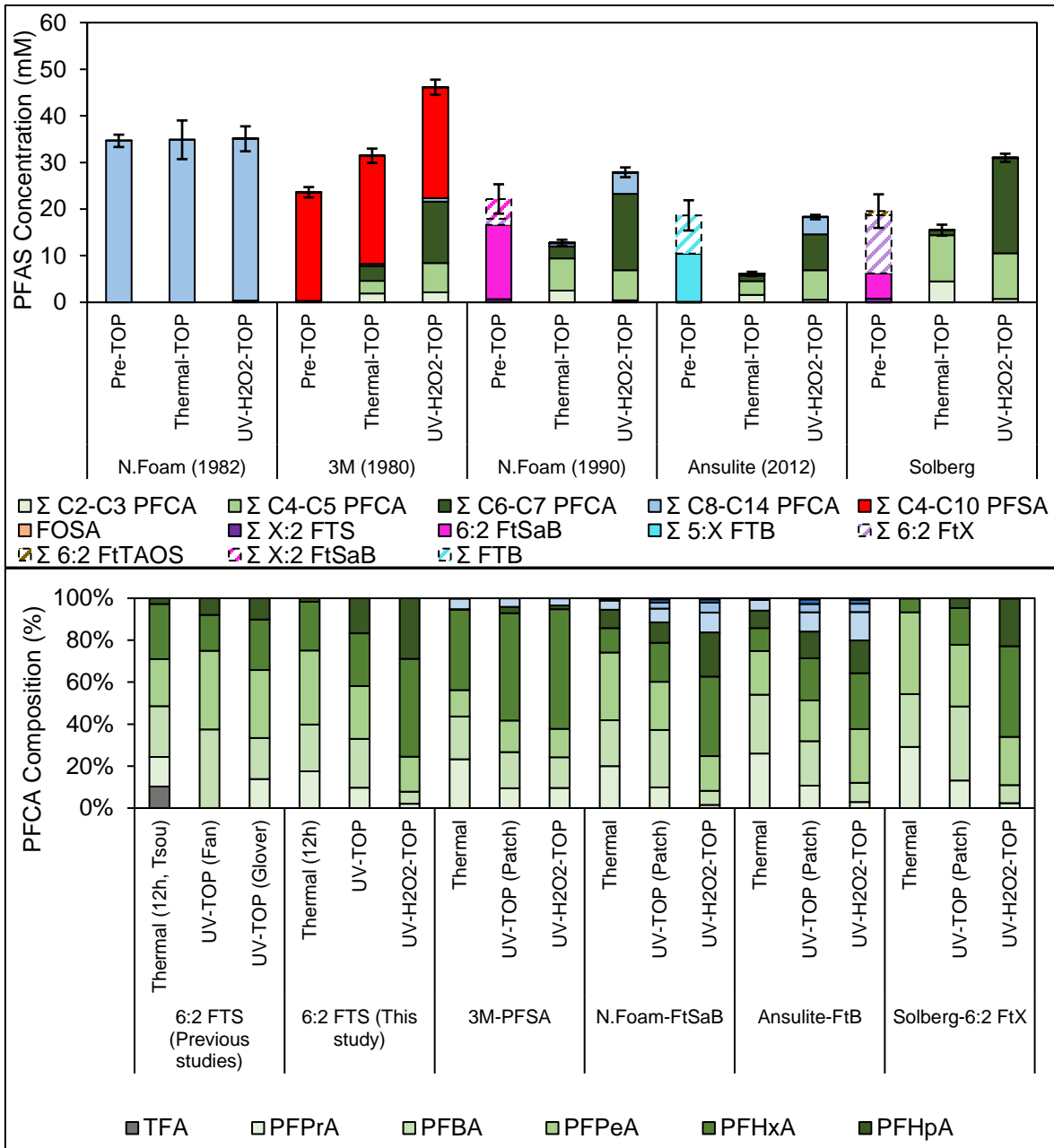


Figure 5.5 – (Top) Absolute concentration of PFAS following application of the thermal- or UV-H₂O₂-TOP assay to five AFFFs, and (Bottom) relativized composition of PFCAs following the oxidation of 6:2 FTS across three different studies, and this study; as well as PFCA composition following the oxidation of the four PFAA-precursor containing AFFFs studied using the stand-alone 12-hour thermal TOP assay (60 mM NaPS, 150 mM NaOH, activated at 85°C for 12 hours), stand-alone UV-TOP assay (60 mM NaPS, 150 mM NaOH, activated with UV for 12 hours), and the UV-H₂O₂-TOP assay (500 mM H₂O₂, activated with UV for 22 hours, followed by 60 mM NaPS, 150 mM NaOH, activated with UV for 12 hours) (Fan et al., 2021; Caitlin M Glover et al., 2024; Patch et al., 2024; Tsou et al., 2023).

Targeted and high-resolution analysis of the AFFF samples identified different major PFAS groups present in different samples, including PFCAs (N. Foam 1980), PFSAs (3M 1980), FtBs (Ansolite-FtB), FtSaBs (N. Foam-FtSaB), and FtTAoSs (Solberg-6:2 FtX). The Solberg AFFF formulation was also found to contain significant concentrations of 6:2 fluorotelomer sulfonamido propyl methyl hydroxymethyl ammonium (6:2 FTtSaPrMeOHMeAN) (Luo et al., 2020). The Solberg AFFF is the only AFFF studied that did not contain any >C6 PFAA precursor homologues, in comparison to the N. Foam 1990 and Ansolite AFFFs which were labelled as C6 AFFFs but contained longer-chain homologues (e.g. 8:2 FtSaB, 7:1:2 FtB).

In comparison to the UV-H₂O₂-TOP assay, the thermal TOP assay resulted in poor conversion of the PFAA precursors into their corresponding PFCAs, with the UV-H₂O₂-TOP assay resulting in up to a 3-fold increase in PFAS concentration compared to the thermal TOP assay. Application of the UV-H₂O₂-TOP assay resulted in up to a 2.6-fold increase in total PFAS concentration in the AFFF formulations. The Ansolite-FtB AFFF formulation had very little increase to the total concentration of PFAS post-oxidation, due to those AFFF samples being well characterized by the expanded analytical suite, which includes TFA, PFPrA, 6:2 FtSaB, 5:3 FtB, and 5:1:2 FtB. This once again reinforces the need to expand targeted analytical methods to include increasingly prevalent PFAA precursors like 6:2 FtSaB and 5:3 FtB, as current analytical targeted suites are becoming increasingly irrelevant with increasingly complex AFFF chemistry.

The PFCA composition following the oxidation of 6:2 FTS is very similar across the different stand-alone thermal and UV-activated TOP assays reported above, with UV-activation typically resulting in more formation of PFHpA (8-17% vs 3%), similar formation of PFHxA (17-25% vs 25%), and less formation of the shorter-chain PFCAs (C₂-C₅). As discussed by previous work and other authors, better preservation of the PFAA chain length post-oxidation allows for improved determination of the PFAA precursor structure, while also allowing for better computation of total PFAS concentration (Patch et al., 2022). As can be seen, the addition of H₂O₂ as an oxidative pre-treatment, even 100 mM for 2 hours, dramatically shifts the PFCA formation to more PFHpA (29%) and PFHxA (47%), resulting in >75% of the PFCA composition being C₆/C₇. The use of the UV-H₂O₂-TOP assay also results in higher proportions of longer-chain PFCAs for the three fluorotelomer-dominant AFFF formulations.

5.4.5. UV-H₂O₂ Assay Mechanism

The application of UV-H₂O₂ to 6:2 FTS resulted in several PFAS oxidation products, including PFCAs, hydroxyl-substituted fluorotelomer sulfonates, and hydroxyl-substituted PFCAs. The subsequent application of the UV-TOP assay (UV-H₂O₂-TOP) resulted in the oxidation of these non-target products to their terminal PFCAs, resulting in a complete or near-complete PFCa field. The following mechanism was developed to identify the transformation pathways responsible for converting 6:2 FTS (and likely other fluorotelomers) to PFCAs (Figure 5.6).

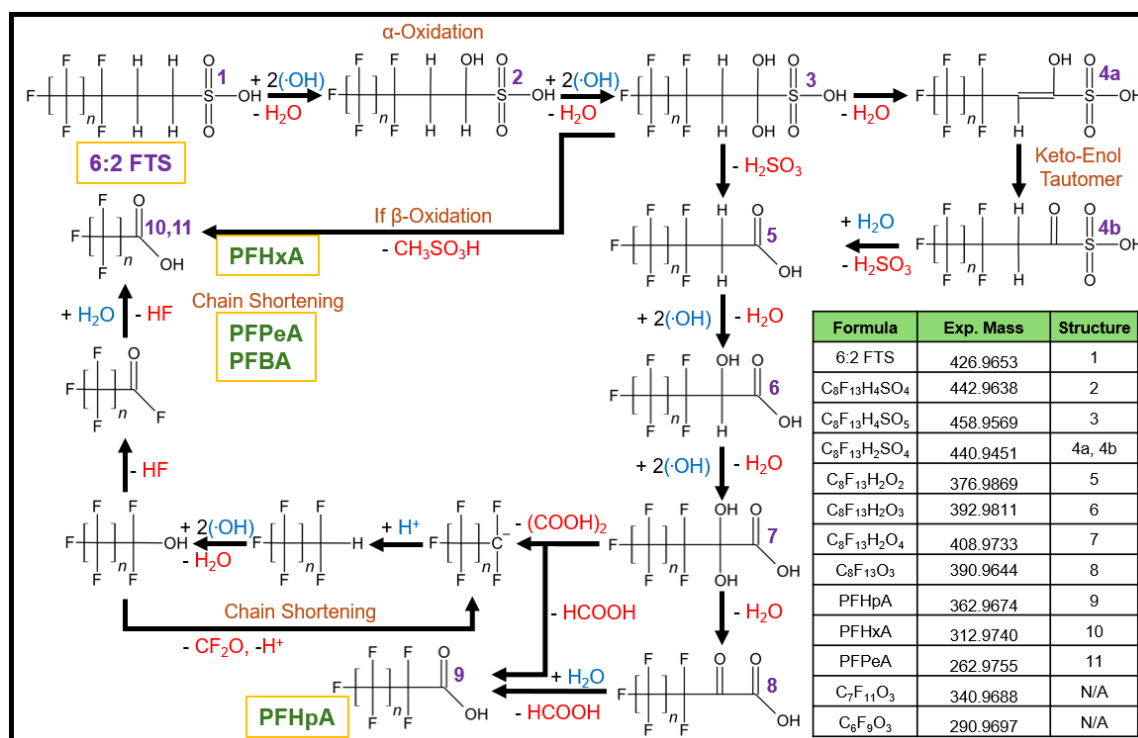


Figure 5.6 – Transformation mechanism of 6:2 FTS oxidatively converted into PFCAs in the UV-H₂O₂ system at neutral pH, with inlaid identified structures and their experimentally measured masses.

6:2 FTS (Figure 6, structure 1) first undergoes hydrogen abstraction with a hydroxyl radical, with the resulting fluorotelomer radical undergoing radical combination with a second hydroxyl radical, yielding the -H/+OH 6:2 FTS (structure 2). This two-step reaction can occur again, resulting in the -2H/+2OH 6:2 FTS molecule (structure 3). The substitutions shown in Figure 6 indicate two substitutions on the α -carbon, but it is important to note that these reactions may also happen on the β -carbon, resulting in three total different substitution options. Progressing from the α -substituted structure (structure 3), an elimination reaction could occur, resulting in the loss of water

and the formation of enol-substituted 6:2 FTS (structure 4a), which can undergo tautomerization to form the ketone-substituted structure (structure 4b). Progressing from either structure 3 or structure 4b, the molecule(s) can undergo a desulfonation reaction to form 6:2 fluorotelomer carboxylic acid (structure 5). If the oxidation of 6:2 FTS took place on the β -carbon, this reaction instead would result in the removal of methane sulfonic acid, forming PFHpA (structure 3 \rightarrow 10). Progressing from 6:2 FTCA, the fluorotelomer will undergo two, two-step reactions with hydroxyl radicals to form the -2H/+2OH 6:2 FTCA molecule (structure 7). From this molecule, three reaction pathways are possible, initiated by the oxidation of one of the alcohols to the carbonyl. The first two reactions both result in PFHpA (structure 9), either directly through a decarboxylation reaction, or first through a condensation reaction (structure 8), followed by subsequent reaction with water to achieve the decarboxylation. The third reaction results in the loss of oxalic acid from the molecule, forming the perfluoroalkyl anion, which undergoes subsequent reactions with hydroxyl radicals and water to form PFHxA (structure 10). This reaction can also deviate after the formation of the perfluoroalkyl alcohol, which progresses through a chain-shortening mechanism to form PFPeA and PFBA.

It is important to note that this proposed mechanism attempted to incorporate all the identified oxidation products but could not include the $C_7F_{11}O_3^-$ or $C_6F_9O_3^-$ structures identified. At this point in time, the exact nature of these two structures is unknown, as they could be part of the main mechanism (suggesting some type of -F/+OH reaction, which has only been observed in reduction-driven systems like UV/S+I (O'Connor et al. 2023)), or they could be terminal end products that do not get oxidized in the UV-H₂O₂ system, but do get oxidized in the UV-TOP system (potentially an alkaline hydrolysis reaction).

5.5. Conclusions

This study aimed to develop and optimize a UV-activated tandem analytical assay for the enhanced characterization of PFAS in complex matrices. This entailed the development of a novel UV-H₂O₂ assay, with considerations as to the optimal pH (5-9), upper H₂O₂ concentration limit (500 mM), and activation rate (64 mM H₂O₂ h⁻¹). This also involved further optimization of the previously developed UV-TOP assay, including the identification of NaPS as a superior oxidant due to its increased solubility, the identification of different effective reagent doses (10 mM NaPS/25 mM NaOH, up to 200 mM NaPS/500 mM NaOH) for particularly clean or complex matrices, and a comparison of the PFCA yield following application of the thermal TOP, UV-TOP, and UV-H₂O₂-

TOP assays for 6:2 FTS and five different AFFF samples. The results presented herein identify that the UV-H₂O₂-TOP assay allows for effective characterization of PFAS concentrations present in aqueous matrices, with the post-oxidation PFCA profile providing insights into PFAA precursor structures. The expansion of the targeted analytical suite to include common PFAA precursors like 6:2 FtSaB, 5:3 FtB, and 5:1:2 FtB serves to further improve the accuracy of PFAS characterization both pre- and post-oxidation. The UV- H₂O₂-TOP assay is an excellent tool to use in combination with other methods if available, namely, with the non-targeted technique used in the present study (LC-HRMS), as well as with other techniques like F-NMR, or total organic fluorine determination methods. The UV- H₂O₂-TOP assay is an excellent tool to use in combination with other methods if available, namely, with the non-targeted technique used in the present study (LC-HRMS), as well as with other techniques like F-NMR, or total organic fluorine determination methods. This study would benefit from future work applying sample pre-concentration techniques, like solid phase extraction, to improve the detection and quantitation limits of this method to meet increasingly stringent drinking water regulations.

5.6. Acknowledgements

This work was supported by Natural Sciences and Engineering Research Council (Canada) Discovery grants of Weber and Koch. The authors would like to acknowledge Taylor Vereecken and Anbareen Farooq for their assistance with TOC measurements.

5.7. References

- Al Amin, M., Luo, Y., Nolan, A., Robinson, F., Niu, J., Warner, S., Liu, Y., Dharmarajan, R., Mallavarapu, M., Naidu, R., Fang, C., 2021. Total oxidisable precursor assay towards selective detection of PFAS in AFFF. *J Clean Prod* 328, 129568. <https://doi.org/10.1016/j.jclepro.2021.129568>
- Antell, E.H., Yi, S., Olivares, C.I., Ruyle, B.J., Kim, J.T., Tsou, K., Dixit, F., Alvarez-Cohen, L., Sedlak, D.L., 2023. The Total Oxidizable Precursor (TOP) Assay as a Forensic Tool for Per- and Polyfluoroalkyl Substances (PFAS) Source Apportionment. *ACS ES and T Water*. <https://doi.org/10.1021/acsestwater.3c00106>
- Barzen-Hanson, K.A., Roberts, S.C., Choyke, S., Oetjen, K., McAlees, A., Riddell, N., McCrindle, R., Ferguson, P.L., Higgins, C.P., Field, J.A., 2017. Discovery of 40 Classes of Per- and Polyfluoroalkyl Substances in Historical Aqueous Film-Forming Foams (AFFFs) and AFFF-Impacted Groundwater. *Environ Sci Technol*. <https://doi.org/10.1021/acs.est.6b05843>
- Bečanová, J., Melymuk, L., Vojta, Š., Komprdová, K., Klánová, J., 2016. Screening for perfluoroalkyl acids in consumer products, building materials and wastes. *Chemosphere* 164, 322–329. <https://doi.org/10.1016/j.chemosphere.2016.08.112>
- Brennan, N.M., Evans, A.T., Fritz, M.K., Peak, S.A., von Holst, H.E., 2021. Trends in the regulation of per- and polyfluoroalkyl substances (PFAS): A scoping review. *Int J Environ Res Public Health* 18. <https://doi.org/10.3390/ijerph182010900>
- Buxton, G. V., Greenstock, C.L., Helman, W.P., Ross, A.B., 1988. Critical Review of rate constants for reactions of hydrated electrons, hydrogen atoms and hydroxyl radicals ($\cdot\text{OH}/\cdot\text{O}$ in Aqueous Solution. *J Phys Chem Ref Data* 17, 513–886. <https://doi.org/10.1063/1.555805>
- Casson, R., Chiang, S.Y.D., 2018. Integrating total oxidizable precursor assay data to evaluate fate and transport of PFASs. *Remediation* 28, 71–87. <https://doi.org/10.1002/rem.21551>
- Dai, X., Xie, Z., Dorian, B., Gray, S., Zhang, J., 2019. Comparative study of PFAS treatment by UV, UV/ozone, and fractionations with air and ozonated air. *Environ Sci (Camb)* 5, 1897–1907. <https://doi.org/10.1039/c9ew00701f>
- Di Battista, V., Rowe, R.K., Patch, D., Weber, K., 2020. PFOA and PFOS diffusion through LLDPE and LLDPE coextruded with EVOH at 22 °C, 35 °C, and 50 °C. *Waste Management* 117, 93–103. <https://doi.org/10.1016/j.wasman.2020.07.036>
- Duchesne, A.L., Brown, J.K., Patch, D.J., Major, D., Weber, K.P., Gerhard, J.I., 2020. Remediation of PFAS-Contaminated Soil and Granular Activated Carbon by Smoldering Combustion. *Environ Sci Technol* 54, 12631–12640. <https://doi.org/10.1021/acs.est.0c03058>
- Eriksson, U., Yeung, L.W.Y., Fredriksson, F., Anna, K., 2022. Analysis and characterization of novel fluorinated compounds used in surface treatments products. *Chemosphere* 302. <https://doi.org/10.1016/j.chemosphere.2022.134720>
- Fan, X., Bao, Y., Mumtaz, M., Huang, J., Yu, G., 2021. Determination of total oxidizable precursors in foam surfactants and foam contaminated water based on UV-activated persulfate oxidation. *Science of the Total Environment* 763, 142943. <https://doi.org/10.1016/j.scitotenv.2020.142943>
- Fennell, B.D., Fowler, D., Mezyk, S.P., McKay, G., 2023. Reactivity of Dissolved Organic Matter with the Hydrated Electron: Implications for Treatment of Chemical Contaminants in Water with Advanced Reduction Processes. *Environ Sci Technol* 57, 7634–7643. <https://doi.org/10.1021/acs.est.3c00909>

- Fennell, B.D., Mezyk, S.P., McKay, G., 2021. Critical Review of UV-Advanced Reduction Processes for the Treatment of Chemical Contaminants in Water. *ACS Environmental Au*. <https://doi.org/10.1021/acsenvironau.1c00042>
- Fennell, B.D., Odorisio, A., McKay, G., 2022. Quantifying Hydrated Electron Transformation Kinetics in UV-Advanced Reduction Processes Using the Re-,UVMMethod. *Environ Sci Technol* 56, 10329–10338. <https://doi.org/10.1021/acs.est.2c02003>
- Glover, Caitlin M, Pazoki, F., Munoz, G., Liu, J., 2024. Enhancing Total Oxidizable Precursor Assay for Characterization of PFAS: UV Versus Heat Activation. Pre-print.
- Glover, Caitlin M., Pazoki, F., Munoz, G., Sauv e, S., Liu, J., 2024. Applying the modified UV-activated TOP assay to complex matrices impacted by aqueous film-forming foams. *Science of the Total Environment* 924. <https://doi.org/10.1016/j.scitotenv.2024.171292>
- Goldstein, S., Aschengrau, D., Diamant, Y., Rabani, J., 2007. Photolysis of aqueous H₂O₂: Quantum yield and applications for polychromatic UV actinometry in photoreactors. *Environ Sci Technol* 41, 7486–7490. <https://doi.org/10.1021/es071379t>
- Hendricks, J., 1953. *Industrial Fluorochemicals*.
- Herzke, D., Olsson, E., Posner, S., 2012. Perfluoroalkyl and polyfluoroalkyl substances (PFASs) in consumer products in Norway - A pilot study. *Chemosphere* 88, 980–987. <https://doi.org/10.1016/j.chemosphere.2012.03.035>
- Houtz, E., Wang, M., Park, J.S., 2018. Identification and Fate of Aqueous Film Forming Foam Derived Per- and Polyfluoroalkyl Substances in a Wastewater Treatment Plant. *Environ Sci Technol* 52, 13212–13221. <https://doi.org/10.1021/acs.est.8b04028>
- Houtz, E.F., Higgins, C.P., Field, J.A., Sedlak, D.L., 2013. Persistence of perfluoroalkyl acid precursors in AFFF-impacted groundwater and soil. *Environ Sci Technol* 47, 8187–8195. <https://doi.org/10.1021/es4018877>
- Houtz, E.F., Sedlak, D.L., 2012. Oxidative conversion as a means of detecting precursors to perfluoroalkyl acids in urban runoff. *Environ Sci Technol* 46, 9342–9349. <https://doi.org/10.1021/es302274g>
- Hutchinson, S., Rieck, T., Wu, X.L., 2020. Advanced PFAS precursor digestion methods for biosolids. *Environmental Chemistry* 17, 558–567. <https://doi.org/10.1071/EN20008>
- Iavetz, R., Lewin, M., Morschel, G., Slee, D., Lim, C., Nolan, A., Grimison, C., Centner, M., Mcgrath, S., Symons, B., 2019. PFAS TOP Assay Interlaboratory Study Supporting Analytical Laboratories 557–558.
- Janda, J., N dler, K., Scheurer, M., Happel, O., N urenberg, G., Zwiener, C., Lange, F.T., 2019. Closing the gap-inclusion of ultrashort-chain perfluoroalkyl carboxylic acids in the total oxidizable precursor (TOP) assay protocol. *Environ Sci Process Impacts* 21, 1926–1935. <https://doi.org/10.1039/c9em00169g>
- Kaiser, A.M., Saracevic, E., Schaar, H.P., Weiss, S., Hornek-Gausterer, R., 2021. Ozone as oxidizing agent for the total oxidizable precursor (TOP) assay and as a preceding step for activated carbon treatments concerning per- and polyfluoroalkyl substance removal. *J Environ Manage* 300, 113692. <https://doi.org/10.1016/j.jenvman.2021.113692>
- Koda, E., Miskowska, A., Siczka, A., 2017. Levels of organic pollution indicators in groundwater at the old landfill and waste management site. *Applied Sciences (Switzerland)* 7. <https://doi.org/10.3390/app7060638>

- Kotthoff, M., Müller, J., Jüriling, H., Schlummer, M., Fiedler, D., 2015. Perfluoroalkyl and polyfluoroalkyl substances in consumer products. *Environmental Science and Pollution Research* 22, 14546–14559. <https://doi.org/10.1007/s11356-015-4202-7>
- Liagkouridis, I., Awad, R., Schellenberger, S., Plassmann, M.M., Cousins, I.T., Benskin, J.P., 2022. Combined Use of Total Fluorine and Oxidative Fingerprinting for Quantitative Determination of Side-Chain Fluorinated Polymers in Textiles. *Environ Sci Technol Lett* 9, 30–36. <https://doi.org/10.1021/acs.estlett.1c00822>
- Liu, X., Fang, L., Zhou, Y., Zhang, T., Shao, Y., 2013. Comparison of UV/PDS and UV/H₂O₂ processes for the degradation of atenolol in water. *J Environ Sci (China)* 25, 1519–1528. [https://doi.org/10.1016/S1001-0742\(12\)60289-7](https://doi.org/10.1016/S1001-0742(12)60289-7)
- Luo, Y.S., Aly, N.A., McCord, J., Strynar, M.J., Chiu, W.A., Dodds, J.N., Baker, E.S., Rusyn, I., 2020. Rapid Characterization of Emerging Per- And Polyfluoroalkyl Substances in Aqueous Film-Forming Foams Using Ion Mobility Spectrometry-Mass Spectrometry. *Environ Sci Technol* 54, 15024–15034. <https://doi.org/10.1021/acs.est.0c04798>
- Lyon, S.W., Grabs, T., Laudon, H., Bishop, K.H., Seibert, J., 2011. Variability of groundwater levels and total organic carbon in the riparian zone of a boreal catchment. *J Geophys Res Biogeosci* 116. <https://doi.org/10.1029/2010JG001452>
- Makhatova, A., Mazhit, B., Sarbassov, Y., Meiramkulova, K., Inglezakis, V.J., Pouloupoulos, S.G., 2020. Effective photochemical treatment of a municipal solid waste landfill leachate. *PLoS One* 15. <https://doi.org/10.1371/journal.pone.0239433>
- Martin, D., Munoz, G., Mejia-Avenida, S., Duy, S.V., Yao, Y., Volchek, K., Brown, C.E., Liu, J., Sauv e, S., 2019. Zwitterionic, cationic, and anionic perfluoroalkyl and polyfluoroalkyl substances integrated into total oxidizable precursor assay of contaminated groundwater. *Talanta* 195, 533–542. <https://doi.org/10.1016/j.talanta.2018.11.093>
- Molot, L.A., Hudson, J.J., Dillon, P.J., Miller, S.A., 2005. Effect of pH on photo-oxidation of dissolved organic carbon by hydroxyl radicals in a coloured, softwater stream. *Aquat Sci* 67, 189–195. <https://doi.org/10.1007/s00027-005-0754-9>
- Morgan, M.S., Van Trieste, P.F., Garlick, S.M., Mahon, M.J., Smith, A.L., 1988. Ultraviolet molar absorptivities of aqueous hydrogen peroxide and hydroperoxyl ion. *Anal Chim Acta* 215, 325–329. [https://doi.org/10.1016/S0003-2670\(00\)85294-0](https://doi.org/10.1016/S0003-2670(00)85294-0)
- Nakabayashi, Y., Nosaka, Y., 2015. The pH dependence of OH radical formation in photo-electrochemical water oxidation with rutile TiO₂ single crystals. *Physical Chemistry Chemical Physics* 17, 30570–30576. <https://doi.org/10.1039/c5cp04531b>
- Nolan, A., Grimison, C., Iavetz, R., Slee, D., Lim, C., 2019. Improving Measurement Reliability of the PFAS TOP Assay 559–560.
- O’Connor, N., Patch, D., Noble, D., Scott, J., Koch, I., Mumford, K.G., Weber, K., 2023. Forever no more : Complete mineralization of per - and poly fl uoroalkyl substances (PFAS) using an optimized UV / sulfite / iodide system. *Science of the Total Environment* 888, 164137. <https://doi.org/10.1016/j.scitotenv.2023.164137>
- Patch, D., O’Connor, N., Koch, I., Cresswell, T., Hughes, C., Davies, J.B., Scott, J., O’Carroll, D., Weber, K., 2022. Elucidating degradation mechanisms for a range of per- and polyfluoroalkyl substances (PFAS) via controlled irradiation studies. *Science of the Total Environment* 832, 154941. <https://doi.org/10.1016/j.scitotenv.2022.154941>

- Patch, D., O'Connor, N., Vereecken, T., Murphy, D., Munoz, G., Ross, I., Glover, C., Scott, J., Koch, I., Sauvé, S., Liu, J., Weber, K., 2024. Advancing PFAS characterization: Enhancing the total oxidizable precursor assay with improved sample processing and UV activation. *Science of The Total Environment* 909, 168145. <https://doi.org/10.1016/j.scitotenv.2023.168145>
- Singh, R.K., Fernando, S., Baygi, S.F., Multari, N., Thagard, S.M., Holsen, T.M., 2019. Breakdown Products from Perfluorinated Alkyl Substances (PFAS) Degradation in a Plasma-Based Water Treatment Process. *Environ Sci Technol* 53, 2731–2738. <https://doi.org/10.1021/acs.est.8b07031>
- Steffens, S.D., Cook, E.K., Sedlak, D.L., Alvarez-Cohen, L., 2021. Under-reporting Potential of Perfluorooctanesulfonic Acid (PFOS) under High-Ionic Strength Conditions. *Environ Sci Technol Lett* 8, 1032–1037. <https://doi.org/10.1021/acs.estlett.1c00762>
- Tsou, K., Antell, E., Duan, Y., Olivares, C.I., Yi, S., Alvarez-Cohen, L., Sedlak, D.L., 2023. Improved Total Oxidizable Precursor Assay for Quantifying Polyfluorinated Compounds Amenable to Oxidative Conversion to Perfluoroalkyl Carboxylic Acids. *ACS ES and T Water*. <https://doi.org/10.1021/acsestwater.3c00224>
- Turner, L.P., Kueper, B.H., Jaansalu, K.M., Patch, D.J., Battye, N., El-Sharnouby, O., Mumford, K.G., Weber, K.P., 2021. Mechanochemical remediation of perfluorooctanesulfonic acid (PFOS) and perfluorooctanoic acid (PFOA) amended sand and aqueous film-forming foam (AFFF) impacted soil by planetary ball milling. *Science of the Total Environment* 765, 142722. <https://doi.org/10.1016/j.scitotenv.2020.142722>
- Wang, Z., Buser, A.M., Cousins, I.T., Demattio, S., Drost, W., Johansson, O., Ohno, K., Patlewicz, G., Richard, A.M., Walker, G.W., White, G.S., Leinala, E., 2021. A New OECD Definition for Per- And Polyfluoroalkyl Substances. *Environ Sci Technol* 55, 15575–15578. <https://doi.org/10.1021/acs.est.1c06896>
- Xia, C., Diamond, M.L., Peaslee, G.F., Peng, H., Blum, A., Wang, Z., Shalin, A., Whitehead, H.D., Green, M., Schwartz-Narbonne, H., Yang, D., Venier, M., 2022. Per- and Polyfluoroalkyl Substances in North American School Uniforms. *Environ Sci Technol* 56, 13845–13857. <https://doi.org/10.1021/acs.est.2c02111>
- Yin, R., Anderson, C.E., Zhao, J., Boehm, A.B., Mitch, W.A., 2023. Controlling contaminants using a far-UVC-based advanced oxidation process for potable reuse. *Nature Water* 1, 555–562. <https://doi.org/10.1038/s44221-023-00094-5>
- Zhao, S., Ma, H., Wang, M., Cao, C., Yao, S., 2013. Study on the role of hydroperoxyl radical in degradation of p-nitrophenol attacked by hydroxyl radical using photolytical technique. *J Photochem Photobiol A Chem* 259, 17–24. <https://doi.org/10.1016/j.jphotochem.2013.02.012>
- Zhu, H., Kannan, K., 2020. Total oxidizable precursor assay in the determination of perfluoroalkyl acids in textiles collected from the United States. *Environmental Pollution* 265, 114940. <https://doi.org/10.1016/j.envpol.2020.114940>

6. Shining a Light on Hidden PFAS: Development of a UV-Reducible Organic Fluorine Assay and Tandem UV-H₂O₂-TOP-ROF Assay for Enhanced Analysis of PFAS.

David Patch†, Natalia O'Connor†, Ellie Ahmed†, Erika Houtz**, Michael Bentel, Ian Ross††, Jennifer Scott†, Iris Koch†, Kela Weber†*

† Environmental Sciences Group, Department of Chemistry and Chemical Engineering, Royal Military College of Canada, Kingston, ON, Canada K7K 7B4.

†† Department of Chemical and Environmental Engineering, University of Cincinnati.

††† ECT2, 125 Industrial Way, Portland, ME 04103

†††† CDM Smith, 75 State St #701, Boston, MA 02109

* Corresponding Author:

Email: Kela.Weber@rmc.ca

Phone: 613-541-6000 ext. 3633

The authors declare no competing financial interest.

6.1. Introduction

Current analytical methodologies for analyzing PFAS rely on the use of liquid chromatography (LC) tandem mass spectrometers, including triple quadrupole mass spectrometry (LC-MS/MS), time-of-flight mass spectrometry (LC-ToF-MS) and ion trap (orbitrap) high resolution mass spectrometry (LC-HRMS) (Rehman et al., 2023). Several newer methodologies have been developed to improve PFAS characterization, including fluorine inductively coupled plasma mass spectrometry (F-ICP-MS), fluorine-nuclear magnetic resonance imaging spectroscopy (^{19}F -NMR), and combustion ion chromatography (CIC) (Heuckeroth et al., 2021; Lewis et al., 2023; McDonough et al., 2019). These methods have varying tradeoffs in robustness, selectivity, and sensitivity, and in many cases, allow for semi-quantitation of potential ‘non-target’ PFAS either as individual compounds or as surrogate fluorine measurements, but require considerable resource investment and highly trained personnel (McDonough et al., 2019). This resource and experiential requirement can present a hurdle for smaller/newer research groups or industry groups while also substantially limiting the ability to analyze PFAS outside of a standard analytical laboratory environment. Furthermore, as the number of detected PFAS continues to outpace commercially available reference materials, there exists a need for the development of low-cost, portable, and easy-to-use chemical assays capable of either augmenting existing analytical methods or standing alone as their own (indirect) PFAS analytical instruments. The rapid growth of PFAS remediation research lends itself to modification into PFAS analytical methods.

Houtz and Sedlak (2012) adapted a conventional remediation method, in-situ chemical oxidation, into an innovative analytical assay that is performed in the laboratory to oxidatively convert PFAA precursors into terminal PFCA products. This total oxidizable precursor (TOP) assay employed potassium persulfate under heated (85°C) and highly alkaline ($\text{pH} > 13$) conditions to generate sulfate radicals, which in turn are converted into hydroxyl radicals, which break down C-H bonds through hydrogen radical abstraction, eventually resulting in oxidation of the non-fluorinated C-C bonds to fully fluorinated alkyl products (typically PFCAs). Since its development, various modifications have been explored including increased reagent concentrations, multiple oxidation cycles, the use of different activators, the use of different persulfate salts, and the use of hydrogen peroxide as an oxidative pre-treatment for overcoming high organic matter concentrations (Al Amin et al., 2021; Casson and Chiang, 2018; Dai et al., 2019; Eriksson et al., 2022; Iavetz et al.,

2019; Janda et al., 2019; Kaiser et al., 2021; Martin et al., 2019; Nolan et al., 2019; Zhu and Kannan, 2020).

To further complement PFAS analysis, many groups employ a total organic fluorine determination which utilizes PFAS destruction technology (e.g. combustion) to convert PFAS to free fluoride, which is then measured to determine the total amount of organic fluorine present in the sample. While methods like combustion ion chromatography are effective, they require expensive infrastructure and can struggle with larger sample sizes. To address this issue, other PFAS destruction technologies can be investigated to achieve complete PFAS mineralization. Several authors have highlighted the susceptibility of PFAS to degradation using reductive technologies generating aqueous electrons (Abusallout et al., 2021; Bentel et al., 2020, 2019; Liu et al., 2021; Patch et al., 2022; Tenorio et al., 2020; Trojanowicz et al., 2020, 2019, 2018). Bentel et al. (2019) demonstrated significant defluorination of PFCAs using UV-activated sulfite but encountered challenges with more resistant PFASs. O'Connor et al. (2023) further explored sulfite, iodide, and/or phenol for PFAS destruction, confirming sulfite and iodide's effectiveness together, achieving ~80% defluorination of PFBS (O'Connor et al., 2023). Through optimization experiments, O'Connor et al. (2023) demonstrated complete defluorination of PFAS, including PFBS, in deionized water by increasing sulfite and iodide concentrations, with a protocol achieving >99.99% defluorination of PFBS within eight hours. This method's ability to achieve complete defluorination within a short timeframe suggests its potential for adaptation into a low-cost, user-friendly analytical chemical assay for determining total organic fluorine load by measuring post-reductive destruction free fluoride concentration.

The present study sought to develop an integrated, UV-activated analytical methodology that exploits both oxidative and reductive technologies to achieve complete characterization of PFAS present within a sample. To this end, this manuscript focuses on three main objectives: 1) the development of a modified UV-activated sulfite/iodide system (UV/S+I) to defluorinate the PFAS present in the sample which, after measurement with a fluoride-ion selective electrode, is used to determine the concentration of reducible organic fluorine (UV-ROF) measure of total organic fluorine; 2) the integration of the UV-ROF assay after the UV-H₂O₂ and UV-H₂O₂-TOP assays; and 3) the application of the tandem UV-H₂O₂-TOP-ROF assay to a selection of PFAS-containing samples. The samples analyzed in the third objective include liquid matrices, such as AFFFs; a distilled regenerable ion exchange solution (“still bottoms”) from an AFFF-impacted groundwater

treatment system that contained very high levels of PFAS; and water containing organic matter and inorganic ions. The method will also be used to analyze the two solid matrices soils and AFFF-containing swabs, and commercial products consisting of cosmetics, textiles, and a surface treatment spray.

6.2. *Materials and Methods*

6.2.1. *Reagents and Materials*

6:2 fluorotelomer sulfonate (FTS) was purchased as a powder from Synquest Labs (>97% purity) and used to prepare high concentration stock solutions by dissolving the powder in MilliQ® deionized water. Analytical PFAS standards were purchased from Wellington Labs (Guelph, Ontario) and diluted with 1:1 water/methanol to different concentrations for calibration purposes. Trifluoroacetic acid (TFA) and perfluoropropanoic acid (PFPrA) was purchased from Sigma Aldrich (97%) for calibration purposes. Potassium persulfate (KPS; ACS grade), sodium persulfate (NaPS), ammonium persulfate (AmmPS) sodium hydroxide (NaOH; ACS grade), UV-transparent cuvettes (BrandTech®), cuvette lids, hydrogen peroxide (H₂O₂; 30%), butyl carbitol (BC), and methanol (ACS grade) were purchased from VWR. LC-MS grade water and acetonitrile were purchased from Canadian Life Sciences. Double deionized (DI) water (18 MΩ•cm) was acquired from an in-house Milli-Q® Direct 8 water purification system.

AFFF, AFFF still bottoms, and AFFF-impacted pipes were acquired from internal inventories or provided under an agreement of confidentiality. Cosmetic makeup products were purchased in 2019 and were previously characterized in the literature (Schultes et al., 2018). The two cosmetic products purchased were Shade Adjusting Drops (The Body Shop) and Fresh Nude Foundation, Bali Vanilla (The Body Shop). The firefighting textile was donated in new, unworn condition, by the Department of National Defence. The commercial textile (Hiasan Rectangle Tablecloth – Stain Resistant Waterproof and Spillproof Washable Table Cloth) and surface spray (Gamer Advantage FogAway Anti Fog Spray) were purchased from Amazon.

6.2.2. *UV-H₂O₂, UV-TOP, and UV-ROF Assays*

For the UV-activated H₂O₂ assay, samples were amended with H₂O₂ (100 mM or 500 mM, unless otherwise stated), sub-sampled into UV-transmissible cuvettes, and subjected to UV-activation for up to 22 hours (254 nm, 36 watt lamp, ~2.6 J s⁻¹ L⁻¹ of photon irradiance, described in (Patch et al., 2024). For the UV-activated TOP assay, samples were amended with 60 mM KPS or NaPS and

150 mM NaOH (unless otherwise stated), sub-sampled into UV-transmissible cuvettes, and subjected to UV-activation for at least 4 hours, up to 22 hours (experiment dependent) (Patch et al., 2024). For the UV-activated ROF assay, samples were amended with 50 mM sodium sulfite, 10 mM potassium iodide, 10 mM sodium bicarbonate, and 150 mM NaOH before being sub-sampled into UV-transmissible cuvettes and subjected to UV-activation for at least 4 hours (O'Connor et al., 2023).

For application of the UV-H₂O₂-TOP-ROF assay to the AFFFs, AFFF still bottoms, and solid samples, special QA/QC protocols were taken. Samples were prepared in batches of 24 samples, consisting of six samples prepared in triplicate (18 total), PFAS-spiked blanks (2 total), fluoride-spiked blanks (2 total), and unspiked method blanks (2 total). The third replicate of each sample was amended with native 6:2 FTS, PFOS, and PFOA to evaluate oxidation/reduction completion and act as an internal standard to measure recovery. 6:2 FTS, PFOS, and PFOA were used instead of mass labelled surrogates to enable the use of higher internal standard concentrations. Overall recovery of both PFAS and fluoride in spiked blanks and spiked samples were found to be between 70-110%. No corrections were made based on PFAS or fluoride recovery. In scenarios in which PFAS and/or fluoride recoveries were below 70%, those samples were re-prepared from the beginning with slight method modification(s), including a higher initial sample dilution, a higher dose of persulfate/hydroxide, or a longer duration of activation time.

6.2.3. Initial Method Development and Evaluation

For a summarized list of experiments performed, please see Table 6.1. For a complete description of experiments, please see the Supporting Information (SI).

Table 6.1 – Summarized method development, validation, and implementation employed across this study. (LC-MS/MS = liquid chromatography mass tandem mass spectrometry. GC-MS= gas chromatography mass spectrometry. TOC = Total organic carbon determination. Iodo determ = iodometric colorimetric determination of H₂O₂. F-ISE = fluoride-ion selective electrode). For assays including multiple steps, time is indicated for each step with / (e.g. UV-H₂O₂-TOP would be the UV-H₂O₂ assay for 22 hours, followed by the UV-TOP assay for four hours).

	Experiment Objective	Specific Variable	Sample Type	Assay Type	Assay Time (Hours)	Analysis	Figure(s)
Method Development	Initial Evaluation	AFFF (20,000 - 10x Dilution)	N. Foam - PFCA	ROF	8	F-ISE, LC-MS/MS	1
	UV-H ₂ O ₂ -ROF Integration	Sample Dilution	N. Foam - PFCA	UV-H ₂ O ₂ -ROF	22/4	F-ISE, LC-MS/MS	1
	UV-H ₂ O ₂ -TOP-ROF Integration	Sample Dilution, UV, Heat	6:2 FTS (4 µM)	UV-H ₂ O ₂ -TOP-ROF	22/4/4	F-ISE	1
Implementation	Application	AFFFs	Fifteen AFFF formulations	H ₂ O ₂ -TOP-ROF	22/12/4	F-ISE, LC-MS/MS	2
	Application	AFFF Still Bottoms	One AFFF Still Bottom sample	UV-H ₂ O ₂ -TOP-ROF	22/12/4	LC-MS/MS, F-ISE	3
	Application	Various Samples	Soils, cosmetics, textiles, pipe swabs, surface sprays	UV-H ₂ O ₂ -TOP-ROF, dTOP-UV-ROF	22/12/4 22/4	LC-MS/MS, F-ISE	3

6.2.4. PFAS Analysis

Detailed information on the analytical methodology employed in this study can be found in the SI (Appendix D) and in several previous works (O'Connor et al., 2023; Patch et al., 2022; Turner et al., 2021). Samples were directly analyzed using an expanded target analytical suite (Table C1) on an Agilent 6460 LC-MS/MS and a ThermoFisher Orbitrap Exploris 120 LC-HRMS. Analysis of TFA and PFPrA was exclusive to the Agilent 6460 LC-MS/MS. Samples suspected to contain AFFF PFAA precursors (e.g. AFFF, AFFF-impacted materials) were semi-quantified exclusively on the ThermoFisher Orbitrap Exploris 120 using suspect screening databases previously built for AFFFs and PFAS degradation products (O'Connor et al., 2023; Patch et al., 2024). Inter-instrument variability for these instruments was evaluated in previous work and found to be less than 20% including error (Patch et al. 2024). Inter-instrument variability was monitored throughout this study and was found to agree with previous work (Patch et al. 2024) and be less than 20%. In scenarios

where the deviation on PFAS concentrations between instruments was found to exceed 20%, both samples and calibration standards were re-prepared and re-analyzed.

6.2.5. Fluoride Analysis

Aqueous samples after application of the UV-ROF assay were analyzed for total free fluoride concentration using a fluoride ion-selective electrode (Fisher Scientific Accumet Fluoride Electrode) coupled to a pH/ISE meter (Mettler Toledo). To this end, 0.5 mL of sample was neutralized with 0.05 mL of 10% acetic acid and diluted with 0.5 mL of total ionic strength adjustment buffer (TISAB, Fisher Scientific). Fluoride probe measurements were quantified using a six-point external calibration curve prepared using a standardized fluoride calibration solution (10 ± 0.2 mg/L, Fisher Scientific) from 0.05 mg/L to 5 mg/L. Fluoride-amended samples carried through the UV-ROF assay were found to have a recovery of 70-110%. Free fluoride concentrations, in mg/L, were converted into the equivalent millimolar (mM) or micromolar (μ M) concentrations for comparison to organic fluorine concentrations determined by target LC-MS analysis pre- and post-TOP assay application.

6.3. Results and Discussion

6.3.1. Development of UV-ROF, UV-H₂O₂-ROF, and UV-H₂O₂-TOP-ROF Assays

Work by previous authors have identified the effectiveness of the UV/S+I technology in achieving near complete defluorination of PFAS in a short (<8 hour) timespan (O'Connor et al., 2023). The initial focus of the present study was to investigate the application of the UV/S+I technology as an analytical methodology to determine the total amount of ROF. To this end, the UV-ROF assay was applied directly, and after a UV-H₂O₂ pre-treatment, to a PFCA-dominant AFFF (Figure 6.1A, B). The UV-ROF assay was then applied to 6:2 FTS following application of the UV-H₂O₂-TOP assay (Figure 6.1C).

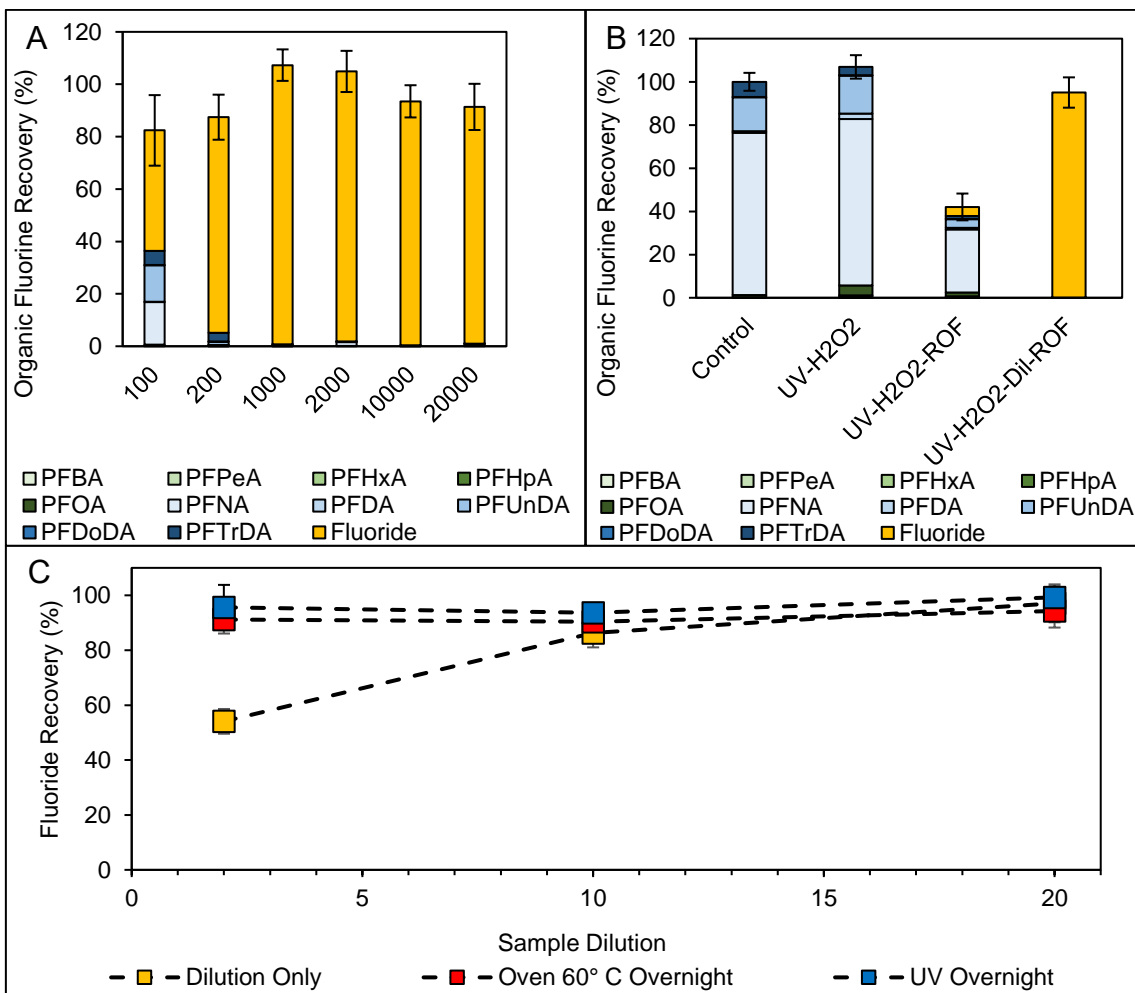


Figure 6.1 – UV-ROF assay applied to different dilutions of N. Foam-PFCA AFFF directly (A), after UV-H₂O₂ pre-treatment (B) or to 10 μM 6:2 FTS after UV-H₂O₂-TOP (C). *UV-ROF conditions:* 50 mM Na₂SO₃, 10 mM KI, 10 mM NaHCO₃, 150 mM NaOH for 4 h; *UV-H₂O₂ conditions:* 500 mM H₂O₂ for 22 hours; *UV-H₂O₂-TOP conditions:* 500 mM H₂O₂ for 22 hours, then 60 mM NaPS, 150 mM NaOH for 4 hours.

Initial application of the UV-ROF assay to the PFCA-dominant AFFF found that total PFAS mineralization was dependent on the extent of sample dilution, with 46±9% defluorination at 100x dilution, and 107±6% defluorination at 1000x dilution. This aligns with previous studies that have applied the UV/S or UV/S+I technologies to dilute AFFFs, where dilutions of up to 60,000x were required to achieve high levels of PFAS destruction (Tenorio et al., 2020). The incomplete defluorination of PFAS at lower dilutions (e.g. 100x) could be due to scavenging of generated aqueous electrons by common AFFF components, such as glycols, alcohols, non-fluorinated surfactants, or inorganic salts (Harding-Marjanovic et al., 2015). It was hypothesized that

implementing the UV-ROF assay after the UV-H₂O₂ or UV-H₂O₂-TOP assays may be beneficial in oxidatively removing organic matter or other potentially interfering species, if the issue of residual oxidants interfering with the UV-ROF assay could be resolved (Figure 6.1B, C).

As identified with both the PFCA-dominant AFFF and 6:2 FTS, direct application of the UV-ROF assay after the UV-H₂O₂ and UV-H₂O₂-TOP assays resulted in incomplete PFAS mineralization, hypothesized to be due to residual oxidants left in the system. Sample dilution proved to be an effective post-oxidation modification to improve fluoride recovery, as can be seen with a fluoride recovery of 95±7% for the PFCA-AFFF (Figure 6.1B, UV-H₂O₂-Dil-ROF) and a fluoride recovery of 97±7% for the 20x dilution of 6:2 FTS (Figure 6.1C, Dilution only 20x). To avoid the loss of sensitivity associated with sample dilution, the input of additional energy in the form of heat (oven, 60°C overnight) or UV light (UV overnight) was investigated to identify if the residual oxidant could be exhausted. In both cases, application of either heat or UV light resulted in near-complete fluoride recovery (Figure 1C, 91±5% for heat at 2x dilution, 96±8% for UV at 2x dilution). The success in achieving near-complete recovery of fluoride following the application of the UV-H₂O₂-TOP-ROF assay to 6:2 FTS provides good support for its application to AFFFs.

6.3.2. UV-H₂O₂-TOP-ROF Assay Evaluation for AFFFs

Following successful development of the UV-ROF assay, and its integration with the UV-H₂O₂ and UV-H₂O₂-TOP assays, the next step was to evaluate its application to a wide range of AFFF formulations. To this end, five AFFFs (NF-82-PFCA, 3M-80-PFSA, NF-90-FtSaB, Ansul-12-FtB, Solberg-FtSaB-FtTAoS) previously characterized using UV-TOP only (Patch et al., 2024) and ten uncharacterized AFFFs were diluted 1000x with DI water and subjected to the UV-H₂O₂-TOP assay, using sodium persulfate (NaPS) in replacement of potassium persulfate (KPS) (Figure D6). Previous work (Tsou et al., 2023) has identified the thermal-activated TOP assay requires a minimum of 12 hours to achieve complete oxidation, so both assays were run for this length of time. This 12 hour activation time also has the added advantage of quenching the oxidant for the subsequent UV-ROF assay (Figure 6.2).

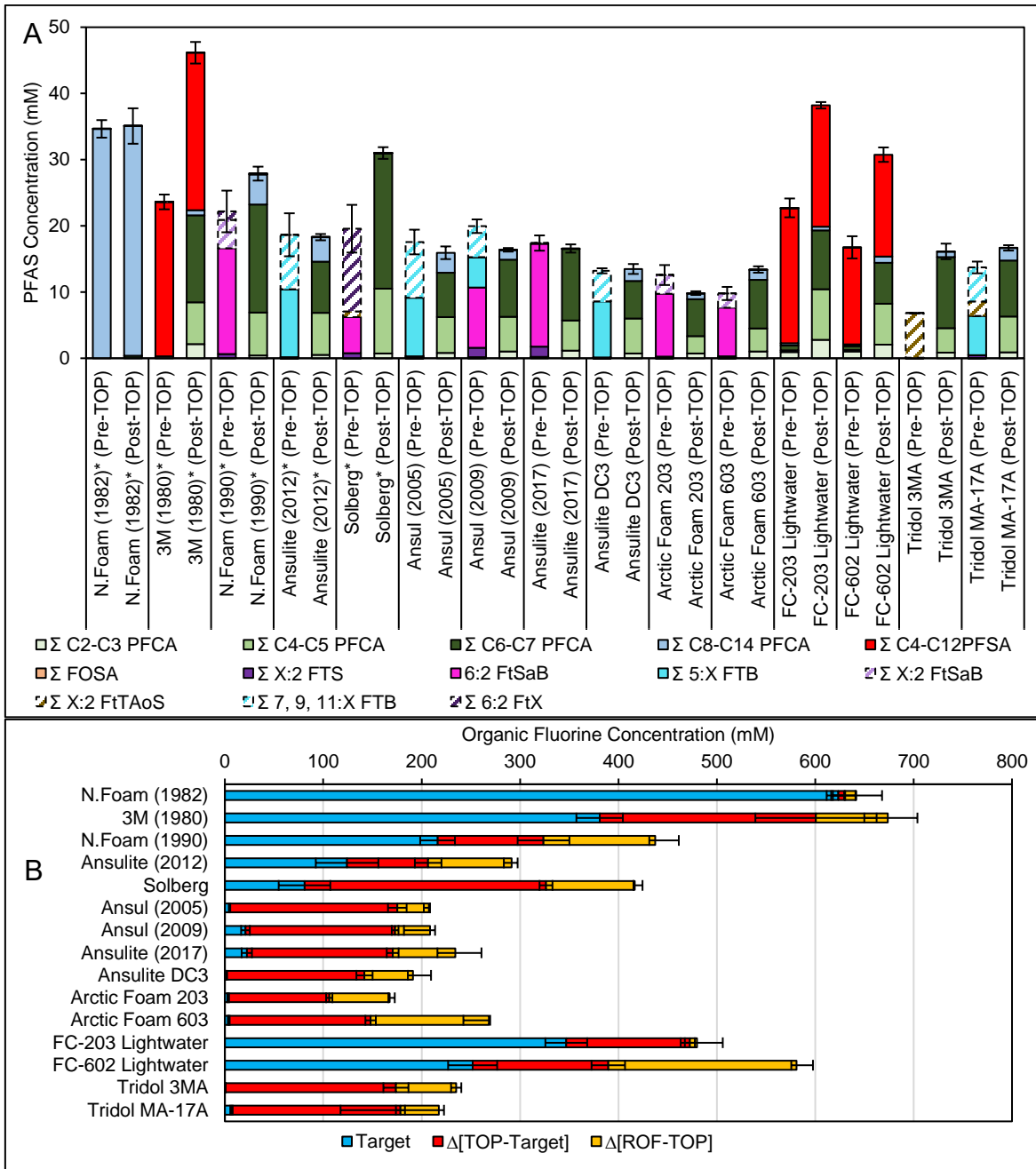


Figure 6.2 – Concentration of PFAS in AFFF formulations evaluated pre-TOP assay and post UV-H₂O₂-TOP assay (100 mM H₂O₂/2h, 60 mM NaPS, 150 mM NaOH 12h), with semi-quantified PFAS in dashed borders with pattern fill (A). Organic fluorine concentrations (mM) calculated from the pre- and post-TOP assay target analysis, and the free fluoride measured after application of the UV-ROF assay. Semi-quantified concentrations excluded the organic fluorine concentrations (B). AFFF with asterisks (*) have also been characterized in previous works (Patch et al. 2024). (ΣFOSA = FOSA, Me-FOSAA, Et-FOSAA; ΣX:2 FTS = 4:2, 6:2, 8:2 FTS; ΣX:2 FtSaB = 8:2 FtSaB, 10:2 FtSaB, semi-quantified using 6:2 FtSaB; ΣX:2 FtTAoS = 6:2, 8:2, semi-quantified using 6:2 FTS; Σ7,9,11:X FTB = 7:3, 7:1:2, 9:3, 9:1:2, 11:3, 11:1:2 FtB, semi-quantified using 5:3 or 5:1:2 FtB).

Targeted and high-resolution analysis of the AFFF samples identified different major PFAS groups present in different samples, including PFCAs (N. Foam 1980), PFSAs (3M 1980, FC-203 Lightwater, FC-206 Lightwater), FtBs (Ansolite 2012, Ansul 2005, Ansul 2009, Ansolite DC3, Tridol MA-17A), FtSaBs (N. Foam 1990, Solberg, Ansul 2009, Ansolite 2017, Arctic Foam 203, Arctic Foam 603), and FtTAoSs (Solberg, Tridol 3MA, Tridol MA-17A). The Solberg AFFF formulation was also found to contain significant concentrations of 6:2 fluorotelomer sulfonamido propyl methyl hydroxymethyl ammonium (6:2 FTtSaPrMeOHMeAN) (Luo et al., 2020).

Application of the UV-H₂O₂-TOP assay resulted in up to a 2.6-fold increase in total PFAS concentration in the AFFF formulations compared to pre-TOP assay concentrations. The N. Foam 1982, Ansul 2009, Ansolite 2017, and Arctic Foam 203 AFFF formulations had very little increase in the total concentration of PFAS post-oxidation, due to those AFFF samples being well characterized by either the targeted (N. Foam 1982) or expanded analytical suite, which includes TFA, PFPrA, 6:2 FtSaB, 5:3 FtB, and 5:1:2 FtB. This reinforces the need to expand targeted analytical methods to include increasingly prevalent PFAA precursors like 6:2 FtSaB and 5:3 FtB, as current analytical targeted suites are becoming increasingly irrelevant with increasingly complex AFFF chemistry.

Application of the UV-ROF assay was found to well characterize the total organofluorine concentration present in all the AFFFs, with the proportion of additional fluoride revealed by the UV-ROF assay being dependent on whether the AFFF formulation is ECF-derived or fluorotelomer (FT)-derived. In ECF-derived (legacy) AFFF formulations, reducible organofluorine concentrations were found to be 6±6% higher than those determined by the TOP assay, whereas in FT-derived (modern) AFFF formulations, reducible organofluorine concentrations were found to be 40±10% higher. This higher organofluorine concentration in the FT-derived AFFF formulations is likely a combination of free fluoride generated during oxidation of the PFAA precursors (e.g. conversion of 6:2 FTS to PFHxA results in a loss of two fluorine atoms) and organofluorine compounds not characterized by the TOP assay.

These results provide strong evidence of the effectiveness of the tandem UV-H₂O₂-TOP-ROF assay for characterizing complex samples containing high concentrations of PFAS. One of the advantages of working with AFFFs is the ability (need) to dilute the samples significantly, thereby reducing the matrix complexity. For this method to be widely applicable, it is important to apply it to other less concentrated sample types, with further modifications being made where appropriate.

6.3.3. *UV-H₂O₂-TOP-ROF Assay Application to Other Matrices*

The initial success of the UV-H₂O₂-TOP-ROF assay for characterizing AFFF represents an ideal scenario where the initial PFAS concentration is high enough that an initial sample dilution can be used to significantly reduce the complexity of the sample. In scenarios where this is not the case, method modification and additional checks may be required to characterize the PFAS. The UV-H₂O₂-TOP-ROF was applied to a wide range of additional matrices including an AFFF-impacted soil (AFFF Soil), soil taken from a fluoropolymer manufacturing site (Industry Soil), a complex sample consisting of an ion exchange regenerant still bottoms from a site treating AFFF-impacted groundwater (AFFF Still Bottoms) two cosmetic foundations (Makeup 1, Makeup 2), two types of textiles, swabs from two different AFFF-impacted pipes, and a surface waterproofing spray (Figure 6.3A, B). The solid samples (soils, makeups, textiles) were also characterized using the direct TOP assay (dTOP), followed by the UV-ROF assay (dTOP-UV-ROF) (Figure 6.3C, D).

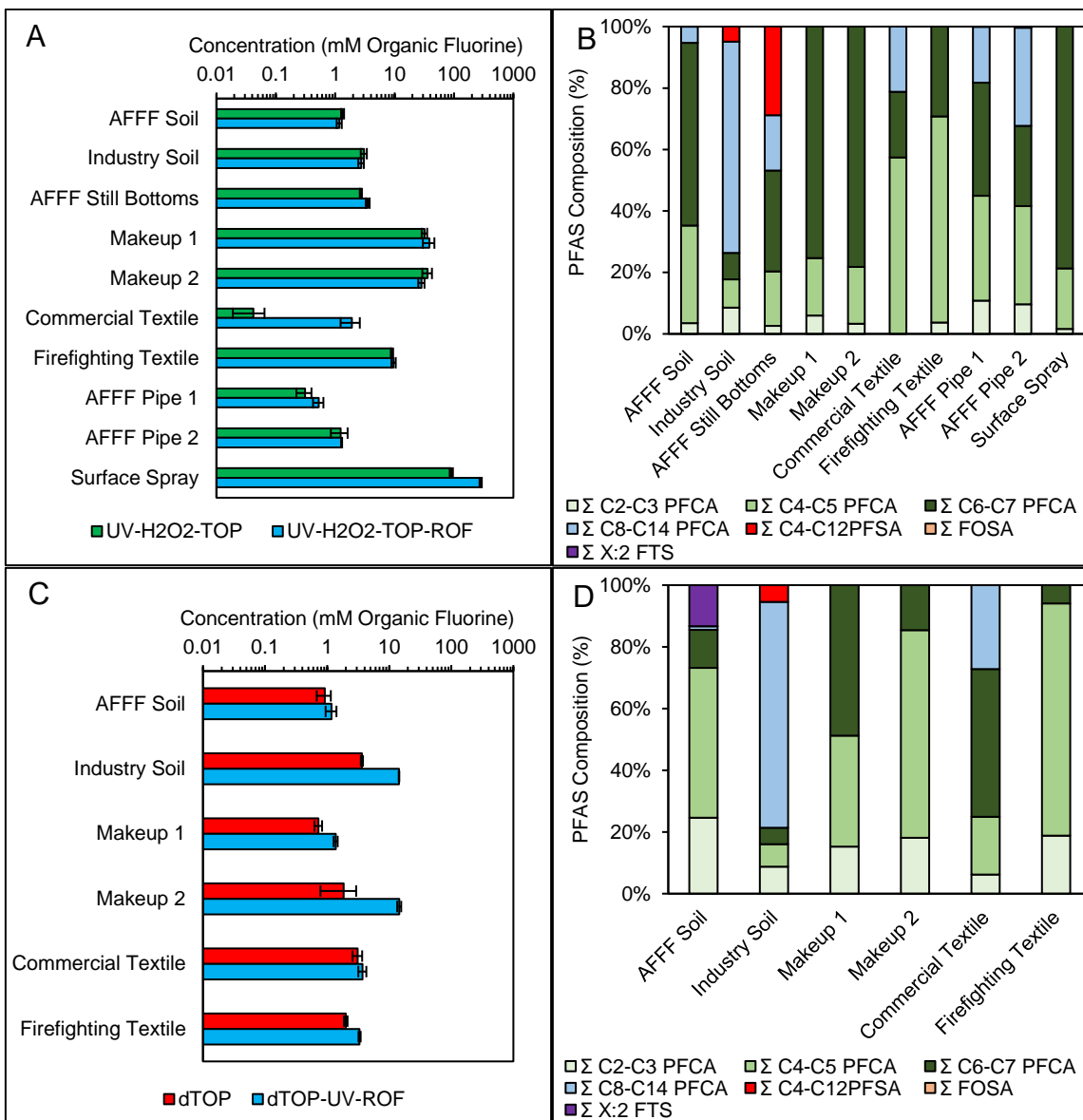


Figure 6.3 – Concentration (A) and relative composition (B) of organic fluorine evaluated after UV-H₂O₂-TOP-ROF assay, compared to concentration (C) and relative composition (D) of organic fluorine evaluated after the dTOP-ROF assay. *UV-H₂O₂-TOP conditions:* 500 mM H₂O₂ for 22 hours, then 60 mM NaPS, 150 mM NaOH for 4 hours; *UV-ROF conditions:* 50 mM Na₂SO₃, 10 mM KI, 10 mM NaHCO₃, 150 mM NaOH for 4 h; *dTOP conditions:* 200 mM NaPS, 500 mM NaOH for 24 hours. Relative standard deviation of organic fluorine concentrations ranges from 2-55% (15% average).

Initial characterization of either H₂O-diluted samples (AFFF still bottoms, surface spray) or methanolic sample extracts revealed different PFAS families, including various saturated and unsaturated PFCAs and PFSA (Industry Soil, AFFF Still Bottoms), FtBs and FtSaBs (AFFF Soil,

AFFF Pipe 1, AFFF Pipe 2), and fluorotelomer phosphate diesters (Makeup 1, Makeup 2, Figure G2). Analysis of the methanolic textile extracts or the surface spray revealed no PFAS present, which was expected based on the suspected PFAS source being side-chain fluoropolymers or fluorotelomer alcohols/methacrylates, respectively. The AFFF still bottoms solution was the most complex sample in terms of PFAS composition, with high resolution analysis revealing an isomeric mix of C₄-C₈ PFCAs, PFSA_s, unsaturated PFOS, and linear 6:2 FTS (Figure D12). The anti-fog surface spray was the most complex sample in terms of PFAS and organic matter concentration, as it contained the highest concentration of PFAS (280 mM organic fluorine) and was found to consist mainly of 6:2 FTOH, butyl carbitol, and 1-butoxy-2-propanol (Figure G1).

Application of the UV-H₂O₂-TOP assay to either methanolic extracts (soils, AFFF pipes), alkaline hydrolysis extracts (makeups, textiles), or DI water dilutions of the liquids (AFFF still bottoms, surface spray) identified significant concentrations of organic fluorine (0.04-90 mM of organic fluorine) (Figure 6.4A). The fluorinated chain length(s) of the PFAA precursors can be derived by considering the PFCA composition in the post-oxidation samples. The two makeup samples and the surface spray contain ≤C₆ PFAA precursors, as indicated by only PFHpA and shorter PFCAs being identified. The AFFF-impacted soil likewise contains mainly ≤C₆ PFAA precursors, but smaller amounts of longer-chain PFAA precursors are also present given the identification of C₈-C₁₄ PFCAs. Similar conclusions can be made when examining the post-oxidation PFCA composition in the dTOP samples, although accurate evaluation is difficult as some PFAA precursors (e.g. 6:2 FTS) were identified post-oxidation, indicating their incomplete conversion to PFCAs (Figure 6.4D).

While both the application of the UV-H₂O₂-TOP-ROF assay and dTOP-ROF assay were effective in identifying the presence and composition of PFAS present in samples, it can be seen that different matrices were characterized more effectively by each method. The UV-H₂O₂-TOP-ROF assay outperformed the dTOP-ROF assay when applied to the makeup samples and the firefighting textile, as can be seen by the higher concentrations of organic fluorine yielded. This is likely due to the presence of dissolved organic carbon that interfered with the dTOP assay, but was likely removed by the UV-H₂O₂ pre-treatment step. The dTOP-ROF assay outperformed the UV-H₂O₂-TOP assay when applied to the industry soil, and the commercial textile. This is likely due to the dTOP assay more effectively converting side-chain fluoropolymers to PFCAs, which were present

on the textiles and possibly present in the Industry Soil (based on soil being taken from a textile manufacturing plant).

Application of the UV-H₂O₂-TOP-ROF assay to the AFFF still bottoms, AFFF pipe swabs and surface spray was effective, revealing concentrations of organic fluorine ranging from 0.5±0.1 mM (AFFF Pipe 1) to 282±12 mM (Surface Spray), with the values determined by the UV-H₂O₂-TOP-ROF assay being either equal to or greater than that determined by the UV-H₂O₂-TOP assay.

Overall, these results show the applicability of the UV-H₂O₂-TOP-ROF assay for the characterization of PFAS present in a variety of aqueous and solid samples, while also identifying the dTOP assay as an effective alternative for oxidation, especially when characterizing side-chain fluoropolymer containing samples like textiles and SFP-impacted materials.

6.3.4. UV-H₂O₂-TOP-ROF Method Analytical Decision Framework

As targetted PFAS analysis has evolved, there is a recognition that analytical methodologies have to maintain a certain level of robustness in the face of increasingly complex sample matrices. However, the degree of robustness should also consider the intensity of the method, ensuring it does not become so laborious or costly so as to prohibit its usage. Since the development of the TOP assay by Houtz and Sedlak in 2012, many studies have sought modifications to improve the robustness, speed, or accuracy of the method. Many of these modifications have culminated in this study, including UV-activation (Fan et al., 2021; Patch et al., 2024), direct quantification of ultra-short chain PFCAs (Janda et al., 2019; Neuwald et al., 2022), H₂O₂ pre-oxidation (Hutchinson et al., 2020), identification of total organic carbon limitations (Tsou et al., 2023), post-oxidation sample processing (Patch et al., 2024), direct quantification of AFFF fluorotelomers (Patch et al., 2024), and the addition of a UV-activated reduction method for the generation of free fluoride, which can be measured as a proxy for the total organic fluorine concentration (Liu et al., 2021; O'Connor et al., 2023). With these modifications in mind, the data collected and presented across this study has been used to establish a methodology decision framework to enable the effective implementation of several assays, including UV-H₂O₂-TOP, UV-H₂O₂-TOP-ROF, and, for textiles dTOP-UV-ROF (Table 2).

Table 6.2 – Developed methodologies for implementation of the UV-H₂O₂-TOP-ROF assay on simple/complex aqueous samples, soils, PFAS-impacted surface swabs, personal care products, and textiles.

		Sample Type					
		Simple Aqueous (e.g. Groundwater)	Complex Aqueous (e.g. AFFF)	Soils	Surface Swabs	Personal Care Products	Textiles
Initial Sample Preparation	Extraction / Preparation	Centrifuge or filter if necessary	Dilute 100x w/ H ₂ O	200 mM NaOH/MeOH, 16 hours.		200 mM NaOH/H ₂ O, 85°C, 16 hours	200 mM NaPS, 500 mM NaOH, 85°, 24 hours
	Screening	LC-MS/MS analysis. Adjust PFAS concentration w/ H ₂ O dilution or SPE/dSPE if necessary.					
Oxidation and Analysis	UV-H ₂ O ₂	50 mM H ₂ O ₂ (>2 hours)	500 mM H ₂ O ₂ (>12 hours)	Evaporate methanol extracts. Neutralize w/ HCl, 500 mM H ₂ O ₂ (>12 hours). Repeat if solution retains color after initial oxidation			N/A
	UV-TOP	20 mM NaPS, 50 mM NaOH, (> 2 hours).	60 mM NaPS, 150 mM NaOH, (> 4 hours). Consider increasing up to 200 mM NaPS, 500 mM NaOH, (> 12 hours) if solution retains color after UV-H ₂ O ₂ application(s)				
	Post-TOP	<ul style="list-style-type: none"> ◆Take sub-sample for UV-ROF analysis ◆Amend with 4% methanolic acetic acid (target MeOH concentration = 25% v:v) ◆If PFAS concentration is low, neutralize w/ acetic acid and clean-up w/ SPE. ◆Analyze w/ LC-MS/MS 					
Reduction and Analysis	UV-ROF	<ul style="list-style-type: none"> ◆Heat sub-sample in UV-cuvette at 60°C overnight to quench residual oxidant ◆Amend w/ 50 mM Na₂SO₃, 10 mM KI, 10 mM NaHCO₃, 150 mM NaOH (4 hours) ◆Neutralize w/ 10% acetic acid, dilute 1:1 w/ TISAB, analyze using F-ISE 					
Data Quality Evaluation		<ul style="list-style-type: none"> ◆ΣPFAS post-TOP ≥ ΣPFAS pre-TOP (molar PFAS units) ◆Fluoride post-ROF ≥ ΣOrganic Fluorine post-TOP (molar fluoride units) ◆PFAS/fluoride recovery in spikes ±30% of theoretical concentration ◆Blanks are non-detect or are used to establish quantification limit 					

For the complete decision-making framework used to build the above methodologies, please see Figure D14. The developed methodologies are modified specifically to six different matrix types and go through four major steps: (1) initial sample preparation and screening, (2) oxidative work-up and analysis, (3) reductive work-up and analysis, and (4) data quality evaluation. Initial sample preparation is either focused on achieving an ideal PFAS concentration (aqueous samples), or extraction of PFAS from the matrix (soils, surface swabs, personal care products, textiles). After samples are extracted, any methanolic sample extracts are evaporated to dryness in UV-transmissible cuvettes. Any highly alkaline samples are neutralized with HCl (pH 5-9). Samples are then subjected to either the 50 mM H₂O₂ assay (for simple/finished aqueous samples) or the

500 mM H₂O₂ assay. Samples are then subjected to either the standard TOP assay (60 mM NaPS, 150 mM NaOH), or the stronger TOP assay (200 mM NaPS, 500 mM NaOH). For samples that are known to be low in dissolved organic matter and PFAS, a weaker TOP assay could be employed (20 mM NaPS, 50 mM NaOH) to effectively complete the PFAS oxidation initiated in the UV-H₂O₂ treatment step. Alternatively, if samples were to be analyzed with as little sample dilution as possible, or there was a desire to avoid salt effects, samples could be analyzed by LC-MS/MS directly after the UV-H₂O₂ assay, with the understanding that fluorotelomer conversion to PFCAs could be as low as 50%. After application of the UV-TOP assay, the methodologies are unified and proceed as described in Table 2.

The above methodologies are supported by the quality control program implemented by the user and evaluated by the analytical laboratory. In this work, two quality control protocols were evaluated, one suited for a research environment, and one suited for a commercial laboratory environment. In both protocols, samples are prepared in replicates, and one of the replicates is spiked with PFAS (native PFAS for the research environment, mass labelled PFAS for the commercial laboratory environment) to track loss over the course of the methods, or changes to the instrument signal during analysis due to matrix effects. In the research environment, samples are spiked with native PFAS to allow for flexibility in spiked PFAS concentration and the selection of appropriate PFAS relevant to the sample. This is also more resource effective, given the cost of native PFAS compounds compared to the mass-labelled counterparts. Several other quality control samples are prepared and evaluated, including PFAS-spiked method blanks, fluoride-spiked replicates, fluoride-spiked blanks, and (if available) appropriate certified reference materials (CRMs) or laboratory reference materials (LRMs).

6.4. Conclusions

This study aimed to develop and optimize a UV-activated tandem analytical assay for the enhanced characterization of PFAS in complex matrices. This work focused on the development of existing UV-activated remediation technology (UV-activated sulfite/iodide) into an analytical tool (UV-ROF), with subsequent development focusing on the ideal quenching protocol required to integrate the UV-ROF assay into the end of the UV-H₂O₂-TOP assay. This work concluded by applying the complete UV-H₂O₂-TOP-ROF assay to a variety of samples, and incorporating the various lessons learned into a decision-making framework, providing end-users of this method with flexibility and

adaptability in the face of ever-increasing analytical requirements for characterizing PFAS concentrations in samples.

6.5. *Acknowledgements*

This work was supported by Natural Sciences and Engineering Research Council (Canada) Discovery grants of Weber and Koch. The authors would like to acknowledge Taylor Vereecken and Anbareen Farooq for their assistance with TOC measurements.

6.6. References

- Abusallout, I., Wang, J., Hanigan, D., 2021. Emerging investigator series: rapid defluorination of 22 per- and polyfluoroalkyl substances in water using sulfite irradiated by medium-pressure UV. *Environ Sci (Camb)* 7, 1552–1562. <https://doi.org/10.1039/d1ew00221j>
- Al Amin, M., Luo, Y., Nolan, A., Robinson, F., Niu, J., Warner, S., Liu, Y., Dharmarajan, R., Mallavarapu, M., Naidu, R., Fang, C., 2021. Total oxidisable precursor assay towards selective detection of PFAS in AFFF. *J Clean Prod* 328, 129568. <https://doi.org/10.1016/j.jclepro.2021.129568>
- Bentel, M.J., Liu, Z., Yu, Y., Gao, J., Men, Y., Liu, J., 2020. Enhanced Degradation of Perfluorocarboxylic Acids (PFCAs) by UV/Sulfite Treatment: Reaction Mechanisms and System Efficiencies at pH 12. *Environ Sci Technol Lett* 7, 351–357. <https://doi.org/10.1021/acs.estlett.0c00236>
- Bentel, M.J., Yu, Y., Xu, L., Li, Z., Wong, B.M., Men, Y., Liu, J., 2019. Defluorination of Per- and Polyfluoroalkyl Substances (PFASs) with Hydrated Electrons: Structural Dependence and Implications to PFAS Remediation and Management. *Environ Sci Technol* 53, 3718–3728. <https://doi.org/10.1021/acs.est.8b06648>
- Casson, R., Chiang, S.Y.D., 2018. Integrating total oxidizable precursor assay data to evaluate fate and transport of PFASs. *Remediation* 28, 71–87. <https://doi.org/10.1002/rem.21551>
- Dai, X., Xie, Z., Dorian, B., Gray, S., Zhang, J., 2019. Comparative study of PFAS treatment by UV, UV/ozone, and fractionations with air and ozonated air. *Environ Sci (Camb)* 5, 1897–1907. <https://doi.org/10.1039/c9ew00701f>
- Di Battista, V., Rowe, R.K., Patch, D., Weber, K., 2020. PFOA and PFOS diffusion through LLDPE and LLDPE coextruded with EVOH at 22 °C, 35 °C, and 50 °C. *Waste Management* 117, 93–103. <https://doi.org/10.1016/j.wasman.2020.07.036>
- Duchesne, A.L., Brown, J.K., Patch, D.J., Major, D., Weber, K.P., Gerhard, J.I., 2020. Remediation of PFAS-Contaminated Soil and Granular Activated Carbon by Smoldering Combustion. *Environ Sci Technol* 54, 12631–12640. <https://doi.org/10.1021/acs.est.0c03058>
- Eriksson, U., Yeung, L.W.Y., Fredriksson, F., Anna, K., 2022. Analysis and characterization of novel fluorinated compounds used in surface treatments products. *Chemosphere* 302. <https://doi.org/10.1016/j.chemosphere.2022.134720>
- Fan, X., Bao, Y., Mumtaz, M., Huang, J., Yu, G., 2021. Determination of total oxidizable precursors in foam surfactants and foam contaminated water based on UV-activated persulfate oxidation. *Science of the Total Environment* 763, 142943. <https://doi.org/10.1016/j.scitotenv.2020.142943>
- Harding-Marjanovic, K.C., Houtz, E.F., Yi, S., Field, J.A., Sedlak, D.L., Alvarez-Cohen, L., 2015. Aerobic Biotransformation of Fluorotelomer Thioether Amido Sulfonate (Lodyne) in AFFF-Amended Microcosms. *Environ Sci Technol* 49, 7666–7674. <https://doi.org/10.1021/acs.est.5b01219>
- Heuckeroth, S., Nxumalo, T.N., Raab, A., Feldmann, J., 2021. Fluorine-Specific Detection Using ICP-MS Helps to Identify PFAS Degradation Products in Nontargeted Analysis. *Anal Chem* 93, 6335–6341. <https://doi.org/10.1021/acs.analchem.1c00031>
- Hutchinson, S., Rieck, T., Wu, X.L., 2020. Advanced PFAS precursor digestion methods for biosolids. *Environmental Chemistry* 17, 558–567. <https://doi.org/10.1071/EN20008>
- Iavetz, R., Lewin, M., Morschel, G., Slee, D., Lim, C., Nolan, A., Grimison, C., Centner, M., Mcgrath, S., Symons, B., 2019. PFAS TOP Assay Interlaboratory Study Supporting Analytical Laboratories 557–558.

- Janda, J., Nödler, K., Scheurer, M., Happel, O., Nürenberg, G., Zwiener, C., Lange, F.T., 2019. Closing the gap-inclusion of ultrashort-chain perfluoroalkyl carboxylic acids in the total oxidizable precursor (TOP) assay protocol. *Environ Sci Process Impacts* 21, 1926–1935. <https://doi.org/10.1039/c9em00169g>
- Kaiser, A.M., Saracevic, E., Schaar, H.P., Weiss, S., Hornek-Gausterer, R., 2021. Ozone as oxidizing agent for the total oxidizable precursor (TOP) assay and as a preceding step for activated carbon treatments concerning per- and polyfluoroalkyl substance removal. *J Environ Manage* 300, 113692. <https://doi.org/10.1016/j.jenvman.2021.113692>
- Lewis, R.E., Huang, C.H., White, J.C., Haynes, C.L., 2023. Using ¹⁹F NMR to Investigate Cationic Carbon Dot Association with Per- and Polyfluoroalkyl Substances (PFAS). *ACS Nanoscience Au* 3, 408–417. <https://doi.org/10.1021/acsnanoscienceau.3c00022>
- Liu, Z., Bentel, M.J., Yu, Y., Ren, C., Gao, J., Pulikkal, V.F., Sun, M., Men, Y., Liu, J., 2021. Near-Quantitative Defluorination of Perfluorinated and Fluorotelomer Carboxylates and Sulfonates with Integrated Oxidation and Reduction. *Environ Sci Technol* 55, 7052–7062. <https://doi.org/10.1021/acs.est.1c00353>
- Luo, Y.S., Aly, N.A., McCord, J., Strynar, M.J., Chiu, W.A., Dodds, J.N., Baker, E.S., Rusyn, I., 2020. Rapid Characterization of Emerging Per- And Polyfluoroalkyl Substances in Aqueous Film-Forming Foams Using Ion Mobility Spectrometry-Mass Spectrometry. *Environ Sci Technol* 54, 15024–15034. <https://doi.org/10.1021/acs.est.0c04798>
- Martin, D., Munoz, G., Mejia-Avendaño, S., Duy, S.V., Yao, Y., Volchek, K., Brown, C.E., Liu, J., Sauvé, S., 2019. Zwitterionic, cationic, and anionic perfluoroalkyl and polyfluoroalkyl substances integrated into total oxidizable precursor assay of contaminated groundwater. *Talanta* 195, 533–542. <https://doi.org/10.1016/j.talanta.2018.11.093>
- McDonough, C.A., Guelfo, J.L., Higgins, C.P., 2019. Measuring total PFASs in water: The tradeoff between selectivity and inclusivity. *Curr Opin Environ Sci Health* 7, 13–18. <https://doi.org/10.1016/j.coesh.2018.08.005>
- Neuwald, I.J., Hu, D., Wiegand, H.L., Valkov, V., Borchers, U., Karsten, N., Scheurer, M., Hale, S.E., Arp, H.P.H., Zahn, D., 2022. Ultra-Short-Chain PFASs in the Sources of German Drinking Water: Prevalent, Overlooked, Difficult to Remove, and Unregulated. <https://doi.org/10.1021/acs.est.1c07949>
- Nolan, A., Grimison, C., Iavetz, R., Slee, D., Lim, C., 2019. Improving Measurement Reliability of the PFAS TOP Assay 559–560.
- O'Connor, N., Patch, D., Noble, D., Scott, J., Koch, I., Mumford, K.G., Weber, K., 2023. Forever no more : Complete mineralization of per - and poly fluoroalkyl substances (PFAS) using an optimized UV / sulfite / iodide system. *Science of the Total Environment* 888, 164137. <https://doi.org/10.1016/j.scitotenv.2023.164137>
- Patch, D., O'Connor, N., Koch, I., Cresswell, T., Hughes, C., Davies, J.B., Scott, J., O'Carroll, D., Weber, K., 2022. Elucidating degradation mechanisms for a range of per- and polyfluoroalkyl substances (PFAS) via controlled irradiation studies. *Science of the Total Environment* 832, 154941. <https://doi.org/10.1016/j.scitotenv.2022.154941>
- Patch, D., O'Connor, N., Vereecken, T., Murphy, D., Munoz, G., Ross, I., Glover, C., Scott, J., Koch, I., Sauvé, S., Liu, J., Weber, K., 2024. Advancing PFAS characterization: Enhancing the total oxidizable precursor assay with improved sample processing and UV activation. *Science of The Total Environment* 909, 168145. <https://doi.org/10.1016/j.scitotenv.2023.168145>

- Rehman, A.U., Crimi, M., Andreescu, S., 2023. Current and emerging analytical techniques for the determination of PFAS in environmental samples. *Trends in Environmental Analytical Chemistry* 37, e00198. <https://doi.org/10.1016/j.teac.2023.e00198>
- Schultes, L., Vestergren, R., Volkova, K., Westberg, E., Jacobson, T., Benskin, J.P., 2018. Per- and polyfluoroalkyl substances and fluorine mass balance in cosmetic products from the Swedish market: Implications for environmental emissions and human exposure. *Environ Sci Process Impacts* 20, 1680–1690. <https://doi.org/10.1039/c8em00368h>
- Tenorio, R., Liu, J., Xiao, X., Maizel, A., Higgins, C.P., Schaefer, C.E., Strathmann, T.J., 2020. Destruction of Per- and Polyfluoroalkyl Substances (PFASs) in Aqueous Film-Forming Foam (AFFF) with UV-Sulfite Photoreductive Treatment. *Environ Sci Technol* 54, 6957–6967. <https://doi.org/10.1021/acs.est.0c00961>
- Trojanowicz, M., Bartosiewicz, I., Bojanowska-Czajka, A., Kulisa, K., Szreder, T., Bobrowski, K., Nichipor, H., Garcia-Reyes, J.F., Nałęcz-Jawecki, G., Męczyńska-Wielgosz, S., Kisała, J., 2019. Application of ionizing radiation in decomposition of perfluorooctanoate (PFOA) in waters. *Chemical Engineering Journal* 357, 698–714. <https://doi.org/10.1016/j.cej.2018.09.065>
- Trojanowicz, M., Bartosiewicz, I., Bojanowska-Czajka, A., Szreder, T., Bobrowski, K., Nałęcz-Jawecki, G., Męczyńska-Wielgosz, S., Nichipor, H., 2020. Application of ionizing radiation in decomposition of perfluorooctane sulfonate (PFOS) in aqueous solutions. *Chemical Engineering Journal* 379, 122303. <https://doi.org/10.1016/j.cej.2019.122303>
- Trojanowicz, M., Bojanowska-Czajka, A., Bartosiewicz, I., Kulisa, K., 2018. Advanced Oxidation/Reduction Processes treatment for aqueous perfluorooctanoate (PFOA) and perfluorooctanesulfonate (PFOS) – A review of recent advances. *Chemical Engineering Journal* 336, 170–199. <https://doi.org/10.1016/j.cej.2017.10.153>
- Tsou, K., Antell, E., Duan, Y., Olivares, C.I., Yi, S., Alvarez-Cohen, L., Sedlak, D.L., 2023. Improved Total Oxidizable Precursor Assay for Quantifying Polyfluorinated Compounds Amenable to Oxidative Conversion to Perfluoroalkyl Carboxylic Acids. *ACS ES and T Water*. <https://doi.org/10.1021/acsestwater.3c00224>
- Turner, L.P., Kueper, B.H., Jaansalu, K.M., Patch, D.J., Battye, N., El-Sharnouby, O., Mumford, K.G., Weber, K.P., 2021. Mechanochemical remediation of perfluorooctanesulfonic acid (PFOS) and perfluorooctanoic acid (PFOA) amended sand and aqueous film-forming foam (AFFF) impacted soil by planetary ball milling. *Science of the Total Environment* 765, 142722. <https://doi.org/10.1016/j.scitotenv.2020.142722>
- Zhu, H., Kannan, K., 2020. Total oxidizable precursor assay in the determination of perfluoroalkyl acids in textiles collected from the United States. *Environmental Pollution* 265, 114940. <https://doi.org/10.1016/j.envpol.2020.114940>

7. Parsimonious Methodology for Synthesis of Silver and Copper Functionalized Cellulose

David Patch†*, Natalia O'Connor†, Debora Meira††, Jennifer Scott†, Iris Koch†, Kela Weber†

† Environmental Sciences Group, Department of Chemistry and Chemical Engineering, Royal Military College of Canada, Kingston, ON, Canada K7K 7B4.

†† Argonne National Laboratory, Lemont, IL, United States of America, 60439

* Corresponding Author:

Email: David.Patch@rmc.ca

The authors declare no competing financial interest.

7.1. Abstract

Metal nanomaterials, such as silver and copper, are often incorporated into commercial textiles to take advantage of their antibacterial and antiviral properties. The goal of this study was to identify the most parsimonious method for the synthesis of silver, copper, or silver/copper bimetallic treated textiles. To accomplish this, eight different methods were employed to synthesize silver, copper, and silver/copper functionalized cotton batting textiles. Using silver and copper nitrate as precursors, different reagents were used to initiate/catalyze the deposition of metal, including: (1) no additive, (2) sodium bicarbonate, (3) green tea, (4) sodium hydroxide, (5) ammonia, (6,7) sodium hydroxide/ammonia at a 1:2 and 1:4 ratio, and (8) sodium borohydride. The use of sodium bicarbonate as a reagent to reduce silver onto cotton has not been used previously in literature and was compared to established methods. All synthesis methods were performed at 80°C for one hour following textile addition to the solutions. The products were characterized by X-ray fluorescence (XRF) analysis for quantitative determination of the metal content and X-ray absorption near edge structure (XANES) analysis for silver and copper speciation on the textile. Scanning electron microscopy (SEM) with energy dispersive X-ray (EDX) and size distribution inductively coupled plasma mass spectrometry (ICP-MS) were used to further characterize the products of the sodium bicarbonate, sodium hydroxide, and sodium borohydride synthesis methods following ashing of the textile. For the silver treatment methods (1 mM Ag⁺), sodium bicarbonate and sodium hydroxide resulted in the highest amounts of silver on the textile (8900 mg Ag/kg textile and 7600 mg Ag/kg textile) and for copper treatment (1 mM Cu⁺) the sodium hydroxide and sodium hydroxide/ammonium hydroxide resulted in the highest amounts of copper on the textile (3800 mg Ag/kg textile and 2500 mg Ag/kg textile). Formation of copper oxide was dependent on the pH of the solution, with 4 mM ammonia and other high pH solutions resulting in majority of the copper on the textile existing as copper oxide, with smaller amounts of ionic-bound copper. The identified parsimonious methods will lend themselves to the efficient manufacturing of antibacterial and antiviral textiles, or the development of multi-functionalized smart textiles.

7.2. Introduction

Metals such as silver and copper have been used in medical, religious, and ornamental applications for thousands of years (Giannossa et al., 2013; Nowack et al., 2011). Many of these applications used bulk metals, such as silver containers for water purification, or ionic salts, such as silver nitrate as a caustic for wound treatment (Alexander, 2009). Advances in material sciences have seen the synthesis of smaller and smaller metal materials, seeking to taking advantage of the increased surface area to volume ratio and the unique properties these metals have compared to the larger bulk counterparts. These materials are often classified according to their size, with fine particles (2,500–100 nm), nanoparticles (100–1 nm), and atom clusters (<1 nm) being the three smallest ranges. The definition of nanoparticles is sometimes expanded to include particles 500 nm and smaller, since these particles still exhibit some nanoscale properties (Drexler, 1986; Fernández et al., 2016; Gubala et al., 2018; Health, 2010).

Metal nanoparticles and nanocomposites are a growing focus of commercialization because of the beneficial qualities these nanomaterials can impart. One of the biggest areas of growth is in the development of nano-functionalized textiles with manufacturers seeking to take advantage of the antibacterial properties of the nanomaterials (Fauss, 2008; Idumah, 2021; Vance et al., 2015). Metal and metal oxide nanoparticles are often utilized as these have enhanced stability and antibacterial efficacy over other oxidation states. Silver is often selected for antibacterial applications, and copper is selected for antiviral and antifungal applications. Silver and copper are the most commonly studied metals used for creating high performance textiles (Figure E1). The COVID-19 pandemic has renewed interest in using nanotechnology for enhanced protectiveness against viral spread (Idumah, 2021). Other than antimicrobial activity, nanoparticles can impart unique properties to textiles including increased conductivity (Gasana et al., 2006; Root et al., 2018), self-cleaning (Allahyarzadeh et al., 2013), electromagnetic interference shielding (Lu et al., 2010) and ultraviolet shielding (Shateri-Khalilabad et al., 2017). A recent push for the development of smart textiles has seen many of these unique properties combined into one material, with many traditional and green synthesis techniques being employed to achieve these multi-application materials (Assylbekova et al., 2022; Baldwin et al., 2021; Darabi et al., 2020; Dhanawansha et al., 2020; Galante et al., 2022; Ibrahim et al., 2021; Salama et al., 2021; Wibawa et al., 2021; Zhu et al., 2020, 2020). For example, work by Guo et al (2021) resulted in the development of a textile that maintained its innate flexibility/permeability, while also exhibiting novel properties including rapid

thermal response, long-time steady heating performance, and antifouling properties while also being conductive and water-resistant (Guo et al., 2021).

There are two common ways to prepare textiles with nanoparticles: ex-situ and in-situ. The ex-situ approach involves first forming metal nanoparticles separately from the textile, using a wet chemical method (Hasan, 2018; Rajendra et al., 2010; Üreyen et al., 2012), a sacrificial anode method (Ditaranto et al., 2016), or a biological method (Cheng et al., 2020; Cuevas et al., 2015; Gaikwad et al., 2013). The particles formed ex-situ are then applied to textiles through immersion or dry padding (El-Rafie et al., 2013). The in-situ approach consists of synthesizing nanoparticles directly onto the textiles, using an electroless plating or a chemical reduction method (Chen et al., 2017; Liu et al., 2017; Rafique et al., 2017; Root et al., 2018; Srikar et al., 2016). Some of these in-situ methods use an added reducing agent (e.g., glucose) (Vigneshwaran et al., 2006) or use the textile polymer itself (e.g., cellulose in cotton textiles) as the reducing agent (Allahyarzadeh et al., 2013; Maryan et al., 2015; Montazer and Allahyarzadeh, 2013). Cellulose is the most popular textile polymer used, due to its aesthetic qualities as well as it being renewable and biocompatible (Figure E1) (Klemm et al., 2005; Miyamoto et al., 1989).

The electron rich functional groups and polymer structure of cellulose allows for initial complexation of the ionic metal and stabilization of the resultant metal nanoparticle (Peng et al., 2016). The extent of deposition, speciation, and morphology of the resultant metal nanoparticle is heavily influenced by the synthesis conditions, including heat, pH, and reagents used (Jiang et al., 2011; Rafique et al., 2017; Shateri-Khalilabad et al., 2017; Sun et al., 2014; Xu et al., 2018; Zhang et al., 2016). To the knowledge of the authors, there have been no previous studies quantitatively characterizing the concentration, speciation, and morphology of the resultant metal materials across different synthesis methods.

The goal of the present study is to identify a parsimonious synthesis method for creating silver, copper, and bimetallic treated textiles by comparing eight different synthesis methods. A selection of novel and popular synthesis methods are examined through a stepwise approach. The ideal synthesis method(s) are ones that result in high concentrations of metal/metal oxide present on the textile with consistent particle morphology.

7.3. Materials and Methods

7.3.1. Reagents

Silver nitrate (ACS), copper (II) nitrate hemipentahydrate (ACS), sodium hydroxide pellets (ACS), ammonia solution (28-30%, ACS), sodium bicarbonate (ACS), Triton X100, and sodium borohydride (ACS) were all purchased from VWR. Cotton batting was purchased from a local supplier in Kingston, Ontario (Stitch by Stitch). Green tea was purchased from a local grocery store (Metro). Deionized water (DI water) was generated using an in-lab filtration system (Milli-Q Direct 8, 18 M Ω).

7.3.2. Preparation

All glassware was cleaned three times with 2% nitric acid and then rinsed with three portions of DI water. 4x4 cm squares of cotton batting (106 g/m²) were cut from the bulk material using a rotary cutter and prepared as follows: (1) washed with 1% Triton X100 solution at 60°C for 30 minutes with agitation (2) rinsed with DI water until no foaming was observed, (3) rinsed with DI water at 60°C for 15 minutes with agitation; and (4) dried overnight in an oven at 40°C. Textiles were trimmed with a rotary cutter after drying to remove any stray strands of batting.

2.3 Synthesis

A summary of the methods and reagents used is provided in Table 1, with a general procedure described in the following paragraphs. A final volume of 13.6 mL of solution and 0.17 ± 0.01 g of cotton batting was used to obtain a volume/textile mass ratio of 80:1, to allow for thorough wetting and mixing of the solutions. Erlenmeyer flasks were filled with DI water, sealed with aluminum foil, and placed into a water bath (digital general water bath, VWR) set to 60°C. Reagents were added as appropriate for each method, shown in Table 1, and agitated for 10 minutes using an orbital shaker.

Table 7.1: Overall synthesis steps performed, including reagents added at each step and analytical methods employed.

Method #	1	2	3	4	5	6	7	8
Short name	Control	NaHCO ₃	NaHCO ₃ + green tea	NH ₃	NaOH	NaOH/ NH ₃ Version1	NaOH/ NH ₃ Version2	NaBH ₄
Step 1: Reagents added and mixed at 60°C for 10 minutes								
Step reagents 1	DI H ₂ O	4 mM NaHCO ₃	4 mM NaHCO ₃	4 mM NH ₃	4 mM NaOH	2 mM NaOH + 4 mM NH ₃	2 mM NaOH + 8 mM NH ₃	DI H ₂ O
Step 2: Metals added and mixed at 60°C for 10 minutes								
Step metals 2	1 mM Ag ⁺ OR 1 mM Cu ²⁺ OR [0.5 mM Ag ⁺ + 0.5 mM Cu ²⁺]							
Step 3: Textile added, temperature set to 80°C								
Step 4: Reagents added								
Step reagents 4	none	none	1% green tea	none	none	none	none	4 mM NaBH ₄
Step 5: Mixed at 80°C for 1 hour								
Step 6: Cooled, drained, textile rinsed with DI H ₂ O at least 3x, and dried at 60°C overnight								
Step 7: Textiles characterized using methods listed below								
XRF	x	x	x	x	x	x	x	x
XANES	x	x	x	x	x	x	x	x
ATR-FTIR		x			x	x		x
SEM/EDX		x			x			x
ISE		x (Ag)						

Silver and/or copper nitrate solutions were added to the flasks to reach the final concentrations listed in Table 1 and mixed for 10 minutes. One textile (4 x 4 cm, 0.17 ± 0.01 g) was added to each Erlenmeyer flask, the water bath temperature was raised to 80°C, and reagents were added for Methods 3 and 8 (see Table 1). Flasks were agitated on an orbital shaker at 30 RPM for one hour. The Erlenmeyer flasks were then removed from the shaker, and 12 mL of room temperature DI water was immediately added to cool the vessel and stop the reaction. The following steps were undertaken to process the textiles: (1) textiles were removed from the solutions and rinsed with 20 mL DI water three times, (2) additional rinses were performed, if necessary, until the rinse solution was clear (e.g., for Method 2) (3) water was gently squeezed from the textiles, and (4) textiles were dried at 60°C in an oven overnight. Synthesis methods were performed in triplicate. A digital camera (Canon SL2) was used to image the textiles after the synthesis reactions to record color change.

Additional experiments were performed to explore the effect of heat, silver/copper competition, and for cellulose analysis. These experiments were performed using synthesis method 6 as it is a well-established method in literature for depositing silver onto different textiles including cotton, polyester, and polyamides (Montazer et al., 2014, 2012a; Montazer and Allahyarzadeh, 2013; Montazer and Komeily Nia, 2015; Textor et al., 2010).

7.3.3. Metal Content Determination

The metal concentration of the textiles following treatment was measured using x-ray fluorescence spectroscopy (Innov-X Systems α -2000 XRF). Textiles were analyzed whole after drying and the concentration determined by using an external calibration curve, since the XRF measurement parameters were set up for soil samples and not applicable to textiles. (See SI for method development of this calibration). Two calibration curve preparation methods were explored to determine the more accurate method. XRF detection limits were identified as ~ 375 mg Ag/kg and ~ 100 mg Cu/kg. Relative standard deviation for replicates was found to be $16 \pm 11\%$.

7.3.4. Metal Speciation

X-ray absorption near edge structure (XANES) analysis was used to perform silver and copper speciation analysis of the bulk textiles. XANES spectra were collected at the Sector 20 insertion device beamline (20ID-C) of the Advanced Photon Source (CLS@APS), within the X-Ray Science Division (XSD), Argonne National Laboratory. XANES spectra of the Ag K α -edge and Cu K α -edge were recorded in fluorescence mode by using a four-element silicon drift detector (Vortex®-ME4 with Xspress 3 pulse processor) while monitoring incident and transmitted intensities in straight ion chamber detectors filled with N₂ gas. Textiles were analyzed as 1 cm x 1 cm subsections rolled and packed in a 3D printed PETG sample holder, held between two layers of Kapton® tape. The Si (111) double crystal monochromator was calibrated using a silver metal foil at 25,514 eV, copper metal foil at 8989 eV, and the incident beam size was 800 μ m. Fitting of XANES spectra was accomplished with Athena software. The silver standard spectra used for fitting had been measured as frozen aqueous dissolved species previously by our group (Gagnon et al., 2019), and included AgNP, AgNO₃, AgO. The copper standards were synthesized in our lab using copper nitrate as a precursor and reacting it with the appropriate reagents to form the desired precipitate (where applicable). After synthesis, standards were washed with three portions of DI water and packed into the same 3D printed sample holder. The Ag (0) and Cu (0) standards used provided

the metals in their zero oxidation state and could not distinguish between nanoparticulate or bulk metallic forms.

7.3.5. Metal Morphology

Complete SEM sample preparation development is described in detail in the SI. Initial SEM analysis of the textiles failed to identify substantial metal materials on the textile surface, despite high concentrations present on the textiles (Figure E3). Cross-sectional analysis of the textiles identified the presence of nanomaterials within the cotton fiber core itself (Figure 7.1). This led to the development of a textile ashing method that allowed for improved metal morphological determination.

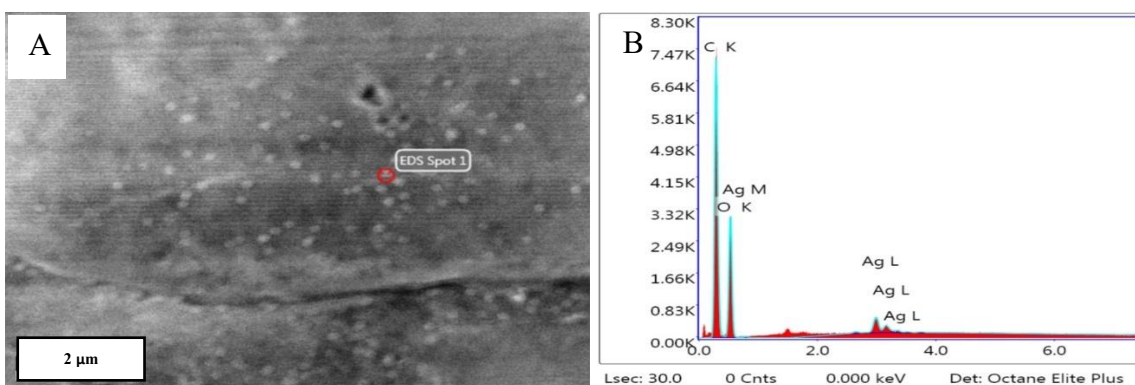


Figure 7.1: Silver nanoparticles found in the cross-section of the cotton fiber following NaHCO_3 silver treatment method.

Separate square subsections of the textiles (approximately 0.1 g) were ashed in ceramic crucibles at 550°C for one hour (Benn and Westerhoff, 2008). The resulting grey ash was dispersed in 1 mL DI water, and diluted to 10 mL with DI water, ultrasonicing the solution at 30 kHz for one minute. A 0.1 mL subsample of the solution was dried onto double-sided carbon tape and analyzed. Surface analysis of the textile samples were analyzed (Quanta 250FED) operating under environmental mode at 100 kPa. EDX (EDAX Octane Elite) was performed for elemental determination. Analysis of the dried ash following reconstitution were analyzed on under high vacuum mode. Images were acquired first at 6000–7500 magnification, then taken at 18–21,000 magnification. ImageJ (NIH) was used to count and determine the spherical diameter for nanoparticles. For non-spherical or oval nanoparticles, the diameter was measured at the shortest dimension.

7.3.6. Fourier-Transform Infrared Spectroscopy (FTIR) Analysis

The FTIR (Thermo Scientific Nicolet-IS10 Attenuated Total Reflection (ATR)-FTIR) spectra of cotton samples were acquired by folding samples twice for a total of four layers before being placed into the active element of the ATR-FTIR.

7.3.7. Ion Selective Electrode (ISE) Analysis

Using a silver ion selective electrode (Fisher Scientific accumet), the kinetics of the NaHCO₃ synthesis method were explored at temperature profile 1 (60 °C heated to 80 °C) and temperature profile 2 (80 °C from the start) by measuring the decrease in ionic silver present in the solution (assumed to correspond to formation of particulate silver on the textile). It is important to note that, as the ISE only measures ionic silver, any release of metallic silver from the textile during synthesis would not be identified. A no-textile control was analyzed using ISE at both temperature profiles to correct for changes to ISE response as a function of temperature. A six-point external calibration curve at the reaction temperature was used to quantify the ionic silver.

7.4. Results and Discussion

7.4.1. Metal Content and Speciation on Textile

Visual inspection of the treated cellulose textiles (see Figure 7.2) allowed for an immediate indication of the effectiveness of the different synthesis methods. Based on the extent of discoloration, the silver synthesis reactions with NaHCO₃, NaOH, or NaOH/NH₃ (Methods 2, 5 and 6) resulted in substantial silver present on the textile (darker brown), whereas copper synthesis methods 4, 5, 6, 7 and 8 appeared to have the most copper present (Figure 7.2). With the combined silver/copper treatment methods, the color trend of the textiles is similar to either their silver or copper textile counterpart, indicating a likely dominance of silver (method 2) or copper (methods 4-8).

	No reagent (1)	NaHCO ₃ (2)	NaHCO ₃ / green tea (3)	NH ₃ (4)	NaOH (5)	NaOH/NH ₃ Version 1 (6)	NaOH/NH ₃ Version 2 (7)	NaBH ₄ (8)
Silver								
Copper								
Silver Copper								

Figure 7.2: Photographic images taken of textiles post-treatment using eight synthesis methods.

XRF analysis confirms some of the observations made from the textile images: for the separate silver and copper textiles, the use of NaHCO₃, NaOH and NaOH/NH₃^{Version1} (Methods 2, 5 and 6) resulted in the highest amounts of silver (Figure 7.3A, S5), and methods 4–8 resulted in comparably high amounts of copper on the textile (Figure 7.3B, S5). For silver/copper bimetallic treatment, the use of NaHCO₃ (Method 2) resulted in highest amount of silver, but methods 4–7 resulted in reduced silver concentrations and copper dominating (Figure 3C, S5).

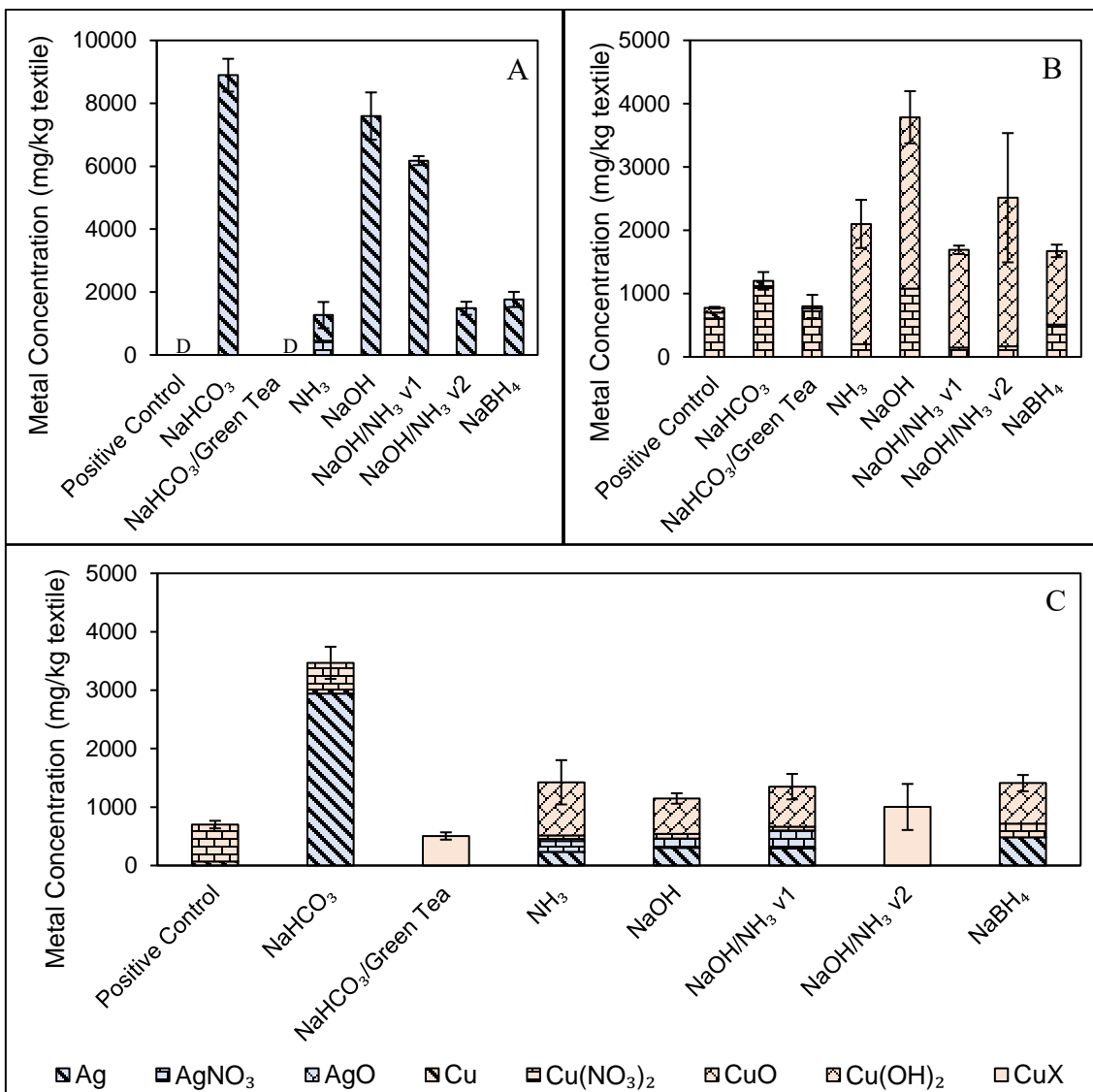


Figure 7.3: Concentration of metal present in the textile following treatment with (A) 1mM silver, (B) 1mM copper, and (C) combined 0.5 mM/0.5 mM silver/copper. CuX are samples that do not have speciation data available. D are samples that were not detected by XRF but have speciation data available.

XANES analysis identified the metal speciation of silver and copper across the synthetic trials. For silver only synthetic trials, all the methods resulted in reduction of the ionic silver into metallic silver (Figure 7.3a).

The speciation of copper using NaBH₄ was expected to be metallic copper, based on NaBH₄ being a strong reducing agent, instead of the copper oxide that was found. It is hypothesized that copper

treated onto the textile underwent oxidation during drying and storage in ambient atmosphere, resulting in the formation of copper oxide.

XANES analysis for the bimetallic textiles identified a significant amount of ionic silver for methods 4-7, which was not present for the silver-only synthetic trials. Given the chemistry of copper oxide formation for methods 4-7, this incomplete reduction is likely due to copper partially outcompeting silver for binding onto the textile.

Due to the novelty of the NaHCO_3 method and the unexpected results additional experiments were performed to investigate the kinetics of reaction as a function of temperature profiles (Figure 7.4), and the final textile concentration as a function of pH (Figure E6).

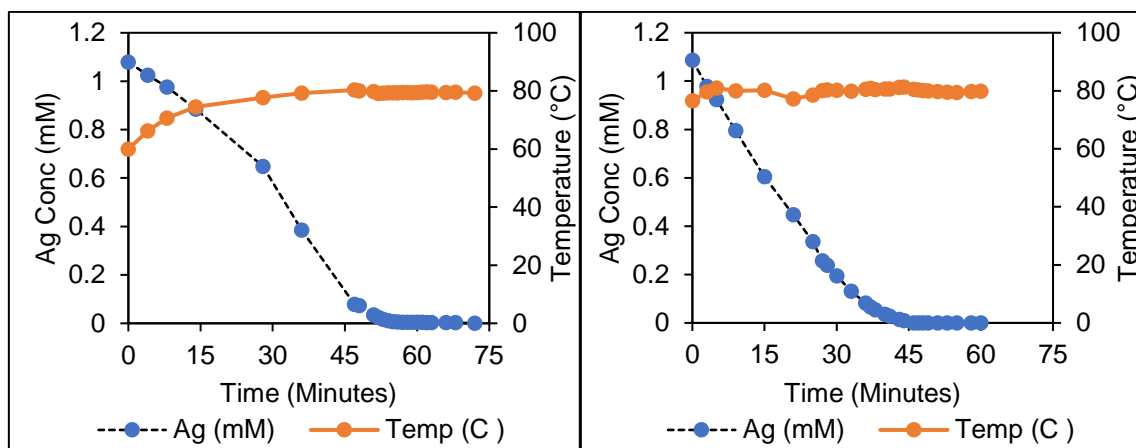


Figure 7.4: Concentration of silver over time with two different temperature profiles using NaHCO_3 synthesis method.

The reduction of silver by cellulose with NaHCO_3 is directly affected by the temperature of the reaction. As temperature is shifted from 60°C to 80°C , the rate of silver reduction increases (Figure 7.4, left) When the reaction temperature is held at 80°C for one hour the silver is reduced at a rate of $0.028 \text{ mM Ag}^+/\text{minute}$, with complete reduction by 46 minutes (Figure 7.4, right). These findings indicate that the temperature of the reaction has an impact on kinetic rates. Unfortunately, while the same kinetic investigation was attempted with the copper reaction the amount of copper present in the solution disappeared immediately upon reaction with the sodium bicarbonate, forming an insoluble copper (II) carbonate complex. The kinetic investigation could not be attempted for other synthesis methods due to the high pH of the reactions damaging the ISE.

While it was originally hypothesized that the effectiveness of NaHCO_3 for silver reduction was due to an optimal pH (pH = 8.24), it was identified that silver was still reduced at pH 6 (5400 ± 510

mg Ag/kg textile), pH 10 (8860 ± 1310 mg Ag/kg textile) and pH 12 (7500 ± 600 mg Ag/kg) (although reduction at pH 10 and 12 is likely due to the NaOH used to adjust the pH). The reduction at pH 6 indicates that the bicarbonate/carbonate ion itself has a key impact on the silver reduction. However, no reduction was found to occur at pH 3, indicating pH still plays a large role in the overall synthesis effectiveness (Figure E6).

7.4.2. Metal Particle Morphology

SEM analysis was performed on silver, copper, and bimetallic treated textiles resulting from the three synthesis methods that gave the most distinct results (Method 2, 5, 8). Initial SEM method development identified that most of the metal particles were present inside the cellulose matrix, requiring ashing of the textiles before analysis. To the author's knowledge this is the first study to identify metal materials present inside the cellulose matrix following in-situ synthesis. While classically defined nanoparticles (<100 nm) were identified, the majority of the particles were found to be between 100 and 500 nm in diameter, which are considered nanomaterials depending on the application and field (Gubala et al., 2018) (Figure 7.5, 7.6). Average silver nanomaterial diameter was found to be 290 ± 147 nm, 226 ± 130 nm, and 270 ± 74 nm for methods 2, 5, and 8 respectively. Average copper nanomaterial diameter was found to be 160 ± 61 nm, 166 ± 72 nm, and 162 ± 54 nm for methods 2, 5, and 8 respectively.

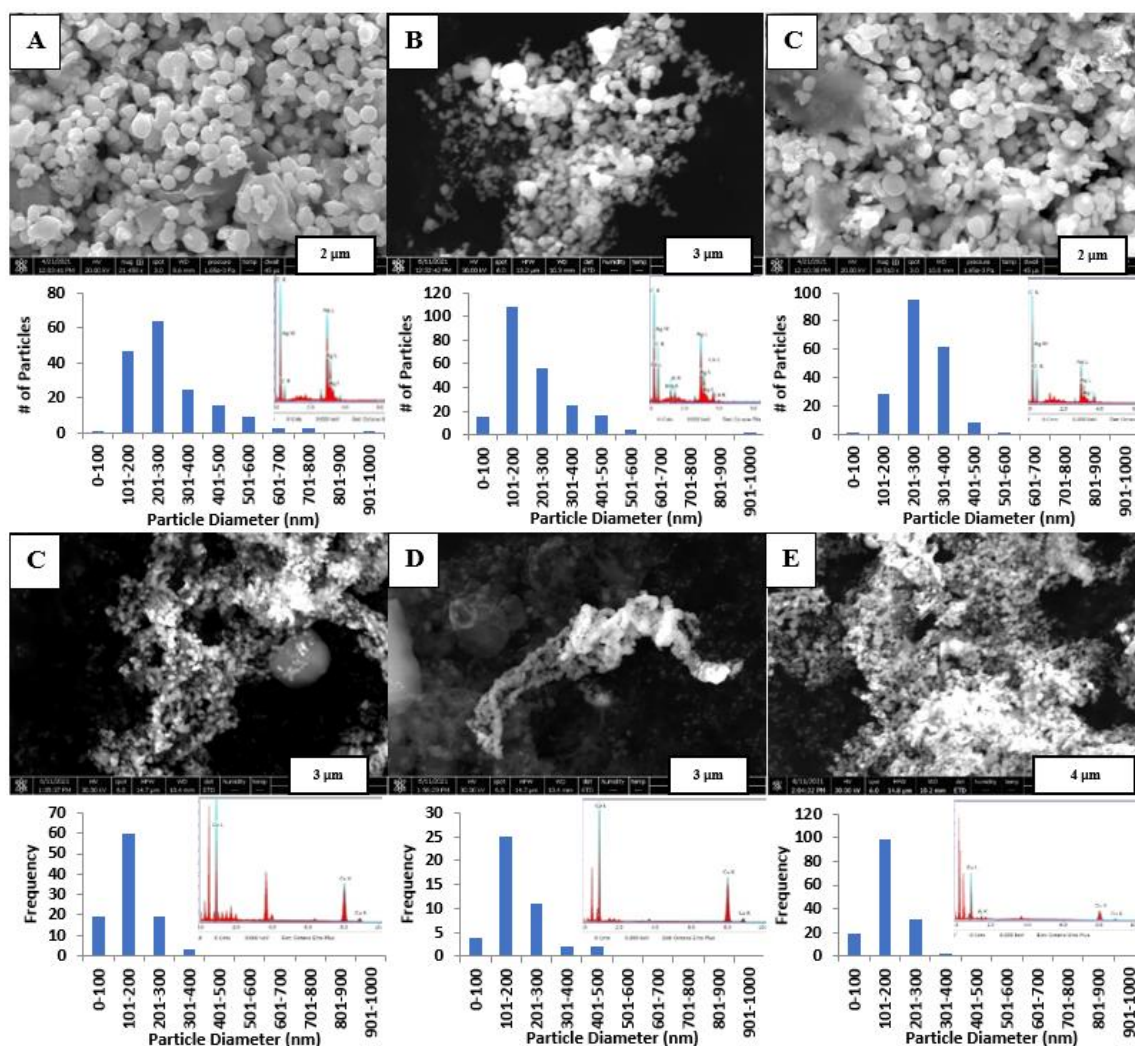


Figure 7.5: SEM analysis, EDX spectra, and ImageJ particle number/diameter determination of silver nanomaterials (A-C) and copper oxide nanomaterials (C-E) using NaHCO_3 (A/C), NaOH (B/D), and NaBH_4 (C/E) synthesis methods.

For the bimetallic treated textiles, the combined presence of silver and copper particles precluded the measurement of the diameters, but visual examination of the SEM images and the corresponding EDX spectra revealed two findings. Use of NaHCO_3 (Method 3) resulted in significantly more silver present than copper, whereas use of NaOH or NaBH_4 resulted in more copper present (predominantly green (copper) shading), which aligns with the XRF concentration results presented previously (Figure 7.6A). Secondly, the silver particles are significantly larger in the bimetallic textiles compared to silver only textiles, with many of them appearing to be well above 500 nm in diameter. Once again, this is likely caused by a lack of binding sites due to

competition with the copper, causing the silver reduction to favor particle growth over new nanoparticle formation. The copper/ copper oxide nanoparticles are relatively unchanged in their diameters (119 ± 36 nm).

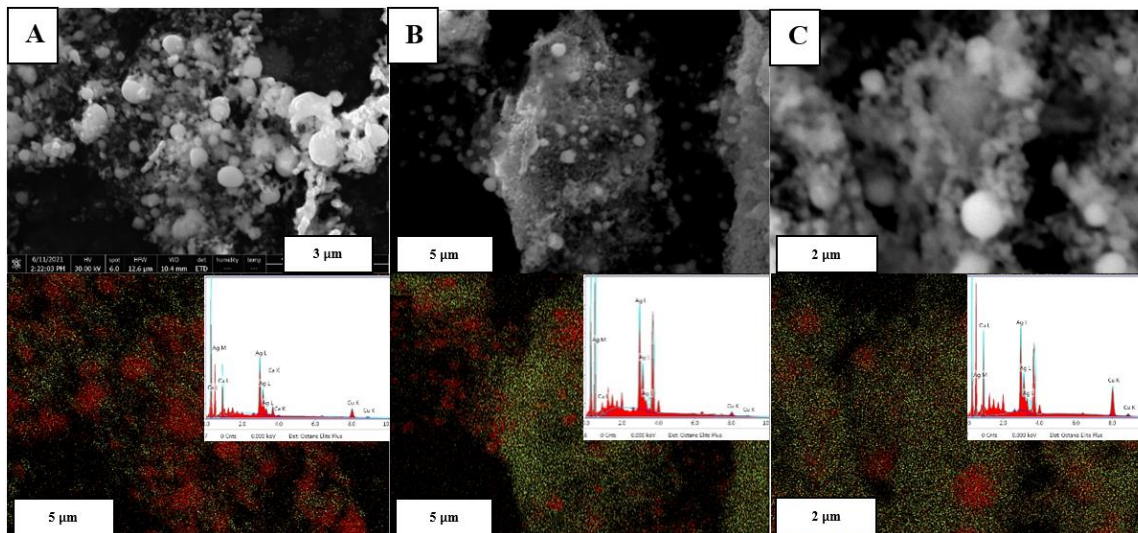


Figure 7.6: SEM analysis (top) and EDX elemental analysis (bottom) on silver (red) and copper (green) nanomaterials following NaHCO_3 (A), NaOH (B), and NaBH_4 (C) synthesis methods.

7.4.3. Role of Heat in Metal-Textile Synthesis

Previous studies have identified that increased temperatures result in increased reaction rates and chemical pathways possible during treatment of cellulose with metal salts (Jiang et al., 2011). The role of heat was qualitatively investigated for silver, copper, and silver/copper treated textiles following treatment with NaOH/NH_3 . The synthesis was either performed at room temperature, with the solution heated after the textile was added, or the solution pre-heated (60°C) before adding the textile.

For silver an increase in heat results in an increase to the amount of silver reduced into the textile. For copper the textile color is different based on the heating profile. When the textile is added to the synthesis solution at room temperature the blue copper complex (copper-tetraammine-hydroxide) immediately binds to the cellulose, stabilizing it against thermal conversion to copper oxide (Figure 7.7). The dark textile color corresponding to copper oxide only occurs when the solution is heated at 60°C before the textile is added. At higher pH ($\text{pH} > 10$) the expected copper complexes are either unstable or are not formed at elevated temperatures in water, resulting in the formation or conversion to copper oxide (Cudennec and Lecerf, 2003). Interestingly for the bimetallic textile the color of the textile resembles copper oxide containing textiles, suggesting a

possible silver-copper complex is formed that results in the deposition of copper oxide. This indicates that at pH >10 the competition between silver and copper could be both physical competition for binding sites and chemical competition for reagents.



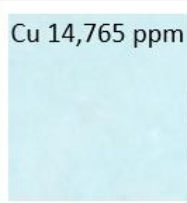
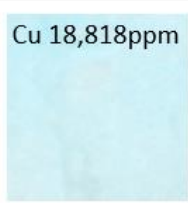

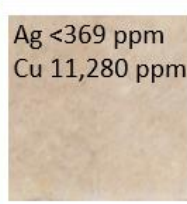
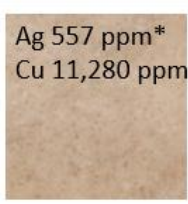
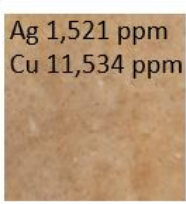
	Room Temperature	60°C After Textile Addition	60°C Before Textile Addition
Silver	Ag 395 ppm*	Ag 26,650ppm 	Ag 55,979 ppm 
Copper	Cu 14,765 ppm 	Cu 18,818ppm 	Cu 22,862 ppm 
Silver Copper	Ag <369 ppm Cu 11,280 ppm 	Ag 557 ppm* Cu 11,280 ppm 	Ag 1,521 ppm Cu 11,534 ppm 

Figure 7.7: Photographs of the synthesis of silver, copper, and silver/copper treated cotton textiles with three different water bath heat treatments using the NaOH/NH₃ Version 1 synthesis method and 10 mM of starting metal concentration. Starred values have one replicate under XRF detection limits.

7.4.4. Silver Copper Competition

The potential for competition between silver and copper was identified in the previous sections from XRF, XANES, and SEM analysis. To investigate this further, synthesis Method 6 (NaOH/NH₃Version1) was used to treat cotton textiles with different concentrations of silver and copper at a fixed (1:1) and variable ratio.

The relationship between the concentration of metal in the textile and in solution was plotted for silver, copper, and silver/copper treated textiles. The slope for the silver only synthesis was found to be 5600 mg Ag/kg textile per mM of reagent (introduced) Ag in solution (R^2 0.98). The slope for the copper only synthesis was found to be 2200 mg Cu/kg textile per mM of Cu in solution (R^2

0.95). For the silver synthesis in the combined silver/copper treatment, the slope for silver decreased dramatically to 240 mg Ag/kg textile per mM of Ag in solution (R^2 0.99), whereas for copper the slope barely decreased (2000 mg Cu/kg textile per mM of Cu in solution, R^2 0.98) (Figure 7.8). This confirms that, when silver and copper are in solution at equal concentrations, copper outcompetes silver for binding onto the textile.

Additionally, by varying the ratio of silver and copper (1:0, 10:1, 5:1, 2:1, 1:1, 0:1) the amount of copper required to outcompete silver can be identified. While the amount of silver decreased slightly with the addition of 0.1 and 0.2 mM of copper, it was within the deviation of the silver with no copper added. The amount of silver present on the textile dropped dramatically with 0.5 mM of copper being added, or a 2:1 ratio. Adding 1 mM of copper (1:1) resulted in further decrease in the amount of silver in the textile, indicating that copper began to significantly outcompete silver between a ratio of 5:1 and 2:1 (Figure 7.8). This explains the dominant amount of silver compared to copper in Ag/Cu synthesis Method 2 (NaHCO_3), as this method showed to result in a large amount of silver but a small amount of copper, resulting in a silver/copper ratio of ~5:1 on the textile. Without any silver present, the amount of copper on the textile increased, indicating that while silver is disproportionately outcompeted by copper, the presence of silver does lead to some inhibition of copper binding to the textile. It is hypothesized that the stabilization of the copper oxide precipitate onto the textile occurs more rapidly than the reduction of silver, leading to the competition phenomena observed.

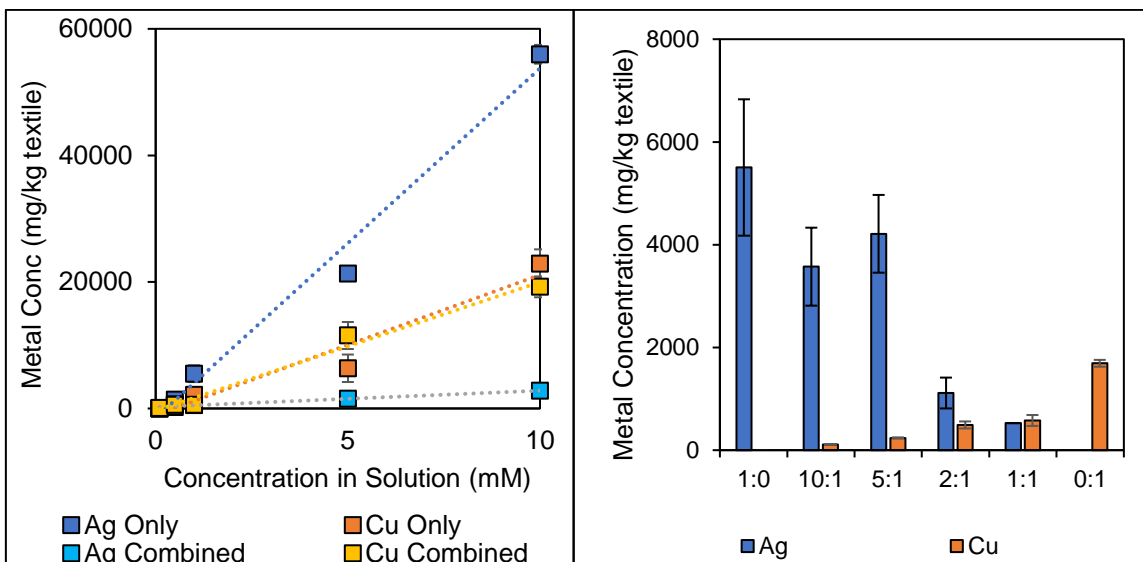


Figure 7.8: Investigation into the effect of reagent concentration on resulting concentration in the textile using the NaOH/NH₃Version1 synthesis method by using a fixed ratio of silver/copper (left) and a variable ratio of silver:copper, with silver held constant at 1 mM (except for 0:1, which had no silver and 1 mM copper) (right).

7.4.5. Cellulose Analysis

ATR-FTIR analysis was performed on samples treated with NaOH/NH₃Version1 (Method 6) with an increasing silver concentration (0.1–10 mM) to identify any changes to the cellulose structure following synthesis (Figure E12). Minor changes to various peak intensities were seen, thought to be due to differences in sample material thickness and homogeneity, and not actual changes to cellulose functional groups. The lack of identifiable functional group changes is expected when considering cellulose polymer chain length (degree of polymerization) for cotton is upwards of 10,000 units, and the reduction of silver only occurs at the termini of the polymer chain, leaving most of the cellulose untouched (Klemm et al., 2005). ATR-FTIR analysis of textiles resulting from Methods 2 (NaHCO₃), 5 (NaOH), and 8 (NaBH₄) further confirm a lack of any functional group transformation (Figure 7.9).

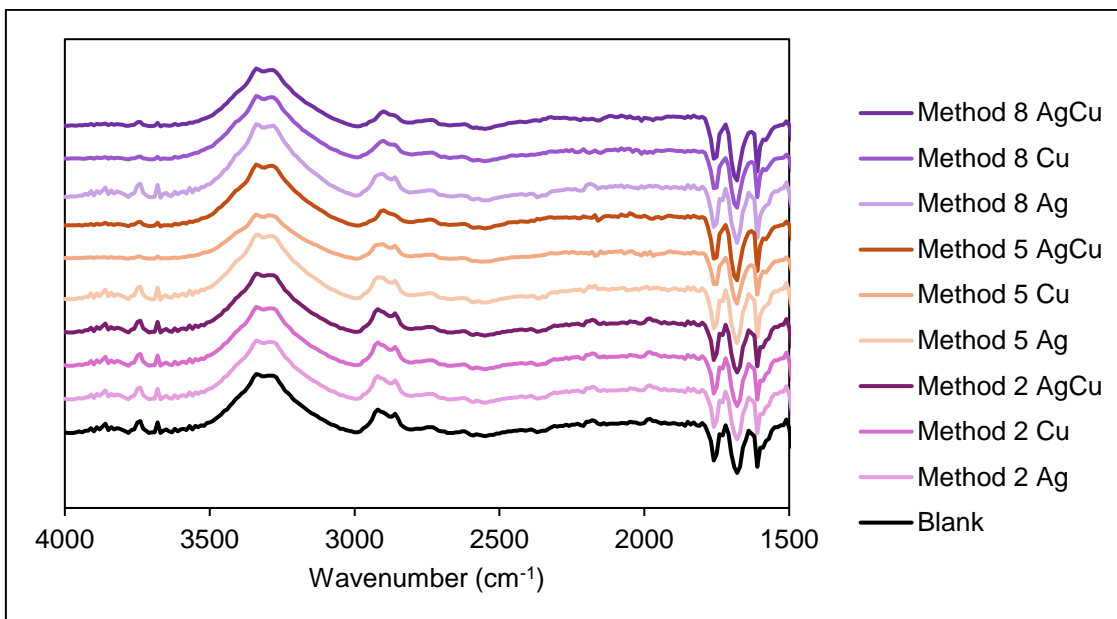


Figure 7.9: ATR-FTIR absorbance spectra for cotton samples using Methods 2 (NaHCO_3), 5 (NaOH) and 8 (NaBH_4) with silver, copper, and silver/copper.

7.4.6. Parsimonious Assessment of the Synthesis Methods

The goal of this investigation was to identify the most parsimonious – successful, simple, and ideally, efficacious – method for creating silver and copper treated textiles by comparing novel and previously identified synthesis methods in a stepwise fashion. The effectiveness of the methods can be identified following comprehensive characterization of the concentration (highest), speciation (non-ionic) and morphology of metal (nanoparticulate) in the textiles.

For silver synthesis methods, treatment with NaHCO_3 or NaOH were assessed as the most parsimonious methods as they resulted in the highest concentrations of silver in the textile in metallic nanoparticulate form (100–500 nm). The use of ammonia, green tea, and NaBH_4 were all found to be ineffective as they reduce and/or stabilize the ionic silver in solution, inhibiting successful binding with the cellulose.

For synthesis of copper-treated textiles, Methods 4–8 were found to be comparable in their effectiveness, as they resulted in the highest concentrations of copper in the textile, forming nanoparticles (50–500 nm, with non-ionic copper speciation (i.e., copper oxide). Of the four methods, use of NaOH was the most parsimonious method as it resulted in the highest total concentration of copper with minimal reagent input.

For the bimetallic synthesis methods, the extent of metal on the textile was influenced by the competition between silver and copper for binding with the textile. The use of NaHCO_3 resulted in a parsimonious silver dominant synthesis method, resulting in a broad range of sizes in silver particles (greater than 1000 nm) interspersed with smaller (~50 to 300 nm) copper nanoparticles. The use of Methods 4–7 resulted in comparable amounts of copper oxide and metallic silver on the textile, with unreduced ionic silver also present. The use of either NH_3 , NaOH , or NaBH_4 were identified as being the most parsimonious balanced silver/copper synthesis method, with NaBH_4 being slightly advantageous due to complete reduction of silver. However, this slight advantage is countered by the toxicity of using NaBH_4 as a reducing agent.

7.4.7. Metal Cellulose Synthesis Mechanism

It is well accepted that ionic metals, such as silver, can be reduced by cellulose in cotton, and this reduction occurs more completely under alkaline conditions and at elevated temperatures (Liu et al., 2013; Tang et al., 2013; Yuen et al., 2013). The exact mechanism of this reduction is not often discussed in detail although some authors suggest that the hydroxyl groups on the cellulose polymer are oxidized into aldehydes, and then into carboxylates (Montazer et al., 2012a). However, silver complexes like those formed using Tollen's Reagent are not reduced in the presence of alcohol-containing compounds in classic chemical tests, whereas they are with aldehydes. Other authors identify that while cellulose itself is not considered a reducing sugar; hemiacetal groups are present at the termini of the polymer chain. These hemiacetals undergo ring-chain tautomerism under basic conditions and with heat (8), converting into aldehyde groups that, like typical reducing sugars such as glucose, can reduce metals (Haskins and Hogsed, 1950; Kongruang et al., 2004; Matsuoka et al., 2011). There is also the potential for alkaline degradation of the cellulose polymer (i.e., the Lobry de Bruyn-Alberda van Ekenstein transformation (van Loon and Glaus, 1998)), resulting in the generation of glucose and other monosaccharides that will readily reduce ionic silver. It is also possible that the pectins and hemicelluloses present in the primary wall and winding layer of cotton fibers are reducing ionic silver, as these compounds have been found to reduce silver when isolated and used as primary reagents (Peng et al., 2011; Zahran et al., 2014).

When no reagents are added, as is the case with the positive control synthesis method, some reduction of silver is observed to be occurring (as detected by XANES). Reduction of ionic silver onto cotton without the use of reagents has been observed previously, with the concentration of silver being related to reaction time and temperature (Jiang et al., 2011; Sadanand et al., 2017).

The reactions for silver explored in this study are shown in equations 1 to 9 below. It is important to note that the silver hydroxide (3) immediately reacts to silver oxide (4) due to the favorable kinetics of the reaction ($pK = 2.88$) (Biedermen and Sillen, 1960) (4). The silver complex formed following addition of NaOH and NH_3 (method 6, 7) is known as Tollen's reagent, which is used to test for aldehydes and alpha-hydroxy ketones and is often used for synthesizing silver-treated textiles (Liu et al., 2013; Montazer et al., 2012a). Reaction of the silver compounds with the aldehyde at the terminal end of the cellulose chain results in reduction of ionic silver to metallic silver, and oxidation of the aldehyde to the carboxylic acid.

If $NaHCO_3$ is added



If only NH_3 is added



If only NaOH



If NH_3 and NaOH are added



Hemiacetal cellulose ring chain tautomerism in the presence of base/heat



Upon addition of cotton textile



The resulting silver nanoparticles (9) are then stabilized by the cellulose inside the cotton fibers, like the stabilization effect that occurs with carboxymethylcellulose (CMC) coated nanoparticles (Garza-Navarro et al., 2013; Hebeish et al., 2010; Liu et al., 2013).

While the speciation of silver on the textile was consistent across the methods, the amount of metal present on the textile varied substantially. This can be explained by the stability of the silver compounds. In the presence of green tea, reduction followed by stabilization via coating occurs, significantly inhibiting any silver deposition onto textile (Ahmad et al., 2019; Arumai Selvan et al., 2018; Asghar et al., 2018; Onitsuka et al., 2019; Rónavári et al., 2017; Sun et al., 2014). In the presence of ammonia (method 4), or high concentrations of ammonia (method 7) significant silver-ammonia complexation occurs, which stabilizes the silver and makes it a weaker oxidizing agent than the corresponding aquo complexes that result with Ag₂O and Ag₂CO₃. When NaBH₄ was added reduction occurred in the solution (a process well understood in the literature) (Dong et al., 2010; Glavee et al., 1995, 1994, 1992; Hynning and Zukoski, 1998; Noordeen et al., 2013; Polte et al., 2012; Wojtysiak and Kudelski, 2012), causing the majority of silver nanomaterials to aggregate and precipitate out of solution before they could be deposited and stabilized by the cellulose (10).



For copper only synthetic trials, methods 1-3 resulted in the copper being deposited as ionic copper; likely intermolecularly bonded with the hydroxyl groups in the cellulose chain. For methods 4-7, which occurred at higher pH (pH >10), the copper was deposited mainly as copper oxide. The reactions for copper explored in this study are shown in equations 11 to 17. When both NaOH and NH₃ are added, a copper-tetraammine-hydroxide complex is eventually formed, similar to the complex known as Schweizer's reagent, which is copper ammonia complex used to dissolve cellulose (14,15). Despite the various complexes that are formed, all of the pH >10 complexes are not stable at elevated temperatures and convert into copper oxide, supporting the speciation results observed (Cudennec and Lecerf, 2003).

If only NaHCO₃ is added



If only NH₃ is added



If only NaOH



If NH_3 and NaOH are added

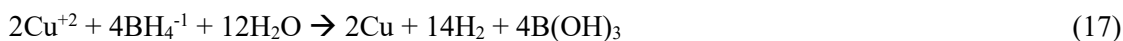


In the presence of heat



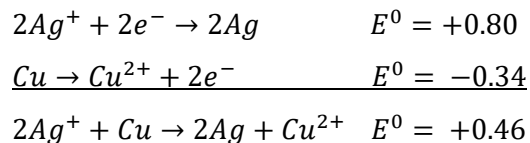
The use of NaHCO_3 and NaHCO_3 /green tea did not have any appreciable effect on the total concentration or speciation of copper on the textile when compared to the reagent-free control, indicating these reagents are superfluous for copper textile synthesis. This was initially unexpected as the antioxidants in green tea (catechins, flavenols) (Wiseman et al., 1997) have been shown capable of reducing other metals like iron and silver (KSV, 2017; Nakhjavani et al., 2017). It is likely the NaHCO_3 precipitated out the ionic copper as copper (II) carbonate before reduction with green tea could occur.

When ionic copper and sodium borohydride react, the initial reduction follows a slightly different path when compared to the ionic silver reduction mechanism. In this reaction, ionic copper reacts with the sodium borohydride to form the reduced copper, hydrogen gas, and boric acid (17) (Glavee et al., 1994).



For silver and copper bimetallic treatment methods it can be seen, based on the speciation and competition results, that the copper synthesis occurs rapidly due to pH-dominated deposition, as discussed in reaction 16. The reduction of ionic silver to metallic silver is, in comparison, a slower process that is further inhibited by the fast deposition of copper oxide nanomaterials into the textile matrix. As such, while the standard reduction reaction (9) is able to proceed, the reaction favours the growth of existing silver nanoparticles instead of the formation of new, smaller silver nanoparticles. It is also possible that, if some metallic copper is being produced, a resulting

spontaneous reduction of the ionic silver onto the surface of the copper occurs, as dictated by their standard reduction potentials.



In summary, the mechanism of synthesis of silver, copper, and bimetallic silver/copper functionalized textiles varies on both the metal and preparation method. For silver, when an existing reducing reagent is not used (catechins, NaBH₄) the silver undergoes reduction with the hemiacetal groups at the end of the cellulose chain following ring-chain tautomerism. The extent of reduction is dependent on temperature and the stability of the resultant silver complex, with less stable complexes undergoing more reduction. For copper, the synthesis is dependent on temperature and pH, with reactions occurring above pH 10 resulting mainly in copper oxide deposition, with some ionic copper complexation also occurring with the hydroxyl functional groups on the cellulose itself.

7.5. Conclusion

This study characterized silver, copper, and silver/copper containing cotton textiles resulting from eight different synthesis methods. The total metal content, metal speciation, and metal morphology of each synthesis reaction has been identified. Additionally, the roles of metal competition, temperature, and pH (treatment with Ag/NaHCO₃) have also been investigated, providing additional mechanistic information.

A NaHCO₃ synthesis method (Method 2) resulted in the highest concentration (8900 ± 500 mg Ag/kg textile) of elemental silver nanoparticles (356 ± 106 nm) in the cotton textile material, representing a successful method for the creation of silver nanoparticle treated textiles. The NaOH synthesis method (Method 5) was also found to result in high concentrations of metallic (silver) and metal-oxide (copper) nanoparticles, representing a successful method for the creation of silver, copper, and bimetallic silver/copper containing textiles.

While the size of the nanoparticles identified in this study are larger than classically defined nanoparticles (<100 nm in diameter), the larger size is potentially advantageous when considering their potential for antimicrobial textile applications. Larger-sized nanoparticles allow for sufficiently small particles to provide an enhanced ability (over sheets or coatings) to inhibit the

growth of bacteria and viruses, while minimizing major nano-specific risk assessment concerns for the product (Gubala et al., 2018; Health, 2010; Ray et al., 2009). The identification of the silver and copper materials being present inside the cellulose matrix suggests that the release of the metal materials during use and washing may be minimal. Future work is planned to evaluate the antimicrobial effectiveness of these silver, copper, and silver/copper treated textiles.

7.6. Acknowledgements

The authors would like to acknowledge Jacob Zachariah, Angela Richard, and Francesca Body for their contributions to the initial literature review. The authors would like to acknowledge Anbareen Farooq for their contribution with proofreading. The authors would also like to thank Dr. Jennifer Snelgrove for training and assistance with the SEM-EDX work, Dr. Fiona Kelly for providing her NexION 300D ICP-MS, as well as Dr. Zou Finfrock for performing XANES speciation analysis. This research used resources of the Advanced Photon Source, an Office of Science User Facility operated for the U.S. Department of Energy (DOE) Office of Science by Argonne National Laboratory and was supported by the U.S. DOE under Contract No. DE-AC02-06CH11357, the Canadian Light Source and its funding partners (Sector 20 work), and DOE and MRCAT member institutions (Sector ID-B). Additional beam time was awarded for research related to COVID applications.

7.7. References

- Ahmad S, Munir S, Zeb N, et al (2019) Green nanotechnology: A review on green synthesis of silver nanoparticles — An ecofriendly approach. *Int J Nanomedicine* 14:5087–5107. <https://doi.org/10.2147/IJN.S200254>
- Alexander JW (2009) History of the medical use of silver. *Surg Infect (Larchmt)* 10:289–292. <https://doi.org/10.1089/sur.2008.9941>
- Allahyarzadeh V, Montazer M, Nejad NH, Samadi N (2013a) In situ synthesis of nano silver on polyester using NaOH/Nano TiO₂. *J Appl Polym Sci* 129:892–900. <https://doi.org/10.1002/app.38907>
- Allahyarzadeh V, Montazer M, Nejad NH, Samadi N (2013b) In situ synthesis of nano silver on polyester using NaOH/Nano TiO₂. *J Appl Polym Sci* 129:892–900. <https://doi.org/10.1002/app.38907>
- Arumai Selvan D, Mahendiran D, Senthil Kumar R, Kalilur Rahiman A (2018) Garlic, green tea and turmeric extracts-mediated green synthesis of silver nanoparticles: Phytochemical, antioxidant and in vitro cytotoxicity studies. *J Photochem Photobiol B* 180:243–252. <https://doi.org/10.1016/j.jphotobiol.2018.02.014>
- Asgar MA, Zahir E, Shahid SM, et al (2018) Iron, copper and silver nanoparticles: Green synthesis using green and black tea leaves extracts and evaluation of antibacterial, antifungal and aflatoxin B1 adsorption activity. *LWT - Food Science and Technology* 90:98–107. <https://doi.org/10.1016/j.lwt.2017.12.009>
- Assylbekova G, Alotaibi HF, Yegemberdiyeva S, et al (2022) Sunlight induced synthesis of silver nanoparticles on cellulose for the preparation of antimicrobial textiles. *J Photochem Photobiol* 11. <https://doi.org/10.1016/j.jpap.2022.100134>
- Baldwin SJ, Slaine PD, Keltie E, et al (2021) Non-Woven Textiles Formed from Contact Drawn Poly(ethylene oxide) Fibers Provide Tunable Filtration and Virucidal Properties via Entrapment of Silver Nanoparticles. *ACS Appl Polym Mater* 3:4245–4255. <https://doi.org/10.1021/acsapm.1c00697>
- Benn TM, Westerhoff P (2008) Nanoparticle silver released into water from commercially available sock fabrics. *Environ Sci Technol* 42:4133–4139. <https://doi.org/10.1021/es7032718>
- Biedermen G, Sillen LG (1960) Studies on the Hydrolysis of Metal Ions. Part 30. A Critical Survey on the Solubility Equilibria of Ag₂O. 9
- Chen H, Liao F, Yuan Z, et al (2017) Simple and fast fabrication of conductive silver coatings on carbon fabrics via an electroless plating technique. *Mater Lett* 196:205–208. <https://doi.org/10.1016/j.matlet.2017.03.070>
- Cheng TH, Yang ZY, Tang RC, Zhai AD (2020) Functionalization of silk by silver nanoparticles synthesized using the aqueous extract from tea stem waste. *Journal of Materials Research and Technology* 9:4538–4549. <https://doi.org/10.1016/j.jmrt.2020.02.081>
- Cudennec Y, Lecerf A (2003) The transformation of Cu(OH)₂ into CuO, revisited. *Solid State Sci* 5:1471–1474. <https://doi.org/10.1016/j.solidstatesciences.2003.09.009>
- Cuevas R, Durán N, Diez MC, et al (2015) Extracellular biosynthesis of copper and copper oxide nanoparticles by *Stereum hirsutum*, a native white-rot fungus from Chilean forests. *J Nanomater* 2015. <https://doi.org/10.1155/2015/789089>
- Darabi S, Hummel M, Rantasalo S, et al (2020) Green Conducting Cellulose Yarns for Machine-Sewn Electronic Textiles. *ACS Appl Mater Interfaces* 12:56403–56412. <https://doi.org/10.1021/acsami.0c15399>

- Dhanawansa KB, Senadeera R, Gunathilake SS, Dassanayake BS (2020) Silver nanowire-containing wearable thermogenic smart textiles with washing stability. *Adv Nano Res* 9:123–131. <https://doi.org/10.12989/anr.2020.9.2.123>
- Ditaranto N, Picca RA, Sportelli MC, et al (2016) Surface characterization of textiles modified by cop-per and zinc oxide nano-antimicrobials. *Surface and Interface Analysis* 48:505–508. <https://doi.org/10.1002/sia.5951>
- Dong X, Ji X, Jing J, et al (2010) Synthesis of triangular silver nanoprisms by stepwise reduction of sodium borohydride and trisodium citrate. *Journal of Physical Chemistry C* 114:2070–2074. <https://doi.org/10.1021/jp909964k>
- Drexler E (1986) The coming era of nanotechnology
- El-Rafie HM, El-Rafie MH, Zahran MK (2013) Green synthesis of silver nanoparticles using polysaccharides extracted from marine macro algae. *Carbohydr Polym* 96:403–410. <https://doi.org/10.1016/j.carbpol.2013.03.071>
- Fauss E (2008) The Silver Nanotechnology Commercial Inventory
- Fernández JG, Fernández-Baldo MA, Berni E, et al (2016) Production of silver nanoparticles using yeasts and evaluation of their antifungal activity against phytopathogenic fungi. *Process Biochemistry* 51:1306–1313. <https://doi.org/10.1016/j.procbio.2016.05.021>
- Gagnon V, Button M, Boparai HK, et al (2019) Influence of realistic wearing on the morphology and release of silver nanomaterials from textiles. *Environ Sci Nano*. <https://doi.org/10.1039/C8EN00803E>
- Gaikwad S, Ingle A, Gade A, et al (2013) Antiviral activity of mycosynthesized silver nanoparticles against herpes simplex virus and human parainfluenza virus type 3. *Int J Nanomedicine* 8:4303–4314. <https://doi.org/10.2147/IJN.S50070>
- Galante AJ, Pilsbury BC, Yates KA, et al (2022) Reactive silver inks for antiviral, repellent medical textiles with ultrasonic bleach washing durability compared to silver nanoparticles. *PLoS One* 17:e0270718. <https://doi.org/10.1371/journal.pone.0270718>
- Garza-Navarro MA, Aguirre-Rosales JA, Llanas-Vázquez EE, et al (2013) Totally ecofriendly synthesis of silver nanoparticles from aqueous dissolutions of polysaccharides. *Int J Polym Sci* 2013:. <https://doi.org/10.1155/2013/436021>
- Gasana E, Westbroek P, Hakuzimana J, et al (2006) Electroconductive textile structures through electrodeless deposition of polypyrrole and copper at polyaramide surfaces. *Surf Coat Technol* 201:3547–3551. <https://doi.org/10.1016/j.surfcoat.2006.08.128>
- Giannossa LC, Longano D, Ditaranto N, et al (2013) Metal nanoantimicrobials for textile applications. *Nanotechnol Rev* 2:307–331. <https://doi.org/10.1515/ntrev-2013-0004>
- Glavee GN, Klabunde KJ, Sorensen CM, Hadjipanayis GC (1992) Borohydride Reductions of Metal Ions. A New Understanding of the Chemistry Leading to Nanoscale Particles of Metals, Borides, and Metal Borates. *Langmuir* 771–773
- Glavee GN, Klabunde KJ, Sorensen CM, Hadjipanayis GC (1995) Chemistry of borohydride reduction of iron(II) and iron(III) ions in aqueous and nonaqueous media. *Inorg Chem* 34:28–35
- Glavee GN, Klabunde KJ, Sorensen CM, Hadjipanayis GC (1994) Borohydride Reduction of Nickel and Copper Ions in Aqueous and Nonaqueous Media. Controllable Chemistry Leading to Nanoscale Metal and Metal Boride Particles. *Langmuir* 10:4726–4730. <https://doi.org/10.1021/la00024a055>

- Gubala V, Johnston LJ, Liu Z, et al (2018) Engineered nanomaterials and human health: Part 1. Preparation, functionalization and characterization (IUPAC Technical Report). *Pure and Applied Chemistry* 90:1283–1324. <https://doi.org/10.1515/pac-2017-0101>
- Guo Z, Wang Y, Huang J, et al (2021) Multi-functional and water-resistant conductive silver nanoparticle-decorated cotton textiles with excellent joule heating performances and human motion monitoring. *Cellulose* 28:7483–7495. <https://doi.org/10.1007/s10570-021-03955-y>
- Hasan R (2018) Production of Antimicrobial Textiles by Using Copper Oxide Nanoparticles. *International Journal of Contemporary Research and Review* 9:20195–20202. <https://doi.org/10.15520/ijcrr/2018/9/08/564>
- Haskins J, Hogsed M (1950) THE ALKALINE OXIDATION OF CELLULOSE. I. MECHANISM OF THE DEGRADATIVE OXIDATION OF CELLULOSE BY HYDROGEN PEROXIDE IN PRESENCE OF ALKALI. 1264–1274
- Hebeish AA, El-Rafie MH, Abdel-Mohdy FA, et al (2010) Carboxymethyl cellulose for green synthesis and stabilization of silver nanoparticles. *Carbohydr Polym* 82:933–941. <https://doi.org/10.1016/j.carbpol.2010.06.020>
- Huning DL van, Zukoski CF (1998) Formation Mechanisms and Aggregation Behavior of Borohydride Reduced Silver Particles. *Langmuir* 7034–7046
- Ibrahim HM, Zaghoul S, Hashem M, El-Shafei A (2021) A green approach to improve the antibacterial properties of cellulose based fabrics using *Moringa oleifera* extract in presence of silver nanoparticles. *Cellulose* 28:549–564. <https://doi.org/10.1007/s10570-020-03518-7>
- Idumah CI (2021) Influence of nanotechnology in polymeric textiles, applications, and fight against COVID-19. *Journal of the Textile Institute* 112:2056–2076. <https://doi.org/10.1080/00405000.2020.1858600>
- Jiang T, Liu L, Yao J (2011) In situ deposition of silver nanoparticles on the cotton fabrics. *Fibers and Polymers* 12:620–625. <https://doi.org/10.1007/s12221-011-0620-4>
- Klemm D, Heublein B, Fink HP, Bohn A (2005) Cellulose: Fascinating biopolymer and sustainable raw material. *Angewandte Chemie - International Edition* 44:3358–3393. <https://doi.org/10.1002/anie.200460587>
- Kongruang S, Han MJ, Breton CIG, Penner MH (2004) Quantitative analysis of cellulose-reducing ends. *Applied Biochemistry and Biotechnology - Part A Enzyme Engineering and Biotechnology* 113:213–231. <https://doi.org/10.1385/ABAB:113:1-3:213>
- KSV G (2017) Green Synthesis of Iron Nanoparticles Using Green Tea leaves Extract. *J Nanomedicine Biotherapeutic Discov* 07:1–4. <https://doi.org/10.4172/2155-983x.1000151>
- Liu B, Li X, Zheng C, et al (2013) Facile and green synthesis of silver nanoparticles in quaternized carboxymethyl chitosan solution. *Nanotechnology* 24:. <https://doi.org/10.1088/0957-4484/24/23/235601>
- Liu KG, Abbasi AR, Azadbakht A, et al (2017) Deposition of silver nanoparticles on polyester fiber under ultrasound irradiations. *Ultrason Sonochem* 34:13–18. <https://doi.org/10.1016/j.ultsonch.2016.04.006>
- Lu Y, Jiang S, Huang Y (2010) Ultrasonic-assisted electroless deposition of Ag on PET fabric with low silver content for EMI shielding. *Surf Coat Technol* 204:2829–2833. <https://doi.org/10.1016/j.surfcoat.2010.02.061>
- Maryan AS, Montazer M, Harifi T (2015) Synthesis of nano silver on cellulosic denim fabric producing yellow colored garment with antibacterial properties. *Carbohydr Polym* 115:568–574. <https://doi.org/10.1016/j.carbpol.2014.08.100>

- Matsuoka S, Kawamoto H, Saka S (2011) Reducing end-group of cellulose as a reactive site for thermal discoloration. *Polym Degrad Stab* 96:1242–1247. <https://doi.org/10.1016/j.polymdegradstab.2011.04.009>
- Miyamoto T, Takahashi S -i, Ito H, et al (1989) Tissue biocompatibility of cellulose and its derivatives. *J Biomed Mater Res* 23:125–133. <https://doi.org/10.1002/jbm.820230110>
- Montazer M, Alimohammadi F, Shamei A, Rahimi MK (2012) In situ synthesis of nano silver on cotton using Tollens' reagent. *Carbohydr Polym* 87:1706–1712. <https://doi.org/10.1016/j.carbpol.2011.09.079>
- Montazer M, Allahyarzadeh V (2013) Electroless plating of silver nanoparticles/nanolayer on polyester fabric using AgNO₃/NaOH and ammonia. *Ind Eng Chem Res* 52:8436–8444. <https://doi.org/10.1021/ie400804n>
- Montazer M, Komeily Nia Z (2015) Conductive nylon fabric through in situ synthesis of nano-silver: Preparation and characterization. *Materials Science and Engineering C* 56:341–347. <https://doi.org/10.1016/j.msec.2015.06.044>
- Montazer M, Shamei A, Alimohammadi F (2014) Synthesis of nanosilver on polyamide fabric using silver/ammonia complex. *Materials Science and Engineering C* 38:170–176. <https://doi.org/10.1016/j.msec.2014.01.044>
- Nakhjavani M, Nikkhah V, Sarafraz MM, et al (2017) Green synthesis of silver nanoparticles using green tea leaves: Experimental study on the morphological, rheological and antibacterial behaviour. *Heat and Mass Transfer/Waerme- und Stoffuebertragung* 53:3201–3209. <https://doi.org/10.1007/s00231-017-2065-9>
- Noordeen S, Karthikeyan K, Parveen M a N (2013) Synthesis of Silver Nanoparticles by using Sodium Borohydride as a Reducing Agent. *International Journal of Engineering Research and Technology* 2:388–397
- Nowack B, Krug HF, Height M (2011) 120 years of nanosilver history: Implications for policy makers. *Environ Sci Technol*. <https://doi.org/10.1021/es103316q>
- Onitsuka S, Hamada T, Okamura H (2019) Preparation of antimicrobial gold and silver nanoparticles from tea leaf extracts. *Colloids Surf B Biointerfaces* 173:242–248. <https://doi.org/10.1016/j.colsurfb.2018.09.055>
- Peng H, Liu Y, Peng W, et al (2016) Green synthesis and stability evaluation of Ag nanoparticles using bamboo hemicellulose. *Bioresources* 11:385–399. <https://doi.org/10.15376/biores.11.1.385-399>
- Peng H, Wang N, Zhang J, Yu Z (2011) Synthesis of silver nanoparticles by using bamboo hemicellulose as template in aqueous solution. *Adv Mat Res* 311–313:149–154. <https://doi.org/10.4028/www.scientific.net/AMR.311-313.149>
- Polte J, Tuaeov X, Wuithschick M, et al (2012) Formation mechanism of colloidal silver nanoparticles: Analogies and differences to the growth of gold nanoparticles. *ACS Nano* 6:5791–5802. <https://doi.org/10.1021/nn301724z>
- Rafique M, Sadaf I, Rafique MS, Tahir MB (2017) A review on green synthesis of silver nanoparticles and their applications. *Artif Cells Nanomed Biotechnol* 45:1272–1291. <https://doi.org/10.1080/21691401.2016.1241792>
- Rajendra R, Balakumar C, Ahammed H, et al (2010) Use of zinc oxide nano particles for production of antimicrobial textiles. *International Journal of Engineering, Science and Technology* 2:202–208. <https://doi.org/10.4314/ijest.v2i1.59113>
- Ray PC, Yu H, Fu PP (2009) Toxicity and environmental risks of nanomaterials: challenges and future needs. *J Environ Sci Health C Environ Carcinog Ecotoxicol Rev* 27:1–35. <https://doi.org/10.1080/10590500802708267>

- Rónavári A, Kovács D, Igaz N, et al (2017) Biological activity of green-synthesized silver nanoparticles depends on the applied natural extracts: A comprehensive study. *Int J Nanomedicine* 12:871–883. <https://doi.org/10.2147/IJN.S122842>
- Root W, Aguiló-Aguayo N, Pham T, Bechtold T (2018a) Conductive layers through electroless deposition of copper on woven cellulose lyocell fabrics. *Surf Coat Technol* 348:13–21. <https://doi.org/10.1016/j.surfcoat.2018.05.033>
- Root W, Aguiló-Aguayo N, Pham T, Bechtold T (2018b) Conductive layers through electroless deposition of copper on woven cellulose lyocell fabrics. *Surf Coat Technol* 348:13–21. <https://doi.org/10.1016/j.surfcoat.2018.05.033>
- Sadanand V, Tian H, Rajulu AV, Satyanarayana B (2017) Antibacterial cotton fabric with in situ generated silver nanoparticles by one-step hydrothermal method. *International Journal of Polymer Analysis and Characterization* 22:275–279. <https://doi.org/10.1080/1023666X.2017.1287828>
- Salama A, Abouzeid RE, Owda ME, et al (2021) Cellulose–silver composites materials: Preparation and applications. *Biomolecules* 11
- SCENIHR (2010) Scientific Basis for the Definition of the Term “Nanomaterial.” Directorate General for Health and Consumers - European Commission 1–43. <https://doi.org/10.2772/ND-The>
- Shateri-Khalilabad M, Yazdanshenas ME, Etemadifar A (2017) Fabricating multifunctional silver nanoparticles-coated cotton fabric. *Arabian Journal of Chemistry* 10:S2355–S2362. <https://doi.org/10.1016/j.arabjc.2013.08.013>
- Srikar SK, Giri DD, Pal DB, et al (2016) Green Synthesis of Silver Nanoparticles: A Review. *Green and Sustainable Chemistry*. *Green and Sustainable Chemistry* 6:34–56. <https://doi.org/10.4236/gsc.2016.61004>
- Sun Q, Cai X, Li J, et al (2014a) Green synthesis of silver nanoparticles using tea leaf extract and evaluation of their stability and antibacterial activity. *Colloids Surf A Physicochem Eng Asp* 444:226–231. <https://doi.org/10.1016/j.colsurfa.2013.12.065>
- Sun Q, Cai X, Li J, et al (2014b) Green synthesis of silver nanoparticles using tea leaf extract and evaluation of their stability and antibacterial activity. *Colloids Surf A Physicochem Eng Asp* 444:226–231. <https://doi.org/10.1016/j.colsurfa.2013.12.065>
- Tang B, Kaur J, Sun L, Wang X (2013) Multifunctionalization of cotton through in situ green synthesis of silver nanoparticles. *Cellulose* 20:3053–3065. <https://doi.org/10.1007/s10570-013-0027-z>
- Textor T, Fouda MMG, Mahltig B (2010) Deposition of durable thin silver layers onto polyamides employing a heterogeneous Tollens’ reaction. *Appl Surf Sci* 256:2337–2342. <https://doi.org/10.1016/j.apsusc.2009.10.063>
- Üreyen ME, Doğan A, Koparal AS (2012) Antibacterial functionalization of cotton and polyester fabrics with a finishing agent based on silver-doped calcium phosphate powders. *Textile Research Journal* 82:1731–1742. <https://doi.org/10.1177/0040517512445331>
- van Loon LR, Glaus MA (1998) Experimental and Theoretical Studies on Alkaline Degradation of Cellulose and its Impact on the Sorption of Radionuclides. 37:2002
- Vance ME, Kuiken T, Vejerano EP, et al (2015) Nanotechnology in the real world: Redeveloping the nanomaterial consumer products inventory. *Beilstein Journal of Nanotechnology* 6:1769–1780. <https://doi.org/10.3762/bjnano.6.181>

- Vigneshwaran N, Nachane RP, Balasubramanya RH, Varadarajan P v. (2006) A novel one-pot “green” synthesis of stable silver nanoparticles using soluble starch. *Carbohydr Res* 341:2012–2018. <https://doi.org/10.1016/j.carres.2006.04.042>
- Wibawa PJ, Nur M, Asy’ari M, et al (2021) Green synthesized silver nanoparticles immobilized on activated carbon nanoparticles: Antibacterial activity enhancement study and its application on textiles fabrics. *Molecules* 26:. <https://doi.org/10.3390/molecules26133790>
- Wiseman SA, Balentine DA, Frei B (1997) Antioxidants in tea. *Crit Rev Food Sci Nutr* 37:705–718. <https://doi.org/10.1080/10408399709527798>
- Wojtysiak S, Kudelski A (2012) Influence of oxygen on the process of formation of silver nanoparticles during citrate/borohydride synthesis of silver sols. *Colloids Surf A Physicochem Eng Asp* 410:45–51. <https://doi.org/10.1016/j.colsurfa.2012.06.012>
- Xu Q, Ke X, Ge N, et al (2018) Preparation of Copper Nanoparticles Coated Cotton Fabrics with Durable Antibacterial Properties. *Fibers and Polymers* 19:1004–1013. <https://doi.org/10.1007/s12221-018-8067-5>
- Yuen CWM, Jiang SX, Kan CW, et al (2013) Polyester metallisation with electroless silver plating process. *Fibers and Polymers* 14:82–88. <https://doi.org/10.1007/s12221-013-0082-y>
- Zahran MK, Ahmed HB, El-Rafie MH (2014) Facile size-regulated synthesis of silver nanoparticles using pectin. *Carbohydr Polym* 111:971–978. <https://doi.org/10.1016/j.carbpol.2014.05.028>
- Zhang S, Tang Y, Vlahovic B (2016) A Review on Preparation and Applications of Silver-Containing Nanofibers. *Nanoscale Res Lett* 11:1–8. <https://doi.org/10.1186/s11671-016-1286-z>
- Zhu HW, Gao HL, Zhao HY, et al (2020a) Printable elastic silver nanowire-based conductor for wash-able electronic textiles. *Nano Res* 13:2879–2884. <https://doi.org/10.1007/s12274-020-2947-x>
- Zhu HW, Gao HL, Zhao HY, et al (2020b) Printable elastic silver nanowire-based conductor for wash-able electronic textiles. *Nano Res* 13:2879–2884. <https://doi.org/10.1007/s12274-020-2947-x>

8. Development and validation of a method for the weathering and detachment of representative nanomaterials from conventional silver-containing textiles

David Patch†, Iris Koch†, Derek Peloquin‡‡, Denis O'Carroll†‡, Kela Weber†*

†Environmental Sciences Group, Department of Chemistry and Chemical Engineering, Royal Military College of Canada, Kingston, ON, Canada K7K 7B4.

‡ School of Civil and Environmental Engineering, University of New South Wales, Sydney NSW 2052, Australia

‡‡Oak Ridge Institute for Science and Education, Oak Ridge, Tennessee 37830, USA

* Corresponding Author:

Email: Kela.Weber@rmc.ca

Phone: 613-541-6000 ext. 6610

The authors declare no competing financial interest.

8.1. Abstract

Nanotoxicology research commonly utilizes pristine nanomaterials for toxicity assessment, which may not be perfectly representative of what is released into environmental systems. The goal of the present study was to develop a method to simulate human weathering of silver-containing textiles. To achieve this goal the roles of physical and chemical stress on X-Static® containing athletic textiles were investigated and compared to data collected from human weathering experiments and literature. Chemical weathering methods (artificial sweat) were used independently and alongside physical weathering methods (3D printed stretching and abrasion instruments). Non-weathered control textiles were found to release 29 ± 11 mg Ag/kg of textile into wash water effluent (ICP-MS), with 16% being released as ionic silver (ICP-MS) and the rest as metallic nanomaterials, nanosheets, and particulates of varying size (SEM/XANES). Real and simulated human weathered textiles released similar amounts of total silver (67 ± 11 mg Ag/kg, 84 ± 13 mg Ag/kg respectively) with the silver released being composed of ionic (1.5%, 2%) and a mixture of metallic and chlorinated nanomaterials, nanosheets, and particulates. The method was shown to effectively detach environmentally representative silver materials from silver-containing textiles and can provide such materials for future studies on the assessment of their fate, transport, and toxicity.

8.2. Introduction

Nanotechnological applications have emerged in recent years to take advantage of the unique physio-chemical properties of nanomaterials resulting from their larger surface area-to-volume ratios (Fauss, 2008). Such applications include their incorporation, along with ionic and metallic silver, into commercial products, which introduces new pathways for silver release into the environment to potentially impact numerous receptors (Fabrega et al., 2009; Kessler, 2011; Nowack et al., 2012). At the same time, the potential for increased reactivity of nanomaterials has led to conclusions that materials at the nanoscale cannot be judged using the same safety regulations as their macro-scale counterparts (Health, 2010; Reidy et al., 2013).

Assessing the risk of nanomaterials is often done with commercially available pristine nanomaterials. While this is vital for establishing the overall potential of risk, possible transformations across the life cycle of a commercial product must be considered as the resulting weathered nanomaterials may have different toxicities compared to their pristine counterparts (Mitrano and Nowack, 2017). Nanomaterials can also be incidentally generated following weathering or dissolution and reduction of products containing conventional metal materials (Glover et al., 2011). Therefore, it is important to understand the initial material present on the product as well as the physical and chemical conditions present during the product's life cycle. These factors may influence the release, transport, and transformation of released materials of concern (Mitrano et al., 2015). Textiles have been identified as a commercial product of concern due to the possibility of metal release during laundering and the possibility of transport onto the skin during use (Lorenz et al., 2012; Nowack et al., 2012; Stefaniak et al., 2014). One of the most common metals used with textiles is silver, with manufacturers seeking to take advantage of silver's antibacterial nature (Drexler, 1986).

One of the biggest influences on the release of silver materials from textiles is the initial type of silver present on the product. Whereas nanomaterial-containing textiles were found to typically release silver similar in characteristics to the silver on the textiles (Mitrano et al., 2014), textiles functionalized with conventional metallic silver were found to release ionic silver, incidentally formed silver nanomaterials, and silver micromaterials (Gagnon et al., 2019). X-Static® containing conventional textiles were noted to be particularly concerning as they were found to release high amounts of silver into solution and have the potential for high amounts of release across multiple

washes (Benn and Westerhoff, 2008; Gagnon et al., 2019; Geranio et al., 2009; Lombi et al., 2014; Lorenz et al., 2012; Mitrano et al., 2014; Mitrano et al., 2015a).

The release of silver into a variety of solutions, including deionized (DI) water (Benn and Westerhoff, 2008), tap water (Gagnon et al., 2019; Mackevica et al., 2017), detergent solutions (Lombi et al., 2014; Mitrano et al., 2014; Mitrano et al., 2016b), artificial sweat (Kulthong et al., 2010; von Goetz et al., 2013), artificial urine (Quadros et al., 2013), and artificial saliva (Mackevica et al., 2017) has been investigated. These studies showed that chemical weathering results in substantial changes to the amount, speciation, size/shape, and stability of released silver materials (Benn and Westerhoff, 2008; Levard et al., 2012; Mitrano et al., 2016, 2014; Wagener et al., 2016).

Other possible variables present across the life cycle of silver-containing textiles have also been studied. Specifically, several groups investigated aging through different experimental designs (Ding et al., 2016; Mitrano et al., 2014; Mitrano et al., 2016b, 2015b), revealing that light exposure, temperature, and humidity could influence silver speciation on the textile as well as influence silver speciation once released into wash water.

Von Goetz et al. investigated the influence of physical weathering by simulating human physical weathering using acrylic spheres during exposure to artificial sweat but noted that, without actual human participants, the method could not be assessed for representativeness (von Goetz et al., 2013). Gagnon et al. investigated the release of silver from X-Static® textiles following human use of the textile, establishing that human weathering resulted in a three-fold increase in the amount of silver released compared to non-weathered textiles (Gagnon et al., 2019). Gagnon identified that the released silver was mainly particulate silver, including spherical nanoparticles, nanoplates, and weathered nanomaterials likely being released because of the breakdown of the silver coating on the textile. Gagnon et al. concluded that development of a simulated human weathering method would allow for better insight into the roles of chemical and physical weathering while also allowing for the generation of weathered nanomaterials for ecotoxicity testing, a gap in methodology that has been highlighted by other studies as well (Gao and Lowry, 2018; Mitrano and Nowack, 2017; Nowack and Mitrano, 2018).

The goal of the present study was to develop a method to simulate human weathering of silver-containing textiles. To achieve this goal, the roles of physical and chemical stress on the silver-containing textiles were investigated and compared to data collected from human weathering

experiments and literature. The developed method will allow for the characterization of the release of environmentally relevant contaminants of emerging concern, such as silver, from commercial textiles.

8.3. Materials and Methods

8.3.1. Textile Characterization

Experiments were conducted using a commercially available athletic textile purchased from Lululemon (T.H.E. Sock). This textile was selected because of its previous use in the literature (Benn and Westerhoff, 2008; Gagnon et al., 2019; Mitrano et al., 2014), its high content (3% according to the label) of X-Static® fiber (a well characterized conventional silver-functionalized fiber), and its potential for long-term silver release (Benn and Westerhoff, 2008). The textiles used in the study weighed 21.4 ± 0.9 grams ($n=30$). Whole socks (in triplicate) were used for all trials instead of sub-sections because preliminary findings showed that the silver in the socks was heterogeneously distributed (Figure E1) and that cutting the textiles into subsections resulted in enhanced silver release due to fragmentation of the textile (Table F2).

8.3.2. Physical Weathering Method

To determine the impact of physical weathering on the release of silver into wash water, two physical weathering instruments were constructed. These physical weathering instruments were 3D printed adaptations of standard industry mechanical weathering equipment used in the textile industry (ISO 13934-1:1999 Tensile Properties of Fabric; ASTM D2594-2004 Standard Test for Stretch; ISO 12947-1-1998 Abrasion Test Method for Textiles). The first instrument simulated stretching (physical weathering-stretched), with one end of the textile secured to a fixed location and the other end of the textile clamped to a moving motor arm, which rotated in an elliptical fashion at a rate of 120 RPM for 90 minutes. The second instrument simulated both stretching and abrasion through a walking motion (physical weathering-walked), with a 3D printed human foot (size 11) on which the textiles were worn, placed inside a shoe, and moved with a motor arm at a rate of 120 RPM for 90 minutes (Figure F2). These instruments were 3D printed (Prusa i3 RepRap) using acrylonitrile butadiene styrene (ABS) filament with a 20% infill density. All printed parts were sanded (120 grit) and sealed with an acetone vapour bath before use. All parts in contact with textile material were rinsed with 2% nitric acid to decontaminate equipment between uses.

8.3.3. Chemical Weathering Method

To simulate chemical weathering conditions, artificial sweat was produced (pH 5.5) following the procedure described by Kulthong et al. (Kulthong et al., 2010) (ISO 105-E04 protocol for color fastness testing) (chemical weathering conditions). Approximately 27 g of artificial sweat solution was loaded onto textiles. This loading was achieved by pipetting 18 g of artificial sweat onto the top of the sock and 9 g onto the bottom of the sock to mimic release amounts and release locations found by Smith et al (Smith, 2013) who examined sweating rates and distribution on the human foot. The 27 grams of sweat utilized in this study was based on male secretion rates, as Smith et al. (2013) identified that male participants secreted more than twice the amount of sweat than compared to female participants. It was noted during loading that this was likely close to the saturation limit of the textiles, which were fully soaked but not dripping. Following chemical weathering for one hour, the textiles were removed, placed in individual open plastic bags to dry for 24 hours, and then washed.

8.3.4. Combined Physical and Chemical Weathering Method

The simulated human weathering of textiles method involved chemical weathering of the textiles first, as described in the chemical weathering method with no drying, followed immediately by one of the two physical weathering methods as described in the physical weathering method. This was done to develop two different simulated human weathering methods, one focused on stretching (chemical/physical weathering-stretched) and one focused on stretching and abrasion (chemical /physical weathering-walked).

8.3.5. Human Weathering Method

Human weathering experiments performed by Gagnon et al. (Gagnon et al., 2019) were replicated, with one male participant wearing the textiles over a period of 4 days. Skin on the bottom of the foot was sampled after the four-day period by using Kapton® tape to remove any materials of interest for analysis.

8.3.6. Standard Wash Method

Following the artificial weathering method, textiles were washed using a modified version of ISO 105-C06. The modifications included the use of acrylic spheres (one-inch diameter) and 2L HDPE (high density polyethylene) bottles to avoid silver present in stainless steel washing machines. Additional information can be found in the supporting information (SI).

8.3.7. Standard Analytical Suite

The analytical techniques used in this study represent many of the techniques used previously in the literature (Gagnon et al., 2019). Total concentrations of silver released into wash water media were determined using inductively coupled plasma mass spectrometry (ICP-MS); size distribution of released silver was measured using filtration/ ICP-MS (5 μm , 0.45 μm , 0.22 μm , 10 kDa) and single-particle ICP-MS (spICP-MS); silver materials were imaged both on the textile and released into wash water media using scanning electron microscopy with energy dispersive x-ray fluorescence (SEM/EDX); and speciation of silver materials was determined on both the textile and released into wash water media using X-ray absorption near-edge structure (XANES) analysis. It is important to note that silver nanomaterials have been found to stick to filter material due to sorption effects. This may cause the largest size fraction of silver reported (>5000 μm) to be over-estimated, and the smaller size fractions of silver reported (<5000 μm) to be under-estimated. Ionic and 100 nm silver positive control samples showed >90% recovery when passed through all filter materials individually, but these may not be appropriate surrogates for tracking potential loss of environmentally relevant weathered materials, where minor sorptive losses may compound across serial size fraction filtering. This potential loss due to filtering does not affect the total concentration of silver reported, however, as this was analyzed without filtering. XANES analysis was performed at the Advanced Photon Source using beamlines at CLS@APS and the Materials Research Collaborative Access Team (MRCAT). Details, QA/QC and additional information can be found in the SI.

8.3.8. Single Particle Analysis

spICP-MS was used to determine nanomaterial distribution in the released wash water with a method cut-off of ~60 nm due to the presence of ionic silver and instrument limitations. To perform these measurements, unfiltered wash water was diluted by a factor of up to 100,000x and introduced through a Meinhardt concentric nebulizer into a cyclonic spray chamber attached to the ICP-MS at a rate of 0.8 mL/min. The ELAN DRC II does not have an established spICP-MS mode so a method was established to collect transient signal data over a 60 second run by setting the number of replicates per run to one and the number of readings per replicate to 6000, with a 10 ms dwell time and 0 ms settling time. Data was collected in a separate CSV file for each sample which was then processed using the single particle calculation tool (SPC, version 2) developed by the

Institute of Food Safety (RIKILT), Netherlands. More information on the single particle method employed can be found elsewhere (Gagnon et al. 2019).

8.4. Results and Discussion

To allow for the development of a simulated human weathering method the contributions of physical and chemical weathering were first explored independently, then combined (chemical, followed by physical, then chemical/physical together). These results were compared with non-weathered control textiles to allow for reference to literature (Mitrano et al., 2014). Results were then compared with human weathering data from literature and the human weathering experiment in the present study.

8.4.1. No Weathering (Control)

SEM analysis of the control textile after washing (Figure 8.1A, F5) shows the X-Static® fiber (thicker, rough coated surface) woven throughout the bulk fabric. Small holes (<5 µm in length) can be seen on the surface of the fiber, which are likely the result of imperfections during manufacturing or release during washing. An EDX image overlay (Figure F6C) and spectrum analysis (Figure 8.1A, F6D) revealed no elements of interest above the detection limits of the EDX method other than silver (chloride concentration reported as 0.00%). XANES analysis also confirmed that the bulk speciation of silver on the textile is mainly elemental silver with smaller proportions of silver oxide (<21%) (Table F3). The silver oxide is likely the result of ionic silver present on the textile after washing and oxidizing during drying. SEM analysis was also performed on a separate textile before washing (Figure F5) showing similar surface morphology and lack of large holes/cracks.

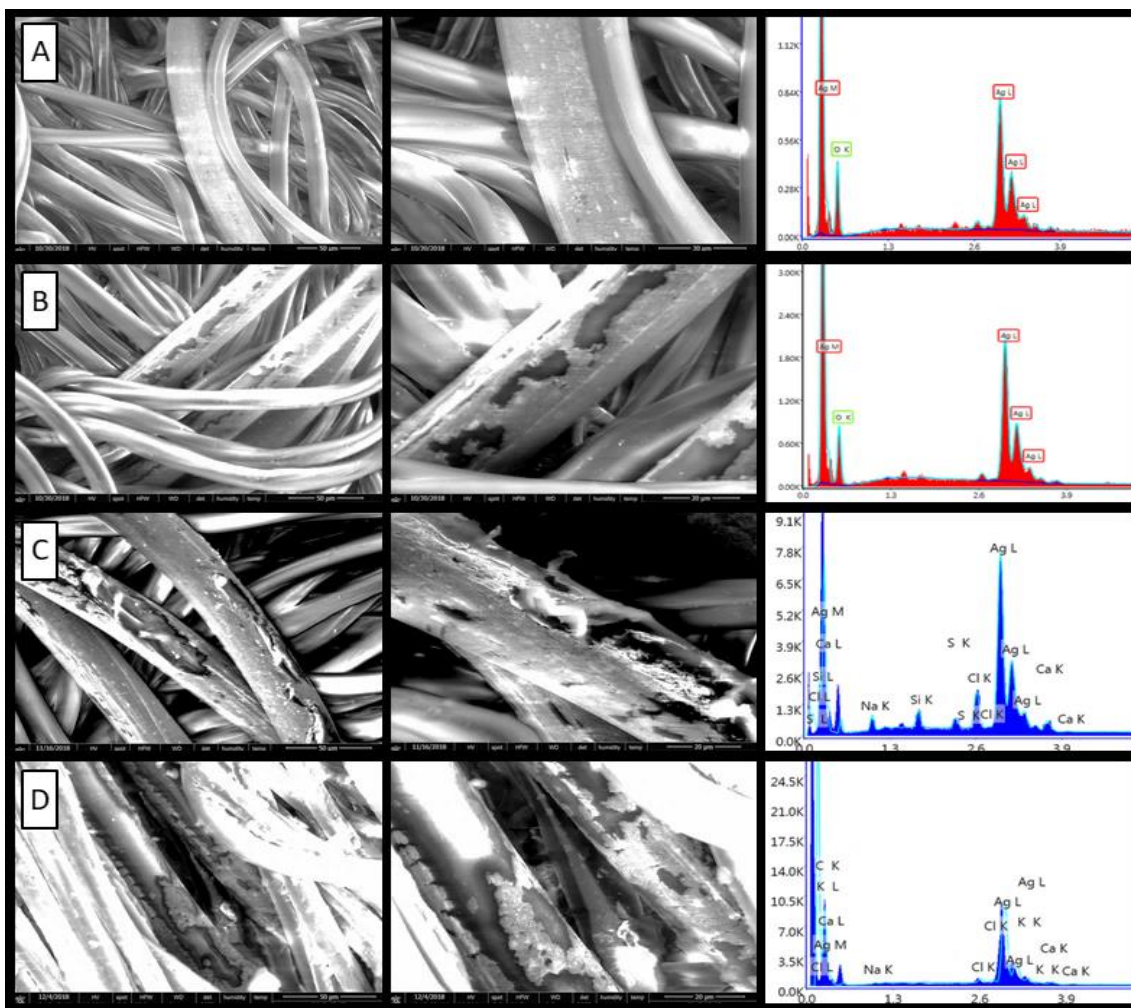


Figure 8.1 – SEM imaging of the X-Static® silver coated fiber in the athletic textile following: (A) no chemical/physical weathering after washing; (B) PhW-W after washing; (C) CW/PhW-W; and (D) human weathering before washing.

The control textiles were found to release 29 ± 11 mg Ag/kg of textile into wash water effluent, which is comparable to released concentrations observed in the literature for similar textiles that were not subjected to weathering (Gagnon et al., 2019; Mitrano et al., 2014). The released silver was 16% ionic, with the remainder a mixture of nanomaterials (Figure 8.2, 8.3) and elemental silver materials of various sizes, as shown by size fractionation results, spICP-MS, and SEM (Figure 2, 3, 4, F13, F14 Table F4).

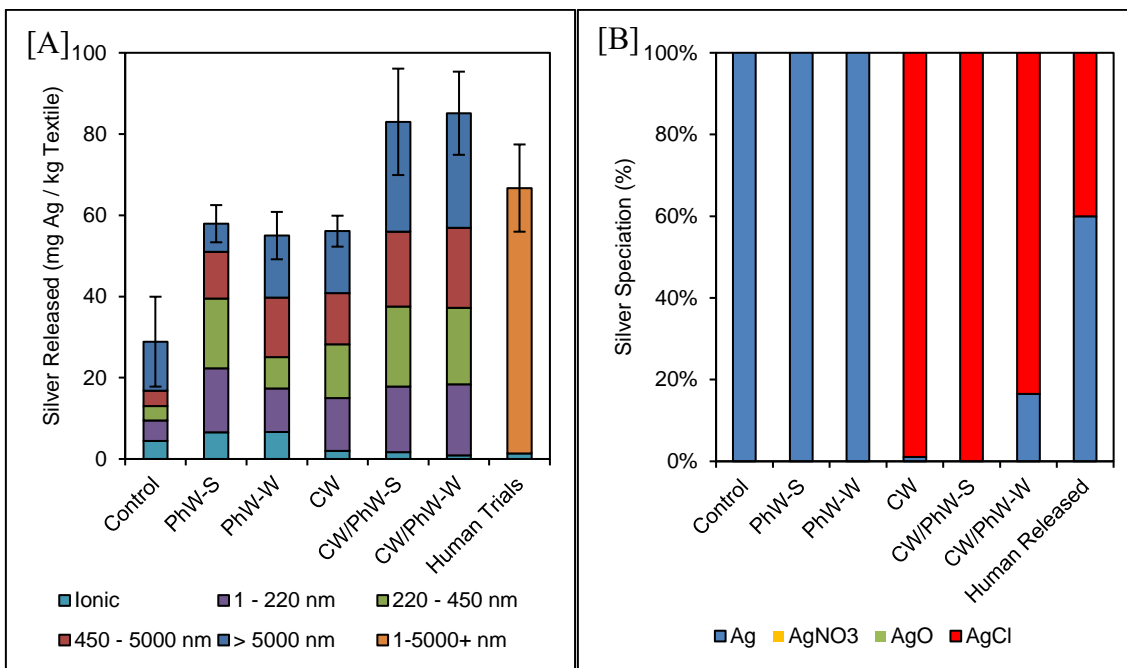


Figure 8.2 – Total concentration, size distribution (A) and speciation (B) of released silver after various weathering methods, with Ag being elemental silver. Human trial data in the left figure was obtained from literature (Gagnon et al., 2019) and only distinguished particulate and ionic silver. (Control = no weathering; PhW-S = physical weathering with stretching; PhW-W = physical weathering with simulated walking; CW = chemical weathering; Human Trials = human release from literature).

Single particle analysis of the conventional silver-containing textiles revealed the presence of incidentally generated silver nanoparticles. The majority of the nanoparticles measured were between 60 and 100 nm in diameter, with some larger particles being measured up to 190 nm in size (Figure 8.3). Other authors in the literature have discussed discrepancies when comparing size distribution data collected from filtering and from spICP-MS, which can be seen in this study. Possible reasons for discrepancies include the difficulty in spICP-MS in differentiating between smaller spherical nanoparticles, larger nanoplates, or nanoparticles of heterogenous chemical composition. It is also possible that these larger particles may settle out of solution through various physical phenomena before introduction into the ICP-MS. The limitations of spICP-MS in general, the limitations of the instrument used in this study for spICP-MS and the characteristics of the released silver suggest that SEM imaging may be a more informative determination of size and shape of the released materials.

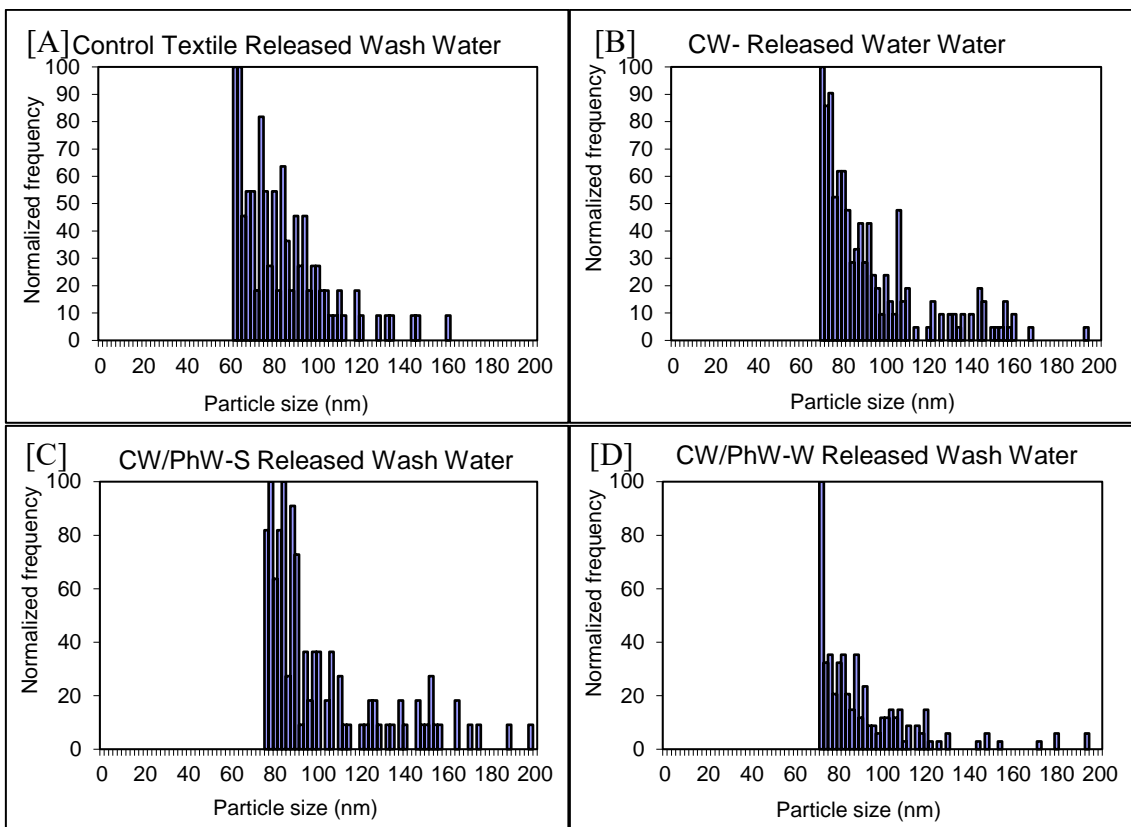


Figure 8.3 – Single particle analysis of released wash water from a ‘control’ textile (A) (no sweat, no weathering) compared to released wash water following sweat exposure (B) and combined chemical/physical weathering (C, D) treatments.

8.4.2. Physical Weathering

By comparing the SEM imaging of the physically weathered textile (Figure 8.1B, F6) to the control textile, it is apparent that physical weathering results in fragmentation of the silver coating, creating large holes of missing silver (approximately 10–50 μm long, up to 10 μm wide). Similar to the control, XANES analysis determined the elemental composition of the textiles to be mainly elemental silver with small amounts of silver oxide (Table F3).

Physical weathering resulted in an increased amount of released silver compared to the control with 58 ± 5 mg Ag/kg textile released following stretching (Physical weathering-stretched) and 55 ± 6 mg Ag/kg textile following artificial walking (Physical weathering-walked) (Tukey, $P < 0.05$) (Figure 8.1). No significant differences were observed in total silver released between the two physical weathering methods or in the percentage of ionic silver released (Tukey, $P > 0.05$) between the control, physical weathering-stretched, and physical weathering-walked experiments. The

released silver materials were of elemental chemical composition and consisted of spherical nanomaterials, nanosheets, and particulates (Figure 8.2, 8.3, 8.4, F12, F13, Table F4).

8.4.3. Chemical Weathering

In contrast to the physical weathering textiles, the SEM imaging of the chemically weathered textile (Figure F7) shows an intact surface, similar to that found in the non-weathered control textile. However, the EDX overlay and spectra analysis confirm co-location of silver and chloride (chloride concentration 0.11%, Cl:Ag ratio 0.0046), which is consistent with a chemical reaction of chloride from the artificial sweat with dissolved ionic silver, likely from the surface of the textile. Despite the EDX overlay showing co-location of silver and chloride, XANES analysis identified the bulk speciation of the textile to be mainly elemental silver with smaller proportions of silver oxide. This suggests that the silver chloride formation shown by EDX is a surface coating, with the majority of the silver still existing as elemental silver (Table F3).

Chemical weathering resulted in a significantly higher amount of released silver (56 ± 4 mg Ag/kg textile) compared to the control (Tukey, $P < 0.05$) (Figure 8.1), but similar amounts compared with physical weathering trials. A significant decrease in the percent of ionic silver was found in the released wash water (3.6%) compared to control and physical weathering (Tukey, $P < 0.05$). This decrease is hypothesized to be attributable to the precipitation of the chloride in the artificial sweat with the silver ions in solution. The released silver materials are of similar size and shape to the materials released by the control trials (Figure 8.2, S2, Table F4), but are primarily composed of silver chloride instead of elemental silver (Figure 8.2, 4).

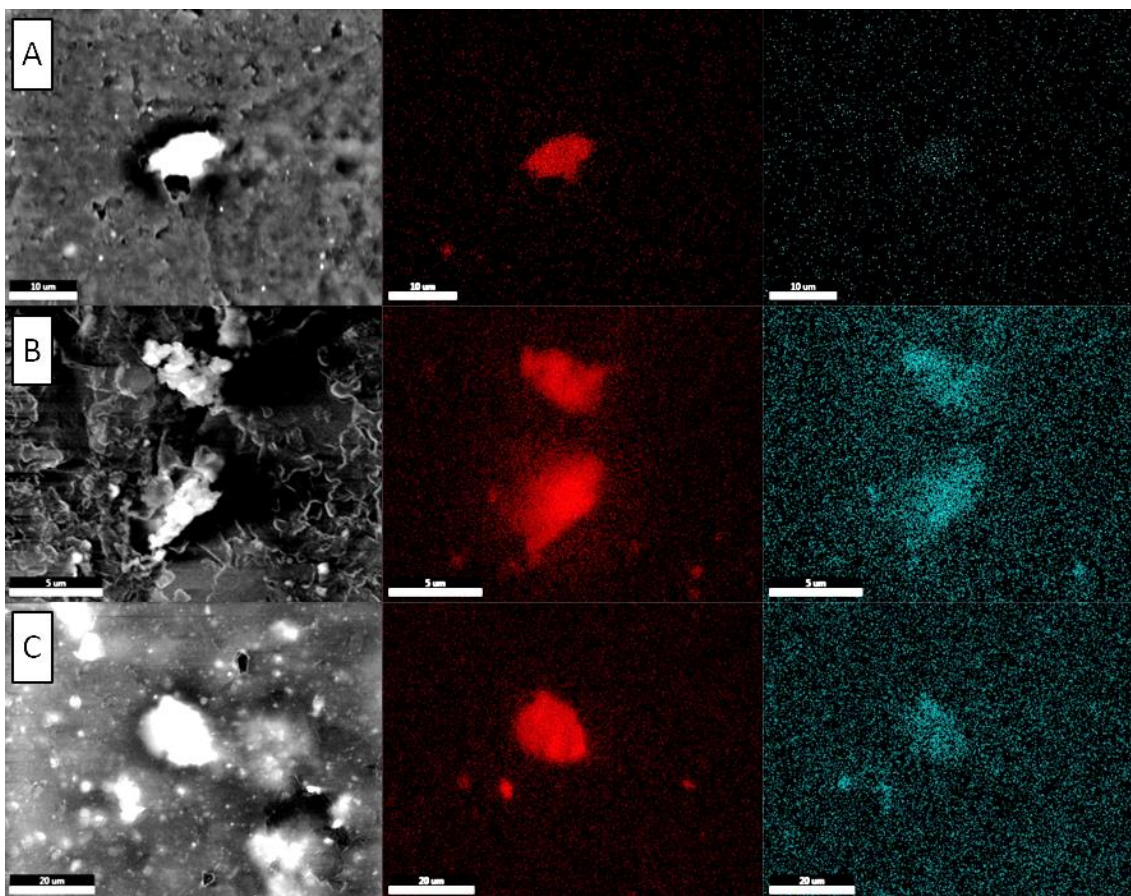


Figure 8.4 – SEM imaging of released silver particles from: (A) a control textile; (B) a CW/PhW-W textile; and (C) a human-weathered textile (C). SEM imaging (left-most panels) shows large micron-sized silver plates surrounded by smaller spherical nanomaterials. EDX overlay shows silver (red, middle panels) and chloride (blue, right-most panels) co-location.

8.4.4. Combined Chemical/Physical Weathering

Imaging of the chemical /physical weathered textiles after washing (Figure 8.1C, S7) shows holes of missing silver and damage to the underlying nylon fiber. The holes are similar in size and shape to those observed in physical weathering trials, supporting the hypothesis that physical weathering is causing the surface deformations. The EDX overlay (Figure F9) also reveals the presence of chloride co-located with the silver on the textile (chloride concentration 1.32%, Cl:Ag ratio 0.0145), as was observed in the chemical weathering trials. The higher percentage of chloride present on the chemicalphysical weathered textiles compared to the chemical weathering-weathered textile is likely due to the enhanced surface area caused by physical weathering, allowing for more surface chlorination to occur. As was the case with the chemical weathering,

XANES analysis indicated that the bulk silver speciation of silver on the textile is elemental silver and silver oxide.

The deformation of the nylon fiber suggests that physical wearing could release microplastic material that is still coated with silver. These silver-coated microplastics could pose a unique toxic exposure pathway to aquatic organisms, as these materials have the toxicological characteristics of both microplastics and silver. These types of particles have not yet been reported in the literature, but the shedding of synthetic polymer fibers from textiles following varying degrees of weathering has been quantified (Carney Almroth et al., 2018; de Falco et al., 2019), indicating it is possible for silver-containing textiles to release silver-containing microfibers into the environment.

Combining physical weathering with chemical weathering results in an increase of the silver release concentrations to 83 ± 13 mg Ag/kg textile for stretching (physical weathering-stretched/chemical weathering) and 85 ± 10 mg Ag/kg textile for artificial walking (physical weathering-walked/chemical weathering) (Figure 8.1). The amount of silver released is significantly higher than the control, physical weathering, and chemical weathering trials (Tukey, $P < 0.05$). As was observed in the chemical weathering trials, the percent of ionic silver released into the wash water ($\sim 1.5\%$) was significantly lower than control and physical weathering wash waters (Tukey, $P < 0.05$). The released silver materials are similar in size/shape (size distribution, particle shape) to that for the materials released by the control trials (Figure 8.2, 8.3, 8.4, F2, Table F4), but are composed of a mixture of elemental silver and silver chloride (Figure 8.2, 8.4).

8.4.5. Comparison to Human Weathering

As was the case with the other textile trials, the speciation of silver on the human weathered textile was found to be mainly elemental silver, with small amounts of silver oxide. SEM images of the human-worn textile prior to washing showed holes of missing silver, similar to those observed in the physically weathered textiles (Figures 8.1D, S8). Co-location of silver and chloride (chloride concentration 1.06%, Cl:Ag ratio 0.0315) was also seen, similar to the chemical weathering textiles. Up to this point it was hypothesized that physical weathering was responsible for loosening the silver-coated surface, which was then removed upon washing. However, observations of removed silver in human weathered textiles prior to washing (as evidenced by the holes) suggests that silver could be migrating off the textile during use, possibly onto skin. SEM images of post-wash human-worn textiles were similar to unwashed textiles, except for the absence of the foreign media (skin, dirt, etc.) seen in the unwashed textile (Figure F10). To further investigate the observations of removed silver before washing, a set of chemical /physical weathered-walked

textiles were prepared and analyzed with SEM before washing. SEM analysis showed holes similar to those found in physical weathering and human trials as well as the co-location of silver and chloride (chloride concentration 1.30%, Cl:Ag 0.0335), like in human weathering trials. This observation of holes before laundering (Figure F11A) supports the hypothesis that silver can migrate from the fiber to another location (skin, inside of a shoe, etc) before washing.

To investigate the fate of the silver missing from the holes, XANES analysis was also performed on Kapton® tape that had been placed on the bottom of the human foot immediately after the textile was removed, following walking (human weathering). Trace amounts of elemental silver were found on the Kapton® tape, confirming that silver materials can migrate from silver-functionalized textiles to human skin.

When comparisons were made to total silver release for actual human use of the same textile from literature (67 ± 11 mg Ag/kg of textile (Gagnon et al., 2019)), statistically similar release was seen in the presence of physical weathering, chemical weathering, and the combined chemical /physical weathering conditions (Tukey, $P > 0.05$) (Gagnon et al., 2019). All trials involving chemical weathering produced percent ionic silver quantities that were statistically indistinguishable from the percent ionic silver seen in the human trial, whereas the control and physical weathering-alone experiments produced ionic silver proportions that were statistically different (Tukey, $P < 0.05$) (Figure 8.2). Particles released from human weathering were a mixture of elemental silver and silver chloride (Figure 8.3), most similar to those released from the chemical /physical weathering trial. SEM analysis also showed the co-location of silver and chloride (chloride concentration 6.12%, Cl:Ag ratio 0.126) (Figure 8.4).

The size distribution analysis (Figure 8.2,(Gagnon et al., 2019)) and SEM imaging of the released silver (Figure 8.4, Table F4) shows silver is released in a wide variety of sizes, including ionic silver, spherical nanoparticles, flat nanoplates, and particulates with sizes up to and larger than 5000 nm in one or more dimensions (ICP-MS, SEM) (Gagnon et al., 2019). It is important to note that due to limitations of SEM it was difficult to identify the thickness of all imaged materials, and particle thickness for materials could only be determined from a small subset of ‘curled’ or angled particles. This variable size distribution has also been observed by others (Gagnon et al., 2019; Mitrano et al., 2014). Such wide variations in size distribution reinforce the idea that silver entering the environment from human weathering of commercial products is different from the type of silver used in nanomaterial exposure research, which is less than 100 nm and of uniform size

distribution(Reidy et al., 2013). In the present study less than 50% of the released silver (by mass) is smaller than 450 nm, with measurements by spICP-MS and SEM indicating the presence of nanoparticles less than 100 nm in diameter.

The concentration, particle size/shape, elemental composition, and coating of the silver released from textiles following human weathering most closely matches the silver released following the chemical /physical weathering-walked method, providing further agreement between simulated and actual human weathering.

8.4.6.Characterization Results and Mechanism

The combined results across all the trials for this study (Table 1) allow for side-by-side comparison of the roles that physical, chemical, combined physical chemical, and human weathering play on the total silver release, ionic silver release, textile coating, and released silver speciation. The size/shape of released silver materials was found to be similar across all trials (a mix of spherical nanoparticles, nanoplates, irregular nanomaterials, and other particulates) and was not included in the summary.

Table 8.1 – Summary of results from various complementary analytical techniques. A, B, C superscripts used to denote statistically different groups, Tukey $P < 0.05$. (Control = no weathering; PhW = average physical weathering; CW = chemical weathering; Human weathering = human release rates from literature (Gagnon et al., 2019))

Trial Name	Total Silver Released (mg Ag/kg textile)	Ionic Silver Released (% , mg Ag/kg textile)	Textile Coating	Released Silver Speciation
Control	29±11 ^B	16 ^A , 4.5	Intact, metallic silver	Metallic
PhW	56±6 ^B	12 ^A , 6.6	Holes, metallic silver	Metallic
CW	56±4 ^B	3.6 ^B , 2.0	Intact, surface chlorination	Mixture of AgCl, Ag ⁽⁰⁾
CW/PhW	84±12 ^C	1.5 ^B , 1.3	Holes, surface chlorination	Mixture of AgCl, Ag ⁽⁰⁾
Human weathering	67±11 ^{BC}	2.0 ^B , 1.3	Holes, surface chlorination	Mixture of AgCl, Ag ⁽⁰⁾

The present study is the first to characterize silver materials released from textiles following human use with SEM and XANES; it builds on the sole previous experiment to investigate human weathering of conventional silver textiles (Gagnon et al., 2019). The present study significantly augments the previous characterization of released silver (nano)materials to highlight the heterogeneous distribution of the released particles, which includes large micrometer silver materials, large silver nanoplates, incidentally generated nanomaterials, and silver potentially attached to microplastics weathered from the textile itself. The released silver following human use of X-Static® containing textiles is a mixture of silver chloride and metallic silver, with small percentages (~2%) of ionic silver.

This study reveals the roles that physical weathering and chemical weathering play separately and together during the use of the textile, allowing for insights into the mechanism of silver released from conventionally functionalized textiles. It is theorized that the release of silver with no weathering is based on dissolution of the metallic silver surface to silver ions. It is possible that silver-containing microplastics could contribute to the release of silver, but identification of these materials was outside the scope of the current study. Physical weathering enhances release by fragmenting the silver coating and increasing the degradation of the textile itself, resulting in more silver and potentially silver-containing microplastics entering the wash water. The chemical weathering mechanisms enhancing release are thought to be the provision of a solution to allow for dissolution, and the subsequent addition of chloride in the artificial sweat, as has been suggested in literature (Spielman-Sun et al., 2018). Specifically, the chloride ions in the sweat react with ionic

silver close to the surface of the silver-coated fibers, forming silver-chloride complexes and driving more dissolution to occur (Gagnon et al., 2019). The combination of physical and chemical weathering is seen as the additive result of both physical and chemical dissolution-based release. By comparing all the trials to the human weathering results it can be demonstrated that combined chemical/physical weathering best simulates human weathering with similar total silver releases, ionic silver releases, released silver size/shape, textile coating, and released silver speciation.

8.5. Conclusion

This study was successful in the development of a method simulating the human weathering of textiles, which results in textile and released silver characteristics like those found following human weathering. This method achieved these results in 90 minutes of continuous action compared to the four days the textiles were worn by humans (Gagnon et al., 2019). This study has identified that human worn silver-containing textiles can release silver before laundering, which could be deposited away from the textile, specifically onto the skin of the foot or to the insides of shoes.

The described method requires minimal resources to implement and can be used to investigate the release of silver materials or other contaminants of emerging concern from textiles including copper, titanium and microplastics. This method generates silver released from textiles (combined ionic, nanomaterial, particulate) that can be used to support ecotoxicology and transport assessments by providing environmentally representative materials.

Given the large amount of silver released from X-Static® containing textiles compared to nanosilver-textiles in the literature, future work would benefit from applying these methods to engineered nanosilver-textiles. These engineered nanosilver textiles release nanomaterials already present on the textile, and not incidentally as was identified in this study (Mitrano et al., 2014). Future work would also benefit from investigating the impact of multiple wearing/washing cycles on the release characteristics of silver from textiles, the potential of silver-doped microplastic generation, and the transport of silver onto the skin of human wearers.

8.6. Acknowledgements

The authors would like to acknowledge Dr. Vincent Gagnon for experimental design input, Dr. Mark Button and Dr. Michelle Nearing for technical input; Sophie Maynard, Kendra Bucholtz, Sarah Denford, Chris Folkins, and Tyler Buote for assistance with experiments; Clarence McEwen for help with development of experimental equipment; and Anbareen Farooq for artificial weathering input. The authors would also like to acknowledge Dr. Jennifer Snelgrove for training and assistance with SEM-EDX work. This research used resources of the Advanced Photon Source, an Office of Science User Facility operated for the U.S. Department of Energy (DOE) Office of Science by Argonne National Laboratory and was supported by the U.S. DOE under Contract No. DE-AC02-06CH11357, the Canadian Light Source and its funding partners (Sector 20 work), and DOE and MRCAT member institutions (Sector 10). We would like to thank Zou Finrock and Debora Motta Meira, beamline scientists at Sector 20, for their support during the experiment. We are deeply grateful to Enzo Lombi (University of South Australia) for his expertise in interpreting silver spectra, and for sharing silver standards data with us for comparison purposes. Lastly the authors would like to acknowledge Environment Canada, Golder Associates, and the National Institute for Standards and Technology.

8.7. References

- Benn, T.M., Westerhoff, P., 2008. Nanoparticle silver released into water from commercially available sock fabrics. *Environmental Science and Technology*. <https://doi.org/10.1021/es7032718>
- Carney Almroth, B.M., Åström, L., Roslund, S., Petersson, H., Johansson, M., Persson, N.K., 2018. Quantifying shedding of synthetic fibers from textiles; a source of microplastics released into the environment. *Environmental Science and Pollution Research* 25, 1191–1199. <https://doi.org/10.1007/s11356-017-0528-7>
- de Falco, F., di Pace, E., Cocca, M., Avella, M., 2019. The contribution of washing processes of synthetic clothes to microplastic pollution. *Scientific Reports* 9, 1–11. <https://doi.org/10.1038/s41598-019-43023-x>
- Ding, D., Chen, L., Dong, S., Cai, H., Chen, J., Jiang, C., Cai, T., 2016. Natural ageing process accelerates the release of Ag from functional textile in various exposure scenarios. *Scientific Reports* 6, 37314. <https://doi.org/10.1038/srep37314>
- Drexler, E., 1986. The coming era of nanotechnology.
- Fabrega, J., Renshaw, J.C., Lead, J.R., 2009. Interactions of silver nanoparticles with *Pseudomonas putida* biofilms. *Environmental Science and Technology* 43, 9004–9009. <https://doi.org/10.1021/es901706j>
- Fauss, E., 2008. The Silver Nanotechnology Commercial Inventory.
- Gagnon, V., Button, M., Boparai, H.K., Nearing, M., O'Carroll, D.M., Weber, K.P., 2019. Influence of realistic wearing on the morphology and release of silver nanomaterials from textiles. *Environmental Science: Nano*. <https://doi.org/10.1039/C8EN00803E>
- Gao, X., Lowry, G. v., 2018. Progress towards standardized and validated characterizations for measuring physicochemical properties of manufactured nanomaterials relevant to nano health and safety risks. *NanoImpact* 9, 14–30. <https://doi.org/10.1016/J.IMPACT.2017.09.002>
- Geranio, L., Heuberger, M., Nowack, B., 2009. The behavior of silver nanotextiles during washing. *Environmental Science and Technology* 43, 8113–8118. <https://doi.org/10.1021/es9018332>
- Glover, R.D., Miller, J.M., Hutchison, J.E., 2011. Generation of metal nanoparticles from silver and copper objects: Nanoparticle dynamics on surfaces and potential sources of nanoparticles in the environment. *ACS Nano* 5, 8950–8957. <https://doi.org/10.1021/nn2031319>
- Health, N.I., 2010. Risks Scientific Basis for the Definition of the Term “Nanomaterial” 1–43. <https://doi.org/10.2772/ND-The>
- Kessler, R., 2011. Engineered nanoparticles in consumer products: understanding a new ingredient. *Environmental health perspectives* 119. <https://doi.org/10.1289/ehp.119-a120>
- Kulthong, K., Srisung, S., Boonpavanitchakul, K., Kangwansupamonkon, W., Maniratanachote, R., 2010. Determination of silver nanoparticle release from antibacterial fabrics into artificial sweat. *Particle and Fibre Toxicology* 7. <https://doi.org/10.1186/1743-8977-7-8>
- Levard, C., Hotze, E.M., Lowry, G. v., Brown, G.E., 2012. Environmental transformations of silver nanoparticles: Impact on stability and toxicity. *Environmental Science and Technology*. <https://doi.org/10.1021/es2037405>
- Lombi, E., Donner, E., Scheckel, K.G., Sekine, R., Lorenz, C., Goetz, N. von, Nowack, B., 2014. Silver speciation and release in commercial antimicrobial textiles as influenced by washing. *Chemosphere*. <https://doi.org/10.1016/j.chemosphere.2014.03.116>

- Lorenz, C., Windler, L., von Goetz, N., Lehmann, R.P., Schuppler, M., Hungerbühler, K., Heuberger, M., Nowack, B., 2012. Characterization of silver release from commercially available functional (nano)textiles. *Chemosphere*. <https://doi.org/10.1016/j.chemosphere.2012.04.063>
- Mackevica, A., Olsson, M.E., Hansen, S.F., 2017. The release of silver nanoparticles from commercial toothbrushes. *Journal of Hazardous Materials*. <https://doi.org/10.1016/j.jhazmat.2016.03.067>
- Mitrano, D.M., Arroyo Rojas Dasilva, Y., Nowack, B., 2015a. Effect of Variations of Washing Solution Chemistry on Nanomaterial Physicochemical Changes in the Laundry Cycle. *Environmental Science and Technology*. <https://doi.org/10.1021/acs.est.5b02262>
- Mitrano, D.M., Limpiteprakan, P., Babel, S., Nowack, B., 2016a. Durability of nano-enhanced textiles through the life cycle: Releases from landfilling after washing. *Environmental Science: Nano* 3, 375–387. <https://doi.org/10.1039/c6en00023a>
- Mitrano, D.M., Limpiteprakan, P., Babel, S., Nowack, B., 2014. Durability of Nanoparticles. <https://doi.org/10.1039/c6en00023a>
- Mitrano, D.M., Lombi, E., Dasilva, Y.A.R., Nowack, B., 2016b. Unraveling the Complexity in the Aging of Nanoenhanced Textiles: A Comprehensive Sequential Study on the Effects of Sunlight and Washing on Silver Nanoparticles. *Environmental Science and Technology* 50, 5790–5799. <https://doi.org/10.1021/acs.est.6b01478>
- Mitrano, D.M., Motellier, S., Clavaguera, S., Nowack, B., 2015b. Review of nanomaterial aging and transformations through the life cycle of nano-enhanced products. *Environment International* 77, 132–147. <https://doi.org/10.1016/j.envint.2015.01.013>
- Mitrano, D.M., Nowack, B., 2017. The need for a life cycle based aging paradigm for nanomaterials: Importance of real-world test systems to identify realistic particle transformations. *Nanotechnology* 28, 1–23. <https://doi.org/10.1088/1361-6528/28/7/072001>
- Mitrano, D.M., Ranville, J.F., Bednar, A., Kazor, K., Hering, A.S., Higgins, C.P., n.d. Tracking dissolution of silver nanoparticles at environmentally relevant concentrations in laboratory, natural, and processed waters using single particle ICP-MS (spICP-MS). <https://doi.org/10.1039/c3en00108c>
- Mitrano, D.M., Rimmelé, E., Wichser, A., Erni, R., Height, M., Nowack, B., 2014. Presence of nanoparticles in wash water from conventional silver and nano-silver textiles. *ACS Nano* 8, 7208–7219. <https://doi.org/10.1021/nn502228w>
- Nowack, B., Mitrano, D.M., 2018. Procedures for the production and use of synthetically aged and product released nanomaterials for further environmental and ecotoxicity testing. *NanoImpact* 10, 70–80. <https://doi.org/10.1016/j.impact.2017.12.001>
- Nowack, B., Ranville, J.F., Diamond, S., Gallego-Urrea, J.A., Metcalfe, C., Rose, J., Horne, N., Koelmans, A.A., Klaine, S.J., 2012. Potential scenarios for nanomaterial release and subsequent alteration in the environment. *Environmental Toxicology and Chemistry*. <https://doi.org/10.1002/etc.726>
- Quadros, M.E., Pierson, R., Tolve, N.S., Willis, R., Rogers, K., Thomas, T.A., Marr, L.C., 2013. Re-lease of silver from nanotechnology-based consumer products for children. *Environmental Science and Technology*. <https://doi.org/10.1021/es4015844>
- Reidy, B., Haase, A., Luch, A., Dawson, K.A., Lynch, I., 2013. Mechanisms of silver nanoparticle re-lease, transformation and toxicity: A critical review of current knowledge and recommendations for future studies and applications. *Materials* 6, 2295–2350. <https://doi.org/10.3390/ma6062295>

Smith, C., 2013. Institutional Repository Design data for footwear: sweating distribution on the human foot. This item was submitted to Loughborough's Institutional Repository (<https://dspace.lboro.ac.uk/>) by the author and is made available under the. *Int. J. Clothing Science and Technology* 25, 43–58.

Spielman-Sun, E., Zaikova, T., Dankovich, T., Yun, J., Ryan, M., Hutchison, J.E., Lowry, G. v., 2018. Effect of silver concentration and chemical transformations on release and antibacterial efficacy in silver-containing textiles. *NanoImpact* 11, 51–57. <https://doi.org/10.1016/j.impact.2018.02.002>

Stefaniak, A.B., Duling, M.G., Lawrence, R.B., Thomas, T.A., LeBouf, R.F., Wade, E.E., Abbas Virji, M., 2014. Dermal exposure potential from textiles that contain silver nanoparticles. *International Journal of Occupational and Environmental Health* 20, 220–234. <https://doi.org/10.1179/2049396714Y.0000000070>

von Goetz, N., Lorenz, C., Windler, L., Nowack, B., Heuberger, M., Hungerbühler, K., 2013. Migration of Ag- and TiO₂- (nano)particles from textiles into artificial sweat under physical stress: Experiments and exposure modeling. *Environmental Science and Technology*. <https://doi.org/10.1021/es304329w>

Wagener, S., Dommershausen, N., Jungnickel, H., Laux, P., Mitrano, D., Nowack, B., Schneider, G., Luch, A., 2016. Textile Functionalization and Its Effects on the Release of Silver Nanoparticles in-to Artificial Sweat. *Environmental Science and Technology*. <https://doi.org/10.1021/acs.est.5b06137>

9. Conclusions and Recommendations

9.1. High Level Conclusions of Current Work

This thesis details the development of robust analytical methodologies to comprehensively characterize two types of emerging contaminants, PFAS and nanomaterials, present in commercial and industrial products. For PFAS, this work was focused on the development of chemical assays to achieve oxidative and reductive conversion of PFAS (known and unknown) to quantifiable end products. These assays were further optimized to work in tandem and supported with high resolution mass spectrometric analysis to provide insights into the identity of different ‘unknown’ PFAS compounds. For nanomaterials, this work was focused on the development of a complementary analytical workflow used for the comprehensive characterization of metal nanomaterials. This work was further supported by the development of a method to simulate human use of textiles, which allowed for the generation of released metal nanomaterials characteristically similar to those released by real human use.

The overarching goal of this thesis was to address the large methodological gap between what can be analyzed using standard, available methods, and what is present in commercial and industrial products. The results presented herein demonstrate that many different products can contain potentially harmful emerging contaminants and standard analytical methods are insufficient in characterizing them. By augmenting existing methods with newly developed assays, or using numerous existing methods in a complementary fashion, one can achieve a more holistic characterization of emerging contaminants.

The work developed in this thesis can be used to screen industrial and commercial products for emerging contaminants and ideally identify the risk they pose before they are released into the environment or used by humans.

9.2. Itemized Conclusions of Current Work

9.2.1. Investigating the Transformation of PFAS Using Gamma Irradiation

The primary goal of this objective was to identify the transformation of PFAS in the presence of reductive and oxidative radicals generated using gamma radiolysis of water. This work was applied to PFOS, PFOA, 6:2 FTS, and a suite of PFAS with varying chain lengths and functional groups. The aqueous electron and hydroxyl radical were hypothesized to be the major reactive radical species present based on the unique PFAS transformation products identified using high resolution

mass spectrometry. These results provide insights into how different reactive radicals can be used to improve PFAS characterization through designed chemical assays. The following conclusions are presented:

- a) PFAS degradation was influenced heavily by pH, PFAS chain lengths, functional group, fluorine saturation, and concentration.
- b) Degradation was highest for long-chain PFCAs at high pH, with degradation rates further enhanced in the presence of minute amounts of methanol.
- c) Degradation was lowest for short-chain PFSAs regardless of pH.
- d) The identification of 80+ fluorinated transformation products allowed for an expanded understanding of PFAS degradation mechanisms, with a unified branching pathway proposed.
- e) The slow degradation of 6:2 FTS using gamma irradiation suggests alternate strategies that employ an oxidative pre-treatment would be best for achieving destruction of fluorotelomer PFAS.
- f) Aqueous electrons are the primary species responsible for initial PFAS degradation, and their application to destroy PFAS for total organic fluorine determination requires a highly alkaline, anoxic environment.

9.2.2. Development of a Tandem UV-H₂O₂-TOP-ROF Assay for Enhanced Characterization of PFAS in Commercial Products and Environmental Matrices

- a) PFAS, particularly PFSAs, are susceptible to poor recoveries in methanolic solutions containing high concentrations of salt, attributed to a precipitation-driven ‘salting out’ effect. This can be mitigated through the inclusion of water (50%) in dilution and preparation solution employed post- sample oxidation.
- b) *UV-TOP*: UV-light is an attractive alternative to thermal energy for the activation of persulfate anions employed in the TOP assay, with UV-activated TOP assay demonstrating higher PFAS recovery, more rapid oxidation, and enhanced preservation of PFCA chain lengths.
- c) *UV-H₂O₂*: The use of UV-activated H₂O₂ results in the mineralization of dissolved organic matter from the system, which otherwise interferes with the TOP assay. The UV-H₂O₂ assay exceeded best under neutral pH conditions, at a concentration of 500 mM, with a UV-activation time of >12 hours.
- d) *UV-H₂O₂-TOP*: The tandem UV-H₂O₂-TOP assay results in further improvements to the preservation of PFCA chain lengths, while also being more robust in the presence of dissolved

organic matter. Sodium persulfate was identified as an effective alternative to potassium persulfate and was found to be effective at concentrations ranging from 20 mM NaPS to 200 mM NaPS.

- e) *UV-ROF*: The developed UV-ROF assay (developed from UV-activated sulfite and iodide PFAS destruction technology) was found to completely mineralize dilute AFFF formulations, providing total organic fluorine measurement of the samples.
- f) *UV-H₂O₂-TOP-ROF*: The UV-ROF assay was modified for incorporation after sample oxidation to form the tandem UV-H₂O₂-TOP-ROF assay. This tandem assay was applied to 15 AFFFs and a broad selection of commercial and environmentally relevant samples with strong success. The direct TOP (dTOP) assay was investigated as an alternate oxidation method, which was demonstrated to be superior when analyzing PFAS-incorporated textiles. The dTOP-UV-ROF assay was also shown to effectively characterize the total organic fluorine concentration present within these samples.
- g) The inclusion of ultra-short chain PFCAs (TFA, PFPrA) and common fluorotelomers (6:2 FtSaB, 5:3 FtB, 5:1:2 FtB) allows for the characterization of more PFAS present in the samples before oxidation, significantly improving the characterization of PFAS pre- and post- TOP assay employment, especially for AFFFs and AFFF-impacted matrices.
- h) The completion of these three studies resulted in the development of an analytical decision-making framework, to support future use and optimization of the method.

9.2.3. Investigating Effective Synthesis Methods for Silver- and Copper-Functionalized Textiles

- a) The use of NaHCO₃ resulted in the most effective silver synthesis method, with the highest concentration of elemental silver nanoparticles being generated into the textile material.
- b) The use of NaOH resulted in the most effective overall synthesis method, yielding high concentrations of elemental silver and copper oxide for all three metal applications (silver only, copper only, silver/copper together).
- c) The nanomaterials developed were, on average, above the classical definition of a nanoparticle (one dimension < 100 nm in size), but this was identified as potentially advantageous due to minimizing nano-specific toxicological concerns.
- d) The metal nanomaterials were identified to be present within the cellulose matrix itself, instead of on the fiber surface as identified in literature.

- e) The complementary analytical techniques employed successfully characterized the metals present on the textile.

9.2.4. Development of a Simulated Weathering Method for Enhanced Characterization of Silver Nanomaterials in Commercial Products and Released Effluent Media

The primary goal of this research was to develop a method to simulate active human use of a commercially available silver-functionalized textile and employ an expanded suite of complementary analytical techniques in characterizing the silver present on the textile and in released laundry effluent. The conclusion of this work is detailed.

- a) The use of 3D printing allowed for the development of two physical weathering techniques, one focused on simulating textile stretching, and one focused on simulating textile stretching and abrasion.
- b) The use of artificial sweat was used to simulate chemical weathering of the textile.
- c) The physical weathering, chemical weathering, and combined physical and chemical weathering techniques resulted in different silver characteristics compared to the no-weathered control, with chemical weathering influencing silver speciation (e.g. formation of silver chloride in the laundry effluent), and physical weathering influencing the concentration of silver released, and deformation of silver from the textile surface. The combined physical/chemical weathering technique resulted in silver being released characteristically similar to that released by active human use trials, indicating the simulated method was successful in simulating human use.
- d) The silver present on the textile was identified to be a thin layer (<100 nm) of electrolessly deposited silver which would act as a long-term source of silver release into the environment.
- e) The use of SEM-EDX identified both silver and underlying nylon deformation from the textile surface, with silver-containing nylon fibers being found fraying from the surface material. This suggests that silver-containing microplastics may be released into the environment from the laundering of these metal-functionalized textiles.

9.3. Recommendations for Future Work

This work and the results presented herein were not generated in a vacuum and builds off the works published by generations of scientists in the fields of PFAS, metal nanomaterials, and analytical chemistry. It is with highest hopes that the works detailed in this thesis are further built upon and

improved by colleagues within the greater scientific community. To this end, the following recommendations are made as a starting point for future work to investigate.

- PFAS UV-H₂O₂-TOP-ROF recommendations:
 1. Employment of pre-concentration techniques (e.g. SPE) to achieve more sensitive detection and quantitation limits with the developed methodology.
 2. Further investigation into PFAS-functionalized textiles, and the application of the tandem UV-assay in identifying the potential for PFAS-containing microplastics released during laundering of the textiles.
 3. The development of a non-mass spectrometric method for quantitation of PFAS in post-oxidation samples, such as a colorimetric assay (e.g. methylene blue active surfactants), F-NMR, or surface enhanced raman spectroscopy (SERS).
- Nanomaterial-functionalized commercial product recommendations:
 1. Expansion of the simulated weathering technique to other CEC-containing textiles, such as titanium dioxide nanoparticles, carbon nanotubes, or PFAS.
 2. Investigation into the potential for nanomaterial-containing microplastic release from textiles, either during laundering, or during other use scenarios (e.g. release during inhalation events if used as medical masks).
 3. Evaluation of the metal-functionalized textiles using antibacterial, antiviral, and antifungal assays, to identify if the metal synthesis methods exert antimicrobial properties with their larger nanoparticle size.

APPENDIX A-G

Appendix A – Supplementary Information for Chapter 3

PFAS and Concentrations Used In Study

Table A1: List of PFAS used in this study.

PFAS Full Name	PFAS Acronym
PFCAs	
Trifluoroacetic acid	TFA
Perfluoropropanoic acid	PFPA
Perfluorobutanoic acid	PFBA
Perfluoropentanoic acid	PFPeA
Perfluorohexanoic acid	PFHxA
Perfluoroheptanoic acid	PFHpA
Perfluorooctanoic acid	PFOA
Perfluorononanoic acid	PFNA
Perfluorodecanoic acid	PFDA
Perfluoroundecanoic acid	PFUdA
Perfluorododecanoic acid	PFDoA
PFSAs	
Perfluorobutane sulfonic acid	PFBS
Perfluorohexane sulfonic acid	PFHxS
Perfluorooctane sulfonic acid	PFOS
Sulfonamides	
Perfluorooctane sulfonamide	FOSA
Fluorotelomer Sulfonate	
6:2 fluorotelomer sulfonate	6:2 FTS

Table A2: Concentration of PFAS used for irradiation experiments.

	PFAS	C ₀ (mg PFAS/L)
PFOA Only	PFOA	1.70
	PFOA	0.03
PFOS Only	PFOS	1.90
	PFOS	0.03
6:2 FTS Only	6:2 FTS	0.50
	6:2 FTS	0.05
PFAS13Suite	PFBA	0.11
	PFPeA	0.14
	PFHxA	0.15
	PFHpA	0.13
	PFOA	0.12
	PFNA	0.14
	PFDA	0.10
	PFUnA	0.10
	PFDoA	0.04
	PFBS	0.13
	PFHxS	0.11
	PFOS	0.09
	FOSA	0.76

Targeted PFAS Analysis

Samples were analyzed using multiple-reaction-monitoring (MRM) mode on an Agilent 6460 MS/MS coupled to an Agilent 1260 high pressure liquid chromatography (HPLC) system using a 50 mm x 2.1 mm x 3 μ m Zorbax C18 analytical column and paired guard column, with a 5 μ L injection volume. The column oven was set to 50°C. Samples were not diluted before analysis and were not spiked with internal standards. Mobile phases consisted of 10 mM ammonium acetate in deionized (DI) water (A) and 10 mM ammonium acetate in acetonitrile (B). The elution profile started at 90% A/10% B at a flow rate of 0.5 mL/min, transitioning to 100% B over 4 minutes, holding for 2 minutes, then equilibrating at starting conditions for 4 minutes. Samples were quantified using an external calibration curve (Wellington Labs). For samples with PFAS concentrations higher than 200 μ g/L, PFAS were quantified with a calibration curve from 10 μ g/L to 2000 μ g/L ($R^2 > 0.99$, detection limit of ~ 5 μ g/L for all PFAS). For samples with PFAS concentrations lower than 200 μ g/L, PFAS were quantified with a calibration curve from 0.1 μ g/L to 250 μ g/L ($R^2 > 0.99$, detection limit of ~ 0.05 μ g/L for all PFAS). Quantification limits were set to the lowest concentration of each calibration curve. Mass spectrometer conditions and multiple-reaction-monitoring (MRM) transitions for all PFAS analyzed can be found in Table A3.

Table A3: Mass spectrometer conditions and MRM transitions for targeted PFAS.

Mass Spectrometer Conditions (Agilent 6460 LC-MS)						
Gas Temp (C)	Gas Flow (L/m)	Nebulizer (PSI)	Sheath Gas (C)	Sheath Gas Flow (L/m)	Capillary (L/m)	Nozzle Voltage (V)
325	9 L/min	30 PSI	30 C	12 L/min	12 L/min	0 V
MRM Transitions						
Compound Name	Precursor Ion (m/z)	Product Ion (m/z)	Fragmentor	Collision Energy	Cell Accelerator Voltage	Polarity
TFA	112.9	69	59	8	2	Negative
PFPA	163	118.8	59	8	2	Negative
PFBA	213	169	72	8	2	Negative
PFPeA	263	219	72	4	2	Negative
PFBS	298.9	99	154	34	2	Negative
PFBS	298.9	80	154	36	2	Negative
PFHxA	313	269	72	8	2	Negative
PFHxA	313	119	72	24	2	Negative
PFPeS	348.9	99	144	40	2	Negative
PFPeS	348.9	80	144	44	2	Negative
PFHpA	363	319	72	8	2	Negative
PFHpA	363	169	72	16	2	Negative
PFHxS	398.9	99	156	40	2	Negative
PFHxS	398.9	80	156	56	2	Negative
PFOA	413	369	72	8	2	Negative
PFOA	413	219	72	16	2	Negative
PFHpS	448.9	99	148	42	2	Negative
PFHpS	448.9	80	148	50	2	Negative
PFNA	463	419	72	8	2	Negative
PFNA	463	219	72	16	2	Negative
FOSA	497.9	169	150	36	3	Negative
FOSA	497.9	48	150	110	3	Negative
PFOS	498.9	99	148	50	2	Negative
PFOS	498.9	80	148	54	2	Negative
PFDA	513	469	72	12	2	Negative
PFDA	513	269	72	16	2	Negative
PFNS	548.9	99	148	52	2	Negative
PFUnDA	563	519	100	12	2	Negative
PFUnDA	563	319	100	20	2	Negative
PFDS	598.9	99	148	56	2	Negative
PFDS	598.9	80	148	60	2	Negative
PFDoDA	613	569	100	8	2	Negative
PFDoDA	613	269	100	24	2	Negative
PFTTrDA	663	619	100	12	2	Negative
PFTTrDA	663	319	100	20	2	Negative
PFDoS	698.9	99	156	62	2	Negative
PFDoS	698.9	80	156	67	2	Negative
PFHxDA	812.9	769	120	12	2	Negative
PFHxDA	812.9	269	120	28	2	Negative

Quality Control

PFAS calibration standards at two different concentrations (50 µg/L, 5 µg/L) were run every 20 samples to measure possible instrument drift. Overall instrument drift was found to be <5% over the duration of the run. Samples were run in batches based on their concentration, with a minimum of four injection blanks (1:1 H₂O/MeOH) run between high concentration and low concentration batches, to eliminate carry over. Sample carry over was found to be <0.1% of previous PFAS concentration. The autosampler injection needle was cleaned between injections using the built-in flush program (Masshunter Acquisition). The needle was washed for 10 seconds with flush solution (20% H₂O, 35% IPA, 45% MeOH). Travel blanks were run before and after each batch to track any contamination from sample preparation and transport. Reagent blanks were run before and after each batch to track any contamination in the used reagents. All blanks were found to be non-detects for PFAS. Targeted PFAS were analyzed in triplicates and were found to exhibit excellent reproducibility.

Non-Targeted Analysis (PFAS Degradation Products)

High concentration samples were analyzed on a ThermoFisher Exploris 120 Orbitrap coupled to a Vanquish ultra-high-performance liquid chromatography (uHPLC) system using a 100 mm x 2.1 mm x 3.0 µm ACME C18 analytical column and paired guard column. Mobile phases consisted of 5 mM ammonium acetate in DI water (A) and acetonitrile (B). The elution profile started at 90% A/10% B with a flow rate of 0.5 mL/min, transitioning to 100% B over 10 minutes, holding for 2 minutes, then equilibrating at starting conditions for 3 minutes. A heated electrospray ionization ion source was used, with a static spray voltage. Both positive and negative ion voltage were 3000 V. Gas was run in static mode, with a sheath gas of 50 (arbitrary units), aux gas of 10 (arbitrary units) and sweep gas of 1 (arbitrary units). The ion transfer tube temperature was set to 325°C, the vaporizer temperature was set to 350°C, and mild trapping was not used. The MS global settings were set to expect an LC peak width of 10 seconds, and the mass was calibration before each sample injection using the RunStart EASY-IC™ system.

Before samples were run, the UHPLC and Orbitrap were flushed with 10% DI water, 90% ACN for a minimum of 1 hour, until baseline ion peak intensity was stable (indicating a clean sample path) and spray stability was <5%. Using the initial orbitrap full scan method, samples were run in the following order: reagent blank, travel blank, 0 kGy, 1 kGy, 2.5 kGy, 5 kGy, 10 kGy, 20 kGy, 40 kGy, 80 kGy, followed by two injection blanks.

Samples from all doses were initially analyzed using a full scan dual polarity method to identify initial degradation products. The analysis method was set up with two 'experiments' (XCalibur® software nomenclature for analytical protocols), one for positive mode analysis and one for negative mode analysis. Each experiment used an orbitrap resolution of 60,000, a scan range of 150-1000 m/z, an RF lens of 70%, a standard automatic gain control (AGC) target, an automatic maximum injection time mode setting, and had in-source fragmentation disabled.

Samples that were exposed to 1 kGy of gamma irradiation were re-run using optimized UHPLC conditions (factory-new ACME C18 column of same dimensions as above, longer elution profile), MS-grade solvents (Fisher Scientific) to achieve better separation, improved peak shape, improved signal intensity, and reduced background noise. Samples were analyzed using full scan data dependent (dd) MS₂ negative polarity method to confirm degradation products and allow for ddMS₂ fragmentation analysis where compound intensity allowed. Full scan analytical method is similar to above, with scan range set to 100-1000 m/z, a ddMS₂ intensity threshold set to 1×10^6 , and a dynamic exclusion method set to exclude after one trigger, with an exclusion duration of 5 seconds. Four data dependent scans were taken for each trigger. An isolation window of 1.2 m/z, fixed collision energy mode, normalized collision energy, HCD 50%, and 15,000 orbitrap resolution were used for the ddMS₂ fragmentation analysis.

The potential transformation byproducts were identified using two methods. The first method was performed by subtracting chromatograms of 0 kGy samples from chromatograms of dosed samples and visually inspecting the resulting chromatogram for new peaks. The second method was to use ddMS₂ mode (set to trigger with a peak intensity $>1.0 \times 10^6$) to identify characteristic PFAS fragments (SO₃, CO₂, CF₃, C₂F₅, etc). Resultant MS/MS data was used to confirm the transformation products identified (Figure A6-S9). If possible, these products were compared to known masses of byproducts found in the literature. For novel products, structures were postulated based on possible reactions and retention time trends. Transformation products were semi-quantified using the calibration curve of the original PFAS. A small number of potential transformation products were not included if their retention time aligned perfectly with a substituted PFCA, as PFCAs fragment readily in the electrospray and may yield false positives. An example of this can be seen in Figure A7, where a potential unsaturated perfluoroalcohol is present (C₈F₁₂OH, m/z 340.9838, 0.74 ppm) in the spectrum for the -F/+CH₂OH substituted PFOA; we opted to not report the potential unsaturated perfluoroalcohol.

Fluoride Analysis

Fluoride analysis was performed using a fluoride ion-selective electrode (Thermo Scientific Orion Fluoride Electrode) on the high concentration PFAS₁₃Suite samples at both pH 7 and 11 after 80 kGy of irradiation. This was done by taking 1 mL of the aqueous sample and mixing it with 1 mL of total ionic strength adjustment buffer (TISAB) and adjusting the final pH to 5.5 with acetic acid. Fluoride probe measurements were quantified using a six-point external calibration curve prepared using a standardized fluoride calibration solution. Detection limit of the fluoride probe was found to be 0.1 mg F/L. Following initial fluoride probe measurements, all samples were spiked with a known amount of fluoride to identify possible matrix effects. Recovery of the internal fluoride spikes were found to be between 79-86%. Sample concentrations were corrected for the fluoride spike recovery. Due to the limited volume of each of the samples, a standard addition curve could not be performed. The amount of fluoride measured was compared to the theoretical expected fluoride based on the extent of PFAS degradation. Fluoride analysis was also performed on the PFOS, PFOA, and 6:2 FTS trials, but due to unusual matrix effects and limited sample volume fluoride results for these trials are not reported.

Comparisons of PFOS and PFOA Degradation to Literature

Some similarities and differences can be observed when comparing PFOS and PFOA degradation results to those in literature. In work by Trojanowicz (2020) the PFOS degradation following 25 kGy of gamma irradiation was ~70% at pH 7 for argon-saturated solutions with a starting concentration of 1 mg/L (Trojanowicz et al., 2020b), compared to 42% and 48% at pH 7 and 11 for nitrogen-saturated solutions with a starting concentration of 1.9 mg/L in this study. The highest degradation for PFOS in this current study was found at the low concentration of PFOS (0.03 mg/L) at pH 11, at which 70% degradation was achieved after 80 kGy of absorbed dose.

In work by Zhang (2014) complete mineralization of PFOA was observed following 126 kGy of absorbed dose. To allow for comparison to this study, the results at ~8 hours of irradiation in Zhang's study (~46 kGy, pH 11) can be examined, which shows almost ~75% degradation of the PFOA. These results are comparable to those found in this study (76±13% degradation, 1.7 mg PFOA/L, pH 11), but a significant amount of the degraded PFOA in this study is converted into shorter-chained PFCAs, whereas Zhang reported substantial mineralization into fluoride (Zhang et al., 2014). Further differences can be found when comparing this work to Trojanowicz, in which 99% of the PFOA is degraded at pH 12.5 with 75% fluoride yield at 50 kGy. It is likely that the enhanced PFOA degradation observed by Trojanowicz is due to the higher pH, which facilitates more aqueous electron generation.

Linear PFOS and 6:2 FTS Degradation Comparison

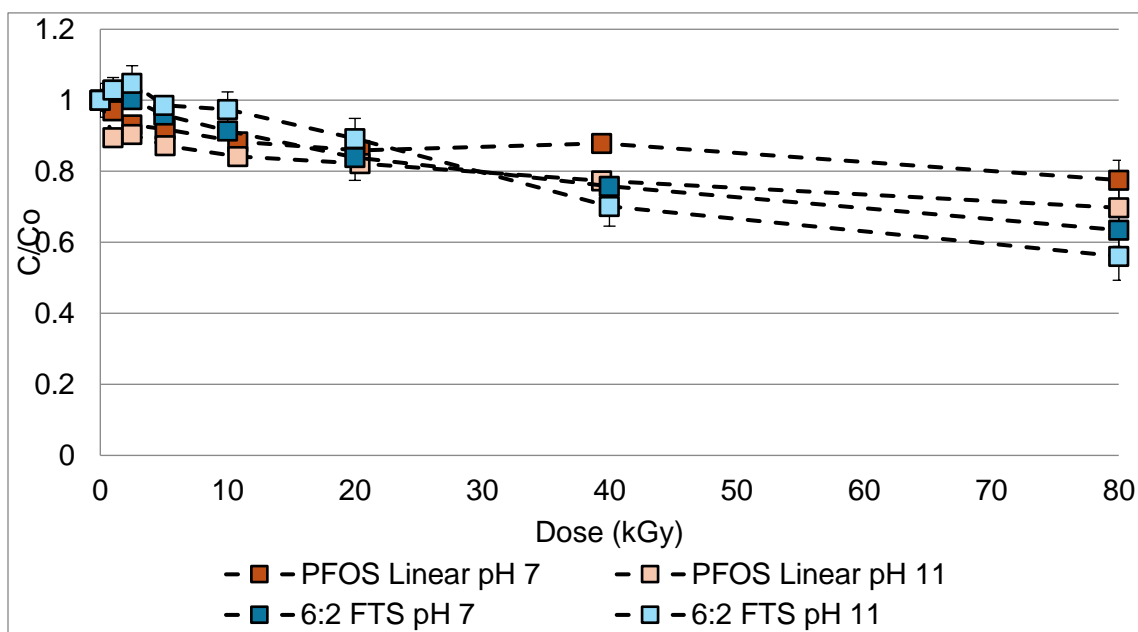


Figure A1: Comparison between 6:2 FTS degradation with linear PFOS at pH 7 and 11.

PFOS Transformation Products

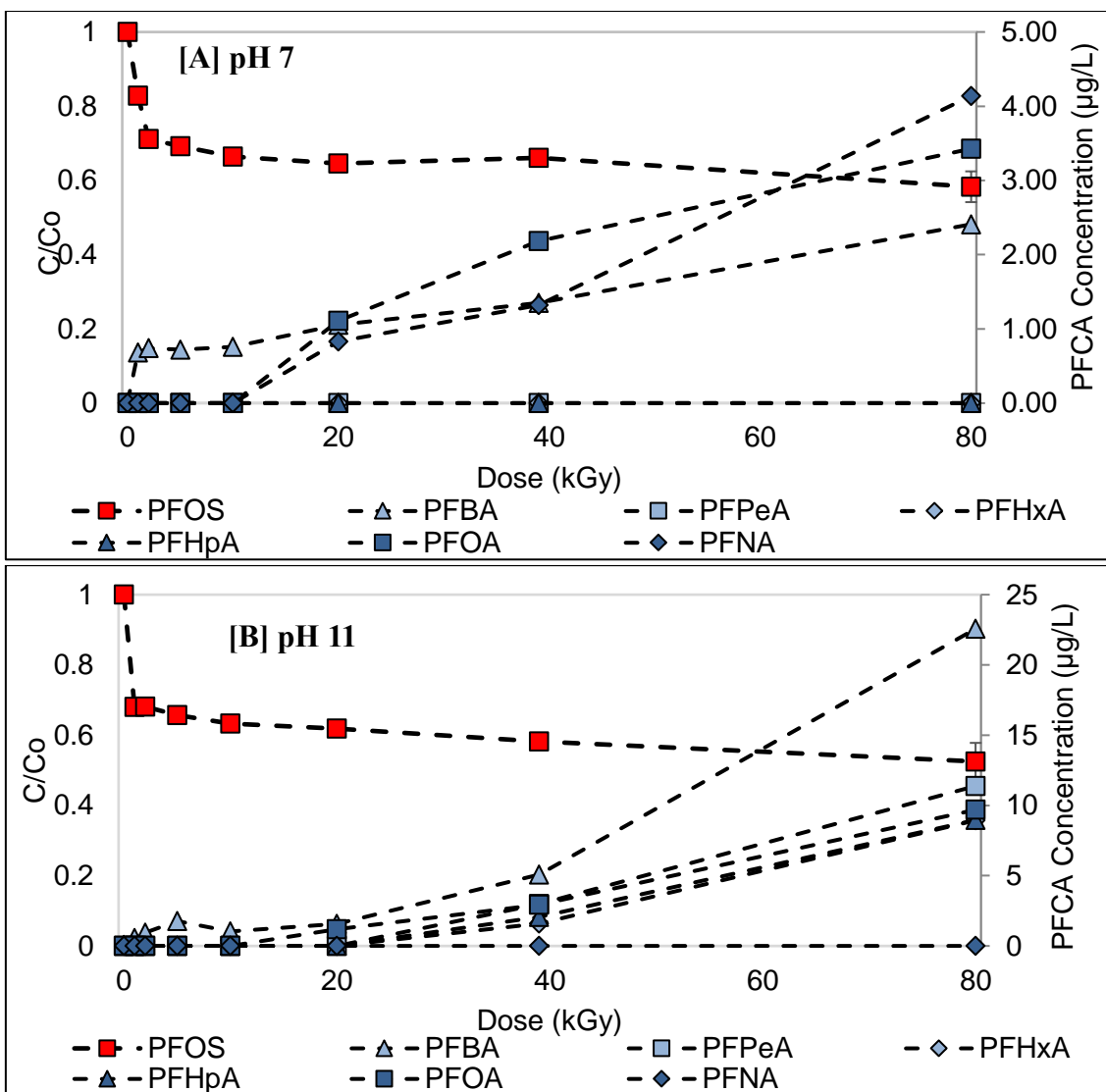


Figure A2: Shorter-chained PFCA formation following irradiation of PFOS at pH 7 (A) and 11 (B). Error bars represent the standard deviation of the replicates (n=3). Some error bars are too small to be shown.

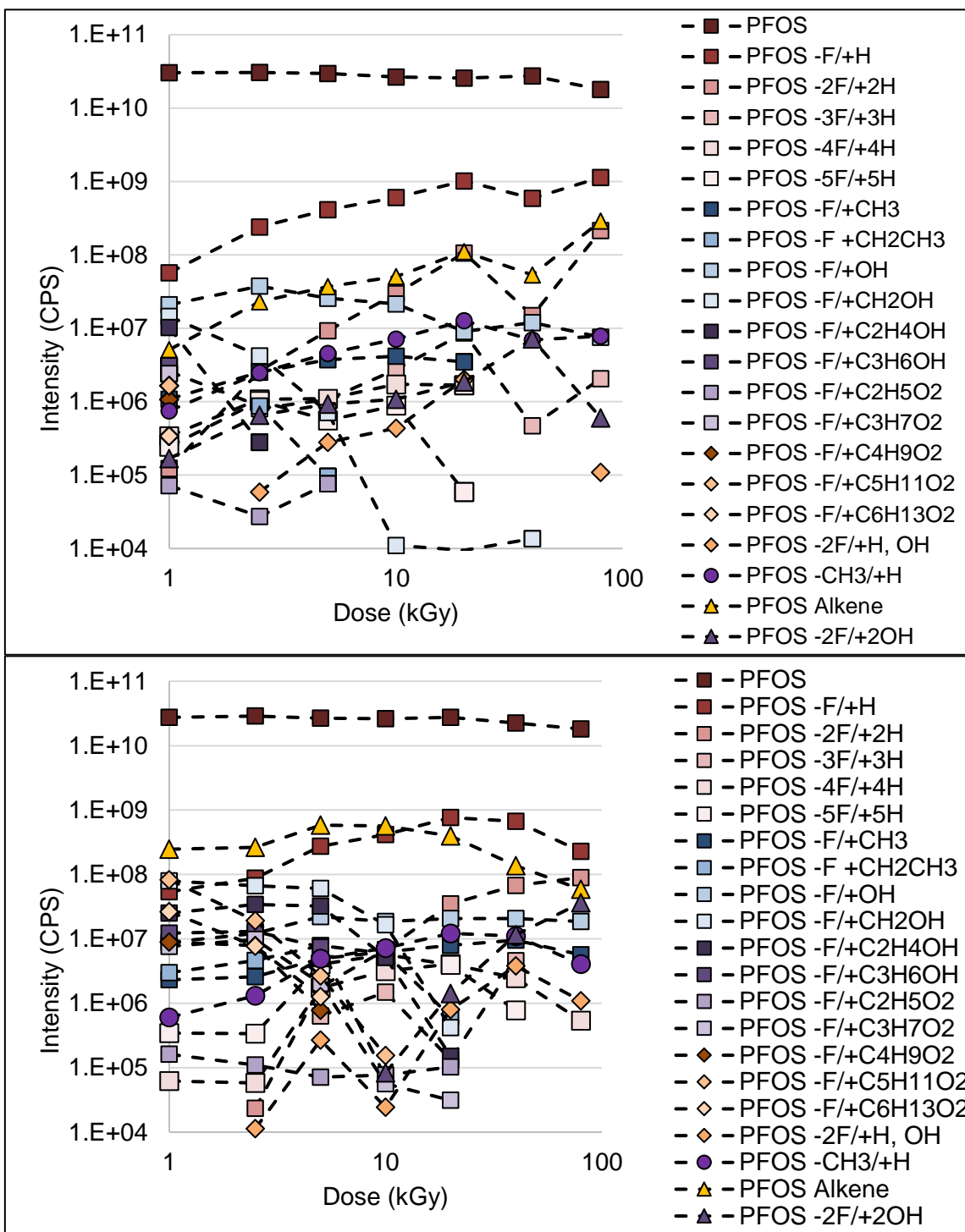


Figure A3: Unquantified polyfluorinated transformation products following PFOS degradation at pH 7 (top) and pH 11 (bottom).

PFOA Transformation Products

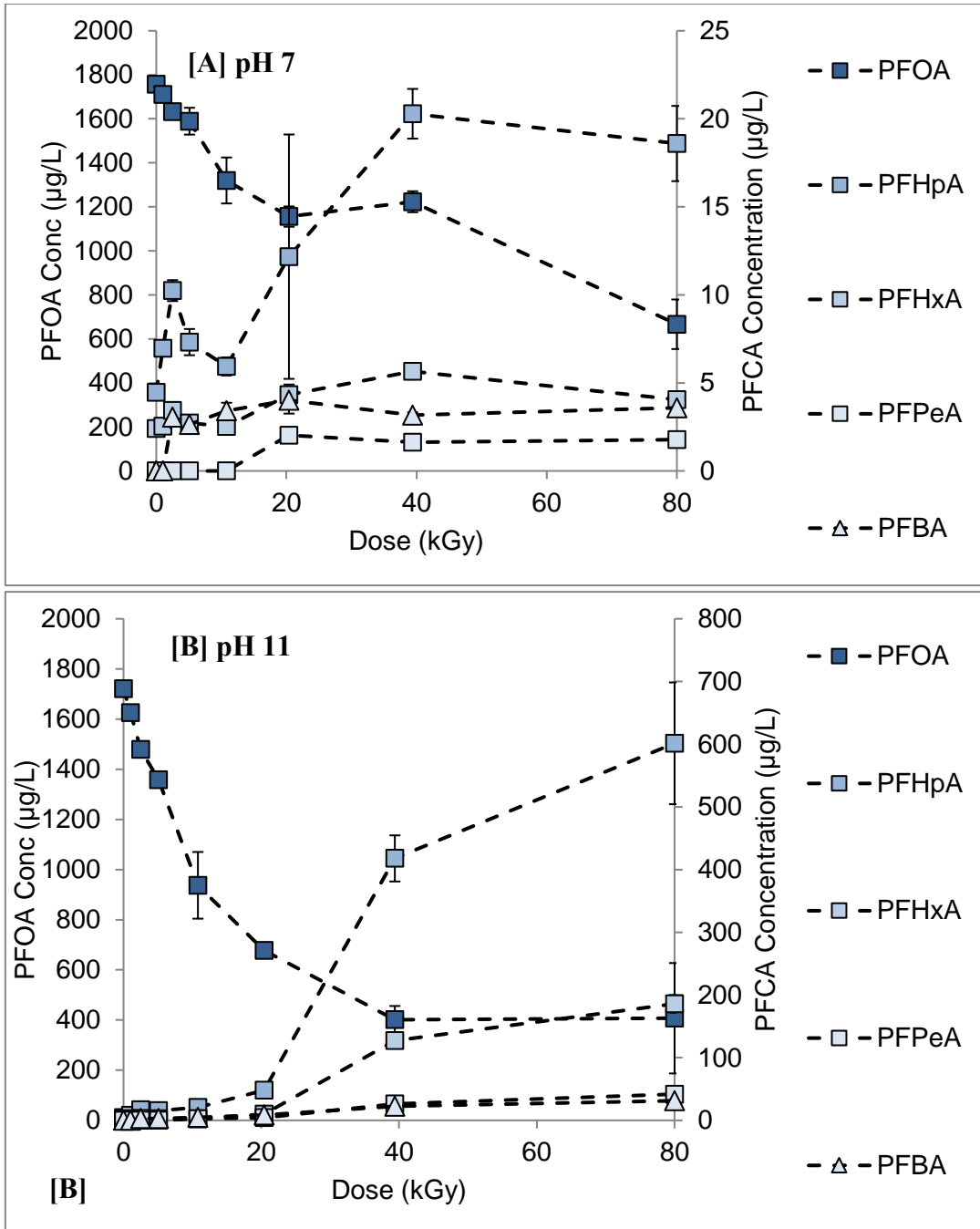


Figure A4: Shorter PFCA formation following irradiation of PFOA at pH 7 (A) and 11 (B). Error bars represent the standard deviation of the replicates. Some error bars are too small to be shown.

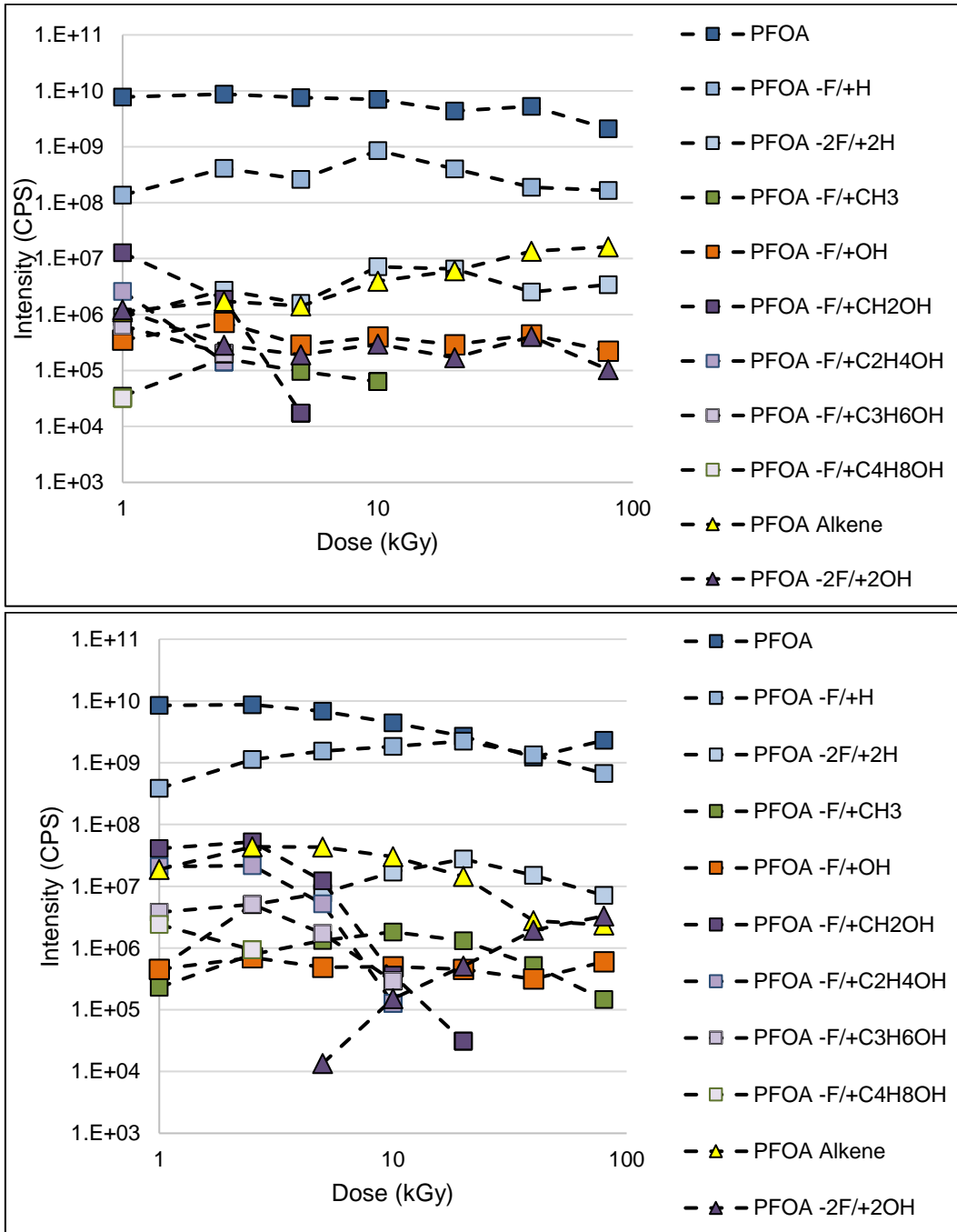


Figure A4: Unquantified polyfluorinated transformation products following PFOA degradation at pH 7 (top) and pH 11 (bottom).

6:2 FTS Transformation Products

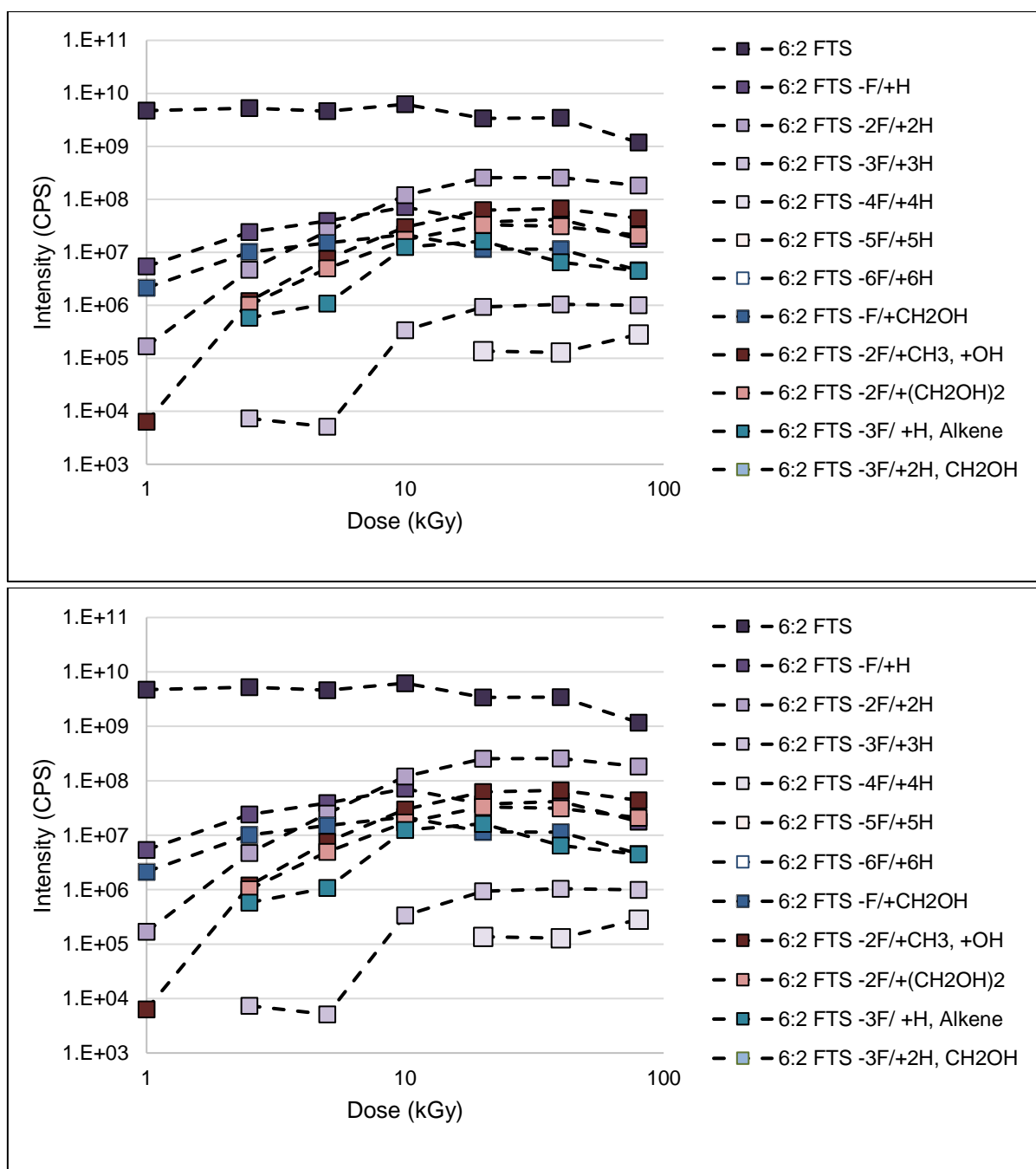


Figure A5: Unquantified polyfluorinated transformation products following 6:2 FTS degradation at pH 7 (top) and pH 11 (bottom).

PFAS Transformation Products – High Resolution Analysis

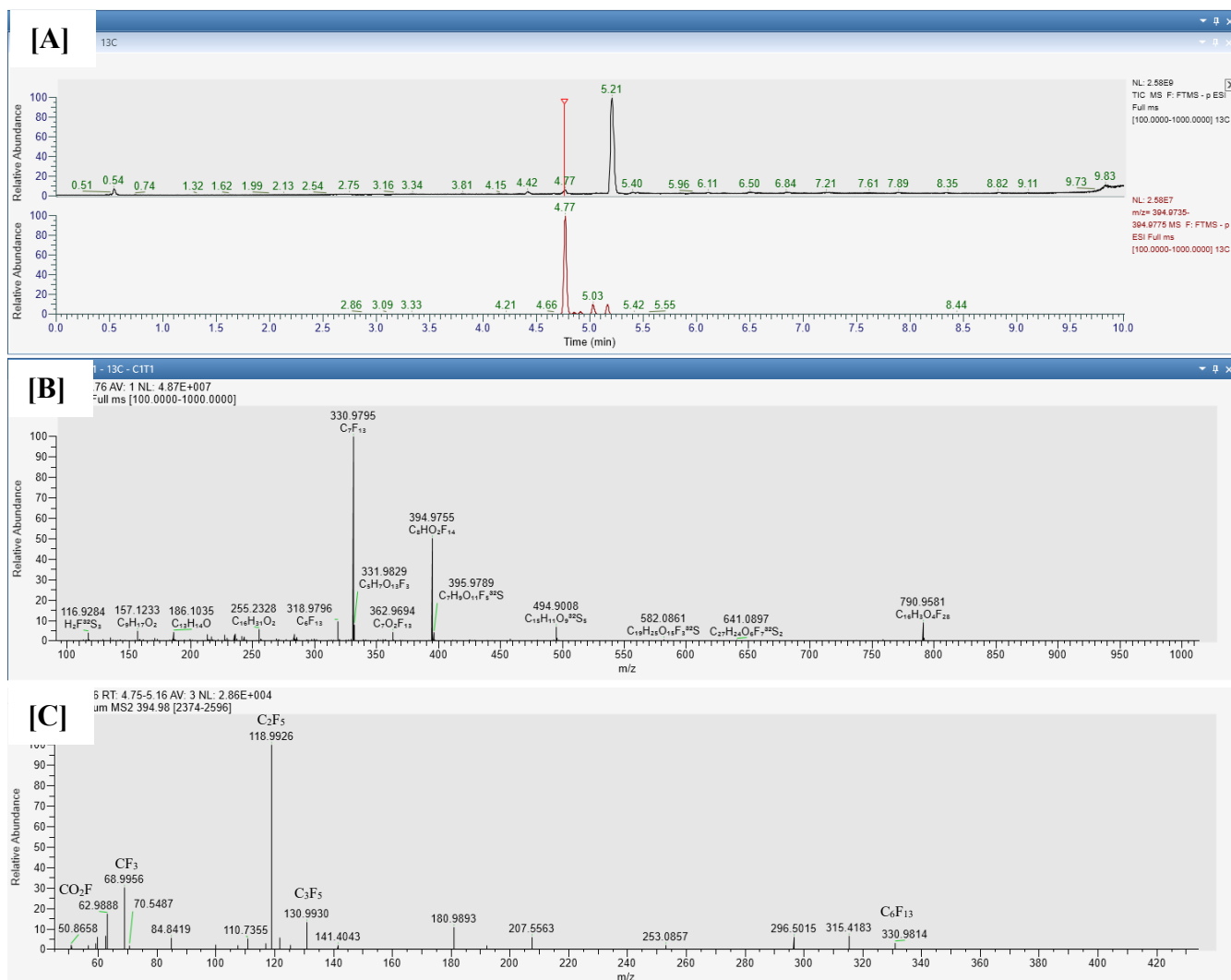


Figure A6: Chromatogram (A), spectrum (B), and ddMS₂ fragmentation (C) analysis of -F/+H substituted PFOA following irradiation at 1 kGy, pH 7.



Figure A7: Chromatogram (A), spectrum (B), and ddMS₂ fragmentation (C) analysis of F/+CH₂OH substituted PFOA following irradiation at 1 kGy, pH 7.

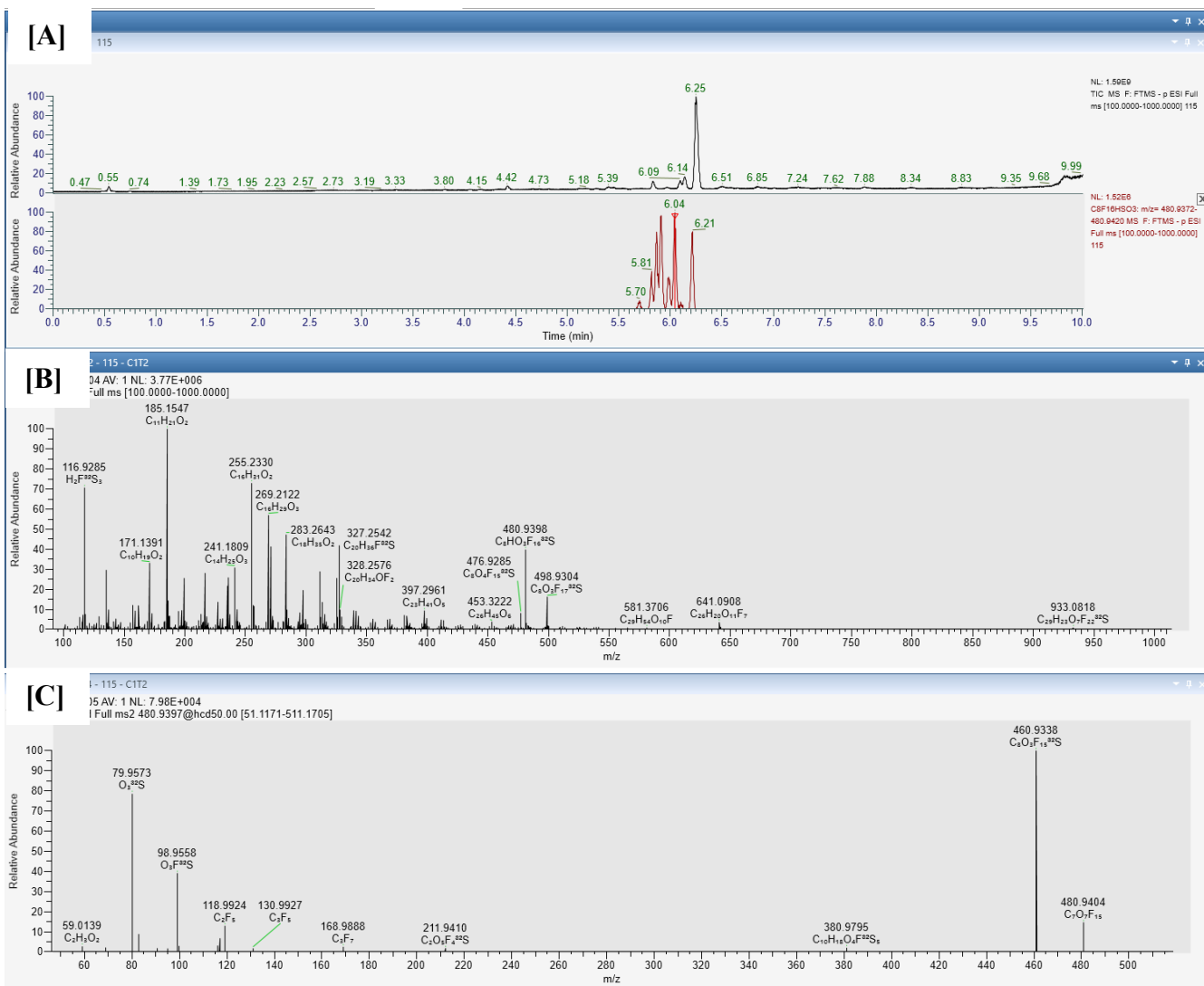


Figure A8: Chromatogram (A), spectrum (B), and ddMS₂ fragmentation (C) analysis of -F/+H substituted PFOS following irradiation at 1 kGy, pH 7.

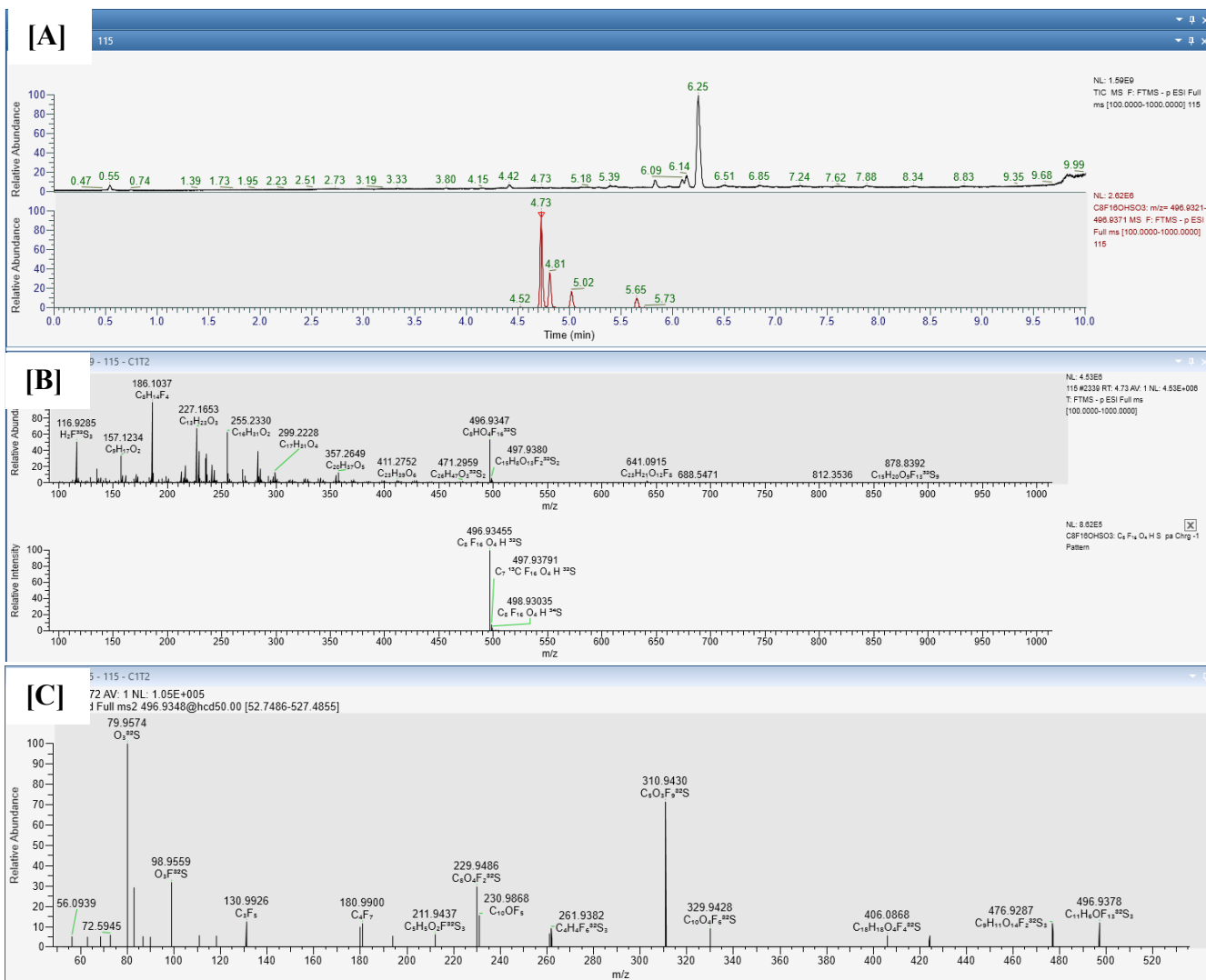


Figure A9: Chromatogram (A), spectrum (B), and ddMS₂ fragmentation (C) analysis of -F/+OH substituted PFOS following irradiation at 1 kGy, pH 7.

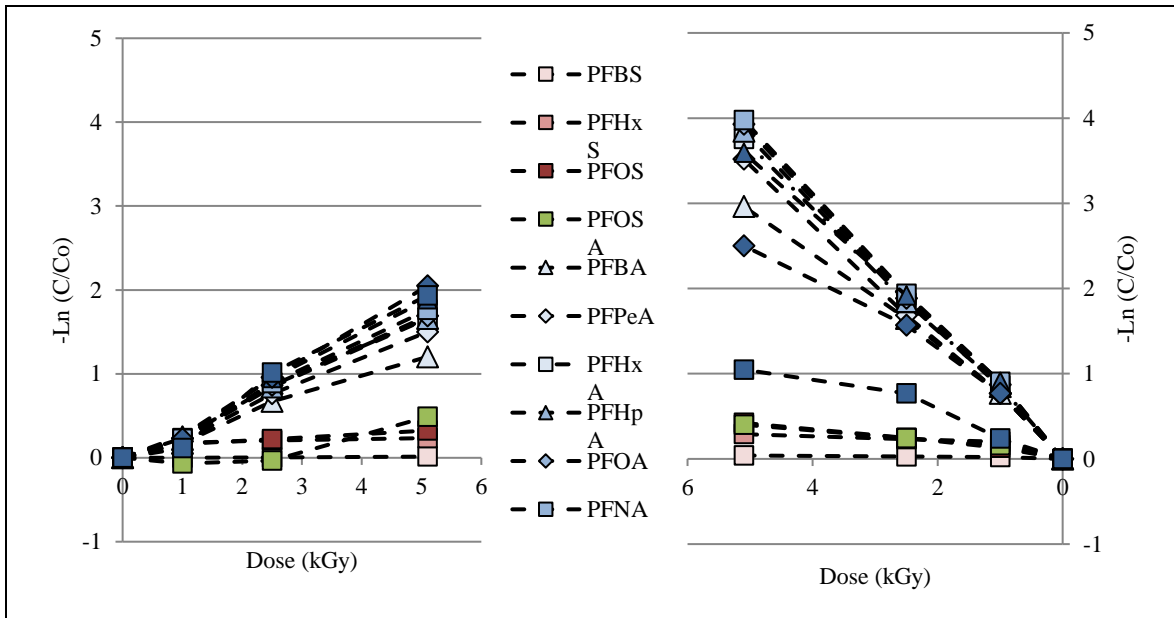


Figure A10: $\ln(C/C_0)$ for all PFAS compounds in the suite from 0-5 kGy at pH 7 (left) and pH 11 (right).

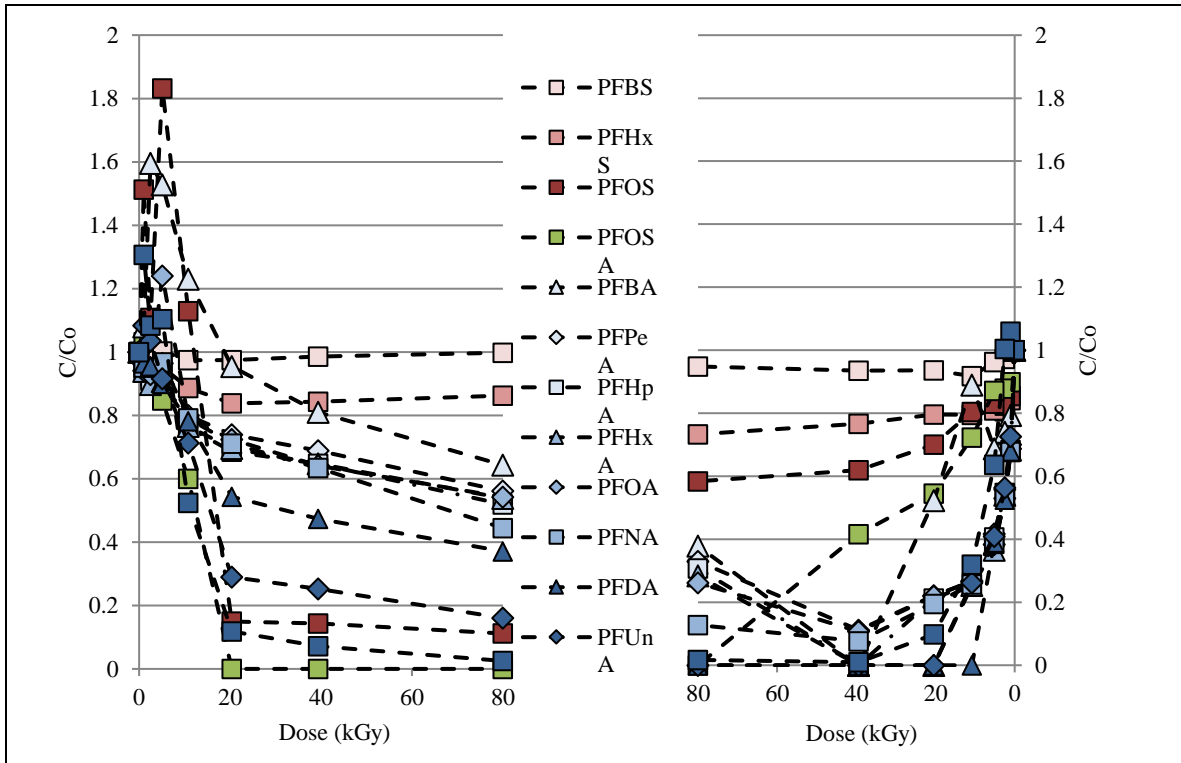


Figure A11: Degradation of mixture of 13 PFAS compounds at low (~ 0.0035 mg individual PFAS / L) at pH 7 (left) and 11 (right) following up to 80 kGy of gamma irradiation.

1 **Table A4:** Summary of total final degradation, degradation rates, and coefficient of determination (RSQ) for differing initial
 2 concentrations of PFAS irradiated at different pH. Rate constant (k) is first order, in kGy^{-1} measured from 0 to 5 kGy .

	PFAS	C_0 (mg PFAS/L)	pH 7			pH 11		
			% Degradation	First Order Rate Constant (kGy^{-1})	RSQ	% Degradation	First Order Rate Constant (kGy^{-1})	RSQ
-COOH Alone	PFOA	1.70	62.1 ± 6.4	0.02	0.93	76.3 ± 12.8	0.05	0.97
	PFOA	0.03	79.4 ± 1.4	0.03	0.86	87.3 ± 11.4	0.11	0.93
-SO ₃ H Alone	PFOS	1.90	41.7 ± 4.1	0.07	0.77	47.5 ± 5.3	0.06	0.49
	PFOS	0.03	36.3 ± 3.5	0.04	0.54	70.4 ± 7.1	0.06	0.53
C ₂ H ₆ SO ₃ H Alone	6:2 FTS	0.50	36.6 ± 4.6	0.01	0.96	43.9 ± 6.8	0.01	0.98
	6:2 FTS	0.05	32.6 ± 3.6	0.00	0.4	22.0 ± 3.2	0.00	0.81
-COOH Mix	PFBA	0.11	89.9 ± 0.5	0.24	0.99	91.5 ± 2.2	0.57	0.99
	PFPeA	0.14	97.4 ± 0.4	0.30	0.99	96.6 ± 1.0	0.68	1.00
	PFHxA	0.15	98.3 ± 0.3	0.33	0.99	98.1 ± 1.0	0.73	1.00
	PFHpA	0.13	99.2 ± 0.1	0.33	0.99	98.8 ± 0.7	0.75	1.00
	PFOA	0.12	99.0 ± 0.2	0.34	1.00	98.8 ± 0.7	0.76	1.00
	PFNA	0.14	99.1 ± 0.1	0.36	0.99	98.8 ± 0.6	0.77	1.00
	PFDA	0.10	99.3 ± 0.0	0.38	1.00	98.4 ± 0.1	0.69	1.00
	PFUnA	0.10	99.5 ± 0.2	0.41	0.99	97.5 ± 1.5	0.48	0.97
	PFDoA	0.04	98.4 ± 0.0	0.40	0.98	94.0 ± 1.1	0.21	0.93
-SO ₃ H Mix	PFBS	0.13	2.2 ± 0.7	0.00	0.21	3.9 ± 1.4	0.01	0.86
	PFHxS	0.11	49.6 ± 0.8	0.02	0.55	37.5 ± 0.0	0.05	0.71
	PFOS	0.09	61.2 ± 1.1	0.04	0.89	45.9 ± 3.4	0.08	0.98
SO ₂ NH ₂ Mix	FOSA	0.76	98.8 ± 1.1	0.10	0.93	69.8 ± 2.6	0.07	0.95

3

4 **Table A5** – First order rate constants calculated for all PFAS degradation trials across three different dose ranges at pH 7 and 11.

	PFAS	Co (mg PFAS/L)	pH 7						pH 11					
			0-5 kGy		0-10 kGy		0-80 kGy		0-5 kGy		0-10 kGy		0-80 kGy	
			First Order Rate Constant (kGy ⁻¹)	RSQ	First Order Rate Constant (kGy ⁻¹)	RSQ	First Order Rate Constant (kGy ⁻¹)	RSQ	First Order Rate Constant (kGy ⁻¹)	RSQ	First Order Rate Constant (kGy ⁻¹)	RSQ	First Order Rate Constant (kGy ⁻¹)	RSQ
-COOH Alone	PFOA	1.70	0.02	0.93	0.03	0.98	0.01	0.93	0.05	0.97	0.06	0.99	0.02	0.78
	PFOA	0.03	0.03	0.86	0.03	0.97	0.02	0.90	0.11	0.93	0.08	0.93	0.02	0.57
-SO3H Alone	PFOS	1.90	0.07	0.77	0.03	0.61	0.00	0.46	0.06	0.49	0.03	0.40	0.00	0.48
	PFOS	0.03	0.04	0.54	0.02	0.49	0.00	0.51	0.06	0.53	0.03	0.49	0.01	0.89
C2H6SO3H Alone*	6:2 FTS	0.50	0.01	0.96	0.01	0.90	0.01	0.96	0.01	0.98	0.00	0.43	0.01	0.98
	6:2 FTS	0.05	0.00	0.94	0.01	0.88	0.00	0.94	0.00	0.81	0.01	0.56	0.00	0.81
-COOH Mix	PFBA	0.11	0.24	0.99	0.22	0.99	0.02	0.43	0.57	0.99	0.37	0.93	0.02	0.10
	PFPeA	0.14	0.30	0.99	0.26	0.99	0.04	0.64	0.68	1.00	0.43	0.93	0.03	0.18
	PFHxA	0.15	0.33	0.99	0.29	0.99	0.04	0.65	0.73	1.00	0.48	0.94	0.03	0.22
	PFHpA	0.13	0.33	0.99	0.30	0.99	0.05	0.75	0.75	1.00	0.49	0.94	0.04	0.27
	PFOA	0.12	0.34	1.00	0.30	0.99	0.05	0.72	0.76	1.00	0.49	0.93	0.04	0.27
	PFNA	0.14	0.36	0.99	0.31	0.99	0.05	0.71	0.77	1.00	0.48	0.92	0.04	0.28
	PFDA	0.10	0.38	1.00	0.32	0.99	0.06	0.71	0.69	1.00	0.42	0.91	0.04	0.31
	PFUnA	0.10	0.41	0.99	0.30	0.96	0.06	0.68	0.48	0.97	0.23	0.78	0.04	0.54
	PFDaA	0.04	0.40	0.98	0.27	0.93	0.04	0.57	0.21	0.93	0.10	0.76	0.03	0.76
-SO3H Mix	PFBS	0.13	0.00	0.21	0.00	0.21	0.00	0.53	0.01	0.86	0.00	0.77	0.00	0.21
	PFHxS	0.11	0.02	0.55	0.02	0.55	0.01	0.88	0.05	0.71	0.02	0.63	0.00	0.56
	PFOS	0.09	0.04	0.89	0.04	0.89	0.01	0.83	0.08	0.98	0.05	0.92	0.01	0.43
-SO2NH2 Mix	FOSA	0.76	0.10	0.93	0.10	0.93	0.06	0.94	0.07	0.95	0.05	0.92	0.01	0.88

5
6
7

Table A6 – Zero order rate constants calculated for all PFAS degradation trials across three different dose ranges at pH 7 and 11.

		Co (mg PFAS/L)	pH 7						pH 11					
			0-5 kGy		0-10 kGy		0-80 kGy		0-5 kGy		0-10 kGy		0-80 kGy	
			Zero Order Rate Constant (ppm/kGy)	RSQ	Zero Order Rate Constant (ppm/kGy)	RSQ	Zero Order Rate Constant (ppm/kGy)	RSQ	Zero Order Rate Constant (ppm/kGy)	RSQ	Zero Order Rate Constant (ppm/kGy)	RSQ	Zero Order Rate Constant (ppm/kGy)	RSQ
-COOH Alone	PFOA	1.70	0.0328	0.93	0.0391	0.98	0.0125	0.88	0.0708	0.96	0.0704	0.99	0.0162	0.69
	PFOA	0.03	0.0008	0.85	0.0009	0.97	0.0003	0.88	0.0024	0.88	0.0014	0.84	0.0003	0.53
-SO3H Alone	PFOS	1.90	0.1032	0.74	0.0456	0.57	0.0056	0.39	0.0948	0.48	0.0397	0.37	0.0059	0.37
	PFOS	0.03	0.0010	0.52	0.0005	0.45	0.0001	0.44	0.0013	0.51	0.0006	0.45	0.0002	0.73
-C2H6S O3H	6:2 FTS	0.50	0.0054	0.64	0.0054	0.89	0.0024	0.93	0.0019	0.09	0.0024	0.42	0.0030	0.96
	6:2 FTS	0.05	0.0007	0.70	0.0006	0.87	0.0002	0.92	0.0008	0.78	0.0004	0.57	0.0001	0.79
-COOH Mix	PFBA	0.11	0.0148	0.95	0.0086	0.86	0.0008	0.35	0.0157	0.78	0.0067	0.57	0.0005	0.17
	PFPeA	0.14	0.0222	0.96	0.0120	0.83	0.0012	0.36	0.0247	0.79	0.0104	0.57	0.0008	0.19
	PFHxA	0.15	0.0236	0.95	0.0123	0.80	0.0012	0.35	0.0248	0.76	0.0103	0.54	0.0008	0.19
	PFHpA	0.13	0.0209	0.95	0.0109	0.81	0.0011	0.36	0.0177	0.77	0.0073	0.54	0.0006	0.20
	PFOA	0.12	0.0187	0.95	0.0097	0.80	0.0010	0.35	0.0161	0.76	0.0066	0.53	0.0005	0.19
	PFNA	0.14	0.0227	0.95	0.0117	0.79	0.0011	0.34	0.0200	0.75	0.0082	0.52	0.0007	0.19
	PFDA	0.10	0.0174	0.94	0.0087	0.77	0.0008	0.33	0.0147	0.74	0.0060	0.52	0.0005	0.19
	PFUnA	0.10	0.0166	0.95	0.0081	0.76	0.0008	0.32	0.0123	0.77	0.0051	0.54	0.0005	0.24
PFDoA	0.04	0.0073	0.91	0.0035	0.73	0.0003	0.31	0.0035	0.88	0.0016	0.67	0.0002	0.50	
-SO3H Mix	PFBS	0.13	0.0004	0.96	0.0001	0.21	0.0000	0.53	0.0009	0.85	0.0005	0.76	0.0000	0.21
	PFHxS	0.11	0.0037	0.61	0.0017	0.52	0.0005	0.81	0.0040	0.68	0.0019	0.59	0.0003	0.48
	PFOS	0.09	0.0046	0.84	0.0028	0.84	0.0006	0.72	0.0051	0.96	0.0030	0.87	0.0003	0.40
-SO2NH 2 Mix	FOSA	0.76	0.0063	0.73	0.0050	0.88	0.0010	0.64	0.0078	0.91	0.0047	0.86	0.0009	0.74

8 **Table A7:** Peak area of different fluorinated compounds identified following PFOS degradation
 9 at pH 7 and 11.

pH 7									
Dose (kGy)	Blank	0	1	2.5	5	10	20	40	80
PFOS	NF	3.23E+10	3.04E+10	3.06E+10	2.96E+10	2.65E+10	2.57E+10	2.76E+10	1.80E+10
PFO-SO2	NF	NF	NF	2.32E+04	2.65E+05	3.89E+05	1.54E+06	NF	5.54E+04
PFO-SO4	NF	2.49E+07	1.59E+07	1.64E+06	2.38E+07	9.15E+06	2.22E+07	NF	4.28E+07
PFOS Alkene	NF	8.78E+07	5.12E+06	2.31E+07	3.70E+07	5.07E+07	1.11E+08	5.35E+07	2.89E+08
PFOS -F/+H	NF	5.74E+06	5.73E+07	2.41E+08	4.13E+08	6.09E+08	1.02E+09	5.90E+08	1.14E+09
PFOS -2F/+2H	NF	4.65E+05	1.23E+05	2.63E+06	9.31E+06	2.96E+07	1.06E+08	1.50E+07	2.15E+08
PFOS -3F/+3H	NF	NF	NF	8.03E+05	1.07E+06	2.77E+06	8.67E+06	4.70E+05	2.07E+06
PFOS -4F/+4H	NF	NF	3.41E+05	1.08E+06	1.10E+06	1.73E+06	1.69E+06	NF	NF
PFOS -5F/+5H	NF	NF	2.45E+05	1.03E+06	5.57E+05	8.90E+05	5.95E+04	NF	NF
PFOS -F/+CH3	NF	NF	1.08E+06	2.53E+06	3.75E+06	4.17E+06	3.49E+06	NF	NF
PFOS -F/+CH2CH3	NF	NF	2.58E+06	8.78E+05	9.58E+04	NF	NF	NF	NF
PFOS -F/+OH	NF	NF	2.11E+07	3.76E+07	2.57E+07	2.15E+07	9.03E+06	1.20E+07	7.57E+06
PFOS -F/+CH2OH	NF	NF	1.45E+07	4.20E+06	7.16E+05	1.10E+04	9.46E+03	1.36E+04	NF
PFOS -F/+C2H4OH	NF	NF	1.02E+07	2.81E+05	NF	NF	NF	NF	NF
PFOS -F/+C3H6OH	NF	NF	3.10E+06	NF	NF	NF	NF	NF	NF
PFOS -F/+C2H5O2	NF	NF	7.22E+04	2.74E+04	7.64E+04	NF	NF	NF	NF
PFOS -F/+C3H7O2	NF	NF	2.42E+06	NF	NF	NF	NF	NF	NF
PFOS -F/+C4H9O2	NF	NF	1.08E+06	NF	NF	NF	NF	NF	NF
PFOS -F/+C5H11O2	NF	NF	1.65E+06	NF	NF	NF	NF	NF	NF
PFOS -F/+C6H13O2	NF	NF	3.40E+05	NF	NF	NF	NF	NF	NF
PFOS -2F/+H, OH	NF	NF	NF	5.89E+04	2.81E+05	4.37E+05	2.01E+06	NF	1.09E+05
PFOS -2F/+2OH	NF	NF	1.68E+05	6.56E+05	9.33E+05	1.08E+06	1.87E+06	7.17E+06	6.00E+05
PFOS -CH3/+H	NF	2.05E+05	7.52E+05	2.50E+06	4.55E+06	7.17E+06	1.27E+07	6.97E+06	7.83E+06
pH 11									
Dose (kGy)	Blank	0	1	2.5	5	10	20	40	80
PFOS	NF	3.41E+10	2.75E+10	2.88E+10	2.66E+10	2.62E+10	2.76E+10	2.25E+10	1.82E+10
PFO-SO2	NF	NF	NF	1.14E+04	NF	2.43E+04	8.23E+05	3.78E+06	1.10E+06
PFO-SO4	NF	1.83E+07	1.23E+06	1.23E+06	8.92E+06	2.71E+06	2.80E+07	1.10E+05	3.13E+07
PFOS Alkene	NF	8.97E+07	2.47E+08	2.63E+08	5.83E+08	5.68E+08	3.97E+08	1.37E+08	5.88E+07
PFOS -F/+H	NF	5.96E+05	5.37E+07	8.72E+07	2.74E+08	4.17E+08	7.66E+08	6.70E+08	2.28E+08
PFOS -2F/+2H	NF	NF	NF	2.33E+04	1.80E+06	6.82E+06	3.49E+07	6.73E+07	8.96E+07
PFOS -3F/+3H	NF	NF	NF	NF	6.35E+05	1.50E+06	1.34E+05	4.58E+06	NF
PFOS -4F/+4H	NF	NF	6.21E+04	5.80E+04	1.73E+06	3.17E+06	4.08E+06	2.45E+06	5.40E+05
PFOS -5F/+5H	NF	NF	3.44E+05	3.38E+05	4.02E+06	5.71E+06	3.95E+06	7.75E+05	NF
PFOS -F/+CH3	NF	NF	2.31E+06	2.59E+06	4.97E+06	6.27E+06	7.94E+06	9.55E+06	5.66E+06
PFOS -F/+CH2CH3	NF	NF	2.99E+06	4.61E+06	7.88E+06	5.93E+06	6.20E+05	NF	NF
PFOS -F/+OH	NF	NF	8.86E+06	1.21E+07	2.22E+07	1.86E+07	2.07E+07	2.07E+07	1.87E+07
PFOS -F/+CH2OH	NF	8.02E+03	7.94E+07	6.66E+07	6.05E+07	1.66E+07	4.20E+05	NF	NF
PFOS -F/+C2H4OH	NF	NF	2.51E+07	3.42E+07	3.24E+07	5.13E+06	1.51E+05	NF	NF
PFOS -F/+C3H6OH	NF	NF	1.22E+07	1.31E+07	7.44E+06	7.05E+04	NF	NF	NF
PFOS -F/+C2H5O2	NF	NF	1.62E+05	1.10E+05	7.15E+04	7.70E+04	1.03E+05	NF	NF
PFOS -F/+C3H7O2	NF	NF	7.67E+06	9.79E+06	2.03E+06	5.62E+04	3.12E+04	NF	NF
PFOS -F/+C4H9O2	NF	NF	8.94E+06	7.85E+06	7.80E+05	NF	NF	NF	NF
PFOS -F/+C5H11O2	NF	NF	8.29E+07	1.92E+07	2.66E+06	1.54E+05	NF	NF	NF
PFOS -F/+C6H13O2	NF	NF	2.65E+07	7.74E+06	1.26E+06	NF	NF	NF	NF
PFOS -2F/+H, OH	NF	NF	NF	1.14E+04	2.69E+05	2.44E+04	8.04E+05	3.80E+06	1.10E+06
PFOS -2F/+2OH	NF	NF	NF	NF	NF	8.34E+04	1.41E+06	1.16E+07	3.61E+07
PFOS -CH3/+H	NF	NF	6.03E+05	1.31E+06	4.94E+06	7.22E+06	1.22E+07	1.10E+07	4.06E+06

10

11 **Table A8:** Peak area of different fluorinated compounds identified following PFOA degradation at pH 7 and 11.

12

pH 7								
Dose	0	1	2.5	5	10	20	40	80
PFOA	8.27E+09	7.70E+09	8.73E+09	7.57E+09	7.08E+09	4.34E+09	5.25E+09	2.09E+09
PFOA Alkene	3.60E+07	1.13E+06	1.73E+06	1.44E+06	3.94E+06	6.09E+06	1.36E+07	1.63E+07
PFOA -F/+H	7.75E+06	1.36E+08	4.14E+08	2.60E+08	8.57E+08	4.00E+08	1.89E+08	1.65E+08
PFOA -2F/+2H	7.35E+04	9.05E+05	2.71E+06	1.59E+06	7.16E+06	6.50E+06	2.52E+06	3.44E+06
PFOA -F/+CH3	NF	3.49E+04	1.65E+05	9.60E+04	6.34E+04	NF	NF	NF
PFOA -F/+OH	7.12E+03	3.51E+05	7.29E+05	2.87E+05	4.00E+05	2.91E+05	4.35E+05	2.22E+05
PFOA -2F/+2OH	5.72E+04	1.22E+06	2.84E+05	1.90E+05	2.98E+05	1.69E+05	4.05E+05	1.04E+05
PFOA -F/+CH2OH	NF	1.28E+07	1.87E+06	1.74E+04	NF	NF	NF	NF
PFOA -F/+C2H4OH	NF	2.61E+06	1.44E+05	NF	NF	NF	NF	NF
PFOA -F/+C3H6OH	NF	6.34E+05	2.00E+05	NF	NF	NF	NF	NF
PFOA -F/+C4H8OH	NF	3.21E+04	NF	NF	NF	NF	NF	NF
pH 11								
Dose	0	1	2.5	5	10	20	40	80
PFOA	8.49E+09	8.49E+09	8.71E+09	6.84E+09	4.40E+09	2.68E+09	1.22E+09	2.31E+09
PFOA Alkene	4.05E+07	1.86E+07	4.36E+07	4.29E+07	3.02E+07	1.43E+07	2.76E+06	2.36E+06
PFOA -F/+H	2.15E+06	3.84E+08	1.13E+09	1.54E+09	1.84E+09	2.24E+09	1.34E+09	6.72E+08
PFOA -2F/+2H	NF	4.68E+05	5.05E+06	7.79E+06	1.69E+07	2.76E+07	1.51E+07	7.09E+06
PFOA -F/+CH3	NF	2.31E+05	7.84E+05	1.32E+06	1.82E+06	1.30E+06	5.23E+05	1.46E+05
PFOA -F/+OH	8.27E+03	4.54E+05	7.01E+05	4.90E+05	5.01E+05	4.54E+05	3.15E+05	6.02E+05
PFOA -2F/+2OH	NF	NF	NF	1.35E+04	1.51E+05	5.10E+05	1.93E+06	3.30E+06
PFOA -F/+CH2OH	NF	4.06E+07	5.23E+07	1.23E+07	3.64E+05	3.09E+04	NF	NF
PFOA -F/+C2H4OH	NF	2.09E+07	2.16E+07	5.18E+06	1.27E+05	NF	NF	NF
PFOA -F/+C3H6OH	NF	3.80E+06	5.09E+06	1.72E+06	2.94E+05	NF	NF	NF
PFOA -F/+C4H8OH	NF	2.40E+06	9.34E+05	NF	NF	NF	NF	NF

13

14 **Table A9:** Peak area of different fluorinated compounds identified following 6:2 FTS degradation at pH 7 and 11.

pH 7									
Dose (kGy)	Blank	0	1	3	5	10	20	40	80
6:2 FTS	NF	4.26E+09	4.71E+09	5.26E+09	4.61E+09	6.21E+09	3.38E+09	3.43E+09	1.18E+09
6:2 FTS -F/+H	NF	NF	5.39E+06	2.41E+07	3.89E+07	7.15E+07	3.74E+07	4.20E+07	1.79E+07
6:2 FTS -2F/+2H	NF	NF	1.68E+05	4.70E+06	2.49E+07	1.20E+08	2.54E+08	2.57E+08	1.83E+08
6:2 FTS -3F/+3H	NF	NF	NF	7.34E+03	5.10E+03	3.38E+05	9.35E+05	1.04E+06	9.98E+05
6:2 FTS -4F/+4H	NF	NF	NF	NF	NF	NF	1.37E+05	1.29E+05	2.84E+05
6:2 FTS -5F/+5H	NF	NF	NF	NF	NF	NF	NF	NF	NF
6:2 FTS -6F/+6H	NF	NF	NF	NF	NF	NF	NF	NF	NF
6:2 FTS -F/+CH₂OH	NF	5.29E+03	2.13E+06	1.01E+07	1.50E+07	2.16E+07	1.16E+07	1.14E+07	4.55E+06
6:2 FTS -3F/+2H, CH₂OH	NF	NF	NF	NF	NF	NF	NF	NF	NF
6:2 FTS -2F/+CH₃, +OH	NF	NF	6.32E+03	1.20E+06	7.52E+06	2.98E+07	6.26E+07	6.71E+07	4.40E+07
6:2 FTS -2F/+(CH₂OH)₂	NF	NF	NF	1.02E+06	4.95E+06	1.72E+07	3.31E+07	3.11E+07	2.09E+07
6:2 FTS -3F/+H, Alkene	NF	NF	NF	5.82E+05	1.08E+06	1.25E+07	1.63E+07	6.48E+06	4.47E+06
pH 11									
Dose (kGy)	Blank	0	1	2.5	5	10	20	40	80
6:2 FTS	NF	4.66E+09	4.42E+09	5.16E+09	4.84E+09	3.89E+09	4.46E+09	2.58E+09	1.74E+09
6:2 FTS -F/+H	NF	NF	9.78E+05	2.75E+06	7.09E+06	7.80E+06	1.53E+07	9.59E+06	1.25E+07
6:2 FTS -2F/+2H	NF	NF	6.70E+03	1.04E+05	1.53E+06	4.20E+06	1.79E+07	2.74E+07	5.38E+07
6:2 FTS -3F/+3H	NF	NF	NF	NF	8.12E+04	1.46E+05	1.22E+06	2.27E+06	5.19E+06
6:2 FTS -4F/+4H	NF	NF	NF	NF	NF	3.42E+04	2.93E+05	9.46E+05	2.92E+06
6:2 FTS -5F/+5H	NF	NF	NF	NF	5.85E+04	2.54E+05	7.72E+05	1.45E+06	2.63E+06
6:2 FTS -6F/+6H	NF	NF	NF	NF	NF	4.04E+04	9.01E+04	2.37E+05	4.49E+05
6:2 FTS -F/+CH₂OH	NF	NF	1.93E+06	3.40E+06	5.06E+06	4.06E+06	5.05E+06	2.93E+06	2.42E+06
6:2 FTS -3F/+2H, CH₂OH	NF	NF	NF	NF	1.09E+06	2.47E+06	5.78E+06	6.94E+06	1.36E+07
6:2 FTS -2F/+CH₃, +OH	NF	NF	1.15E+06	2.93E+06	4.90E+06	4.23E+06	4.97E+06	2.37E+06	1.33E+06
6:2 FTS -2F/+(CH₂OH)₂	NF	NF	2.51E+05	8.00E+05	1.76E+06	2.48E+06	4.54E+06	4.49E+06	4.67E+06
6:2 FTS -3F/+H, Alkene	NF	NF	6.74E+05	3.65E+06	4.05E+07	7.26E+07	1.83E+08	1.20E+08	8.73E+07

15

Table A10 – High resolution mass spectrometry results for identified degradation products of PFOS, PFOA, and 6:2 FTS. Mass error generated by software when compound intensities are at a specific threshold. Mathematical mass error calculated for all compounds.

Group	Accurate Mass	Theoretical Mass	Mass Error (ppm)	Formula	Name
Parent PFOS	498.9301	498.93022	-0.24	C8F17SO3	PFOS
Alkene	460.9332	460.93341	-0.46	C8F15SO3	PFOS Alkene
H Substitution	480.9396	480.93964	-0.08	C8O3F16SH	PFOS -F/+H
H Substitution	462.9492	462.94906	0.30	C8O3F15SH2	PFOS -2F/+2H
H Substitution	444.9584	444.95848	-0.18	C8O3F14SH3	PFOS -3F/+3H
H Substitution	426.9678	426.9679	-0.23	C8O3F13SH4	PFOS -4F/+4H
H Substitution	408.9775	408.97733	0.42	C8O3F12SH5	PFOS -5F/+5H
H Substitution	390.9867	390.98675	-0.13	C8F11SO3H6	PFOS -5F/+5H
OH Substitution	496.9345	496.93455	-0.10	C8F16SO4H	PFOS -F/+OH
H Substitution	430.9428	430.94283	-0.07	C7F14HSO3	PFOS -CF3/+H
OH Substitution	510.9505	510.9502	0.59	C9F16SO4H3	PFOS -F/+CH2OH
OH Substitution	524.9657	524.96585	-0.29	C10F16SO4H5	PFOS -F/+C2H4OH
OH Substitution	538.9813	538.9815	-0.37	C11F16SO4H7	PFOS -F/+C3H6OH
Alkylated	494.9554	494.95529	0.22	C9F16SO3H3	PFOS -F/+CH3
Alkylated	508.9698	508.97094	-2.24	C10F16SO3H5	PFOS -F/+CH2CH3
Carboxylated	540.9612	540.96077	0.79	C10F16SO5H5	PFOS -F/+C2H5O2
Carboxylated	554.9763	554.97642	-0.22	C11F16SO5H7	PFOS -F/+C3H7O2
Carboxylated	568.9921	568.99207	0.05	C12F16SO5H9	PFOS -F/+C4H9O2
Carboxylated	583.0075	583.00772	-0.38	C13F16SO5H11	PFOS -F/+C5H11O2
Carboxylated	597.0233	597.02337	-0.12	C14F16SO5H13	PFOS -F/+C6H13O2
H, OH Substitution	478.9441	478.94398	0.25	C8F15SO4H2	PFOS -2F/+H, OH
OH, OH Substitutor	494.9389	494.93889	0.02	C8F15SO5H2	PFOS -2F/+OH, OH
Sulfate Reduced	482.9353	482.9353	0.00	C8F17SO2	Perfluorooctane-SO2
Sulfate Oxidized	514.9249	514.92513	-0.45	C8F17SO4	Perfluorooctane-SO4
Parent PFOA	412.9662	412.96643	-0.56	C8F15O2	PFOA
Alkene	374.9697	374.96962	0.21	C8F13O2	PFOA Alkene
H Substitution	394.9757	394.97585	-0.38	C8F14O2H	PFOA -F/+H
H Substitution	376.9855	376.98527	0.61	C8F13O2H2	PFOA -2F/+2H
OH Substitution	410.9706	410.97076	-0.39	C8F14O3H	PFOA -F/+OH
OH Substitution	424.9865	424.98641	0.21	C9F14O3H3	PFOA -F/CH2OH
OH Substitution	439.002	439.00206	-0.14	C10F14O3H5	PFOA -F/C2H4OH
OH Substitution	453.0177	453.01771	-0.02	C11F14O3H7	PFOA -F/C3H6OH
OH Substitution	467.0333	467.03336	-0.13	C12F14O3H9	PFOA -F/C4H8OH
OH, OH Substitutor	408.9752	408.9751	0.24	C8F13OH2	PFOA -2F/+OH, OH
Alkylated	408.9914	408.9915	-0.24	C9F14O2H3	PFOA -F/CH3
Parent 6:2 FTS	426.9674	426.9679	-1.17	C8H4F13SO3	6:2 FTS
H Substitution	408.9774	408.97733	0.17	C8H5F12SO3	6:2 FTS -F/+H
H Substitution	390.9868	390.98675	0.13	C8H6F11SO3	6:2 FTS -2F/+2H
H Substitution	372.9963	372.99617	0.35	C8H7F10SO3	6:2 FTS -3F/+3H
H Substitution	355.0057	355.00559	0.31	C8H8F9SO3	6:2 FTS -4F/+4H
H Substitution	337.0153	337.01501	0.86	C8H9F8SO3	6:2 FTS -5F/+5H
H Substitution	319.0243	319.02444	-0.44	C8H10F7SO3	6:2 FTS -6F/+6H
H Sub, Alkene	370.9804	370.98052	-0.32	C8H5F10SO3	6:2 FTS -3F/+H Alkene
OH Sub, Alkylation	420.9972	420.99731	-0.26	C9H8F11SO4	6:2 FTS -2F/+CH3, +OH
OH Substitution	438.9879	438.98811	-0.48	C9F15H7SO3	6:2 FTS -F/+CH2OH
H, OH Substitution	420.9975	420.99731	0.45	C9H8F11SO4	6:2 FTS -2F/+H, CH2OH
H, OH Substitution	403.0069	403.00673	0.42	C9H9F10SO4	6:2 FTS -3F/+2H, CH2OH
Di-OH Substitution	451.008	451.00788	0.27	C10H10F11SO5	6:2 FTS -2F/+(CH2OH)2

Statistical Analysis

Table A11: Two way ANOVA performed for PFOS, showing $P < 0.05$ for concentration, pH, and the interaction of the two variables.

Anova: Two-Factor With Replication (PFOS)						
SUMMARY	pH 7	pH 11	Total			
<i>Low</i>						
Count	3	3	6			
Sum	1.91188	0.886464	2.798344			
Average	0.637293	0.295488	0.466391			
Variance	0.000723	0.004395	0.037096			
<i>High</i>						
Count	3	3	6			
Sum	1.749103	1.576951	3.326054			
Average	0.583034	0.52565	0.554342			
Variance	0.001811	0.003566	0.003138			
<i>Total</i>						
Count	6	6				
Sum	3.660983	2.463415				
Average	0.610164	0.410569				
Variance	0.001897	0.019077				
ANOVA						
<i>Source of Variation</i>	<i>SS</i>	<i>df</i>	<i>MS</i>	<i>F</i>	<i>P-value</i>	<i>F crit</i>
Concentration	0.023207	1	0.023207	8.845473	0.017759	5.317655
pH	0.119514	1	0.119514	45.55433	0.000145	5.317655
Interaction	0.060672	1	0.060672	23.12574	0.00134	5.317655
Within	0.020988	8	0.002624			
Total	0.224381	11				

Table A12: Two way ANOVA performed for PFOA, showing $P > 0.05$ for concentration, pH, and the interaction of the two variables.

Anova: Two-Factor With Replication (PFOA)						
SUMMARY	pH 7	pH 11	Total			
<i>Low</i>						
Count	3	3	6			
Sum	0.616594	0.380674	0.997268			
Average	0.205531	0.126891	0.166211			
Variance	0.018946	0.01303	0.014645			
<i>High</i>						
Count	3	3	6			
Sum	1.138086	0.709157	1.847242			
Average	0.379362	0.236386	0.307874			
Variance	0.004151	0.016273	0.014302			
<i>Total</i>						
Count	6	6				
Sum	1.75468	1.089831				
Average	0.292447	0.181639				
Variance	0.018304	0.015318				
ANOVA						
<i>Source of Variation</i>	<i>SS</i>	<i>df</i>	<i>MS</i>	<i>F</i>	<i>P-value</i>	<i>F crit</i>
Concentration	0.060205	1	0.060205	4.595847	0.064395	5.317655
pH	0.036835	1	0.036835	2.8119	0.132091	5.317655
Interaction	0.003104	1	0.003104	0.236977	0.639454	5.317655
Within	0.104798	8	0.0131			
Total	0.204943	11				

Table A13: Two way ANOVA performed for 6:2 FTS, showing $P < 0.05$ for concentration, interaction and $P > 0.05$ for pH.

Anova: Two-Factor With Replication (6:2 FTS)						
SUMMARY	pH 7	pH 11	Total			
<i>Low</i>						
Count	3	3	6			
Sum	2.022569	2.338341	4.36091			
Average	0.67419	0.779447	0.726818			
Variance	0.001486	0.000321	0.004047			
<i>High</i>						
Count	3	3	6			
Sum	1.908708	1.686617	3.595326			
Average	0.636236	0.562206	0.599221			
Variance	0.00363	0.006413	0.005662			
<i>Total</i>						
Count	6	6				
Sum	3.931277	4.024958				
Average	0.655213	0.670826				
Variance	0.002479	0.016852				
ANOVA						
<i>Source of Variation</i>	<i>SS</i>	<i>df</i>	<i>MS</i>	<i>F</i>	<i>P-value</i>	<i>F crit</i>
Concentration	0.048843	1	0.048843	16.48626	0.003632	5.317655
pH	0.000731	1	0.000731	0.246854	0.632663	5.317655
Interaction	0.024108	1	0.024108	8.137297	0.021394	5.317655
Within	0.023701	8	0.002963			
Total	0.097384	11				

Appendix B – Supplemental Information for Chapter 4

Table B1 – Review of TOP assay methods employed in literature to identify key operational parameters (Al Amin et al., 2021a; Eriksson et al., 2022; Fan et al., 2021; Gökener et al., 2020; Houtz et al., 2018, 2013; Houtz and Sedlak, 2012a; Hutchinson et al., 2020; Janda et al., 2019; Kaiser et al., 2021; Katz et al., 2022; Larsson et al., 2018; Liu et al., 2022; Martin et al., 2019; Neuwald et al., 2022; Rodgers et al., 2022; Rodowa et al., 2020; Schaefer et al., 2022; Schellenberger et al., 2022; Zhang et al., 2019; Zhou et al., 2021; Zhu and Kannan, 2020).

Author	Year	Matrix	Oxidizer	Base	Activator	Time	Quench	MeOH Addition	Cleanup	PFAS Recovery / Yield	Notes
Houtz	2012	Stormwater	KPS (60 mM)	NaOH (150 mM)	Heat (85 C°)	6 hours	Cooled to RT, HCl	No	SPE	6:2 FTS 73±10%	N/A
Houtz	2013	AFFF in groundwater	KPS (60 mM)	NaOH (125 mM)	Heat (85 C°)	6 hours	HCl	Yes	No	N/A	N/A
Larsson	2018	AFFF (13,600x DF)	KPS (54 mM)	NaOH (150 mM)	Heat (85 C°)	6 hours	Cooled ice bath, HCl	No	SPE	N/A	Ultrasonication during and after TOP to desorb PFAS. No headspace
Houtz	2018	AFFF in WWTP water	KPS (60 mM)	NaOH (125 mM)	Heat (85 C°)	6 hours	HCl	Yes	SPE	6:2 FTS 95±4%	N/A
Janda	2019	Methanolic soil extract	KPS (59 mM)	NaOH (150 mM)	Heat (85 C°)	20 hours	Cooled ice bath	No	Evaporation, extraction of residue	PFAS Suite 68-123%	No headspace. 6:2 FTS not measured for PFAS recovery
Martin	2019	Groundwater	KPS (51 mM)	NaOH (167 mM)	Heat (85 C°)	6 hours	HCl	Yes	Centrifuge to remove salt	PFAS Suite 62-112% 6:2 FTS 88±5	Found 80% MeOH in HPLC vial required to avoid sorptive loss
Zhang	2019	Spiked DI water	KPS (5 mM)	NaOH (150 mM)	Heat (85 C°)	6 hours	HNO3	No	SPE	6:2 FTS 67±15%	GenX and other PFEAs were not oxidatively converted
Rodowa	2020	AFFF in groundwater	KPS (30 mM)	NaOH (63 mM)	Heat (85-90 C°)	6 hours	HCl	No	Extracted with 1:9 2,2,2 trifluoroethanol in ethyl acetate	N/A	N/A
Gökener	2020	Feed and egg albumen	KPS (200 mM)	NaOH (500 mM)	Heat (85 C°)	7 hours	Cooled to RT, HCl	No	SPE	PFAS Suite 36-93% EtFOSAA 82±7%	6:2 FTS not measured for PFAS recovery
Hutchinson	2020	Biosolids	KPS (200 mM)	NaOH (250 mM)	Heat (85 C°)	6 hours	Cooled to RT, HCl	No	SPE	N/A	Pre-treated with 5 mL H2O2 at 85 C° for 24 hours
Zhu	2020	Methanolic textile extracts	KPS (128 mM)	NaOH (690 mM)	Heat (85 C°)	6 hours	Cooled to RT, buffered (AmmAc), HCl	No	SPE	PFAS Suite 72-123%	6:2 FTS not measured for PFAS recovery
Zhou	2021	Groundwater	KPS (58 mM)	NaOH (150 mM)	Heat (85 C°)	6 hours	Cooled ice bath, HCl	No	SPE	N/A	Methods written poorly
Al Amin	2021	Spiked DI water	KPS (66 mM)	NaOH (150 mM)	Heat (85 C°)	6 hours	Cooled to RT, HCl, ultrasonication	No	N/A	6:2 FTS ~60% (100 ug/L) 6:2 FTS ~80% (10,000 ug/L)	N/A
Kaiser	2021	Wastewater effluent	Ozone (0.3 mM)	N/A	N/A	N/A	Formic acid, ultrasonication	No	No	PFAS Suite 78±14%	Resulted in conversion of precursors to 6:2 FTS
Fan	2021	Spiked DI water	KPS (60 mM)	NaOH (150 mM)	UV (254 nm, 16x14 watt)	6 hours	Cooled to RT, HCl	No	No	6:2 FTS 100%	Oxidation completed by one hour
Rodgers	2022	Methanol extracts	KPS (60 mM)	NaOH (125 mM)	Heat (85 C°)	6 hours	HCl	No	No	N/A	Commercial product analysis
Neuwald	2022	Drinking water	KPS (74 mM)	NaOH (186 mM)	Heat (85 C°)	20 hours	Cooled ice bath, formic acid	Yes	SPE	EtFOSAA >70%	N/A
Schaefer	2022	Biosolid extracts	KPS (66 mM)	NaOH (166 mM)	Heat (85 C°)	6 hours	Cooled ice bath	No	Subsampled and diluted with alcohol to remove salts	N/A	N/A
Katz	2022	Estuary water	KPS (60 mM)	NaOH (160 mM)	Heat (85 C°)	6 hours	Cooled to RT, HCl	No	SPE	N/A	N/A
Liu	2022	Methanolic soil extracts	KPS (60 mM)	NaOH (125 mM)	Heat (85 C°)	6 hours	Cooled to RT, HCl	Yes	No	PFAS Suite 60-128% 6:2 FTS 74-98%	N/A
Eriksson	2022	Surface treatment products	KPS (60 mM)	NaOH (150 mM)	Heat (85 C°)	6 hours	Cooled ice bath, HCl	No	SPE	6:2 FTS 106±5%	N/A
Schellenberger	2022	Methanolic textile extracts	KPS (58 mM)	NaOH (150 mM)	Heat (85 C°)	6 hours	HCl	No	SPE	EtFOSAA 110±2%	N/A

PFAS Analysis

Samples were analyzed on a ThermoFisher Exploris 120 Orbitrap coupled to a Vanquish ultra-high-performance liquid chromatography (uHPLC) system using a 100 mm x 2.1 mm x 3.0 μ m ACME C18 analytical column and paired guard column. Mobile phases consisted of 5 mM ammonium acetate in DI water (A) and acetonitrile (B). The elution profile started at 90% A/10% B with a flow rate of 0.5 mL/min, transitioning to 100% B over 10 minutes, holding for 2 minutes, then equilibrating at starting conditions for 3 minutes. A diverter valve was used to send the first minute of elution to waste to avoid heavy salt content impacting the MS. A heated electrospray ionization ion source was used, with a static spray voltage. Both positive and negative ion voltage were 3000 V. Gas was run in static mode, with a sheath gas of 50 (arbitrary units), auxiliary gas of 10 (arbitrary units) and sweep gas of 1 (arbitrary units). The ion transfer tube temperature was set to 325°C, the vaporizer temperature was set to 350°C, and mild trapping was not used. The MS global settings were set to expect an LC peak width of 10 seconds, and the mass was calibration before each sample injection using the RunStart EASY-IC™ system.

Before samples were run, the UHPLC and Orbitrap were flushed with 10% DI water, 90% ACN for a minimum of 1 hour, until baseline ion peak intensity was stable (indicating a clean sample path), and spray stability was <5%. The analysis method was set up with two ‘experiments’ (XCalibur® software nomenclature for analytical protocols), one for positive mode analysis and one for negative mode analysis. Each experiment used an orbitrap resolution of 60,000, a scan range of 100-1000 m/z, an RF lens of 70%, a standard automatic gain control target, an automatic maximum injection time mode setting, and had in-source fragmentation disabled. PFAS peak intensities were extracted using XCalibur® software (Processing Setup and Quan Browser) and converted to concentration using an external calibration curve.

PFAS were quantified with an external calibration curve (PFAC-MXB or PFAC-MXC, native mix, Wellington Labs, with additions of TFA, PFPrA, 6:2 FTS, 8:2 FTS, and FOSA) from 0.1 μ g/L to 50 μ g/L ($R_2 > 0.99$, detection limit of ~ 0.05 μ g/L for all PFAS). Quantification limits were set to the lowest concentration of each calibration curve. Detection limits were established by analyzing the matrix blank ten times, and then taking the sum of the mean concentration of the blank and three times the standard deviation of the blank. In situations where blanks yielded no detectable PFAS or signal, the detection limit was set as half of the quantitation limit, and confirmed by analyzing a calibration sample made at 0.05 μ g/L. For this reason, in situations where analysis of the blanks yielded no signal, the detection limit is arbitrarily high.

PFAS calibration verification standards at two different concentrations (50 μ g/L, 5 μ g/L) were run every 20 samples to measure possible instrument drift. Overall instrument drift was found to be <5% over the duration of the run. Samples were run in batches based on their concentration, with a minimum of four injection blanks (1:1 H₂O/MeOH) run between high concentration and low concentration batches, to eliminate carry over. Sample carryover was found to be <0.1% of previous PFAS concentration. The autosampler injection needle was cleaned between injections using the built-in flush program. The needle was washed for 10 seconds with flush solution (20%

H₂O, 35% isopropanol, 45% MeOH). Reagent blanks were run before and after each batch to track any contamination in the used reagents. All blanks were found to be below detection limits for PFAS.

Liquid chromatography – high resolution mass spectrometry (LC-HRMS) analysis was used to identify PFAS precursors in AFFF samples. LC-HRMS analysis was performed as described in previous works (Battye et al., 2022; O’Connor et al., 2023; Patch et al., 2022; Turner et al., 2021). Briefly, full scan data was acquired and PFAS precursors were identified using Background Subtractor (Thermo Fisher Scientific), FreeStyle, Processing Setup, and Quan Browser (all Thermo Fisher Scientific software tools). For each AFFF analysis, a background blank chromatogram (reagent blank) and matrix blank chromatogram were acquired. Chromatograms from each active experiment were blank subtracted and visually inspected for any new peaks. Following potential PFAS precursor identification, a homologue series search was performed using Isotope Simulation in Freestyle. If possible, these products were compared to known masses of AFFF precursors found in the literature and an in-house database of degradation products identified in previous work (Banayan Esfahani and Mohseni, 2022; Barzen-Hanson et al., 2017; Bentel et al., 2020b; D’Agostino and Mabury, 2014; Harding-Marjanovic et al., 2015; Houtz et al., 2013; Liu et al., 2022, 2021b; Martin et al., 2019; Munoz et al., 2021; Patch et al., 2022). Processed data was then inspected with Quan Browser, and exported to Microsoft Excel for data clean-up and interpretation.

PFAS detected by LC-HRMS (Table B5, S6) were semi-quantified to their closest homologue (if available) or their closest pKa homologue. Semi-quantified concentrations were calculated by dividing the PFAS area by the slope of the calibration curve of the related homologue. For 3M-related precursors, compounds were either semi-quantified using PFOS, PFHxS, or PFOSA. For FTSaB or FTB products, these were quantified with their 6:2 FTSaB, 5:3 FTB, or 5:1:2 FTB homologues. For 6:2 FTTAoS and related compounds, these were quantified with 6:2 FTS.

Table B2 – Mass spectrometer conditions used for the Agilent 6460 LC-MS analysis.

Mass Spectrometer Conditions (Agilent 6460 LC-MS)							
Gas Temp (C)	Gas Flow (L/m)	Nebulizer (PSI)	Sheath Gas (C)	Sheath Gas Flow (L/m)	Capillary (L/m)	Nozzle Voltage (V)	
325	9 L/min	30 PSI	30 C	12 L/min	12 L/min	0 V	
MRM Transitions							
Compound Name	Precursor (m/z)	Ion	Product (m/z)	Ion Fragmentor	Collision Energy	Cell Accelerator Voltage	Polarity
TFA	112.9	69	59	59	8	2	Negative
PFPA	163	118.8	59	59	8	2	Negative
PFBA	213	169	72	72	8	2	Negative
PFPeA	263	219	72	72	4	2	Negative
PFBS	298.9	99	154	154	34	2	Negative
PFBS	298.9	80	154	154	36	2	Negative
PFHxA	313	269	72	72	8	2	Negative
PFHxA	313	119	72	72	24	2	Negative
PFPeS	348.9	99	144	144	40	2	Negative
PFPeS	348.9	80	144	144	44	2	Negative
PFHpA	363	319	72	72	8	2	Negative
PFHpA	363	169	72	72	16	2	Negative
PFHxS	398.9	99	156	156	40	2	Negative
PFHxS	398.9	80	156	156	56	2	Negative
PFOA	413	369	72	72	8	2	Negative
PFOA	413	219	72	72	16	2	Negative
PFHpS	448.9	99	148	148	42	2	Negative
PFHpS	448.9	80	148	148	50	2	Negative
PFNA	463	419	72	72	8	2	Negative
PFNA	463	219	72	72	16	2	Negative
FOSA	497.9	169	150	150	36	3	Negative
FOSA	497.9	48	150	150	110	3	Negative
PFOS	498.9	99	148	148	50	2	Negative
PFOS	498.9	80	148	148	54	2	Negative
PFDA	513	469	72	72	12	2	Negative
PFDA	513	269	72	72	16	2	Negative
PFNS	548.9	99	148	148	52	2	Negative
PFUnDA	563	519	100	100	12	2	Negative
PFUnDA	563	319	100	100	20	2	Negative
PFDS	598.9	99	148	148	56	2	Negative
PFDS	598.9	80	148	148	60	2	Negative
PFDoDA	613	569	100	100	8	2	Negative
PFDoDA	613	269	100	100	24	2	Negative
PFTTrDA	663	619	100	100	12	2	Negative
PFTTrDA	663	319	100	100	20	2	Negative

Statistical Analysis

Three replicates were performed for each quenching method. Nine replicates were used for the pre-oxidation controls to provide a baseline concentration to compare recoveries. A total of 12 different quenching protocols were investigated. A three-way analysis of variance (ANOVA), followed by a series one-way ANOVAs were performed followed by Tukey post hoc tests (XLSTAT®). The ANOVA was performed twice, with PFOS and mass labelled PFOS as the dependent variables. Quenching reagents (acetic acid or acidified methanol), dilution type (whole sample or sub-sample dilution), and quenching time (immediate, cooled to room temperature, cooled in ice) were investigated as the categorical independent variables for each ANOVA.

Volume-Normalized Photon Irradiance to the Solution at 254 nm

The volume-normalized photon irradiance to the solution ($\text{mJ s}^{-1} \text{L}^{-1}$) were calculated for the UV-activated TOP experiments as described in literature (Banayan Esfahani and Mohseni, 2022; Bolton and Stefan, 2002; Chen et al., 2022b; Fennell et al., 2021; O'Connor et al., 2023; Tenorio et al., 2020). An actinometry solution containing 0.6 M KI (9.96 g), 0.1 M KIO₃ (2.14 g), and 0.01 M Na₂B₄O₇ (0.201 g) was prepared to 100 mL with deionized water and used within four hours of preparation. The UV lamp was turned on and warmed up for 10 minutes before actinometry experiments. The formation of triiodide was measured at 352 nm using a UV-vis spectrophotometer, and all photons entering the solution were assumed to be totally absorbed by the opaque (at 254 nm) solution (Thermo Fisher Scientific Genesys 20). Samples were taken at regular intervals for the first five minutes of the reaction, and the slope (absorbance vs seconds) was converted into concentration (molarity vs seconds) by dividing the absorbance by the molar absorptivity of triiodide at 254 nm ($27600 \text{ M}^{-1} \text{ cm}^{-1}$) and the pathlength of the cuvette (1 cm).

Volume-normalized photon irradiance (P_I) ($\text{mJ s}^{-1} \text{L}^{-1}$) by the 36 W lamp to the cuvettes was calculated in accordance with the below formula.

$$P_I = \frac{d[I_3^-]}{dt} * \frac{1}{\Phi} * U_{254nm}$$

Where $d[I_3^-]/dt$ is the rate of triiodide formation for cuvette ($3.8 \times 10^{-6} \text{ M s}^{-1}$), Φ is the quantum yield of triiodide at 22°C (0.69 moles Einstein⁻¹), and U_{254nm} is the molar photon energy at 254 nm (472,000 J/Ein). Therefore, the volume-normalized photon irradiance was calculated at $2.6 \text{ J s}^{-1} \text{L}^{-1}$ for the cuvette system. The cuvettes were positioned approximately 3.5 centimeters away from the lamp and rotated around the lamp using a rotary stand.

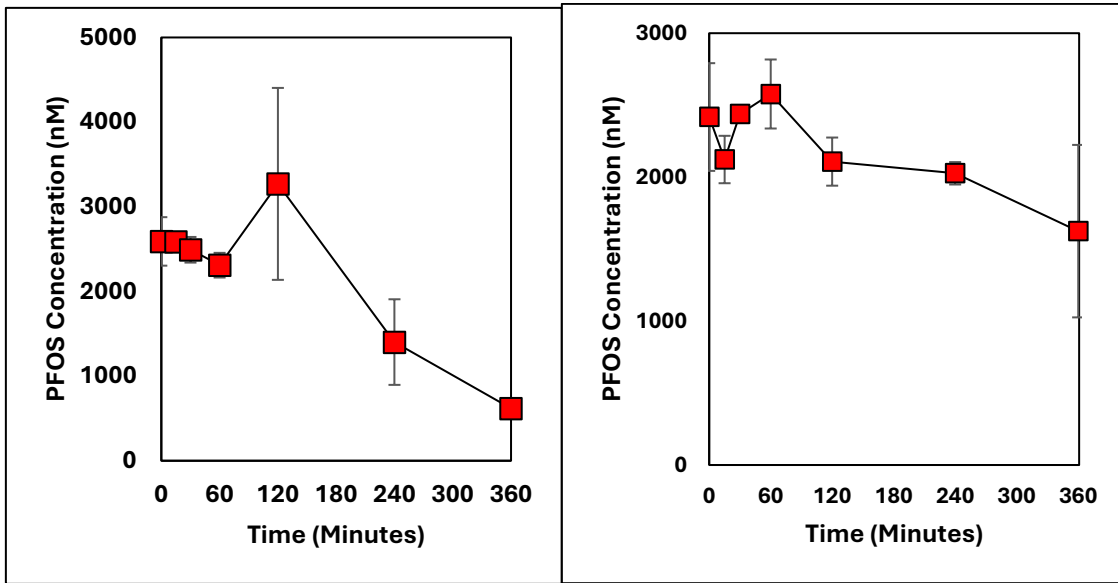


Figure B1 – PFOS concentrations during thermal-activated (left) and UV-activated (right) TOP assays before implementation of meticulous quenching protocols. Samples here quenched with 0.25 mL methanol only, with no consideration of pre-quench mixing.

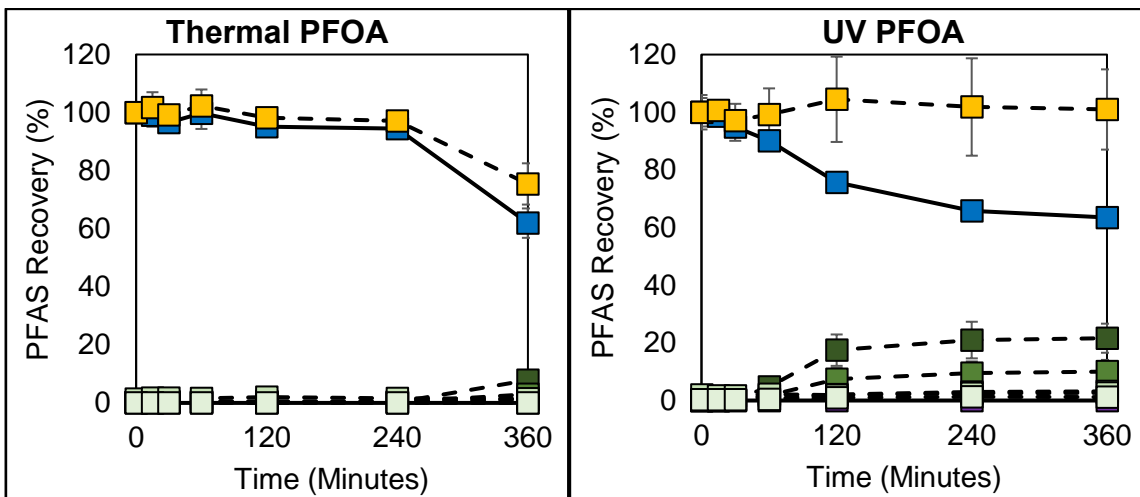


Figure B2 – Investigation of PFOA following thermal and UV-activated TOP assay. The NaOH concentration employed in these experiments was later identified to be less than 150 mM, leading to significant PFCA conversion with time. One mL samples were quenched immediately with 0.25 mL of acidified methanol (4% acetic acid) and sub-sampled.

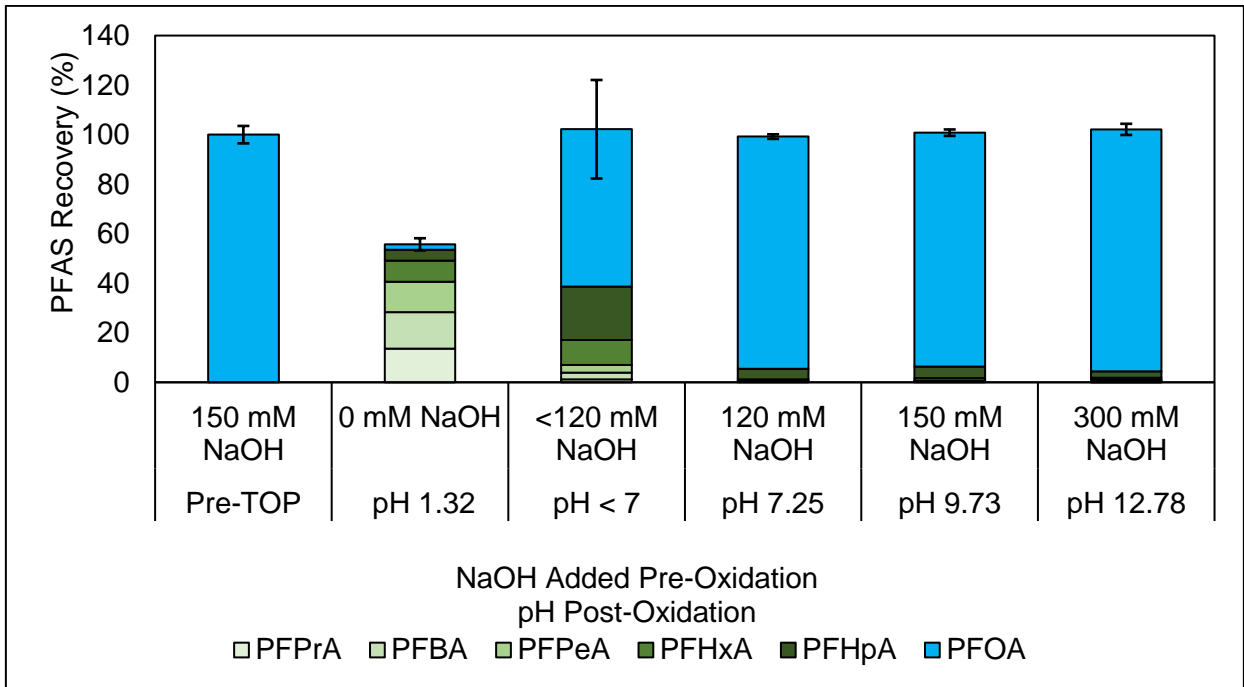


Figure B3 – UV-activated oxidation of PFOA with different initial concentrations of NaOH and pH measured after oxidation. The <120 mM NaOH sample was acquired during initial TOP assay investigations, before implementation of pH tracking in the method.

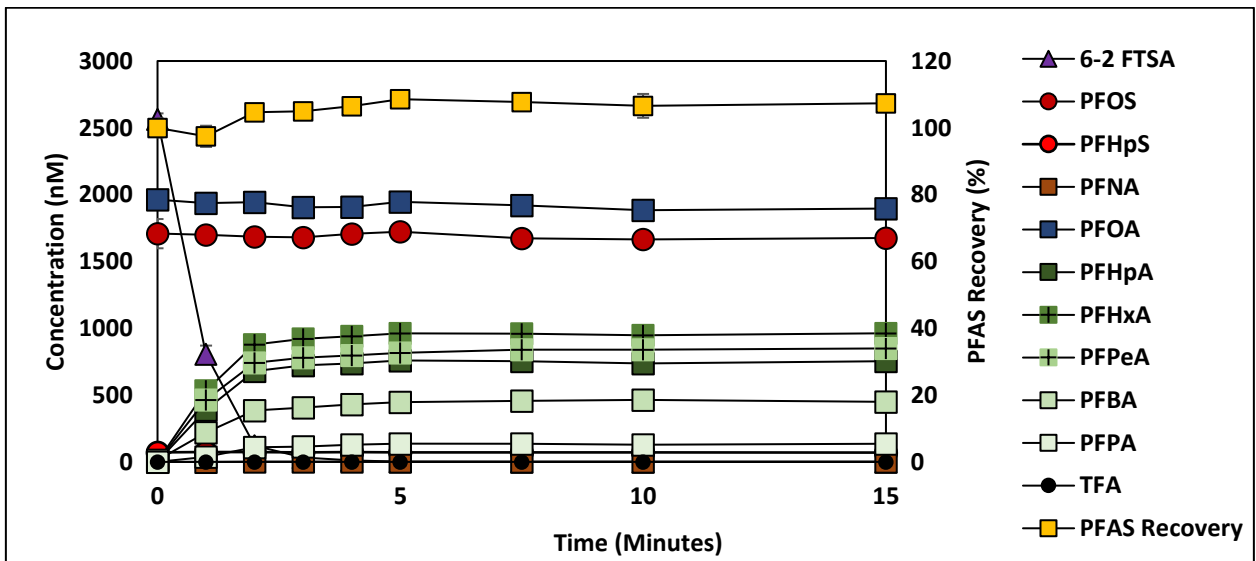


Figure B4 – Intensive time sampling of PFOS, PFOA, and 6:2 FTS following UV-activated TOP assay.

Table B3 – Different statistical groups following three-way ANOVA on PFOS and three-way ANOVA on PFOS corrected data. Quenching reagent, quenching interval, and dilution type were all selected as independent variables.

	Quench Reagent		Quench Interval				Dilution Type	
	Acetic Acid	Methanol/ Acetic Acid	Control	Immediate	Cooled Ice	Cooled RT	Sub-Sample	Whole Sample
PFOS	A	B	A	B	B	B	A	B
PFOS Corrected	A	A	A	A	B	B	A	A

Table B4 – Different statistical groups following eight, one-way ANOVAs employed with quenching interval used as the independent variable and PFOS concentration used as the dependent variable.

		Sub-Sample Dilution		Whole Sample Dilution	
		PFOS	PFOS Corrected	PFOS	PFOS Corrected
		Acetic Acid	Control	A	A
	Immediate	B	AB	B	A
	Cooled on Ice	B	B	B	B
	Cooled to RT	B	C	B	B
Methanol and Acetic Acid	Control	A	A	A	A
	Immediate	B	AB	B	AB
	Cooled on Ice	B	B	B	B
	Cooled to RT	B	C	B	AB

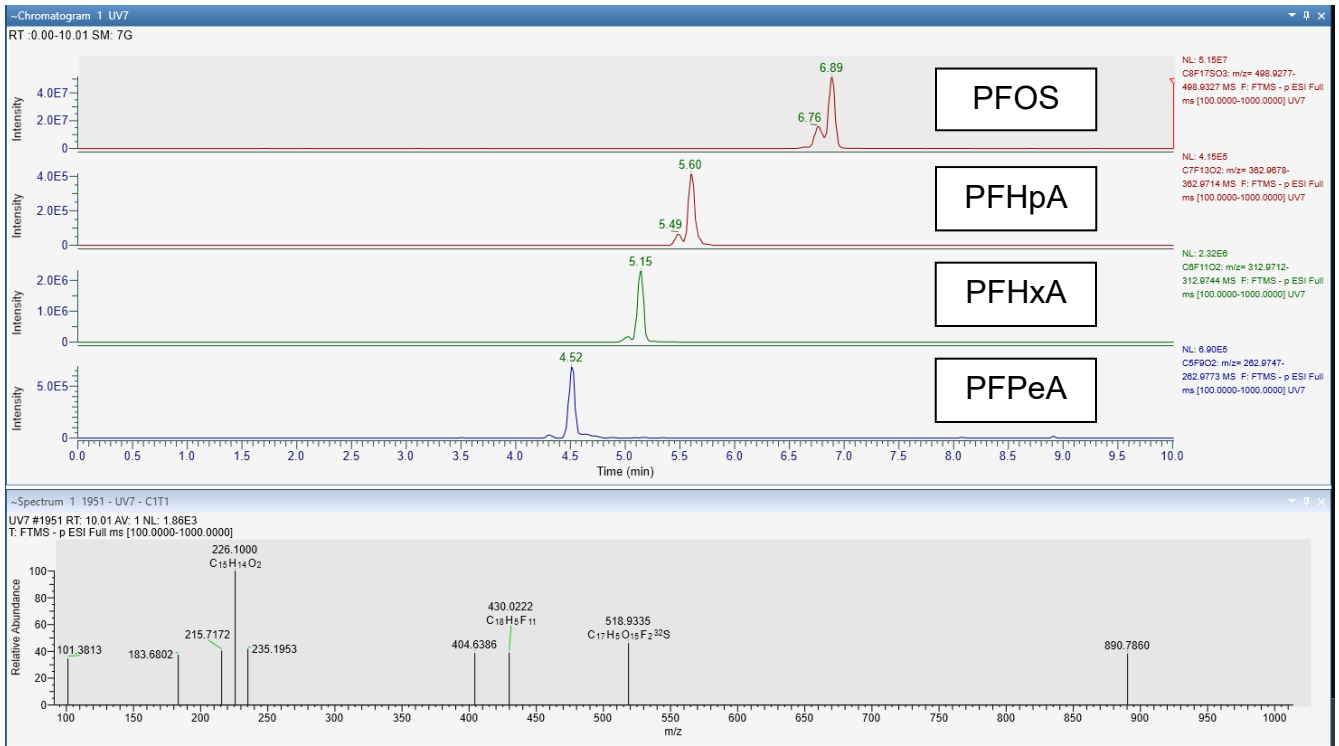


Figure B5 – Chromatograms of PFOS, PFHpA, PFHxA, and PFPeA in the 3M AFFF sample following UV oxidation, showing the presence of branched isomers.

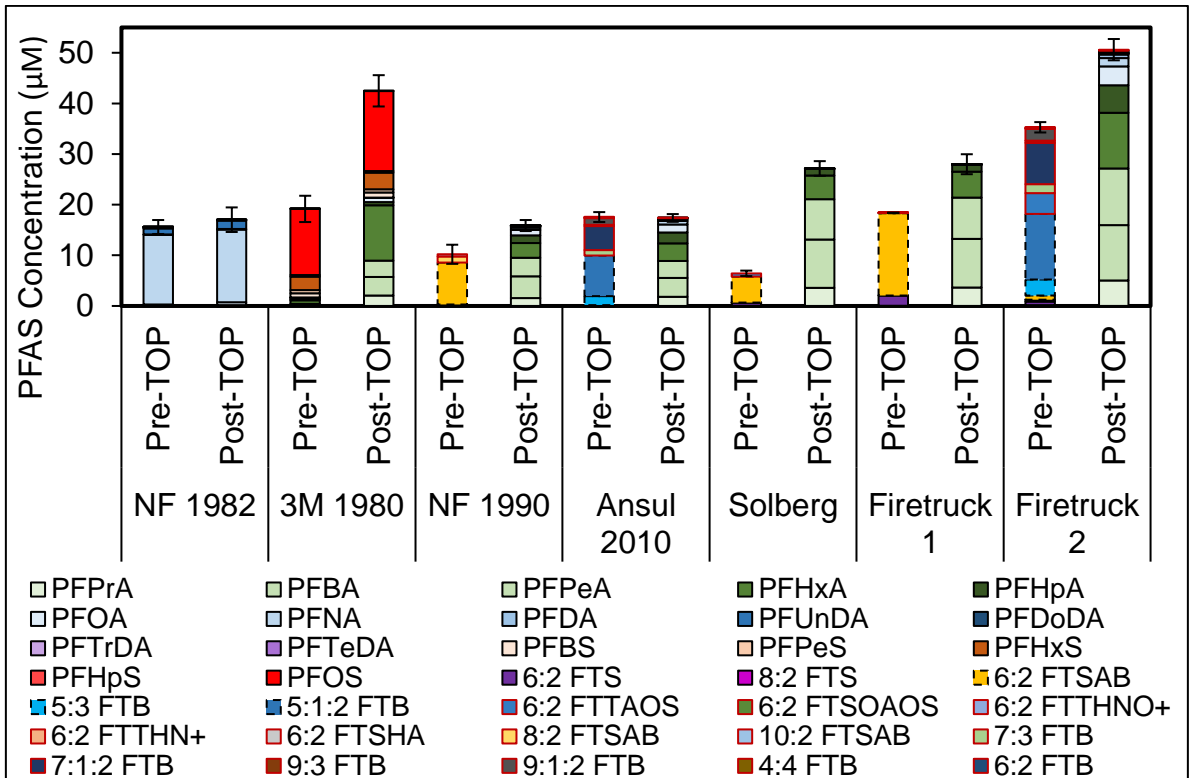


Figure B6 – PFAS concentration determined using standard analytical suite (black border), expanded analytical suite (dashed black border), and semi-quantified according to closest homologues (red border)

Table B5 – PFAS precursors identified in the 3M AFFF following 10,000 fold dilution in DI water.

Acronym	Name	LC-MS ionization mode	m/z (analyzed)	Found In
8-F5S-PFSA	Pentafluorosulfide perfluorooctane sulfonate	Negative	606.8962	3M
9-F5S-PFSA	Pentafluorosulfide perfluorononane sulfonate	Negative	656.8933	3M
O-PFOS	Oxa-perfluorooctane sulfonate	Negative	514.9252	3M
O-PFNS	Oxa-perfluorononane sulfonate	Negative	564.9227	3M
8-U-PFSA	Unsaturated perfluorooctane sulfonate	Negative	610.9246	3M
N-SP-FHxSA	N-sulfopropyl perfluorohexane sulfonamide	Negative	519.9565	3M
N-diHOPAmHOB-FPeSA	N-dihydroxy propyldimethylammoniohydroxybutyl perfluoropentane sulfonamide	Negative	537.0927	3M
N-diHOPAmHOB-FHxSA	N-dihydroxy propyldimethylammoniohydroxybutyl perfluorohexane sulfonamide	Negative	587.0894	3M
N-diHOPAmHOB-FPeSAPS	N-dihydroxy propyldimethylammoniohydroxybutyl perfluoropentane sulfonamidopropyl sulfonate	Negative	569.0973	3M
N-diHOPAmHOB-FHxSAPS	N-dihydroxy propyldimethylammoniohydroxybutyl perfluorohexane sulfonamidopropyl sulfonate	Negative	709.0931	3M
N-SPAmP-FHxSAPS	N-sulfopropyl dimethylammoniopropyl perfluorohexane sulfonamidopropyl sulfonate	Negative	727.0494	3M
N-HOEAmP-FBSAPS	N-hydroxyethyl dimethylammoniopropyl perfluorobutane sulfonamidopropyl sulfonate	Positive	551.0930	3M
N-HOEAmP-FPeSAPS	N-hydroxyethyl dimethylammoniopropyl perfluoropentane sulfonamidopropyl sulfonate	Positive	601.0895	3M
N-HOEAmP-FHxSAPS	N-hydroxyethyl dimethylammoniopropyl perfluorohexane sulfonamidopropyl sulfonate	Positive	651.0862	3M
N-HOEAmP-FHpSAPS	N-hydroxyethyl dimethylammoniopropyl perfluoroheptane sulfonamidopropyl sulfonate	Positive	701.0831	3M
N-HOEAmP-FOSAPS	N-hydroxyethyl dimethylammoniopropyl perfluorooctane sulfonamidopropyl sulfonate	Positive	751.0802	3M
PFBSAmS	Perfluorobutane sulfonamidoalkyl ammonium	Positive	399.0784	3M
PFPeSAmS	Perfluoropentane sulfonamidoalkyl ammonium	Positive	449.0751	3M
PFHxSAmS	Perfluorohexane sulfonamidoalkyl ammonium	Positive	499.0718	3M
PFOSAmS	Perfluorooctane sulfonamidoalkyl ammonium	Positive	549.0683	3M
PFHxSAm	Perfluorohexane sulfonamidoalkyl amine	Positive	485.0562	3M
N-SPrAmPr-FHxSA	N-sulfopropyl dimethylammoniopropyl perfluorohexane sulfonamide	Positive	607.0600	3M
N-SPrAmPr-FEtSAPrS	N-sulfopropyl dimethylammoniopropyl perfluoroethane sulfonamido propyl sulfonate	Positive	529.0823	3M
N-SPrAmPr-FPrSAPrS	N-sulfopropyl dimethylammoniopropyl perfluoropropane sulfonamido propyl sulfonate	Positive	579.0732	3M
N-SPrAmPr-FBSAPrS	N-sulfopropyl dimethylammoniopropyl perfluorobutane sulfonamido propyl sulfonate	Positive	629.0705	3M
N-SPrAmPr-FPeSAPrS	N-sulfopropyl dimethylammoniopropyl perfluoropentane sulfonamido propyl sulfonate	Positive	679.0671	3M
EtOH-AmPr-FHxSA	N-hydroxyethyl dimethylammoniopropyl perfluorohexane sulfonamide	Positive	529.0822	3M

Table B6 – PFAS precursors identified in the National Foam (1990) and Ansul (2012) AFFF following 10,000 fold dilution in DI water.

Acronym	Name	LC-MS ionization mode	<i>m/z</i> (analyzed)	Found In
8:2 FTThAd-PeA	8:2 fluorotelomer thioamido pentanoic acid	Negative	693.0683	National (1990) Foam
6:2 FTSAB	6:2 fluorotelomer sulfonamidopropyl betaine	Positive	571.0923	National (1990) Foam
8:2 FTSAB	8:2 fluorotelomer sulfonamidopropyl betaine	Positive	671.0860	National (1990) Foam
10:2 FTSAB	10:2 fluorotelomer sulfonamidopropyl betaine	Positive	771.0793	National (1990) Foam
6:2 FTA	6:2 fluorotelomer sulfonamido N-dimethyl amine	Positive	513.0869	National (1990) Foam
6:2 demethyl-FTA	6:2 fluorotelomer sulfonamido N-methyl amine	Positive	499.0722	National (1990) Foam
8:2 demethyl-FTA	8:2 fluorotelomer sulfonamido N-methyl amine	Positive	599.0676	National (1990) Foam
6:2 FTSHA	6:2 fluorotelomerthiohydroxyl ammonium	Positive	496.0948	Ansul (2012)
8:2 FTSHA	8:2 fluorotelomerthiohydroxyl ammonium	Positive	596.0887	Ansul (2012)
10:2 FTSHA	10:2 fluorotelomerthiohydroxyl ammonium	Positive	696.0852	Ansul (2012)
5:3 FTB	5:3 fluorotelomer betaine	Positive	414.0915	Ansul (2012)
7:3 FTB	7:3 fluorotelomer betaine	Positive	514.0854	Ansul (2012)
9:3 FTB	9:3 fluorotelomer betaine	Positive	614.0788	Ansul (2012)
11:3 FTB	11:3 fluorotelomer betaine	Positive	714.0721	Ansul (2012)
5:1:2 FTB	5:1:2 fluorotelomer betaine	Positive	432.0821	Ansul (2012)
7:1:2 FTB	7:1:2 fluorotelomer betaine	Positive	532.0762	Ansul (2012)
9:1:2 FTB	9:1:2 fluorotelomer betaine	Positive	632.0691	Ansul (2012)
11:1:2 FTB	11:1:2 fluorotelomer betaine	Positive	732.0630	Ansul (2012)
4:4 FTB	4:4 fluorotelomer betaine	Positive	378.1107	Ansul (2012)
6:4 FTB	6:4 fluorotelomer betaine	Positive	478.1042	Ansul (2012)
8:4 FTB	8:4 fluorotelomer betaine	Positive	578.0978	Ansul (2012)
10:4 FTB	10:4 fluorotelomer betaine	Positive	678.0914	Ansul (2012)
6:2 FTB	6:2 fluorotelomer betaine	Positive	450.0729	Ansul (2012)
8:2 FTB	8:2 fluorotelomer betaine	Positive	550.0667	Ansul (2012)
10:2 FTB	10:2 fluorotelomer betaine	Positive	650.0603	Ansul (2012)
4:1:3 FTB	4:1:3 fluorotelomer betaine	Positive	396.1012	Ansul (2012)
6:1:3 FTB	6:1:3 fluorotelomer betaine	Positive	496.0947	Ansul (2012)

Appendix C – Supplemental Information for Chapter 5

PFAS Analysis

Samples were analyzed on either on a ThermoFisher Exploris 120 Orbitrap coupled to a Vanquish ultra-high-performance liquid chromatography (UHPLC) system (herein referred to as LC-HRMS), or an Agilent 6460 Triple Quadrupole MS/MS coupled to an Agilent 1260 HPLC system. On the Orbitrap LC-HRMS, PFAS were separated using a 100 mm x 2.1 mm x 3.0 μ m ACME C18 analytical column and paired guard column. On the Agilent QQQ LC-MS, PFAS were separated using a 150 mm x 2.1 mm x 3.0 μ m ACME C18 analytical column and paired guard column. Mobile phases consisted of 5 mM ammonium acetate in DI water (A) and acetonitrile (B). The elution profile started at 90% A/10% B with a flow rate of 0.5 mL/min, transitioning to 100% B over 10 minutes, holding for 2 minutes, then equilibrating at starting conditions for 3 minutes. A diverter valve was used to send the first minute of elution to waste to avoid heavy salt content impacting the MS. A heated electrospray ionization ion source was used, with a static spray voltage. Both positive and negative ion voltage were 3000 V. Gas was run in static mode, with a sheath gas of 50 (arbitrary units), auxiliary gas of 10 (arbitrary units) and sweep gas of 1 (arbitrary units). The ion transfer tube temperature was set to 325°C, the vaporizer temperature was set to 350°C, and mild trapping was not used. The MS global settings were set to expect an LC peak width of 10 seconds, and the mass was calibrated before each sample injection using the RunStart EASY-IC™ system.

Before samples were run, the UHPLC and Orbitrap were flushed with 10% DI water, 90% ACN for a minimum of 1 hour, until baseline ion peak intensity was stable (indicating a clean sample path), and spray stability was <5%. The analysis method was set up with two ‘experiments’ (XCalibur® software nomenclature for analytical protocols), one for positive mode analysis and one for negative mode analysis. Each experiment used an orbitrap resolution of 60,000, a scan range of 100-1000 m/z, an RF lens of 70%, a standard automatic gain control target, an automatic maximum injection time mode setting, and had in-source fragmentation disabled. PFAS peak intensities were extracted using XCalibur® software (Processing Setup and Quan Browser) and converted to concentration using an external calibration curve.

PFAS were quantified with an external calibration curve (PFAC-MXB or PFAC-MXC, native mix, Wellington Labs, with additions of TFA, PFPrA, 6:2 FTS, 8:2 FTS, and FOSA). Quantification limits were set to the lowest concentration of each calibration curve. Detection limits were established by analyzing the matrix blank ten times, and then taking the sum of the mean concentration of the blank and three times the standard deviation of the blank. In situations where blanks yielded no detectable PFAS or signal, the detection limit was set as half of the quantitation limit, and confirmed by analyzing a calibration sample made at 0.05 μ g/L. For this reason, in situations where analysis of the blanks yielded no signal, the detection limit is arbitrarily high. For a complete list of the analytes measured using the expanded analytical method, please see Table C1.

Table C1 – PFAS directly quantified in the expanded analytical suite using an Agilent 6460 LC-MS (QQQ) and/or a ThermoFisher Exploris 120 Orbitrap (Orbi).

Analyte	Instrument Detect. Limit (µg/L)	Instrument Quant. Limit (µg/L)	Linear Dynamic Range (µg/L)	RSQ	Instrument
TFA	0.50	1	1 - 102.9	0.9998	QQQ
PFPtA	0.10	0.50	0.5 - 100.0	0.9993	QQQ
PFBA	0.05	0.10	0.1 - 104.0	0.9997	QQQ, Orbi
PFPeA	0.10	0.50	0.5 - 104.0	0.9999	QQQ, Orbi
PFHxA	0.05	0.10	0.1 - 52.7	0.9998	QQQ, Orbi
PFHpA	0.05	0.10	0.1 - 52.7	0.9998	QQQ, Orbi
PFOA	0.05	0.10	0.1 - 52.7	0.9999	QQQ, Orbi
PFNA	0.05	0.10	0.1 - 52.7	0.9999	QQQ, Orbi
PFDA	0.05	0.10	0.1 - 104.0	0.9992	QQQ, Orbi
PFUnDA	0.05	0.10	0.1 - 104.0	0.9993	QQQ, Orbi
PFDoA	0.05	0.10	0.1 - 104.0	0.9996	QQQ, Orbi
PFTTrDA	0.05	0.10	0.1 - 52.7	0.9999	QQQ, Orbi
PFTeDA	0.05	0.10	0.1 - 52.7	0.9999	QQQ, Orbi
PFBS	0.05	0.10	0.1 - 52.7	0.9997	QQQ, Orbi
PFPeS	0.05	0.10	0.1 - 52.7	0.9990	QQQ, Orbi
PFHxS	0.05	0.10	0.1 - 102.7	0.9998	QQQ, Orbi
PFHpS	0.05	0.10	0.1 - 52.7	0.9991	QQQ, Orbi
PFOS	0.05	0.10	0.1 - 101.5	0.9990	QQQ, Orbi
PFNS	0.05	0.10	0.1 - 52.7	0.9990	QQQ, Orbi
PFDS	0.05	0.10	0.1 - 52.7	0.9999	QQQ, Orbi
PFOSA	0.05	0.10	0.1 - 51.0	0.9980	QQQ, Orbi
6:2 FTS	0.06	0.11	0.1 - 54.6	0.9998	QQQ, Orbi
8:2 FTS	0.10	0.50	0.5 - 47	0.9981	QQQ, Orbi
6:2 FTSaB	0.17	1.70	1.7 - 171.2	0.9995	Orbi
5:3 FTB	0.17	1.70	1.7 - 166.9	0.9979	Orbi
5:1:2 FTB	0.19	1.90	1.9 - 185.9	0.9973	Orbi
Fluoride	50	100	100 - 5000	0.9999	F-ISE

PFAS calibration verification standards at two different concentrations (50 µg/L, 5 µg/L) were run every 20 samples to measure possible instrument drift. Overall instrument drift was found to be <5% over the duration of the run. Samples were run in batches based on their concentration, with a minimum of four injection blanks (1:1 H₂O/methanol (MeOH)) run between high concentration and low concentration batches, to eliminate carry over. Sample carryover was found to be <0.1% of previous PFAS concentration. The autosampler injection needle was cleaned between injections using the built-in flush program. The needle was washed for 10 seconds with flush solution (20% H₂O, 35% isopropanol, 45% MeOH). Reagent blanks were run before and after each batch to track any contamination in the used reagents. All blanks were found to be below detection limits for PFAS.

Liquid chromatography – high resolution mass spectrometry (LC-HRMS) analysis was used to identify PFAS precursors in AFFF samples. LC-HRMS analysis was performed as described in previous works (Battye et al., 2022; O’Connor et al., 2023; Patch et al., 2022; Turner et al., 2021). Briefly, full scan data was acquired and PFAS precursors were identified using Background Subtractor (Thermo Fisher Scientific), FreeStyle, Processing Setup, and Quan Browser (all Thermo Fisher Scientific software tools). For each AFFF

analysis, a background blank chromatogram (reagent blank) and matrix blank chromatogram were acquired. Chromatograms from each active experiment were blank subtracted and visually inspected for any new peaks. Following potential PFAS precursor identification, a homologue series search was performed using Isotope Simulation in Freestyle. If possible, these products were compared to known masses of AFFF precursors found in the literature and an in-house database of degradation products identified in previous work (Banayan Esfahani and Mohseni, 2022; Barzen-Hanson et al., 2017; Bentel et al., 2020b; D'Agostino and Mabury, 2014; Harding-Marjanovic et al., 2015; Houtz et al., 2013; Liu et al., 2022, 2021b; Martin et al., 2019; Munoz et al., 2021; Patch et al., 2022). Processed data was then inspected with Quan Browser and exported to Microsoft Excel for data clean-up and interpretation.

Analysis of Butyl Carbitol

Butyl carbitol was analyzed for parent compound concentration and total organic carbon concentration using a GC-MS and total organic carbon (TOC) analyzer respectively. GC-MS analysis was performed using a Thermo Scientific 1310 GC, with a GC-VMS 30m x 0.25 mm x 1.40 μm column, coupled to a Thermo Scientific ISQ7000 mass spectrometer. Initial GC temperature was set to 50°C for 1 minute, before ramping to 240°C at a rate of 20°C/minute. Butyl carbitol was detected at 4.5 minutes and was confirmed using the NIST MS Search 2.4 database to match the fragmentation pattern to library records. TOC was determined using an Analytika Jena TOC/TN analyzer operating under standard manufacturer conditions.

Identification of Organic Matter Inhibition Concentration

To identify the critical concentration of oxidation inhibition, 6:2 FTS (6 μM , ~2.5 mg/L) was amended with different concentrations of butyl carbitol (0, 0.5, 1, 5, 10, 50, 100, and 250 mM) and subjected to the UV-TOP assay for two hours. Following oxidation, samples were quenched with 0.25 mL methanolic acetic acid (4% acetic acid in MeOH), diluted 20x with 1:1 H₂O/MeOH and analyzed using LC-MS/MS.

H₂O₂ Pre-Treatment Initial Method Development

6 μM of 6:2 FTS (~2.5 mg/L) was amended with different concentrations of butyl carbitol (0, 0.5, 1, 5, 10, 50, 100, and 250 mM) and hydrogen peroxide (H₂O₂, 500 mM). A second set of solutions were prepared as above but amended with 150 mM of sodium hydroxide (NaOH, pH 13.2). The solutions were then subsampled (1 mL) into UV-transmissible cuvettes and activated with UV-light for 22 hours. After oxidation, the first set of solutions (no pH adjustment) were diluted 20x with 1:1 H₂O/MeOH and analyzed using LC-MS/MS. The second set of solutions were neutralized with 0.1 mL of 10% acetic acid, diluted 20x with 1:1 H₂O/MeOH, and analyzed. The results from this initial work are not directly shown in this manuscript, but formed the basis for the optimization experiments.

H₂O₂ Pre-Treatment Method Optimization (Figure 5.1)

Results from the first phase of method development identified that the concentration of H₂O₂, the pH of the solution, and the duration of UV activation would play key roles in ensuring maximum removal of dissolved organic matter (DOM). Therefore, a series of experiments were identified to explore these variables.

In the first experiment, 6:2 FTS (~7 μM) was amended with 500 mM of H₂O₂ and adjusted to various pHs (2.6, 5, 6.6, 9.2, 11, and 13) with either NaOH or hydrochloric acid (HCl). An unadjusted sample was also prepared, which had a pre-oxidation pH of 5.7. After preparation, the solutions were subsampled into UV-transmissible cuvettes and activated with UV light for 22 hours. Samples were then neutralized with either acetic acid or ammonium hydroxide and diluted 20x with 1:1 H₂O/MeOH for analysis.

In the second and third experiments, 6:2 FTS (~4 μM) or butyl carbitol (10 mM) was amended with different concentrations of H₂O₂ (0.1, 1, 5, 50, 100, 500, 1000, 4000 mM), subsampled into UV-transmissible cuvettes, and activated with UV-light for 22 hours. 6:2 FTS samples were then diluted 20x with 1:1 H₂O/MeOH for analysis using LC-MS/MS. Butyl carbitol samples were diluted to varying concentrations and analyzed using both gas chromatography – mass spectrometry (GC-MS) and total organic carbon (TOC).

In the fourth experiment, 100 mM of H₂O₂ was prepared in DI water, loaded into UV-transmissible cuvettes, and activated with UV-light for 2.5 hours. Samples were taken at regular time intervals and analyzed for total H₂O₂ concentration using an iodometric colorimetric determination method (Liang et al., 2008; Tantawi et al., 2019). In brief, samples were diluted (up to 1000x) with DI water before being amended with 70 mM of sodium bicarbonate, 60 mM of potassium iodide, and adjusted to pH 3.5 with phosphoric acid. Samples were then left to sit under dark conditions at room temperature for 20 minutes to allow for the H₂O₂ to react with the dissolved iodide and form triiodide, which was resulting measured at 352 nm using a UV-vis spectrometer (Burgess and Davidson, 2012). H₂O₂ did not decrease in concentration in the UV-free control sample, indicating that UV-light is required to meaningfully initiate the reaction over a 2.5 hour time scale.

Tandem UV-H₂O₂ and UV-TOP Assay (Figure 5.2, 5.3)

After the initial development and optimization of the UV-H₂O₂ assay, it was applied to solutions of 6:2 FTS amended with different concentrations of butyl carbitol (previously described) for 22 hours with no pH adjustment. Following the UV-H₂O₂ assay, the samples were diluted 1:1 with a double strength TOP assay solution (120 mM potassium persulfate, 300 mM NaOH, to achieve final concentrations of 60 mM and 150 mM, respectively) and subjected to the UV-TOP assay for four hours.

Investigation of Persulfate Salt and Concentration (Figure C4)

One of the limitations of using potassium persulfate as an oxidant is its poor solubility in water compared to sodium persulfate. To investigate if sodium or ammonium persulfate would be an effective substitution, the UV-activated TOP assay was applied to 20 μM of 6:2 FTS for 4 hours using 60 mM of NaPS, KPS, and ammonium persulfate (AmmPS) and 150 mM of NaOH. Samples were then neutralized with methanolic acetic acid (4% acetic acid, 0.25 mL of methanol to 1 mL of post-oxidation sample) and analyzed using LC-MS/MS. Following this investigation, different concentrations of NaPS were investigated for application after the UV-H₂O₂ assay (22 hours), ranging from 1 mM to 200 mM, with NaOH added at a concentration of 2.5x the persulfate concentration. The different concentrations of NaPS were evaluated using 6:2 FTS, to evaluate PFAS oxidation extent, as well as PFOS and PFOA to measure any salting out or matrix effects. Samples were then UV-activated for 12 hours after amendment with NaPS and NaOH, neutralized with methanolic acetic acid, and analyzed using LC-MS/MS.

PFCA Yield of Different Fluorotelomers (Figure 5.4)

The PFCA yield of different fluorotelomers were evaluated using the UV-H₂O₂-TOP system. First, the fluorotelomer standards (Wellington Labs) were evaporated to dryness and reconstituted in DI water. After this reconstitution, the standards were further diluted to create ~200 ppb stock solutions, which were amended first with 500 mM H₂O₂ (UV-activated for 22 hours), followed by amendment with 60 mM NaPS, 150 mM NaOH (UV-activated for 4 hours). After application of the full UV-H₂O₂-TOP, systems were quenched with 4% acetic acid in methanol (1 mL methanolic acetic acid to 3 mL of post-oxidation solution), and then diluted 20-fold with 1:1 H₂O:MeOH into HPLC vials for analysis.

Thermal-TOP, Tandem UV-H₂O₂, UV-TOP Validation (Figure 5.5)

After the initial success of the tandem UV-H₂O₂/TOP assays, the method was applied to 6:2 FTS and five different diluted (100x w/ DI water) AFFF formulations and compared against a 12 hour thermal TOP assay. All five AFFF formulations have been previously characterized (NF-1982, 3M-1980, NF-1990, Ansul-2012, Solberg) and have been identified as being PFCA, PFSA, FtSaB, FtB, and 6:2 FtTAoS dominant, respectively (Patch et al. 2024). AFFF formulations were diluted 100x in DI water to prepare dilute AFFF samples. For the thermal-TOP assay, samples were diluted 20x further and amended with 60 mM NaPS, 150 mM NaOH, and activated in a water bath at 85°C for 12 hours. For the UV-H₂O₂ assay, the AFFF samples were diluted 10x from their 100x diluted stock with DI water and amended with H₂O₂ to a final concentration of 500 mM H₂O₂ before being subjected to the UV-H₂O₂ assay for 22 hours. Following initial oxidation, samples were amended 1:1 with a modified TOP assay solution (final concentration 60 mM sodium persulfate, 150 mM

NaOH) and oxidized for 12 hours to align with the thermal-TOP assay activation time. After oxidation, samples were neutralized with methanolic acetic acid (4% acetic acid in MeOH), and diluted for LC-MS/MS analysis. Samples were prepared in triplicate, with the third sample being amended with 6:2 FTS, PFOS, and PFOA to evaluate oxidation/reduction completion and act as an internal standard to measure recovery. Overall recovery of both PFAS and fluoride was found to be between 70-110%. No corrections were made based on PFAS or fluoride recovery.

Extended Results and Discussion

Understanding the Role of pH, Concentration, and Activation Rate in the UV-H₂O₂ Assay

Following oxidation of 6:2 FTS in the UV-H₂O₂ system, it was identified that pH 5.0-9.2 resulted in the highest molar yield of perfluoroalkyl acids (PFAAs, 53-63%), with the non-pH adjusted system (pH 5.7) having the highest molar yield (62±1%), while the pH 9.2 had the highest yield of PFHpA. At pH 2.6, 6:2 FTS and PFCAs were recovered, indicating that while oxidation did occur, it was not complete and was significantly inhibited under acidic conditions. In contrast, at pH 11 and higher, 80-110% of 6:2 FTS was recovered with <3% conversion to PFCAs being identified (Figure C1).

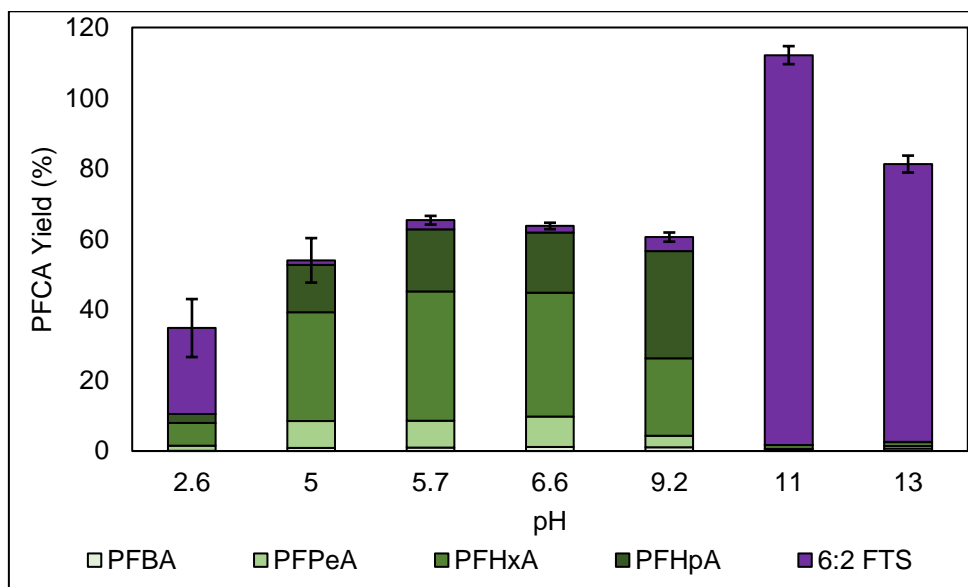


Figure C1 – Influence of pH on PFCA yield in the UV-H₂O₂ assay using 500 mM of H₂O₂ activated with UV for 22 hours.

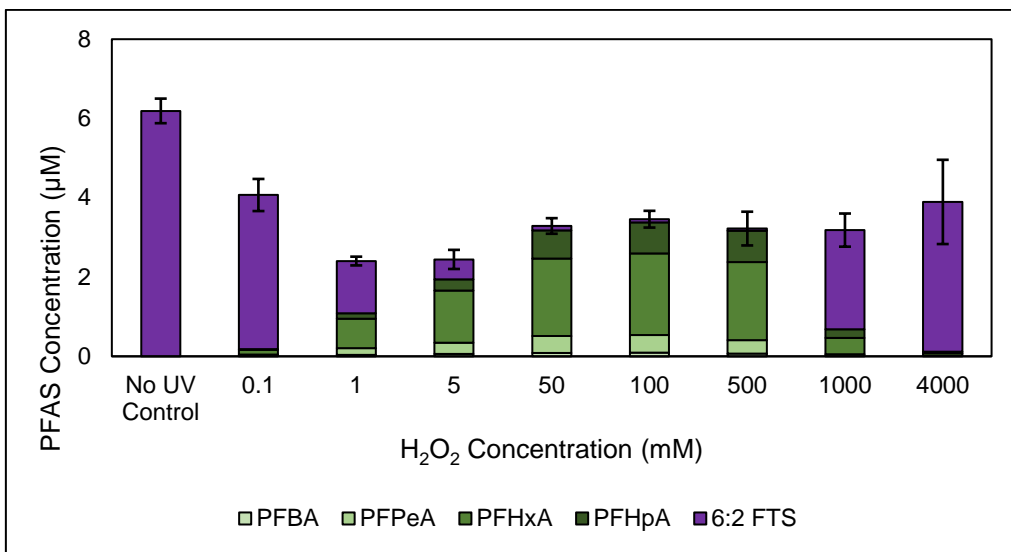


Figure C2 – Percent recovery of PFCAs and 6:2 FTS (6 µM) after application of the UV-H₂O₂ assay with different concentrations of H₂O₂. Error bars are the sum of the standard deviation of the triplicates, and the error of the control samples.

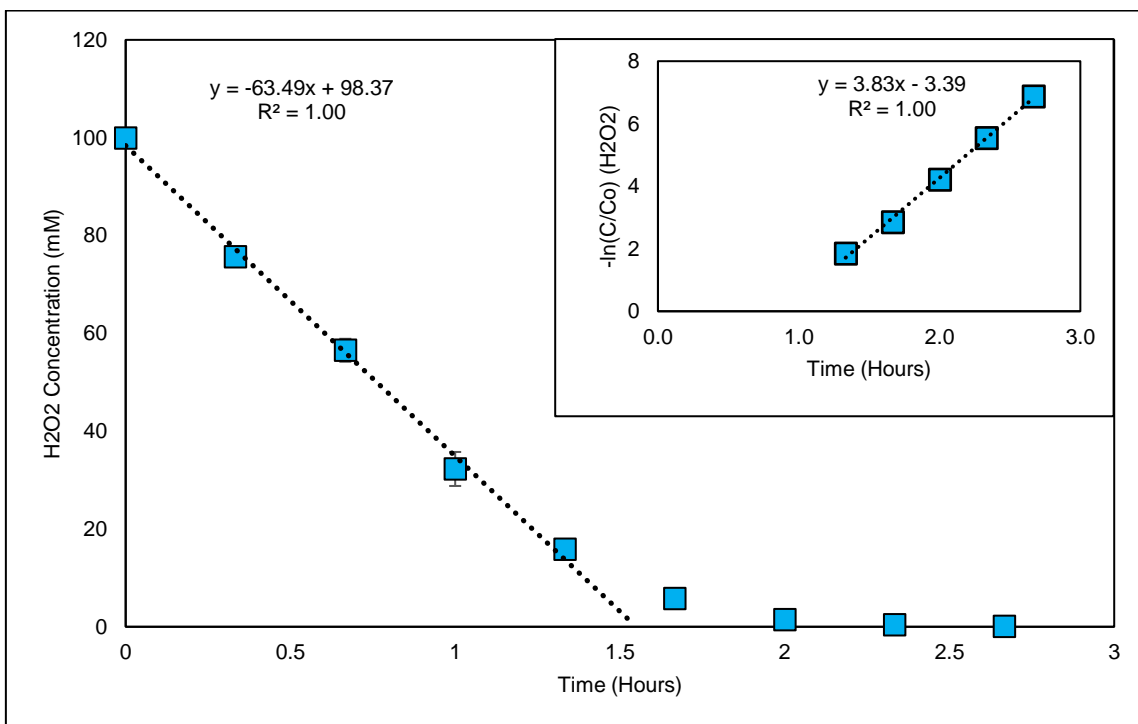


Figure C3 – Zero-order (0-1.33 h) and first order (1.33-2.66 h) activation rate of 100 mM H₂O₂ in the UV-H₂O₂ system.

Selection of Persulfate Salt and Concentration in the UV-H₂O₂-TOP Assay

One of the drawbacks in using potassium persulfate as an oxidant is its poor solubility in water (~160 mM KPS) relative to sodium persulfate (~2.3 M NaPS) and ammonium persulfate (3.5 M AmmPS), which often requires multiple cycles of the TOP assay to be applied when higher oxidant dose is required. To this end, the effectiveness of KPS, NaPS, and AmmPS were investigated for the oxidative conversion of 6:2 FTS to PFCAs, followed by the investigation of different concentrations of NaPS at an NaPS:NaOH ratio of 1:2.5 to PFOS, PFOA, and 6:2 FTS (Figure C4).

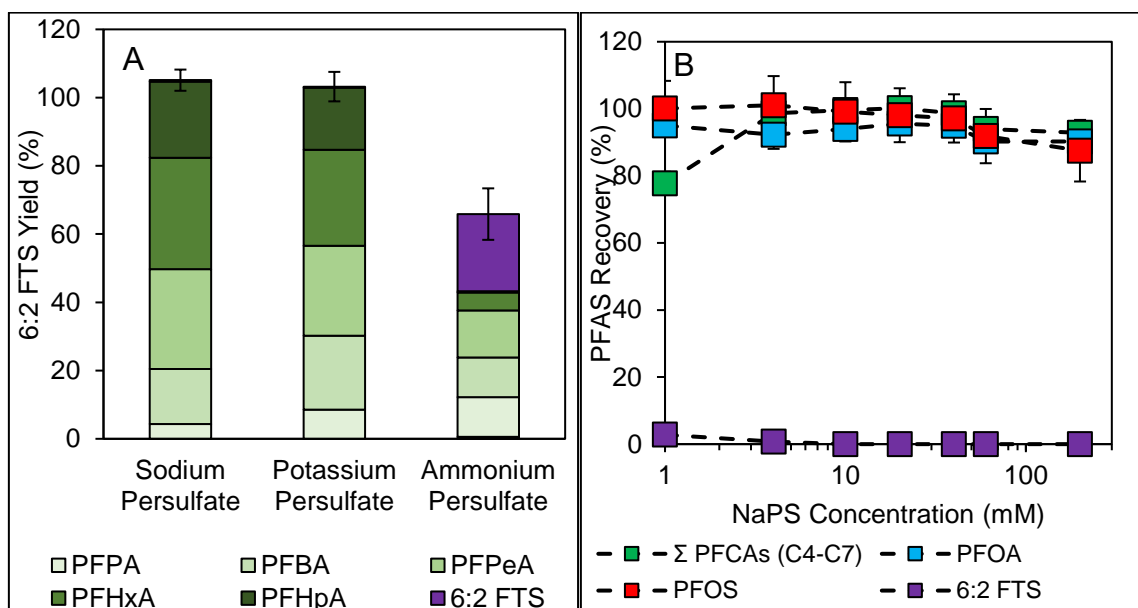


Figure C4 – (A) UV-activated TOP assay applied to 6:2 FTS (20 μ M) for 4 hours using 60 mM NaPS, KPS, and ammonium persulfate and 150 mM NaOH. (B) Investigation of variable concentrations of NaPS (1 mM, 4 mM, 10 mM, 20 mM, 40 mM, 60 mM, 200 mM) and NaOH (2.5x the concentration of persulfate) on the UV-activated oxidation of 6:2 FTS (5 μ M) following UV-H₂O₂ (500 mM H₂O₂) pre-oxidation.

Of the three persulfate salts investigation, sodium persulfate and potassium persulfate both achieved complete oxidation of 6:2 FTS, with very similar proportions of PFCAs being found. Interestingly, the use of ammonium persulfate resulted in incomplete oxidation of 6:2 FTS and overall incomplete PFAS recovery, likely due to the ammonium ion itself reacting with hydroxyl radicals and quenching the available oxidant.

It was hypothesized that the use of the UV-H₂O₂ assay as a pre-treatment would enable lower persulfate concentrations to be used to effectively convert PFAA precursors into PFCAs. Additionally, the higher solubility of NaPS would enable higher oxidant doses to be used for the UV-H₂O₂-TOP assay in situations where samples contained high concentrations of TOC. It was identified that a reagent concentration of 10 mM of NaPS, 25 mM NaOH was required to completely oxidize the remaining 6:2 FTS and achieve complete recovery of PFCAs (100 \pm 2%), with recovery of PFCAs, PFOA, and 6:2 FTS remaining consistent up to 40 mM NaPS/100 mM NaOH. At 60 mM NaPS and 200 mM NaPS, a slight decrease in PFAS recovery was noted (93 \pm 2% PFCAs, 90 \pm 3% PFOA, 88 \pm 9% PFOS at 200 mM NaPS, 500 mM NaOH), likely due to the higher salt concentrations causing a slight matrix effect.

The identification of NaPS as an effective alternative to KPS is attractive due to its higher solubility and wide range of concentration effectiveness (10 mM NaPS – 200 mM NaPS). These results will benefit when dealing with highly TOC-containing samples, requiring a higher oxidant concentration even after UV-H₂O₂

pre-treatment, or when dealing with very neat aqueous samples where the UV-H₂O₂ assay does majority of the oxidation and the UV-TOP assay is used at a lower reagent dose to simply complete the PFAS oxidation.

Greyscale Version of Figure 5.5

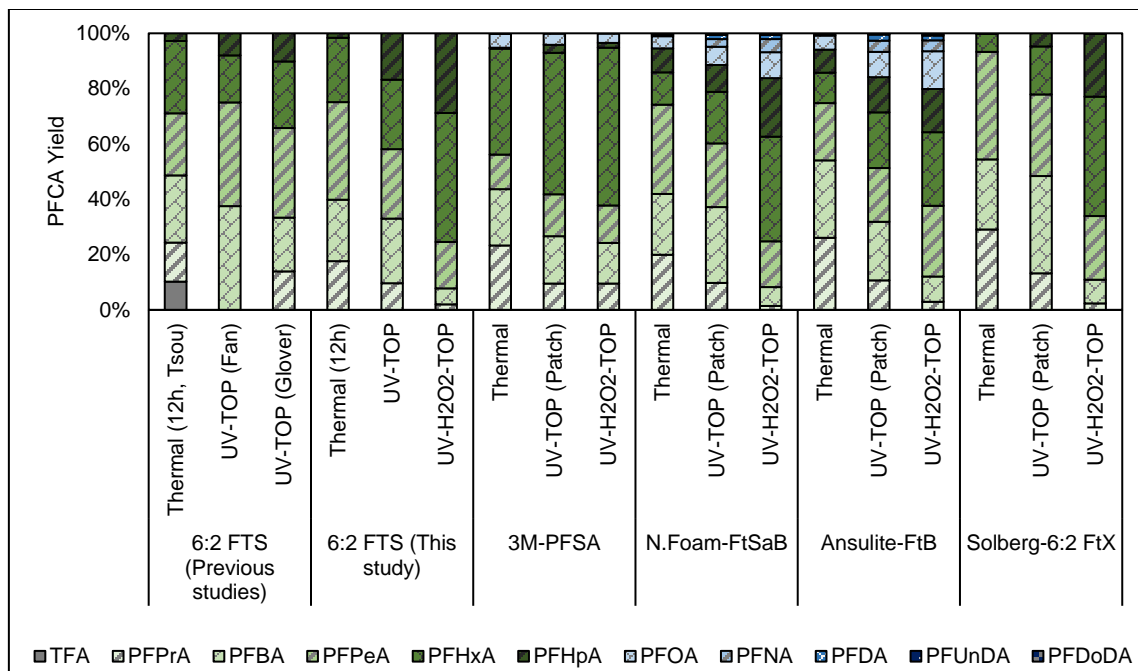
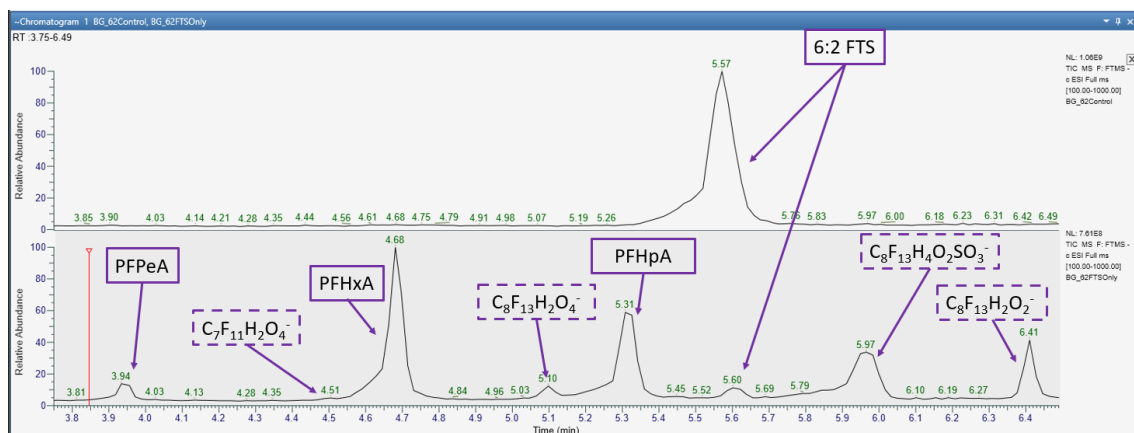


Figure C5 – Relativized composition of PFCAs following the oxidation of 6:2 FTS across three different studies, and this study; as well as PFCA composition following the oxidation of four AFFFs studied using the stand-alone 12 hour thermal TOP assay, stand-alone UV-TOP assay, and the UV-H₂O₂-TOP assay (Fan et al., 2021; Caitlin M Glover et al., 2024; Patch et al., 2024; Tsou et al., 2023).

UV-H₂O₂ Transformation Products of 6:2 FTS



Formula	Experimental Mass	Theoretical Mass	Delta	Fragments
C8F13H2O2	376.9869	376.9853	4.43	C7F11, C7F12H, C7F13H2
C8F13H4SO5	458.9569	448.9577	-1.8	C6F13
C8F13H2SO4	440.9451	440.9472	-4.63	N/A
6:2 FTS	426.9653	426.9679	-6.06	N/A
PFHpA	362.9674	362.9696	-6.05	C6F13, C3F7
C8F13O3	390.9644	390.9645	-0.33	C6F13
C8F13H2O4	408.9733	408.9751	-4.33	C6F13, C7F13O2
PFHxA	312.9740	312.9728	3.64	C5F11, C5F9O, C4F7, C2F5
C7F11O3	340.9688	340.9677	3.22	C5F11
C8F13H2O3	392.9811	392.9802	2.34	N/A
PFPeA	262.9755	262.9760	-1.79	C4F9, C4F7O
C6F9O3	290.9697	290.9709	-4.06	C4F9
C8F13H4SO4	442.9638	442.9628	2.21	C6F11

Figure C6 – (Top) Chromatogram of PFCAs and 6:2 FTS transformation products following oxidation using UV-H₂O₂ (500 mM H₂O₂, 22 hours), and the high-resolution identification of the transformation products, alongside the most prevalent ddMS₂ fragments.

References

- Banayan Esfahani, E., Mohseni, M., 2022. Fluence-based photo-reductive decomposition of PFAS using vacuum UV (VUV) irradiation: Effects of key parameters and decomposition mechanism. *J Environ Chem Eng* 10, 107050. <https://doi.org/10.1016/j.jece.2021.107050>
- Barzen-Hanson, K.A., Roberts, S.C., Choyke, S., Oetjen, K., McAlees, A., Riddell, N., McCrindle, R., Ferguson, P.L., Higgins, C.P., Field, J.A., 2017. Discovery of 40 Classes of Per- and Polyfluoroalkyl Substances in Historical Aqueous Film-Forming Foams (AFFFs) and AFFF-Impacted Groundwater. *Environ Sci Technol*. <https://doi.org/10.1021/acs.est.6b05843>
- Battye, N.J., Patch, D.J., Roberts, D.M.D., O'Connor, N.M., Turner, L.P., Kueper, B.H., Hulley, M.E., Weber, K.P., 2022. Use of a horizontal ball mill to remediate per- and polyfluoroalkyl substances in soil. *Science of The Total Environment* 835, 155506. <https://doi.org/https://doi.org/10.1016/j.scitotenv.2022.155506>
- Bentel, M.J., Liu, Z., Yu, Y., Gao, J., Men, Y., Liu, J., 2020. Enhanced Degradation of Perfluorocarboxylic Acids (PFCAs) by UV/Sulfite Treatment: Reaction Mechanisms and System Efficiencies at pH 12. *Environ Sci Technol Lett* 7, 351–357. <https://doi.org/10.1021/acs.estlett.0c00236>
- Burgess, A.E., Davidson, J.C., 2012. A kinetic-equilibrium study of a triiodide concentration maximum formed by the persulfate-iodide reaction. *J Chem Educ* 89, 814–816. <https://doi.org/10.1021/ed200055t>
- D'Agostino, L.A., Mabury, S.A., 2014. Identification of Novel Fluorinated Surfactants in Aqueous Film Forming Foams and Commercial Surfactant Concentrates. *Environ Sci Technol* 48, 121–129. <https://doi.org/10.1021/es403729e>
- Fan, X., Bao, Y., Mumtaz, M., Huang, J., Yu, G., 2021. Determination of total oxidizable precursors in foam surfactants and foam contaminated water based on UV-activated persulfate oxidation. *Science of the Total Environment* 763, 142943. <https://doi.org/10.1016/j.scitotenv.2020.142943>
- Fennell, B.D., Fowler, D., Mezyk, S.P., McKay, G., 2023. Reactivity of Dissolved Organic Matter with the Hydrated Electron: Implications for Treatment of Chemical Contaminants in Water with Advanced Reduction Processes. *Environ Sci Technol* 57, 7634–7643. <https://doi.org/10.1021/acs.est.3c00909>
- Glover, C.M., Pazoki, F., Munoz, G., Liu, J., 2024. Enhancing Total Oxidizable Precursor Assay for Characterization of PFAS: UV Versus Heat Activation. Pre-print.
- Harding-Marjanovic, K.C., Houtz, E.F., Yi, S., Field, J.A., Sedlak, D.L., Alvarez-Cohen, L., 2015. Aerobic Biotransformation of Fluorotelomer Thioether Amido Sulfonate (Lodyne) in AFFF-Amended Microcosms. *Environ Sci Technol* 49, 7666–7674. <https://doi.org/10.1021/acs.est.5b01219>
- Houtz, E.F., Higgins, C.P., Field, J.A., Sedlak, D.L., 2013. Persistence of perfluoroalkyl acid precursors in AFFF-impacted groundwater and soil. *Environ Sci Technol* 47, 8187–8195. <https://doi.org/10.1021/es4018877>
- Liang, C., Huang, C.F., Mohanty, N., Kurakalva, R.M., 2008. A rapid spectrophotometric determination of persulfate anion in ISCO. *Chemosphere* 73, 1540–1543. <https://doi.org/10.1016/j.chemosphere.2008.08.043>
- Liu, M., Munoz, G., Vo Duy, S., Sauv e, S., Liu, J., 2022. Per- and Polyfluoroalkyl Substances in Contaminated Soil and Groundwater at Airports: A Canadian Case Study. *Environ Sci Technol* 56, 885–895. <https://doi.org/10.1021/acs.est.1c04798>
- Liu, Z., Bentel, M.J., Yu, Y., Ren, C., Gao, J., Pulikkal, V.F., Sun, M., Men, Y., Liu, J., 2021. Near-Quantitative Defluorination of Perfluorinated and Fluorotelomer Carboxylates and Sulfonates with Integrated Oxidation and Reduction. *Environ Sci Technol* 55, 7052–7062. <https://doi.org/10.1021/acs.est.1c00353>

Martin, D., Munoz, G., Mejia-Avenida, S., Duy, S.V., Yao, Y., Volchek, K., Brown, C.E., Liu, J., Sauv e, S., 2019. Zwitterionic, cationic, and anionic perfluoroalkyl and polyfluoroalkyl substances integrated into total oxidizable precursor assay of contaminated groundwater. *Talanta* 195, 533–542. <https://doi.org/10.1016/j.talanta.2018.11.093>

Munoz, G., Michaud, A.M., Liu, M., Vo Duy, S., Montenach, D., Resseguier, C., Watteau, F., Sappin-Didier, V., Feder, F., Morvan, T., Houot, S., Desrosiers, M., Liu, J., Sauv e, S., 2021. Target and Nontarget Screening of PFAS in Biosolids, Composts, and Other Organic Waste Products for Land Application in France. *Environ Sci Technol*. <https://doi.org/10.1021/acs.est.1c03697>

O’Connor, N., Patch, D., Noble, D., Scott, J., Koch, I., Mumford, K.G., Weber, K., 2023. Forever no more : Complete mineralization of per - and poly fl uoroalkyl substances (PFAS) using an optimized UV / sulfite / iodide system. *Science of the Total Environment* 888, 164137. <https://doi.org/10.1016/j.scitotenv.2023.164137>

Patch, D., O’Connor, N., Koch, I., Cresswell, T., Hughes, C., Davies, J.B., Scott, J., O’Carroll, D., Weber, K., 2022. Elucidating degradation mechanisms for a range of per- and polyfluoroalkyl substances (PFAS) via controlled irradiation studies. *Science of the Total Environment* 832, 154941. <https://doi.org/10.1016/j.scitotenv.2022.154941>

Patch, D., O’Connor, N., Vereecken, T., Murphy, D., Munoz, G., Ross, I., Glover, C., Scott, J., Koch, I., Sauv e, S., Liu, J., Weber, K., 2024. Advancing PFAS characterization: Enhancing the total oxidizable precursor assay with improved sample processing and UV activation. *Science of The Total Environment* 909, 168145. <https://doi.org/10.1016/j.scitotenv.2023.168145>

Tantawi, O., Baalbaki, A., El Asmar, R., Ghauch, A., 2019. A rapid and economical method for the quantification of hydrogen peroxide (H₂O₂) using a modified HPLC apparatus. *Science of the Total Environment* 654, 107–117. <https://doi.org/10.1016/j.scitotenv.2018.10.372>

Tsou, K., Antell, E., Duan, Y., Olivares, C.I., Yi, S., Alvarez-Cohen, L., Sedlak, D.L., 2023. Improved Total Oxidizable Precursor Assay for Quantifying Polyfluorinated Compounds Amenable to Oxidative Conversion to Perfluoroalkyl Carboxylic Acids. *ACS ES and T Water*. <https://doi.org/10.1021/acsestwater.3c00224>

Turner, L.P., Kueper, B.H., Jaansalu, K.M., Patch, D.J., Battye, N., El-Sharnouby, O., Mumford, K.G., Weber, K.P., 2021. Mechanochemical remediation of perfluorooctanesulfonic acid (PFOS) and perfluorooctanoic acid (PFOA) amended sand and aqueous film-forming foam (AFFF) impacted soil by planetary ball milling. *Science of the Total Environment* 765, 142722. <https://doi.org/10.1016/j.scitotenv.2020.142722>

Appendix D – Supplemental Information for Chapter 6

PFAS Analysis

Samples were analyzed on a ThermoFisher Exploris 120 Orbitrap coupled to a Vanquish ultra-high-performance liquid chromatography (UHPLC) system (herein referred to as LC-HRMS) using a 100 mm x 2.1 mm x 3.0 μ m ACME C18 analytical column and paired guard column. Mobile phases consisted of 5 mM ammonium acetate in DI water (A) and acetonitrile (B). The elution profile started at 90% A/10% B with a flow rate of 0.5 mL/min, transitioning to 100% B over 10 minutes, holding for 2 minutes, then equilibrating at starting conditions for 3 minutes. A diverter valve was used to send the first minute of elution to waste to avoid heavy salt content impacting the MS. A heated electrospray ionization ion source was used, with a static spray voltage. Both positive and negative ion voltage were 3000 V. Gas was run in static mode, with a sheath gas of 50 (arbitrary units), auxiliary gas of 10 (arbitrary units) and sweep gas of 1 (arbitrary units). The ion transfer tube temperature was set to 325°C, the vaporizer temperature was set to 350°C, and mild trapping was not used. The MS global settings were set to expect an LC peak width of 10 seconds, and the mass was calibrated before each sample injection using the RunStart EASY-IC™ system.

Before samples were run, the UHPLC and Orbitrap were flushed with 10% DI water, 90% ACN for a minimum of 1 hour, until baseline ion peak intensity was stable (indicating a clean sample path), and spray stability was <5%. The analysis method was set up with two ‘experiments’ (XCalibur® software nomenclature for analytical protocols), one for positive mode analysis and one for negative mode analysis. Each experiment used an orbitrap resolution of 60,000, a scan range of 100-1000 m/z, an RF lens of 70%, a standard automatic gain control target, an automatic maximum injection time mode setting, and had in-source fragmentation disabled. PFAS peak intensities were extracted using XCalibur® software (Processing Setup and Quan Browser) and converted to concentration using an external calibration curve.

PFAS were quantified with an external calibration curve (PFAC-MXB or PFAC-MXC, native mix, Wellington Labs, with additions of TFA, PFPrA, 6:2 FTS, 8:2 FTS, and FOSA). Quantification limits were set to the lowest concentration of each calibration curve. Detection limits were established by analyzing the matrix blank ten times, and then taking the sum of the mean concentration of the blank and three times the standard deviation of the blank. In situations where blanks yielded no detectable PFAS or signal, the detection limit was set as half of the quantitation limit, and confirmed by analyzing a calibration sample made at 0.05 μ g/L. For this reason, in situations where analysis of the blanks yielded no signal, the detection limit is arbitrarily high. For a complete list of the analytes measured using the expanded analytical method, please see Table D1.

Table D1 – PFAS directly quantified in the expanded analytical suite using an Agilent 6460 LC-MS (QQQ) and/or a ThermoFisher Exploris 120 Orbitrap (Orbi).

Analyte	Instrument Detect. Limit (µg/L)	Instrument Quant. Limit (µg/L)	Linear Dynamic Range (µg/L)	RSQ	Instrument
TFA	0.50	1	1 - 102.9	0.9998	QQQ
PFPPrA	0.10	0.50	0.5 - 100.0	0.9993	QQQ
PFBA	0.05	0.10	0.1 - 104.0	0.9997	QQQ, Orbi
PFPeA	0.10	0.50	0.5 - 104.0	0.9999	QQQ, Orbi
PFHxA	0.05	0.10	0.1 - 52.7	0.9998	QQQ, Orbi
PFHpA	0.05	0.10	0.1 - 52.7	0.9998	QQQ, Orbi
PFOA	0.05	0.10	0.1 - 52.7	0.9999	QQQ, Orbi
PFNA	0.05	0.10	0.1 - 52.7	0.9999	QQQ, Orbi
PFDA	0.05	0.10	0.1 - 104.0	0.9992	QQQ, Orbi
PFUnDA	0.05	0.10	0.1 - 104.0	0.9993	QQQ, Orbi
PFDoA	0.05	0.10	0.1 - 104.0	0.9996	QQQ, Orbi
PFTTrDA	0.05	0.10	0.1 - 52.7	0.9999	QQQ, Orbi
PFTeDA	0.05	0.10	0.1 - 52.7	0.9999	QQQ, Orbi
PFBS	0.05	0.10	0.1 - 52.7	0.9997	QQQ, Orbi
PFPeS	0.05	0.10	0.1 - 52.7	0.9990	QQQ, Orbi
PFHxS	0.05	0.10	0.1 - 102.7	0.9998	QQQ, Orbi
PFHpS	0.05	0.10	0.1 - 52.7	0.9991	QQQ, Orbi
PFOS	0.05	0.10	0.1 - 101.5	0.9990	QQQ, Orbi
PFNS	0.05	0.10	0.1 - 52.7	0.9990	QQQ, Orbi
PFDS	0.05	0.10	0.1 - 52.7	0.9999	QQQ, Orbi
PFOSA	0.05	0.10	0.1 - 51.0	0.9980	QQQ, Orbi
6:2 FTS	0.06	0.11	0.1 - 54.6	0.9998	QQQ, Orbi
8:2 FTS	0.10	0.50	0.5 - 47	0.9981	QQQ, Orbi
6:2 FTSaB	0.17	1.70	1.7 - 171.2	0.9995	Orbi
5:3 FTB	0.17	1.70	1.7 - 166.9	0.9979	Orbi
5:1:2 FTB	0.19	1.90	1.9 - 185.9	0.9973	Orbi
Fluoride	50	100	100 - 5000	0.9999	F-ISE

PFAS calibration verification standards at two different concentrations (50 µg/L, 5 µg/L) were run every 20 samples to measure possible instrument drift. Overall instrument drift was found to be <5% over the duration of the run. Samples were run in batches based on their concentration, with a minimum of four injection blanks (1:1 H₂O/methanol (MeOH)) run between high concentration and low concentration batches, to eliminate carry over. Sample carryover was found to be <0.1% of previous PFAS concentration. The autosampler injection needle was cleaned between injections using the built-in flush program. The needle was washed for 10 seconds with flush solution (20% H₂O, 35% isopropanol, 45% MeOH). Reagent blanks were run before and after each batch to track any contamination in the used reagents. All blanks were found to be below detection limits for PFAS.

Liquid chromatography – high resolution mass spectrometry (LC-HRMS) analysis was used to identify PFAS precursors in AFFF samples. LC-HRMS analysis was performed as described in previous works (Battye et al., 2022; O’Connor et al., 2023; Patch et al., 2022; Turner et al., 2021). Briefly, full scan data was acquired and PFAS precursors were identified using Background Subtractor (Thermo Fisher Scientific), FreeStyle, Processing Setup, and Quan Browser (all Thermo Fisher Scientific software tools). For each AFFF analysis, a background blank chromatogram (reagent blank) and matrix blank chromatogram were acquired. Chromatograms from each active experiment were blank subtracted and visually inspected for any new

peaks. Following potential PFAS precursor identification, a homologue series search was performed using Isotope Simulation in Freestyle. If possible, these products were compared to known masses of AFFF precursors found in the literature and an in-house database of degradation products identified in previous work (Banayan Esfahani and Mohseni, 2022; Barzen-Hanson et al., 2017; Bentel et al., 2020b; D'Agostino and Mabury, 2014; Harding-Marjanovic et al., 2015; Houtz et al., 2013; Liu et al., 2022, 2021b; Martin et al., 2019; Munoz et al., 2021; Patch et al., 2022). Processed data was then inspected with Quan Browser and exported to Microsoft Excel for data clean-up and interpretation.

UV-ROF Validation and Impact of Oxidation Pre-Treatment on UV-ROF Assay (Figure 1)

To evaluate the validity of the UV-ROF assay (50 mM Na₂SO₃, 10 mM KI, 10 mM NaHCO₃, and 150 mM NaOH), it was applied to different dilutions of a PFCA-dominant AFFF (N. Foam – PFCA, also referred to as N. Foam 1982). After application of the UV-ROF assay, samples were neutralized with 10% acetic acid (to pH 5.5) and diluted 1:1 with TISAB, before being analyzed for total fluoride using a F-ISE.

To evaluate the impact of the UV-H₂O₂ assay on overall reduction effectiveness, an 1000x dilution of the PFCA-dominant AFFF was amended with H₂O₂ (500 mM) and either activated with UV-light or kept in the dark for 22 hours. Following the oxidation pre-treatment, samples were either subjected to the UV-ROF assay directly, or after a 20x dilution factor with DI water. After application of the UV-ROF assay, samples were neutralized with 10% acetic acid (to pH 5.5) and diluted 1:1 with TISAB, before being analyzed for total fluoride using a F-ISE.

To evaluate the impact of the UV-H₂O₂-TOP assay on overall reduction effectiveness, ~4 μM of 6:2 FTS was first amended with H₂O₂ (500 mM) and activated with UV-light for 22 hours. Following the oxidation pre-treatment, samples were subjected to the UV-TOP assay (60 mM NaPS, 150 mM NaOH) for 4 hours, before either: receiving an additional 18 hours of UV (to exhaust residual oxidant), sitting in an oven at 60°C for 18 hours (to exhaust residual oxidant), or being directly diluted and subjected to the UV-ROF assay (to evaluate the impact of residual oxidant at different dilutions). After application of the UV-ROF assay, samples were neutralized with 10% acetic acid (to pH 5.5) and diluted 1:1 with TISAB, before being analyzed for total fluoride using a F-ISE.

Application of UV-H₂O₂-TOP-ROF Assay to AFFFs (Figure 2)

The UV-H₂O₂-TOP-ROF assay was applied to 15 diluted (100x w/ DI water, additional 10x dilution factor after H₂O₂-TOP) AFFF samples (15 total) using 500 mM H₂O₂ (activated for 22 hours), followed by 60 mM NaPS, 150 mM NaOH (activated for 22 hours). After the UV-H₂O₂-TOP assays, a 0.2 mL subsample of the samples were taken, amended with 0.1 mL of DI water, and 0.3 mL of 100 mM Na₂SO₃, 20 mM KI, 20 mM NaHCO₃, and 300 mM NaOH (to reach final concentrations of 50 mM Na₂SO₃, 10 mM KI, 10 mM NaHCO₃, and 150 mM NaOH) and activated by UV light to complete the UV-ROF assay for 4 hours. The remaining post-oxidation samples were quenched with 0.25 mL of methanolic acetic acid and diluted between 20x and 100x with 1:1 H₂O/MeOH before LC-MS/MS analysis. After application of the UV-ROF assay, samples were neutralized with 10% acetic acid (to pH 5.5) and diluted 1:1 with TISAB, before being analyzed for total fluoride using a F-ISE.

Application of the UV-H₂O₂-TOP-ROF Assay to AFFF Still Bottoms (Figure 3).

It was hypothesized that method modification may be required for analysis of the AFFF still bottoms sample, due to the suspected high concentrations of organic matter and inorganic ions. To this end, the AFFF still bottoms sample was diluted 10x with DI water and subjected to the UV-H₂O₂-TOP assay, with the TOP assay concentration being increased to 200 mM NaPS, 500 mM NaOH. Subsequent application of the UV-ROF assay and preparations for LC-MS, F-ISE analyses were performed as described for the AFFF samples without modification.

Application of the UV-H₂O₂-TOP-ROF Assay to Assorted Samples (Figure 3).

Sample preparation methods for the UV-H₂O₂-TOP-ROF and dTOP-UV-ROF were developed with consideration to the PFAS identified in the initial characterization (or lack there-of, in the case of the textiles and surface spray). Sample preparation methods were dependent on the type of sample (e.g. solid, liquid, gel), and the complexity of the sample (e.g. high concentrations of dissolved organic matter). Initially, all solid samples (soils, makeups, and textiles) samples were extracted with basic and acidic methanol (Mejia-Avenidaño et al., 2017b; Munoz et al., 2018; Nickerson et al., 2020), but this was found to result in considerable extraction of either very high concentrations of alkaline-soluble organic matter (e.g. humic and fulvic acids present in the soils) which precipitated during the UV-H₂O₂ assay under neutral pH and interfered with the UV-TOP assay, or water-insoluble waxes and polymers (makeups and textiles) which resulted in significant precipitation when reconstituting the samples into water. The methanolic extracts also identified no PFAS present on the textiles, despite having been previously identified as containing PFAS. To overcome these challenges, the soils and AFFF-impacted pipe swabs were extracted only with basic methanol, whereas the makeup and textile samples were extracted using alkaline hydrolysis (500 mM KOH, H₂O, 85°C, 24 hours). The soils, makeup, and textile samples were also extracted using the direct TOP (dTOP) assay. Both alkaline hydrolysis and the dTOP assay have been used to previously characterize PFAS-containing materials, including those that contain side-chain fluoropolymers (SFPs) that are not extracted by standard basic methanol methods (O'Carroll et al., 2020; Zweigle et al., 2023, 2022).

Following sample preparation, the sample extracts (methanolic, or alkaline hydrolysis) or post-direct oxidation solutions (dTOP) were prepared for application of the UV-H₂O₂-TOP-ROF or UV-ROF assays respectively. The AFFF still bottoms sample was used to investigate necessary assay modifications as it was identified as the most complex in terms of PFAS concentration, type, and presence of complex organic/inorganic ions. Initial application of the UV-H₂O₂-TOP-ROF method to an undiluted subsample of the AFFF still bottoms was found to be ineffective in both oxidizing the PFAA precursors to PFCAs and reducing the resultant PFAS into free fluoride. Diluting the sample 10-fold and increasing the persulfate/hydroxide concentrations from 60 mM/150 mM to 200 mM/500 mM allowed for successful implementation of the tandem assay, as determined by complete oxidation of the 6:2 FTS natively present in the sample, and complete recovery of PFCAs following oxidation of additional 6:2 FTS added to the sample as a quality control assessment.

After sample extraction, methanolic extracts were evaporated to dryness in the UV-transmissible cuvettes at 60°C in an oven, before being reconstituted in DI water and neutralized with HCl. Hydrolysis extracts were pipetted into UV-transmissible cuvettes and likewise neutralized with HCl. The samples were then subjected to the UV-H₂O₂-TOP assay (amended to a final concentration of 500 mM H₂O₂ and activated with UV for 22 hours, followed by an amendment to a final concentration of 60 mM NaPS, 150 mM NaOH and activated with UV for 22 hours) before being sub-sampled for the UV-ROF assay. The UV-ROF assay and subsequent workups for analysis were performed as was done for the AFFF samples without modification.

Extended Results and Discussion

High Resolution Analysis of AFFF Still Bottoms Sample

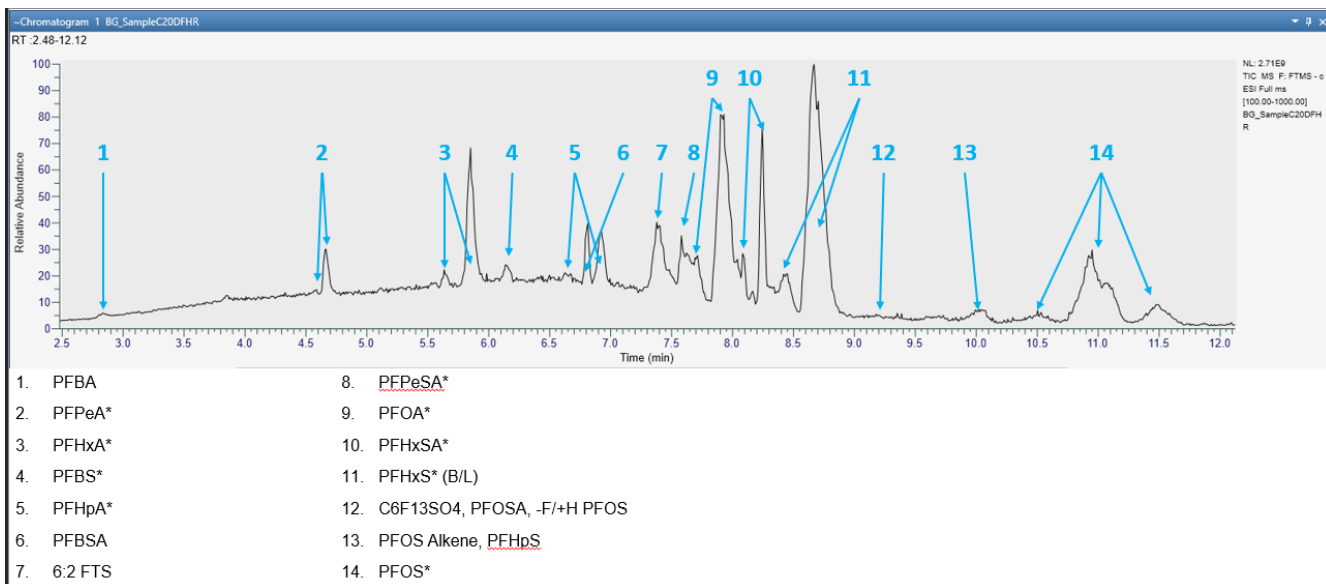


Figure D1 – High resolution analysis of AFFF still bottoms sample, revealing several PFCA, PFSA, PFSAms, and 6:2 FTS. PFAS with asterisks are a mixture of branched and linear isomers.

PFAS Composition of Additional Samples Post-UV-H₂O₂-TOP and Post-dTOP

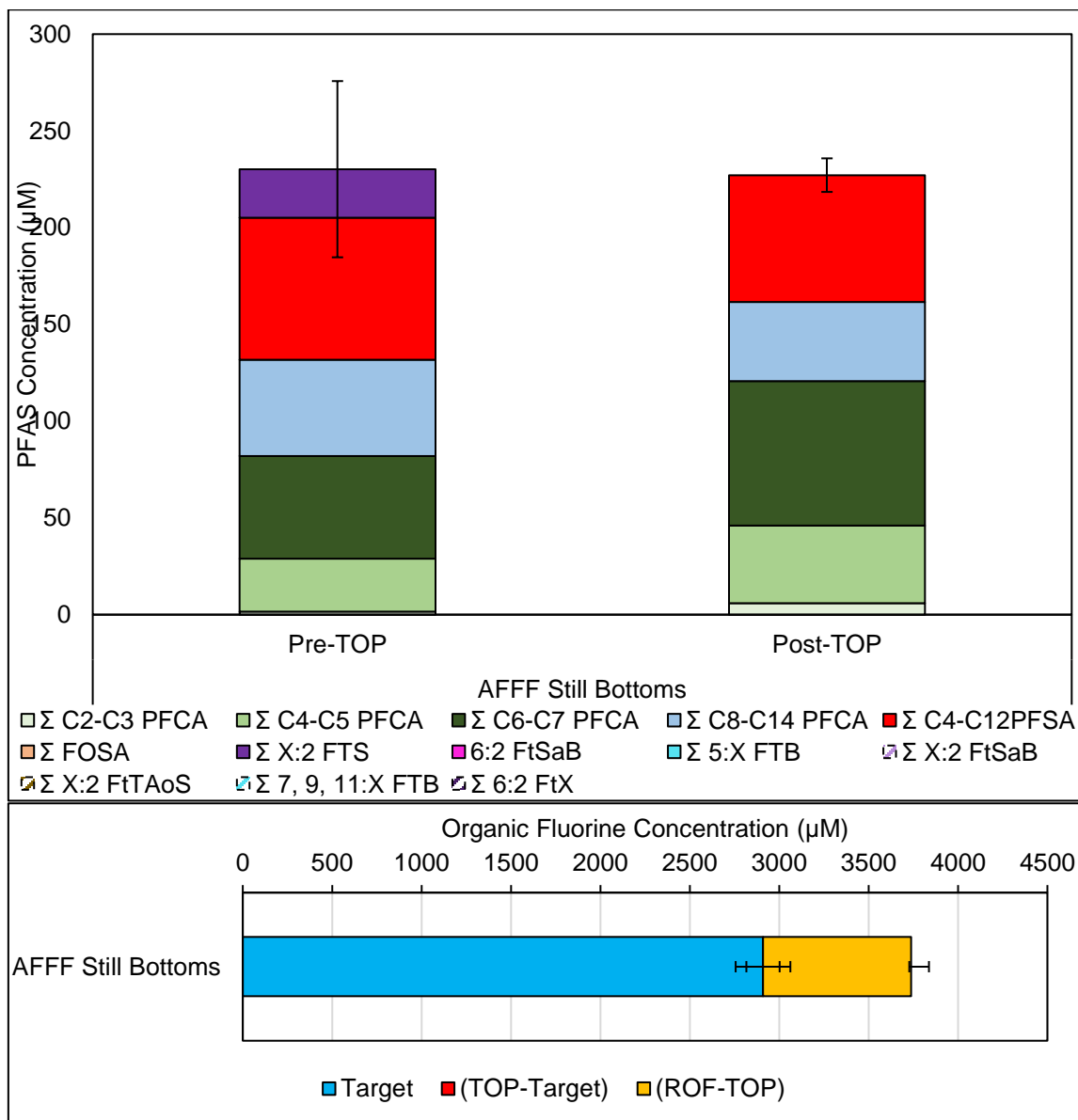


Figure D2 – (A) Concentration of PFAS of pre-TOP assay and post-UV-H₂O₂-TOP applied to diluted AFFF still bottoms (200 mM NaPS, 500 mM NaOH), (B) Organic fluorine concentration of post UV-H₂O₂-TOP-ROF assay (50 mM Na₂SO₃, 10 mM KI, 10 mM NaHCO₃, 150 mM NaOH).

UV- H₂O₂-TOP-ROF Method Analytical Decision Framework Expanded

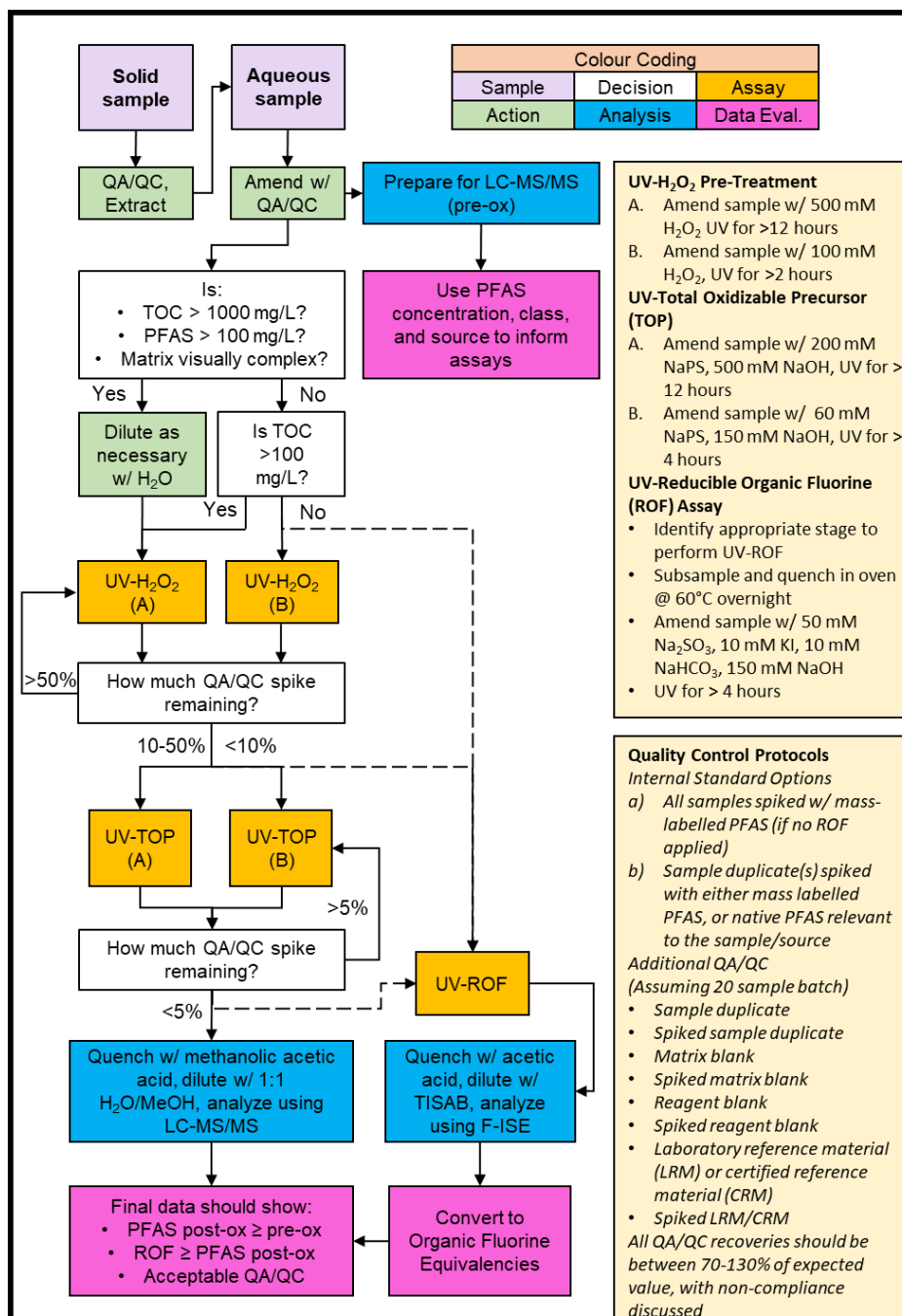


Figure D14 - Decision framework for implementation of the UV-H₂O₂-TOP-ROF assay, expanded to show detailed decision flow chart.

The initial framework begins by preparing the starting sample for work-up and analysis. In the case of solid materials (e.g. soils, sorptive materials, textiles, biota), they are amended with QA/QC spikes (to be discussed later), extracted using an appropriate protocol, and are evaporatively exchanged into water overnight without any external gasses.

In the case of soils, the extraction protocol would be alkaline methanol extractions (200 mM NaOH), as developed by Nickerson and later modified by Munoz (Liu et al., 2022; Mejia-Avendaño et al., 2017a; Nickerson et al., 2020). In this study, the HCl-MeOH extraction was performed but excluded from work-up, as analysis showed less than 5% extraction of PFAS, and combining the HCl extract with the MeOH extracts led to significant matrix effects which interfered with the TOP assay and led to PFAS loss. Depending on the matrix being extracted, combination of the extracts either led to precipitation of dissolved metals, forming a floc, or led to the precipitation of alkaline-soluble organic matter, which also formed a floc. In the case of the alkaline-soluble organic matter, it was able to be oxidatively digested using the UV-H₂O₂ assay but required multiple rounds to achieve complete oxidation.

In the case of textiles or cosmetic products, two different extraction protocols were evaluated: the direct TOP assay (dTOP), and a modified total hydrolysis of precursors (THP) assay (500 mM KOH, 85°C, 24 hours) (O'Carroll et al., 2020; Zweigle et al., 2023). These were performed after standard alkaline MeOH extractions yielded no PFAS from the textiles tested. Both the dTOP assay and the alkaline hydrolysis assay resulted in significant concentrations of PFAS being extracted from the textiles and makeup, but the dTOP (200 mM NaPS, 500 mM NaOH, 85°C for 24 hours) was found to result in consistently higher concentrations of PFCAs for the textiles compared to alkaline hydrolysis. The drawback of the dTOP method is it results in a standard thermal-TOP assay distribution of PFCAs, skewing to a shorter distribution than compared to the UV-TOP method.

After solid extracts are reconstituted in water, or if starting with an aqueous sample, samples are amended with appropriate QA/QC spikes (if not performed already), then sub-sampled and prepared for LC-MS/MS analysis to determine pre-oxidation PFAS concentrations. In scenarios where the PFAS concentration may be high, then a serial dilution would be employed, with analysis starting at the highest diluted samples. In scenarios where the PFAS concentration may be low, or the sample matrix is particularly complex, samples may need to be cleaned up with solid phase extraction (SPE), centrifuged, filtered, or alkaline digested.

Following initial sample analysis of the pre-oxidized sample using LC-MS/MS, the concentration and type of detected PFAS should be considered in the context of the sample location and potential PFAS source to determine the type and concentration of unknown PFAS. For example, high concentrations of PFSAs, or mixed isomers of PFSAs/PFCAs would indicate a legacy ECF-derived PFAS source, which may have 2-10x more PFAS concentration existing as unknown organofluorine species (e.g. PFSAMs). However, the presence 6:2 FTS and/or a mix of linear PFCAs would indicate a modern fluorotelomer-derived PFAS source, which could have a PFAS concentration up to 100x higher than indicated by standard targeted analytical suites. If little-to-no PFAS compounds were detected, but other qualities indicate there may be PFAS compounds present such as sample foaming or proximity to a potential PFAS source (e.g. landfill, manufacturing facility), then a direct application of the UV-ROF assay may be required to better estimate total PFAS concentration. A direct UV-ROF application can also be used in scenarios where regular access to an LC-MS/MS is limited, or on-site determination of organofluorine concentrations are required. An example of this may be following the surface wipe of an AFFF-impacted pipe surface, or evaluation of an applied remediation technology.

After the initial PFAS concentration (pre-oxidation) is evaluated, the samples can be further adjusted with DI water dilution if necessary. Based on the total organic carbon (TOC) limitations identified in this study, any samples appearing highly visually complex, or known to contain a TOC > 1000 mg/L may require dilution with DI water, or multiple oxidation cycles. Additionally, while the assays employed are not negatively impacted by high concentrations of PFAS, the ability to dilute samples to a PFAS concentration range of >1-10 mg/L (for application of the full UV-H₂O₂-TOP-ROF assay) or >10-1000 µg/L (for application of the UV-H₂O₂-TOP assay) has advantages for further minimizing any matrix effects and

improving accuracy. Lastly, the sample pH should be checked before moving to the UV-H₂O₂ assay stage, due to the previously identified optimal pH range of the assay. This is of particular concern when dealing with bicarbonate-rich waters (pH >8) or limestone-dominant solid materials, as dissolved carbonates can directly impact the UV-H₂O₂ assay. If sample pH is above 7-8, then the sample may be lightly acidified with HCl to pH 5-7 to ensure removal of bicarbonates. After samples are appropriately adjusted, they can be subjected to the UV-H₂O₂ assay (excluding dTOP samples).

In this study, a short UV-H₂O₂ (100 mM H₂O₂, >2 hours UV) and long UV-H₂O₂ (500 mM H₂O₂, >12 hours UV) were tested with good agreement and validation. In scenarios where the sample is clean and has a low TOC (e.g. groundwater, finished waters), then the short UV-H₂O₂ would be appropriate to ensure the formation of longer-chain PFCAs and ensuring no TOC concentration remains. In scenarios where the sample has a moderate TOC concentration of 100-1000 mg/L, then the long UV-H₂O₂ should be selected to ensure complete TOC removal. After employment of the UV-H₂O₂ assay, the QA/QC spikes could be evaluated (if possible) for the concentration remaining. If majority (>50%) of the QA/QC spike is remaining, then the UV-H₂O₂ assay should be repeated, possibly with a 10x DI water dilution before re-application. This may indicate mischaracterization of the TOC concentration of the sample matrix, or the presence of hydroxyl-radical specific quenching species (e.g. bicarbonate, alcohols).

If all, or most, of the QA/QC spike is oxidatively consumed, then the sample can undergo more complete oxidation using the UV-TOP assay. Once again, if samples are relatively simple and QA/QC spikes have been converted, then the short UV-TOP assay may be applied, which involves amending the sample with 60 mM NaPS and 150 mM NaOH. If moderate amounts of the QA/QC spike remain, and significant PFCA formation is noted, then the higher-dose UV-TOP assay may be applied, which involves amending the sample with 200 mM NaPS and 500 mM NaOH. In this study, the use of a low-dose TOP assay was also investigated (5 mM NaPS, 15 mM NaOH) for use with relatively clean groundwater samples with low PFAS concentrations. This allowed for direct injection of the sample after quenching with acidified MeOH post-TOP assay, which improved detection limits. The use of a low-dose TOP assay should be a last resort, as it was found to be highly sensitive to interferences from matrix effects, even after application of the UV-H₂O₂ assay.

Sample pH should be monitored closely before and after application of the UV-TOP to ensure the post-oxidation samples do not shift to pH < 7, as this can result in predominant generation of sulfate radicals and will breakdown PFCAs present in the sample. It is at this stage that the practicality of the UV-TOP assay duration must be considered if the UV-ROF assay is going to be applied afterwards. In this study, the two main methods identified to quench the post-oxidation sample before applying the UV-TOP assay was through additional UV application (overnight), or overnight heat application (oven, 60°C). Previous work by Javed has identified the potential for minor PFCA degradation with extended UV application (Javed et al., 2020), therefore the use of the oven to quench is advantageous. However, this may exasperate thermal diffusion of PFAS into the plastic UV-cuvettes. Both UV and thermal quenching have been investigated with statistically similar results, so the exact method of quenching is a practical choice at the discretion of the user.

If the UV-ROF assay is to be applied after the UV-H₂O₂-TOP assay, then a sub-sample of the post-oxidation sample is taken (before quenching with methanolic acetic acid) and, if not quenched by excess UV, quenched using heat and amended with reagents for the UV-ROF assay. In this study, the sample is amended to a final reagent concentration 50 mM Na₂SO₃, 10 mM KI, 10 mM NaHCO₃, and 150 mM NaOH. If 500 mM of NaOH was used in the previous UV-TOP assay, then the sample should be diluted at least 3.5x in the amendment to bring the NaOH concentration to the described concentration. It is important to note that, with newer developments in UV-reduction technology, the UV-ROF assay may be modified with different reagent concentrations or may be modified to include sequential additions of Na₂SO₃, as described by (O'Connor et al., 2023). The modification of sequential Na₂SO₃ may be required for samples dominated by high concentrations of short- and ultra-short PFASs.

After sub-sampling of the post-oxidation sample, or if the UV-ROF assay is not being applied, the sample is quenched directly into the cuvette with methanolic acetic acid (4% acetic acid) at a ratio of 1 part quench to

3 parts post-oxidation sample. The sample is then vortexed and left to sit overnight at 4°C to ensure desorption of sorbed PFAS. It is possible that sitting overnight is not required, but immediate analysis after quenching was not evaluated in this study.

After the full application of the UV-H₂O₂-TOP, and if applicable, ROF assay, then the data needs to be processed and mathematically converted to appropriate units depending on the application of the final data. For comparison of pre-oxidation and post-oxidation PFAS concentrations, PFAS concentrations in mass/mass or mass/volume units will be converted to molarity units. For comparison of pre/post-oxidation PFAS concentrations and mineralized fluoride concentrations, units will need to be converted into organic fluorine equivalencies (mM of fluorine).

References

- Banayan Esfahani, E., Mohseni, M., 2022. Fluence-based photo-reductive decomposition of PFAS using vacuum UV (VUV) irradiation: Effects of key parameters and decomposition mechanism. *J Environ Chem Eng* 10, 107050. <https://doi.org/10.1016/j.jece.2021.107050>
- Barzen-Hanson, K.A., Roberts, S.C., Choyke, S., Oetjen, K., McAlees, A., Riddell, N., McCrindle, R., Ferguson, P.L., Higgins, C.P., Field, J.A., 2017. Discovery of 40 Classes of Per- and Polyfluoroalkyl Substances in Historical Aqueous Film-Forming Foams (AFFFs) and AFFF-Impacted Groundwater. *Environ Sci Technol*. <https://doi.org/10.1021/acs.est.6b05843>
- Battye, N.J., Patch, D.J., Roberts, D.M.D., O'Connor, N.M., Turner, L.P., Kueper, B.H., Hulley, M.E., Weber, K.P., 2022. Use of a horizontal ball mill to remediate per- and polyfluoroalkyl substances in soil. *Science of The Total Environment* 835, 155506. <https://doi.org/https://doi.org/10.1016/j.scitotenv.2022.155506>
- Bentel, M.J., Liu, Z., Yu, Y., Gao, J., Men, Y., Liu, J., 2020. Enhanced Degradation of Perfluorocarboxylic Acids (PFCAs) by UV/Sulfite Treatment: Reaction Mechanisms and System Efficiencies at pH 12. *Environ Sci Technol Lett* 7, 351–357. <https://doi.org/10.1021/acs.estlett.0c00236>
- Burgess, A.E., Davidson, J.C., 2012. A kinetic-equilibrium study of a triiodide concentration maximum formed by the persulfate-iodide reaction. *J Chem Educ* 89, 814–816. <https://doi.org/10.1021/ed200055t>
- Buxton, G. V., Greenstock, C.L., Helman, W.P., Ross, A.B., 1988. Critical Review of rate constants for reactions of hydrated electrons, hydrogen atoms and hydroxyl radicals ($\cdot\text{OH}/\cdot\text{O}^-$ in Aqueous Solution. *J Phys Chem Ref Data* 17, 513–886. <https://doi.org/10.1063/1.555805>
- D'Agostino, L.A., Mabury, S.A., 2014. Identification of Novel Fluorinated Surfactants in Aqueous Film Forming Foams and Commercial Surfactant Concentrates. *Environ Sci Technol* 48, 121–129. <https://doi.org/10.1021/es403729e>
- Duchesne, A.L., Brown, J.K., Patch, D.J., Major, D., Weber, K.P., Gerhard, J.I., 2020. Remediation of PFAS-Contaminated Soil and Granular Activated Carbon by Smoldering Combustion. *Environ Sci Technol* 54, 12631–12640. <https://doi.org/10.1021/acs.est.0c03058>
- Fan, X., Bao, Y., Mumtaz, M., Huang, J., Yu, G., 2021. Determination of total oxidizable precursors in foam surfactants and foam contaminated water based on UV-activated persulfate oxidation. *Science of the Total Environment* 763, 142943. <https://doi.org/10.1016/j.scitotenv.2020.142943>
- Fennell, B.D., Fowler, D., Mezyk, S.P., McKay, G., 2023. Reactivity of Dissolved Organic Matter with the Hydrated Electron: Implications for Treatment of Chemical Contaminants in Water with Advanced Reduction Processes. *Environ Sci Technol* 57, 7634–7643. <https://doi.org/10.1021/acs.est.3c00909>
- Glover, C.M., Pazoki, F., Munoz, G., Liu, J., 2024. Enhancing Total Oxidizable Precursor Assay for Characterization of PFAS: UV Versus Heat Activation. Pre-print.
- Goldstein, S., Aschengrau, D., Diamant, Y., Rabani, J., 2007. Photolysis of aqueous H₂O₂: Quantum yield and applications for polychromatic UV actinometry in photoreactors. *Environ Sci Technol* 41, 7486–7490. <https://doi.org/10.1021/es071379t>
- Harding-Marjanovic, K.C., Houtz, E.F., Yi, S., Field, J.A., Sedlak, D.L., Alvarez-Cohen, L., 2015. Aerobic Biotransformation of Fluorotelomer Thioether Amido Sulfonate (Lodyne) in AFFF-Amended Microcosms. *Environ Sci Technol* 49, 7666–7674. <https://doi.org/10.1021/acs.est.5b01219>
- Hayyan, M., Hashim, M.A., Alnashef, I.M., 2016. Superoxide Ion: Generation and Chemical Implications. *Chem Rev* 116, 3029–3085. <https://doi.org/10.1021/acs.chemrev.5b00407>

- Houtz, E.F., Higgins, C.P., Field, J.A., Sedlak, D.L., 2013. Persistence of perfluoroalkyl acid precursors in AFFF-impacted groundwater and soil. *Environ Sci Technol* 47, 8187–8195. <https://doi.org/10.1021/es4018877>
- Javed, H., Lyu, C., Sun, R., Zhang, D., Alvarez, P.J.J., 2020. Discerning the inefficacy of hydroxyl radicals during perfluorooctanoic acid degradation. *Chemosphere* 247. <https://doi.org/10.1016/j.chemosphere.2020.125883>
- Liang, C., Huang, C.F., Mohanty, N., Kurakalva, R.M., 2008. A rapid spectrophotometric determination of persulfate anion in ISCO. *Chemosphere* 73, 1540–1543. <https://doi.org/10.1016/j.chemosphere.2008.08.043>
- Liu, M., Munoz, G., Vo Duy, S., Sauv e, S., Liu, J., 2022. Per- and Polyfluoroalkyl Substances in Contaminated Soil and Groundwater at Airports: A Canadian Case Study. *Environ Sci Technol* 56, 885–895. <https://doi.org/10.1021/acs.est.1c04798>
- Liu, Z., Bentel, M.J., Yu, Y., Ren, C., Gao, J., Pulikkal, V.F., Sun, M., Men, Y., Liu, J., 2021. Near-Quantitative Defluorination of Perfluorinated and Fluorotelomer Carboxylates and Sulfonates with Integrated Oxidation and Reduction. *Environ Sci Technol* 55, 7052–7062. <https://doi.org/10.1021/acs.est.1c00353>
- Martin, D., Munoz, G., Mejia-Avenida, S., Duy, S.V., Yao, Y., Volchek, K., Brown, C.E., Liu, J., Sauv e, S., 2019. Zwitterionic, cationic, and anionic perfluoroalkyl and polyfluoroalkyl substances integrated into total oxidizable precursor assay of contaminated groundwater. *Talanta* 195, 533–542. <https://doi.org/10.1016/j.talanta.2018.11.093>
- Mejia-Avenida, S., Munoz, G., Sauv e, S., Liu, J., 2017. Assessment of the Influence of Soil Characteristics and Hydrocarbon Fuel Cocontamination on the Solvent Extraction of Perfluoroalkyl and Polyfluoroalkyl Substances. *Anal Chem* 89, 2539–2546. <https://doi.org/10.1021/acs.analchem.6b04746>
- Morgan, M.S., Van Trieste, P.F., Garlick, S.M., Mahon, M.J., Smith, A.L., 1988. Ultraviolet molar absorptivities of aqueous hydrogen peroxide and hydroperoxyl ion. *Anal Chim Acta* 215, 325–329. [https://doi.org/10.1016/S0003-2670\(00\)85294-0](https://doi.org/10.1016/S0003-2670(00)85294-0)
- Munoz, G., Michaud, A.M., Liu, M., Vo Duy, S., Montenach, D., Resseguier, C., Watteau, F., Sappin-Didier, V., Feder, F., Morvan, T., Houot, S., Desrosiers, M., Liu, J., Sauv e, S., 2021. Target and Nontarget Screening of PFAS in Biosolids, Composts, and Other Organic Waste Products for Land Application in France. *Environ Sci Technol*. <https://doi.org/10.1021/acs.est.1c03697>
- Nickerson, A., Maizel, A.C., Kulkarni, P.R., Adamson, D.T., Kornuc, J.J., Higgins, C.P., 2020. Enhanced Extraction of AFFF-Associated PFASs from Source Zone Soils. *Environ Sci Technol* 54, 4952–4962. <https://doi.org/10.1021/acs.est.0c00792>
- O’Carroll, D.M., Jeffries, T.C., Lee, M.J., Le, S.T., Yeung, A., Wallace, S., Battye, N., Patch, D.J., Manefield, M.J., Weber, K.P., 2020. Developing a roadmap to determine per- and polyfluoroalkyl substances-microbial population interactions. *Science of the Total Environment* 712. <https://doi.org/10.1016/j.scitotenv.2019.135994>
- O’Connor, N., Patch, D., Noble, D., Scott, J., Koch, I., Mumford, K.G., Weber, K., 2023. Forever no more : Complete mineralization of per - and poly fl uoroalkyl substances (PFAS) using an optimized UV / sulfite / iodide system. *Science of the Total Environment* 888, 164137. <https://doi.org/10.1016/j.scitotenv.2023.164137>
- Patch, D., O’Connor, N., Koch, I., Cresswell, T., Hughes, C., Davies, J.B., Scott, J., O’Carroll, D., Weber, K., 2022. Elucidating degradation mechanisms for a range of per- and polyfluoroalkyl substances (PFAS) via controlled irradiation studies. *Science of the Total Environment* 832, 154941. <https://doi.org/10.1016/j.scitotenv.2022.154941>

- Patch, D., O'Connor, N., Vereecken, T., Murphy, D., Munoz, G., Ross, I., Glover, C., Scott, J., Koch, I., Sauvé, S., Liu, J., Weber, K., 2024. Advancing PFAS characterization: Enhancing the total oxidizable precursor assay with improved sample processing and UV activation. *Science of The Total Environment* 909, 168145. <https://doi.org/10.1016/j.scitotenv.2023.168145>
- Tantawi, O., Baalbaki, A., El Asmar, R., Ghauch, A., 2019. A rapid and economical method for the quantification of hydrogen peroxide (H₂O₂) using a modified HPLC apparatus. *Science of the Total Environment* 654, 107–117. <https://doi.org/10.1016/j.scitotenv.2018.10.372>
- Tsou, K., Antell, E., Duan, Y., Olivares, C.I., Yi, S., Alvarez-Cohen, L., Sedlak, D.L., 2023. Improved Total Oxidizable Precursor Assay for Quantifying Polyfluorinated Compounds Amenable to Oxidative Conversion to Perfluoroalkyl Carboxylic Acids. *ACS ES and T Water*. <https://doi.org/10.1021/acsestwater.3c00224>
- Turner, L.P., Kueper, B.H., Jaansalu, K.M., Patch, D.J., Battye, N., El-Sharnouby, O., Mumford, K.G., Weber, K.P., 2021. Mechanochemical remediation of perfluorooctanesulfonic acid (PFOS) and perfluorooctanoic acid (PFOA) amended sand and aqueous film-forming foam (AFFF) impacted soil by planetary ball milling. *Science of the Total Environment* 765, 142722. <https://doi.org/10.1016/j.scitotenv.2020.142722>
- Yin, R., Anderson, C.E., Zhao, J., Boehm, A.B., Mitch, W.A., 2023. Controlling contaminants using a far-UVC-based advanced oxidation process for potable reuse. *Nature Water* 1, 555–562. <https://doi.org/10.1038/s44221-023-00094-5>
- Zhao, S., Ma, H., Wang, M., Cao, C., Yao, S., 2013. Study on the role of hydroperoxyl radical in degradation of p-nitrophenol attacked by hydroxyl radical using photolytical technique. *J Photochem Photobiol A Chem* 259, 17–24. <https://doi.org/10.1016/j.jphotochem.2013.02.012>
- Zweigle, J., Capitain, C., Simon, F., Roesch, P., Bugsel, B., Zwiener, C., 2023. Non-extractable PFAS in functional textiles - characterization by complementary methods: oxidation, hydrolysis, and fluorine sum parameters. *Environ Sci Process Impacts* 25, 1298–1310. <https://doi.org/10.1039/d3em00131h>

Appendix E – Supplemental Information for Chapter 7

Literature Review Summary

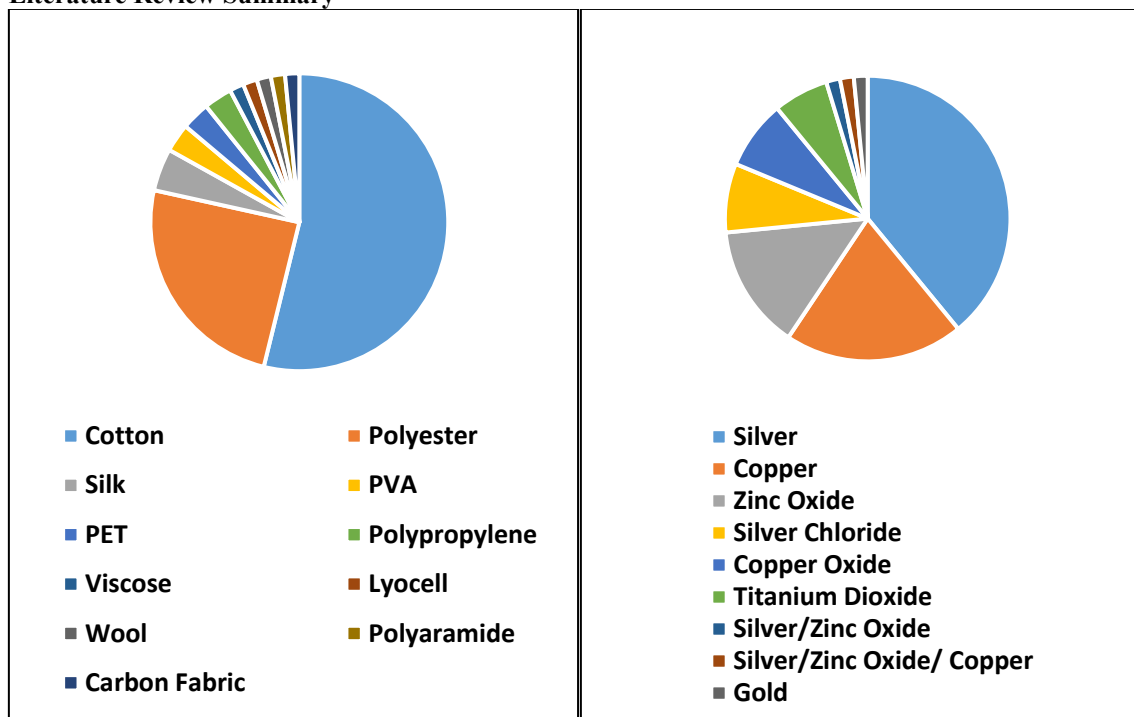


Figure E1: Assessment of most popular textile (cotton) and metals (silver, copper) for synthesis of metal-treated textiles for studies from 2005-2020 (n=65).

Metal Content Calibration

The first calibration curve was prepared by taking washed and dried sections of untreated cotton batting and drying different amounts of a silver nitrate or copper nitrate solution onto it which was then analyzed using XRF, with concentration of the XRF being plotted against the theoretical concentration on the textile. However, it was found that the ionic solution did not dry homogeneously and much of it dried onto the weigh boats used to hold the solution. Due to concerns about the accuracy of this calibration method a second method was developed.

Using sodium hydroxide and ammonia, textiles were treated with silver, copper, or silver and copper using the previously described synthesis method. Once dry, the textiles were analyzed on the XRF to obtain the XRF signal. The textiles were then digested using Piranha solution (4:1 H₂SO₄:H₂O₂), in 0.04 g textile and 2.5 mL solution quantities with heating followed by 1 mL of HNO₃, diluted with DI water and analyzed using an inductively coupled plasma mass spectrometer (NexION 300D) for total silver and copper concentration using rhodium as an internal standard. The XRF concentration was then plotted against the ICP-MS concentration to generate a linear calibration curve. Given the accuracy of the second calibration curve method, the silver and copper XRF signals were calibrated using the ICP-MS calibration curve (Figure E2).

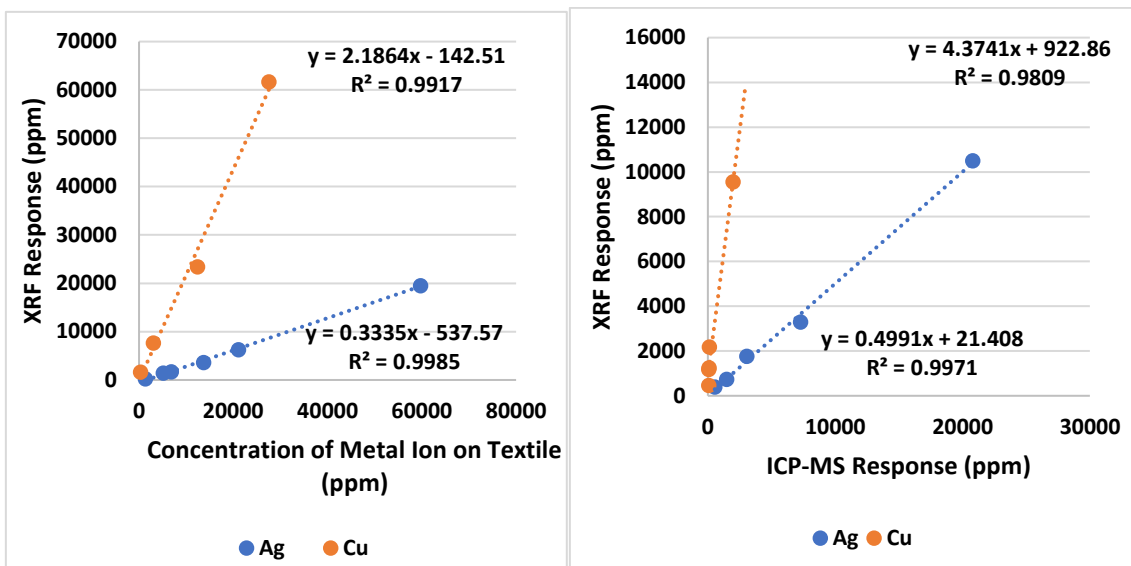


Figure E2: Calibration curve converting XRF response (in ppm) to concentration of metal on the textile using the theoretical amount of metal dried on the textile (left) and ICP-MS determined concentration (right).

SEM Sample Preparation Development

Initial SEM method development was performed on textile subsamples (1x1 cm) from method 2 (NaHCO_3), method 5 (NaOH) and method 8 (NaBH_4). For silver treatment methods 2 and 5, no silver was found on the surface of the textile (Figure E3a), while method 8 had small amounts of silver nanoparticles present on the surface (Figure E3b, S3c). For copper treatment methods 2, 5, and 8, copper nanoparticles were found on the surface in small patches, but not consistently (Figure E3d).

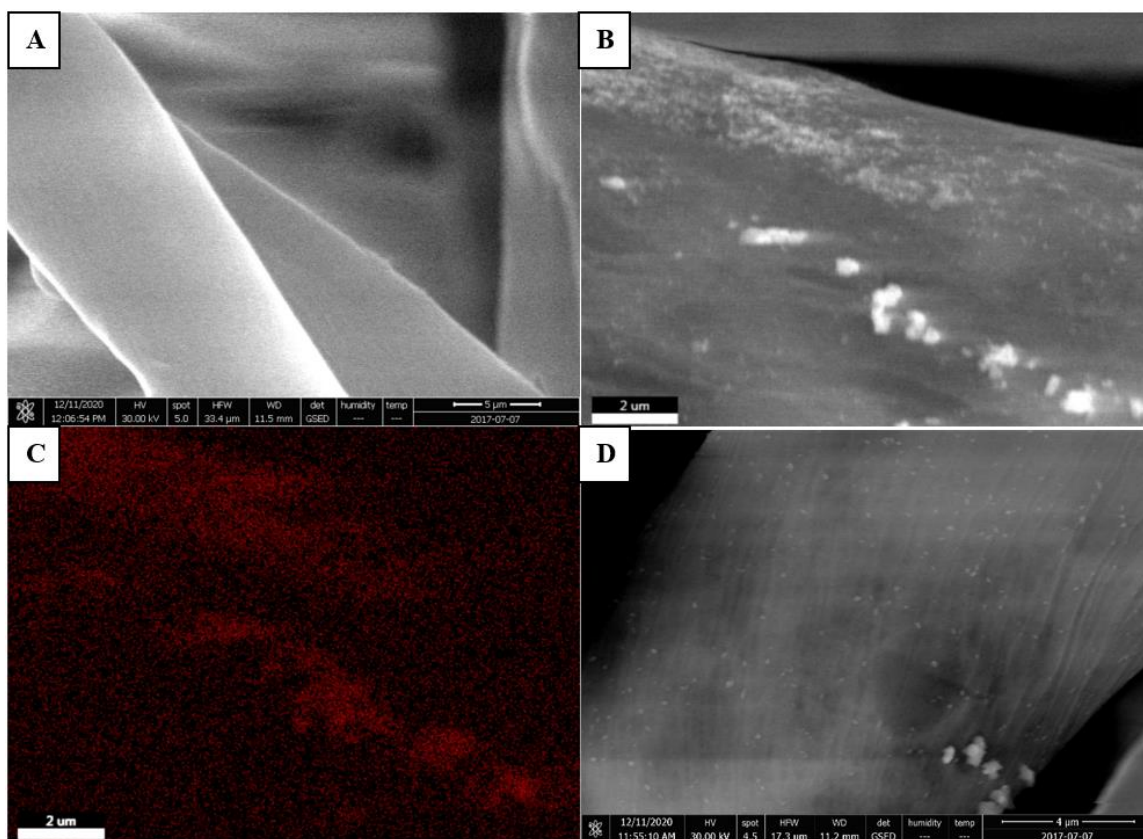


Figure E3: SEM image from NaHCO₃ treatment method, showing no silver present on the cotton fiber surface (A). Image of silver particles and nanoparticles on the surface of the cotton fiber following NABH₄ treatment method (B), with EDX image overlay confirming silver (red, C). Image of copper nanoparticles present on the surface of the textile following NaHCO₃ treatment method (D).

Following the failure to find any silver nanoparticles or substantial copper nanoparticles on the surface of the textile, it was identified that structure of cotton fiber, while mainly cellulosic, does have a cuticle and outer wall which consists of waxes, pectin, and polysaccharides. Given the porous nature of cotton fibers and the waxy (French and Kim, 2018), less reactive surface cuticle, it was hypothesized that the nanomaterials were present inside the fiber and not on the surface. To confirm this, a cross-section of a silver-treated cotton fiber was prepared by rolling a section of cotton between Kapton tape which was then cut horizontally with a scalpel. While most fibers deformed almost immediately under the electron beam, an image and EDX spectra were acquired confirming the internal location of the particles (Figure 1). While ex-situ synthesized silver nanoparticles have been theorized to be entrapped in cross-linked cellulose, this is (to the author's knowledge) the first study to identify the presence of silver and copper nanomaterials inside the cotton fibers (Montazer et al., 2012b).

Once the location of the nanomaterials was confirmed the textiles (0.1 grams) were ashed, redispersed in DI water (5 mL), then dried onto carbon tape stubs and analyzed.

SEM analysis of the dried ash solution revealed a large amount of silver particles, which dried into clusters on the double-sided carbon tape (Figure E4). Further magnification of the image acquisition shows spherical and semi-spherical nanoparticles making up majority of the clusters. Some larger particles of ash were also found in the clusters of silver materials as well. This ashing method was then repeated with a higher dilution factor (10 mL DI water : 0.1 grams textile) and ultrasonicated (60 seconds) to reduce particle clustering during drying. This method yielded less clustering and resulted in better SEM characterization.

It is important to note that some of the nanoparticles may be undergoing sintering, resulting in a positive bias in the reported particle diameters(Benn and Westerhoff, 2008a). However, due to difficulties in cross-section analysis of the fibers this method was still employed.

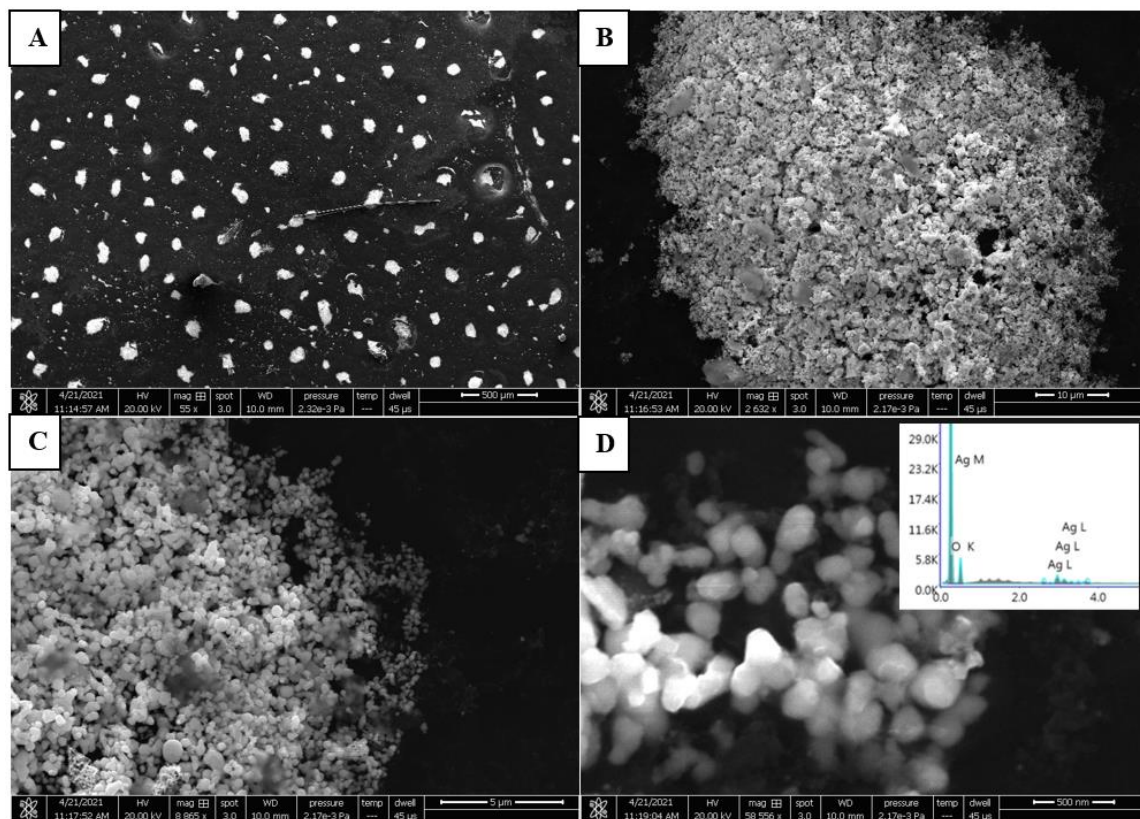


Figure E4: SEM analysis of silver nanoparticles dried onto double-sided carbon tape from the NaHCO_3 ashed textile.

XANES Relativized Data

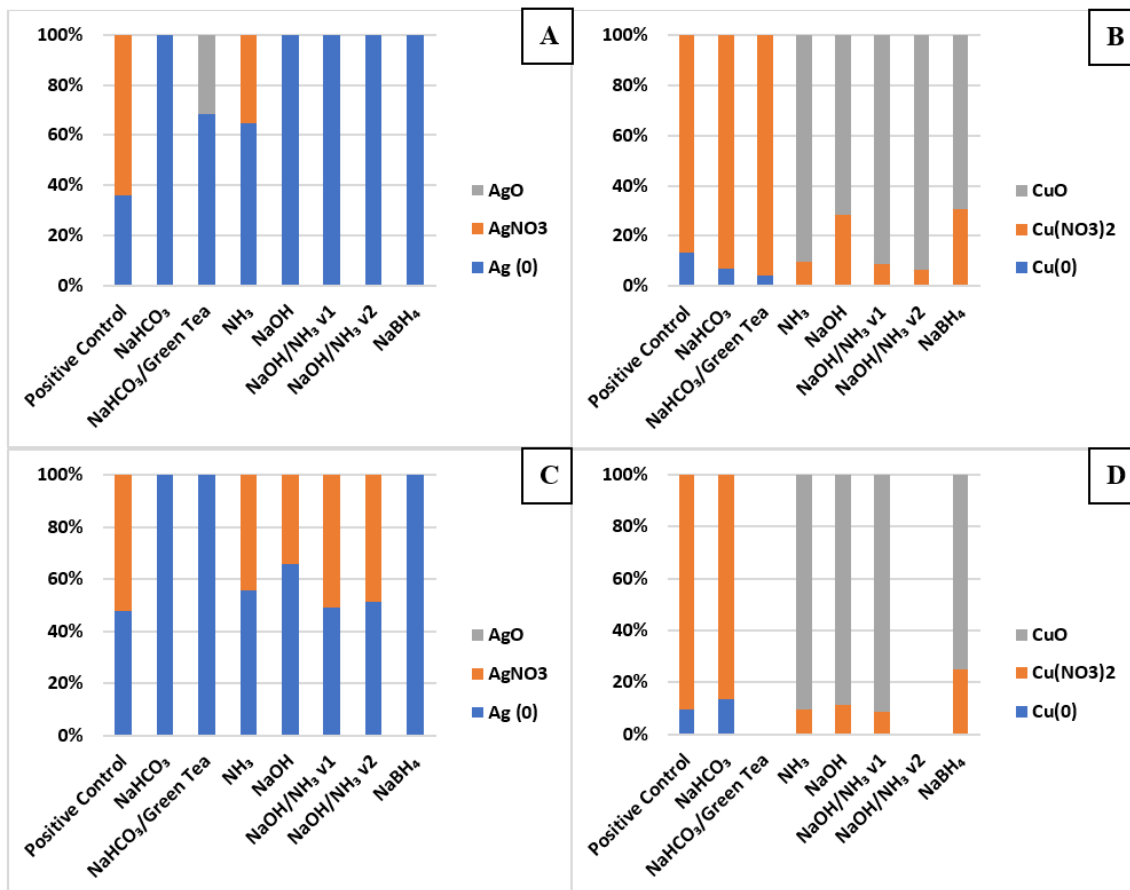


Figure E5: XANES speciation of silver (A), copper (B) independently on the textile and silver (C), copper (D) combined on the textile

NaHCO₃ Role of pH

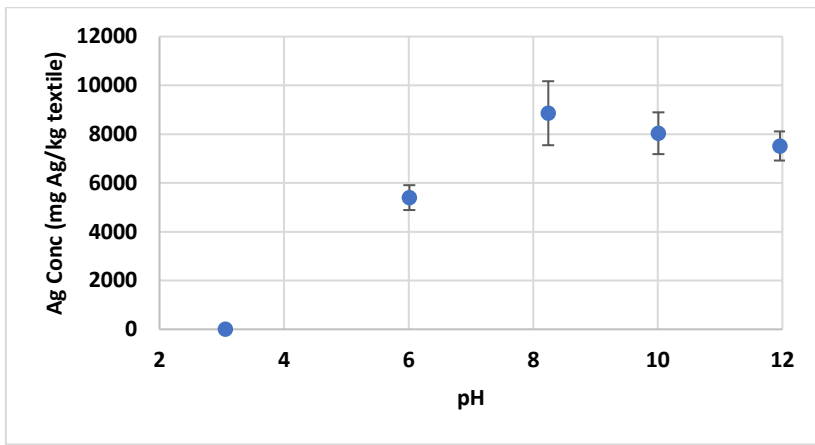


Figure E6: XRF analysis of the textiles following treatment with silver and NaHCO₃, investigating the role of pH.

Silver/Copper Competition

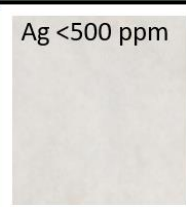
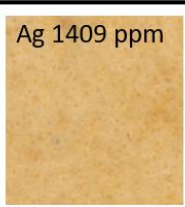
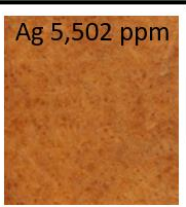

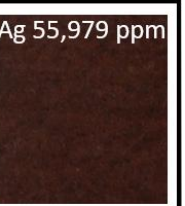
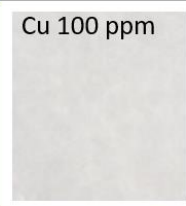
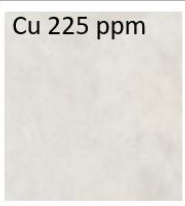
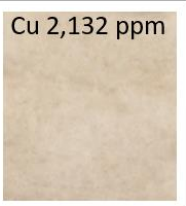

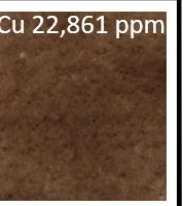
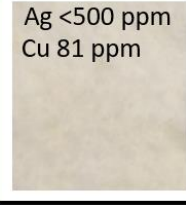
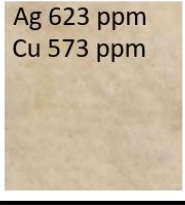
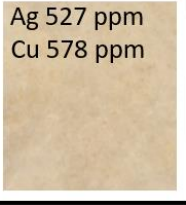
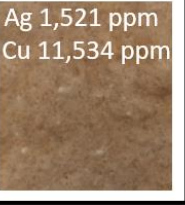
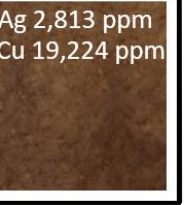
	0.1 mM	0.5 mM	1 mM	5 mM	10 mM
Silver	Ag <500 ppm 	Ag 1409 ppm 	Ag 5,502 ppm 	Ag 21,340 ppm 	Ag 55,979 ppm 
Copper	Cu 100 ppm 	Cu 225 ppm 	Cu 2,132 ppm 	Cu 6,356 ppm 	Cu 22,861 ppm 
Silver Copper	Ag <500 ppm Cu 81 ppm 	Ag 623 ppm Cu 573 ppm 	Ag 527 ppm Cu 578 ppm 	Ag 1,521 ppm Cu 11,534 ppm 	Ag 2,813 ppm Cu 19,224 ppm 

Figure E7: Textile analysis of the investigation into the effect of reagent concentration on concentration present on the textile following NaOH/NH₃Version1 synthesis method.

XANES and FTIR Spectra

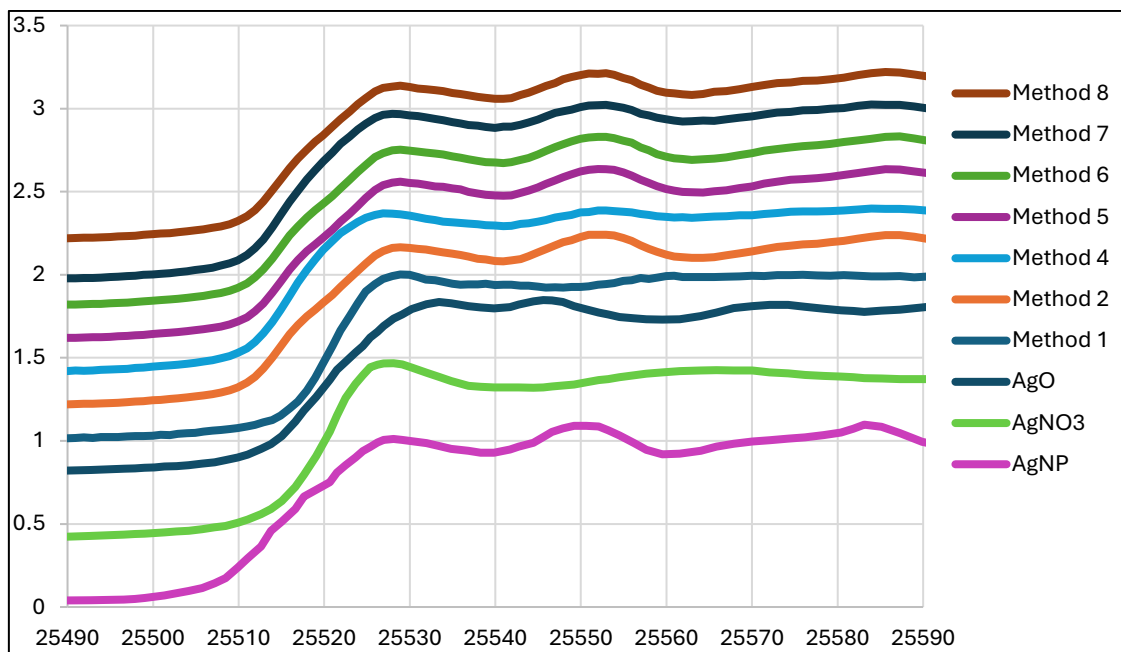


Figure E8: XANES chromatograms for synthesis methods 1-8 following treatment with only silver.

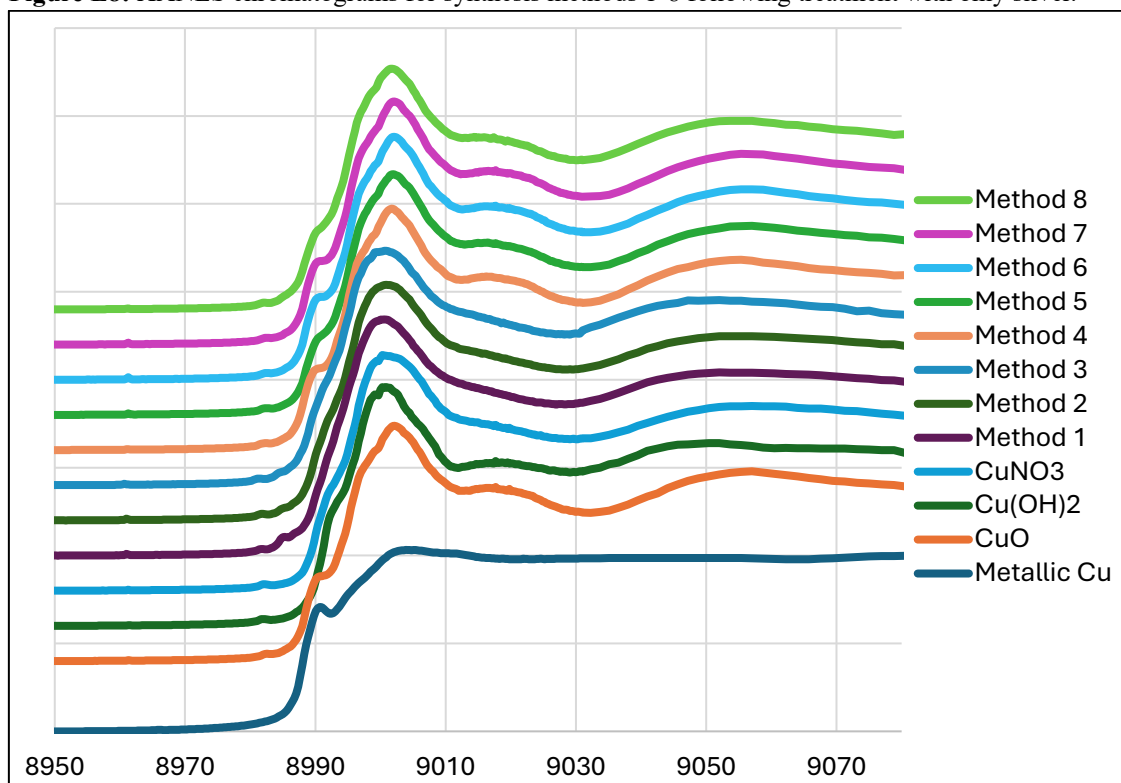


Figure E9: XANES chromatograms for synthesis methods 1-8 following treatment with only copper.

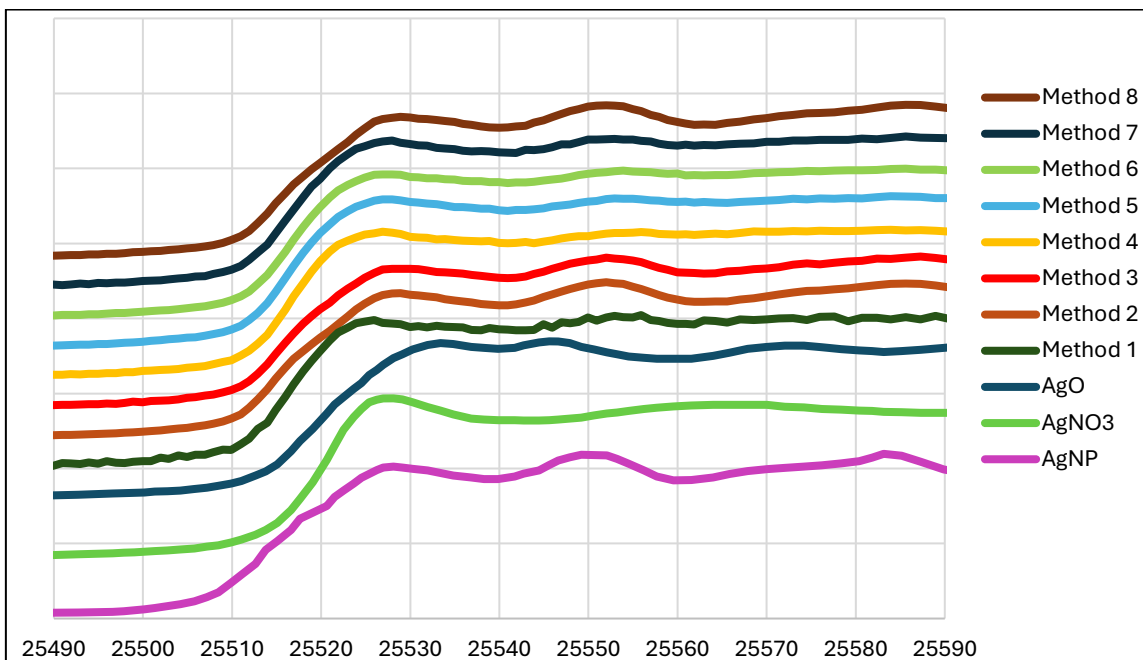


Figure E10: XANES chromatograms for synthesis methods 1-8 following treatment with silver and copper (silver shown).

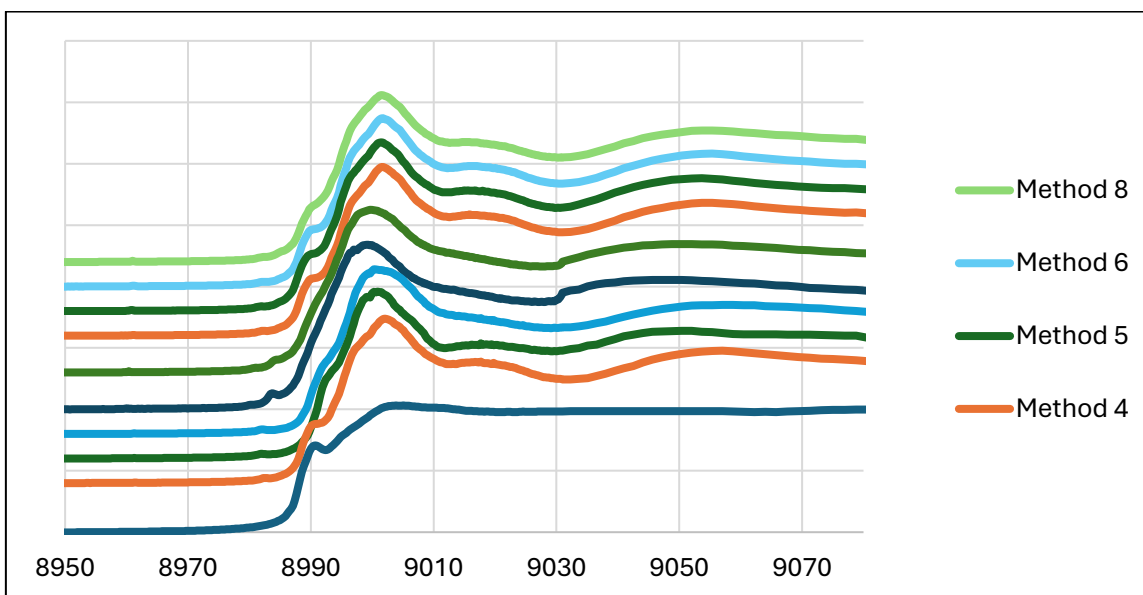


Figure E11: XANES chromatograms for synthesis methods 1-8 following treatment with silver and copper (copper shown).

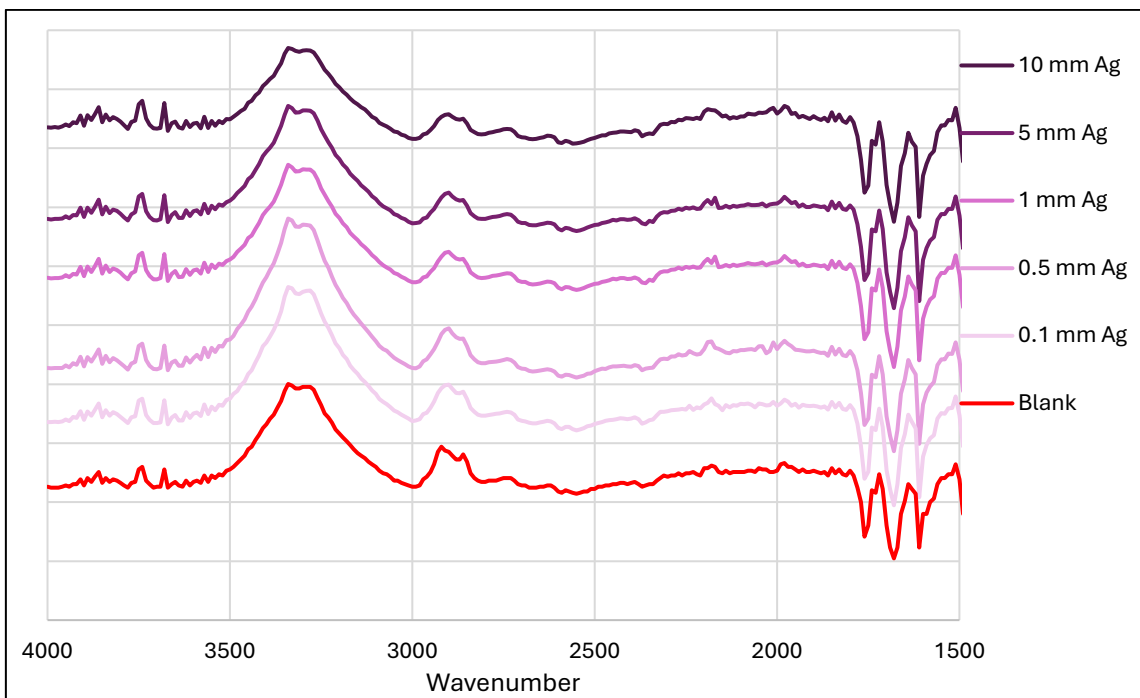


Figure E12: ATR-FTIR spectra for cotton samples following treatment with silver nitrate and NaOH/NH₃
Version 1.

Appendix F – Supplemental Information for Chapter 8

Analytical Suite

Total Silver Analysis

Equal parts of wash and rinse samples were combined to create a sample representative of the total release event for characterization. The solutions were sequentially filtered through a series of filters with pore sizes of 5 μm , 0.45 μm , 0.22 μm , and 10 kilodalton, and an unfiltered portion was also retained. Each of these filtered portions and the unfiltered portion were then analyzed using ICP-MS (ELAN DRC II, Perkin Elmer) following digestion by aqua regia to determine the total concentration and size distribution of released silver. Aqua regia digestion procedures were performed by digesting 0.50 mL of combined wash water with 1 mL of freshly prepared aqua regia (1:3 v/v concentrated nitric:hydrochloric acids, Fisher), at 80°C for 2 hours in an oven, followed by diluting with 8.5 mL of DI water.

The digests were analyzed on an ICP-MS optimized for mass and sensitivity daily by using a 1 $\mu\text{g/L}$ tuning solution (Inorganic Ventures). The instrument conditions for ICP-MS were: nebulizer gas flow 1.11 L/min, lens voltage 8.5V, ICP-radio frequency power 1300W. A 6-point calibration curve over the range of 0–250 $\mu\text{g/L}$ (Silver Standard for ICP, Fluka Analytical) was used, and plasma and matrix effects were corrected using rhodium as an internal standard (20 $\mu\text{g/L}$ Rh Standard, Fluka). Continuing calibration checks (CCC) were analyzed every 15 samples at a high (50 $\mu\text{g/L}$) and low (5 $\mu\text{g/L}$) concentration with results within 10% of expected values. DI water analyzed before and after being taken through the washing method were found to be below the limit of detection (LOD) of 1 $\mu\text{g Ag/L}$, and DI water spiked with ionic silver taken through the same procedure as the samples (method spike) showed spiked recoveries (>90%) which were within acceptable limits.

Silver Morphology and Surface Speciation Analysis

SEM/EDX was used to image both the textiles and the released wash water from the textiles. SEM was also used as a preliminary investigation into silver speciation by looking at the co-location of silver with other elements. Samples were analyzed on a Quanta 250FED operating under environmental mode at 100 kPa. EDX was performed using an EDAX Octane Elite. 1 x 1cm subsamples of textiles were cut and mounted onto an SEM sample stage using thermoplastic. Wash water samples were collected via vacuum filtration onto a 0.025 nm cellulose filter. Filtered material was then transferred onto an SEM sample mount with thermoplastic.

Bulk Silver Speciation Analysis

X-ray absorption near edge structure (XANES) analysis was used to perform silver speciation analysis of the bulk released silver solution and the textiles. XANES spectra were collected at the Sector 20 insertion device beamline (20ID-C) of the Advanced Photon Source (CLS@APS), within the X-Ray Science Division (XSD), Argonne National Laboratory. XANES spectra of the Ag K α -edge were recorded in fluorescence mode by using a four-element silicon drift detector (Vortex®-ME4 with Xspress 3 pulse processor) while monitoring incident and transmitted intensities in straight ion chamber detectors filled with N₂ gas. One sample of wash water from human weathering was analyzed at the Materials Research Collaborative Access Team (MRCAT) Sector 10-BM, in fluorescence mode with a Vortex single-element silicon drift diode detector. Textiles were analyzed as 1cm x 1cm subsections rolled and packed in an aluminum sample holder, held between two layers of Kapton® tape. Wash water samples were soaked onto a Kimwipe® and packed in an aluminum sample holder, held between two layers of Kapton® tape. The wash water from human weathering was analyzed (at MRCAT Sector 10) at a later date, with 2 mL of this wash water dried onto a filter under vacuum and in the dark. The filter was sealed in Kapton® tape, then sectioned into 3 sections that were stacked for analysis. During irradiation and measurements, the samples collected at Sector 20 were kept at 80 K inside a stainless steel chamber with Kapton® tape windows (APS construction, with NorCal clamps) kept under a 8 mTorr vacuum (Agilent Technologies Turbo-V 81-AG) with electronic cooling (Lakeshore 331 Temperature Controller with DT-600 Series silicon dioxide cryogenic temperature sensor). The Si(111)

double crystal monochromator was calibrated using a silver metal foil at 25,514 eV, the incident beam size was 800 μm , and the reference Ag foil was measured simultaneously with samples. XANES spectra were fit within -20 to +30 eV to E0 using Athena software. The standard spectra used for fitting had been measured as frozen aqueous dissolved species previously by our group¹, and included AgNP, AgNO₃, AgO, AgCl, Ag₃PO₄, and Ag₂S. It is important to note that the AgNP standard used identifies silver in its zero oxidation state, and therefore cannot distinguish between nanoparticulate or bulk metallic silver.

Standard Wash Method

The detergent solution consisted of 4 ± 0.05 grams of Tide Original® diluted to 1L with deionized (DI) water. The water was previously heated to 40°C and the pH of the Tide® solution was measured using a pH probe (Accumet) with an average pH of 8.1 ± 0.3 . 150 mL of detergent solution was added to a 2L HDPE bottle containing one sock and ten one-inch acrylic spheres¹. The bottle was then put onto an orbital shaker inside an incubator at 40°C, and agitated at a rate of 150 RPM for 1 hour. After this time, the sock was removed, gently pressed with gloved hands to remove absorbed wash water, and a sub-sample of the wash water was collected, discarding the rest. This represents the completion of the wash cycle before the start of the rinse cycle. The sock was then put back into the 2L HDPE bottle and 150 mL DI water at 40°C was added. The bottle was placed onto the shaker table and agitated for 5 minutes as described for the wash cycle. After the rinse cycle was complete, the textile was removed, gently pressed with a gloved hand to remove absorbed rinse water, and a sub-sample of the rinse water was collected. The textile was then dried on a wire drying rack, covered with a large thick cloth to protect the washed textiles from direct light exposure. Three replicates were conducted for each textile trial.

Materials

Table F1: Materials and reagents used in ICP-MS and total silver concentration work.

Chemical/Material	Supplier	Use
Eppendorf Conical Tubes	VWR	Sample storage, transport, dilution
5µm, 0.45 µm, 0.22 µm syringe filters	Thermo Scientific Canada	Size fractionation
10 kDa centrifuge filter	Thermo Scientific Canada	Ionic silver determination
Nitric acid (TraceMetal Grade)	Fischer Scientific Canada	Glassware cleaning, aqua regia digestion, ICP-MS
Hydrochloric Acid, ACS Plus, 36.5%	Fischer Scientific Canada	Aqua regia digestion

1.1. List of ingredients in Tide Liquid Original Detergent

https://www.pg.com/productsafety/ingredients/household_care/laundry_fabric_care/Tide/Tide_Liquid_Original.pdf

- Alcohol Sulfate
- Dimethicone
- Mannanase
- Alcoholethoxy Sulfate
- Disodium
- Diaminostilbene Disulfonate
- Polyethylene Glycol 4000
- Alkyldimethylamine Oxide
- DTPA
- Polyethyleneimine Ethoxylate
- Amylase
- Ethanol
- Propylene Glycol
- Borax
- Ethanolamine
- Protease
- Calcium Formate
- Fragrance
- Sodium Fatty Acids
- Citric Acid
- Laureth-9
- Sodium Formate
- Diethylene Glycol
- Linear Alkylbenzene Sulfonate
- Sodium Hydroxide
- Diquaternium Ethoxysulfate
- Liquitint™ Blue
- Water

Textile Characterization

Experiments were conducted using a commercially available textile purchased from Lululemon™ (T.H.E. Sock). This textile was selected because of its use previously in literature research and for its content of X-Static® fiber (3% according to label), a well characterized fiber coated in silver. Textiles, on average, weighed 21.4 +/- 0.9 grams (n=30). Previous researchers cut sub-sections from the textile for use in release experiments (references). We found that cutting sub-sections from the textile resulted in increased release concentrations (Table F2). Moreover, our X-ray fluorescence (XRF) analysis of the socks demonstrated that silver is distributed heterogeneously on the textile, which could bias experimental results when obtained subsections (Figure F1). For this reason, socks were kept whole for artificial weathering and silver release experiments. Information on the silver-containing textile used such as silver speciation, particle size, functionalization, and actual silver content was limited. Investigation of patents related to the silver-coated X-Static® Fiber also yielded limited information, but it is hypothesized that the silver functionalization occurs through an electroless (chemical, non-galvanic) deposition process onto a nylon core to form the X-Static fiber. This fiber is then woven into the textile to add the silver to the overall textile. SEM with EDX imaging was used to confirm this hypothesis. Textiles were cut into 1cm x 1cm squares and measured under SEM operating in environmental mode (ESEM). Wash water was dried onto carbon table mounted on an SEM stub and analyzed under both ESEM and SEM mode. ImageJ was used to determine dimensions of released materials.

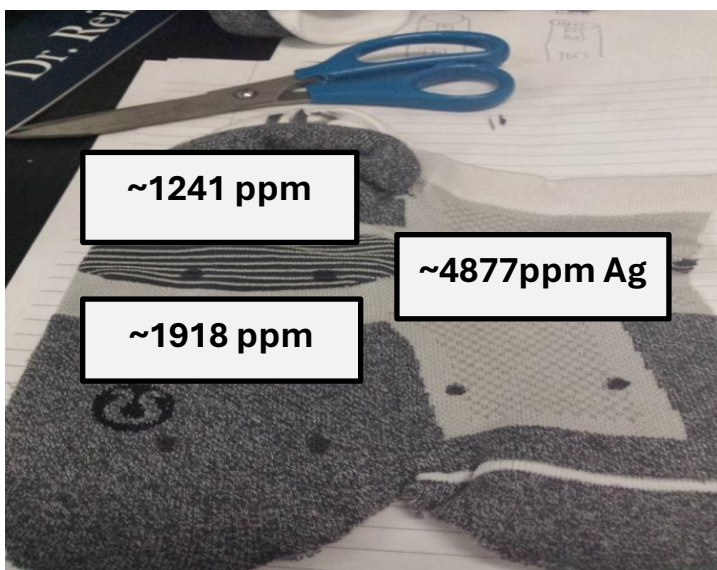


Figure F1: XRF-determined concentration of silver in different areas of the textile

Table F2: Influence of cutting textile subsections on the release into wash water

Textile Treatment	Silver Release	Wash
Whole Sock	2.2 ± 0.6 mg/L	
Cut-Up Sock	6.5 ± 0.2 mg/L	

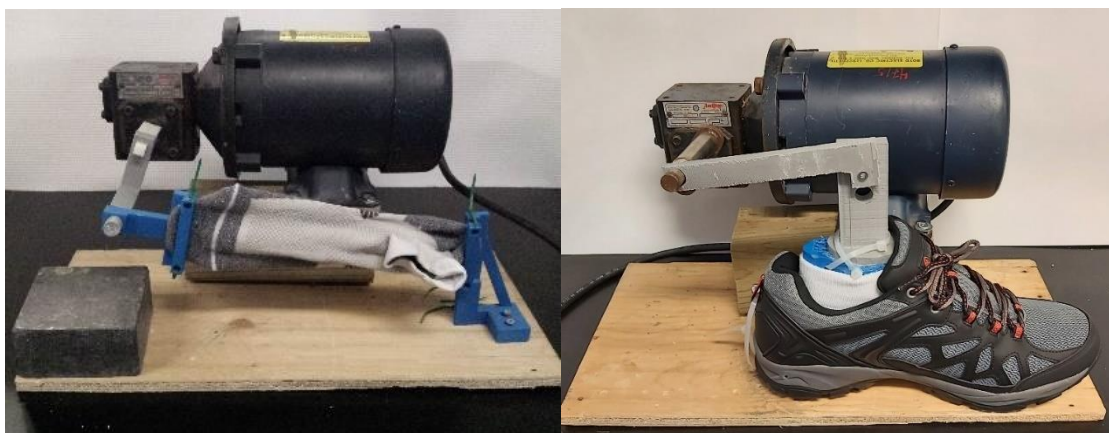


Figure F2: Physical weathering apparatus focused on stretching (left, PhW-S) and stretching/abrasion (right, PhW-W).

XANES Analysis

Table F3: XANES analysis results summary table. Results generated using ATHENA linear combination fitting (LCF) to compare the spectra generated by the sample against known standards. Reduced chi-squared and R-factor are used to determine the goodness of fit for the LCF.

Textile Trial	AgNP %	AgNO3 %	AgO %	AgCl %	Reduced Sq	Chi-	R-Factor
Control	79.5	0.0	20.5	0.0	0.00018		0.00113
PhW-S	81.6	0.0	18.4	0.0	0.000024		0.025037
PhW-W	99.1	0.0	0.9	0.0	0.00025		0.001883
CW	86.0	0.0	14.0	0.0	0.000031		0.032975
CW/PhW-S	100.0	0.0	0.0	0.0	0.00025		0.001997
CW/PhW-W	96.0	0.0	4.0	0.0	0.00032		0.002193
Human Weathered	79.7	0.0	20.3	0.0	0.0002431		0.001737
Wash Water Trial	AgNP %	AgNO3 %	AgO %	AgCl %	Reduced Sq	Chi-	
Control	100.0	0.0	0.0	0.0	0.02800		0.43
PhW-S	100.0	0.0	0.0	0.0	0.015000		0.153962
PhW-W	100.0	0.0	0.0	0.0	0.00084		0.005838
CW	1.1	0.0	0.0	98.9	0.000542		0.003443
CW/PhW-S	0.0	0.0	0.0	100.0	0.00010		0.051651
CW/PhW-W	16.5	0.0	0.0	83.5	0.00033		0.00208
Human Released	60.0	0.0	0.0	40.0	0.00007		0.000437
Onto Foot	100.0	0.0	0.0	0.0	0.00200		0.014788

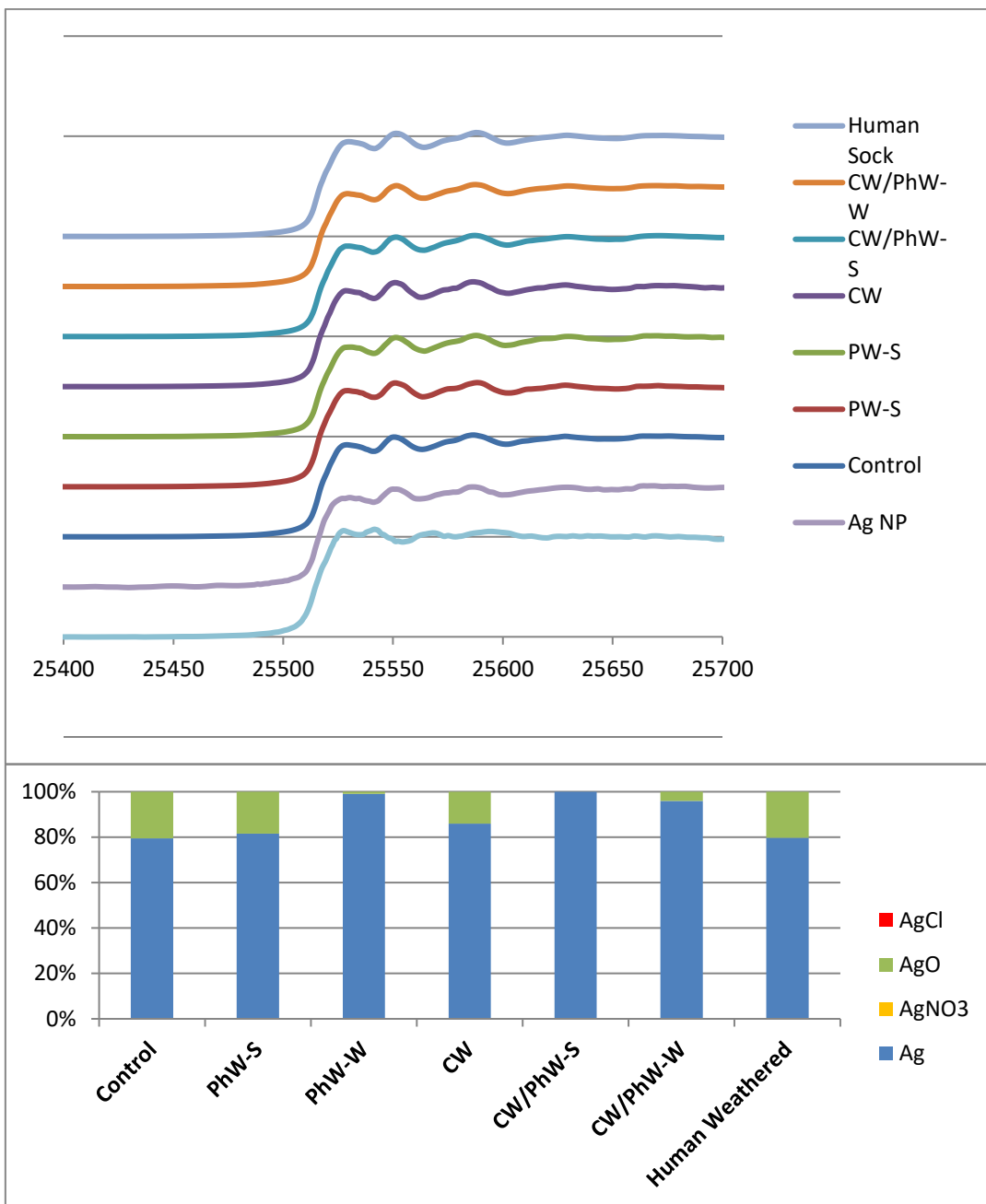


Figure F3: XANES spectra (top) and results of linear combination fitting (bottom) for textiles after weathering and washing. See text for definition of abbreviations.

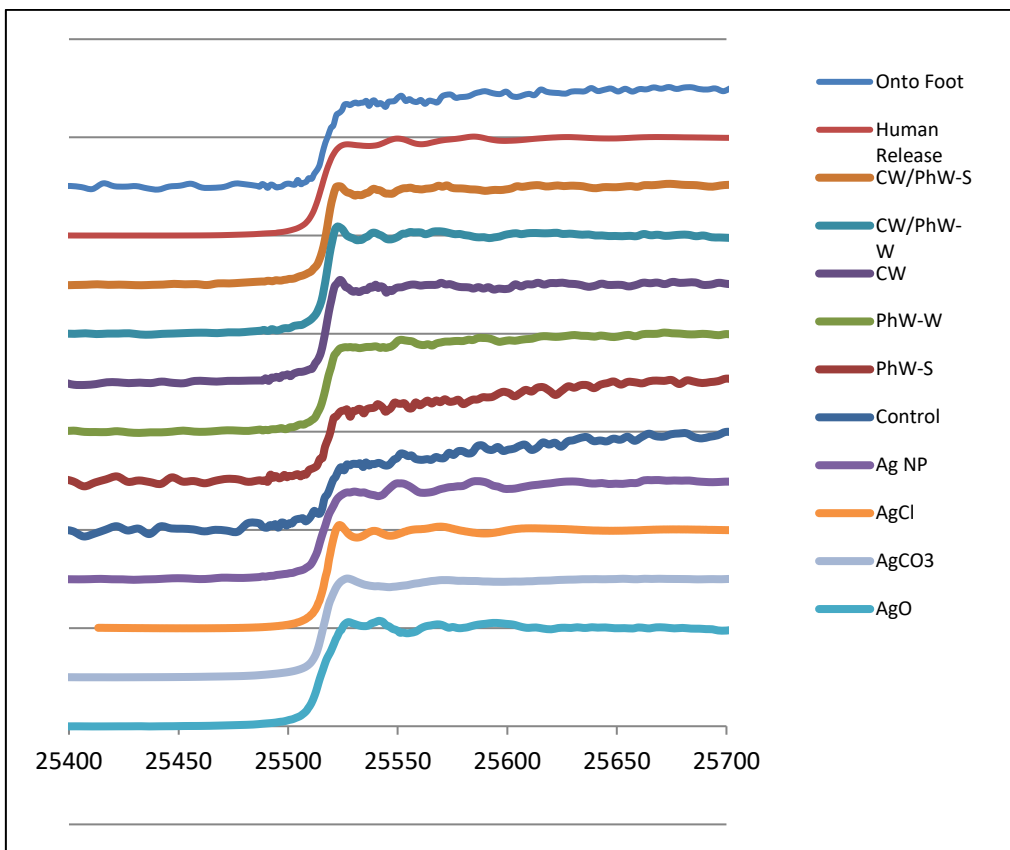
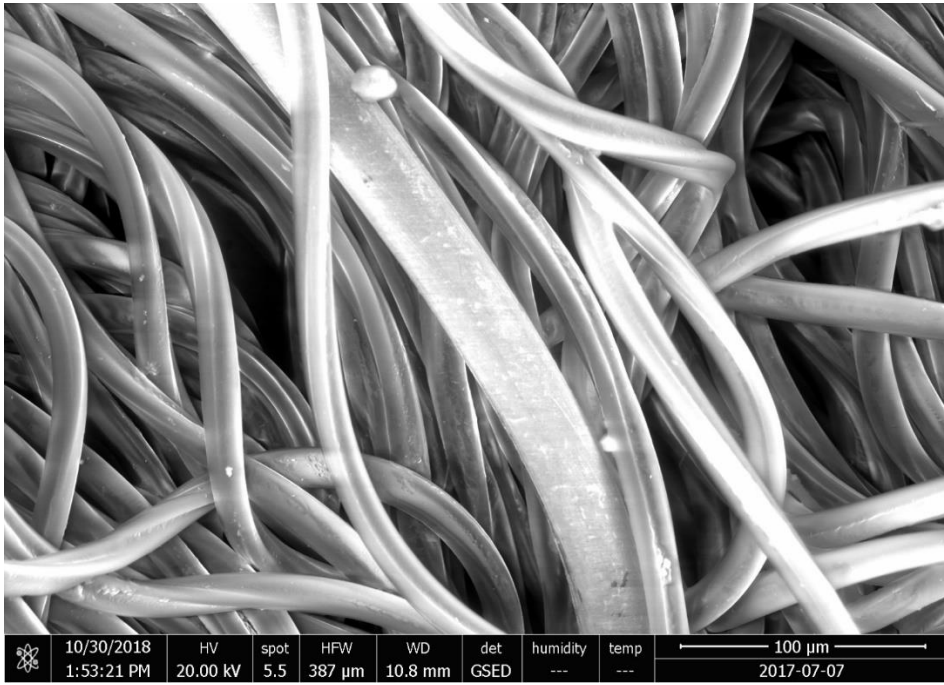


Figure F4: XANES spectra of released wash water after weathering and washing



3. **Figure F5 – SEM image of unwashed X-Static® functionalized textile.**

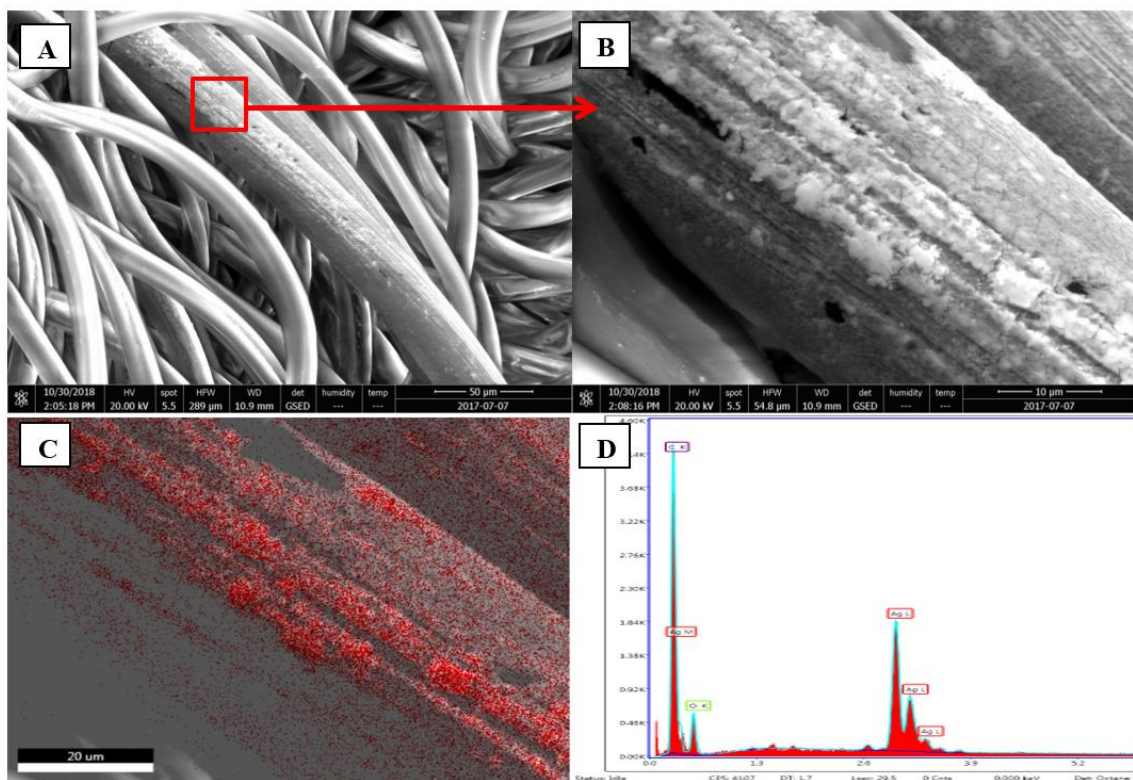


Figure F6 – SEM images of a control textile following washing (A). Close-up magnification of the surface, revealing irregular coating with small holes (B). EDX overlay confirms the presence of silver (red) on the surface and an absence of silver in the cracks/holes (C). EDX Spectrum of Figure 3.3, showing only silver, carbon, and oxygen (D).

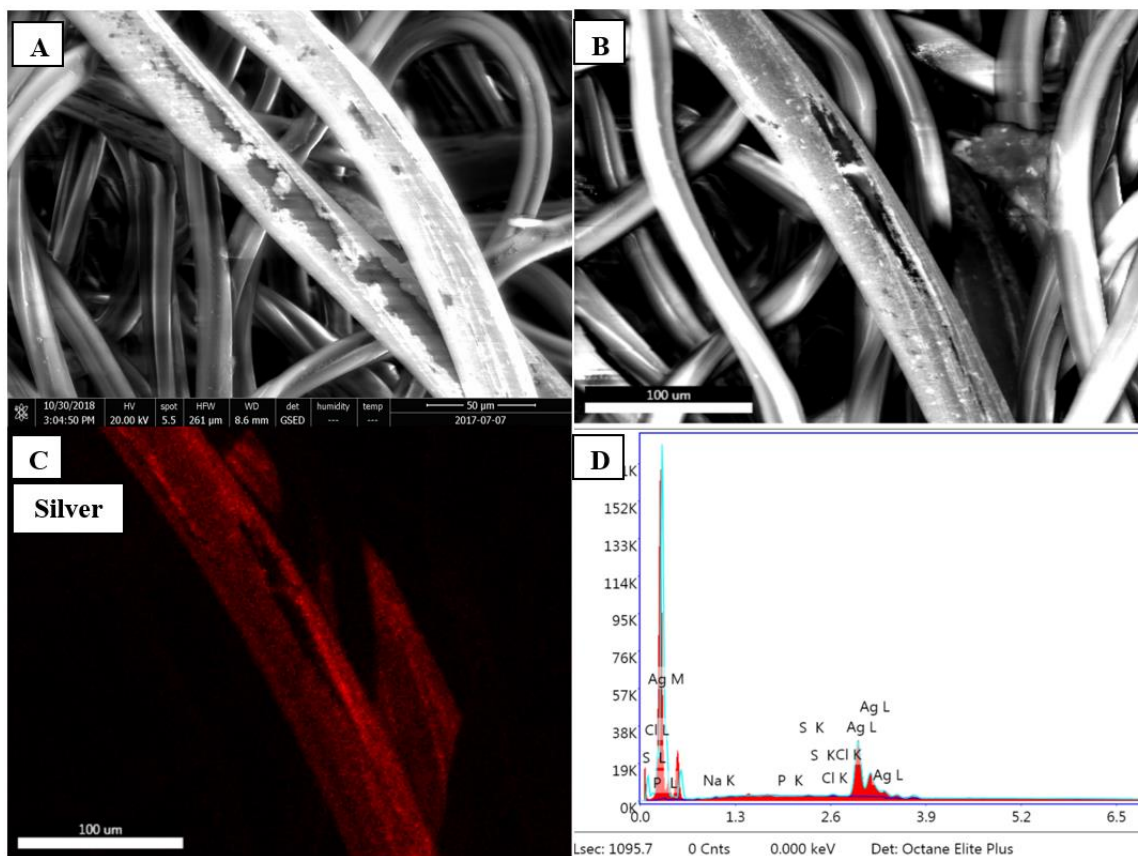


Figure F7 – SEM imaging of an PhW-W textile after showing large holes of missing silver (A,B). EDX image overlay confirms missing silver (C). Spectrum analysis shows only silver in the spectrum (D).

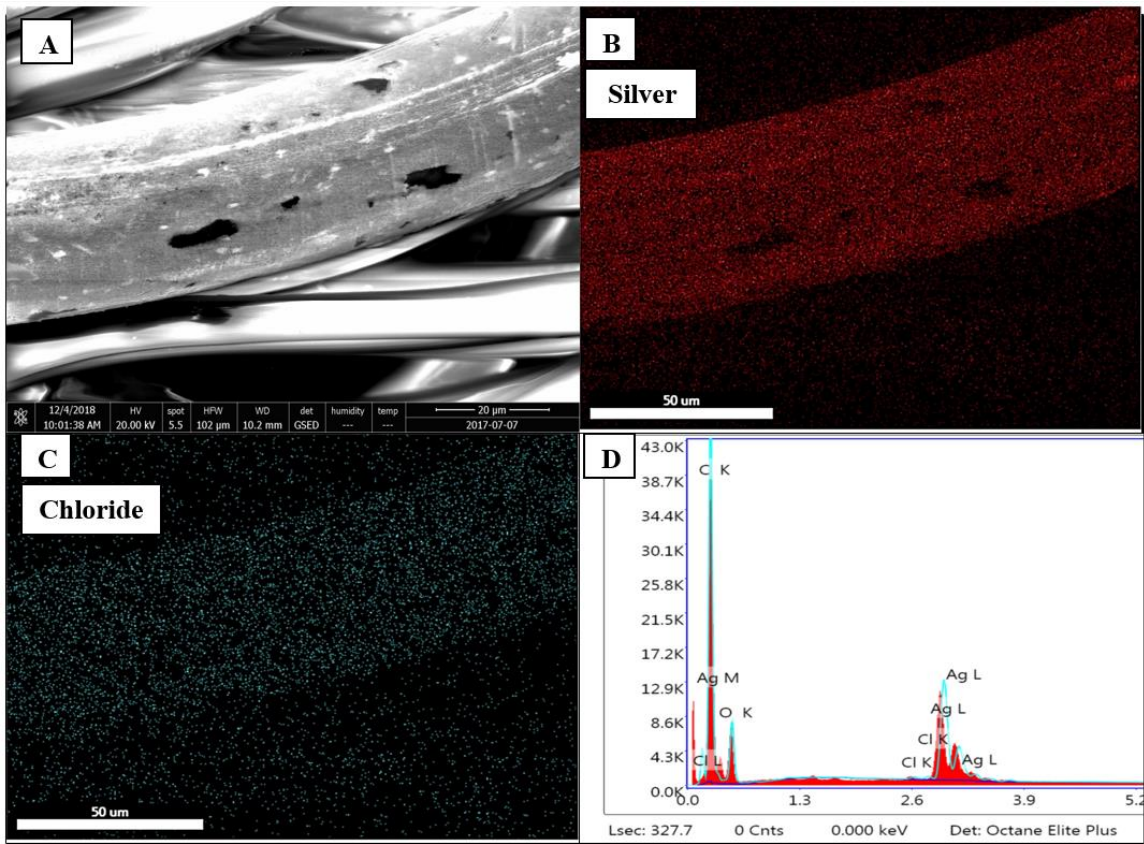


Figure F8– SEM imaging of a CW textile after washing with no holes or large cracks in the textile surface (A). EDX image overlay shows silver (B) and chloride (C) co-located, with spectra showing trace amounts of chloride (D).

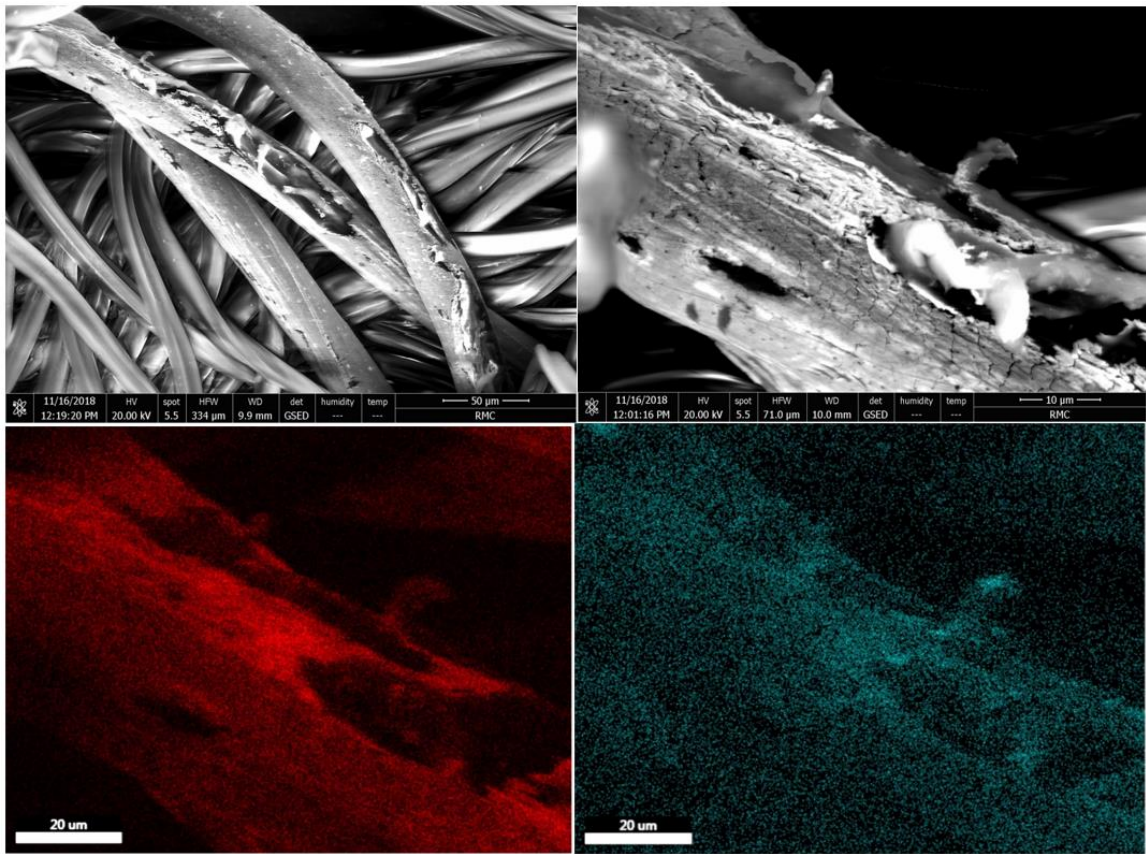


Figure F9 – SEM imaging of an CW/PhW-W textile after washing with large holes, cracks, and deformation to the silver-coated nylon surface (A,B). EDX overlay showing silver (C) and chloride (D).

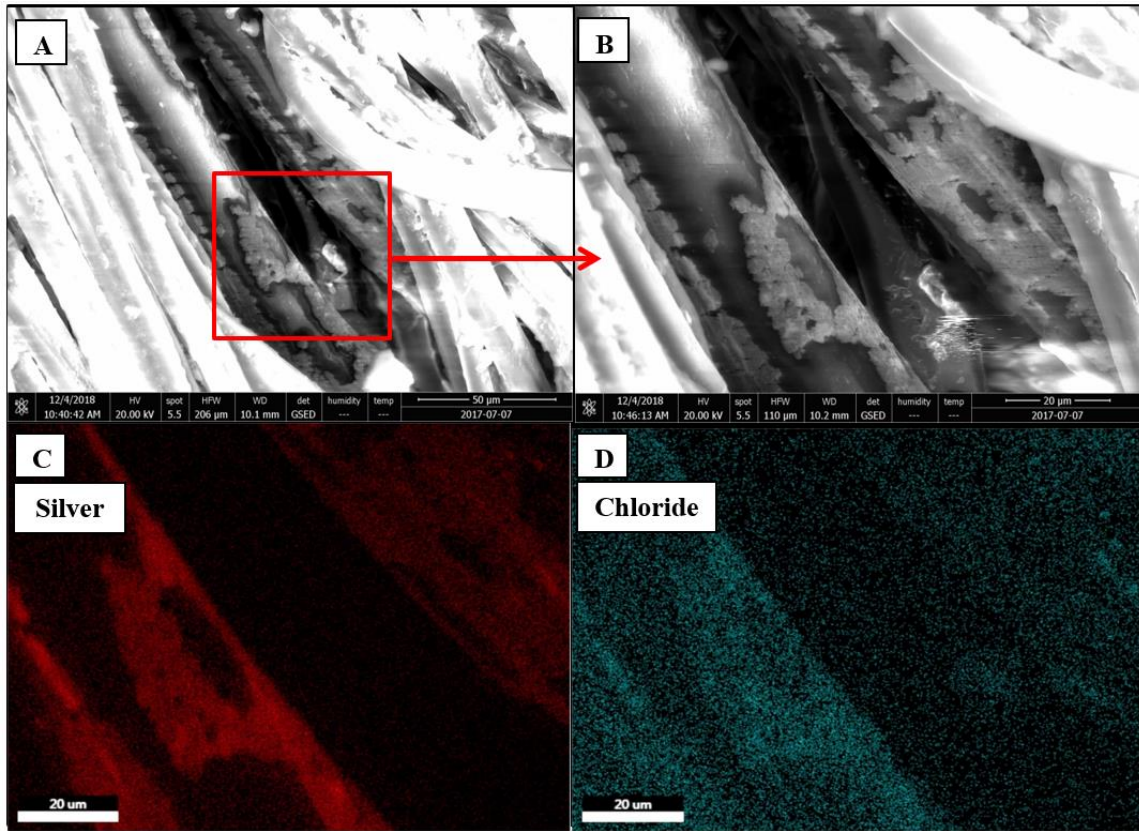


Figure F10 – SEM imaging of unwashed human weathered textile (A,B), showing similar holes/cracking as observed in artificially weathered textiles (see Figure F6 for comparison). EDX-overlay of silver (C) and chloride (D) also show similar co-location as observed in artificial textiles.

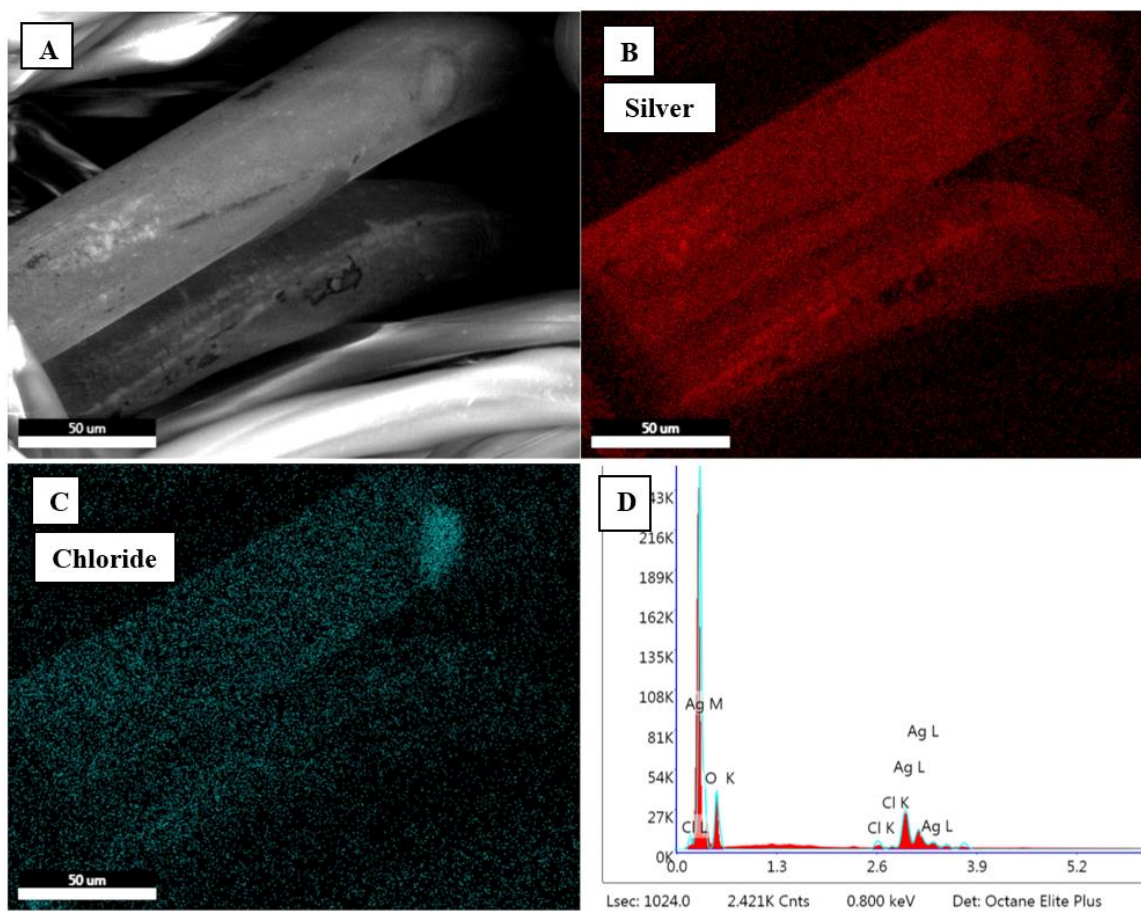


Figure F11 – SEM imaging of washed human weathered textile (A), showing similar holes/cracking as observed in artificially weathered textiles (see Figure F6 for comparison). EDX-overlay of silver (B) and chloride (C) also show similar co-location as observed in artificial textiles.

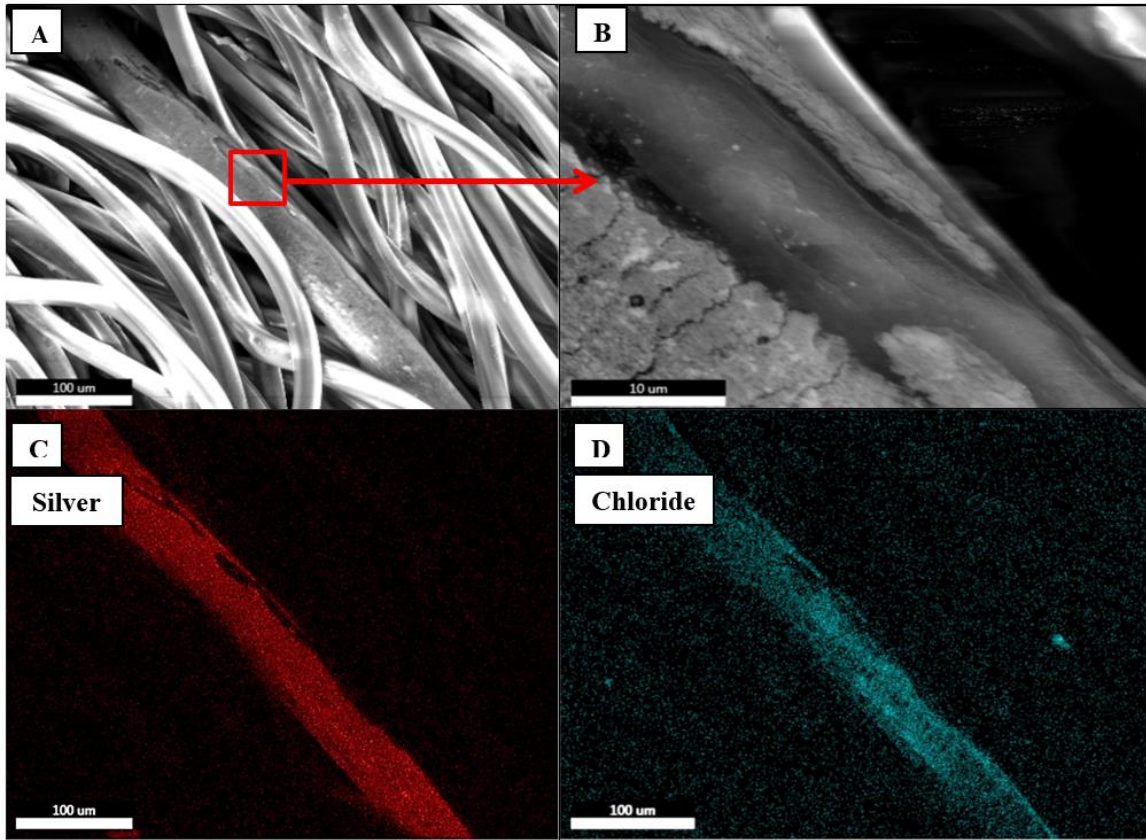


Figure F12 – SEM imaging of unwashed artificially weathered textile, showing similar holes/cracks as observed in post-washed artificially weathered textiles (A,B). EDX-overlay of silver (C) and chloride (D) also show similar co-location as observed in post-washed physically weathered textiles with sweat.

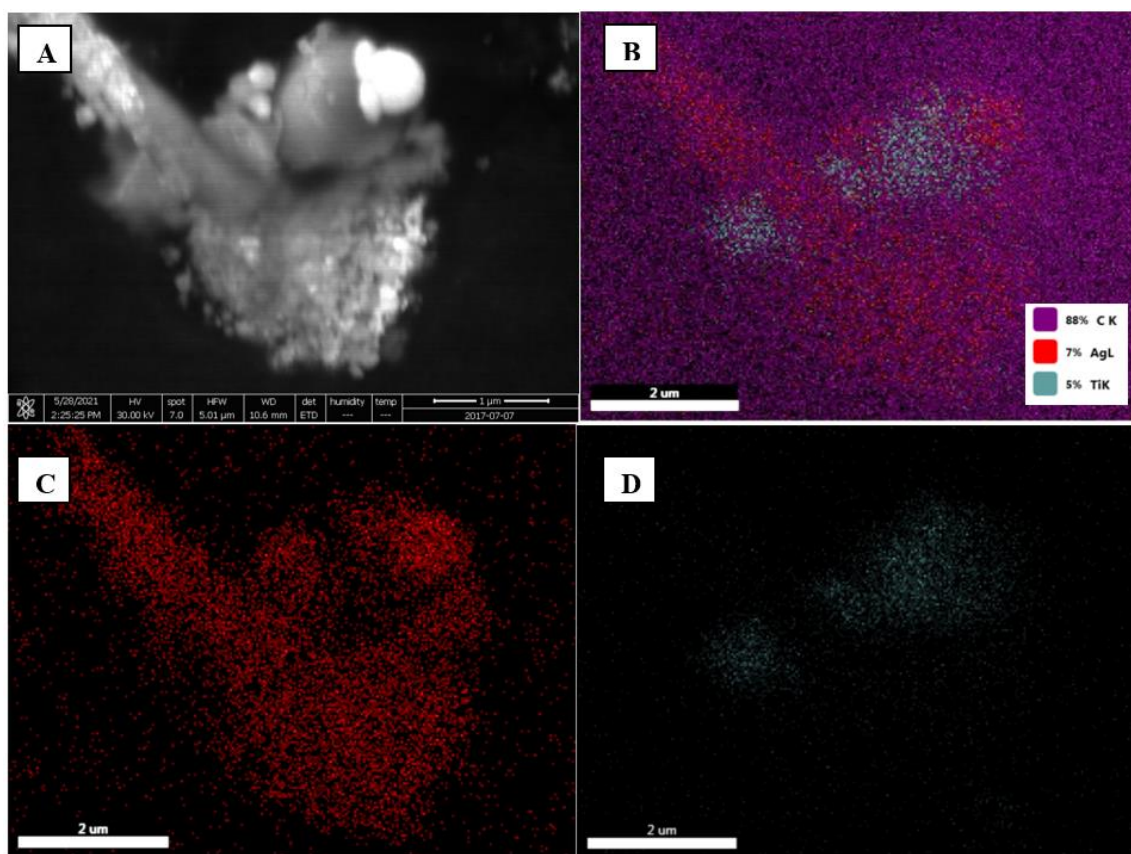


Figure F13: SEM image of silver (nano)materials and titanium materials released from an unweathered control textile following washing (A). Particle diameters ranged from 46-553 nm (average 131 ± 118 nm, significant skew due to large 553 nm particle in the top right of A). EDX identifies majority of the structure as silver with two overlapping particles of titanium (B). Individual EDX imaging of silver (C) and (D) also shown for clarity.

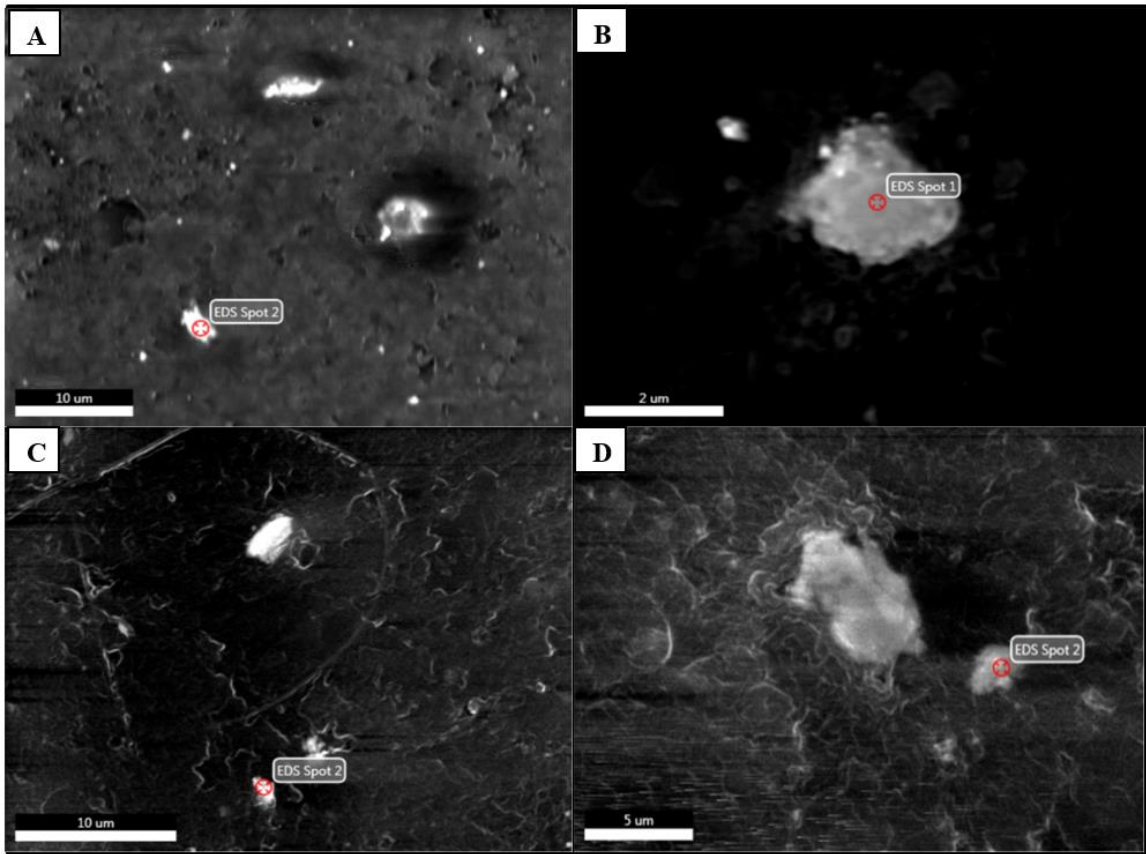


Figure F14 – SEM imaging of released silver particles the following release scenarios: control (A), PhW-W only (B), CW (C), PhW-W/CW (D). SEM imaging shows large micron-sized silver plates surrounded by smaller nanoparticles.

Table F4: Particle longest dimension, aspect ratio, and thickness of released silver materials from textiles.

Release Experiment	Particle Diameter (nm)	Aspect Ratio (L/W) of Released Particles	Particle Thickness (nm)
Control	3900 ± 2500	1.9±0.7	97 ± 47
PhW-S	2400 ± 900	1.6±0.6	
PhW-W	3200 ± 1600	1.7±0.3	
CW	2500 ± 1400	1.9±0.8	
CW/PhW-S	4500 ± 2200	1.7±0.3	
CW/PhW-W	2200 ± 1200	1.6±0.8	
Human Weathered	6900 ± 5800	1.7±0.7	

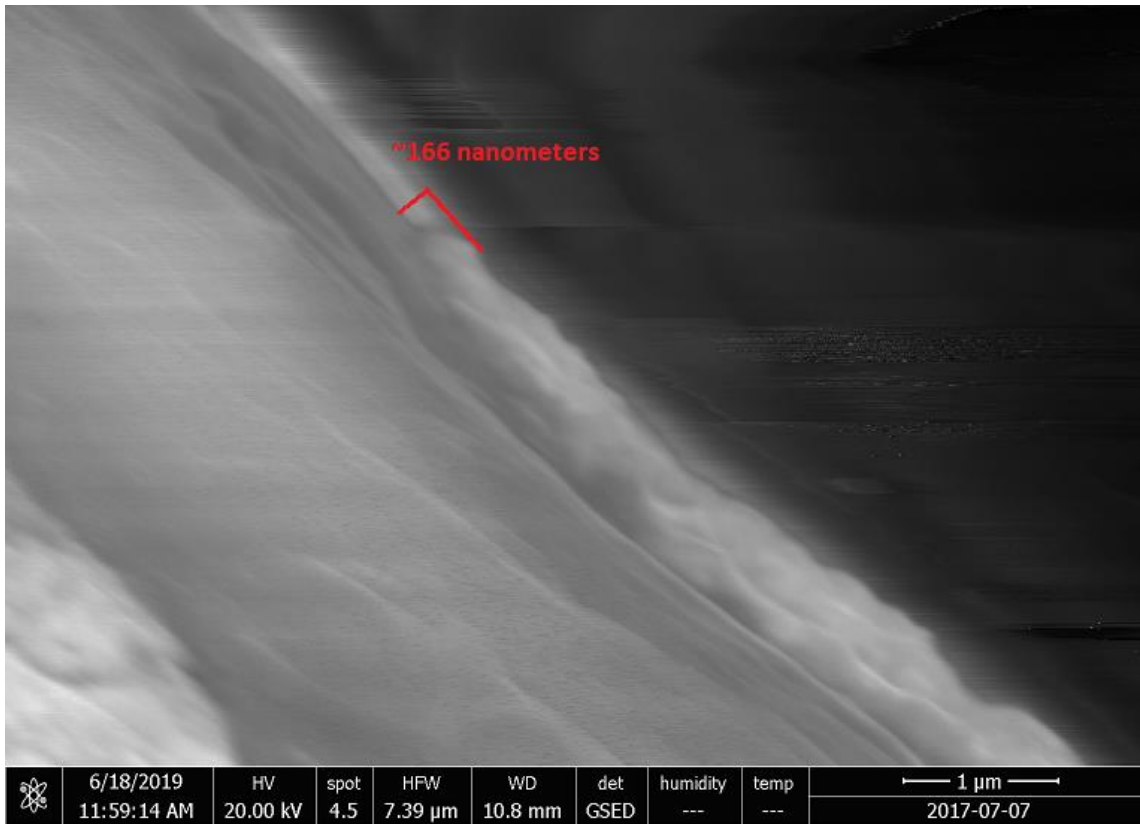


Figure F15: Approximate thickness of silver coating based on SEM imaging. Thickness was determined by taking the raised height from the nylon surface to the top of the silver coating.

Statistics on Total/Ionic Releases of Silver

Statistical analysis was performed using XLSTAT in Microsoft Excel®, on total concentrations of released silver (mg Ag/L wash water) and relative proportion of released ionic silver to determine significant differences across trials. One-way ANOVA was used with Tukey post-hoc tests.

Table F5: Chemical Weathering vs No Chemical Weathering Silver Concentrations One-Way ANOVA with Tukey post-hoc test. N=3

Treatment / Tukey (HSD) / Analysis of the differences between the categories with a confidence interval of 95% (Ag Release):

Contrast	Difference	Standardized difference	Critical value	Pr > Diff	Significant
Chemical Weathering vs No Chemical Weathering	1940.589	4.026	2.776	0.016	Yes
Tukey's d critical value:			3.926		

Category	LS means	Standard error	Lower bound (95%)	Upper bound (95%)	Groups
Chemical Weathering	4000.635	340.870	3054.227	4947.043	A
No Chemical Weathering	2060.046	340.870	1113.638	3006.454	B

Summary of all pairwise comparisons for Treatment (Tukey (HSD)):

Category	LS means (Ag Release)	Groups
Chemical Weathering	4000.635	A
No Chemical Weathering	2060.046	B

Table F6: No Chemical Weathering ionic one-way ANOVA showing similar ionic silver percentages across the three no sweat trials

Trial Name / Tukey (HSD) / Analysis of the differences between the categories with a confidence interval of 95% (No Sweat):

Contrast	Difference	Standardized difference	Critical value	Pr > Diff	Significant
Control vs Stretch	4.088	0.531	3.068	0.859	No
Control vs Walked	3.330	0.433	3.068	0.904	No
Walked vs Stretch	0.758	0.099	3.068	0.995	No
Tukey's d critical value:			4.339		

Category	LS means	Standard error	Lower (95%) bound	Upper (95%) bound	Groups
Control	15.482	5.442	2.165	28.798	A
Walked	12.152	5.442	-1.164	25.468	A
Stretch	11.394	5.442	-1.923	24.710	A

Summary of all pairwise comparisons for Trial Name (Tukey (HSD)):

Category	LS means(No Sweat)	Groups
Control	15.482	A
Walked	12.152	A
Stretch	11.394	A

Table F7: Chemical Weathering ionic one-way ANOVA showing similar ionic silver percentage across the three sweat trials and human release. N=3 for each trial.

Trial Name / Tukey (HSD) / Analysis of the differences between the categories with a confidence interval of 95% (Sweat):

Contrast	Difference	Standardized difference	Critical value	Pr > Diff	Significant
Control vs Walked	2.567	2.746	3.202	0.095	No
Control vs Human	1.669	1.785	3.202	0.346	No
Control vs Stretch	1.582	1.692	3.202	0.387	No
Stretch vs Walked	0.986	1.055	3.202	0.724	No
Stretch vs Human	0.087	0.094	3.202	1.000	No
Human vs Walked	0.898	0.961	3.202	0.774	No
Tukey's d critical value:			4.529		

Category	LS means	Standard error	Lower (95%) bound	Upper (95%) bound	Groups
Control	3.627	0.661	2.102	5.151	A
Stretch	2.045	0.661	0.521	3.569	A

Human	1.958	0.661	0.433	3.482	A
Walked	1.059	0.661	-0.465	2.584	A

Summary of all pairwise comparisons for Trial Name (Tukey (HSD)):

Category	LS means(Sweat)	Groups
Control	3.627	A
Stretch	2.045	A
Human	1.958	A
Walked	1.059	A

Table F8: Total silver release from no chemical weathering trials one-way ANOVA comparing total silver released. N=3 for each trial

Treatment / Tukey (HSD) / Analysis of the differences between the categories with a confidence interval of 95% (No Sweat):

Contrast	Difference	Standardized difference	Critical value	Pr > Diff	Significant
Stretch vs Control	2072.161	4.625	3.068	0.009	Yes
Stretch vs Walk	209.041	0.467	3.068	0.889	No
Walk vs Control	1863.120	4.159	3.068	0.014	Yes
Tukey's d critical value:			4.339		

Category	LS means	Standard error	Lower bound (95%)	Upper bound (95%)	Groups
Stretch	4132.207	316.792	3357.044	4907.370	A
Walk	3923.166	316.792	3148.003	4698.329	A
Control	2060.046	316.792	1284.883	2835.209	B

Summary of all pairwise comparisons for Treatment (Tukey (HSD)):

Category	LS means(No Sweat)	Groups
Stretch	4132.207	A
Walk	3923.166	A
Control	2060.046	B

Table F9: Total silver release from chemical weathering trials one-way ANOVA. N=3 for each trial

Treatment / Tukey (HSD) / Analysis of the differences between the categories with a confidence interval of 95% (Sweat):

Contrast	Difference	Standardized difference	Critical value	Pr > Diff	Significant
Walk vs Control	2071.304	3.465	3.010	0.023	Yes
Walk vs Human Use	1314.226	2.539	3.010	0.108	No
Walk vs Stretch	150.735	0.252	3.010	0.994	No
Stretch vs Control	1920.569	3.213	3.010	0.036	Yes
Stretch vs Human Use	1163.491	2.248	3.010	0.170	No
Human Use vs Control	757.078	1.462	3.010	0.490	No
Tukey's d critical value:			4.256		

Category	LS means	Standard error	Lower bound (95%)	Upper bound (95%)	Groups
Walk	6071.939	422.669	5141.650	7002.228	A
Stretch	5921.204	422.669	4990.914	6851.493	A
Human Use	4757.712	298.872	4099.899	5415.526	A B
Control	4000.635	422.669	3070.346	4930.924	B

Summary of all pairwise comparisons for Treatment (Tukey (HSD)):

Category	LS means(Sweat)	Groups
Walk	6071.939	A
Stretch	5921.204	A
Human Use	4757.712	A B
Control	4000.635	B

Table F10: Two-way ANOVA comparing no CW to CW results, showing significance of sweat. N=3 for each trial

Analysis of variance (Released Silver (Y)):

Source	DF	Sum of squares	Mean squares	F	Pr > F
Model	3	32990035.627	10996678.542	31.650	< 0.0001
Error	14	4864319.332	347451.381		
Corrected Total	17	37854354.959			

Computed against model $Y=Mean(Y)$

Model parameters (Released Silver (Y)):

Source	Value	Standard error	t	Pr > t	Lower bound (95%)
Intercept	5977.279	277.869	21.511	< 0.0001	5381.308
Treatment X1-No Sweat	-1959.453	277.869	-7.052	< 0.0001	-2555.423
Treatment X1-Sweat	0.000	0.000			
Treatment X2-Control	-1967.212	340.319	-5.780	< 0.0001	-2697.124
Treatment X2-Stretch	29.153	340.319	0.086	0.933	-700.759
Treatment X2-Walked	0.000	0.000			

Equation of the model (Released Silver (Y)):

Released Silver (Y) = 5977.27869219963-1959.45273491499*Treatment X1-No Sweat-1967.21179196536*Treatment X2-Control+29.1528773288094*Treatment X2-Stretch

Standardized coefficients (Released Silver (Y)):

Source	Value	Standard error	t	Pr > t	Lower bound (95%)
Treatment X1-No Sweat	-0.676	0.096	-7.052	< 0.0001	-0.881
Treatment X1-Sweat	0.000	0.000			
Treatment X2-Control	-0.639	0.111	-5.780	< 0.0001	-0.877
Treatment X2-Stretch	0.009	0.111	0.086	0.933	-0.228
Treatment X2-Walked	0.000	0.000			

Appendix G – Supplemental Information for Thesis

Table G1 – Group names of PFAS, with abbreviations, general structure, and examples.

Group Name	Abbreviation	General Structure	Chain Length Nomenclature	Example (N=5)	Example (N=6)	Example (N=7)	Example (N=8)
Perfluorocarboxylic Acid	PFCA	$(CF_2)_{n-1}COOH$	IUPAC	PFPeA	PFHxA	PFHpA	PFOA
Perfluorosulfonic Acid	PFSA	$(CF_2)_nSO_3H$	IUPAC	PFPeS	PFHxS	PFHpS	PFOS
Perfluorosulfonamide	PFSA _m	$(CF_2)_nSO_3NH_2$	IUPAC	PFPeSA _m	PFHxSA _m	PFHpSA _m	PFOSA, FOSA
Alkyl Perfluorosulfonamido Acetic Acid	Alykl-PFSA _m	$(CF_2)_nSO_3N(CH_2)_y(CH_3)_z(CH_2)COOH$	IUPAC		MeFHXSAA		MeFOSAA, EtFOSAA
Fluorotelomer Sulfonate	FTS	$(CF_2)_n(CH_2)_2SO_3H$	N:2		6:2 FtS		8:2 FtS
Fluorotelomer Sulfonamido Betaine	FtSaB	$(CF_2)_n(CH_2)_2SO_2NHC_3H_6N(CH_3)_2COOH$	N:2		6:2 FtSaB		8:2 FtSaB
X:3 Fluorotelomer Betaine	FtB	$(CF_2)_n(CH_2)_3N(CH_3)_2COOH$	N:3	5:3 FtB		7:3 FtB	
X:1:2 Fluorotelomer Betaine	FtB	$(CF_2)_n(CFH)_1(CH_2)_2N(CH_3)_2COOH$	N:1:2	5:1:2 FtB		7:1:2 FtB	
Fluorotelomer Thioether Amido Sulfonate	FtTAoS	$(CF_2)_n(CH_2)_2S(CH_2)_2CONHC(CH_3)_2(CH_2)SO_3H$	N:2		6:2 FtTAoS		8:2 FtTAoS

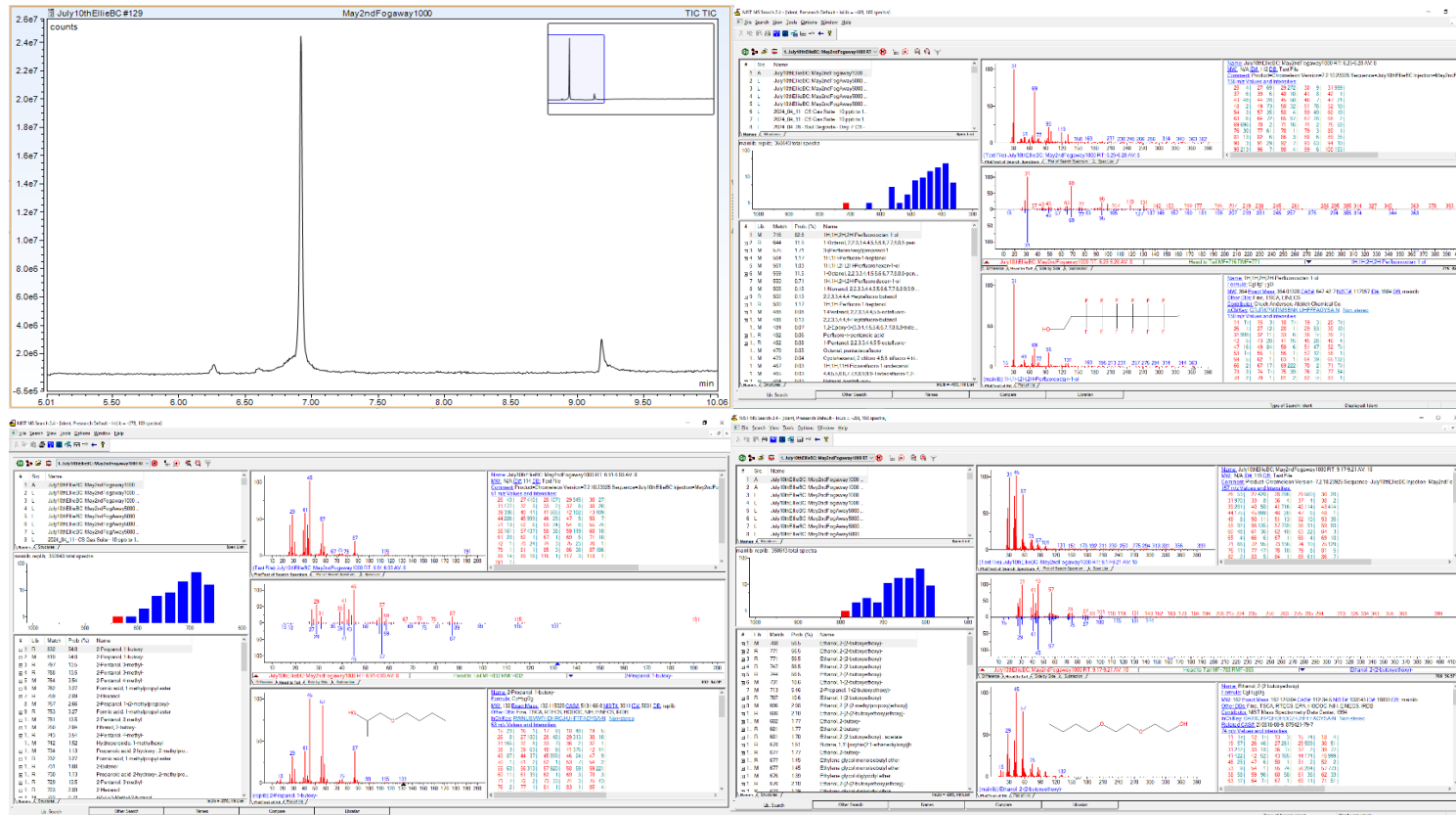


Figure G1 – Gas Chromatography chromatogram and database matches confirming the presence of 6:2 FTOH, 1-butoxy-2-propanol, and butyl carbitol found in the Fog Away commercial surface treatment spray.

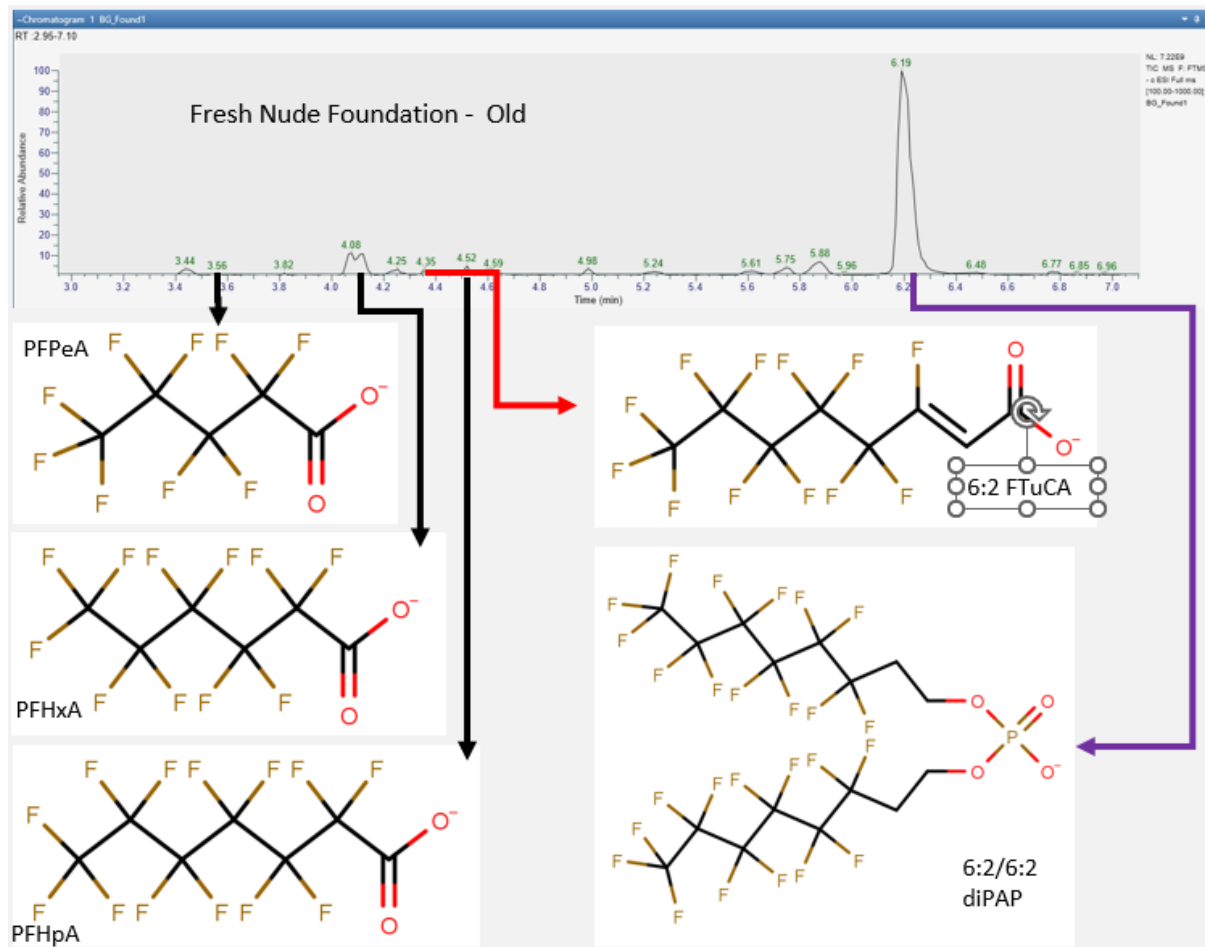


Figure G2 – LC-HRMS chromatogram and structures of PFAS found in Fresh Nude Foundation (Makeup 1).

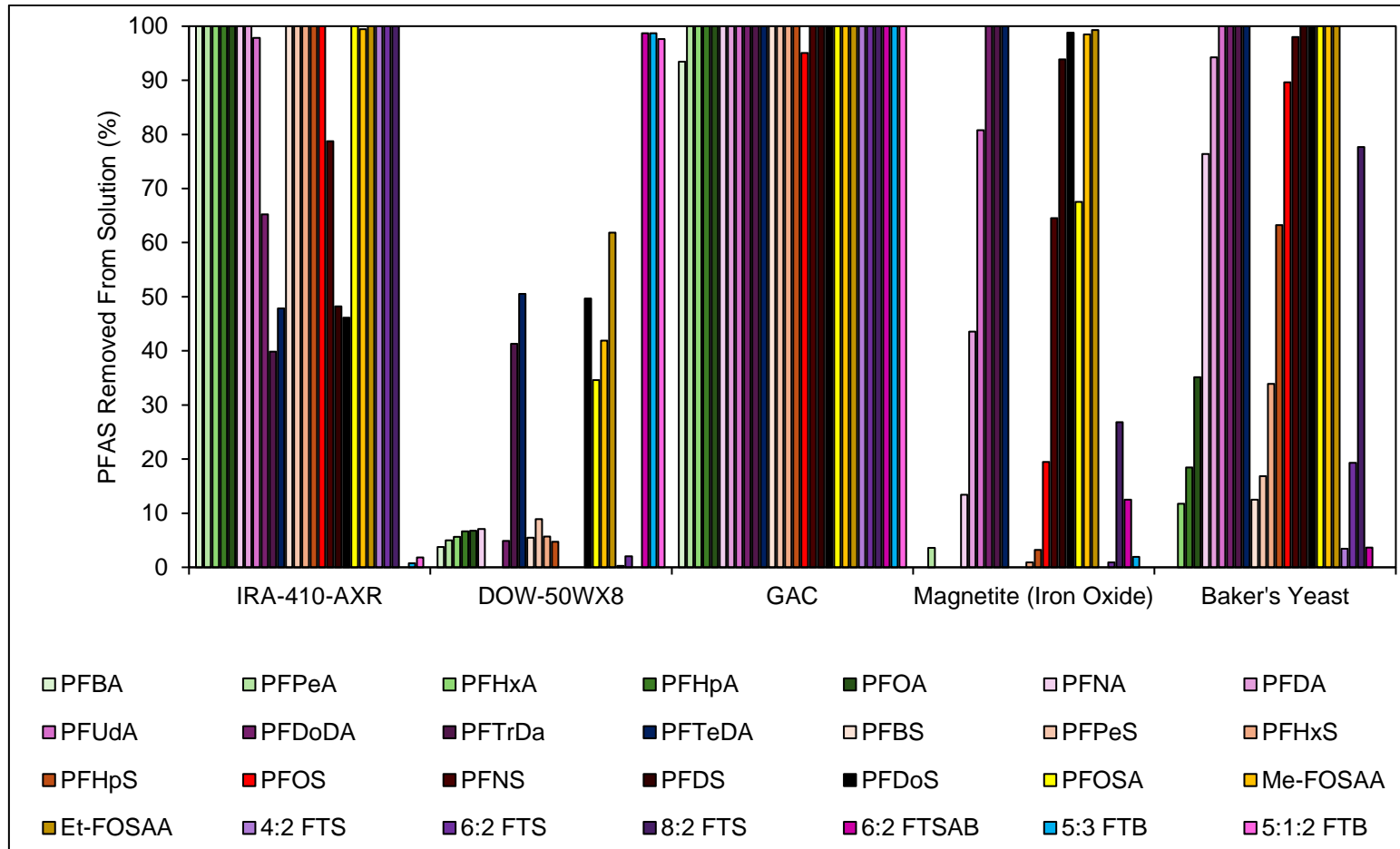


Figure G3 – Removal of ~1 µg/L PFAS from an aqueous solution (pH 5.6) using a 1:100 sorbent:solution ratio for 24 hours.

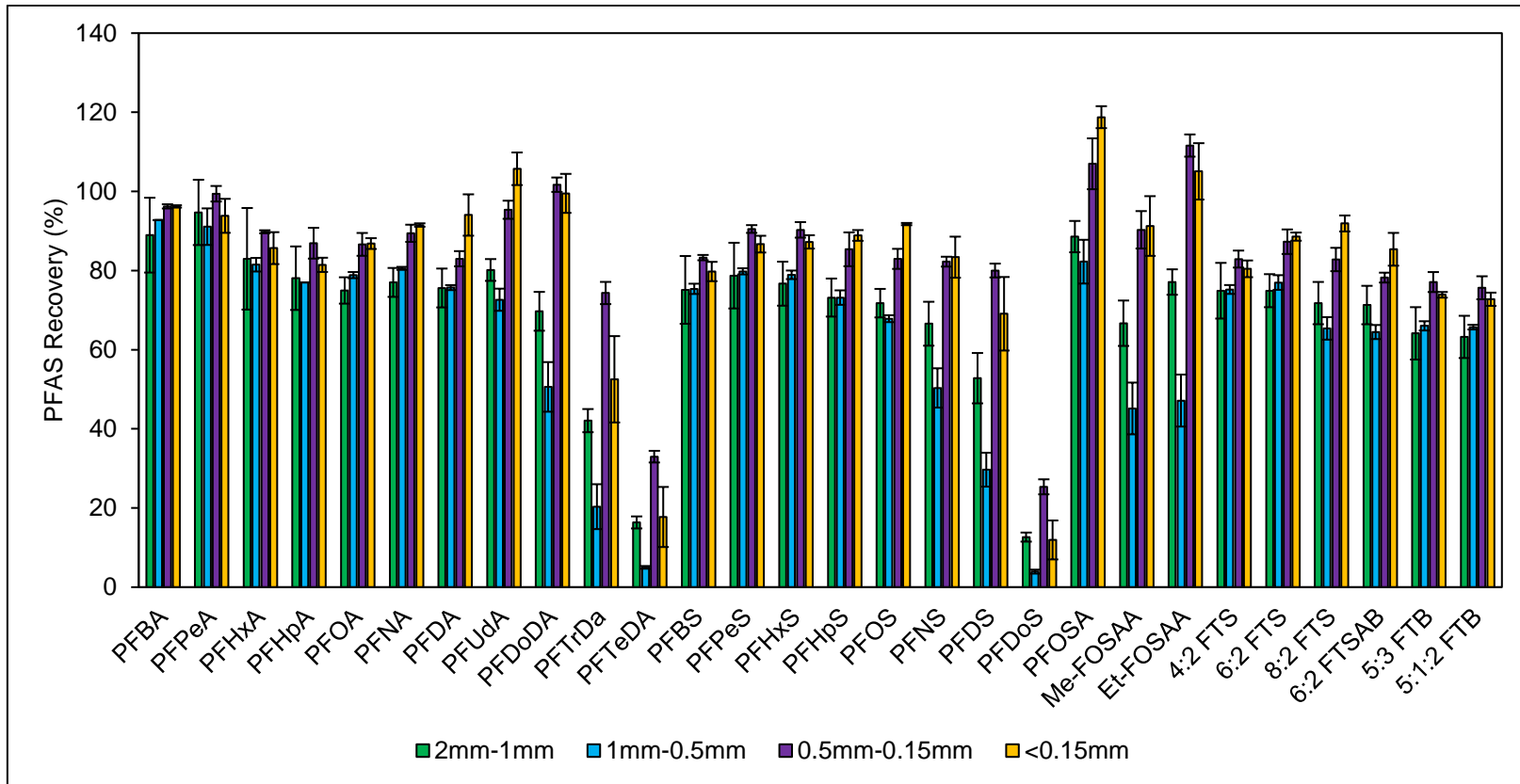


Figure G4 – Recovery of PFAS following sorption onto different size fractions of GAC (1:100 ratio, 24-hour sorption time) and extraction using two methanolic extractions (24-hour first extraction, 2 hours second extraction).

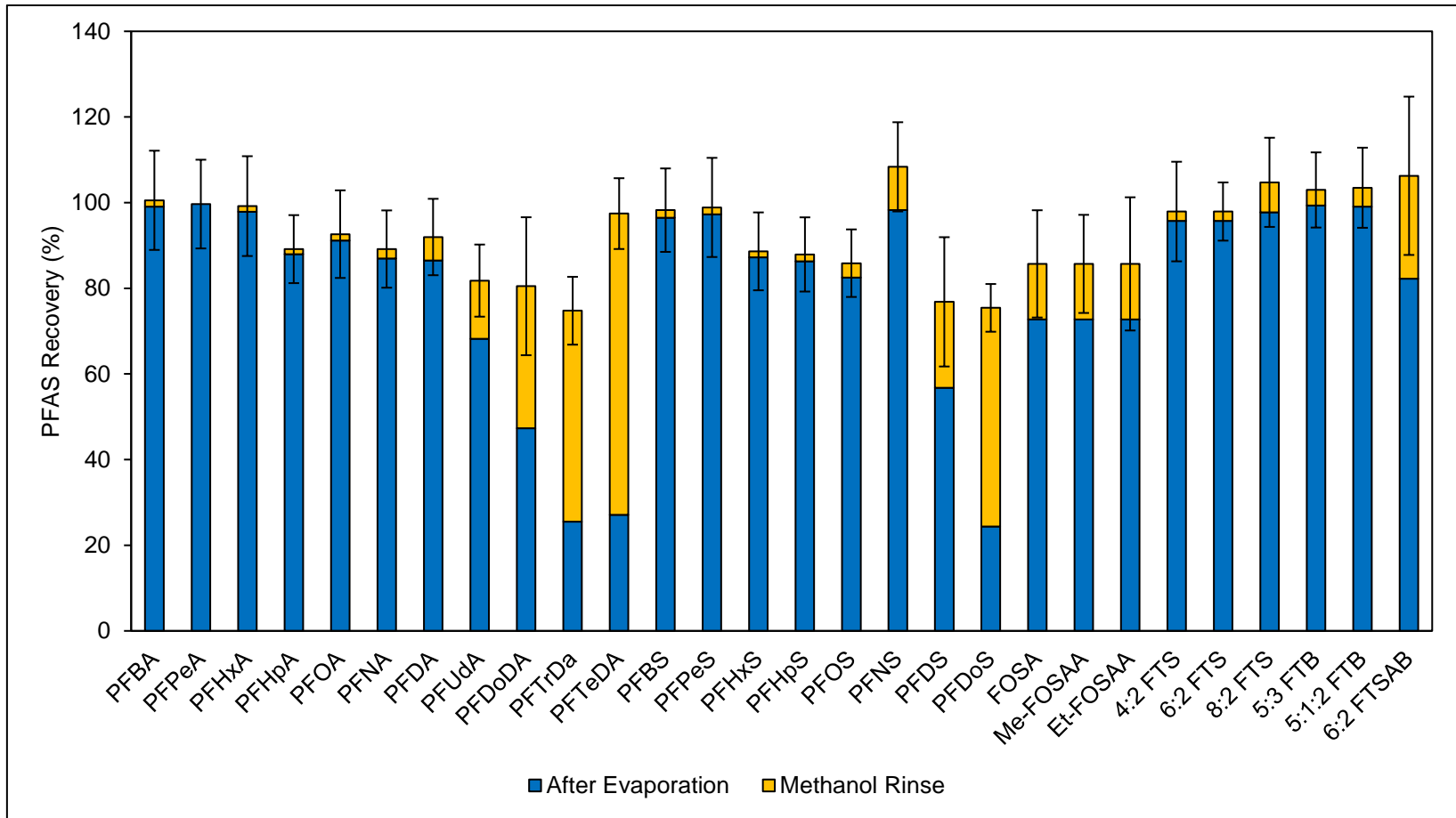


Figure G5 – Recovery of PFAS (~40 µg/L) following evaporative exchange into water (1 part sample, 4 parts water) at 50°C for 6 hours, evaluated either right away (After Evaporation) or after a methanolic rinse of the container (Methanol Rinse).

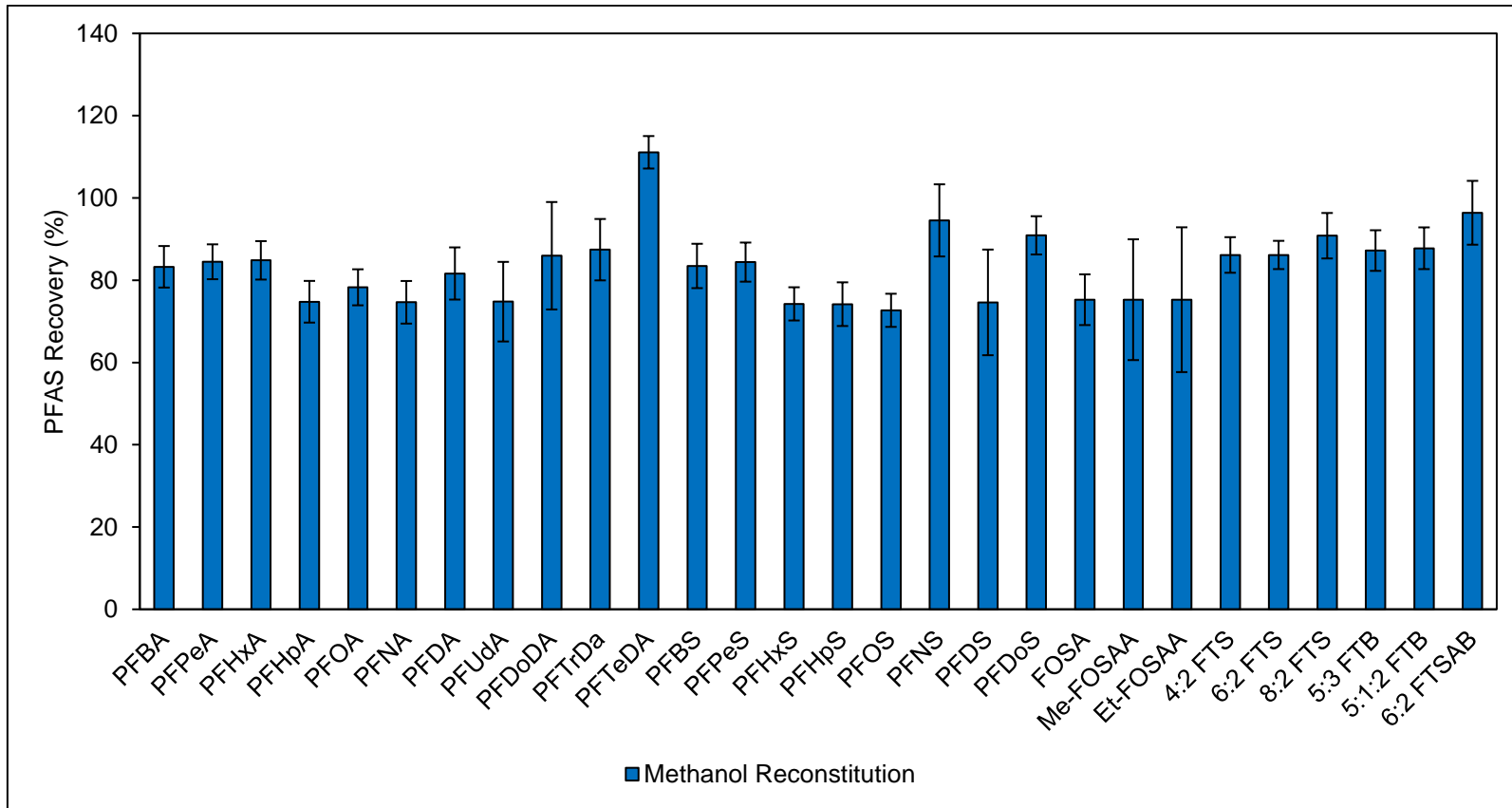


Figure G6 – Recovery of PFAS (~40 µg/L) following evaporation to dryness at 50°C for 6 hours, and subsequent reconstitution of the sample directly into methanol.

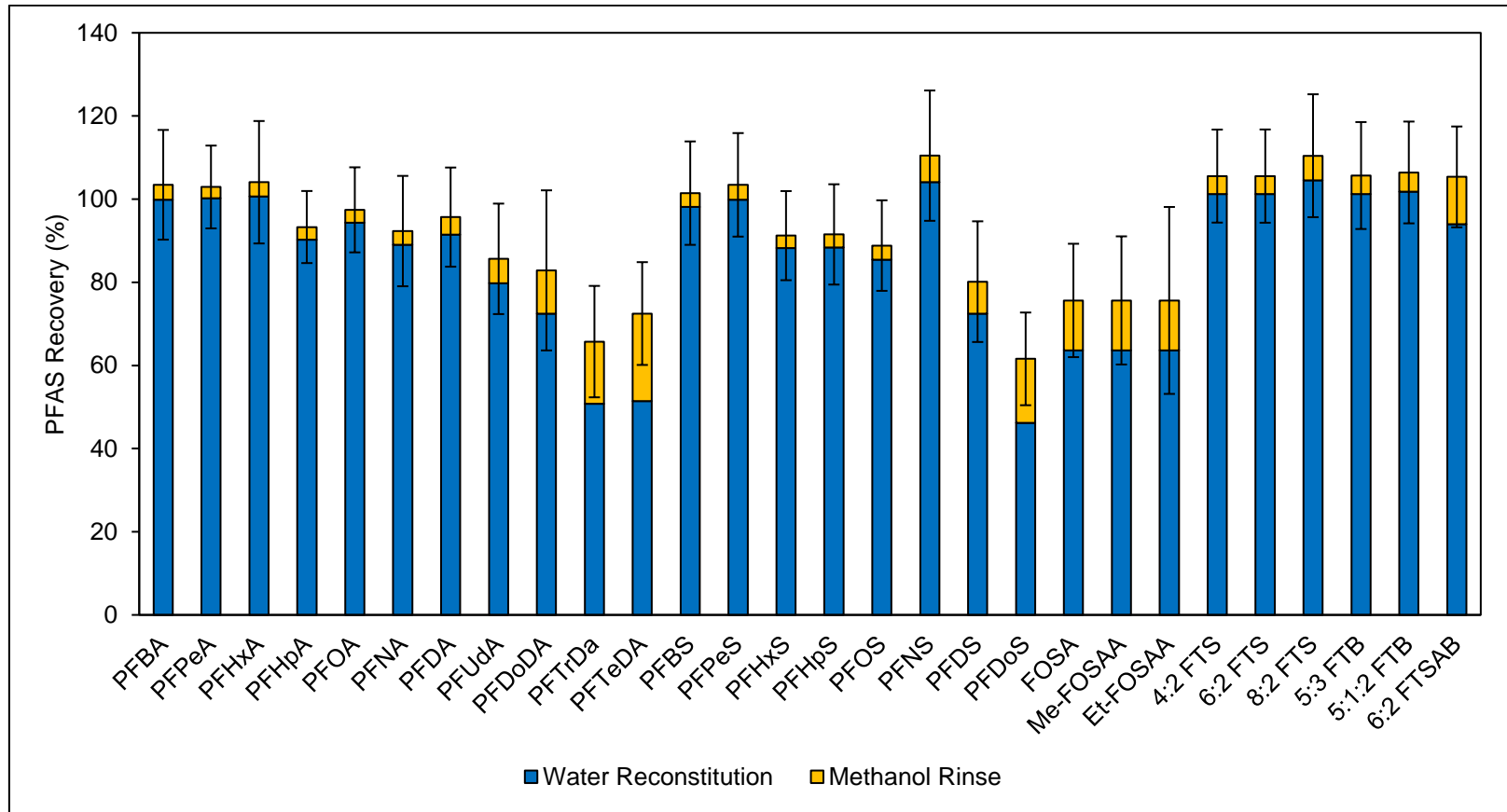


Figure G7 – Recovery of PFAS (~40 µg/L) following evaporation to dryness at 50°C for 6 hours, and subsequent reconstitution of the sample directly into DI water, followed by a methanolic rinse of the container.

Group	PFAS	99% Water, 1% MeOH								50% H2O, 50% MeOH							
		HPLC Glass				PP C-Tube				HPLC Glass				PP C-Tube			
		8 Hours		24 Hours		24 Hours		21 Days		8 Hours		24 Hours		24 Hours		21 Days	
		Recovery	+/-	Recovery	+/-	Recovery	+/-	Recovery	+/-	Recovery	+/-	Recovery	+/-	Recovery	+/-	Recovery	+/-
PFCA	PFBA	96	2	89	2	106	3	113	1	96	5	88	2	104	2	108	1
	PFPeA	98	3	89	3	106	1	118	8	93	1	90	5	96	2	103	6
	PFHxA	98	2	91	2	120	5	127	10	93	1	90	4	100	3	113	16
	PFHpA	94	6	88	3	105	4	91	3	94	5	84	0	102	4	94	4
	PFOA	94	7	89	2	102	8	82	8	94	6	86	3	105	4	90	13
	PFNA	94	10	81	3	80	7	73	3	95	5	90	2	98	0	85	14
	PFDA	84	4	77	0	50	4	69	3	91	9	92	5	99	3	95	17
	PFUdA	61	7	52	2	34	6	36	1	94	6	88	6	97	3	92	10
	PFDODA	47	5	20	2	34	5	13	1	89	6	86	4	108	3	88	10
	PFTTrDA	43	8	9	2	36	4	5	3	101	10	95	12	116	9	91	6
	PFTeDA	45	1	9	1	31	5	2	0	83	1	77	24	120	9	88	11
PFSA	PFBS	93	5	85	1	108	1	108	3	91	7	86	0	102	2	106	4
	PFPeS	95	5	87	1	101	1	93	3	94	2	89	0	104	1	98	9
	PFHxS	94	8	87	1	107	3	79	5	93	6	86	2	105	2	86	17
	PFHpS	92	1	86	1	91	5	79	4	90	2	88	2	98	1	90	14
	PFOS	89	6	83	1	72	6	73	3	94	7	86	2	103	2	87	7
	PFNS	74	3	69	0	40	5	46	4	96	3	88	0	102	2	95	7
	PFDS	52	7	35	2	35	6	17	2	94	9	86	4	105	4	94	7
	PFDoS	42	7	8	1	40	6	5	2	99	10	97	15	116	5	97	4
FOSA	PFOSA	52	5	42	5	36	4	34	4	87	4	89	2	110	1	101	2
	Me-FOSAA	74	7	64	0	34	3	39	2	93	7	85	4	106	1	83	15
	Et-FOSAA	58	5	47	2	36	3	24	4	90	4	89	2	110	6	86	16
Fluorotelomer	4:2 FTS	94	2	84	1	106	3	108	2	92	3	88	1	102	1	105	1
	6:2 FTS	94	7	83	1	103	1	86	6	94	5	86	1	104	1	94	9
	8:2 FTS	80	4	74	1	53	4	60	4	90	5	88	2	102	1	86	18
	6:2 FTSAB	73	3	67	0	55	5	45	5	94	4	89	1	97	4	81	29
	5:3 FTB	91	3	86	2	105	3	72	3	91	1	88	3	103	2	99	10
	5:1:2 FTB	90	5	84	1	100	2	63	7	93	3	84	2	101	3	119	11

Figure G8 – Recovery of PFAS (~ 1µg/L) after being stored in a HPLC borosilicate glass vials (8 hours, 24 hours storage time) or 15 mL polypropylene centrifuge tube (24 hours, 21 days storage time) at 4°C with different solvent compositions of water and methanol.